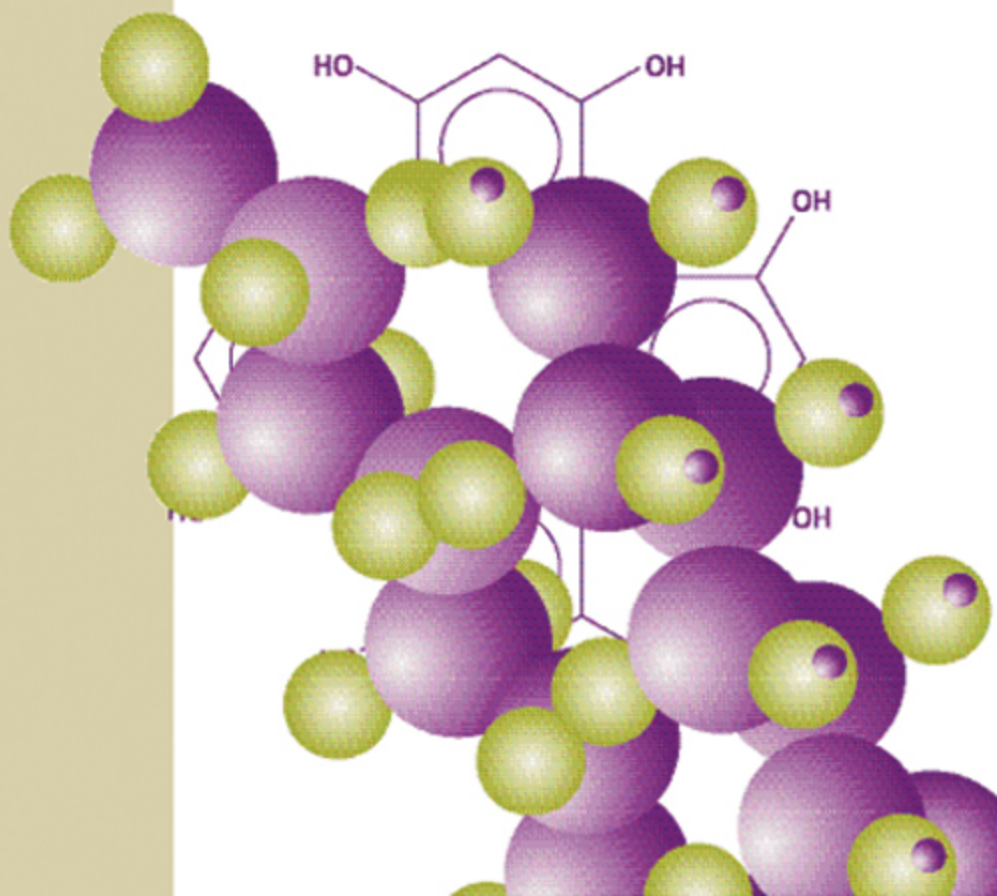


NANOTECHNOLOGY SERIES

# Organic and Inorganic Nanostructures

Alexei Nabok



# Organic and Inorganic Nanostructures

For a listing of recent titles in the *Artech House MEMS Series*,  
turn to the back of this book

# Organic and Inorganic Nanostructures

Alexei Nabok



**ARTECH  
HOUSE**

BOSTON | LONDON  
[artechhouse.com](http://artechhouse.com)

**Library of Congress Cataloging-in-Publication Data**

A catalog record of this book is available from the Library of Congress.

**British Library Cataloguing in Publication Data**

Nabok, Alexei

Organic and inorganic nanostructures. —(Artech House MEMS series)

1. Nanotechnology 2. Nanostructures 3. Thin films

I. Title

602.5

ISBN 1-58053-818-5

**Cover design by Igor Valdman**

© 2005 ARTECH HOUSE, INC.

685 Canton Street

Norwood, MA 02062

All rights reserved. Printed and bound in the United States of America. No part of this book may be reproduced or utilized in any form or by any means, electronic or mechanical, including photocopying, recording, or by any information storage and retrieval system, without permission in writing from the publisher.

All terms mentioned in this book that are known to be trademarks or service marks have been appropriately capitalized. Artech House cannot attest to the accuracy of this information. Use of a term in this book should not be regarded as affecting the validity of any trademark or service mark.

International Standard Book Number: 1-58053-818-5

10 9 8 7 6 5 4 3 2 1

# Contents

Preface	<i>ix</i>
Acknowledgments	<i>xi</i>
<b>CHAPTER 1</b>	
Introduction	1
1.1 A Brief History of Nanorevolution	1
1.2 Physical Limitations of Traditional Semiconductor Electronics	2
1.3 Quantum Nanoelectronic Devices and Quantum Computing	4
1.4 Revolutionary Nanotechnologies	6
1.5 Solid State Against Soft Matter in Nanotechnologies	9
1.6 The Book Structure	11
References	11
<b>CHAPTER 2</b>	
Wet Technologies for the Formation of Organic Nanostructures	13
2.1 Traditional Chemical Routes for Nanostructure Processing	13
2.1.1 Formation of Colloid Nanoparticles	13
2.1.2 Self-Assembly of Colloid Nanoparticles	15
2.1.3 Electrodeposition of Nanostructured Materials	16
2.1.4 Sol-Gel Deposition	18
2.2 Electrostatic Self-Assembly	23
2.2.1 The Idea of Electrostatic Self-Assembly	23
2.2.2 ESA Deposition in Detail	24
2.2.3 ESA Deposition Equipment	27
2.2.4 Composite ESA Films	29
2.3 Langmuir-Blodgett Technique	33
2.3.1 LB Classics	33
2.3.2 Special Types of LB Films—Composite LB Films	43
2.3.3 Formation of II-VI Semiconductor Particles in LB Films	48
2.4 Spin Coating	54
2.5 Résumé	58
References	59

**CHAPTER 3**

Structural Study of Organic/Inorganic Nanocomposites	71
3.1 Morphology and Crystallography of Nanostructured Materials Prepared by Chemical Routes	71
3.1.1 Methods of Morphology Study	72
3.1.2 Methods of Crystallography Study	75
3.1.3 The Layer-by-Layer Structure of Thin Films	76
3.1.4 Morphology of LB Films Containing Nanoparticles	79
3.1.5 Morphology and Crystallography of Chemically Self-Assembled Nanoparticles	81
3.1.6 The Morphology and Structure of Sol-Gel and Electrodeposited Materials	84
3.2 Elemental and Chemical Composition of Organic/Inorganic Nanostructures	87
3.2.1 Experimental Methods of Composition Study	87
3.2.2 Examples of Composition Study of Materials Prepared by Chemical Routes	88
3.2.3 Control of Impurities in Chemically Deposited Nanostructures	90
References	92

**CHAPTER 4**

Optical Properties of Organic/Inorganic Nanostructures	95
4.1 Optical Constants of Organic/Inorganic Nanostructures	95
4.1.1 Method of Ellipsometry	95
4.1.2 Method of SPR	100
4.1.3 Optical Constants of Thin Organic Films	104
4.1.4 Optical Parameters of Organic Films Containing Nanoparticles	110
4.2 The Effect of Quantum Confinement on Optical Properties of Low-Dimensional Systems	114
4.2.1 Electron in a Quantum Box	114
4.2.2 Quantum Confinement and the Main Optical Properties of Low-Dimensional Semiconductor Structures	116
4.3 Optical Spectra Semiconductor Nanoparticles in Organic Films	122
4.3.1 Semiconductor Nanoparticles in LB and Spun Films	122
4.3.2 Semiconductor Nanoparticles in Electrostatically Self-Assembled Films	127
References	129

**CHAPTER 5**

Electron Transport in Organic/Inorganic Nanostructures	133
5.1 Conductivity of Thin Films	133
5.1.1 Definitions and Experimental Methods	133
5.1.2 Conductivity of Nanocrystalline Materials	138
5.1.3 Organic Semiconductors	141
5.2 Electron Tunneling	144
5.2.1 The Concept and Main Features of Electron Tunneling	144
5.2.2 Electron Transfer Through Thin Organic Films	146

5.2.3	Electron Tunneling Through Multilayered LB Films	149
5.2.4	Resonance Tunneling	151
5.2.5	Inelastic Tunneling and Inelastic Tunneling Spectroscopy	154
5.3	Single Electron Phenomena	155
5.3.1	Coulomb Blockade and Staircase I-V Characteristics	155
5.3.2	Single-Electron Devices and Their Practical Realization	158
5.3.3	Single-Electron Phenomena in Organic Films Containing Nanoparticles	160
	References	162

## CHAPTER 6

	Applications of Organic/Inorganic Nanostructures in Microelectronics and Optoelectronics	171
6.1	Organic Films in Conventional Microelectronics	171
6.1.1	Organic Films as Insulating and Passivating Layers	171
6.1.2	Active Organic/Inorganic Devices	172
6.2	Organic/Inorganic Optoelectronic Devices	174
6.2.1	Nanostructured Photovoltaic Devices and Solar Cells	175
6.2.2	Light-Emitting Devices	181
6.2.3	Optical Memory Devices	183
6.3	Quantum Nanoelectronic Devices	185
6.3.1	Quantum Computing	186
6.3.2	Practical Realization of Arrays of Quantum Dots	188
	References	190

## CHAPTER 7

	Chemical and Biosensors	205
7.1	Classification and Main Parameters of Chemical and Biosensors	205
7.1.1	Main Definitions and Classification of Sensors	205
7.1.2	Parameters of Sensors	208
7.2	Physical Transducing Principles for Sensors	212
7.2.1	Gravimetric Sensors	212
7.2.2	Electrical and Electrochemical Sensors	215
7.2.3	Optical Sensors	220
7.3	Nanostructured Materials for Sensing	231
7.3.1	Sensors Based on Inorganic Materials	231
7.3.2	Sensors Based on Organic Materials	232
7.3.3	Organic Vapor Sensors Based on Calixarenes	233
7.4	Biosensors	238
7.4.1	Composite Membranes for Biosensing	238
7.4.2	Immune Sensors	240
7.4.3	Enzyme Sensors	245
	References	251

	About the Author	261
	Index	263





# Preface

This book is an attempt to summarize the knowledge and personal experience accumulated throughout 18 years of work in the field of physics and technology of thin organic films, organic-inorganic nanostructures, and chemical and biosensing.

Initially the book was planned as a research monograph, but later in the process of writing I introduced a quite substantial scientific background in every chapter in order to make the subject more understandable for a wide scientific audience. Then I realized that the book might be very useful for postgraduate and even undergraduate students. The book contains the original scientific results obtained by the author, as well as substantial literature reviews in every chapter, which makes it useful for academics and researchers working in the field of nanotechnology.

I began writing with the enthusiasm and the feeling that I knew something about science in my field. Now, I am not that sure about it. I learned a lot during the writing of this book, but I also realized how vast and fast-growing the area of nanotechnology is, and how small my contribution to it is. Several times I wanted to quit and occupy myself with something less stressful. I finished the book anyway, and I hope some people will make use of it.



# Acknowledgments

I would like to thank Dr. O. S. Frolov (Kiev Research Institute of Microdevices), Professor Yu. M. Shirshov, a supervisor of my Ph.D. research, and Professor B. A. Nesterenko (both from the Institute of Semiconductor Physics, Academy of Sciences of the Ukraine), who have helped me throughout my research career to become a scientist.

I would like to thank all my colleagues and friends from the Institute of Semiconductor Physics, Academy of Sciences of the Ukraine (Kiev), Sheffield Hallam and Sheffield Universities (United Kingdom), and the other universities and research institutes in the Ukraine, Russia, and the United Kingdom, at which I worked and collaborated all these years. I would like to acknowledge the contribution of my colleagues from Sheffield Hallam University (particularly Professor Asim Ray and Dr. Aseel Hassan) to our joint publications, which were often quoted in this book.

I appreciate very much a great deal of help from Mr. Alan Birkett (Sheffield) with checking the proper use of the English language.

Finally, I want to express my love and special appreciation to my wife Valentina for being supportive and patient with me during the process of writing this book.



# Introduction

## 1.1 A Brief History of Nanorevolution

At the turn of twenty-first century, we entered nanoworld. These days, if you try to run a simple Web search with the keyword “nano,” thousands and thousands of references will come out: nanoparticles, nanowires, nanostructures, nanocomposite materials, nanoprobe microscopy, nanoelectronics, nanotechnology, and so on. The list could be endless.

When did this scientific nanorevolution actually happen? Perhaps, it was in the mid-1980s, when scanning tunneling microscopy was invented. Specialists in electron microscopy may strongly object to this fact by claiming decades of experience in observing features with nearly atomic resolution and later advances in electron-beam lithography. We should not omit molecular beam epitaxy, the revolutionary technology of the 1980s, which allows producing layered structures with the thickness of each layer in the nanometer range. Colloid chemists would listen to that with a wry smile, and say that in the 1960s and 1970s, they made Langmuir-Blodgett (LB) films with extremely high periodicity in nanometer scale. From this point of view, the nanorevolution was originated from the works of Irving Langmuir and Katherine Blodgett [1, 2] in 1930s, or from later works of Mann and Kuhn [3–5], Aviram and Ratner [6], and Carter [7], which declared ideas of molecular electronics in the 1970s. What is the point of such imaginary arguments? All parties were right. We cannot imagine modern nanotechnology without any of the above-mentioned contributions. The fact is that we are in the nanoworld now, and the words with prefix “nano-” suddenly have become everyday reality. Perhaps it is not that important how it happened (since it has become history already). However, we should realize the reason why it happened.

A driving force of the nanorevolution is a continuous progress in microelectronics towards increasing the integration level of integrated circuits (IC), and thus the reduction in the size of active elements of ICs. This is well illustrated by Moore’s law [8] in Figure 1.1.

It was monitored during the last four decades that the size of active elements (e.g., transistors) reduces by a factor of two every 18 months. Of course, there were some deviations from this law, and the graph in Figure 1.1 requires some kind of error bars. However, a thick trend line, which may cover error margins, demonstrates the above behavior clearly. What is behind Moore’s law? It is not just physics, microelectronic engineering, and technology alone, all of which have a spontaneous character of development. I believe that Moore’s law is a free market

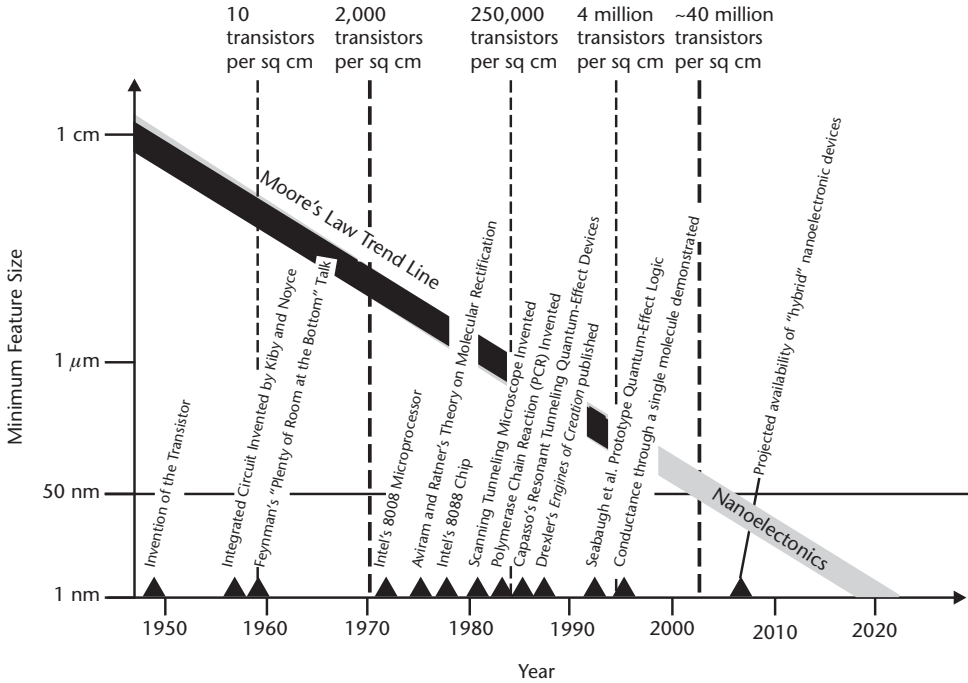


Figure 1.1 Moore's law. (From: [8]. © 1996 MITRE Corporation. Reprinted with permission.)

economy law, which reflects the growing public demand in microelectronic devices, and the competition between microelectronic companies.

Let's leave the economic aspects of Moore's law to economists, and start discussing physics. As one can see, the critical line of one micron was crossed in the 1990s, which means we entered the nanoelectronics era at that time. Electron beam lithography had started to overtake the conventional UV photolithography, which cannot provide submicron resolution. Smart technological approaches in microelectronics, such as VMOS, DMOS, and vertical CMOS transistors, also allowed the ability to meet the demands of the steadily growing market of personal computers. What is next? Can we further scale down the existing electron devices, based mostly on the field effect in semiconductors? The answer is *no*, because of obvious physical limitations of semiconductor microelectronics.

## 1.2 Physical Limitations of Traditional Semiconductor Electronics

Scaling down of the dimensions of semiconductor devices may have following consequences.

- Decreasing of the thickness of insulating layers, thus increasing the electric field, and the probability of field related effects, such as electron tunneling and avalanche breakdown;
- Dispersion of bulk properties of materials;
- Quantum phenomena in low dimensional systems;
- Problems of heat dissipation;

- Limitation of computing speed.

Let's discuss them one by one. Typical thickness of the gate oxide in MOSFETs with several microns of the channel length is about 100 nm. A typical gate voltage of 5V will create an electric field of  $5 \cdot 10^8$  V/m, which is a fairly large voltage, but less than avalanche breakdown limit. Submicron MOS devices must have a much smaller thickness of gate oxide, in the range from 20 to 30 nm. If the same gate voltage is applied, the electric field increases in the range from  $1.7 \cdot 10^9$  to  $2.5 \cdot 10^9$  V/m, which increases the probability of the avalanche breakdown or electron tunneling through much thinner triangular barriers.

We previously considered semiconductor material to be an approximately homogeneous medium, which is true for relatively large devices (more than  $1 \mu\text{m}$  in size). Even a 10% deviation of the impurity concentration in the material would not result in significant changes of characteristics of MOSFETs (e.g., threshold voltage, channel current). What will happen if we scale down the size of the elements? How this will affect the properties of semiconductor materials, for example impurity concentration? In case of typical p-type (boron doped) silicon with the concentration of doping impurity  $N_A = 10^{22} \text{ m}^{-3}$ , the surface concentration of boron would be  $N_{AS} = (N_A)^{2/3} \approx 5 \cdot 10^{14} \text{ m}^{-2} = 500 \mu\text{m}^{-2}$ . For a MOS transistor with the channel of  $1 \mu\text{m} \times 1 \mu\text{m}$ , we have 500 atoms of boron under the gate. It is not that much, but still enough to consider the material as a uniform solid-state medium. However, if we reduce the size of a MOSFET down to  $0.1 \mu\text{m} \times 0.1 \mu\text{m}$ , we have only five atoms of boron under the gate. They are statistically distributed, so the number of atoms could be 6, 7 or 3, 4. Therefore, the threshold voltage of these MOSFETs will be varied substantially, so that some of these devices may not be working at all. What shall we do? Increasing the impurity concentration is not an ideal solution to the problem, only a temporary measure. The problem reoccurs in the course of further scaling down. Additionally, the side effects of reducing the depletion width followed by increasing of the electric field, and thus increasing the probability of avalanche or tunneling breakdown in *p-n* junctions, should be taken into account in highly doped semiconductor materials. The conclusion is obvious—MOSFETs with dimensions of less than 100 nm are not feasible.

Quantum phenomena begin to affect the properties of materials when the dimensions are less than 10 nm, which is currently not the case. The energy structure of low dimensional solid states, [e.g., two-dimensional (thin films), one-dimensional (quantum wires), and zero-dimensional (quantum dots)], changes dramatically in comparison to that in three-dimensional bulk materials. On the other hand, quantum phenomena may have a rather positive effect on the progress of solid-state microelectronics. The phenomena of quantum confinement, such as Coulomb blockade and resonance tunneling, have stimulated the development of novel quantum electronic devices, which may constitute the foundation of future nanoelectronics.

Heat dissipation is another problem of super VLSI. Even the least power consuming CMOS logic gates, which do not conduct current in both "1" and "0" logic states, release the power of about  $10^{-5}$ W per gate. Super CMOS VLSI with a range from  $10^6$  to  $10^7$  transistors have from 10W to 100W of power to dissipate. For example, a Pentium IV processor produces 80W of power, and requires a quite sophisticated cooling system. Next generations of VLSI must be built on devices consuming less power.

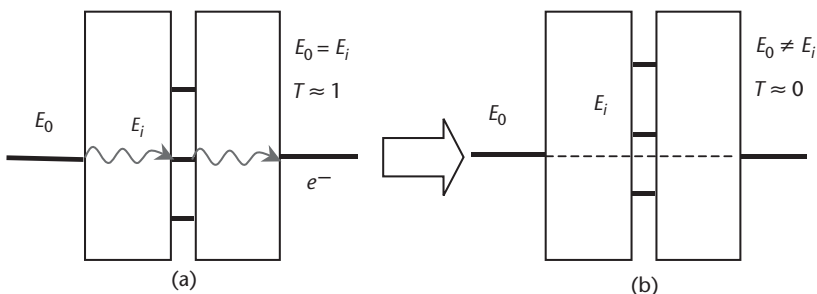


The further increase of computing speed is a very difficult and complex problem, which includes the use of new materials, novel quantum electronic devices, and novel principles of computing and computer architecture. It is well known that III-V semiconductors having high values of charge carrier mobility can offer much higher operational frequency than silicon devices. However, despite obvious functional advantages of III-V semiconductor devices, 95% of the microelectronics market is occupied with the more technological and cost-efficient silicon devices. A shift towards III-V semiconductor materials is expected in near future, when novel quantum devices, particularly resonance tunneling devices (RTD), will become more common. The operational speed of novel quantum devices and the novel principles of computer architecture are the subjects of discussion in the next section.

### 1.3 Quantum Nanoelectronic Devices and Quantum Computing

The physical limitations of semiconductor microelectronics described above became obvious long ago. One of the suggested alternatives was molecular electronics. This subject was booming in the 1980s, when a number of research laboratories were launched in the United States, the United Kingdom, Germany, France, Japan, and Russia (i.e., the former U.S.S.R.), and started working on the development of molecular electronic devices. Many interesting and fascinating ideas of logic devices based on one molecule or group of molecules, and revolutionary novel principles of molecular computing systems were suggested at that time. Although most of these ideas have not yet been fulfilled, the efforts were not wasted. The research in molecular electronics and thin organic films forced the technology and instrumentation into the nanometer zone. The architecture of quantum computing systems has been developed theoretically and modeled with existing computing facilities, resulting in artificial neuron networks and cellular automata becoming available in modern software packages. The development of solid-state electronics has also been stimulated by alternative research in molecular systems. Eventually, molecular electronics moved towards sensors and biosystems, while solid-state electronics prevailed with several brilliant ideas of quantum electron devices. It worth mentioning here three major breakthrough developments: (1) resonance tunneling devices, (2) single-electron devices, and (3) quantum dots.

RTDs are based upon the phenomenon of an electron tunneling through a complex barrier having intermediate electron states. As shown in Figure 1.2, when the

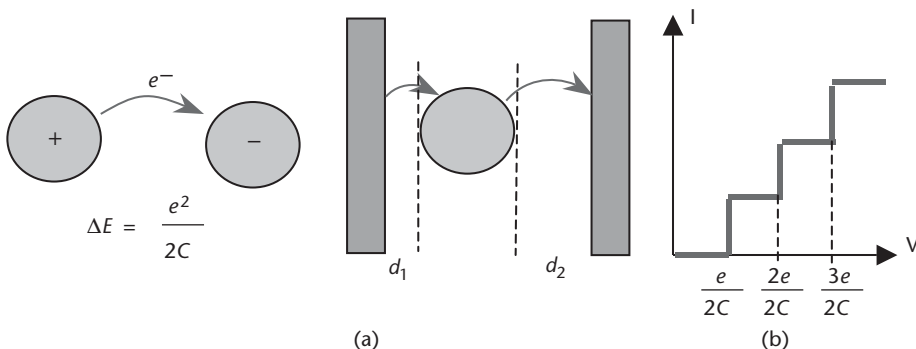


**Figure 1.2** The scheme of resonance tunneling through the barrier having intermediate electron states in (a) resonance conditions and (b) energy mismatching conditions.

energy level of electrons in the source matches one of the intermediate levels, the probability of tunneling increases dramatically (theoretically up to one), even if the total barrier thickness is larger than the tunneling distance. When the energies do not match, the probability of electron tunneling is practically equal to zero. The realization of this idea was achieved with GaAs/AlGaAs layered structures produced by molecular beam epitaxy (MBE) [9]. It allowed the scaling down in size of RTD devices to 50 nm. Currently, these devices are on the market, and the next generation of super VLSI will be most likely built on RTDs.

The idea of single-electron devices derived from the discovery of the phenomenon of Coulomb blockade in early 1990s by K. Licharev [10, 11] and H. Grabert and M. Devoret [12]. The operational principle of SEDs is very simple, and is illustrated in Figure 1.3. The transfer of a single electron between two particles, separated by the tunneling distance, will create a potential barrier  $\Delta E = \frac{e^2}{2C}$  (see Figure 1.3), where  $C = \epsilon r$  is the capacitance of the particles proportional to their radius. If particles are relatively large, this potential barrier is much less than  $kT$  even at very low temperatures, so that the other electrons are able to move practically unhindered between these particles, ignoring the potential barrier. However, the reduction in the particle size may lead to a different situation, when the potential barrier is comparable to or even higher than  $kT$  at a certain temperature. In this case, the potential barrier caused by the transfer of a single electron will prevent further electron transfer, and this effect is called Coulomb blockade. The first observation of the Coulomb blockade was achieved on 300-nm indium particles at 4.2<sup>0</sup>K [10]. Furthermore, the Coulomb blockade can be observed at room temperature in much smaller particles, with the size in the range from 3 to 5 nm. Such observation on 3-nm CdS nanoparticles, formed within Langmuir-Blodgett films, was reported recently in [13, 14].

Under Coulomb blockade conditions, the electron transfer between two electrodes via asymmetrically sandwiched nanoparticles (the separations  $d_1$  and  $d_2$  must be different) displays the staircase-like I-V characteristic, as shown in Figure 1.3. The transfer of one electron from the source to the nanoparticle will create a potential barrier of  $\frac{e}{2C}$ . There would be no current until the external bias voltage exceeds this value. The consecutive electron transitions will occur at bias voltages of



**Figure 1.3** (a) The effect of Coulomb blockade, and (b) the single-electron transistor having a staircase I-V characteristic.

$\frac{2e}{2C}, \frac{3e}{2C}$ , and so forth. Thus, a staircase-like I-V characteristic is typical for single-electron devices. Such behavior has been demonstrated at room temperatures on nanostructures by different research groups [15–17]. At the same time, an extensive theoretical work has resulted in a variety of single-electron logic gates [11], and they may constitute the elementary base of super VLSI in near future.

Another very attractive idea for future quantum computing systems involves quantum dots (QD) [18, 19]. These are regularly arranged nano-objects (e.g., nano-clusters, nanoislands, nanoparticles, macromolecules), separated by nanometer distances in order to provide the relay mechanism of charge transport. QDs will be a subject of more detailed discussion in following chapters. The most important idea to mention here is that new types of computing systems can be built on QDs (i.e., neurone networks or cellular automata [20]), operating on the principles of parallel computing. The future of nanoelectronics is believed to be in QD systems, which combine elements in nanometer dimensions with low power consumption, high operating frequency, and high reliability.

Great progress also can be expected in molecular electronics, although it is not a subject of this review. The idea to have molecules as active elements in computing systems is still very much attractive, and molecular QDs seem to be the most promising direction in molecular computers. The cellular automata architecture [7] might be able to solve the key problem of molecular electronics—addressing of individual molecules. Instead of the “wiring” of every molecular active element, it is better to organize them in networks with fast connections between nearest neighbors, and to provide only the input and output to the molecular web.

## 1.4 Revolutionary Nanotechnologies

Tremendous progress in solid-state electronics is based on several revolutionary technologies: (1) molecular beam epitaxy (MBE) and relative methods; (2) scanning nanoprobe microscopy; and (3) electron beam lithography. There might be many more, but these three greatly enhance the scaling down of electron devices to a nanometer range.

MBE, a method of precise high vacuum deposition of different compounds automatically controlled by several analytical techniques, allows the formation of layered systems, consisting of metals, insulators, and semiconductors, with the thickness resolution in fractions of nanometers. The realization of RDTs and semiconductor lasers on GaAs/AlGaAs superlattices is an industrial routine nowadays [8]. Regular arrays of QDs can be also formed by self-aggregation of thin InAs layers deposited onto the surface of GaAs using MBE [21].

Perhaps, the most impressive achievement in nanotechnology was the invention of scanning tunneling microscopy (STM) in 1986 [22], followed by the explosive development of relative techniques, such as atomic force microscopy (AFM) [23], and a dozen different scanning nanoprobe techniques in the subsequent 10 to 15 years. The fact that the Nobel prize for the invention of STM was given to Gerd Binnig and Heinrich Rohrer in 1986, only 4 years after the first publication, highlights the extreme importance of this method. For the first time in history (not taking into

account quite complicated methods of point-projection field-emission and ion-emission microscopy [24]), scientists obtained the instrument enabling them to observe features in atomic and molecular scale, with relative ease. I would say that nanotechnology was launched from there.

Genius and simplicity go together. Nothing can be simpler than STM, which is based on the exponential dependence of tunneling current on the distance. A sharp tungsten tip fixed on the XYZ piezoceramic transducer is the main part of the STM instrument, shown schematically in Figure 1.4. The scanning of the tip in the X-Y plane is organized by respective sweep voltages applied to the transducer, while the tunneling current measured between the tip and the studied conductive substrate provides a feedback voltage to the Z terminal of the ceramic transducer. By keeping the tunneling current constant during the scanning of the sample in XY plane, the recording of the voltage on the Z terminal would reproduce the surface profile in atomic scale. One of the classical STM images of the surface of highly oriented pyrolytic graphite (HOPG) is shown in Figure 1.5 [25].

The idea of STM is really simple. That is why it was reproduced many times, and developed further by different research groups, companies, and even individuals. In early 1990s, a colleague and friend of mine from the Institute of Physics, Academy of Science of the Ukraine, built his own STM on the transducer, consisting of three piezoceramic tubes from an old fashioned LP head glued together. It was a crude instrument sensitive to all sorts of external influences, but was able to produce pseudo-3D images of the surfaces of mica, graphite, and other materials, using an XY recorder.

The scanning nanoprobe method is not only an analytical tool, but also a nanotechnological tool. A simple nanolithography can be realized by scratching soft organic coatings with a tungsten STM tip. Another way of nanopatterning is the anode oxidation of thin metal films under the tip. However, an amazing application of STM is the possibility of moving atoms around. Figure 1.6 shows schematically

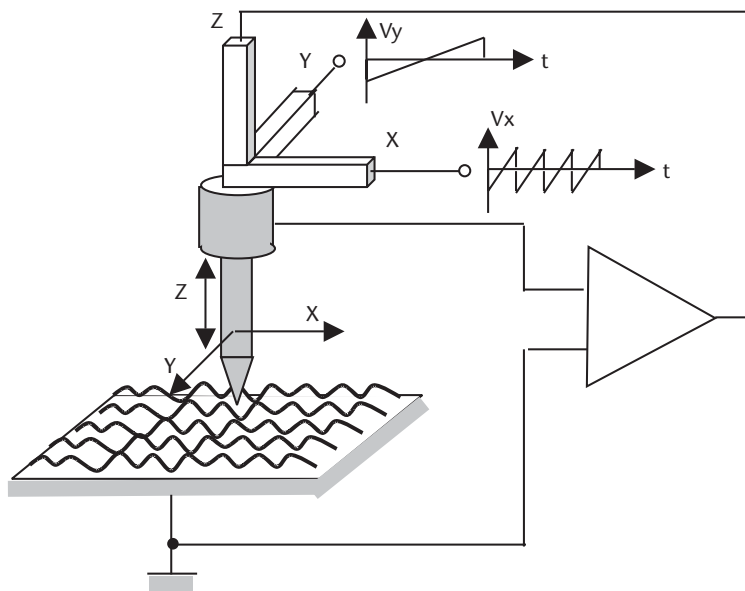
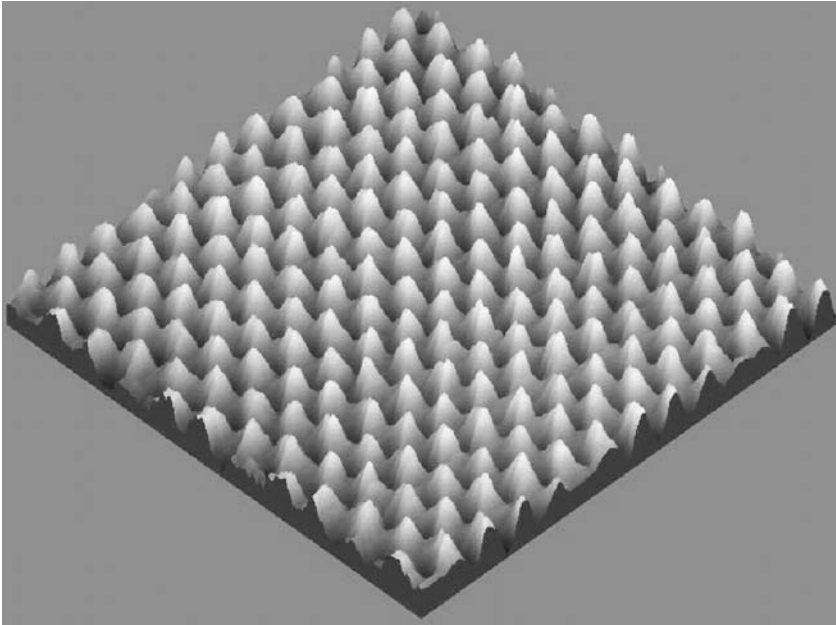
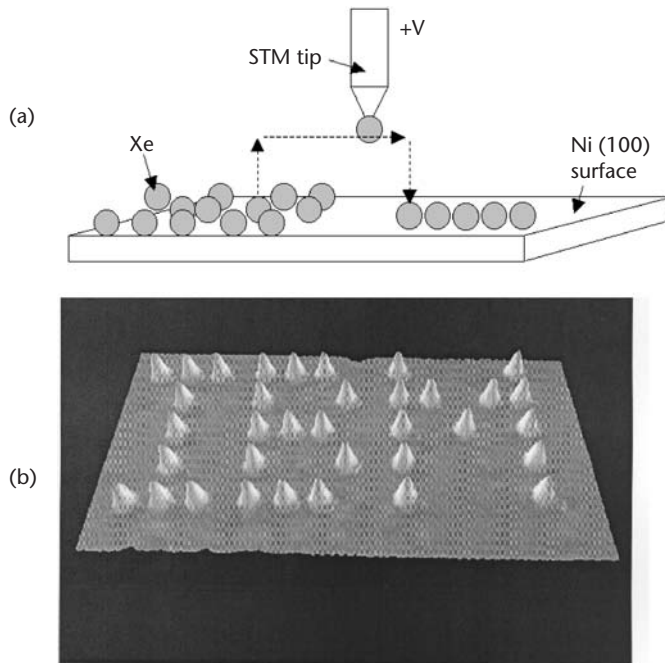


Figure 1.4 A simplified scheme of STM.



**Figure 1.5** Pseudo-3D STM image of the surface of HOPG. (From: [25].)

how atoms can be attracted to the STM tip by applying the appropriate voltage, moved away, and then placed where required. A very impressive advertising of IBM has been achieved by writing the company logo with Xe atoms on a (100) Ni surface using the above technique [26] (see Figure 1.6). The verdict that STM manipulation



**Figure 1.6** (a) The scheme of STM atomic manipulation, and (b) the IBM logo made on Ni(100) surface with Xe atoms using STM manipulation. (From: [27].)

is too slow to build atom-by-atom nanoelectronic elements in large numbers may not be right. It was reported recently on the development of a matrix of STM tips operating simultaneously [28]. With such tools, the STM fabrication of nanocomputers does not appear to be too much of a fantasy.

Finally, there is electron beam lithography [29], which came as a logical development of scanning electron microscopy (SEM). The  $\lambda/2$  diffraction limit of the conventional optical UV lithography could provide a theoretical resolution of 130 nm when a mercury light source ( $\lambda = 360$  nm) was used. However, a practical resolution of about  $1 \mu\text{m}$  can only be achieved due to the difficulties in focusing the light beam. The use of X-ray light sources can obviously improve the resolution, but X-ray systems are quite complex, and not safe in everyday exploitation. The diffraction limit also can be overcome with the help of near-field optical lithography [30]. However, this method still relies on the use of conventional metal/glass masks with nanofeatures, which have to be produced by some other means. Yet the application of such masks suffers from dust particles and other defects.

Electron beam lithography gives a much better solution. First, there is practically no diffraction limit, since the wavelength of high energetic electrons is incredibly small (e.g., electrons of typical energy of 10 keV have  $\lambda = 0.12$  nm). In practice, taking into account the problems of electron beam focusing, a resolution of few nanometers is now achievable. Second, electron beam lithography performs in a vacuum, thus making this method free of dust and other contamination. Finally, electron beam lithography may not require intermediate masks, since the pattern can be simply formed by the programmed scanning of the wafer with the electron beam.

## 1.5 Solid State Against Soft Matter in Nanotechnologies

Decades of extensive research in molecular electronics have resulted in remarkable progress in chemical methods of nanotechnology. The technology of thin organic films has improved to perfection. In addition to the traditional Langmuir-Blodgett technique, new methods of chemical and electrostatic self-assembly appeared. The progress in organic colloid and polymer chemistry was enormous. Thousands and thousands of new organic compounds of high purity were synthesized. The compounds have very interesting optical and electrical properties, enabling them to form complexes with other molecules, thus making them suitable for self-assembly and sensing, for example. The same can be said about polymer chemistry, which currently produces both conducting and light emitting polymers [31], and polyionic compounds capable of building electrostatically self-assembled composite multilayers [32]. Colloid chemistry achieved commercial production of various inorganic colloid particles of different natures [33], such as metals (Au, Pt, Ag, and Co), semiconductors (II-VI, III-V, and IV materials), insulators ( $\text{TiO}_2$ ,  $\text{SiO}_2$ , mica, and polymers), and magnetic materials ( $\text{Fe}_2\text{O}_3$ ). These colloid particles are pure, stable, uniform, and precise in their size, down to nanometer range.

Biochemistry is a special issue (beyond the scope of this book), because of the tremendous progress in the synthesis of biocomponents, experimental methodology, modeling, and the understanding of bioprocesses. The twenty-first century would be a century of biotechnology, rather than nanotechnology, if we would be

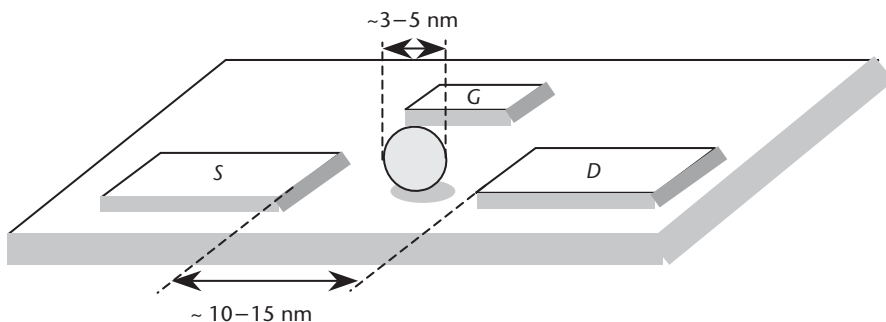
able to distinguish between them. Future nanoelectronics also can be bioelectronics, an industrial reproduction of the most powerful (though moody) data processing and decision-making machine—the human brain.

In many aspects, it is much more convenient to use nanosized elements produced by chemical methods, rather than by very complicated and expensive physical methods such as MBE. For example, resonance tunneling devices or semiconductor lasers can be produced by electrostatic self-assembly, the technique providing precision similar to MBE, but at a much lower cost. The parameters of these multilayered materials may not be as good as those produced with MBE, but perhaps it would be sufficient for some applications.

The same applies to QDs. The use of MBE for QD formation is not convincing. Nano-islands of InAs formed as a result of self-aggregation of a thin MBE layer of InAs on the surface of GaAs are not perfect, with the size dispersion in the nanometer range and irregularities in the planar arrangement [22]. At the same time, the size dispersion of colloid nanoparticles is one order of magnitude less, and colloid particles can be arranged in an exceptionally regular manner using the method of chemical self-assembly [34]. A monolayer of chemically (via thiol route) self-assembled gold nanoparticles, having formed a nearly perfect two-dimensional lattice following a close packing order, demonstrates the advantage of a chemical approach. Further patterning of such self-assembled layers is possible either with the e-beam or STM lithography.

The first experimental observation of the Coulomb blockade and staircase-like I-V characteristics at room temperature has been done with STM on CdS nanoparticles formed in fatty acid LB films [13, 14]. More practical single electron devices can be realized by a simple trapping of metal or semiconductor nanoparticles in the planar tunneling junctions, as shown in Figure 1.7.

It would be wrong to suggest that organic film technologies will take over the solid-state technology. They would instead complement each other, bringing together the advantages of each. In all of the applications mentioned above, nanostructures produced by chemical routes were integrated with traditional elements (e.g., metal contacts, tunneling junctions) produced by conventional solid-state technologies, such as metal deposition and e-beam lithography. This demonstrates a general trend of chemical and physical methods to complement each other, so future nanoelectronic systems will be manufactured using complex methods.



**Figure 1.7** The schematic of a single electron transistor with a CdS nanoparticle trapped into a planar tunneling junction.



## 1.6 The Book Structure

This book is dedicated to inorganic nanostructures formed by chemical routes. The technology of the formation of such structures will be described in Chapter 2. Chapters 3, 4, and 5 will review the structure, the optical properties, and the electrical properties of nanostructures, respectively. The effect of size quantization on optical properties of nanostructured materials and quantum phenomena in conductivity will be described in detail there. Chapters 6 and 7 describe different applications of organic/inorganic nanostructures in quantum electron devices, light emitters and other optoelectronic devices, and chemical and biosensors.

### References

- [1] Langmuir, I., "Forces Near the Surfaces of Molecules," *Chem. Rev.*, Vol. 6, No. 4, 1930, pp. 451–479.
- [2] Blodgett, K. B., "Monomolecular Films of Fatty Acids on Glass," *J. Amer. Chem. Soc.* Vol. 56, No. 2, 1934, pp. 495–495.
- [3] Kuhn, H., *Naturwiss.*, Vol. 54, 1967, p. 429.
- [4] Mann, B., and H. Kuhn, "Tunneling Through Fatty Acid Salt Monolayers," *J. Appl. Phys.* Vol. 42, No. 11, 1971, pp. 4398–4405.
- [5] Kuhn, H., D. Möbius, and H. Bücher, "Molecular Assemblies," in *Physical Methods of Chemistry*, A. Weissberger, and B. Rossiter, (eds.), Vol. 1, Part 3B, Chapter 7, New York: John Wiley & Sons, 1972.
- [6] Aviram, A., and M. Ratner, "Molecular Rectifiers," *Chem. Phys. Lett.*, Vol. 29, No. 2, 1974, pp. 277–283.
- [7] Carter, F. L., "The Molecular Device Computer: Point of Departure for Large Scale Cellular Automata," *Physica D*, Vol. 10, No. 1–2, 1984, pp. 175–194.
- [8] Montemerlo, M. S., et al., *Technologies and Design for Electronic Nanocomputers*, MITRE Corporation, McLean, VA, 1996.
- [9] Nichols, K. B., et al., "Fabrication and Performance of In<sub>0.53</sub>Ga<sub>0.47</sub>As/AlAs Resonant Tunneling Diodes Overgrown on GaAs/AlGaAs Heterojunction Bipolar Transistors," in *Compound Semiconductors 1994*, H. Goronkin, and U. Mishra, (eds.), *Institute of Physics Conference Series*, Vol. 141, 1995, pp. 737–742.
- [10] Averin, D. V., and K. K. Likharev, "Coulomb Blockade of Single-Electron Tunneling, and Coherent Oscillations in Small Tunnel-Junctions," *J. Low Temp. Phys.*, Vol. 62, No. 3–4, 1986, pp. 345–373.
- [11] Likharev, K. K., "Single-Electron Devices and Their Applications," *Proc. IEEE*, Vol. 87, No. 4, 1999, pp. 606–632.
- [12] Grabert, H., and M. Devoret, *Single Charge Tunneling*, New York: Plenum, 1992.
- [13] Facci, P., et al., "Room-Temperature Single-Electron Junction," *Proc. NAS USA*, Vol. 93, No. 20, 1996, pp. 10556–10559.
- [14] Erokhin, V., et al., "Observation of Room Temperature Monolectron Phenomena on Nanometer-Sized CdS Particles," *J. Phys. D: Appl. Phys.*, Vol. 28, No. 12, 1995, pp. 2534–2538.
- [15] Clarke, L., et al., "Room-Temperature Coulomb Blockade-Dominated Transport in Gold Nanocluster Structures," *Semicond. Sci. & Technol.*, Vol. 13, No. 8A, 1998, pp. A111–A114.
- [16] Schoonveld, W. A., et al., "Coulomb Blockade Transport in Single-Crystal Organic Thin-Film Transistors," *Nature*, Vol. 404 (6781), 2000, pp. 977–980.



- [17] Durrani, Z. A. K., "Coulomb Blockade, Single-Electron Transistors and Circuits in Silicon," *Physica E-Low-Dimensional Systems & Nanostructures*, Vol. 17, No. 1–4, 2003, pp. 572–578.
- [18] Bakshi, P., D. A. Broido, and K. Kempa, "Spontaneous Polarization of Electrons in Quantum Dashes," *J. Appl. Phys.*, Vol. 70, No. 9, 1991, pp. 5150–5152.
- [19] Tougaw, P. D., and C. S. Lent, "Quantum Cellular Automata: Computing with Quantum Dot Molecules," in *Compound Semiconductors 1994*, H. Goronkin, and U. Mishra, (eds.), *Institute of Physics Conference Series*, Vol. 141, 1995, pp. 781–786.
- [20] Adams, D. M., et al., "Charge Transfer on the Nanoscale: Current Status," *J. Phys. Chem.*, Vol. 107, No. 28, 2003, pp. 6668–6697.
- [21] Ploog, K. H., and O. Brandt, "InAs Monolayers and Quantum Dots in a Crystalline GaAs Matrix," *Semicond. Sci. & Techn.*, Vol. 8, No. 1, 1993, pp. S229–S235.
- [22] Binning, G., et al., "Surface Studies by Scanning Tunneling Microscopy," *Phys. Rev. Lett.*, Vol. 49, No. 1, 1982, pp. 57–61.
- [23] Albrecht, T. R., and C. F. Quate, "Atomic Resolution Imaging of a Nonconductor by Atomic Force Microscopy," *J. Appl. Phys.*, Vol. 62, No. 7, 1987, pp. 2599–2602.
- [24] Muller, E. W., *Z. Physik*, Vol. 131, 1951, 136–141.
- [25] Lee, Park STM, <http://www.physics.purdue.edu/nanophys/stm.html>.
- [26] Eigler, D. M., et al., "Imaging Xe with a Low-Temperature Scanning Tunneling Microscope," *Phys. Rev. Lett.*, Vol. 66, No. 9, 1991, pp. 1189–1192.
- [27] <http://www.almaden.ibm.com/vis/stm/auto.html>.
- [28] Requicha, A. A. G., "Massively Parallel Nanorobotics for Lithography and Data Storage," *Int. J. Robotic Research*, Vol. 18, No. 3, 1999, pp. 344–350.
- [29] Campbell, S., *The Science and Engineering of Microelectronics Fabrication*, Oxford, England: Oxford University Press, 1996.
- [30] Alkaisi, M. M., R. J. Blaikie, and S. J. McNab, "Nanolithography in the Evanescent Near Field," *Adv. Mater.* Vol. 13, No. 12–13, 2001.
- [31] Saxena, V., and B. D. Malhotra, "Prospects of Conducting Polymers in Molecular Electronics (Review)," *Current Appl. Phys.* Vol. 3, No. 2–3, 2003, pp. 293–305.
- [32] Lvov, Y. M., and G. Decher, "Assembly of Multilayer Ordered Films by Alternating Adsorption of Oppositely Charged Macromolecules," *Crystall. Reports*, Vol. 39, No. 4, 1994, pp. 696–716.
- [33] Fendler, J., and F. Meldrum, "The Colloid-Chemical Approach to Nanostructured Materials," *Adv. Mater.*, Vol. 7, No. 7, 1995, pp. 607–632.
- [34] Dorogi, M., et al., "Room-Temperature Coulomb-Blockade from a Self-Assembled Molecular Nanostructure," *Phys. Rev. B*, Vol. 52, No. 12, 1995, pp. 9071–9077.

# Wet Technologies for the Formation of Organic Nanostructures

## 2.1 Traditional Chemical Routes for Nanostructure Processing

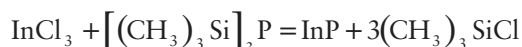
Chemical methods of material processing were known for years, existing in parallel with physical methods of film deposition. Recent advances in electron microscopy and scanning nanoprobe microscopy (STM, AFM) have revealed that some of the materials produced by the chemical methods have distinctive nanocrystalline structure. Furthermore, due to the achievements of colloid chemistry in the last 20 years, a large variety of colloid nanoparticles have become available for film deposition. This has stimulated great interest in further development of chemical methods as cost-effective alternatives to such physical methods as: thermal evaporation; magnetron sputtering; chemical and physical vapor deposition (CVD, PVD); and molecular beam epitaxy (MBE). This chapter will review chemical methods of film deposition, with the emphasis on novel techniques for nanostructured materials processing.

### 2.1.1 Formation of Colloid Nanoparticles

The most advanced chemical method for nanostructured materials processing is the deposition of colloid inorganic particles. Recent achievements in colloid chemistry have made a large variety of colloid compounds commercially available. The list of colloid nanoparticles with uniform (low-dispersed) dimensions in the range from 3 to 50 nm includes the noble metals (e.g., Au, Ag, Pt, Pd, and Cu), semiconductors (e.g., Si, Ge, III-V and II-VI, and metal oxides), insulators (e.g., mica, silica, different ceramic materials, polymers), and magnetic materials (e.g., Fe<sub>2</sub>O<sub>3</sub>, Ni, Co, and Fe). The growth of colloid particles is usually stabilized during synthesis by adding surfactants to the reagents [1]. Therefore, the stable nanoparticles produced are coated with a thin shell of functionalized hydrocarbons, or some other compounds. Typical examples of the chemistry of formation of colloid nanoparticles are shown below.

Gold stable colloids can be prepared by the reduction of AuCl<sub>4</sub> with sodium borohydride in the presence of alkanethiols [2]. Other colloids, such as Ag, CdS, CdSe, and ZnS, can be prepared in a similar way.

InP nanocrystals can be synthesized by the following reaction, with temperatures ranging from 150°C to 280°C

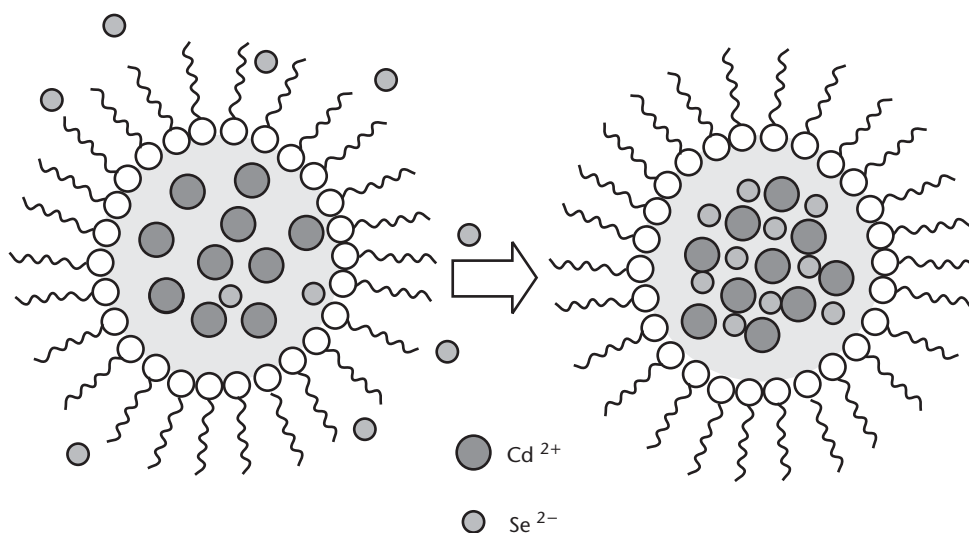


in the presence of either primary amines, tri-*n*-octylphosphine (TOP), or tri-*n*-octylphosphine oxide (TOPO) as stabilizing agents, preventing further InP aggregation [3]. The particles appear to be monodispersed, with a mean cluster size varying from 2.2 to 6 nm depending on the stabilizer used. The particles show strong resonance luminescence after etching in HF.

Cobalt monodispersed nanocrystals can be produced by rapid pyrolysis of the organic precursor  $\text{Co}(\text{CO})_8$  in an inert Ar-atmosphere, and in the presence of organic surfactants, such as oleic acid and trioctylphosphonic acid at high temperatures [4]. The particles appear to have ideal spherical, cubical, or rod-like shapes, with sizes in the range from 3 to 17 nm depending on surfactant concentration. The Co particles demonstrate superparamagnetic-ferromagnetic transition.

CdTe nanoparticle colloids can be prepared by the reaction of  $\text{Na}_2\text{Te}$  with  $\text{CdI}_2$  in methanol at  $-78^\circ\text{C}$ . The diameter of CdTe colloid particles is in the range from 2.2 to 2.5 nm [5].

An alternative method for the formation of stabilized colloid particles is to utilize self-assembled membranes, such as micelles, microemulsions, liposomes, and vesicles [1]. Typical dimensions are from 3 to 6 nm for reverse micelles in aqueous solutions, from 5 to 100 nm for emulsions, and from 100 to 800 nm for vesicles. Liposomes are similar to vesicles, but they have bilayer membranes made of phospholipids. Such membranes may act as the reaction cage during the formation of nanoparticles, and may prevent their further aggregation. The idea of the formation of nanoparticles inside micelles is to trap respective cations there. This can be done by sonification of the mixture of required salts and surfactants. Since the permeability of the membrane for anions is about 100 times higher than for cations, the formation of nanoparticles takes place within micelles, with a constant supply of anions from outside. The process of the formation of CdSe clusters within a reverse micelle is shown schematically in Figure 2.1. A number of different colloids, such as CdSe [6], silver oxide [7], iron oxide [8], aluminum oxide [9], and cobalt ferrite [10, 11], were prepared using the above methods.



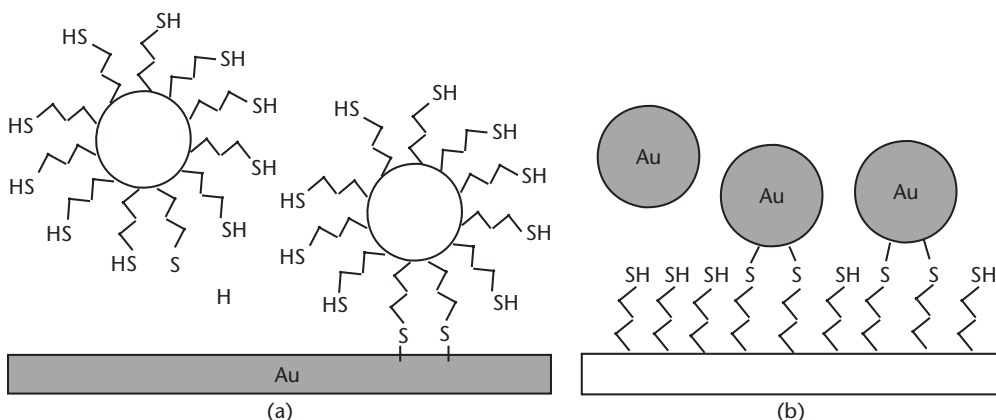
**Figure 2.1** Schematic diagram of the formation of CdSe nanoparticles within a reverse micelle.

### 2.1.2 Self-Assembly of Colloid Nanoparticles

The deposition of colloid nanoparticles onto solid substrates can be accomplished by different methods, such as simple casting, electrostatic deposition, Langmuir-Blodgett, or spin coating techniques, which will be discussed in detail later in this chapter. However, the simplest method of nanoparticles deposition, which gives some remarkable results, is the so-called self-assembly or chemical self-assembly method. This method, which was first introduced by Netzer and Sagiv [12], is based upon strong covalent bonding of the adsorbed objects (i.e., monomer or polymer molecules and nanoparticles) to the substrate via special functional groups. It is known, for example, that the compounds containing thiol (SH) or amine ( $\text{NH}_2$ ) groups have strong affinity to gold. The silane group ( $\text{SiH}_3$ ) with silicon is another pair having very strong affinity. Such features can be exploited for the film deposition of nanoparticles (modified, for example, with SH groups) onto the surface of bare gold, or vice versa, gold clusters onto the surface modified with thiol groups, as shown schematically in Figure 2.2.

The first work on the self-assembly of gold colloid particles capped with alkanethiols was done by Brust and coworkers [2]. This routine has been adopted by other scientists for the deposition of self-assembled monolayers of different colloid nanoparticles (e.g., Ag [13], CdS [14], CdSe [15], and ZnS [16]), which were prepared using mercapto-alcohols, mercaptocarboxylic acids, and thiophenols as capping agents. Self-assembled nanoparticles usually show well-ordered lateral structures, proved by numerous observations with SEM, STM, and AFM. Two-dimensional ordering in self-assembled nanoparticle monolayers can be substantially improved by thermal annealing at temperatures ranging from  $100^\circ\text{C}$  to  $200^\circ\text{C}$ , depending on the material used.

The use of bifunctional  $\text{HS}-(\text{CH}_2)_{10}-\text{COOH}$  bridging molecules, which combines both the affinity of thiol groups to gold and carboxylic group to titania, can provide more flexibility in the self-assembly. Both self-assembly routes were exploited for deposition of  $\text{TiO}_2$  nanoparticles onto the gold surface [17]. In the first one, unmodified  $\text{TiO}_2$  nanoparticles were self-assembled onto the gold surface, coated with a monolayer of  $\text{HS}-(\text{CH}_2)_{10}-\text{COOH}$ ; while in the second one,  $\text{TiO}_2$



**Figure 2.2** Two examples of the self-assembly of (a) alkylthiol modified nanoparticles onto bare gold and (b) pure Au particles onto alkylthiol modified surface.

nanoparticles stabilized with HS-(CH<sub>2</sub>)<sub>10</sub>-COOH were self-assembled onto the bare gold surface.

For some time, chemical self-assembly was limited to the formation of organized monolayers. The use of bifunctional bridge molecules overcomes this relative disadvantage. For example, multilayers of Au colloid particles can be deposited using dithiol spacing layers. A similar routine was applied for the fabrication of Au/CdS superlattices [18, 19].

### 2.1.3 Electrodeposition of Nanostructured Materials

Electrodeposition is one of the first chemical (or rather electrochemical) methods for the formation of inorganic coatings on solid surfaces. The formation of metal coatings on the anode by means of electrolysis of respective metal salts has been known since the nineteenth century. During the last few decades, this method has spread to other materials, such as II-VI and II-V semiconductor materials, with the main application in photovoltaic devices and solar cells.

Two types of electrodeposition can be distinguished from a large number of publications on this topic: (1) combination of the formation of stabilized colloid particles with their electrodeposition, and (2) electrodeposition (i.e., electrophoresis) of preformed colloid nanoparticles.

The first route is more traditional, and is based on the well-developed technique of electroplating. In order to form nanostructured materials, some kind of surfactants should be added to the electrolyte solution. The surfactants act as a stabilizing agent to coat nanocrystals and to prevent them from further aggregation, and therefore the formation of large grains of material. The review papers [20, 21] present a variety of materials, including metals, semiconductors, ceramics, and polymers, deposited in this way. A classical example of gold nanoparticles deposition is given in [22]. Monodispersed gold nanoparticles of a few nanometers were fabricated and deposited simultaneously on the silicon surface by the galvanostatic reduction of H<sub>2</sub>AuCl<sub>4</sub> in the presence of dodecanethiol.

The traditional, purely electrochemical way for the limitation of the growth of bulk materials is the use of pulse electrochemistry. The deposition of silver clusters from a cyanide-containing electrolyte onto indium-tin oxide electrodes using potentiostatic double-pulse method was reported in [23]. Clusters with particle diameters ranging from 100 to 300 nm can be prepared within minutes.

Ensembles of sulfur-capped, cadmium sulfide nanocrystals (CdS/S) have been synthesized using a new variant of the electrochemical/chemical method [24]. Cadmium clusters were first electrodeposited from an aqueous Cd<sup>2+</sup> plating solution using a train of 8- to 10-ms pulses, separated by approximately 1-second "mixing" segments at the open circuit potential. These Cd nanoparticles then were oxidized to Cd(OH)<sub>2</sub>, and CdS/S nanoclusters were obtained by exposure of Cd(OH)<sub>2</sub> nanoparticles to H<sub>2</sub>S at 300°C. The CdS/S nanocrystals obtained exhibit a very narrow (15 to 35 meV) photoluminescence (PL) emission line at 20°K.

The role of the substrate is a very important factor for electrodeposition. In some cases, highly ordered substrate surfaces can stimulate growth of monodispersed nanoclusters. For example, the electrochemical deposition and reoxidation of Au on the basal plane of highly oriented pyrolytic graphite (HOPG) immersed in a 5-mM AuCl<sub>4</sub>/6-M LiCl solution results in the formation of Au nanoparticles, with a

height of 3.3 nm and a diameter of 10 nm, as confirmed by SEM and AFM study [25]. The effect of low energy surfaces like graphite or H-terminated silicon on electrodeposition of metals was reviewed in [26].

Electrodeposition of different materials onto organic templates stimulates the formation of nanostructures. Nanoparticles of Ni, Ru, and Ni-Ru oxides have been prepared by electrodeposition of these metals coordinated into the dendrimer molecules, and their electrochemical and catalytic activities have been evaluated. The dendrimer molecules used were amine- and hydroxyl-terminated poly(amidoamine) dendrimers [27]. Self-assembled nanostructures of copper were grown by electrodeposition on a thin conducting polymer (polypyrrole) film electropolymerized on a gold electrode. The shapes, sizes, and densities of the nanostructures were found to depend on the thickness of the polypyrrole thin film, which provides an easy means of control of the morphology of these nanostructures [28]. Cadmium selenide nanoparticles were prepared at gold electrodes modified with molecular templates. The molecular templates were obtained by properly arranging thiolated beta-cyclodextrin self-assembled monolayers (SAMs) on gold electrodes. Selenium was first deposited on a SAM-modified gold electrode at an appropriate potential, followed by reduction to  $\text{HSe}^-$  in a solution containing  $\text{Cd}^{2+}$ , leading to the deposition of CdSe. CdSe particles as small as 1 to 2 nm have been observed with electrochemical AFM [29].

An extremely promising approach to electroplating via arrested and templated electrodeposition was recently discussed in [30]. This offers novel routes to the formation of nanosized structures, such as nanowires, by using porous substrates. The following examples demonstrate the potential of this approach. Rod-shaped gold particles were obtained by electrodeposition of gold in the nanoporous anodized alumina attached to a conductive support [31]. After dissolution of the alumina, the rods were released from the support. Coagulation was prevented by adsorption of poly(vinylpyrrolidone) on the gold surface. The length of the golden rods obtained can be tuned between 40 and 730 nm, and the diameter is between 12 and 22 nm. In [32], alumina membranes containing pores of 200 nm in diameter were replicated electrochemically with metals (Au and Ag) to make free-standing nanowires several microns in length. Wet layer-by-layer assembly of nanoparticles ( $\text{TiO}_2$  or  $\text{ZnO}$ )/polymer thin films was carried out in the membrane between electrodeposition steps to give nanowires containing rectifying junctions. This method has shown a great future for electroplated Pd, Cd, Mo, Au, Ag, and Cu nanowires, having diameters of a few tens of nanometers and a length of millimeters, for different electronic applications, ranging from the interconnection of nanoparticles to the active electronic devices and sensors, as discussed in [33].

Nanoporous alumina membranes are easily obtained by controlled anodization of aluminum surfaces in aqueous acids. Their properties, such as optical transparency, temperature stability, and pores of variable widths and lengths, make them a unique material to be filled by optically or magnetically interesting elements and compounds on the nanoscale. Magnetic nanowires of Fe, Co, and Ni can be formed by ac deposition from aqueous solutions. Gold colloids are generated inside the pores by growing smaller particles, or by using prepared particles. Siloxanes, gallium nitride, and cadmium sulphide have been made inside the pores from appropriate precursors, resulting in photoluminescent alumina membranes [34].



Nanometer-sized iron particles with diameters in the range from 5 to 11 nm can be grown within a silica gel matrix by electrodeposition. Electron diffraction shows the presence of an oxide (either  $\text{Fe}_3\text{O}_4$  or  $\text{Fe}_2\text{O}_3$ ) shell on these particles, which causes ferrimagnetic behavior [35].

An interesting example of patterned electrodeposition is given in [36], where submonolayer assembly of monodispersed Au (core)-Cu (shell) nanoparticles of 20 nm in diameter was prepared by electrodeposition of Cu on the monolayer of self-assembled Au nanoparticles. Under suitable potential, Cu was found to be selectively electrodeposited on the Au nanoparticles rather than on the surrounding organic monolayer.

The effect of the substrate crystallography on the nanostructure of electrodeposited material was demonstrated in [37]. In this work, CdSe nanoparticles were electrodeposited on mechanically strained gold, the latter achieved by controlled bending of gold films evaporated on mica. It was shown that both the size and bandgap of the electrodeposited CdSe quantum dots can be varied by applying mechanical strain to the Au substrate during deposition. This is attributed to changes in the lattice spacing of the strained {111} Au, and consequently in the lattice mismatch between the Au and the CdSe.

The successful exploitation of the electrophoretic approach in electrodeposition was demonstrated in the following works, where preformed nanoparticles were electrodeposited onto different substrates, including porous materials. A three-dimensional array of gold nanoparticles was assembled on a nanostructured  $\text{TiO}_2$  template by subjecting the colloidal gold suspension to a dc electric field (50V to 500V) [38]. By varying both the concentration of gold colloids in toluene and the applied voltage, it is possible to control the thickness of nanostructured gold film without inducing aggregation effects. The electrophoretic deposition of ZnO nanopowder (nano-ZnO) in aqueous media has been described in [39]. A cationic polyelectrolyte (polyethylenimine, PEI) was used to disperse and modify the surfaces of the ZnO nanoparticles. The electrophoretic deposition (EPD) was conducted via cathodic electrodeposition from stable low viscosity suspensions. In [40], a detailed study concerning the size-selective electrochemical preparation of  $\text{R}_4\text{N}^+\text{Br}^-$  stabilized palladium colloids is presented. Such colloids were readily obtainable using a Pd anode, with the surfactant serving as the electrolyte and stabilizer. It was shown that parameters, such as solvent polarity, current density, charge flow, and distance between electrodes and temperature, can be used to control the size of the Pd nanoparticles in the range from 1.2 to 5 nm. This strategy was also exploited for the deposition of bimetallic Pt/Pd nanoparticles.

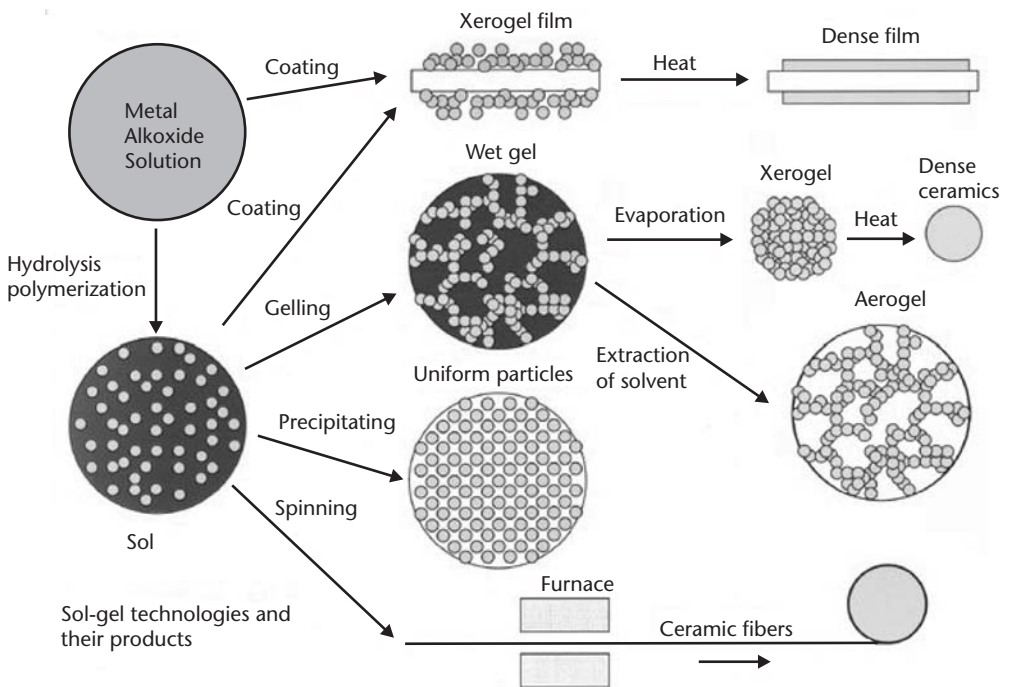
An interesting combination of electrophoresis and nanoscopic lateral patterning was demonstrated in [41]. In this work, copper electrodeposition was carried out by *in situ* electrochemical STM on Au(111) electrodes covered by complete decanethiol monolayers. It was found that 2- to 5-nm Cu nanoparticles were formed at certain electrical potentials on the surface of bare gold. Nanoparticle heights correspond to one atomic layer of Cu.

#### 2.1.4 Sol-Gel Deposition

Sol-gel is another purely chemical route for the formation of inorganic nanostructured materials. This method was known for many years, but was resurrected about

20 years ago [42]. The revival and further development of this method was mostly related to growing interest in ceramic materials. The sol-gel method offers a unique opportunity for ceramic fabrication at relatively low temperatures, often at room temperature. Later the sol-gel method was successfully adopted for the processing of a wide variety of materials, from monolithic ceramic and glasses, to fine powders, thin films, ceramic fibers, microporous inorganic membranes, and extremely porous aerogel materials [43]. The classification of sol-gel technology and products was given by Blinker and Scherrer [44], and well illustrated by the diagram in Figure 2.3. The main idea of the sol-gel process is the spontaneous formation of a dual phase material (gel), containing a solid skeleton filled with solvent, from the solution (sol), containing either solid clusters or required chemical reagents (e.g., inorganic precursors and stabilizing agents). Further transformation of the gel phase is driven by the evaporation of the solvent, and the subsequent formation of the xerogel phase. The sol-xerogel transformation may take place in the bulk of the solution, but it works much more effectively when the solution is spread over the surface of solid substrate. Thin xerogel films (in the range of 100 nm) can be formed on the solid substrates by dip coating, spin coating, or spraying of the solution. Heating of the xerogel completely removes solvent molecules, and perhaps stabilizers, therefore leading to further aggregation of inorganic clusters and the formation of solid materials, either bulk or in the form of thin films. Subsequent repeating of the routine allows the formation of thicker multilayered films.

A quick, supercritical drying carried out at high temperature leads to the formation of the aerogel, an extremely porous (greater than 75% porosity) material. On the other extreme, a very slow evaporation of the solvent at ambient conditions

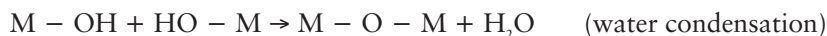
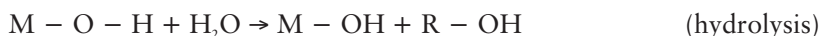


**Figure 2.3** Sol-gel technology and their products. (From: [44]. © 1990 Academic Press, Inc. Reprinted with permission.)



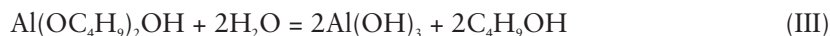
causes the precipitation of solid phase, and eventually yields fine, uniform particles. As shown in Figure 2.3, the sol-gel was implemented in the industrial processing of ceramic materials in the form of sheets, tubes, and fibers [45–47]. Despite the presence of a large number of different forms and applications of sol-gel materials, thin film deposition is the main focus of this chapter.

The chemistry of the sol-gel process is largely based on an alkoxide solution route. Alkoxides are traditional organometallic precursors for silica, alumina, titania, zirconia, and other metal oxides [1]. The sol-gel reaction, ignited by a catalyst, starts with the hydrolysis of alkoxides in the water-alcohol mixed solution, followed by poly-condensation reactions, as shown in the scheme below [44]:



The metals are  $M = \text{Si, Ti, Al, Zr, } \dots$ . Typical alkoxides are: tetraethyl orthosilicate ( $\text{Si}(\text{OC}_2\text{H}_5)_4$  or TEOS), tetramethyl orthosilicate ( $\text{Si}(\text{OCH}_3)_4$  or TMOS), Zr(IV)-propoxide, and Ti(IV)-butoxide. The hydrolysis can be triggered by changes in the solution pH. Acidic solutions are typically transparent, but become opaque at alkaline pH. This critical pH value indicates a transition point, when the reaction of hydrolysis becomes irreversible, and the sol-gel process begins.

A typical chain of reactions for the formation of alumina from aluminum-sec-butoxide in a mixture of water and ethanol [1] is shown here:

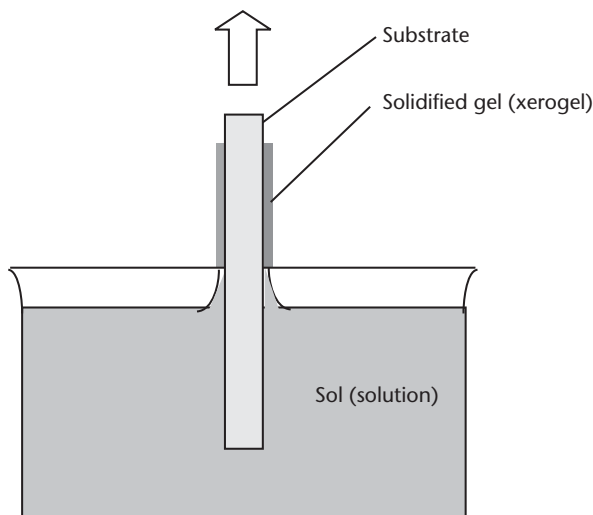


The reactions (I) and (III) correspond to hydrolysis, and the reactions (II) and (IV) correspond to polycondensation.

The above scheme was exploited for the formation of multicomponent oxides. Several alkoxides working together can result in the formation of composite ceramic materials—for example, yttrium aluminum garnet [48] or a whole range of zeolites [49].

An alternative route of sol-gel reaction lies in the usage of colloidal sols as precursors [1]. In this case, the reaction of the agglomeration of colloid nanoparticles can be catalyzed by changes in either pH or colloid concentration.

The sol-gel reaction is very often performed in the dip-coating regime, in which the solid substrate is slowly pulled out from the solution containing the required chemicals. The reaction known as gelation (i.e., sol-gel transition of the solution in contact with the atmosphere) takes place in a thin liquid layer wetting the substrate, as shown schematically in Figure 2.4. The xerogel coating obtained requires additional annealing to remove the residual solvent. The thickness of the resulting

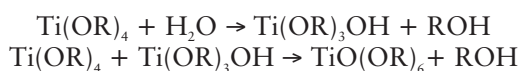


**Figure 2.4** The schematic of the sol-gel dip-coating technique.

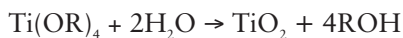
inorganic layer depends on the viscosity of the solution, the withdrawal speed, and the wetting conditions of the substrate (i.e., the contact wetting angle between the solution and the substrate).

The final stage of the formation of thin solid films prepared by the sol-gel route is annealing. As previously mentioned, two processes occur during annealing: (1) final evaporation of solvent from the film matrix, and (2) further aggregation and sintering of nanoclusters. The resulting films are typically polycrystalline, with the grain size ranging from 10 to 20 nm.

Thin films of titania ( $\text{TiO}_2$ ), a very popular material for the application in photovoltaic devices and solar cells, are usually produced by hydrolysis and polycondensation of titanium alkoxides, according to a following scheme [50]:



The reaction stops at the stage of the formation of  $\text{TiO}_2$  with the inclusion of two water molecules:



Further thermal treatment of titania colloid was studied with differential thermal analysis (DTA) [50]. It was shown that pure colloidal solution undergoes endothermic dehydration in the temperature range from  $80^\circ\text{C}$  to  $150^\circ\text{C}$ . An exothermic peak between  $250^\circ\text{C}$  and  $550^\circ\text{C}$  showed the formation of  $\text{TiO}_2$  anatase phase in the course of further oxidation of organic residuals and crystallization, while the peak at about  $800^\circ\text{C}$  indicated the recrystallization to  $\text{TiO}_2$  rutile phase.

A typical example of thin films of titania produced by the dip-coating sol-gel technique is given in [51, 52]. The solution was prepared from a mixture of 5 ml glacial acetic acid ( $\text{CH}_3\text{COOH}$ ) and 6.3 ml titanium (IV) isopropoxide ( $\text{Ti}[\text{OCH}(\text{CH}_3)_2]_4$ ) in 50 ml anhydrous ethanol. The films were transferred to the

surface of ITO-coated glass during its withdrawal from the sol at a speed of 250 mm/min. After deposition, the samples were allowed to dry in air for 24 hours, and then underwent thermal treatment at 550°C for 5 hours in air. In order to avoid cracks in the film, the heating and cooling of the samples were ramped at a rate of about 1°C/min. A typical thickness of the solid TiO<sub>2</sub> films obtained was about 50 nm. Thicker films can be obtained by several consecutive sol-gel depositions. Structure and morphology study of the films, obtained with SEM, AFM, and X-ray diffraction (XRD), revealed their nanocrystalline structure with a grain size of approximately 10 nm. The results of XRD also showed that TiO<sub>2</sub> clusters have an anatase crystallographic structure. The titania films produced by sol-gel route have found their application in photovoltaic devices and solar cells.

Another common method of performing sol-gel reaction is spin coating, in which the solution is dispensed onto the substrate rotating at high speed. The method of spin coating, as well as its combination with sol-gel, will be discussed later in the chapter.

The sol-gel deposition of thin films of a large number of materials for various applications was reported within the last decade. The following examples demonstrate the versatility of the sol-gel method for thin film deposition.

As reported in [53], films of zinc oxide were deposited on the surface of polished pyrex glass by sol-gel spin coating from a solution of zinc acetate in methanol. The coating solution of 0.2 ml was dropped, and spun at 3,000 r/min for 20 seconds in air. The sample was then dried at 80°C for 10 minutes, followed by annealing in air at temperatures ranging from 500°C to 575°C for 20 minutes. ZnO films with a thickness in the range from 160 to 250 nm were produced by repeating the above cycle 10 times. The films obtained showed a resistivity of 28 (Ω·cm) at room temperature, and the adsorption edge in near-UV range of 380 nm, which corresponds to an energy bandgap of 3.2 eV.

Nanostructured tungsten oxide (WO<sub>3</sub>) thin films were prepared by the sol-gel method following the inorganic route, in which alcohol solutions contained tungsten salts as precursors. The WO<sub>3</sub> films were deposited by dip-coating on glass substrates [54]. In [55], MoO<sub>3</sub>, WO<sub>3</sub>, and Mo/W binary compounds were deposited by the sol-gel spin coating technique on Si/Si<sub>3</sub>N<sub>4</sub> substrates provided with Pt interdigitated electrodes, and annealed at 450°C for 1 hour. Electrical responses to different gases, such as 30 ppm CO and 1 ppm NO<sub>2</sub>, were obtained. Thin films of other mixed metal oxides (e.g, Mo, Ti, Sn, and W), prepared by sol-gel technique, found their application for gas sensing [56].

Silica/titania composite films were prepared by the sol-gel method [57]. The systematic modifications of the silica matrix as a function of modified Ti-alkoxide contents (Au nanocrystals doped TiO<sub>2</sub>/SiO<sub>2</sub> mixed oxide thin films) have been investigated by the sol-gel process.

Ni and mixed Ni-Co oxide films were formed on Pt substrates by the sol-gel technique, and studied electrochemically in 1 M NaOH solutions. All sol-gel films under study were found to be amorphous [58].

Thin iron oxide films (70 to 1,500 nm) were deposited by the dip-coating method from iron-ion-containing sols, which were made from a FeCl<sub>3</sub>·6H<sub>2</sub>O precursor precipitated with ammonium hydroxide [59]. Homogeneous sols were obtained after peptization of precipitates with the addition of acetic acid (approximately 60 mol.%),

and no organics were added, in order to adjust the sol viscosity for depositing the xerogel film. These films displayed electrochromism, which disappeared after heat treatment at 500°C, when the  $\alpha$ -Fe<sub>2</sub>O<sub>3</sub> phase with a larger grain size of approximately 27 nm was formed.

The sol-gel method allows the introduction of organic molecules into inorganic matrix. For example, conducting polyaniline thin films were prepared by entrapping a water-suspended matrix by the sol-gel route [60]. The presence of metal oxides, such as TiO<sub>2</sub> and Al<sub>2</sub>O<sub>3</sub>, increases the film conductivity up to 17 (S cm<sup>-1</sup>) after heat treatment at 85°C.

The colloid-alkoxide mixture approach in the sol-gel method allows the formation of different semiconductor materials [61]. For example, SiO<sub>2</sub>/CdS-nanoparticle composite films were prepared by the sol-gel route [62]. The films were characterized by studying microstructural [XRD and transmission electron microscopy (TEM)] and optical (transmittance and photoluminescence) properties. The average radii of the nanoparticles varied as the cube root of the annealing time. The preparation of concentrated sols and transparent stiff gels of II-VI semiconductor nanocrystals is reported in [63]. A two-step process for the production of cadmium sulphide is reported. Sol stabilization and gelation control are achieved through successive passivation and depassivation of the surface of the nanocrystals, which are modified with thiols. The general principles of the method are not restricted to chalcogenide systems, and thus enlarge the range of applications of the inorganic sol-gel process.

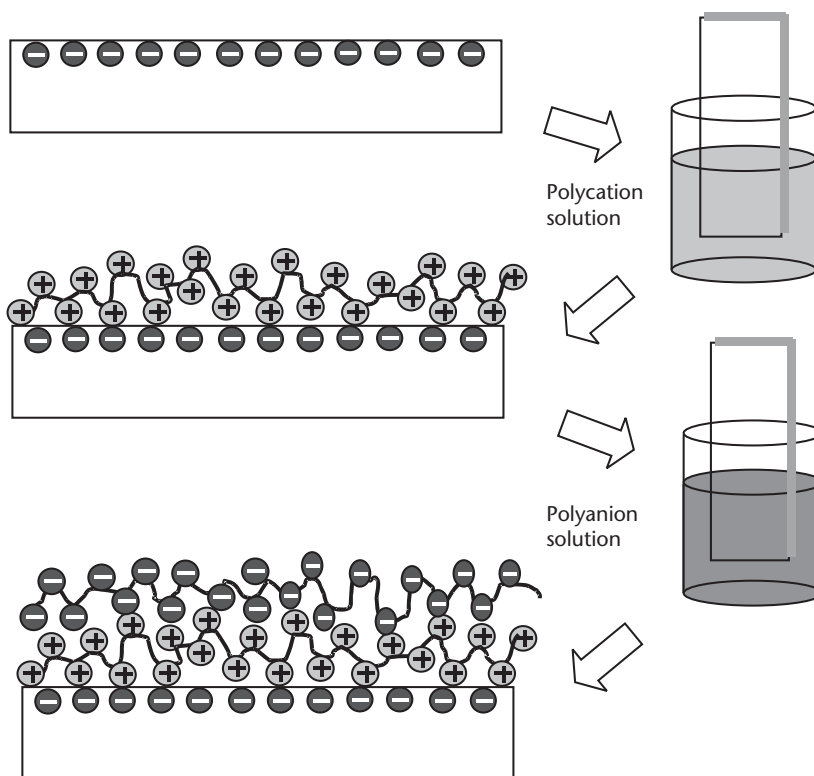
Great interest in GaN, a very promising material for blue light emitting diodes (LEDs) has stimulated the development of its new cost-effective processing technologies, such as sol-gel. A simple chemical reaction of gallium nitrate, incorporated into a silica gel precursor to form gallium oxide and the nitride, leads to a composite material with nanocrystals of the hexagonal phase of GaN, with an average diameter of approximately 5 nm, embedded in a silica matrix [64]. Thin films of GaN have been successfully deposited on Al<sub>2</sub>O<sub>3</sub> (100) substrates by the sol-gel technique [65].

## 2.2 Electrostatic Self-Assembly

### 2.2.1 The Idea of Electrostatic Self-Assembly

The technique of electrostatic self-assembly (ESA), also known as polyelectrolyte self-assembly or electrostatic layer-by-layer deposition, is based upon electrostatic interaction between polymers containing cation and anion groups. The method was developed at the beginning of the 1990s by G. Decher and colleagues [66–72], although historically this idea was suggested earlier [73, 74]. The ESA method became extremely popular, and within the following decade was adopted and further developed in many research laboratories [75–119].

Multilayered polymer films can be deposited onto an electrically charged substrate by its sequential dipping in solutions of polycations and polyanions. This process is shown schematically in Figure 2.5. Starting from a negatively charged substrate, the first layer of polycations can be deposited by simply dipping the sample into a polycation solution. At this stage, positively charged ionic groups of the polymer interact electrostatically with the substrate, leaving a number of positive ions available for further binding. The next layer of polyanions can be transferred



**Figure 2.5** The sequence of layer-by-layer electrostatic deposition: the negatively charged substrate, the dipping into polycation solution, the polycation layer deposited, the dipping into polyanion solution, and the polyanion layer deposited.

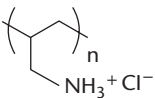
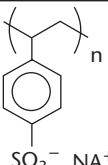
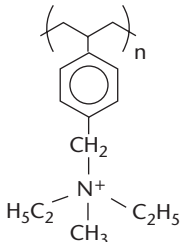
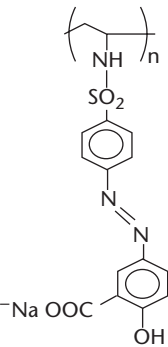
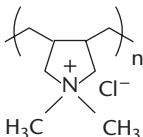
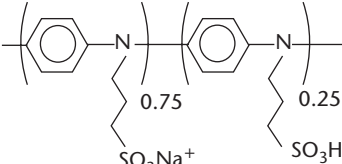
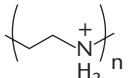
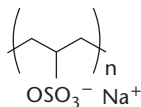
onto the substrate by dipping the sample into a polyanion solution. This deposition routine can be repeated many times, accompanied by the washing out of nonbound polyanion molecules after each layer deposited.

### 2.2.2 ESA Deposition in Detail

A number of polycations and polyanions are presently commercially available, and the most common compounds are listed in Table 2.1. These compounds usually exist in the form of salts, and dissociate in water or other polar solvents, splitting into the polymer chain, containing ionic groups (either anionic or cationic) and the counter-ions. Typically, polyions are deposited from their aqueous solutions, ranging from 1 to 2 mg/mL, although polyelectrolyte concentration is not a very important parameter. The deposition can be carried out in solutions that are much more diluted, but it may require longer deposition time. It has been reported that variations in polyion concentration in the range from 0.1 to 5 mg/mL do not dramatically affect the layer thickness, although the use of smaller concentrations, down to 0.01 mg/mL, has resulted in thinner films [72].

The polyelectrolyte deposition process can be separated into two stages. The first stage is the anchoring of polyion chains onto the surface, caused by the electrostatic attraction between a small number of ions and electrically charged adsorption sites. This stage is relatively fast, lasting only a few seconds. During a much longer second stage of polyion adsorption, the remaining adsorption sites must be filled.

**Table 2.1** The Most Common Polyions Used for ESA Deposition

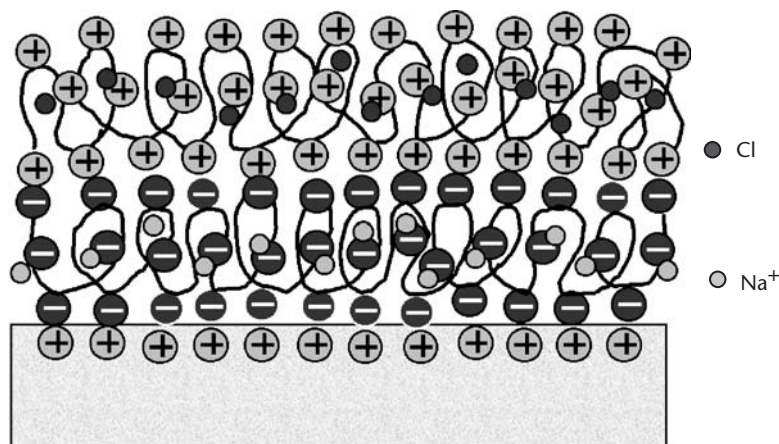
<i>Polycations</i>		<i>Polyanions</i>	
Poly(allyamine) hydrochloride PAA or PAH		Poly(styrenesulphonate) sodium salt PSS	
PVBA		Poly(carboxyhydroxy-phenylazo) benzene sulphonamido-ethanedyl Na salt (PAZO)	
Poly(dimethyldiallyl-ammonium) chloride PDDA		Poly(anilinepropanesulphonic) acid (PAPSA)	
Poly(ethyleneimine) PEI (protonated)		Poly(vinylsulphate) potassium salt PVS	

This requires the adjustment and penetration of the polycation chains between the anchored ones, and thus takes a much longer time, usually up to 20 minutes. In practice, 10 minutes is sufficient, since 97% of polyions are adsorbed within that interval [72].

The thickness of the polyanion/polycation layer depends on the compounds used. For example, the thickness of a PAA/PSS layer is about 1 nm. The combination of a relatively long deposition time, and a small thickness of the film repeating unit, makes the whole ESA process quite elaborate. The thickness of a film repeating unit can be increased by adding other salts to the polyion solutions. For example, the addition of NaCl salt to both polyelectrolyte solutions causes the incorporation of  $\text{Cl}^-$  and  $\text{Na}^+$  ions into the polyanion and polycation layers, respectively, as shown in Figure 2.6.

As a result, the bilayer thickness can be increased by a factor of three to five times, depending on the salt concentration. This is the way to accelerate the ESA deposition; however, the presence of ions in the film may cause electrical instabilities of ESA films, and this may be crucial for many electronic applications.

Another important practical question is whether or not to dry the sample after washing. The common point of view is that drying is important for successful ESA



**Figure 2.6** ESA film produced from solutions containing other salts.

deposition, although many researchers do not use drying at all, since it reduces deposition rate and may block deposition completely [95, 117]. Both opinions have their points. The highly polar water molecules may interact with the excessive electric charges of the top polyion layer, keeping neutrality and preserving ion groups from unnecessary interaction, and possibly discharging. At the same time, drying the sample in a neutral gas, such as nitrogen or argon, should not do any harm to the polymer layer [95, 117]. However, in practice, the presence of oxygen and other impurities, as well as dust particles, may partially compensate the electric charge of the top polyion layer, and thus reduce deposition efficiency or even completely block it. The easiest recipe for successful ESA deposition is, therefore, to keep the sample surface wet. If the sample drying option is used, it has to be done properly in inert gases, in order to avoid contamination and discharging of the top polyion layer. Substrate preparation is another very important issue to consider. For successful binding of the first polyelectrolyte layer, the substrate surface must be electrically charged. The first ESA films were produced on glass substrates positively charged by oxygen, argon, methane, or polysiloxane plasma [68, 72, 79]. This kind of treatment provides a 2- to 50-nm-thick electrically charged layer on the surface of materials of any kind [68]. Charging of the surface can be achieved much more easily by chemical modification. For instance, the surfaces of glass or quartz slides, or of silicon (either oxidized or only having native oxide on top), usually contain a certain concentration of  $\text{OH}^-$  groups. The list of compounds can be extended for all kinds of metal oxide surfaces, such as  $\text{Al}-\text{Al}_2\text{O}_3$ ,  $\text{TiO}_2$ , ITO, and so on. Such natural surface charges may be sufficient to begin ESA deposition, although the first few layers may suffer from poor surface coverage. The charge of these oxide surfaces can be increased by treatment in alkali solutions. In our work, we were using the following recipe [105]: sonification in 1% KOH solution in 60% ethanol for 20 to 30 minutes at approximately  $60^\circ\text{C}$  (this temperature is reached automatically during ultrasonic treatment for the above time). After such treatment, the surface became saturated with  $\text{OH}^-$ , and thus negatively charged. The surface of another important practical material, silicon nitride ( $\text{Si}_3\text{N}_4$ ), is normally positively charged due to the presence of  $\text{NH}_2^+$  groups. This charge can be increased by refreshing the nitride surface in HF solution. The surfaces of noble metals (e.g., Au, Ag, and Pt) are highly polarizable, and become



slightly negatively charged in contact with polycations. The surfaces can be further modified by self-assembled monolayers of short hydrocarbons with a thiol group on one end, and either a sulphonic- or amino-group on the other one.

*Advantages and Disadvantages of ESA Deposition* The films produced by this method have a number of obvious advantages over conventional LB, spin coating, and casting techniques. First of all, the films are much more mechanically stable due to much stronger Coulomb interaction, both between the polymer layers, and between the first layer and substrate, as compared to weak Van der Waals forces in LB films, for example. Another advantage of polyelectrolyte films lies in their typical polymer structure without pinholes, characteristic defects for LB films. The latter lead to better dielectric and masking properties of ESA films. Therefore, industrial implementation of ESA films as very thin insulating and masking layers has become a reality.

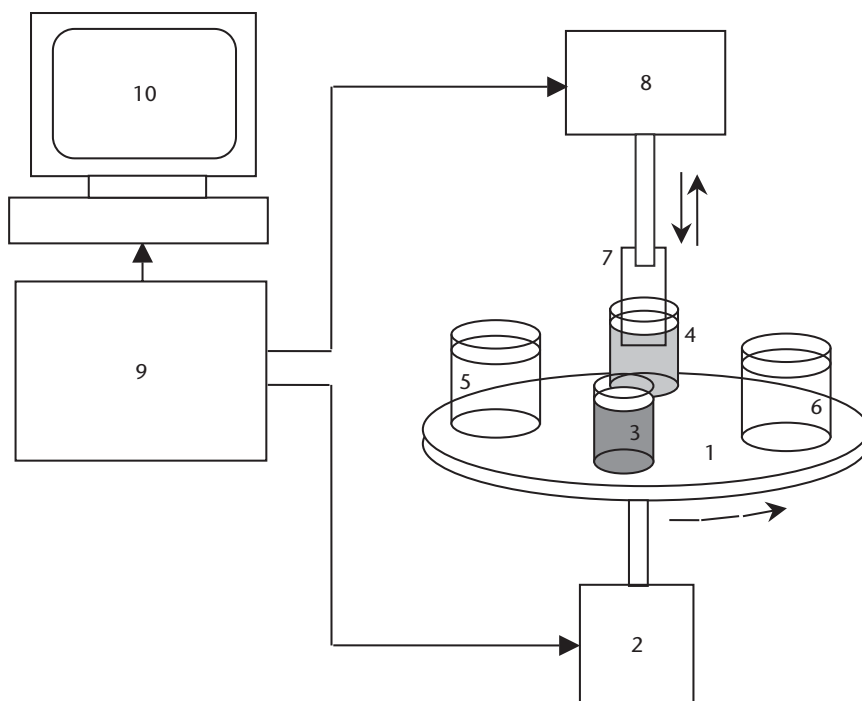
ESA films are less ordered, as compared to LB films, which is a relative disadvantage of ESA technique. This results in less periodicity in the film's layer-by-layer structure, but the precision of the overall film thickness is still very good, especially in nanometer range. Another drawback of ESA technique is low deposition speed, which restricts the use of this method to relatively thin film formation. However, the greatest benefit of the ESA technique lies in the possibility of incorporating other electrically charged objects, such as organic macromolecules, proteins, and inorganic nanoparticles, into the polymer matrix by simple alternation with oppositely charged polyions [67–72]. The extension of the ESA technique to deposition of composite films was very logical, and a large number of publications on this topic soon appeared.

### 2.2.3 ESA Deposition Equipment

Since ESA deposition is a time consuming process, the development of automatic deposition setup is beneficial for large-scale research work in this field. Many research groups, therefore, have developed their own deposition equipment. One of the first ESA deposition machines in the United Kingdom was designed and made in-house at Sheffield Hallam University in 1997 [118]. This construction, which is schematically shown in Figure 2.7, comprises a plastic dish (1), rotated by a stepper motor (2), with four beakers placed on it: two beakers contain polycation (3) and polyanion (4) solutions, respectively, the other two (5,6) contain water. The substrate is fixed in the holder (7) of the dipping mechanism (8). The stepper motor and the dipper are interfaced to PC (10) via IO card (9).

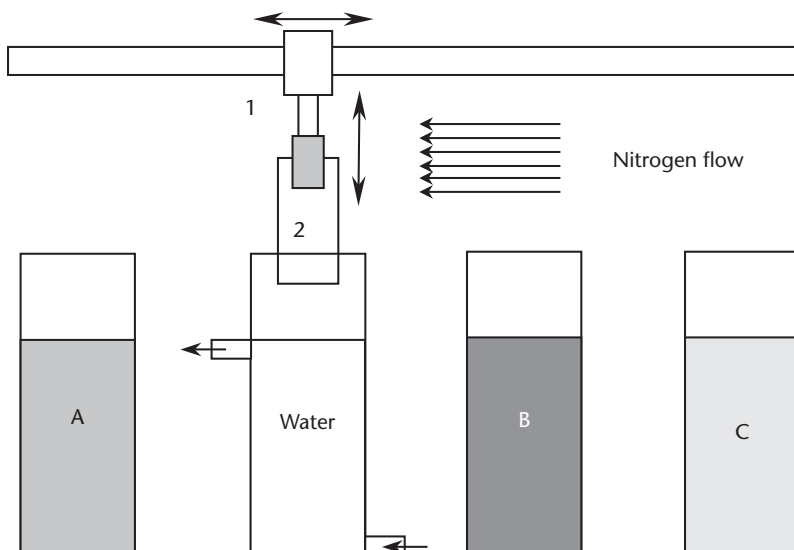
The deposition routine consists of dipping electrically charged (e.g., positively charged) substrate into the beaker containing a polyanion solution for a certain time, typically 10 to 20 minutes; then withdrawing the sample, rotating the dish 90°, and washing the sample in Millipore water by dipping and withdrawing several times; then turning the dish another 90°, and dipping into polycation solution for another 10 to 20 minutes, and so on. The process is interrupted after completion of the required number of cycles. We only need to change the washing water after each 10 to 20 cycles, in order not to cross-contaminate polyanion and polycation solutions. The described instrument provides only basic functions for ESA deposition, leaving room for further development. Similar equipment is now commercially available from NIMA, in the United Kingdom.





**Figure 2.7** Experimental setup for electrostatic self-assembly.

A much more advanced instrument was developed recently in Japan [120, 121]. As shown in Figure 2.8, it comprises several compartments filled with polyelectrolyte solutions, or some other compounds to be deposited, and a washing compartment with circulated water. The sample moves from one compartment to another by a computer controlled dipping mechanism (robotic arm). The deposition rate is monitored by a quartz crystal microbalance (QCM) sensor, placed on the holder next to



**Figure 2.8** Schematic diagram of the advanced ESA deposition machine.

the sample. The samples can be dried with a stream of nitrogen gas after each washing step. The whole system is placed in a clean, dust-free cabinet. For large-scale industrial production, the deposition equipment can be further developed into a conveyor type machine, operating nonstop with a large number of samples.

#### 2.2.4 Composite ESA Films

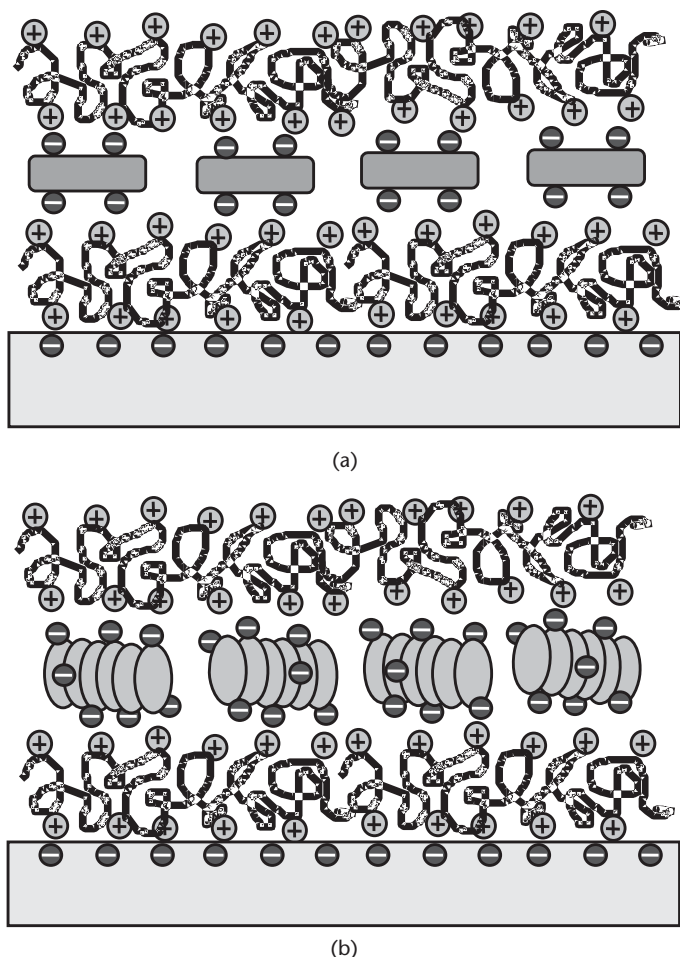
As was mentioned previously, many other electrically charged objects, such as organic macromolecules, bioobjects (e.g., proteins, immune-components, DNA, cells, and viruses), and inorganic and polymer particles, can be incorporated into the polymer film matrix by simple alternation with layers of polyions of opposite charge. In order to be suitable for ESA deposition, these objects must have the electric charge distributed over the whole surface. In this case, part of the electric charge will be engaged in binding the polyion underlayer, while the remaining charge will be available for binding the next polyion layer. This requirement can be easily achieved for inorganic particles (metallic, semiconducting, or insulating), either having native surface charge, or being chemically modified. Proteins are also electrically charged depending on their isoelectric point and the pH of the buffer solution. As regards to organic macromolecules, they must contain several ionic groups in a three-dimensional arrangement. The following examples of composite ESA films demonstrate the high versatility of this deposition technique.

*ESA Films Containing Other Organic Macromolecules* Many organic macromolecules (e.g., organic dyes) containing ionic groups can be deposited by ESA technique. The most common ionic substituting groups are  $\text{SO}_3^- \text{Na}^+$  and  $\text{NH}_3^+$ , although many others can be used. Additionally, the molecule must contain more than one ionic group in a three-dimensional configuration. It allows the binding of chromophore molecules on top of the polyion layer, leaving some groups for electrostatic binding of the next polyion layer, as shown schematically in Figure 2.9(a). Sometimes, two-dimensional molecules, or even molecules containing a single ionic group, can be deposited by the ESA method. This is possible due to the aggregation of organic molecules in solution. In this case, molecular aggregates having ionic groups randomly oriented meet the above criteria for ESA deposition, as illustrated in Figure 2.9(b).

In our earlier work, the molecules of cyclo-tetra-chromotroplene (CTCT) were successfully deposited by the ESA method. As shown in Figure 2.10, CTCT molecules having four  $\text{SO}_3^- \text{Na}^+$  groups and a boat-like three-dimensional configuration are ideally suitable for ESA deposition [122].

Two-dimensional molecules of Copper Phthalocyanine (CuPc) having four  $\text{SO}_3^- \text{Na}^+$  substituting groups represent a good example of deposition of molecular aggregates, as was previously illustrated in Figure 2.9. CuPc molecules are known to form so-called H-aggregates in the shape of three-dimensional molecular stacks and are thus suitable for ESA deposition. Molecules containing only one ionic group, such as Thymol Blue sulphonic sodium salt, can form similar molecular stacks with  $\text{SO}_3^-$  groups pointed in different directions (see Figure 2.9), and therefore can be deposited by the ESA method.

*Embedding of Biomolecules into ESA Films* The ESA method is particularly attractive for the immobilization of biomolecules, such as proteins, enzymes,

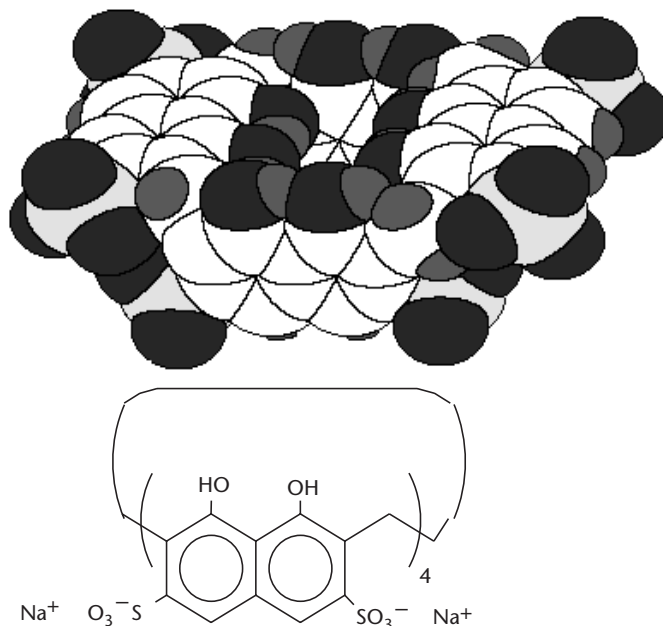


**Figure 2.9** Incorporation of organic macromolecules into PESA films: (a) monomer molecules containing ionic groups in three-dimensional conformation; and (b) molecular aggregates.

immune components, DNA, and viruses [119]. A polyanion matrix provides a natural surrounding for protein molecules, so that they retain their activity for a long time [119, 122–124]. Therefore, the most promising application of the ESA technique is the incorporation of various chemical components into the membrane using the same deposition routine, and the formation of composite membranes for various chemical and biosensors [119, 122–124].

Immobilization of proteins onto the surface of solid states is the first and the most important step for biosensor development. It is known that proteins immobilized directly onto the surface of a solid state tend to change their secondary structure, and to lose their function as a result [125]. There are several methods of protein immobilization, which can be used to prevent such undesirable transformations. The most common method is covalent binding of proteins to the surface, using an intermediate layer of glutaraldehyde [126]. Another approach is encapsulation of proteins, either within alginate gel [127], or lipid LB films [128], which provide a natural environment for proteins.

The immobilization of proteins by means of ESA [68, 85, 104, 119] combines strong binding by electrostatic interaction with structural stability of proteins in



**Figure 2.10** Chemical structure and configuration of cyclo-tetra-chromotropylene (CTCT) molecules.

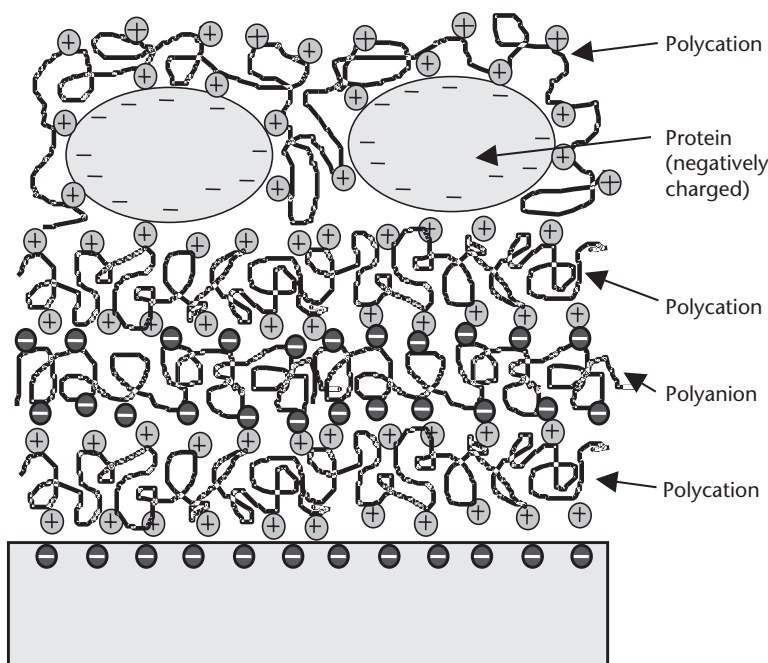
polyelectrolyte membranes, and a high permeability of the latter. The ESA method has proved to be the most successful for protein immobilization, since biomolecules can keep their function for a considerably long time (up to several months).

Protein molecules are known to have both negatively charged carboxylic acid groups and positively charged amino-groups in their structure. The electrostatic balance of protein molecules depends on the pH of the buffer solution. At the isoelectric point, the balance is achieved, and results in a net zero electric charge of protein molecules. Below this point (i.e., at acidic pH), proteins are positively charged; above it (i.e., at alkaline pH), negatively charged. Because of the three-dimensional globular structure of proteins, they automatically fulfill the main suitability criterion for ESA deposition. A typical structure of ESA films containing proteins is shown schematically in Figure 2.11.

Numerous experimental attempts of ESA deposition of different biomolecules, such as albumins, enzymes, immunoglobulins, DNA, light-harvesting complexes, and viruses. Biocompounds and specific conditions of their ESA deposition are summarized in Table 2.2.

*Embedding of Inorganic Particles into ESA Films* As described earlier, inorganic particles of different nature (metallic, semiconducting, or insulating), with their size varying from several nanometers to several micrometers, can be incorporated into ESA films by simple alternation with polyions. The only requirement is to have the surface of these particles electrically charged.

Some of these particles have the surface electrically charged naturally. For example, oxide materials, such as  $\text{SiO}_2$ ,  $\text{Al}_2\text{O}_3$ ,  $\text{TiO}_2$ , and  $\text{SnO}_2$ , under normal atmospheric conditions, have their surfaces coated with adsorbed hydroxide groups (OH), and therefore are negatively charged. The same applies to most metals (i.e., Al, Cu, Ti, Ag, and Fe) which are usually covered with a thin native oxide layer.



**Figure 2.11** The incorporation of biomolecules into the PESA films.

**Table 2.2** Experimental Data for ESA Deposition of Biomolecules

<i>Biomolecule</i>	<i>Isoelectric Point</i>	<i>pH for ESA Deposition</i>	<i>Electric Charge</i>	<i>Polyions to Alternate With</i>
Albumin	4.9	8		PDDA <sup>+</sup>
Cytochrome	10.1	4.5	+	PSS <sup>-</sup>
Lysozyme	11	4.0	+	PSS <sup>-</sup>
Myoglobin	7	4.0	+	PSS <sup>-</sup>
Hemoglobin	6.8	4.5	+	PSS <sup>-</sup>
Glucose oxidase	4.2	6.5	-	PEI <sup>+</sup> , PDDA <sup>+</sup>
Catalase	5.5	6.5–8.0	-	PEI <sup>+</sup>
Urease		8.2	-	PAA <sup>+</sup>
Cholinesterase		8.0	-	PAA <sup>+</sup>
Protein A		8.2	-	PAA <sup>+</sup>
Immunoglobulin	6.8	7.5	-	PDDA <sup>+</sup>
		8.4	-	PAA <sup>+</sup>
Bacteriorhodopsin	6.0	9.4	-	PDDA <sup>+</sup>
Carnovirus		7.0	-	PAH <sup>+</sup>

Such objects can be incorporated into the ESA film by alternation with polycation layers. Noble metals, such as Au and Pt, do not have a native oxide layer. Because of a large concentration of free electrons, these materials can be easily polarized by polycations and can form electrostatic bonds.

On the other hand, the electrical charge of these particles can be formed, enhanced, or even altered by their chemical modification. It is done during the initial stage of colloid stabilization, when the growth of particles is terminated at some stage by coating their surface with functional groups. A typical example of such processes is stabilization of gold colloid with thiol-containing compounds. The modification of gold nanoparticles with short hydrocarbons containing a thiol-group on one end and  $\text{SO}_3^-\text{Na}^+$  on the other end will result in negatively

charged particles, while thiol-amine compounds will form positively charged gold colloid particles.

Usually fine inorganic particles may exist in the form of colloid suspensions and thus can be deposited in the same way as polyions—by sequential dipping of the substrate in the respective solutions. The larger particles of submicron or micron size can sediment very quickly, and thus require continuous stirring.

The technology of the deposition of large varieties of inorganic particles was described in detail by Fendler and Kotov [91, 92]. Composite films containing layers of metal (e.g., gold), semiconductor, and insulating (e.g., mica, clay) particles were produced by the ESA method [91, 92, 129, 130]. Such nanoparticle engineering allows formation of systems having unique electrical properties, such as conducting or semiconducting two-dimensional layers separated by layers of dielectrics [129, 130]. ESA films containing semiconductor nanoparticles have found very promising applications in optoelectronics, particularly as tuneable photoluminescent and electroluminescent devices [131–135]. Layers of  $\text{TiO}_2$  nanoparticles can be deposited by the ESA technique with a view to application in photovoltaic devices [136, 137].

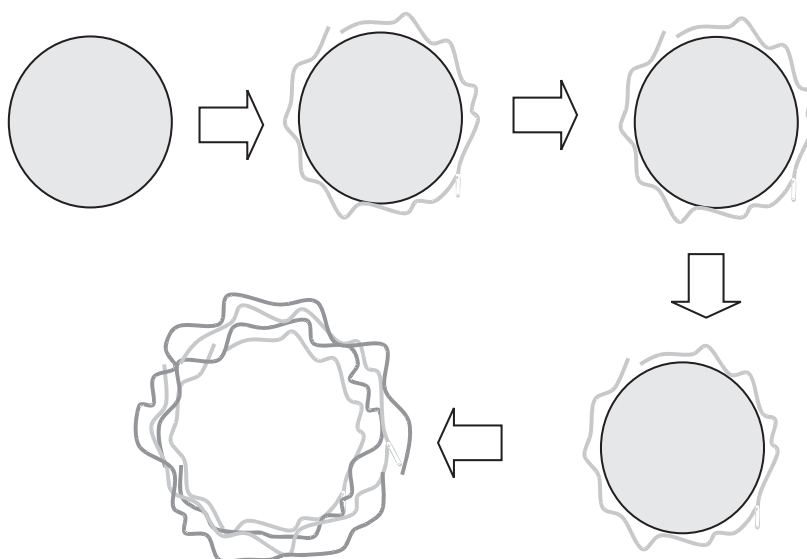
Another way to modify inorganic particles is to coat them with a layer (or several layers) of polyions [138]. Slightly negatively charged metal particles can be coated with layers of polycation (e.g., by mixing the particles with a solution of PAH). Then, the particles can be separated from the PAH solution in a high-speed centrifuge. This process can be repeated several times by sequential dipping in PSS and PAH solutions to form a multilayer ESA coating.

This idea was later exploited for the formation of hollow polyelectrolyte shell-particles. Figure 2.12 illustrates this process, which starts from the polymer (polystyrene) core beads coated several times with PAH and PSS layers to form polymer beads embedded into a polyelectrolyte multilayered shell. Finally, the polymer core can be dissolved in a strong acid, leaving a hollow PAH/PSS shell. This elegant idea has a great potential in nanobiotechnology (e.g., in the development of drug delivery systems). Different nanosized objects, such as proteins, antibodies, and various drugs, can be encapsulated in polymer shells [138], delivered to a certain place, and then released.

## 2.3 Langmuir-Blodgett Technique

### 2.3.1 LB Classics

The method of Langmuir-Blodgett films was established between 1920 and 1930. The main idea of this technique lies in the formation of a monolayer of closely packed amphiphilic molecules on the surface of the aqueous subphase, followed by film transfer onto the solid substrate during its up-and-down movement through the water surface. The study of the molecular layers on the water surface was derived from nineteenth century work by Pockels [139] and Lord Rayleigh [140] on the behavior of fatty acid molecules on the water surface. For the first time, the surface pressure–area isotherms were measured, and it was proven that fatty acids form true monolayers on the water surface. In 1920s, Langmuir continued the experimental study of different amphiphilic molecules in more detail [141]. The precise



**Figure 2.12** The sequence of the formation of hollow polyelectrolyte shells: initial negatively charged polystyrene core-particle; after coating with PAH layer; after coating with PSS layer; after several PAH/PSS layers deposited; and after dissolving of the core-particle in acid.

instrumentation for this study (i.e., the Langmuir trough and Langmuir balance) was developed, and the monolayers' behavior was described theoretically. For this work, Irving Langmuir received a Nobel Prize in 1932 "for discoveries and investigations in surface chemistry." Later in 1930s, his student and colleague Katharine Blodgett developed the technique of multilayer film growth by sequential deposition of preformed amphiphilic monolayers onto solid surfaces [142]. From this work, the name Langmuir-Blodgett (LB) films was derived. Since then, for years, this subject was regarded as exotic, having a very limited usage in the field of colloid chemistry, with no foreseeable industrial implementation. The only application that appeared in the 1970s was the use of highly periodic (in normal direction) LB films of heavy metal salts of fatty acids as dispersion gratings for the X-ray spectral region. However, even at that time, the industry realized the difficulties of large-scale implementation of LB technology. The revival of this topic happened at the end of the 1960s and at the beginning of the 1970s, when ideas of molecular systems and molecular electronics appeared [143–145]. The number of publications on LB films peaked in the 1980s and at the beginning of the 1990s. Those readers who are interested in a detailed study of LB technique can refer to a number of review papers and books on the technology, physical chemistry, and applications of LB films published at that time [146–152].

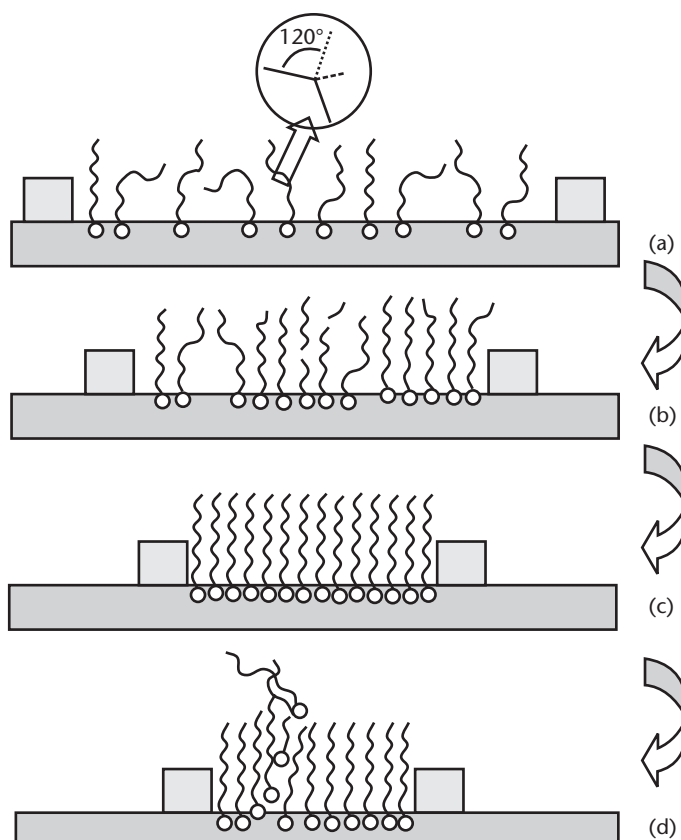
The LB film method has developed dramatically since then. Several companies, such as Joyce Loyble, Lauda, NIMA, and KSV, have been competing on the market, offering their technological equipment for LB deposition. Later in the 1990s, the number of publications started to drop, mainly because the high expectations of the LB film method in molecular electronics were not fulfilled. Despite the unique properties of LB films regarding their high ordering and thickness precision, the industrial implementation of this technique was limited by the poor mechanical and



thermal stability of LB films. LB films are poorly adhesive, too soft and fragile, and therefore can be easily damaged during preparation and exploitation. Both advantages and disadvantages of LB film methods will be discussed later.

Now, it is time to describe briefly the basics of the LB method. These films can be produced from special kinds of molecules, called amphiphilic, which contain a hydrophilic head group and a hydrophobic tail. Fatty acids are a typical example of these types of molecules. These molecules, having the general chemical formula  $(\text{CH}_3-(\text{CH}_2)_n-\text{COOH})$ , contain a highly polar  $\text{COOH}$  head group and a nonpolar  $(\text{CH}_2)_n-\text{CH}_3$  hydrocarbon chain. Such molecules in contact with water will occupy a place on the water surface, with the polar head groups interacting with the dipole moments of the water molecules and thus submerged in the water; and the hydrophobic chains repelled from the water (see Figure 2.13). An alternative possibility for amphiphilic molecules is to form micelles in the water bulk. A small concentration of micelles in the order of  $10^{-6}$  M is always present in the water/fatty acid mixtures; however, the majority of amphiphilic molecules exist on the water surface. That is why they are sometimes called surface-active compounds or surfactants.

The molecular monolayer can be formed on the water surface by spreading a solution of amphiphilic molecules in some volatile solvent. After evaporation of the solvent molecules, a layer of amphiphiles is formed. Because every two adjacent



**Figure 2.13** The consecutive stages of the formation of Langmuir monolayer: (a) two-dimensional gaseous state, (b) two-dimensional liquid state, (c) two-dimensional solid state, and (d) collapse of the monolayer.



CH<sub>2</sub> groups in the chain have three possible directions for the C-C bond, fatty acid molecules are quite flexible, and may have different spatial configurations when placed in low concentrations on the water surface, as shown in Figure 2.13(a). The monolayer can be compressed by restricting the area occupied by the amphiphilic molecules. This can be accomplished in different ways, and will be discussed in the section on LB equipment. As a result of this monolayer compression, fatty acid molecules start to interact with each other, and are stretched and reduced in their flexibility, as shown in Figure 2.13(b). Soon, the monolayer may reach a stage when all the molecules are stretched and closely packed, as shown in Figure 2.13(c). In this two-dimensional solid-state phase, the monolayer can be transferred onto solid substrates. Further compression may lead to so-called “monolayer collapse,” as shown in Figure 2.13(d), when the closely packed order is broken, causing some molecules to fall out of the monolayer and form a multilayered structure on the water surface.

The state of the monolayer can be characterized by the parameter of the surface pressure ( $\Pi$ ), defined as the difference between the surface tensions of pure water ( $\sigma_0$ ) and of water covered by the monolayer ( $\sigma$ ):

$$\Pi = \sigma_0 - \sigma$$

There are two practical methods for the experimental determination of the surface pressure. The first and most common method, the Wilhelmy balance method, is based upon the measurement of the weight of a hydrophilic plate partially submerged in the water. As shown in Figure 2.14(a), an extra weight  $\Delta W$  of the water meniscus is proportional to the surface tension:

$$\Delta W = P\sigma \cos \theta$$

where  $P$  is the perimeter of the plate and  $\theta$  is the wetting angle. When a sheet of filter paper having absolute wetting ( $\theta = 0$ ) is used as a plate

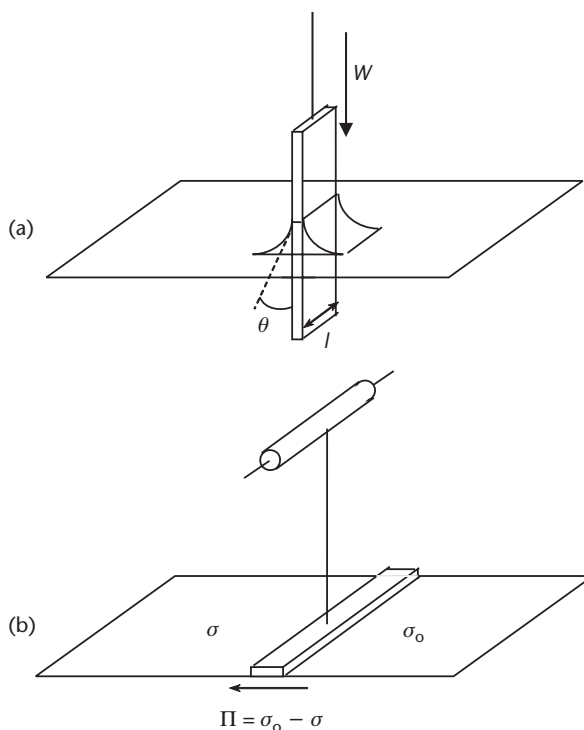
$$\Delta W = 2l\sigma$$

where  $l$  is the width of the paper (the paper thickness is simply neglected). In effect, the Wilhelmy balance measures the surface tension, the readings of which can be easily recalibrated to  $\Pi$ .

Another method called the Langmuir balance, which was used in the early LB years, measures the value of the surface pressure. The main element of this construction is a floating barrier parting the water surface coated with the monolayer from the pure water surface. The torsion of a rod connected at one end to that barrier is proportional to the surface pressure [see Figure 2.14(b)]. This method yields absolute values of the surface pressure, but it is quite difficult to use, due to problems of separation of the two compartments, cleaning of the partition, and vibrations.

The behavior of the molecular monolayer on the water surface can be well-described by the dependence of the monolayer surface pressure ( $\Pi$ ) versus the area occupied by a single molecule ( $A$ ), often called as  $\Pi$ - $A$  diagrams. Phase diagrams are quite complicated even for the simplest fatty acid molecules, and they were described in detail in many publications; see, for example, [153].

A schematic  $\Pi$ - $A$  diagram is presented in Figure 2.15. At very low surface concentrations of molecules (high area per molecule), as shown in Figure 2.13(a), the

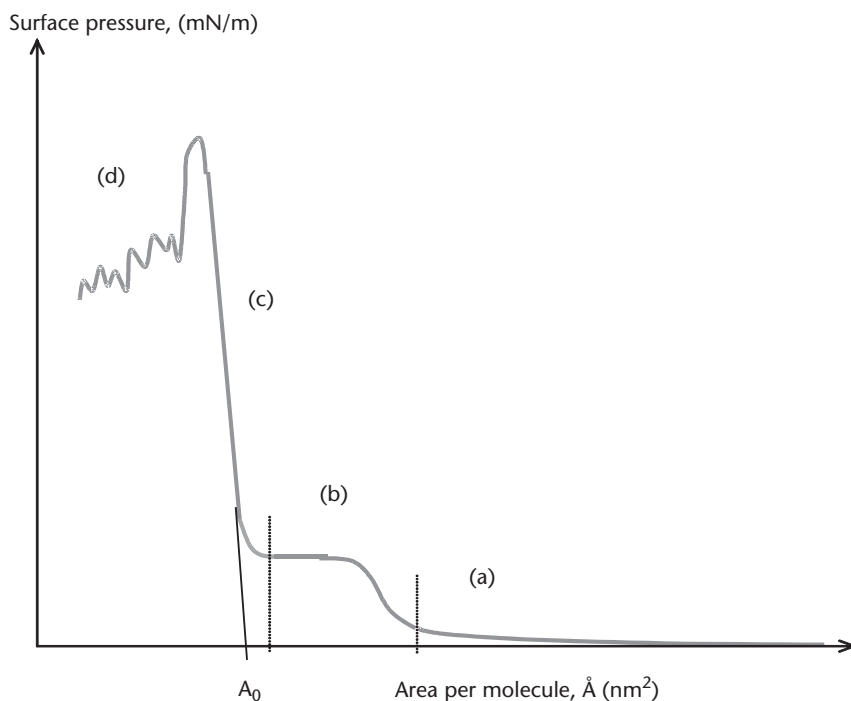


**Figure 2.14** Measurements of surface pressure with (a) Wilhelmy and (b) Langmuir balances.

monolayer behaves like two-dimensional ideal gas, and shows a very small (up to 1 mN/m) increase in  $\Pi$ , as shown in Figure 2.15(a). Further compression of the monolayer leads to a quasi-liquid two-dimensional stage, with the characteristic increase in the surface pressure followed by its saturation [see Figure 2.13(b) and Figure 2.15(b)]. Finally, in the stage of closely packed molecules, the monolayer can be described as a two-dimensional solid-state phase with a characteristic steep linear increase in the surface pressure [see Figure 2.13(c) and Figure 2.15(c)]. The extrapolation of the linear part of  $\Pi$ - $A$  diagram to intercept the  $A$  axis yields a characteristic value of the area per molecule in the condensed state ( $A_0$ ) (see Figure 2.15). It is assumed that the monolayer, having been transferred onto the solid substrate molecules, retains the same occupancy area of  $A_0$ . Further compression of the monolayer leads to its collapse, which appears on the  $\Pi$ - $A$  diagram as a drop in the surface pressure, followed by its irregular changes or oscillations [see Figures 2.13(d) and 2.15(d)].

It should be noted that only selected compounds from the fatty acids family, having a number of carbon atoms between 14 and 24, are suitable for LB film deposition [152]. The acids lighter than  $C_{14}$  are liquids at room temperature, and thus cannot exist in the solid form, either on the water surface or on the solid substrate. The compounds with the chain longer than  $C_{24}$  are too flexible, and thus tend to form fragile and unstable layers on the water surface.

The next stage of the formation of LB films is the deposition of monolayers of amphiphilic molecules compressed to the two-dimensional solid phase stage. In classical LB technique, it is fulfilled by the sequential dipping and withdrawing of the substrate into the water subphase. In the case of hydrophobic substrate, the

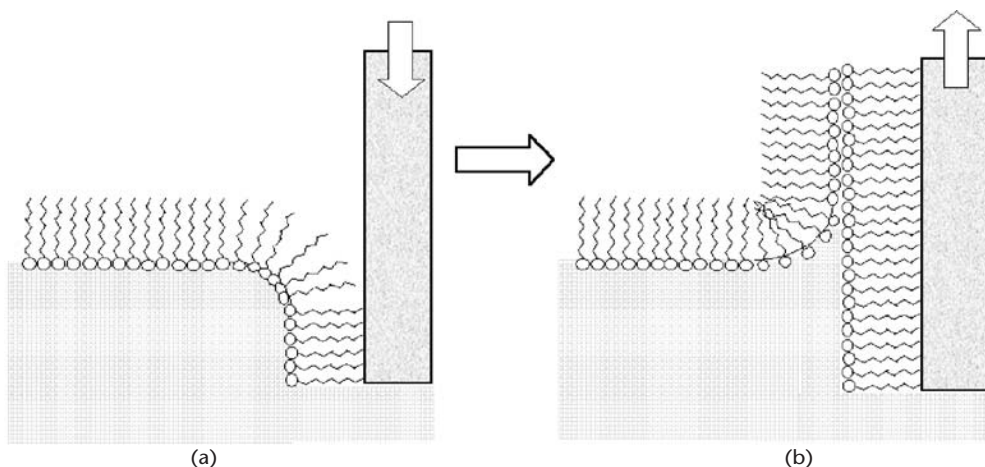


**Figure 2.15** Typical  $\Pi$ -A diagram of the Langmuir monolayer. (a) 2D gas state; (b) 2D liquid state; (c) solid state; and (d) monolayer collapse.

deposition process starts from dipping. In this case, the contact angle at a triple contact point substrate/air/water is much larger than  $90^\circ$  and usually lies in the range from  $120^\circ$  to  $130^\circ$ , which turns amphiphilic molecules with their hydrophobic chains towards the substrate. The first monolayer can be transferred onto the substrate surface in the course of the substrate downstroke, as shown in Figure 2.16(a). On withdrawing, the contact angle between the substrate surface, coated with one amphiphilic layer with head groups on top, is less than  $90^\circ$ , so that the floating layer is oriented with their head groups towards the substrate. Due to the interaction between polar groups, the next layer can be transferred to the substrate, as shown in Figure 2.16(b). This process can be repeated many times resulting in the formation of a multilayered film on the solid substrate. This is the most common Y-type of LB films, when molecules in the film are oriented head-to-head and tail-to-tail, and the period of the obtained molecular structure (in the direction perpendicular to the film surface) is equal to the double molecular length (see Figure 2.17). There are another two types of LB film structure, X and Z, also shown in Figure 2.17, which have periods of a single molecular length.

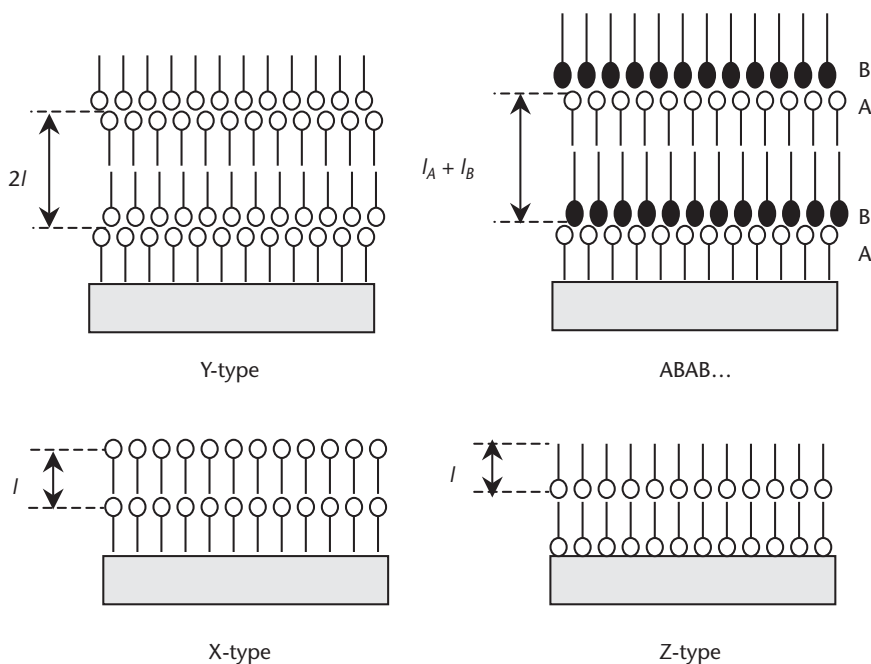
Another type of LB film, called alternative LB layers (or ABAB... layers), as shown in Figure 2.17, can be built using a double-compartment LB trough, by dipping the substrate into the compartment containing monolayer A, and withdrawing from the compartment containing monolayer B. More detailed discussion of different constructions of an LB trough will be given later. An important parameter of LB film deposition is the transfer ratio:

$$T = A_l/A_s$$



**Figure 2.16** Langmuir-Blodgett deposition process: (a) dipping a hydrophobic substrate, and (b) withdrawing the substrate.

where  $A_L$  is the reduction in the total area occupied by the monolayer, and  $A_S$  is the area of the substrate coated with the film. The value of  $T = 1$  indicates an ideal film transfer; however, in practice, its deviation from unity of about  $\pm 10\%$  is acceptable. The values of  $T$  sufficiently lower than unity indicate poor (patchy) coating, while  $T > 1$  is an attribute of the formation of supermonolayer structure. Very often LB were produced from fatty acid bivalent metal salts, which can be formed on the water surface according to the following reaction:



**Figure 2.17** Different types of LB film deposition: Y-type, alternative layers (ABAB...), X-type, and Z-type.

To perform such reactions in the monolayer, respective salts of bivalent metals, such as  $\text{Cd}^{2+}$ ,  $\text{Pb}^{2+}$ , and  $\text{Cu}^{2+}$ , typically with the concentration in the range of  $10^{-4}$  M, have to be added to the water subphase. Such monolayers are much more stable as compared to those formed from pure fatty acid molecules, and thus yield much better quality LB films. In fact, LB films of fatty acid metal salts were classical objects of colloid chemistry for many decades, starting from works by Langmuir and Blodgett.

As was already mentioned, there exist a number of commercial instruments for LB deposition based on different principles of monolayer compression and substrate dipping. Typical examples of LB troughs are shown schematically in Figures 2.18 and 2.19. A very common technique of moving barriers, shown in Figure 2.18, was implemented in NIMA and KSV troughs. In this case, the trough, usually made of PTFE, is filled with water up to the brim, so that the convex meniscus is formed. One or two PTFE barriers, which are rested on the trough brim, can slide right and left driven by stepper-motors, and thus control the area occupied by the monolayer. In order to reduce the through volume, they are usually made quite shallow (a few millimeters deep) all around the well, where the substrate is to dip (see Figure 2.18).

All types of LB troughs have one thing in common: an automatic system to control the surface pressure during film deposition. It consists of a surface pressure sensor (typically, the Wilhelmy balance described earlier). A differential amplifier compares the signal from the pressure sensor with the reference signal, corresponding to a target pressure, and provides a negative feedback to the stepper-motor responsible for barriers movement.

Another principle of the monolayer compression, called “a constant perimeter tape,” as shown in Figure 2.19, uses a PTFE-coated tape stretched between PTFE bobbins; some of them were fixed, and the others mounted on a moving frame. Such

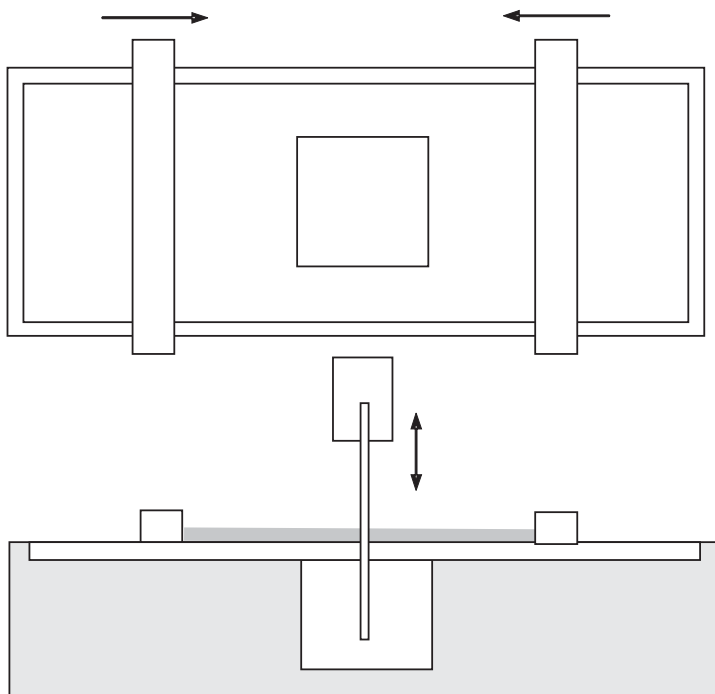
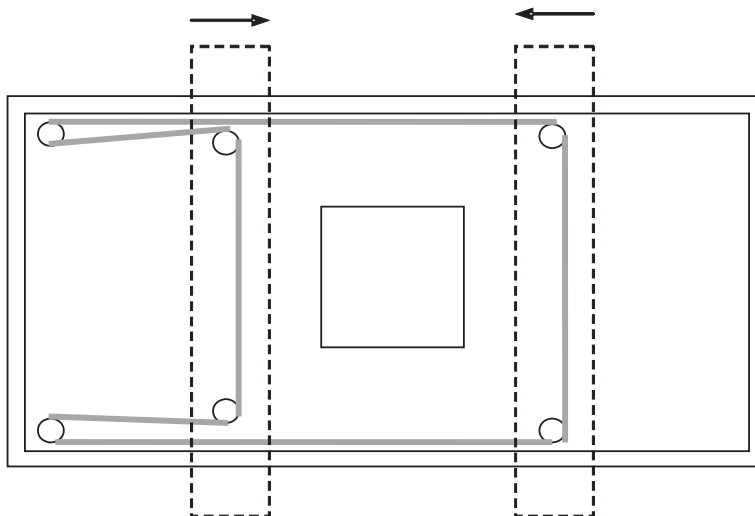


Figure 2.18 LB trough with moving barriers.



**Figure 2.19** LB trough equipped with constant perimeter tape.

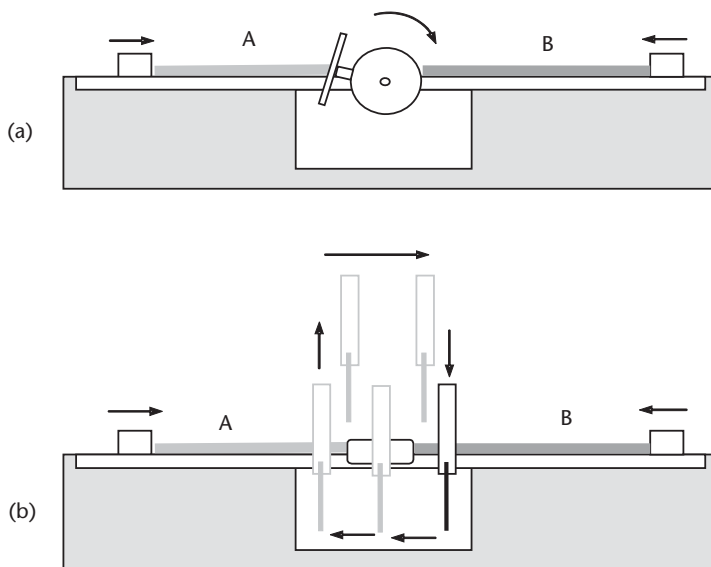
constant perimeter tape, partially dipped into the water in the LB trough, provides the control of the monolayer area. Joyce Loyble and Lauda troughs are equipped with such monolayer compression system.

Most of the modern LB troughs are equipped with dipping mechanisms for alternative LB layers deposition. Two of the most common constructions of such dippers are the rotor, as shown in Figure 2.20(a), and the gate, as shown in Figure 2.20(b). In the first configuration, the substrate is fixed on a PTFE cylindrical rotor, which separates compartments A and B of the trough. As shown in Figure 2.20(a), during the rotation, the sample goes down through the monolayer A, then moves underwater to the compartment B, and emerges through the monolayer B. NIMA troughs are equipped with such rotor mechanism.

Another option, realized in KSV troughs, comprises the partition of the trough surface with the gate made of two flat PTFE coated springs, as shown in Figure 2.20(b). The sample holder fixed on the PTFE coated arm can move vertically and horizontally to perform the cycle, as illustrated by Figure 2.20(b). Both constructions suffer the cross-contamination of the compartments A and B, which is more essential for rotor systems. At the same time, the construction of a rotating dipper is simpler, which makes NIMA equipment less expensive than KSV.

LB deposition seems to be quite an easy technique; however, there are many external factors affecting the successful film transfer, and thus the quality of LB films. These factors are named and discussed next.

1. *Water contamination.* As was discussed earlier, the presence of metal ions may lead to the formation of fatty acid salts on the water surface. In contrast to bivalent metals, which act as a beneficial factor for the monolayer stabilization, other metal ions, for example  $\text{Na}^+$  and  $\text{K}^+$ , even in low concentrations in the range of  $10^{-6}$  M, can adversely affect the monolayer. Changes in the subphase pH may affect the dissociation of COOH head groups and the salt formation. These impurities in water may adversely effect the LB film deposition.



**Figure 2.20** LB trough for alternative layers deposition equipped with: (a) a rotor, and (b) a gate dipper.

2. *Surface contamination.* The contamination of the surface by other amphiphilic molecules is another crucial factor affecting LB film deposition. The contamination of the water surface by other amphiphilic compounds or simply by any grease in the smallest amounts in the range of nanograms may cause significant changes in the monolayer  $\Pi$ -A diagram and, therefore, may hamper the LB film deposition. Therefore, the cleaning of the LB trough with organic solvents (e.g., chloroform or isopropanol) is a very important part of the successful LB deposition. An accidental touch of the water surface with a finger usually causes irreversible contamination of the monolayer, and requires thorough cleaning of the water surface using an air-suction pump, or even requires complete replacement of the water subphase with additional trough cleaning.
3. *Dust contamination.* The presence of dust particles of micron or submicron dimensions on the water surface produces a huge impact on the formation of the molecular monolayer having a thickness of at least two orders of magnitude smaller. Such surface disturbances may trigger the so-called slow collapse of the monolayer, which appeared as a spontaneous reduction of the surface area under a constant surface pressure. The formation of two- and three-folds of the monolayer is the most likely mechanism of the slow collapse.
4. *Vibration.* Vibration is another factor causes monolayer collapse. That is why LB trough should be placed on an antivibration table to reduce low-frequency vibrations. High-frequency vibrations can be substantially reduced by using a plate made of natural stone (e.g., granite or marble).

Apart from these items, there are many other factors affecting the successful film deposition. These include: the subphase contents, the choice of solvent, the concentration of spreading solution, the evaporation time, the value of the target surface

pressure, the monolayer compression speed, the dipping speed for both down- and up-strokes, and the drying time. Taking into consideration all the above details, successful LB deposition requires a great deal of experience and patience.

### 2.3.2 Special Types of LB Films—Composite LB Films

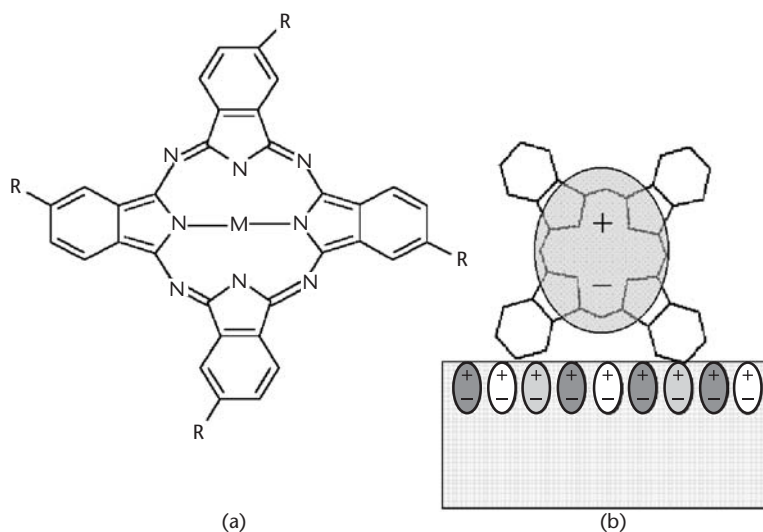
In the 1980s and 1990s, when the LB film method was considered as the main technology for molecular electronics, the range of amphiphilic compounds for LB film formation synthesized at that time was vast. Apart from various types of long-chain hydrocarbons (saturated and nonsaturated) with different head groups, the list includes different organic functional molecules (i.e., dyes, cavitands, macrocomplexes, and polymers), modified with respective hydrocarbons and head groups [152]. The main criterion for good amphiphilic compounds is to have a balance between the hydrophobic interaction between hydrocarbon tails and the attraction of head groups to the aqueous subphase. The domination of the hydrophobic part may result in the instability of monolayers on the water surface (slow collapse), and the formation of supermonolayer structures. In this case, the film transfer is not stable, with the transfer ratio deviating substantially from unity. Domination of the hydrophilic interaction may result in the inclusion of water into LB film structure, and thus cause a poor transfer ratio during the sample upstroke. In extreme cases, the layer can be peeled off from the substrate in the course of the upstroke.

*LB Films of Phthalocyanines* Sometimes amphiphilic properties are not necessary to form monolayers on the water surface. An interesting example of this type of property is phthalocyanines (Pcs), which are a large group of organic dyes [154] having a general chemical structure as shown in Figure 2.21. The main trend for these compounds is to form molecular aggregates (stacks) [154]. This tendency can be controlled by using different substituting groups and central atoms [155]. However, in all cases, the main building block of the monolayer is the molecular stacks lying on the water surface (see, for example, [156]). Pc molecules having 18  $\pi$ -electrons can be easily polarized within the molecular plane by the external electric field; for example, originated from the oriented dipole moments on the water surface. Such polarization, as shown schematically in Figure 2.21, makes stacked Pc molecules behave like amphiphiles. The formation of the monolayer and its transfer depend very much on hydrophilic-hydrophobic balance in Pc molecular aggregates.

*Calixarene LB Films* Another relatively new object for LB film deposition are calixarenes, a typical example of cavitand compounds, initially suggested as selective receptors for molecular recognition [157]. Chemical structures of two of the most common branches of these compounds, namely calix[4]resorcinarenes (C[4]RA) and calix[n]arenes (C[n]A), where  $n = 4, 6, 8$ , are shown in Figures 2.22 and 2.23, respectively.

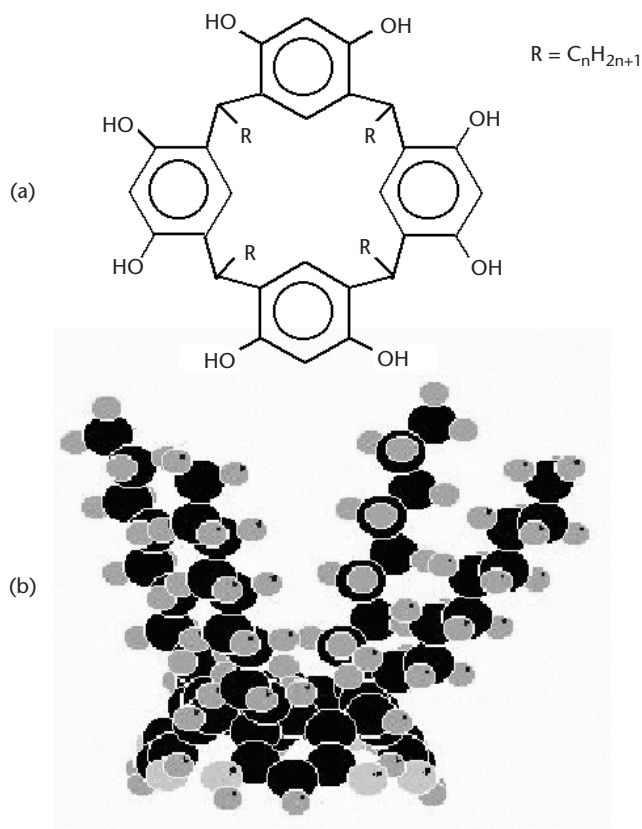
Both types of molecules consist of calixarene baskets modified on the upper rim with hydrocarbons (or other hydrophobic groups), and with the OH polar head groups on the lower rim. Such modifications make these molecules amphiphilic, and thus suitable for LB film deposition. The first publication on calixarene LB films appeared in 1995 [158], and this subject was developed further in subsequent years. The distinctive features of amphiphilic calixarenes lie in the combination of



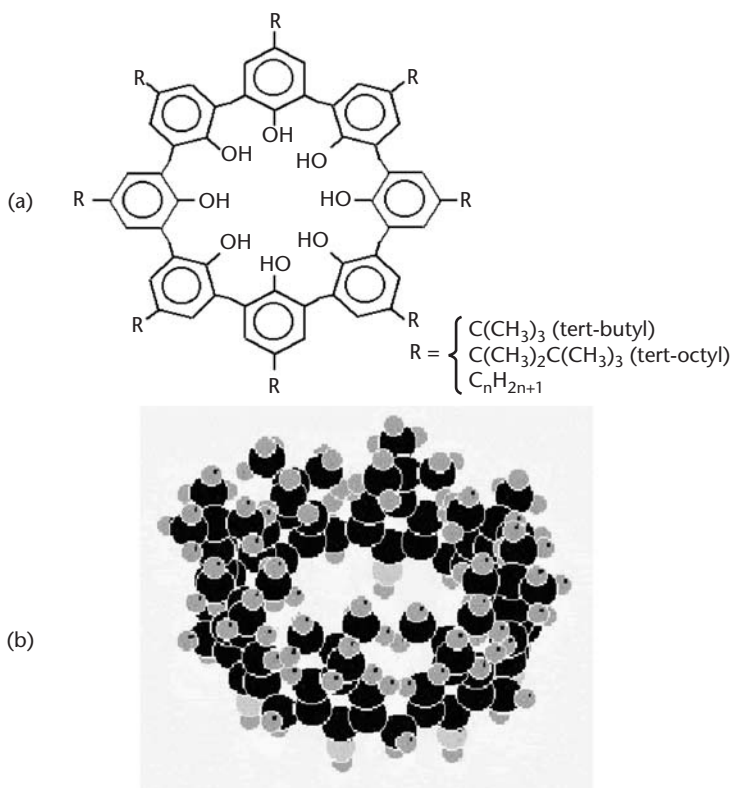


**Figure 2.21** (a) Chemical structure of phthalocyanines, and (b) polarization of Pc molecules on the water surface.

relatively rigid calixarene basket with flexible hydrophobic chains, and results in a strong hydrophobic interaction between LB layers well balanced by a large number



**Figure 2.22** Amphiphilic calix[4]resorcinarene: (a) chemical structure, and (b) pseudo-3D quick-fill model.

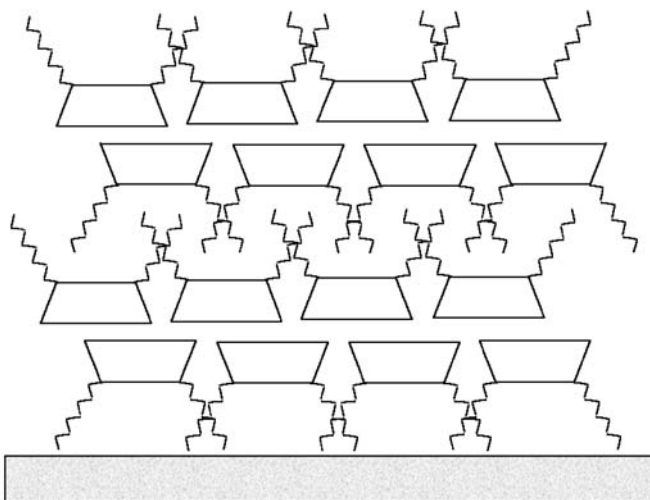


**Figure 2.23** Amphiphilic calix[8]arenes: (a) chemical structure, and (b) pseudo-3D quick-fill model.

of hydrophilic groups on the lower rim. The structure study of calixarene LB films using different methods, such as  $\Pi$ -A isotherms, low angle X-ray diffraction, ellipsometry and surface plasmon resonance (SPR), allowed us to propose a layer-by-layer structure for these films, as shown in Figure 2.24. The interdigitation of hydrocarbon chains explains a strong hydrophobic interaction between calixarene molecules. Further study [159] has shown that some calixarenes behave not like traditional amphiphilic molecules, but form aggregates in the solution prior to LB deposition. As a result, LB films of calixarenes appeared to be much less ordered in the normal direction, as compared to the classical LB films of fatty acids.

Calixarene LB films represent a unique example of nanoporous film. Such pores, which have typical dimensions in nanometer range, were formed by calixarene, cavities, empty spaces between calixarene baskets, and between hydrocarbon chains. Absorption of various gases and vapors is therefore expected in such films. Indeed, calixarene LB films have found their application as sensitive membranes in sensors of organic solvent vapors, such as benzene, toluene, and hexane [160]. Moreover, a nanoporous matrix of calixarene LB films is quite flexible, and, therefore, can accommodate large foreign objects including macromolecules, polymers, and inorganic nanoparticles. These properties of calixarene LB films are a subject of the following paragraphs.

*LB Deposition of Nonamphiphilic Objects* The mechanism of polarization of phthalocyanine molecules on the water surface can explain the pseudo-amphiphilic

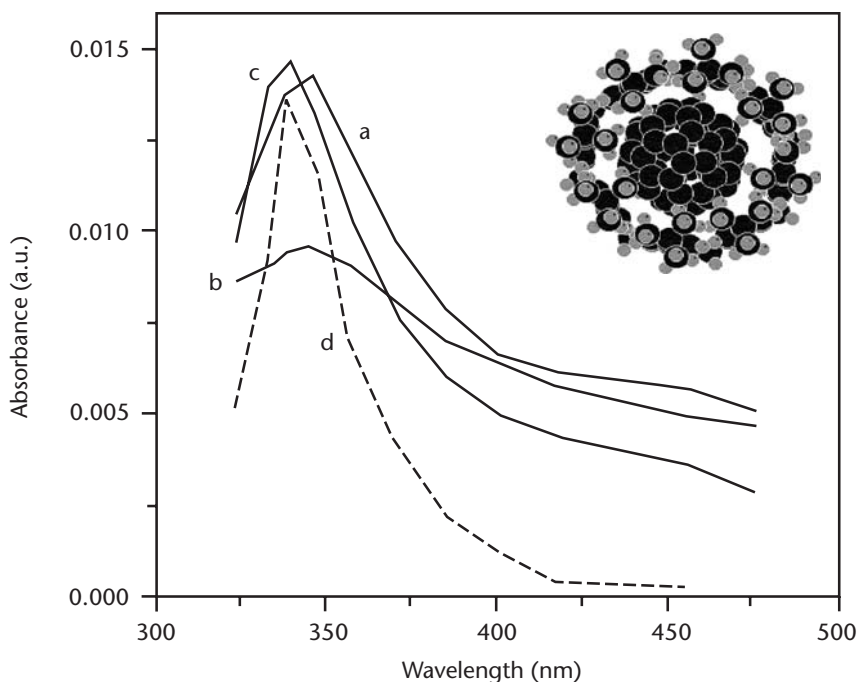


**Figure 2.24** Schematic representation of calix[4]resorcinarene LB film.

behavior of many other objects. It is known, for example, that nonamphiphilic fullerenes  $C_{60}$  and  $C_{70}$  can form stable monolayers on the water surface. The reason for this is a large number of  $\pi$ -electrons in fullerenes, which can be polarized on the air-water interface. At the same time, the transfer of  $C_{60}$  and  $C_{70}$  onto the solid substrates using LB technique is problematic, because of the lack of hydrophobic interaction between fullerene molecules. The modification of fullerene molecules with some functional groups (e.g., hydrocarbons) may improve film transfer [161], but the unique symmetry of fullerenes will be lost. The idea of mixing of nonamphiphilic fullerenes with some other amphiphilic compounds was suggested in [162], and calixarenes were found to be the most suitable candidates to form such mixtures. It was demonstrated that  $C_{60}$  molecules can be successfully mixed with different calixarene derivatives, and then transferred onto solid substrates [162]. However, in most cases,  $C_{60}$  molecules do not form a homogeneous mixture with calixarenes, but rather form aggregates. Optical absorption spectra of those  $C_{60}$ /calixarene mixed LB films shows the broadening and red shift of the absorption band at 344 nm in respect to the spectral band of  $C_{60}$  monomers in solution at 335 nm, the fact attributed to the aggregation of  $C_{60}$  molecules (see Figure 2.25).

Only in the case of using tertbutyl-calix[8]arene, is the absorption band of  $C_{60}$  close to that in solution, as shown in Figure 2.25(c). The explanation of such behavior lies in the known fact of the formation of  $C_{60}$ /Calix[8]arene inclusion complex, as shown in the inset to Figure 2.25, which is exploited in [163] for the separation of the  $C_{60}$  fraction from higher mass fullerenes  $C_{70}$  and  $C_{86}$ . The formation of inclusion complexes between amphiphilic calix[4]resorcinarenes and octasubstituted metal free phthalocyanines was reported in [164]. In this work, measurements of optical absorption spectra of C[4]RA/ $H_2$ Pc mixed monolayers on the water surface demonstrated braking of Pcs aggregates and gradual spectra transformations towards the characteristic spectrum of monomer  $H_2$ Pc molecules, along with the increase of the surface pressure.

The above approach was successfully adopted for LB deposition of nonamphiphilic polymers, such as polyaniline (PAN) and polyphenylsulfide (PPS). Both polymers are too hydrophilic, and thus not suitable for LB deposition. Mixtures of the



**Figure 2.25** Optical absorption spectra of  $C_{60}$  incorporated into different matrices: (a) C[4]RA; (b) phosphorilated C[4]RA; (c) C[8]A; and (d) liquid toluene. Inset shows the pseudo-3D model of  $C_{60}$ /C[8]A inclusion complex. (From: [162]. © 1997 Elsevier. Reprinted with permission.)

above polymers with the amphiphilic C[4]RA of different molar weight ratio from 5:1 to 1:5 were formed and transferred onto solid substrates [165, 166]. The resultant films found their application in gas sensing. Because of the high gas permeability of calixarene matrix, composite LB films of PPS/C[4]RA showed much faster response to ozone as compared to pure PPS spun films [166].

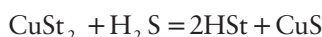
This method of LB was successfully exploited for the immobilization of globular protein molecules onto different solid substrates, which is an important part of biosensor research and development. In fact, the incorporation of proteins into the phospholipid LB film structure is the most effective way of protein immobilization, very close to the natural environment for proteins embedded into lipid biomembranes. The majority of proteins are not amphiphilic, but soluble in water, so that they cannot form stable monolayers on the water surface. On the other hand, a high solubility of proteins is advantageous for their LB deposition. Proteins dissolved in the aqueous subphase, and being electrically charged (depending on the solution pH), can be electrostatically attached to the phospholipid monolayer on the air-water interface. The transfer of such phospholipid/protein complexes onto the solid substrate can be done by horizontal lifting, often called as Langmuir-Schaeffer (LS) method [167]. A number of successful experimental attempts of the immobilization of different biomolecules, such as valinomycin [168], enzymes [169], and biotin-streptavidin systems [170], by means of LB technique have been done during last 10 to 15 years for biosensing applications [171, 172].

As previously mentioned, metal and semiconductor colloid particles were often stabilized with hydrophobic radicals, such as alkyl-thiols, which makes them suitable for LB deposition. These nanoparticles, which high electron density, can be

polarized on the water surface, while alkyl chain fur surrounding nanoparticles provides hydrophobic interaction. The mechanism of the nanoparticles' polarization, illustrated in Figure 2.26, is similar to that proposed for phthalocyanine molecules and other nonamphiphilic compounds. As a result, colloid nanoparticles can form stable monolayers on the water surface, and can be transferred onto solid substrates with either the Langmuir-Shaeffer (see the scheme in Figure 2.26) or the Langmuir-Blodgett methods.

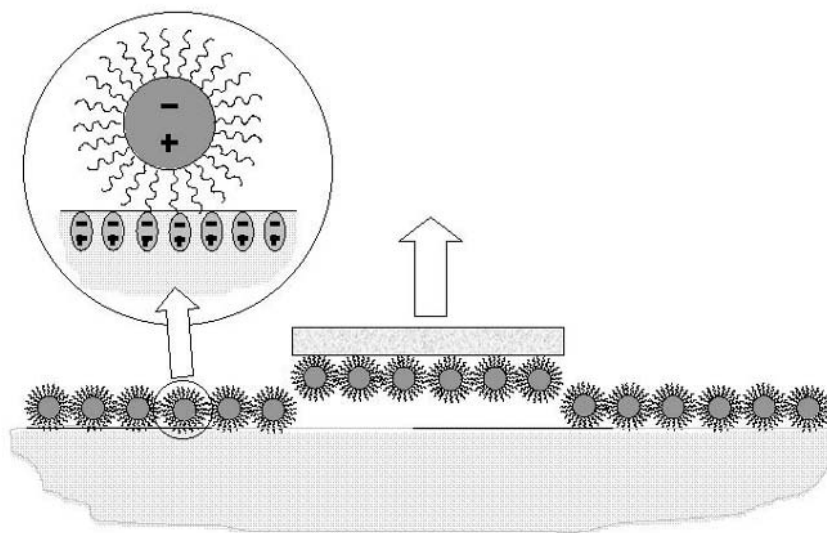
### 2.3.3 Formation of II-VI Semiconductor Particles in LB Films

An elegant method of the formation II-VI semiconductor nanoparticles was proposed by Barraud and colleagues [173]. The initial idea was to form two-dimensional semiconducting layers by exposure of copper stearate LB films to  $H_2S$  gas:



However, instead of the expected conducting CuS planes within each stearic acid bilayer, LB films appeared to be nonconductive, but containing small CuS aggregates. The driving force of CuS aggregation is a general trend of conserving the surface energy of metal sulphide nuclei and the formation of larger particles. The process of the formation of metal sulphide particles is illustrated in Figure 2.27.

The formation of II-VI semiconductor nanoparticles, and the physical properties of such objects, were studied intensively by Barraud and his colleagues, as well as by many other scientists working in this area [174–179]. This approach was quickly expanded to cover the whole range of II-VI compounds, with bivalent metals of Cu, Cd, Pb, Hg, and S, and Se as counterparts from the VI group. Different fatty acids, as well as other amphiphilic compounds, were tried for LB film matrix formation

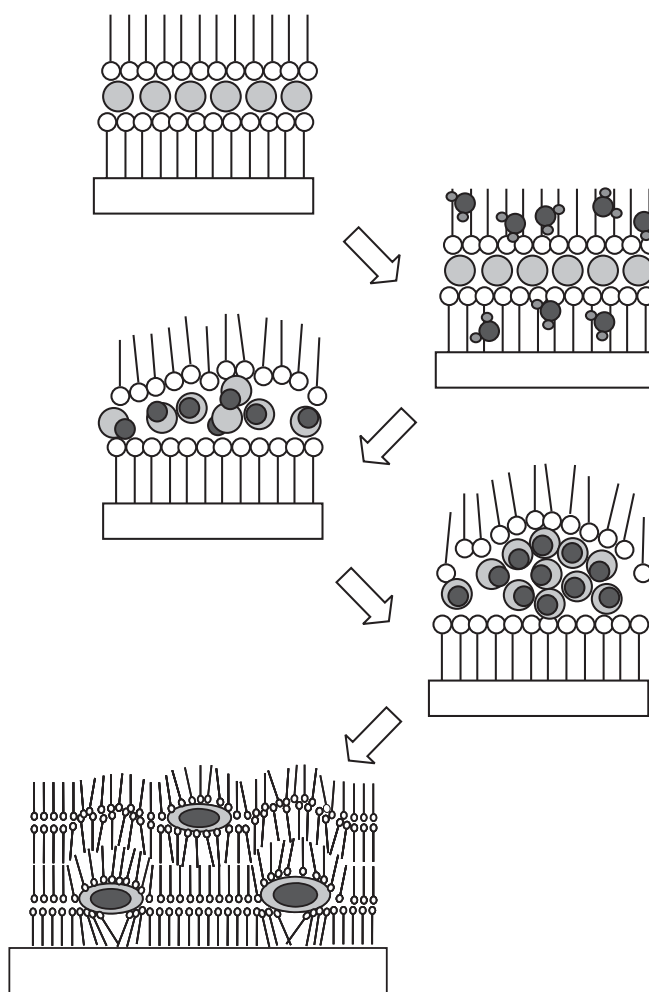


**Figure 2.26** Formation of the nanoparticle monolayer on the water surface, and its LS transfer of the onto the substrate. The inset illustrates the polarization of colloid particles on the water surface.

[178–181]. The size of metal-sulphide clusters, typically estimated from UV-vis absorption spectra measurements, was in the range from 3 to 5 nm. The formation of such particles was confirmed with different methods, including optical techniques of SPR, ellipsometry and photoluminescence (PL) [182], X-ray photoelectron spectroscopy (XPS) [178], TEM, electron diffraction [180], STM, and AFM [180, 183].

The use of LB films of cavitand amphiphilic compounds, particularly tert-octyl-calix[4(or 8)]arene carboxylic Cd salt, has resulted in the formation of much smaller CdS clusters with the size of 1.5 nm [178]. It was suggested that the presence of calixarene cavities restricts the aggregation of CdS by capturing some CdS molecules and small CdS clusters within calixarene cavities.

An attempt at modeling of the formation of II-VI semiconductor nanoparticles within LB films has been done recently [184]. The situation is similar to the formation of CdS/CdSe nanoclusters in halcogenide glass, which was theoretically described by Lifschits and Slezov [185]. The formation of primary CdS/CdSe nuclei



**Figure 2.27** Consecutive stages of the formation of CdS nanoparticles in LB films of cadmium stearate (CdSt<sub>2</sub>) (from top to bottom): initial bilayer of CdSt<sub>2</sub>; formation of CdS during exposure to H<sub>2</sub>S gas; nucleation of CdS; and further aggregation and the formation of larger CdS clusters.

occurred in the course of cooling down the glass malt oversaturated with the above impurities. Further aggregation was driven by the reduction in the surface energy of CdS/CdSe, and by the material supply due to diffusion. The above processes have resulted in the asymmetrical size dispersion of CdS/CdSe particles, called the Lifschits and Slezov distribution.

In our case of the formation of CdS nanoparticles in LB films, two-dimensional diffusion of CdS should be considered. It was also assumed that CdS nuclei were already formed, and further aggregation was driven by the reduction in the surface energy (surface tension) of those primary clusters. For the sake of simplicity, spherical CdS clusters were considered. Assuming that CdS grains develop further due to a slow, quasi-stationary diffusion, the distribution of CdS molecules in the LB film obeys Laplace's equation:

$$\Delta C(x, y) = 0 \quad (2.1)$$

where  $C(x, y)$  is the two-dimensional concentration of CdS. Unlike the three-dimensional situation [185], where the solution of Laplace's equation decays at infinity as  $1/r$ , in the two-dimensional case it grows logarithmically with the distance from a single grain. Therefore, the quasi-stationary average concentration is determined self-consistently by the size distribution of the grains. The radial distribution of CdS concentration near the grain is given by:

$$C(r) = \frac{(C_{0a} - C_{av}) \ln(r/d_0)}{\ln(a/d_0)} + C_{av} \quad (2.2)$$

where  $C_{0a}$  is the equilibrium concentration near the grain of the radius  $a$ ,  $C_{av}$  is the average concentration in the film, and  $d_0$  is a parameter of the system of the grains that we determine self-consistently. According to [185],

$$C_{0a} = C_{0\infty} (1 + 2\sigma v/kTa) \quad (2.3)$$

where  $\sigma$  is the surface tension and  $v$  is the molar volume of solid CdS. The parameter  $C_{0\infty}$  is the equilibrium concentration of CdS molecules near the grain of an infinite-size. The whole distribution of CdS concentration in the film is given by:

$$C(x, y) = C_{av} + \sum_i \frac{(C_{0\infty} (1 + 2\sigma v/kTa_i) - C_{av}) \ln(r_i/d_0)}{\ln(a_i/d_0)} \quad (2.4)$$

where  $r_i \sqrt{(x - x_i)^2 + (y - y_i)^2} < d_0$  is the distance from the  $i$ th grain, and parameter  $d_0$  is approximately three times less than the intergrain distance. To derive the time-dependent equation for the variation of the grain size  $a_i$ , we assume that the grains remain spherical during coalescence. The total diffusion flux near the grain is then

$$I(a_i) = -2\pi r D \frac{\partial C(r)}{\partial r} \quad (2.5)$$



where  $D$  is the two-dimensional diffusion coefficient. As a result, we have a time-dependent equation for  $a_i$ :

$$\frac{da_i}{dt} = D\nu \frac{C_{av} - C_{0\infty} (1 + 2\sigma v/kTa_i)}{2a_i^2 \ln(a_i/d_0)} \quad (2.6)$$

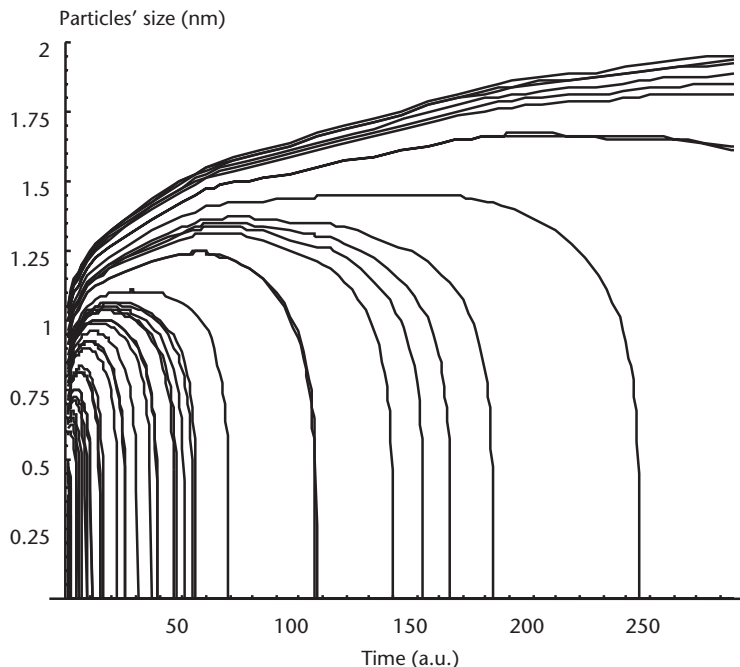
Note that the parameter  $C_{av}$  is also time dependent, to ensure the CdS conservation. Similar to the Lifshitz-Slezov model [185], we can define critical radius

$$a^* = \frac{2\sigma v C_{0\infty}}{kT(C_{av} - C_{0\infty})} \quad (2.7)$$

Equation (2.6) shows that large grains with  $a_i > a^*$  grow slowly, whereas small grains ( $a_i < a^*$ ) disappear within the finite time of  $\tau \sim a^3/DC_{av}\nu$  for  $C_{av} \sim C_{0\infty}$  or  $\tau \sim a^4 kt/DC_{0\infty}\sigma v^2$ . Numerical simulation of the (2.6) is shown in Figure 2.28.

The initial condition was set for particles distributed randomly, with sizes less than 1 nm, and with initial  $C_{av}$  corresponding to  $a^* = 0.5$  nm. The obtained evolution function of the particles' size  $f(a)$  in the two-dimensional case at large times is similar to that in the Lifshitz-Slezov model [185]. It also has a peak at  $a = a^*$ , and it is not very sensitive to the initial conditions. However,  $f(a)$  is flatter at small  $a$ , and drops more rapidly at large  $a$  than in the three-dimensional case. The average concentration in the two-dimensional case decreases slower than in the three-dimensional case, and the critical radius depends on time as  $a^*(t) \sim a_0^* t^{1/4}$ .

The results of the above simulation are in good agreement with the experimental absorption spectroscopy study on the evolution of CdS particles. As shown in

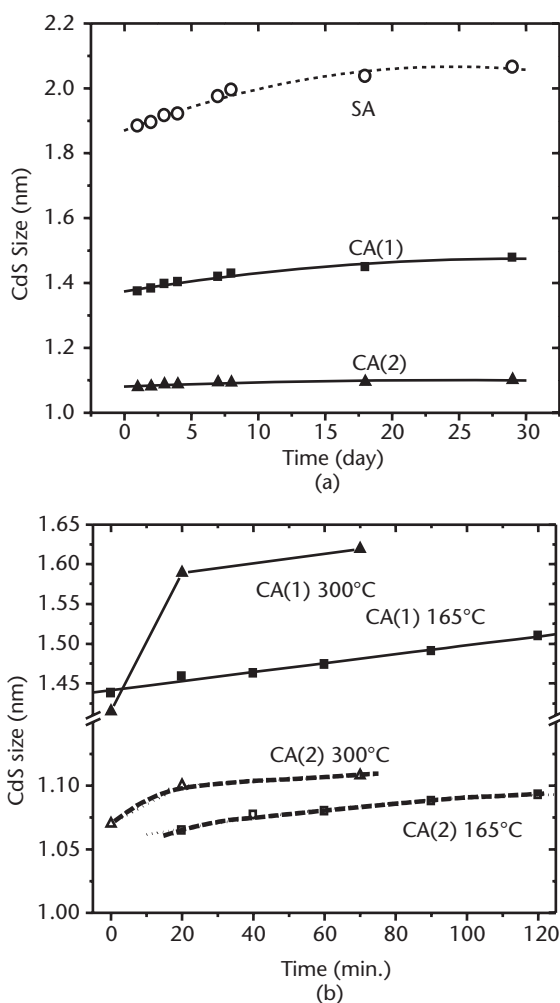


**Figure 2.28** Size evolution of CdS grains (*From*: [184]. © 2002 Institute of Physics. Reprinted with permission.)

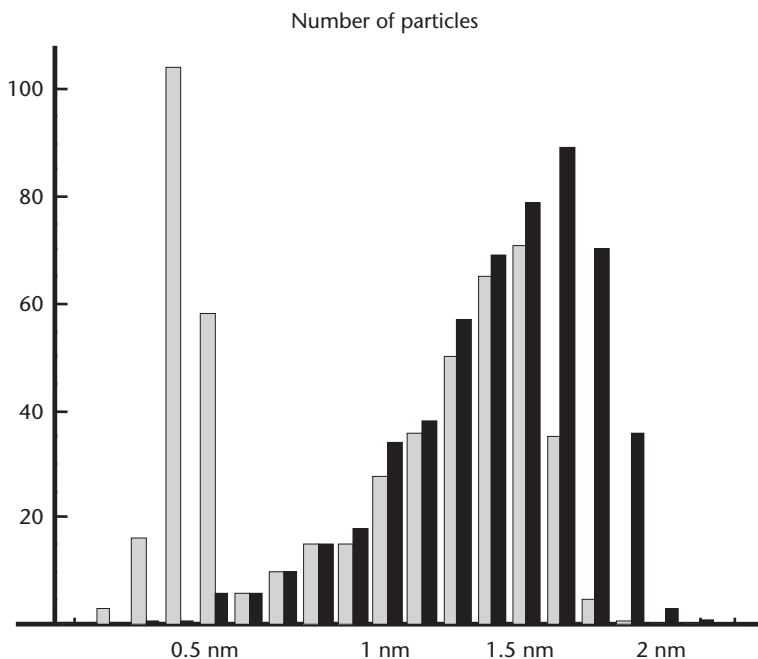


Figure 2.29(a), the increase in the nanoparticle size was observed for both stearic acid and calixarene LB films at room temperature in the course of a several measurements during one month. The size increase of 12.5% for CdS clusters in SA LB films is much larger than the values of 4.4% and 0.9% for two characteristic sizes obtained, respectively, from the first and second absorption peaks in CA LB films. This fact supports the idea of the suppressed aggregation in CA LB films. At elevated temperatures, the particles' growth in CA films is much more noticeable, as illustrated by Figure 2.29(b). Two characteristic sizes of 1.42 and 1.08 nm for CdS nanoparticles in calixarene LB films can be related, respectively, to the clusters formed between the calixarene molecules and clusters within calixarene cavities having size of approximately 1 nm.

The size dispersion function for CdS particles in stearic acid LB films, shown in Figure 2.30 as black bars, closely resembles the Lifshitz–Slezov distribution for bulk halcogenide glass samples. Restrictions on the value of diffusion coefficient ( $D$ ),



**Figure 2.29** Time dependencies of the size of CdS nanoparticles in LB films of stearic acid (SA) and calix[4]arene [CA(1) and CA(2)], obtained from the first and second absorption peaks, respectively, monitored at (a) room temperature and (b) elevated temperatures.

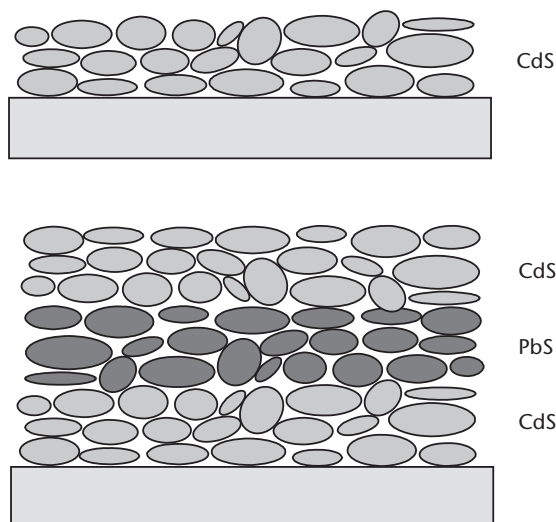


**Figure 2.30** Size dispersion for CdS nanoparticles in stearic acid LB films (black bars), and for calixarene LB films (gray bars). (From: [184]. © 2002 Institute of Physics. Reprinted with permission.)

imposed during the simulation, resulted in a double peak distribution function, shown as gray bars in Figure 2.30. This result gives an excellent qualitative agreement with the experimentally obtained size distribution of CdS clusters in calixarene LB films. This confirms once again the mechanism of the restricted diffusion of CdS in calixarene LB films, due to the capturing of some CdS molecules within CA cavities. For SA films, the segregation, described by (2.6), remains longer until  $a_i$  becomes very small, which explains why the typical size of large grains in SA is greater than in CA films.

The LB film approach has attracted the attention of many scientists and engineers, due to its technological simplicity and exciting applications in single-electron devices and semiconductor superlattices. Single-electron quantum processes will be discussed later in the book. Pure II-VI semiconducting layers can be formed from the LB film/metal sulphide composites described above, by washing out the LB film matrix in some volatile organic solvents [186] (see Figure 2.31). This seemingly easy procedure requires, however, a high level of thoroughness. The substrate has to be placed into a shallow plastic beaker horizontally until the solvent evaporates completely, otherwise the flow of liquid solvent may carry away CdS material together with the organic. This procedure has to be repeated several times until all organic molecules removed. Yet the above procedure has to be performed in the super-clean environment in order to prevent contamination of II-VI materials. This approach was successfully implemented for the formation of thin films of different metal sulphide materials, namely, CdS, PbS, ZnS, and CuS [183, 186–188].

Furthermore, semiconductor superlattices can be produced from LB films containing layers of different II-VI nanoparticles; for example, CdS/PbS, as shown in Figure 2.31. Such superlattices, consisting of wide and narrow bandgap



**Figure 2.31** Formation of CdS layers and CdS/PbS superlattices by washing out the organic film in chloroform.

semiconductors, can be used for the development of resonance tunneling devices [189] or light-emitting devices (lasers) [190]. From this point of view, the technology for the formation of semiconductor superlattices can be considered as an extremely attractive alternative to very expensive technologies, such as MBE.

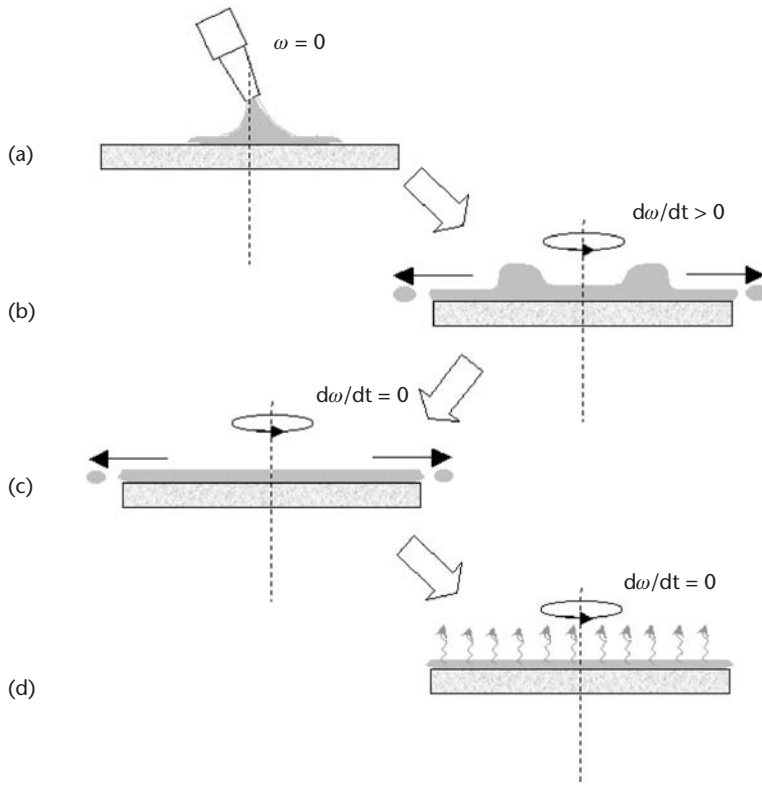
## 2.4 Spin Coating

The method of spin coating was known for decades as a main technique for the deposition of polymer layers onto flat solid surfaces, and particularly for photoresist deposition in microelectronics fabrication. The idea is very simple, and consists of spreading of a polymer solution onto the substrate fixed on a stage, rotating at a speed in the order of thousands of revolutions per minute. Under the influence of the central force, the polymer solution spreads evenly over the large area and dries out, due to the solvent evaporation during the rotation. After additional baking at elevated temperatures, a polymer layer is finally formed on the surface.

The process of spin coating can be formally split in four stages, as shown in Figure 2.32: (1) dispersion of the solution onto the solid substrate, (2) acceleration to its nominal rotation speed, (3) thinning of a liquid layer during rotation at a constant nominal speed dominating by viscous force, and (4) hardening of the coating dominating by solvent evaporation. In practice, especially when highly volatile solvents used, the last two stages overlap.

The hydrodynamic theoretical model was developed for the two last stages of spin coating (i.e., viscose and evaporation dominated stages) [191, 192]. In the viscose domination stage, the equilibrium between centrifugal and viscous forces takes place according to a following equation:

$$\eta \frac{\partial^2 v}{\partial z^2} = -\rho \omega^2 r \quad (2.8)$$



**Figure 2.32** Four stages of spin coating: (a) solution dispersion, (b) acceleration, (c) viscous force domination during steady spinning, and (d) solvent evaporation domination during steady spinning.

where  $z$  and  $r$  correspond to the vertical and radial directions, respectively, in the cylindrical coordinates;  $\eta$  and  $\rho$  are, respectively, the viscosity and density of the fluid;  $v$  is the fluid velocity, and  $\varpi = 2\pi f$  is the rotation frequency. The film was considered to be uniform, that is, the film thickness  $h$  is invariant on the radius. The solution of the (2.8) with the flow continuity condition

$$\frac{dh}{dt} = -\frac{2\rho\omega^2}{3\eta} h^3 \quad (2.9)$$

and the appropriate boundary conditions yields a following expression for the film thickness:

$$h = h_0 \left[ 1 + \left( \frac{4\rho\omega^2}{3\eta} \right) h_0 t \right]^{-\frac{1}{2}} \quad (2.10)$$

In this formula,  $h_0$  is the initial film thickness at  $t = 0$ , which corresponds to the beginning of stage 3 of a stable rotation. The evaporation of solvent from the spun fluid was not considered at the above situation, so that both the fluid density and viscosity remain constant. Therefore, the dependencies of  $h \sim \omega^{-1}$  and  $h \sim t^{-1/2}$  are characteristic for stage 3 of the spin coating.

The evaporation of solvent, which is a crucial part of the formation of a solid spun film, can be taken into account by adding the evaporation rate  $e$  in the continuity condition:

$$\frac{dh}{dt} = -\frac{2\rho\omega^2}{3\eta}h^3 - e \quad (2.11)$$

Both parameters in (2.11),  $\rho$  and  $\eta$ , are becoming time dependent because of the condensing and hardening of the spun fluid during solvent evaporation. The exact solution of (2.11) is difficult, and requires numerical calculations. That is why stage 4 of spin coating, entirely controlled by solvent evaporation, was introduced in [192]. Respective critical values of  $\rho_0$ ,  $\eta_0$ , and  $c_0$  for the fluid concentration can be introduced as:

$$(1 - c_0) \frac{2\rho_0\omega^2}{3\eta_0} = e \quad (2.12)$$

From this point onwards, the evaporation has become dominating, and the viscous term can be excluded from (2.11). The solution for the expected final thickness of a spun film is given by the following formula:

$$h_f = c_0(1 - c_0)^{-\frac{1}{3}} \left( \frac{\rho_0}{\eta_0} \right)^{\frac{1}{3}} \omega^{-\frac{2}{3}} e^{\frac{1}{3}} \quad (2.13)$$

If the evaporation rate is constant during stage 4, which may take place for highly volatile solvents, then  $h_f \sim \omega^{-2/3}$ . However, the evaporation rate can be also dependent on the spinning speed as  $e \sim \omega^{1/2}$ , considering the air flow above the sample. In this case,  $h_f \sim \omega^{-1/2}$ , the dependence observed in many practical cases, especially when less volatile solvents were used [193, 194].

The theory was developed further by taking into account the dependencies of  $\rho(z)$  and  $\eta(z)$ , due to the surface evaporation and to the formation of a more condensed surface skin layer [195], as well as due to the consideration of the non-Newtonian character of the spun fluid [196, 197]. The effect of an external gas flow on the uniformity of spin coated films was studied in [198, 199]. The first two stages of spin coating (i.e., fluid dispensing and acceleration) are very difficult to model, although several successful attempts in this direction have been done [200, 201]. The conditions for these two stages, such as the means of fluid dispensing, the concentration and the amount of the dispensed fluid, and the duration and ramp of the acceleration, were often found empirically from the experimental criterion of the homogeneous final coating. For example, in the case of the use of extremely volatile solvents, such as chloroform, the dispensing of the solution must take place in the beginning of the acceleration, otherwise the fluid will start to dry out before reaching steady rotation conditions [159].

The method of spin coating, unraveled from the photoresist deposition, has found its place in many other applications. Different compounds, not necessarily polymers, are suitable for spin coating, with the only criterion of its solubility in

some relatively volatile organic solvents. Different organic dye molecules [159, 202, 203], or organic macromolecules and complexes [204–208], were deposited by spin coating for various applications, mostly for the formation of sensing membranes in chemical sensors. As a matter of fact, all amphiphilic compounds designed for LB deposition can be deposited by spin coating technique. Of course, the films produced would not have the same high level of order in the normal direction as LB films, but in many cases the order is not required. For example, uneven surfaces made with materials of different wetting properties, such as the surface of quartz crystals with evaporated golden electrodes and spring contacts, can be unified by spin coating of amphiphilic calixerenes prior their LB deposition [200, 201]. In all of the cases mentioned above [159, 202–209], the appropriate conditions for spin coating, [e.g., the type of solvent, the solution concentration, the amount of solution dispensed, and the parameters of spinning (time, ramp and spin speed)], were found experimentally. In these cases, when highly volatile solvents, such as hexane, benzene, toluene, and particularly chloroform, were used, the dependencies of  $h_f \sim \omega^{-2/3}$  and  $h_f \sim c$  for the film thickness on the spin speed and solution concentration, respectively, were found. This is in a good agreement with (2.6) for constant rate evaporation. The use of less volatile solvents, such as alcohols (e.g., ethanol, methanol, isopropanol, or THF), has resulted in the dependence of  $h_f \sim \omega^{-1/2}$ .

The following examples demonstrate how the method of spin coating has been exploited for the fabrication of thin films of stabilized colloid nanoparticles for a wide range of industrial applications. Nanometer-size gold particles were deposited onto the surface of fused silica modified with 3-aminopropyltrimethoxysilane by means of spin coating [210]. The combination of a fast spin coating method with self-assembly conditions for gold nanoparticles and  $\text{NH}_2$  terminated silica surface has resulted in reproducible and homogeneous films of gold nanoparticles. The AFM study shows a regular arrangement of Au-clusters in these films. Method of spin coating has been recently deployed for the deposition of Ni nanoparticles as a precursor for the formation of carbon nanotubes [211]. Thin ceramic films of  $\text{Y}_2\text{O}_3$  doped  $\text{CeO}_2$  nanocrystalline powders with the particle size from 10 to 15 nm have been formed with spin coating technique [212]. Conductive antireflecting coatings for commercial computer displays have been produced recently by spin coating of antimony tin oxide, indium tin oxide, and noble metal nanoparticles [213].

The method of spin coating has been applied in the formation of nanoparticles and nanocrystalline materials. For example, thin films containing Ag nanoparticles were prepared by spin coating of polymers (polyvinylalcohol and polyvinylpyrrolidone) mixed with silver nitrate, and followed by thermal annealing [214]. A recently proposed combination of sol-gel reactions with the method of spin coating [215, 216] has resulted in high quality nanostructured inorganic materials. In contrast to the conventional dip-coating sol-gel technique, the steady spinning state produces a much faster sol-gel reaction over the whole surface of thin fluid film. As a result, inorganic films produced by sol-gel spin coating are more homogeneous, and contain fewer defects as compared to dip-coated sol-gel films. Several types of nanostructured inorganic materials, such as titanium dioxide ( $\text{TiO}_2$ ) [217, 218] and zinc sulphide ( $\text{ZnS}$ ) [219], were recently produced with this method, for the application in photovoltaic devices and solar cells.

**Table 2.3** Comparison of Different Chemical Techniques for Nanostructured Materials Processing

<i>Technology</i>	<i>Adhesion</i>	<i>Thermal Stability</i>	<i>Mechanical Properties</i>	<i>Thickness Precision</i>	<i>Level of Ordering</i>	<i>Industrial Compatibility</i>
<i>Electrodeposition</i>	Good	High (material depending)	Reasonable	Rather poor (tens of nanometers)	Polycrystalline	Very good
<i>Sol-gel</i>	Good	High (material depending)	Good	Rather poor (tens of nanometers)	Amorph. or polycrystalline	Very good
<i>Chemical self-assembly</i>	Strong	Rather poor and depends on organic materials used	Reasonable	Very high (tenths of nanometer range)	High level 2D order	Reasonable
<i>Electrostatic (or Polyelectrolyte) self-assembly</i>	Strong	Rather poor and depends on the polyelectrolyte used	Reasonable	High (nanometer range)	Good layer-by-layer order	Reasonable
<i>Langmuir-Blodgett</i>	Poor	Poor	Poor	Very high (tenths of nanometers)	High level of layer-by-layer order	Poor (practically incompatible)
<i>Spin coating</i>	Poor	Poor	Poor	Rather poor (tens of nanometers)	Amorph. or polycrystalline	Very good

## 2.5 Résumé

The review of different chemical (wet) technologies for the formation of nanostructured materials shows a growing interest in these methods by industry. Wet technologies offer cost-effective alternatives, and become competitive with such traditional solid-state methods as evaporation, sputtering, chemical and physical vapor deposition, and molecular beam epitaxy. For many applications (e.g., ceramic materials processing), chemical routes are already playing the major role in industry.

The properties of the nanostructured materials, produced by different chemical methods, vary greatly. Table 2.3 is an attempt to classify these chemical technologies, and to compare the main features of the thin films produced.

This classification can be helpful in choosing the right deposition technique for a certain material and for particular application. As one can see, the techniques of electrodeposition and sol-gel have become very popular, due to a reasonable combination of good adhesion, and thermal and mechanical stability with the industrial compatibility. However, these methods cannot achieve a high level of thickness precision, which is required for the fabrication of nanoelectronic devices.

On the other hand, the Langmuir-Blodgett technique, poorly rated by industry, is irreplaceable when it comes to subnanometer thickness precision, and layer-by-layer order. The application of the LB method for semiconductor nanoparticle formation, followed by the removal of the organic film matrix, is a very promising technique, because of the improved thermal stability of the material and high thickness precision in nanometer range. This technique may present a real alternative to MBE for the fabrication of semiconductor superlattices.

A well-established industrial method of spin coating has an unfortunate combination of poor adhesion and mechanical properties, with low ordering and thickness precision. However, this method, apart from polymers (photoresist) deposition, has

found its application in the formation of sensing membranes in chemical and biosensors fabrication. Yet, the combination of the spin coating and sol-gel techniques is very popular for the processing of a variety of materials.

The technique of chemical self-assembly is unique, regarding the two-dimensional order in the monolayers of self-assembled nanoparticles. Therefore, this technique may have a great future in the formation quantum dots for nanoelectronic devices. The technique of electrophoresis seems to be very promising for the formation of thin two-dimensional ordered layers of nanoparticles, and can compete in this aspect with the chemical self-assembly technique.

The combination of the above-mentioned chemical techniques is a very promising area, which may boost the advantages and reduce the drawbacks of individual methods. A very successful combination of spin coating and sol-gel techniques was already mentioned. Other examples are LB/self-assembly (either chemical or electrostatic), and electrophoresis/self-assembly.

A more detailed analysis of structural features, and optical and electrical properties of different nanostructured materials produced by chemical routes, as well as their applications, will be discussed later in the following chapters.

## References

- [1] Edelstein, A. S., and R. C. Cammarata, (eds.), *Nanomaterials, Synthesis, Properties and Applications*, Bristol, PA: IoP Publishing, 1996.
- [2] Brust, M., et al., "Synthesis of Thiol-Derivatized Gold Nanoparticles in a 2-Phase Liquid-Liquid System," *J. Chem. Soc.- Chem. Comm.*, Vol. 7, 1994, pp. 801–802.
- [3] Talapin, D. V., et al., "Synthesis of Surface-Modified Colloidal Semiconductor Nanocrystals and Study of Photoinduced Charge Separation and Transport in Nanocrystal-Polymer Composites," *Physica E*, Vol. 14, No. 1–2, 2002, pp. 237–241.
- [4] Puentes, V. F., and K. M Krishnan, "Synthesis, Structural Order and Magnetic Behavior of Self-Assembled Epsilon-Co Nanocrystal Arrays," *IEEE Trans. on Magnetics*, Vol. 37, No. 4, 2001, pp. 2210–2212.
- [5] Schultz, D. L., et al., "High Quality CdTe Films from Nanoparticle Precursors," *IEEE, 25th PVSC*, Washington, D.C., May 13–17, 1996, pp. 929–932.
- [6] Cortan, A. R., et al., "Nucleation and Growth of CdSe on ZnS Quantum Crystallite Seeds, and Vice Versa, in Inverse Micelle Media," *J. Am. Chem. Soc.*, Vol. 112, No. 4, 1990, pp. 1327–1332.
- [7] Mann, S., et al., "Precipitation Within Unilamellar Vesicles. 2. Membrane Control of Ion-Transport," *J. Chem. Soc.-Dalton Trans.*, No. 4, 1983, pp. 771–774.
- [8] Mann, S., J. P. Hannington, and R. J. P. Williams, "Phospholipid-Vesicles as a Model System for Biomineralization," *Nature*, Vol. 324, No. 6097, 1986, pp. 565–567.
- [9] Bhandarkar, S., and A. Bose, "Synthesis of Nanocomposite Particles by Intravesicular Coprecipitation," *J. Colloid Interface Sci.*, Vol. 135, No. 2, 1990, pp. 541–550.
- [10] Yaacob, I. I., S. Bhandarkar, and A. Bose, "Synthesis of Aluminum Hydroxide Nanoparticles in Spontaneously Generated Vesicles," *J Mater. Research*, Vol. 8, No. 3, 1993, pp. 573–577.
- [11] Li, S., et al., "Cobalt-Ferrite Nanoparticles: Correlations Between Synthesis Procedures, Structural Characteristics and Magnetic Properties," *IEEE Trans. on Magnetics*, Vol. 37, No. 4, 2001, pp. 2350–2352.
- [12] Netzer, L., and J. Sagiv, "A New Approach to Construction of Artificial Monolayer Assemblies," *J. Am. Chem. Soc.*, Vol. 105, No. 3, 1983, pp. 674–676.



- [13] Collier, C. P., et al., "Reversible Tuning of Silver Quantum Dot Monolayers Through the Metal-Insulator Transition," *Science*, Vol. 277, No. 5334, 1997, pp. 1978–1981.
- [14] Lover, T., et al., "Vibrational Spectroscopic Study of Thiophenolate-Capped Nanoclusters of CdS and of Cadmium Thiophenolate Complexes," *Chem. Mater.* Vol. 9, No. 4, 1997, pp. 967–975.
- [15] Rogach, A. L., et al., "Synthesis and Characterization of a Size Series of Extremely Small Thiol-Stabilized CdSe Nanocrystals," *J. Phys. Chem. B*, Vol. 103, No. 16, 1999, pp. 3065–3069.
- [16] Vogel, W., et al., "Structure and Stability of Monodisperse 1.4-nm ZnS Particles Stabilized by Mercaptoethanol," Vol. 16, No. 4, 2000, pp. 2032–2037.
- [17] Rizza, R., et al., "Self-Assembly of Monolayers of Semiconductor Nanocrystallites," *Chem. Mater.*, Vol. 9, No. 12, 1997, pp. 2969–2982.
- [18] Sarathy, K. V., et al., "Superlattices of Metal and Metal-Semiconductor Quantum Dots Obtained by Layer-by-Layer Deposition of Nanoparticle Arrays," *J. Phys. Chem. B*, Vol. 103, No. 3, 1999, pp. 399–401.
- [19] Nakanishi, T., B. Ohtani, and K. Uosaki, "Fabrication and Characterization of CdS-Nanoparticle Mono- and Multilayers on a Self-Assembled Monolayer of Alkanedithiols on Gold," *J. Phys. Chem. B*, Vol. 102, No. 9, 1998, pp. 1571–1577.
- [20] Searson, P. C., and T. F. Moffat, "Electrodeposition of Semiconductor Materials," *Crit. Rev. Surf. Chem.*, Vol. 3, 1994, p. 171.
- [21] Ross, C., "Electrodeposited Multilayer Thin-Films," *Annu. Rev. Mater. Sci.*, Vol. 24, 1994, pp. 159–188.
- [22] Zhang, P., P. S. Kim, and T. K. Sham, "Electrochemical Route for the Fabrication of Alkanethiolate-Capped Gold Nanoparticles," *Appl. Phys. Lett.*, Vol. 82, No. 9, 2003, pp. 1470–1472.
- [23] Sandmann, G., H. Dietz, and W. Plieth, "Preparation of Silver Nanoparticles on ITO Surfaces by a Double-Pulse Method," *J. Electroanal. Chem.*, Vol. 491, No. 1–2, 2000, pp. 78–86.
- [24] Gorer, S., and R. M. Penner, "Multipulse Electrochemical/Chemical Synthesis of CdS/S Core/Shell Nanocrystals Exhibiting Ultranarrow Photoluminescence Emission Lines," *J. Phys. Chem. B*, Vol. 103, No. 28, 1999, pp. 5750–5753.
- [25] Boxley, C. J., et al., "Electrochemical Deposition and Reoxidation of Au at Highly Oriented Pyrolytic Graphite. Stabilization of Au Nanoparticles on the Upper Plane of Step Edges," *J. Phys. Chem. B*, Vol. 107, No. 2, 2003, pp. 451–458.
- [26] Penner, R. M., "Mesoscopic Metal Particles and Wires by Electrodeposition," *J. Phys. Chem. B*, Vol. 106, No. 13, 2002, pp. 3339–3353.
- [27] Kim, J. W., and S. M. Park, "Electrochemical Preparation of Ru-Ni Binary Nanoparticles and Their Applications to Electro-Oxidation of Ethanol," *Electrochem. Solid State Lett.*, Vol. 3, No. 8, 2000, pp. 385–388.
- [28] Sarkar, D. K., et al., "Growth of Self-Assembled Copper Nanostructure on Conducting Polymer by Electrodeposition," *Solid State Commun.*, Vol. 125, No. 7–8, 2003, pp. 365–368.
- [29] Choi, S. J., et al., "Electrochemical Preparation of Cadmium Selenide Nanoparticles by the Use of Molecular Templates," *J. Electrochem. Soc.*, Vol. 148, No. 9, 2001, pp. C569–C573.
- [30] Riley, D. J., "Electrochemistry in Nanoparticle Science," *Curr. Opin. Colloid Interface Sci.*, Vol. 7, No. 3–4, 2002, pp. 186–192.
- [31] Van der Zande, B. M. I., et al., "Colloidal Dispersions of Gold Rods: Synthesis and Optical Properties," *Langmuir*, Vol. 16, No. 2, 2000, pp. 451–458.
- [32] Kovtyukhova, N. I., et al., "Layer-by-Layer Assembly of Rectifying Junctions in and on Metal Nanowires," *J. Phys. Chem. B*, Vol. 105, No. 37, 2001, pp. 8762–8769.
- [33] Walter, E. C., et al., "Electronic Devices from Electrodeposited Metal Nanowires," *Microelectron. Eng.*, Vol. 61–2, 2002, pp. 555–561.

- [34] Schmid, G., "Materials in Nanoporous Alumina," *J. Mater. Chem.*, Vol. 12, No. 5, 2002, pp. 1231–1238.
- [35] Banerjee, S., et al., "Magnetic Properties of Oxide-Coated Iron Nanoparticles Synthesized by Electrodeposition," *J. Magn. Magn. Mater.*, Vol. 219, No. 1, 2000, pp. 45–52.
- [36] Cao, L. Y., P. Diao, and Z. F. Liu, "Preparation of Au (Core)-Cu (Shell) Nanoparticles Assembly by Electrodeposition," *Acta Physico-Chimica Sinica*, Vol. 18, No. 12, 2002, pp. 1062–1067.
- [37] Ruach-Nir, I., et al., "Structural Effects in the Electrodeposition of CdSe Quantum Dots on Mechanically Strained Gold," *Adv. Funct. Mater.*, Vol. 13, No. 2, 2003, pp. 159–164.
- [38] Chandrasekharan, N., and P. V. Kamat, "Assembling Gold Nanoparticles as Nanostructured Films Using an Electrophoretic Approach," *Nano Lett.*, Vol. 1, No. 2, 2001, pp. 67–70.
- [39] Tang, F. Q., T. Uchikoshi, and Y. Sakka, "Electrophoretic Deposition Behavior of Aqueous Nanosized Zinc Oxide Suspensions," *J. Am. Ceram. Soc.*, Vol. 85, No. 9, 2002, pp. 2161–2165.
- [40] Reetz, M. T., et al., "Size-Selective Electrochemical Preparation of Surfactant-Stabilized Pd-, Ni- and Pt/Pd Colloids," *Chem.-Eur. J.*, Vol. 7, No. 5, 2001, pp. 1084–1094.
- [41] Gilbert, S. E., O. Cavalleri, and K. Kern, "Electrodeposition of Cu Nanoparticles on Decanethiol-Covered Au(111) Surfaces: An In Situ STM Investigation," *J. Phys. Chem.*, Vol. 100, No. 30, 1996, pp. 12123–12130.
- [42] Sakka, S., "Sol-Gel Synthesis of Glasses—Present and Future," *Am. Ceram. Soc. Bull.*, Vol. 64, No. 11, 1985, pp. 1463–1466.
- [43] Pier, A. C., *Introduction to Sol-Gel Processing*, Norwell, MA: Kluwer, 1998.
- [44] Blinker, C. J., and G. W. Scherrer, *Sol-Gel Science: The Physics and Chemistry of Sol-Gel Processing*, San Diego, CA: Academic Press, 1990.
- [45] Kozuka, H., H. Kuroki, and S. Sakka, "Flow Characteristics and Spinnability of Sols Prepared from Silicon Alkoxide Solution," *J. Non-Cryst. Solids*, Vol. 100, No. 1–3, 1988, pp. 226–230.
- [46] Sakka, S., et al., "Formation of Sheets and Coating Films from Alkoxide Solutions," *J. Non-Cryst. Solids*, Vol. 63, No. 1–2, 1984, pp. 223–235.
- [47] Gallagher, D., and L. Klein, "Silica Membranes by the Sol-Gel Process," *J. Colloid Interface Sci.*, Vol. 109, No. 1, 1986, pp. 40–45.
- [48] Hay, R. S., "Phase-Transformations and Microstructure Evolution in Sol-Gel Derived Yttrium-Aluminum-Garnet Films," *J. Mater. Res.*, Vol. 8, No. 3, 1993, pp. 578–604.
- [49] Klinowski, J., "Recent Advances in Solid-State NMR of Zeolites," *Ann. Rev. Mater. Sci.*, Vol. 18, 1998, pp. 189–218.
- [50] Harizanov, O., and A. Harizanova, "Development and Investigation of Sol-Gel Solutions for the Formation of TiO<sub>2</sub> Coatings," *Solar Energy Mater. Solar Cells*, Vol. 63, No. 2, 2000, pp. 185–195.
- [51] Ray, A. K., et al., "Optical Studies on Sol-Gel Derived Titanium Dioxide Films," *IEE Proc.-Sci. Meas. Technol.*, Vol. 147, No. 6, 2000, pp. 301–305.
- [52] Ray, A. K., S. M. Tracey, and S. N. B. Hodgson, "Photoelectric Measurements on Chloroaluminium Phthalocyanine/Titanium Oxide Heterojunctions," *J. Sol-Gel Sci. & Technol.*, Vol. 22, No. 1–2, 2001, pp. 15–22.
- [53] Natsume, Y., and H. Sakata, "Zinc Oxide Films Prepared by Sol-Gel Spin-Coating," *Thin Solid Films*, Vol. 372, No. 1–2, 2000, pp. 30–36.
- [54] Badilescu, S., and P. V. Ashrit, "Study of Sol-Gel Prepared Nanostructured WO<sub>3</sub> Thin Films and Composites for Electrochromic Applications," *Solid State Ion.*, Vol. 158, No. 1–2, 2003, pp. 187–197.
- [55] Galatsis, K., et al., "MoO<sub>3</sub>, WO<sub>3</sub> Single and Binary Oxide Prepared by Sol-Gel Method for Gas Sensing Applications," *J. Sol-Gel Sci. Technol.*, Vol. 26, No. 1–3, 2003, pp. 1097–1101.

- [56] Kaciulis, S., et al., "Investigation of Thin Films of Mixed Oxides for Gas-Sensing Applications," *Surf. Interface Anal.*, Vol. 34, No. 1, 2002, pp. 672–676.
- [57] Jung, M. W., "Synthesis and Structural Analysis of Au-Doped  $\text{TiO}_2/\text{SiO}_2$  Mixed Oxide Films Prepared by Sol-Gel Process," *J. Sol-Gel Sci. Technol.*, Vol. 19, No. 1–3, 2000, pp. 563–568.
- [58] Serebrennikova, I., and V. I. Birss, "Electrochemical Behavior of Sol-Gel Produced Ni and Ni-Co Oxide Films," *J. Electrochem. Soc.*, Vol. 144, No. 2, 1997, pp. 566–572.
- [59] Orel, B., et al., "Electrochromism of Iron-Oxide Films Prepared Via the Sol-Gel Route by the Dip-Coating Technique," *Thin Solid Films*, Vol. 246, No. 1–2, 1994, pp. 131–142.
- [60] Hori, T., et al., "Preparation of Conducting Film Composed of Polyaniline and Metal Oxide by Sol-Gel Method," *J. Mater. Res.*, Vol. 14, No. 1, 1999, pp. 5–7.
- [61] Livage, J., and D. Ganguli, "Sol-Gel Electrochromic Coatings and Devices: A Review," *Sol. Energy Mater. Sol. Cells*, Vol. 68, No. 3–4, 2001, pp. 365–381.
- [62] Bhattacharjee, B., et al., "Studies on CdS Nanoparticles Dispersed in Silica Matrix Prepared by Sol-Gel Technique," *Eur. Phys. J. B*, Vol. 31, No. 1, 2003, pp. 3–9.
- [63] Malier, L., J. P. Boilot, and T. Gacoin, "Sulfide Gels and Films: Products of Non-Oxide Gelation," *J. Sol-Gel Sci. Technol.*, Vol. 13, No. 1–3, 1998, pp. 61–64.
- [64] Yang, Y., et al., "From  $\text{Ga}(\text{NO}_3)_3$  to Nanocrystalline GaN: Confined Nanocrystal Synthesis in Silica Xerogels," *Mater. Lett.*, Vol. 43, No. 5–6, 2000, pp. 240–243.
- [65] Sardar, K., A. R. Raju, and G. N. Subbanna, *Solid State Comm.*, Vol. 125, No. 6, 2003, pp. 355–358.
- [66] Lvov, Y., G. Decher, and H. Möhwald, "Assembly, Structural Characterization, and Thermal-Behavior of Layer-by-Layer Deposited Ultrathin Films of Poly(vinyl sulfate) and Poly(allylamine)," *Langmuir*, Vol. 9, 1993, pp. 481–486.
- [67] Lvov, Y., G. Decher, and G. Sukhorukov, "Assembly of Thin-Films by Means of Successive Deposition of Alternate Layers of DNA and Poly(allylamine)," *Macromolecules*, Vol. 26, No. 20, 1993, pp. 5396–5399.
- [68] Lvov, Y., et al., "Assembly of Polyelectrolyte Molecular Films onto Plasma-Treated Glass," *J. Phys. Chem.*, Vol. 97, No. 49, 1993, pp. 12835–12841.
- [69] Lvov, Y., F. Essler, and G. Decher, "Combination of Polycation Polyanion Self-Assembly and Langmuir-Blodgett Transfer for the Construction of Superlattice Films," *J. Phys. Chem.*, Vol. 97, No. 51, 1993, pp. 13773–13777.
- [70] Decher, G., Y. Lvov, and J. Schmitt, "Proof of Multilayer Structural Organization in Self-Assembled Polycation Polyanion Molecular Films," *Thin Solid Films*, Vol. 244, No. 1–2, 1994, pp. 772–777.
- [71] Lvov, Y., et al., "Successive Deposition of Alternate Layers of Polyelectrolytes and a Charged Virus," *Langmuir*, Vol. 10, No. 11, 1994, pp. 4232–4236.
- [72] Lvov, Y., and G. Decher, "Assembly of Multilayer Ordered Films by Alternating Adsorption of Oppositely Charged Macromolecules," *Crystallography Reports*, Vol. 39, No. 4, 1994, pp. 696–616.
- [73] Iler, R., "Multilayers of Colloid Particles," *J. Colloid Interface Sci.*, Vol. 21, 1966, p. 569.
- [74] Fromhertz, P., and W. Baumeister, (eds.), *Electron Microscopy at Molecular Dimension*, Berlin, Germany: Springer-Verlag, 1980.
- [75] Zumbrunnen, H. R., and F. C. Anson, "Electrostatic Binding of Anions and Cations to Graphite-Electrodes Coated with a Polyelectrolyte Containing Both Positive and Negative Charges," *J. Electroanal. Chem.*, Vol. 152, No. 1–2, 1983, pp. 111–124.
- [76] Iyoda, T., et al., "Cationic Polypyrrole Composites with Anionic Functional Molecules," *J. Chem. Soc.-Faraday Trans.*, Vol. 87, No. 11, 1991, pp. 1765–1769.
- [77] Mao, G., et al., "Self-Assembly of Photopolymerizable Bolaform Amphiphile Monolayers and Multilayers," *Langmuir*, Vol. 9, No. 12, 1993, pp. 3461–3470.

- [78] Buchhammer, H. M., G. Petzold, and K. Lunkwitz, "The Interaction Between Oppositely Charged Polyelectrolytes in the Presence of Solid-Surfaces," *Colloid Surfaces A*, Vol. 76, 1993, pp. 81–85.
- [79] Hong, J. D., et al., *Progr. Colloid Polym. Sci.*, Vol. 93, 1993, p. 98.
- [80] Schmitt, J., et al., "Internal Structure of Layer-by-Layer Adsorbed Polyelectrolyte Films—A Neutron and X-Ray Reflectivity Study," *Macromolecules*, Vol. 26, No. 25, 1993, pp. 7058–7063.
- [81] Decher, G., et al., "New Nanocomposite Films for Biosensors—Layer-by-Layer Adsorbed Films of Polyelectrolytes, Proteins or DNA," *Biosens. Bioelectron.*, Vol. 9, No. 9–10, 1994, pp. 677–684.
- [82] Tronin, A., Y. Lvov, and C. Nicolini, "Ellipsometry and X-Ray Reflectometry Characterization of Self-Assembly Process of Polystyrenesulfonate and Polyallylamine," *Colloid Polym. Sci.*, Vol. 272, No. 10, 1994, pp. 1317–1321.
- [83] Cheung, J., A. Fou, and M. Rubner, "Molecular Self-Assembly of Conducting Polymers," *Thin Solid Films*, Vol. 244, No. 1–2, 1994, pp. 985–989.
- [84] Kleinfeld, E., and G. Ferguson, "Stepwise Formation of Multilayered Nanostructural Films from Macromolecular Precursors," *Science*, Vol. 265, No. 5170, 1994, pp. 370–373.
- [85] Lvov, Y., et al., "Assembly of Multicomponent Protein Films by Means of Electrostatic Layer-by-Layer Adsorption," *J. Am. Chem. Soc.* Vol. 117, No. 22, 1995, pp. 6117–6123.
- [86] Korneev, D., et al., "Neutron Reflectivity Analysis of Self-Assembled Film Superlattices with Alternate Layers of Deuterated and Hydrogenated Polystyrenesulfonate and Polyallylamine," *Physica B*, Vol. 213, 1995, pp. 954–956.
- [87] Ramsden, J., Y. Lvov, and G. Decher, "Determination of Optical-Constants of Molecular Films Assembled Via Alternate Polyion Adsorption," *Thin Solid Films*, Vol. 254, No. 1–2, 1995, pp. 246–251.
- [88] Mao, G. Z., et al., "Interactions, Structure, and Stability of Photoreactive Bolaform Amphiphile Multilayers," *Langmuir*, Vol. 11, No. 3, 1995, pp. 942–952.
- [89] Ferreira, M., and M. Rubner, "Molecular-Level Processing of Conjugated Polymers. 1. Layer-by-Layer Manipulation of Conjugated Polyions," *Macromolecules*, Vol. 28, No. 21, 1995, pp. 7107–7114.
- [90] Cooper, T., A. Campbell, and R. Crane, "Formation of Polypeptide-Dye Multilayers by an Electrostatic Self-Assembly Technique," *Langmuir*, Vol. 11, No. 7, 1995, pp. 2713–2718.
- [91] Kotov, N. A., I. Dekany, and J. N. Fendler, "Layer-by-Layer Self-Assembly of Polyelectrolyte-Semiconductor Nanoparticle Composite Films," *J. Phys. Chem.*, Vol. 99, No. 35, 1995, pp. 13065–13069.
- [92] Fendler, J., and F. Meldrum, "The Colloid-Chemical Approach to Nanostructured Materials," *Adv. Mater.*, Vol. 7, No. 7, 1995, pp. 607–632.
- [93] Hammond, P., and G. Whitesides, "Formation of Polymer Microstructures by Selective Deposition of Polyion Multilayers Using Patterned Self-Assembled Monolayers as a Template," *Macromolecules*, Vol. 28, No. 22, 1995, pp. 7569–7571.
- [94] Sano, M., Y. Lvov, and T. Kunitake, "Formation of Ultrathin Polymer Layers on Solid Substrates by Means of Polymerization-Induced Epitaxy and Alternate Adsorption," *Annu. Rev. Mater. Sci.*, Vol. 26, 1996, pp. 153–187.
- [95] Onda, M., et al., "Molecularly Flat Films of Linear Polyions and Proteins Obtained by the Alternate Adsorption Method," *Jpn. J. Appl. Phys.* 2, Vol. 36, No. 12A, 1997, pp. L1608–L1611.
- [96] Hoogeveen, N. G., et al., "Formation and Stability of Multilayers of Polyelectrolytes," *Langmuir*, Vol. 12, No. 15, 1996, pp. 3675–3681.
- [97] Sukhorukov, G., et al., "Assembly of Polyelectrolyte Multilayer Films by Consecutively Alternating Adsorption of Polynucleotides and Polycations," *Thin Solid Films*, Vol. 285, 1996, pp. 220–223.

- [98] Sukhorukov, G. J. Schmitt, and G. Decher, "Reversible Swelling of Polyanion/Polycation Multilayer Films in Solutions of Different Ionic Strength," *Ber. Bunsen. Ges. Phys. Chem.*, Vol. 100, No. 6, 1996, pp. 220–223.
- [99] Von Klitzig, R., and H. Möhwald, "Transport Through Ultrathin Polyelectrolyte Films," *Thin Solid Films*, Vol. 285, 1996, pp. 352–356.
- [100] Von Klitzig, R., and H. Möhwald, "A Realistic Diffusion Model for Ultrathin Polyelectrolyte Films," *Macromolecules*, Vol. 29, No. 21, 1996, pp. 6901–6906.
- [101] Brynda, E., and M. Houshka, "Multiple Alternating Molecular Layers of Albumin and Heparin on Solid Surfaces," *J. Colloid Interface Sci.*, Vol. 183, No. 1, 1996, pp. 18–25.
- [102] Ichinose, I., et al., "Layer-by-Layer Assembly of Aqueous Bilayer Membranes on Charged Surfaces," *Chem. Lett.*, No. 4, 1996, pp. 257–258.
- [103] Cheung, J., W. Stockton, and M. Rubner, "Molecular-Level Processing of Conjugated Polymers .3. Layer-by-Layer Manipulation of Polyaniline Via Electrostatic Interactions," *Macromolecules*, Vol. 30, No. 9, 1997, pp. 2712–2716.
- [104] Ariga, K., Y. Lvov, and T. Kunitake, "Assembling Alternate Dye-Polyion Molecular Films by Electrostatic Layer-by-Layer Adsorption," *J. Am. Chem. Soc.*, Vol. 119, No. 9, 1997, pp. 2224–2231.
- [105] Lvov, Y., S. Yamada, and T. Kunitake, "Nonlinear Optical Effects in Layer-by-Layer Alternate Films of Polycations and an Azobenzene-Containing Polyanion," *Thin Solid Films*, Vol. 300, No.1–2, 1997, pp. 107–112.
- [106] Schmitt, J., et al., "Metal Nanoparticle/Polymer Superlattice Films: Fabrication and Control of Layer Structure," *Adv. Mater.*, Vol. 9, No. 1, 1997.
- [107] Bliznyuk, V. N., F. Rinderspacher, and V. V. Tsukruk, "Dendrimer Self-Assembled Films," *Abstr. Papers Amer. Chem. Soc.*, Vol. 213, Part 2, 1997, p. 522.
- [108] Tsukruk, V., F. Rinderspacher, and V. Bliznyuk, "Self-Assembled Multilayer Films from Dendrimers," *Langmuir*, Vol. 13, No. 8, 1997, pp. 2171–2176.
- [109] Lvov, Y., et al., "Alternate Assembly of Ordered Multilayers of SiO<sub>2</sub> and Other Nanoparticles and Polyions," *Langmuir*, Vol. 13, No. 23, 1997, pp. 6195–6203.
- [110] Liu, Y., A. Wang, and R. Claus, "Layer-by-Layer Electrostatic Self-Assembly of Nanoscale Fe<sub>3</sub>O<sub>4</sub> Particles and Polyimide Precursor on Silicon and Silica Surfaces," *Appl. Phys. Lett.*, Vol. 71, No. 16, 1997, pp. 2265–2267.
- [111] Tsukruk, V., et al., "Electrostatic Deposition of Polyionic Monolayers on Charged Surfaces," *Macromolecules*, Vol. 30, No. 21, 1997, pp. 6615–6625.
- [112] Laurent, D., and J. Schlenoff, "Multilayer Assemblies of Redox Polyelectrolytes," *Langmuir*, Vol. 13, No. 6, 1997, pp. 1552–1557.
- [113] Yoo, D., S. Shiratori, and M. Rubner, "Controlling Bilayer Composition and Surface Wettability of Sequentially Adsorbed Multilayers of Weak Polyelectrolytes," *Macromolecules*, Vol. 31, No. 13, 1998, pp. 4309–4018.
- [114] Lvov, Y., et al., "High-Speed Multilayer Film Assembly by Alternate Adsorption of Silica Nanoparticles and Linear Polycation," *Chem. Commun.*, No. 1, 1998, pp. 1229–1230.
- [115] Caruso, F., et al., "Electrostatic Self-Assembly of Silica Nanoparticle—Polyelectrolyte Multilayers on Polystyrene Latex Particles," *J. Am. Chem. Soc.*, Vol. 120, No. 33, 1998, pp. 8523–8524.
- [116] Schlenoff, J., H. Ly, and M. Li, "Charge and Mass Balance in Polyelectrolyte Multilayers," *J. Am. Chem. Soc.*, Vol. 120, No. 30, 1998, pp. 7626–7634.
- [117] Lvov, Y., et al., "A Careful Examination of the Adsorption Step in the Alternate Layer-by-Layer Assembly of Linear Polyanion and Polycation," *Colloids & Surfaces A*, Vol. 146, No. 1–3, 1999, pp. 337–346.
- [118] Nabok, A. V., A. K. Hassan, and A. K. Ray, "Optical and Electrical Characterisation of Polyelectrolyte Self-Assembled Thin Films," *Mater. Sci. & Eng. C*, No. 8–9, 1999, pp. 505–508.



- [119] Lvov, Y., and H. Mohwald, (eds.), *Protein Architecture. Interfacing Molecular Assemblies and Immobilization Biotechnology*, New York: Marcel Dekker, 2000, p. 167.
- [120] Shiratori, S., "Method and Apparatus for Forming Films by Alternative Deposition," Patent PCT/JP99/04432, Japan.
- [121] Shiratori, S., T. Ito, and T. Yamada, "Apparatus for the Alternative Layers Deposition," *Proc. 9th Intern. Conf. Organised Organic Films (LB9)*, Potsdam, Germany, August 28–September 2, 2000.
- [122] Nabok, A. V., et al., "Polyelectrolyte Self-Assembled Thin Films Containing Cyclo-Tetrachromotropyene for Chemical and Biosensing," *Mater. Sci. & Eng. C*, No. 8–9, 1999, pp. 123–126.
- [123] Caruso, F., et al., "Ultrathin Multilayer Polyelectrolyte Films on Gold: Construction and Thickness Determination .1," *Langmuir*, Vol. 13, No. 13, 1997, pp. 3422–3426.
- [124] Caruso, F., et al., "Assembly of Alternating Polyelectrolyte and Protein Multilayer Films for Immunosensing .2," *Langmuir*, Vol. 13, No. 13, 1997, pp. 3427–3433.
- [125] Andrade, J. D., (ed.), *Surface and Inrefacial Aspects of Biomedical Polymers*, New York: Plenum, 1985, Vol. 2, p. 1.
- [126] Sakayan, N. N., et al., *Laboratornoe Delo*, No. 12, 1988, pp. 63–66 (in Russian).
- [127] Ortega, N., M. D. Busto, and M. PerezMateos, "Optimisation of Beta-Glucosidase Entrapment in Alginate and Polyacrylamide Gels," *Bioresource Technol.*, Vol. 64, No. 2, 1998, pp. 105–111.
- [128] Bersina, T. S., et al., "Langmuir-Blodgett Films Composed of Monolayers of Amphiphilic Molecules and Adsorbed Soluble Proteins," *Thin Solid Films*, Vol. 285, 1996, pp. 757–761.
- [129] Kotov, N. A., I. Dekany, and J. H. Fendler, "Layer-by-Layer Self-Assembly of Polyelectrolyte-Semiconductor Nanoparticle Composite Films," *J. Phys. Chem.*, Vol. 99, No. 35, 1995, pp. 13065–13069.
- [130] Fendler, J., and F. C. Meldrum, "The Colloid-Chemical Approach to Nanostructured Materials," *Adv. Mater.*, Vol. 7, No. 7, 1995, pp. 607–632.
- [131] Gao, M., B. Richter, and S. Kirstein, "White-Light Electroluminescence from a Self-Assembled Q-CdSe/PPV Multilayer Structures," *Adv. Mater.*, Vol. 9, No. 10, 1997.
- [132] Gao, M., et al., "Strongly Photoluminescent CdTe Nanocrystals by Proper Surface Modification," *J. Phys. Chem. B*, Vol. 102, No. 34, 1998, pp. 8360–8363.
- [133] Gao, M., et al., "Electroluminescence Studies on Self-Assembled Films of PPV and CdSe Nanoparticles," *J. Phys. Chem. B*, Vol. 102, No. 21, 1998, pp. 4096–4103.
- [134] Gao, M., et al., "Photoluminescence and Electroluminescence of CdSe and CdTe Nanoparticles," in "Innovative Light Emitting Materials," P. Vincenzini and G. C. Righini, (eds.), *Adv. Sci. Technol.*, Vol. 27, 1999, pp. 347–358.
- [135] Gao, M., et al., "Electroluminescence of Different Colors from Polycation/CdTe Nanocrystal Self-Assembled Films," *J. Appl. Phys.*, 87, No. 5, 2000, pp. 2297–2302.
- [136] Bliznyuk, V. N., A. Campbell, and V. V. Tsukruk, "Organized Multilayer Films of Charged Organic Latexes," *Organic Thin Films ACS Symposium Series*, Vol. 695, 1998, pp. 220–232.
- [137] Bliznyuk, V., et al., "Self-Assembled Nanocomposite Polymer Light-Emitting Diodes with Improved Efficiency and Luminance," *Adv. Mater.*, Vol. 11, No. 15, 1999.
- [138] Caruso, F., "Nanoengineering of Particle Surfaces," *Adv. Mater.*, Vol. 13, No. 1, 2001, pp. 11–22.
- [139] Pockels, A., *Nature*, Vol. 43, 1891, p. 437.
- [140] Lord Rayleigh, *Phil. Mag.* Vol. 48, 1899, p. 321.
- [141] Langmuir, I., "Forces Near the Surfaces of Molecules," *Chem. Rev.*, Vol. 6, No. 4, 1930, pp. 451–479.
- [142] Blodgett, K. B., "Monomolecular Films of Fatty Acids on Glass," *J. Amer. Chem. Soc.*, Vol. 56, No. 2, 1934, p. 495.

- [143] Kuhn, H., *Naturwiss.*, Vol. 54, 1967, p. 429.
- [144] Kuhn, H., D. Möbius, and H. Bücher, *Physical Methods of Chemistry*, A. Weissberger and B. Rossiter, (eds.), Vol. 1, Part 3B, Chapter 7, New York: John Wiley & Sons, 1972.
- [145] Mann, B., and H. Kuhn, "Tunneling Through Fatty Acid Salt Monolayers," *J. Appl. Phys.* Vol. 42, No. 11, 1971, p. 4398–4405.
- [146] Roberts, G. G., (ed.), *Langmuir-Blodgett Films*, New York: Plenum Press, 1990.
- [147] Aviram, A., (ed.), *Molecular Electronics: Science and Technology*, St. Thomas, Virgin Islands: American Institute of Physics, 1991.
- [148] Lazarev, P. I., and P. Dordrecht, (eds.), *Molecular Electronics: Materials and Methods*, Boston, MA: Kluwer, 1991.
- [149] Ashwell, G. J., (ed.), *Molecular Electronics*, Taunton, MA: Research Studies Press, 1992.
- [150] Tredgold, R. H., *Order in Thin Organic Films*, Cambridge, England: Cambridge University Press, 1994.
- [151] Petty, M. C., M. R. Bryce, and D. Bloor, (eds.), *An Introduction to Molecular Electronics*, London, England: Edward Arnold, 1995.
- [152] Petty, M. C., *Langmuir-Blodgett Films: An Introduction*, Cambridge, England: Cambridge University Press, 1996.
- [153] Bibo, A. M., and I. R. Peterson, "Defect Annealing Rate in Monolayers Displaying a Smectic-L Phase," *Thin Solid Films*, Vol. 210, No. 1–2, 1992, pp. 515–518.
- [154] Lehn, J. M., and C. W. Rees, (eds.), *Molecular Semiconductors: Photoelectric Properties and Solar Cells*, Berlin, Germany: Springer-Verlag, 1985.
- [155] Han, R. A., "Molecular Structure and Monolayer Properties," in *Langmuir-Blodgett Films*, G. G. Roberts, (ed.), New York: Plenum Press, 1990, pp. 17–92.
- [156] Dimitriev, O. P., et al., "Effect of Structure of Langmuir-Blodgett Tetrasubstituted Copper Phthalocyanine Films on their Optical-Absorption Spectra," *Ukr. Fiz. Zhurn.* Vol. 38, No. 10, 1993, pp. 1573–1579 (in Russian).
- [157] Gutsche, C. D., *Calixarenes*, Cambridge, England: Royal Society of Chemistry, 1989.
- [158] Nabok, A. V., et al., "Complexing Properties of Calix[4]resorcinolarene LB Films," *Thin Solid Films*, Vol. 259, No. 2, 1995, pp. 244–247.
- [159] Hassan, A. K., et al., "Surface Plasmon Resonance Studies on Spin Coated Films of Azobenzene-Substituted Calix-4-resorcinolarene Molecules," *IEE Proceedings—Sci. Meas. Technol.*, Vol. 147, No. 3, 2000, pp. 137–140.
- [160] Nabok, A. V., A. K. Hassan, and A. K. Ray, "Condensation of Organic Vapors Within Nanoporous Calixarene Thin Films," *J. Mater. Chemistry*, Vol. 10, 2000, pp. 189–194.
- [161] Wang, J. Y., et al., "Fullerene Films and Fullerene Dodecylamine Adduct Monolayers at Air-Water Interfaces Studied by Neutron and X-Ray Reflection," *Thin Solid Films*, Vol. 242, No. 1–2, 1994, pp. 40–44.
- [162] Kazantseva, Z. I., et al., "Structure and Electronic Properties of Langmuir-Blodgett Films of Calixarene/Fullerene Composites," *Supramol. Sci.*, Vol. 4, No. 3–4, 1997, pp. 341–347.
- [163] Atwood, J. L., G. A. Koutsantonis, and C. L. Raston, "Purification of C-60 and C-70 by Selective Complexation with Calixarenes," *Nature*, Vol. 368, No. 6468, 1994, pp. 229–231.
- [164] Nabok, A. V., et al., "Inclusion Phenomena in Mixed Floating Layers Containing Phthalocyanines," *Thin Solid Films*, Vol. 327–329, 1998, pp. 104–109.
- [165] Lavrik, N. V., et al., "Composite Polyaniline/Calixarene Langmuir-Blodgett Films for Gas Sensing," *Nanotechnology*, No. 7, 1996, pp. 1–5.
- [166] Nabok, A. V., et al., "Composite Calixarene/Noxon Langmuir-Blodgett Films for Ozone Sensing," *IEE Proceedings—Sci. Meas. Technol.*, Vol. 147, No. 4, 2000, pp. 153–157.
- [167] Langmuir, I., and V. J. Schaefer, "Activities of Urease and Pepsin Monolayers," *J. Am. Chem. Soc.*, Vol. 60, No. 6, 1938, pp. 1351–1360.

- [168] Howarth, V. A., et al., "The Deposition and Characterization of Multilayers of the Ionophore Valinomycin," *Thin Solid Films*, Vol. 160, No. 1–2, 1988, pp. 483–489.
- [169] Zhu, D. G., et al., "On the Formation of Langmuir-Blodgett Films Containing Enzymes," *Thin Solid Films*, Vol. 176, No. 1, 1989, pp. 151–156.
- [170] Hoffamn, M., et al., "Molecular Recognition in Biotin-Streptavidin Systems and Analogs at the Air-Water-Interface," *Thin Solid Films*, Vol. 210, No. 1–2, 1992, pp. 780–783.
- [171] Swart, R. M., "Monolayers and Multilayers of Biomolecules," in *Langmuir-Blodgett Films*, G. G. Roberts, (ed.), New York: Plenum Press, 1990, pp. 273–316.
- [172] Petty, M. C., "Application of Multilayer Films to Molecular Sensors—Some Examples of Bioengineering at the Molecular-Level," *J. Biomed. Eng.*, Vol. 13, No. 3, 1991, pp. 209–214.
- [173] Raudel-Teixier, A., J. Lelup, and A. Barraut, "Insertion Compounds in LB Films," *Mol. Cryst. Liq. Cryst.*, Vol. 134, No. 1–4, 1986, pp. 347–354.
- [174] Zylberajch, G., A. Raudel-Teixier, and A. Barraut, "2D Monomolecular Inorganic Semiconductors, Inserted in a Langmuir-Blodgett Matrix," *Synth. Metals*, Vol. 27, No. 3–4, 1988, pp. B609–B614.
- [175] Weller, H., et al., "Photochemistry of Semiconductor Colloids .14. Photochemistry of Colloidal Semiconductors—Onset of Light-Absorption as a Function of Size of Extremely Small CdS Particles," *Chem. Phys. Let.*, Vol. 124, No. 6, 1986, pp. 557–560.
- [176] Smotkin, E. S., et al., "Size Quantization Effects in Cadmium-Sulfide Layers Formed by a Langmuir-Blodgett Technique," *Chem. Phys. Let.*, Vol. 152, No. 2–3, 1988, pp. 265–268.
- [177] Facci, P., et al., "Formation of Ultrathin Semiconductor-Films by CdS Nanostructure Aggregation," *J. Phys. Chem.*, Vol. 98, No. 50, 1994, pp. 13323–13327.
- [178] Nabok, A. V., et al., "Nanoparticles in Langmuir-Blodgett Films of Calixarene," *Langmuir*, 1997, Vol. 13, No. 12, pp. 3198–3201.
- [179] Nabok, A. V., et al., "Size-Quantization in Extremely Small CdS Clusters Formed in Calixarene Langmuir-Blodgett Films," *Thin Solid Films*, Vol. 327–329, 1998, pp. 510–515.
- [180] Nabok, A. V., et al., "Formation of CdS Nanoclusters Within LB Films of Calixarene Derivatives and Study of Their Size-Quantization," *Mater. Sci. & Eng. C*, Vol. 8–9, 1999, pp. 171–177.
- [181] Wang, L. J., et al., "A Study on Inorganic Nanoparticles Amphiphilic Oligomer in Nanoordered Multilayer," *Mol. Cryst. & Liq. Cryst. Sci. & Technol., Section A*, Vol. 294, 1997, pp. 473–478.
- [182] Nabok, A. V., et al., "II-VI Semiconductor Nanoparticles Formed by Langmuir-Blodgett Film Technique: Optical Study," *IEEE Trans. on Nanotechnology*, Vol. 2, No. 1, 2003, pp. 44–49.
- [183] Erokhin, V., et al., "Fatty Acid-Based Monoelectron Device," *Biosens. & Bioelectron.*, Vol. 12, No. 7, 1997, pp. 601–606.
- [184] Nabok, A. V., et al., "Evolution of CdS Nanoparticles Self-Assembled Within Two-Dimensional Langmuir-Blodgett Layers," *J. Phys. D*, Vol. 35, No. 13, 2002, pp. 1512–1515.
- [185] Lifshitz, I. M., and V. V. Slezov, "Kinetics of Diffusive Decomposition of Saturated Solid Solutions," *Soviet Physics (JETP)*, Vol. 35, 1959, pp. 331–339.
- [186] Facci, P., V. Erokhin, and C. Nicolini, "Formation and Characterization of an Ultrathin Semiconductor Polycrystal Layer for Transducer Applications," *Biosens. & Bioelectr.*, Vol. 12, No. 7, 1997, pp. 607–611.
- [187] Erokhin, V., et al., "Preparation of Semiconductor Superlattices from LB Precursor," *Thin Solid Films*, Vol. 327, 1998, pp. 503–505.
- [188] Erokhin, V., et al., "Semiconductor Nanoparticles for Quantum Devices," *Nanotechnology*, Vol. 9, No. 3, 1998, pp. 158–161.



- [189] Montemerlo, M. S., et al., *Technology and Design for Electronic Nanocomputers*, McLean, VA: MITRE Corporation, 1996.
- [190] Yoffe, A. D., "Semiconductor Quantum Dots and Related Systems: Electronic, Optical, Luminescence and Related Properties of Low Dimensional Systems," *Adv. Phys.*, Vol. 50, No. 1, 2000, pp. 1–208.
- [191] Emslie, A. G., F. T. Bonner, and L. G. Peck, "Flow of a Viscous Liquid on a Rotating Disk," *J. Appl. Phys.*, Vol. 29, No. 5, 1958, pp. 858–862.
- [192] Meyerhofer, D., "Characteristics of Resist Films Produced by Spinning," *J. Appl. Phys.*, Vol. 49, No. 7, 1978, pp. 3993–3997.
- [193] Sukanek, P. C., "Dependence of Film Thickness on Speed in Spin Coating," *J. Electrochem. Soc.*, Vol. 138, No. 6, 1991, pp. 1712–1719.
- [194] Sukanek, P. C., "Anomalous Speed Dependence in Polyimide Spin Coating," *J. Electrochem. Soc.*, Vol. 144, No. 11, 1997, pp. 3959–3962.
- [195] Birnie, D. P., "Combined Flow and Evaporation During Spin Coating of Complex Solutions," *J. Non-Cryst. Sol.*, Vol. 218, 1997, pp. 174–178.
- [196] Acrivos, A., M. J. Shan, and E. E. Petersen, "On the Flow of a Non-Newtonian Liquid on a Rotating Disk," *J. Appl. Phys.*, Vol. 31, No. 6, 1960, pp. 963–967.
- [197] Britten, J. A., and I. M. Thomas, "Non-Newtonian Flow Effects During Spin Coating Large-Area Optical Coatings with Colloidal Suspensions," *J. Appl. Phys.*, Vol. 71, No. 2, 1992, pp. 972–979.
- [198] Bornside, D. E., et al., "The Effects of Gas-Phase Convection on Mass-Transfer in Spin Coating," *J. Appl. Phys.*, Vol. 73, No. 2, 1993, pp. 585–600.
- [199] Oztekin, A., D. E. Bornside, and R. A. Brown, "The Connection Between Hydrodynamic Stability of Gas-Flow in Spin-Coating and Coated Film Uniformity," *J. Appl. Phys.*, Vol. 77, No. 6, 1995, pp. 2297–2308.
- [200] Borkar, A. V., et al., "Spin-Coating of Viscoelastic and Nonvolatile Fluids over a Planar Disk," *Phys. Fluids*, Vol. 6, No. 11, 1994, pp. 3539–3553.
- [201] Frayse, N., and G. M. Homsy, "An Experimental Study of Rivulet Instabilities in Centrifugal Spin-Coating of Viscous Newtonian and Non-Newtonian Fluids," *Phys. Fluids*, Vol. 6, No. 4, 1994, pp. 1491–1503.
- [202] Critchley, S. M., et al., "Deposition of Ordered Phthalocyanine Films by Spin Coating," *J. Mater. Chem.*, Vol. 2, No. 2, 1992, pp. 157–159.
- [203] Ten Grotenhuis, E., J. C. Van Miltenburg, and J. P. Van der Eerden, "Preparation of Anthracene Micro-Crystals by Spin-Coating and Atomic Force Microscopy Study of the Molecular Packing," *Chem. Phys. Lett.*, Vol. 261, 1996, pp. 558–562.
- [204] Hassan, A. K., et al., "Thin Films of Calix-4-resorcinarene Deposited by Spin Coating and Langmuir-Blodgett Techniques: Determination of Film Parameters by Surface Plasmon Resonance," *Mater. Sci. & Engineer. C*, Vol. 8–9, 1999, pp. 257–261.
- [205] Hassan, A. K., et al., "Spun Films of Novel Calix-4-resorcinarene Derivatives for Benzene Vapor Sensing," *Sensors & Actuators B*, Vol. 77, 2001, pp. 638–641.
- [206] Hassan, A. K., et al., "Kinetic Study of BTEX Vapor Adsorption onto Surfaces of Calix-4-resorcinarene Films," *Appl. Surf. Sci.*, Vol. 182, 2001, pp. 49–54.
- [207] Skabara, P. J., et al., "The First Example of a Polythiophene Bearing Fused Tetrathiafulvalene Units," *Material Research Society Symposium Proceedings*, Vol. 665, 2001, Materials Research Society, pp. C2.1.1–C2.1.8.
- [208] Ray, A. K., et al., "Organic Vapors Sensor," U.K. patent No. 0217125.4, 24/7/2002.
- [209] Holloway, A. F., et al., "Impedance Analysis of the Thickness Shear Mode Resonator for Organic Vapor Sensing," *Sensors and Actuators*, Vol. 99, 2004, pp. 355–360.
- [210] Liu, F. K., et al., "Rapid Fabrication of High Quality Self-Assembled Nanometer Gold Particles by Spin Coating Method," *Microelectron. Eng.*, Vol. 67, No. 8, 2003, pp. 702–709.
- [211] Choi, G. S., et al., "Mass Production of Carbon Nanotubes Using Spin-Coating of Nanoparticles," *Microelectronic Engineering*, Vol. 66, No. 1–4, 2003, pp. 77–82.

- [212] Yang, X., and M. N. Rahman, "Thin Films by Consolidation and Sintering of Nanocrystalline Powders," *J. European Ceramic Soc.*, Vol. 17, No. 1997, pp. 525–535.
- [213] Ishibara, Y., et al., "Applications of the Particle Ordering Technique for Conductive Antireflection Films," *Thin Solid Films*, Vol. 411, No. 1, 2002, pp. 50–55.
- [214] Fritzsche, W., et al., "In-situ Formation of Ag-containing Nanoparticles in Thin Polymer Films," *Nanostructured Materials*, Vol. 10, No. 1, 1998, pp. 89–97.
- [215] Van Hardeveld, R. M., et al., "Deposition of Inorganic Salts from Solution on Flat Substrates by Spin-Coating: Theory, Quantification and Application to Model Catalysts," *Appl. Surf. Sci.*, Vol. 84, No. 4, 1995, pp. 339–346.
- [216] Partridge, A., et al., "Nanocluster Formation by Spin Coating: Quantitative Atomic Force Microscopy and Rutherford Backscattering Spectrometry Analysis," *J. Vac. Sci. Technol., B*, Vol. 14, No. 2, 1996, pp. 585–592.
- [217] Li, Y., et al., "Titanium Dioxide Films for Photovoltaic Cells Derived from a Sol-Gel Process," *Solar Energy Materials & Solar Cells*, Vol. 56, No. 2, 1999, pp. 167–174.
- [218] Hassan, A. K., et al., "Structural and Electrical Studies on Sol-Gel Derived Spun TiO<sub>2</sub> Thin Films," *J. Phys. D*, Vol. 36, 2003, pp. 1120–1125.
- [219] Bhattacharjee, B., et al., "Synthesis and Optical Characterization of Sol-Gel Derived Zinc Sulphide Nanoparticles Confined in Amorphous Silica Thin Films," *Mater. Chem. Phys.*, Vol. 78, No. 2, 2002, pp. 272–379.



# Structural Study of Organic/Inorganic Nanocomposites

This chapter is dedicated to the structural study of nanomaterials produced by chemical routes (e.g., either electrodeposited or by use of sol-gel materials), nanoparticles deposited by both chemical and electrostatic self-assembly and formed within LB films. Although the structural study is perhaps the most developed part of the science of organic films, reflected in a number of review papers and monographies [1–19], it is worth repeating some key methods and problems in this field. The control of the structure and particularly of the impurities is very important for industrial applications. Very often, the optical and electrical properties of the materials made with chemical methods suffer from poor reproducibility, because of the structural disorder and presence of uncontrolled impurities. This resembles the situation with semiconductor materials between 1950 and 1960, when the properties of materials produced in different laboratories varied greatly. The chapter also contains short descriptions of various experimental methods for morphology, crystallography, and chemical composition study.

## 3.1 Morphology and Crystallography of Nanostructured Materials Prepared by Chemical Routes

The structural study of materials was always of a high priority, because the physical properties of materials depend very much on their structure. There are several levels of structural study, which start with the investigation of the morphology of the material surfaces, closely related to their in-plane ordering. Many nanostructured materials prepared with the help of layer-by-layer deposition techniques, such as LB or electrostatic self-assembly, have a distinctive periodicity in the direction normal to the surface, which determines their main electrical and optical properties. This is why the study of the layer-by-layer structure of such materials is of crucial importance.

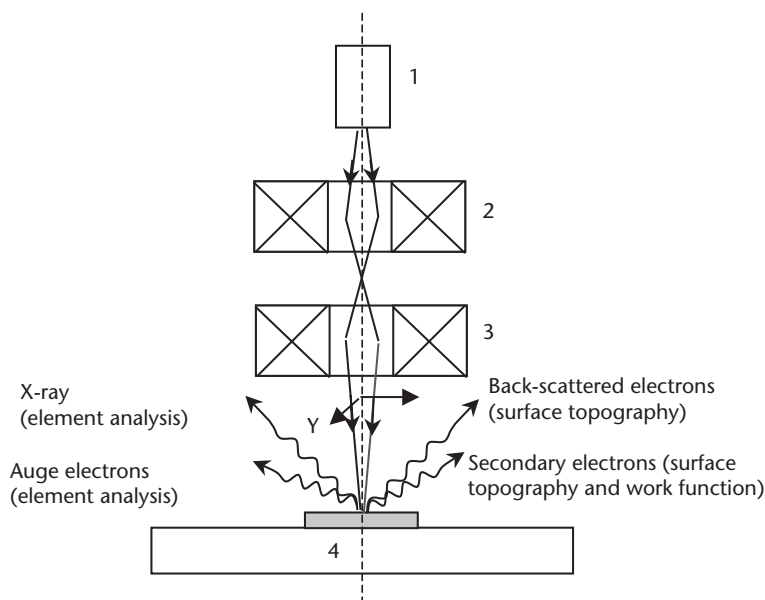
The materials consisting of colloid nanoparticles have a tendency to form two-dimensional structures according to the close packing order. This trend can stimulate the formation of multilayered quasi-3D structures of closely packed nanoparticles. The final stage of structural study is the crystallography of individual nanoparticles, clusters, and grains of materials. This is a very interesting and important subject, since the crystallography of nanoclusters, which consist of several

hundred to several thousand atoms, is very often different from that of their respective bulk materials.

The planar order of nanostructures deposited by chemical routes has become an important issue, because of the competition with solid-state nanotechnology capable of the fabrication of fine two-dimensional structures. The main concern is with the layers of nanoparticles produced by chemical self-assembly, because methods of electrostatic self-assembly and LB are not capable of producing two-dimensional ordered arrays of nanoparticles. The features of the lateral arrangement of particles, which are buried under layers of either closely packed amphiphilic compounds or polymers, are usually smeared and difficult to observe. In the case of relatively thick (quasi-3D) films, produced by electrodeposition and sol-gel techniques, the morphology study usually reveals polycrystallites. Therefore, the quality of these materials can be assessed by the size of the crystallites and by the presence of preferential orientation, which may cause anisotropy of the electrical and optical properties of materials.

### 3.1.1 Methods of Morphology Study

Electron microscopy is one of the traditional and well-established methods in surface science. SEM operates in a vacuum, with a high energy electron beam (typically from 5 to 20 keV) focused into a spot of several tens of nanometers in diameter (or fractions of nanometers in modern high-resolution instruments) [20]. Because of the very short wavelength of the electrons used (e.g., electrons with an energy of  $10^4$  eV have a wavelength  $\lambda_e =$  equal to 0.12 nm), the resolution of SEM is limited by the beam diameter and image distortions, (e.g., astigmatism) introduced by the focusing system. A complex electromagnetic system provides both the formation of the electron beam and its scanning over the sample surface (see Figure 3.1). The electrons that are



**Figure 3.1** The scheme of SEM: (1) electron gun, (2) electromagnetic beam focusing system, (3) electromagnetic X,Y scanner, and (4) specimen.

reflected (backscattered) from the surface, or the emitted secondary electrons, are collected with a sensitive detector to provide imaging of the studied surfaces [20].

SEM can be used to study samples of different nature and shape, practically without any limitations. Ideally, the samples for SEM study should be conductive to avoid electrical charging the sample with an electron beam, which is a side effect causing image distortion. Therefore, the samples of insulating materials for SEM study are recommended to coat (decorate) with thin metal film. This reproduces the surface profile. Another possible characteristic of SEM lies in the film damage caused by high energy electrons, which is particularly important for organic film study. The interpretation of SEM images of composite samples may not always be straightforward. This is especially true for secondary electron images, which represent a combination of both the surface and the work function profiles [20].

TEM produces images by a high energy focused electron beam penetrating through the material, so that materials for TEM study are meant to be thin films. Sample preparation for TEM study is therefore a very important experimental stage, and usually requires deposition of a studied material onto fine metal meshes or hollow carbon substrates. Resolution of TEM is higher than of SEM, and reaches angstrom level in the best instruments. Since the electrons' energy in TEM is normally higher than in SEM, this increases the danger of samples being damaged by high energy electrons, which is particularly important in studying thin organic films [21].

We cannot imagine the morphology study of materials without scanning nanoprobe techniques, such as STM, AFM, and many other techniques derived from them. Examples include magnetic force microscopy (MFM), electrochemical force microscopy (ECFM), linear force microscopy (LFM), surface potential microscopy (SPM), and scanning near-field optical microscopy (SNOM).

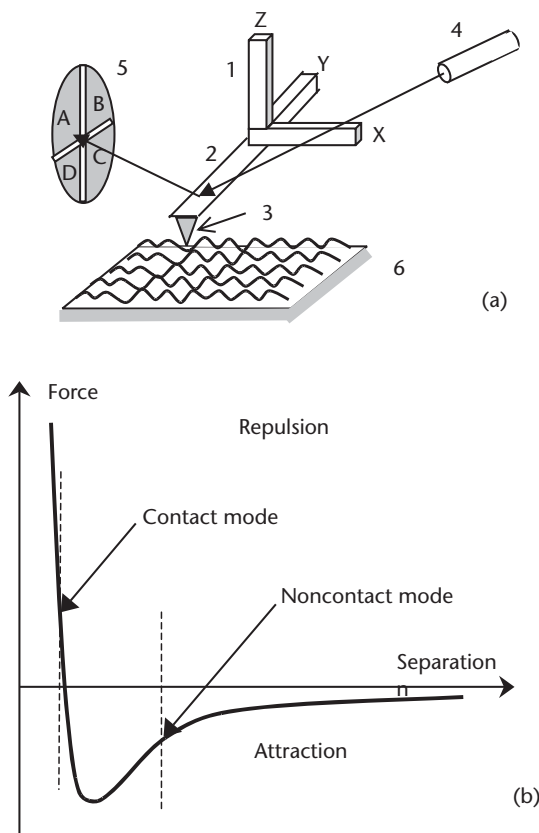
STM, the first nanoprobe technique, briefly described in Chapter 1, was suitable for studying conducting materials. The AFM method, developed soon after STM, was more universal and applicable to all kinds of surfaces. The basic idea of AFM is slightly different from STM, and is illustrated in Figure 3.2(a). Although the main unit is the same [X,Y,Z piezo-ceramic positioner (1)], the principle of registration of vertical movement of the tip (3), which is usually made by CVD of  $\text{Si}_3\text{N}_4$  on a flexible cantilever (2), is optical. The laser beam reflected from the cantilever is registered with the position sensitive photodetector (5). This construction is universal, and is adopted by the majority of scanning nanoprobe instruments [18, 19].

Many nanoprobe scanning techniques (e.g., MFM, ECFM, and LFM) derived from AFM deploy modified tips to measure magnetic, electrostatic, or specific bio-interaction forces. The measurements of the ac current between the vibrating conducting (metallized) AFM tip and the surface allow the measurement of the surface potential ( $\varphi$ ), according to the following formula:

$$I = \frac{dQ}{dt} = \varphi \frac{dC}{dt} \quad (3.1)$$

where  $C$  is the tip capacitance. This is a realization of a Kelvin probe, with a lateral resolution in nanometer range called surface potential microscopy (SPM).

SNOM is a unique method that allows the overcoming of the diffraction limit in optical microscopy. It stands apart from the rest of the nanoprobe techniques, because it exploits the registration of the light scattered in the gap between the



**Figure 3.2** (a) The scheme of AFM: the X,Y,Z piezo-ceramic positioner (1), the cantilever (2), the tip (3), the laser (4), the position-sensitive photodetector (5), and the studied surface (6); and (b) the atomic force diagram. Set points for the contact and noncontact modes are indicated with dotted lines.

nanotip and the studied surface on the distances much smaller than the wavelength of the light under study [22]. The lateral resolution of SNOM is usually on an order of 10 less than that of AFM.

AFM can operate in three different modes—contact mode, noncontact mode, and tapping mode [18, 19]. Figure 3.2(b) shows the dependence of the interaction force on the distance between the tip and the sample surface. At larger distances from the surface, the attraction force is dominating, while the repulsion force starts to dominate at smaller distances (in the range of a few angstroms).

In the contact mode, the tip is brought into close contact with the sample surface, so that the force between the tip and the sample becomes repulsive. The deflection of the cantilever caused by this force is registered with a photodetector. The signal is compared to the predefined value of deflection (force), and the dc feedback system generates a certain voltage applied to the Z-part of the piezo-ceramic to keep the value of deflection (force) constant. This dc voltage measures the surface roughness. The vertical resolution of the AFM contact mode is in the range of  $10^{-2}$  nm, while the lateral resolution could reach the values less than 1 nm, depending mostly on the tip radius [18, 19]. The disadvantage of the contact mode is that it could damage both the sample and the tip. The tip could leave scratches in the surface of soft materials, and the tip could be broken on hard rough surfaces. Consequently, the

scan speed should be kept very low (usually less than 1 Hz), depending on the studied surface.

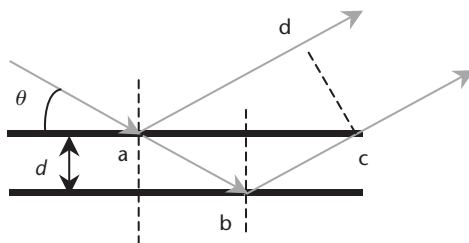
If the set-point is chosen in a range from 5 to 10 nm away from the surface, the tip will be attracted to the surface, and thus cause the cantilever to bend towards it. The surface profile can be recorded by maintaining the same value of the cantilever deflection, by using a feedback system. This is called the noncontact mode. Since the attraction force is much weaker than the repulsion force, the cantilever is vibrated in order to deploy more sensitive ac registration techniques. The resolution of the non-contact AFM is much lower in comparison to the registration of the contact mode; however, the scanning is much faster, making this method suitable for studying large and rough surfaces of various natures.

The tapping mode combines the advantages of both previous approaches. The cantilever is set to oscillate at frequencies in the range from 100 to 500 kHz, with an amplitude of approximately 20 nm, so that the tip is just touching (i.e., tapping) the surface [18, 19]. The amplitude of these oscillations depends on the distance from the surface, and thus provides a measure of the surface roughness. At the same time, recording the phase of oscillations may give the information on the visco-elastic properties of the material [18, 19]. For example, inclusion of materials with different mechanical properties will cause a contrast in phase images. The resolution of tapping mode AFM is almost the same as that of contact mode, but it is faster and much less damaging than noncontact AFM.

The majority of scanning nanoprobe techniques can be deployed in ultrahigh vacuum as well as in air and liquids, which make these methods universal for studying a large range of objects—atomically clean surfaces, various nanostructure surfaces, and real surfaces of materials—using both chemical and biological processes.

### 3.1.2 Methods of Crystallography Study

Diffraction is one of the most powerful methods of the structural study of materials, which may involve either X-ray, electrons, or neutrons. Disregarding the type of irradiation used, the same Bragg diffraction conditions can be applied to find positions of minimum and maximum intensity in the pattern. A zero phase shift between two or more waves, reflected from the regular pattern of the studied sample, gives the maximal intensity, while the waves in opposite phase will cancel each other and yield minimal intensity. For example, in the case of light reflection from a layered structure with a spacing ( $d$ ) between the reflecting planes, the Bragg conditions for diffraction maxima can be obtained by subtracting the pathlengths  $abc$  and  $ad$ , as shown in Figure 3.3 [23]:



**Figure 3.3** The calculation of a path-length difference in diffraction experiments.



$$2d \sin \theta = n\lambda, \quad n = 1, 2, 3, \dots \quad (3.2)$$

where  $\lambda$  is the wavelength and  $\theta$  is the angle of incidence.

Generally speaking, the diffraction pattern reflects the distribution in reciprocal space of either the electron density in electron diffraction or atomic density in neutron diffraction. Therefore, the profile of electron or atomic density can be extracted from the respective diffraction patterns.

Diffraction pattern can be registered as a whole two-dimensional image on the luminescent screen (in case of electron diffraction), or by scanning the angle of incidence of the beam and recording its intensity on reflection (in X-ray and neutron diffraction). In the latter method, often referred to as  $\theta-2\theta$  configuration, the rotation of the sample on an angle  $\theta$  is linked with the rotation of the detector on  $2\theta$ , and very often the experimental data was presented in the intensity versus  $2\theta$ .

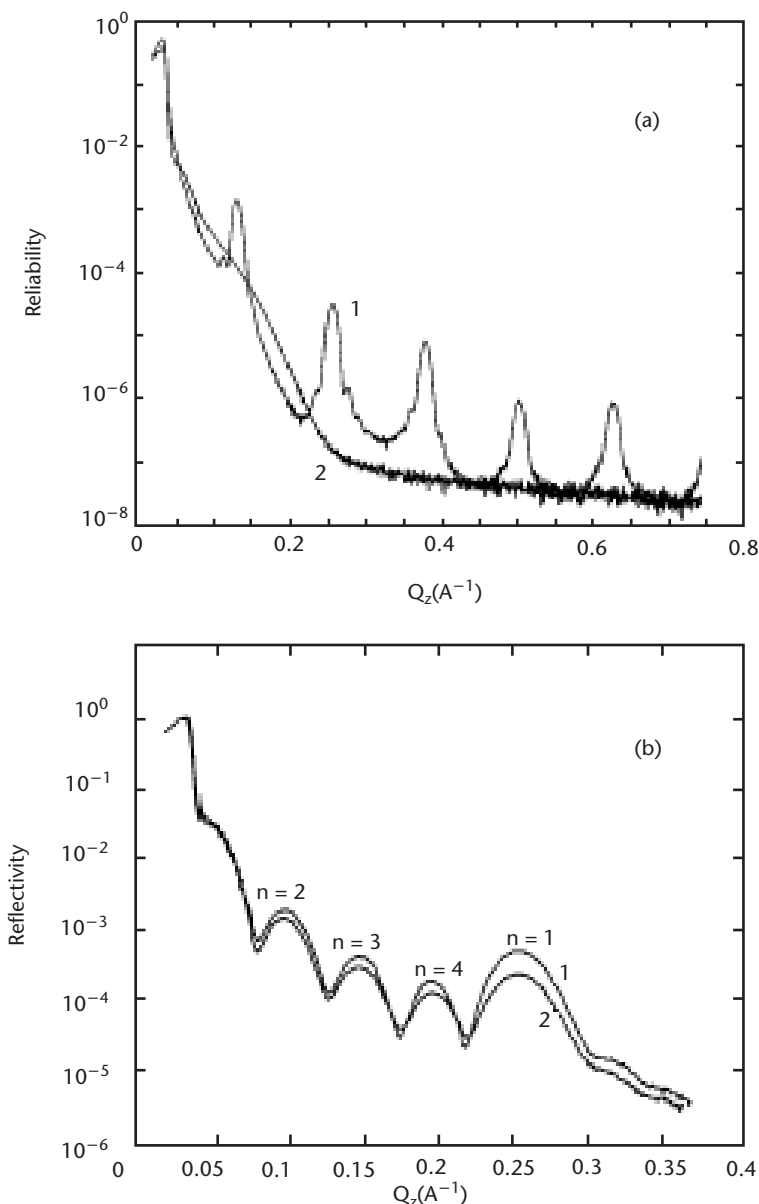
The interpretation of diffraction patterns obtained from two-dimensional and quasi-3D systems includes calculating the characteristic distances in different crystallographic directions using Bragg's formula (3.2), and comparing the obtained values to the database of the parameters of known crystallographic lattices. The parameters of elementary unit cells for particular crystallographic lattices can be also found.

### 3.1.3 The Layer-by-Layer Structure of Thin Films

We now discuss films produced by LB or layer-by-layer electrostatic deposition techniques. These are usually studied using the method of small angle X-ray diffraction (SAXD), with the X-ray beam hitting the sample at grazing angles ranging from  $1^\circ$  to  $5^\circ$  [4–9]. LB films, having a highly periodical layer-by-layer structure, are exemplary objects for such study. A typical SAXD pattern registered for multilayered LB films of fatty acids (i.e., stearic acid Cd salt) is shown in Figure 3.4(a) [24]. The seven diffraction fringes observed (only five of which are shown) demonstrate the high periodicity of the film in normal direction. This is not a unique occurrence, since observations of 10 to 12 diffraction fringes were reported in similar systems.

The interplane distance ( $d$ ) can be easily evaluated from the position of each diffraction maximum. For the above system, the value of 5.03 nm was evaluated, which corresponds closely to a double chain-length of stearic acid. It is interesting to observe dramatic changes in the diffraction pattern of the same film after exposure to  $H_2S$  gas. All Bragg peaks disappear, indicating a randomized structure caused by the formation of CdS clusters within LB film. The LB films of some other compounds may not have such a high level of periodicity. For example, LB films of calixarene Cd salt show only one broad Bragg diffraction maximum [see Figure 3.4(b)] [24], which yields a value of  $d = 2.47$  nm as an interlayer distance. At the same time, there are several small maxima observed at the angles below the first Bragg peak. They are called interference fringes (or Kiessig fringes), and represent the interference of electromagnetic waves reflected both from the top film surface and from the bottom film/substrate interface. A total film thickness ( $D$ ) can therefore be calculated from the position of the Kiessig fringes [13, 25]:

$$n\lambda = 2D \sin \theta_n, \quad n = 1, 2, 3, \dots \quad (3.3)$$

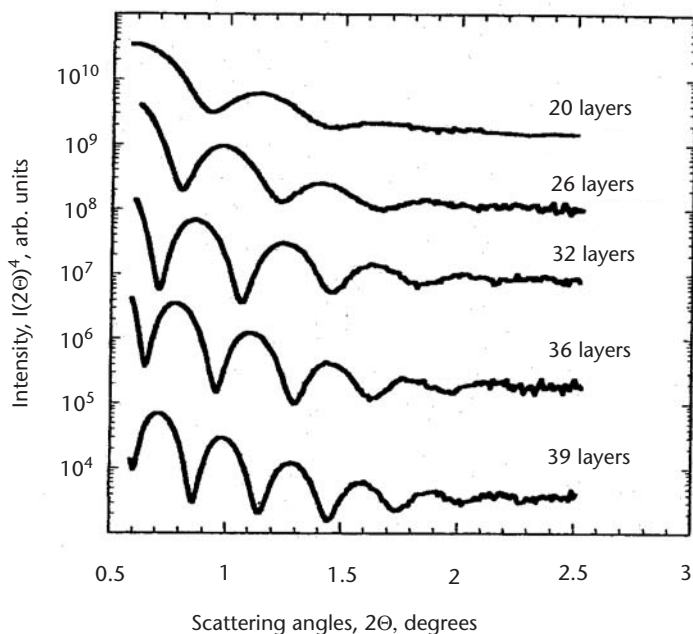


**Figure 3.4** SAXD patterns (a) for LB films (5 bilayers) of Cd stearate, and (b) for calix[8]-resorcinarene both before (curve 1) and after (curve 2) exposure to  $\text{H}_2\text{S}$  gas. (From: [23]. © 1998 Elsevier. Reprinted with permission.)

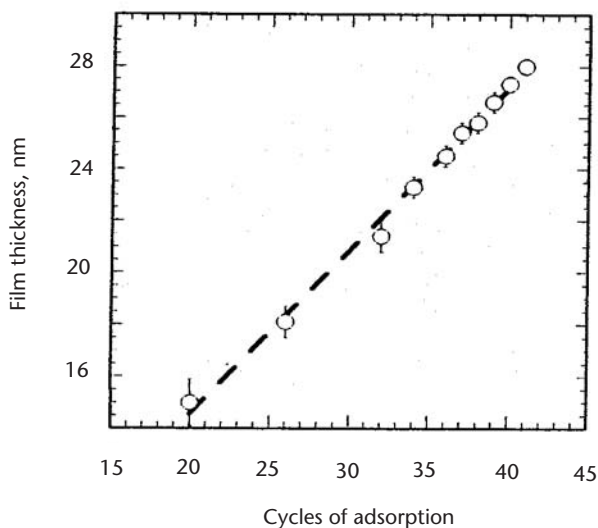
For this particular object [see Figure 3.4(b)], calculations yield  $D = 13.2$  nm, which is very close to the thickness of 10 layers or 5 bilayers ( $5d = 5 \times 2.47 = 12.35$  nm) of calix[8]arene LB film [24]. The formation of CdS clusters within LB film of calixarene Cd salt has little effect on SAXD pattern [see Figure 3.4(b)], because the film is not well-ordered in the first place.

Electrostatically self-assembled films produced by consecutive deposition of polycations and polyanions onto electrically charged substrates (see Chapter 2) are supposed to have periodic structure in the normal direction. However, this suggestion is not confirmed by X-ray and neutron diffraction. The SAXD pattern of one of

the classical example of polyelectrolyte films (i.e., PVSA/PAH film) shows no Bragg peaks, but only Kiessig interference fringes [see Figure 3.5(a)] [25]. It is somehow expected, considering the quite flexible polymer structure and interpenetration of



(a)



(b)

**Figure 3.5** (a) SAXD pattern of (PVS/PAH)<sub>n</sub> film. The corresponding number of layers (n) shown near their respective curves. (b) The dependence of the film thickness on the number of adsorbed PVS/PAH layers. (From: [24]. © 2000 Marcel Dekker, Inc. Reprinted with permission.)

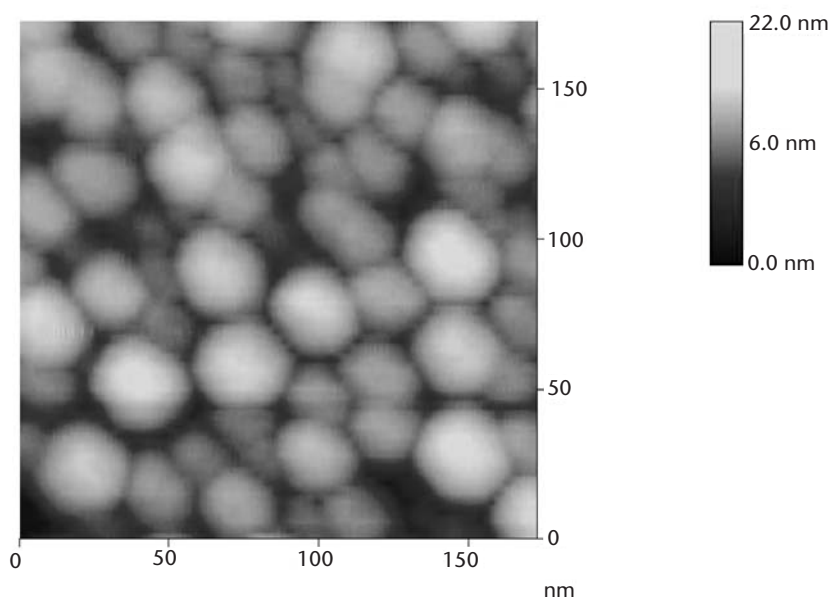
polycation and polyanion chains. As a matter of fact, the absence of Bragg diffraction may not be only attributed to a poor layer-by-layer ordering, but also to the lack of contrast in either electron or atomic density. Both polymers (PAA and PAH) consist mostly of carbon, and thus do not show significant difference in electron density (in X-ray diffraction experiments), nor in atomic nuclear density (in neutron scattering experiments) [13, 25].

As one can see from Figure 3.5(a), the number of Kiessig fringes increases with the increase of in number of PVS/PAH layers deposited. From the slope of the dependence of the film thickness compared to the number of PVS/PAH layers deposited [see Figure 3.5(b)], the thickness of the PVS/PAH repeating unit was found to be  $1.34 \pm 0.03$  nm [25].

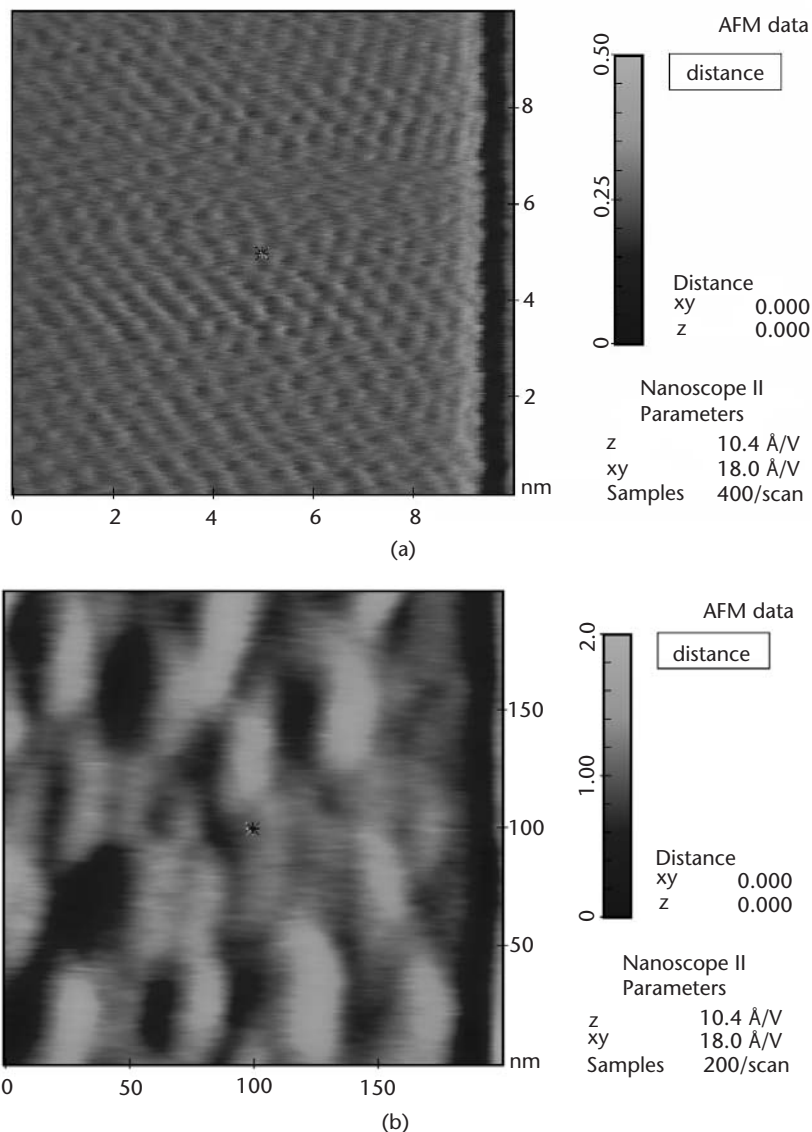
### 3.1.4 Morphology of LB Films Containing Nanoparticles

As described in Chapter 2, nanoparticles can be formed within LB films, or can be deposited by electrostatic self-assembly. In both cases, particles appeared to be covered with the “blanket” of thin organic films, which obviously causes broadening and smearing of the features on STM/AFM images. AFM images of CdS nanoparticles formed within LB films of stearic acid are shown in Figure 3.6 [26].

CdS particles are randomly distributed but have a trend for further aggregation. Yet CdS clusters show a hint of hexagonal facets, which most likely is the consequence of their hexagonal (wurzite) crystallographic lattice. The appearance of wurzite structure instead of cubic zinc blend, typical for bulk CdS, is an interesting fact predicted theoretically for nanoclusters of some II-VI semiconductor materials [27]. Our experiments on similar objects with the AFM contact mode, having generally higher resolution than the tapping mode, were less successful. AFM images in Figure 3.7 show the transformation from a regular two-dimensional pattern of



**Figure 3.6** Tapping mode AFM image (Nanoscope III a) of CdS nanoparticles formed within a bilayer of stearic acid LB film.



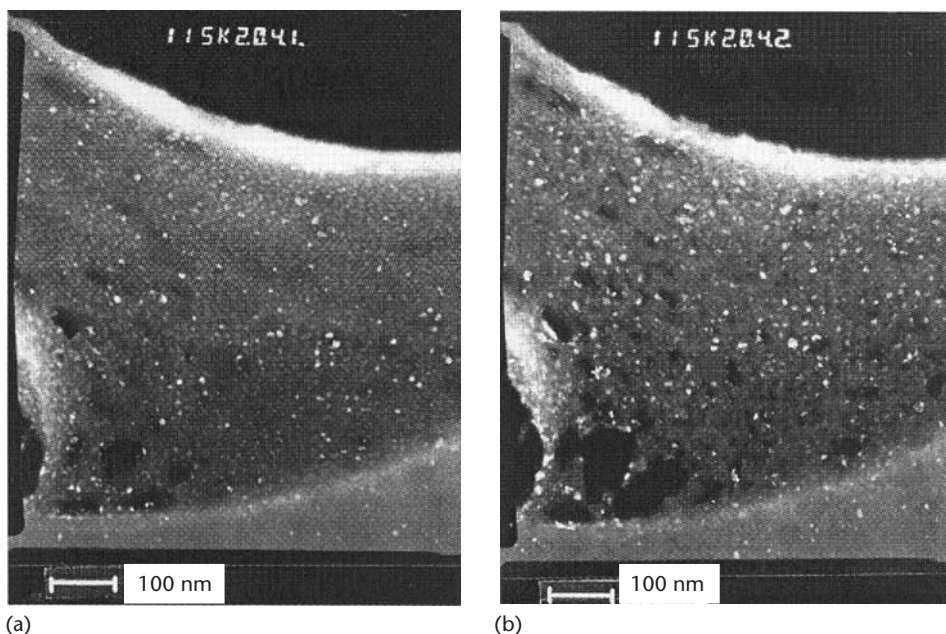
**Figure 3.7** Contact mode AFM images (Nanoscope II) of cadmium stearate LB film (a) before and (b) after exposure to H<sub>2</sub>S gas. (From: [27]. © 1999 Elsevier. Reprinted with permission.)

closely packed cadmium stearate molecules in LB film [see Figure 3.6(a)], to a rough and irregular surface after the formation of CdS clusters within LB film, caused by exposure to H<sub>2</sub>S gas [28].

Comparison of AFM tapping and contact modes shows clearly the advantage of the former for this particular application. Perhaps the presence of rigid CdS clusters under a relatively soft layer of stearic acid may contribute to the formation of the AFM tapping mode image and produce better contrast as a result.

CdS nanoparticles formed within LB films are too small to be seen with SEM, but they were observed with TEM, as shown in Figures 3.8 [29].

This experiment demonstrates the effect of a high-energy (200-keV) electron beam of a Philips CM20 TEM instrument on the CdS particle growth. Two TEM images in Figure 3.8, taken with a time interval of 5 minutes, clearly show an increase



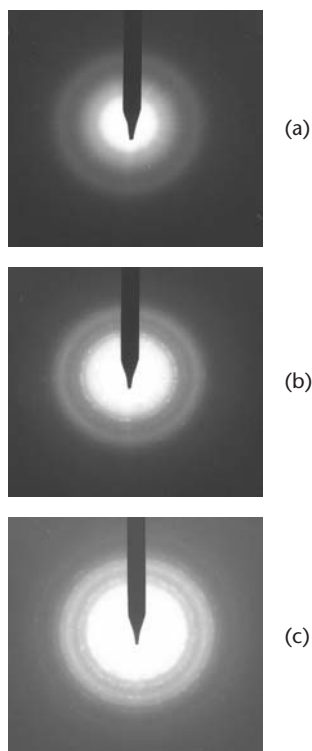
**Figure 3.8** (a) TEM images of calix[8]arene LB films (10 layers) containing CdS clusters, with a magnification of 115,000. (b) Same images, taken 5 minutes later. (From: [28]. © 2000 American Institute of Physics. Reprinted with permission.)

in the cluster size. This was further confirmed with electron diffraction measured with the same instrument, but with an unfocused ( $0.5\text{-}\mu\text{m}$  spot) electron beam. Three diffraction patterns measured subsequently in 5-minute time intervals show gradual changes from diffused rings of the fresh sample [Figure 3.9(a)] to the spotted rings [Figure 3.9(b, c)]. This is in line with the transformation from the amorphous background structure of the hollow carbon substrate to a more pronounced crystalline structure, due to the growth of CdS clusters. The pattern in Figure 3.9(c) yields the spacing values of 0.226, 0.16, and 0.133 nm. The last two values correspond closely to the same parameter of a cubic (zinc blend) lattice  $a_0 = 0.567 \pm 0.012$  nm [29], which is less than a value of 0.583 nm for bulk CdS, and is in line with predictions of Ramakrishna's theory [27]. The spacing value of 0.16 nm does not fit into zinc blend structure, but corresponds to a hexagonal (wurtzite) lattice, or a mixture of the two.

### 3.1.5 Morphology and Crystallography of Chemically Self-Assembled Nanoparticles

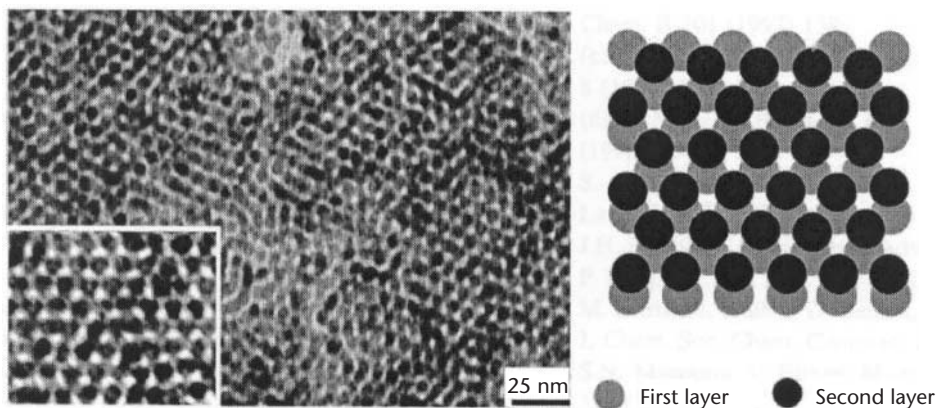
In contrast to the previous deposition techniques (i.e., LB and electrostatic self-assembly), nanoparticles, which are chemically self-assembled onto the solid substrates, tend to form regular two-dimensional structures, especially after annealing at moderate temperatures. The type of two-dimensional structure, which usually follows the trend of close packing arrangement, depends on the particles' shapes. For example, a simple hexagonal pattern is formed by spherical nanoparticles. A classical example of such structures is gold colloid particles chemically self-assembled onto the surface of gold via thiol groups. The observation of such structures is possible with scanning nanoprobe microscopy, such as STM and AFM, as well as with TEM and high resolution SEM.





**Figure 3.9** Electron diffraction pattern registered on calix[8]arene LB film containing CdS clusters. Photos (a), (b), and (c) correspond to subsequent 5-minute irradiation with a focused 200-keV electron beam. (From: [28]. © 2000 American Institute of Physics. Reprinted with permission.)

As an example, Figure 3.10 shows high resolution TEM images of 5-nm thiol stabilized Au colloid particles, deposited on a carbon-coated copper grid from their solution in chloroform, demonstrating a well-ordered structure of two layers of gold nanoparticles [30]. The observed hexagonal in-plane structure of Au particles, as well as the position of the second layer with respect to the first layer, corresponds to the close packing principle.



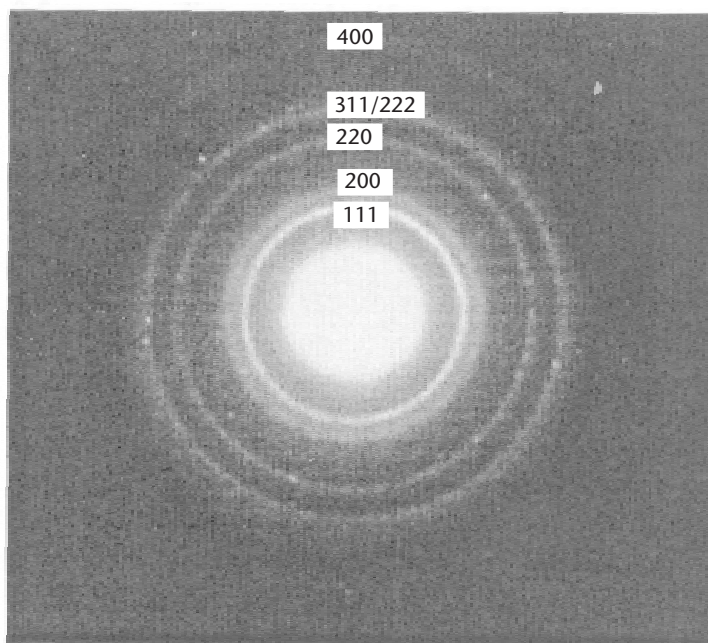
**Figure 3.10** TEM images of gold nanoparticle film deposited onto the carbon-coated copper grid from a 1-mg/mL solution in chloroform. The schematic structure of two close packed layers of spherical particles is shown on the right. (From: [29]. © 2002 Elsevier. Reprinted with permission.)

Two levels of crystallography must be considered here: first, the arrangement of nanoparticles in two- or three-dimensional structures, and second, the crystallography of the nanoparticles themselves.

The following example of Au colloid nanoparticles prepared in the presence of low generation poly(amidoamine) dendrimer [31] shows a combination of two levels of crystallography. TEM images of gold colloid deposited onto a carbon-coated copper grid revealed randomly scattered Au-colloid particles, ranging in size from 2 to 3 nm. An electron diffraction pattern of the same object in Figure 3.11 shows well-resolved rings, corresponding to (111), (200), (220), (311), and (232) planes of a face-centered cubic (f.c.c.) lattice of Au clusters.

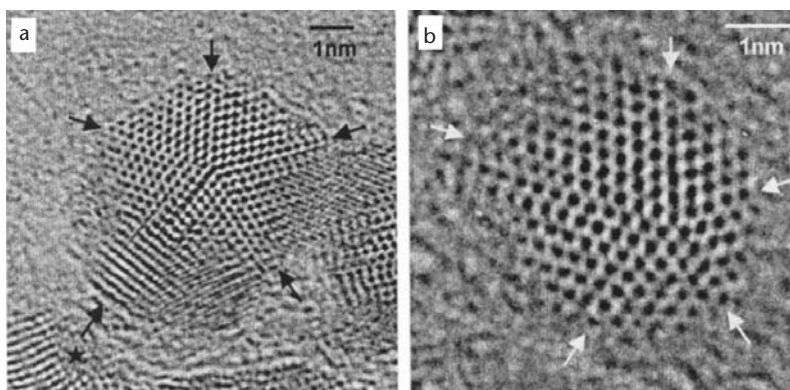
A unique case of five-fold symmetry of 10-nm gold nanoparticles, dispersed from their solution in toluene on hollow carbon film, was observed with high-resolution electron microscopy (HREM) [32] (see Figure 3.12). An ARM-1250 instrument operating at 1,250 keV and with a resolution of 0.13 nm was deployed for this study. Five-fold symmetry is allowed only in small particles, and it is in line with previously reported cases of five-fold symmetry appearing on early stages of the formation of f.c.c. structures. Five-fold  $\langle 111 \rangle$  symmetry is observed for both nanoparticles; however, the structure of a smaller particle [Figure 3.12(b)] is less distorted than that of the larger one [Figure 3.12(a)].

The films of II-VI, III-V, and metal oxide semiconductor nanoparticles are very popular objects for a structural study. One example of CdS nanoparticles formed within LB films was already discussed earlier in Section 3.1.4. In that case, the system represented a combination of randomly distributed CdS clusters, which contributed to a diffuse halo on the electron diffraction pattern and a zinc blend/wurtzite mixed structure of CdS, giving rise to diffraction rings and spots. ZnS nanoparticles



**Figure 3.11** Electron diffraction pattern of Au colloid nanoparticles deposited onto carbon-coated copper grid. (From: [30]. © 2003 Elsevier. Reprinted with permission.)





**Figure 3.12** HREM images of a gold nanoparticles on the hollow carbon surface: (a) 5-nm particle, and (b) 3.8-nm particle. Twin planes are indicated as arrows. (From: [31]. © 2000 Elsevier. Reprinted with permission.)

prepared by the sol-gel route and confined in amorphous silica thin film are another typical example of a combination of random distribution of ZnS clusters in the matrix and fine crystallographic lattice of ZnS clusters, as can be judged from TEM/ED experimental results [33]. Much better crystallography of PbS nanoparticles incorporated into zeolite was observed in [34]; however, their in-plane distribution is still random. Well-pronounced electron diffraction spots imply some kind of preferential orientation of PbS clusters.

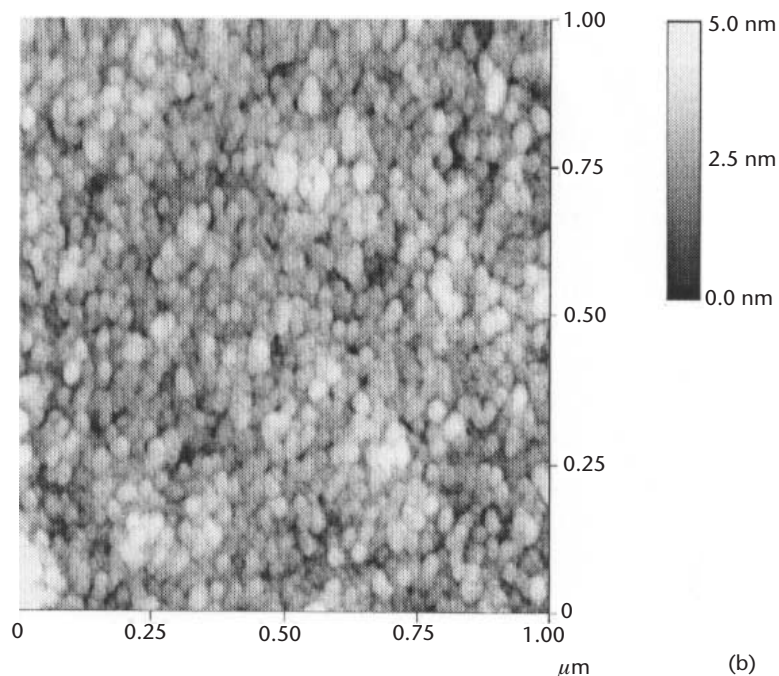
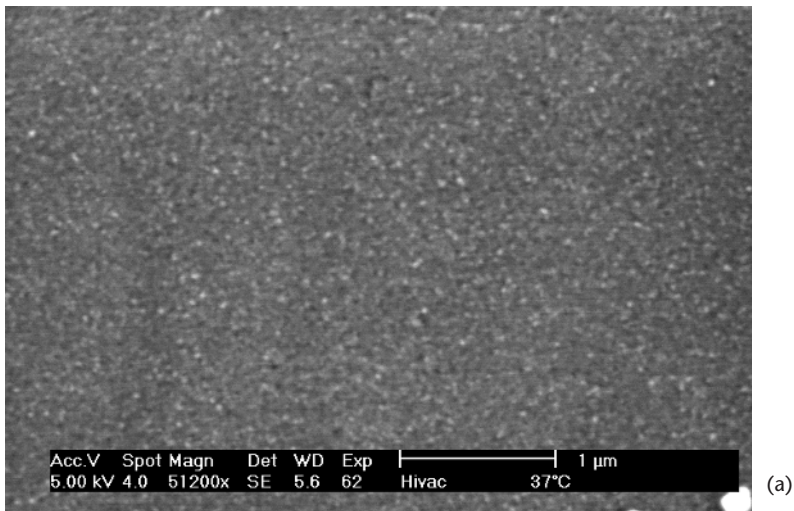
### 3.1.6 The Morphology and Structure of Sol-Gel and Electrodeposited Materials

The materials produced by sol-gel or electrodeposition techniques are polycrystalline, with the size of crystallites (i.e., grains or domains) varying from micrometers down to nanometers. In the latter case, materials can be called nanocrystalline, or even amorphous, in which case, crystallites become very small and comparable to atomic distances, thus losing their long-range crystalline order. Thermal annealing of electrodeposited or sol-gel materials leads to increasing grain size. Typical examples of the structure of sol-gel materials are shown in the Figure 3.13. Both SEM and AFM images of TiO<sub>2</sub> films, prepared by the sol-gel route combined with spin coating deposition technique from titanium isopropoxide catalyzed by acetic acid [35], show similar domain structure. However, AFM offers better resolution and contrast of images, and allows the estimation of mean grain size to be from 20 to 25 nm.

A typical XRD pattern of the above TiO<sub>2</sub> sol-gel material [35] gives two diffraction peaks at  $2\theta = 25.41^\circ$  and  $48.12^\circ$ , corresponding, respectively, to (101) and (200) crystallographic directions in the TiO<sub>2</sub> anatase-type structure. The size of crystallites can be estimated from the half-width ( $\beta$ ) of the diffraction peaks using the semi-empirical Scherrer formula [36]:

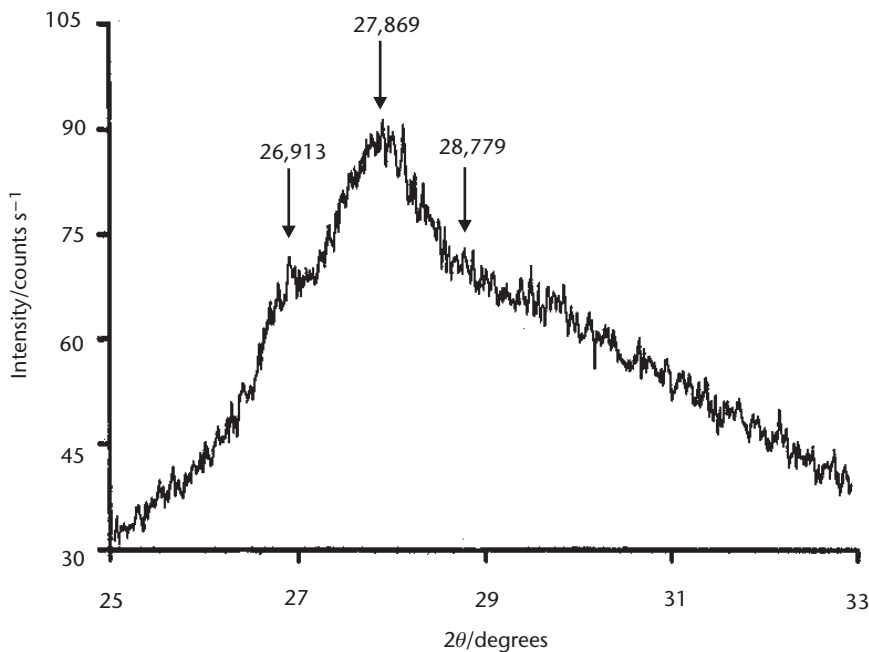
$$l_{101} = \frac{0.89\lambda}{\beta \cos \theta} \quad (3.4)$$

Such calculations yield a value of 18 nm, which corresponds closely to the direct observation of TiO<sub>2</sub> grains with AFM [see Figure 3.13(b)]. AFM and XRD



**Figure 3.13** (a) SEM and (b) tapping mode AFM images of  $\text{TiO}_2$  sol-gel material. (From: [34]. © 2003 Institute of Physics. Reprinted with permission.)

both show a correlation between the grain size of sol-gel  $\text{TiO}_2$  material and a spin speed during deposition—slower spinning produces larger grains [35]. Electrodeposition is another simple and cost-effective technique for the formation of nanostructured materials. The number of publications on this subject has increased dramatically within the last few years, because of the growing application of these materials in photovoltaic devices, solar cells, light emitters, and other semiconductor devices [37–39].



**Figure 3.14** XRD pattern of 41 period InAs/InSb superlattice produced by electrodeposition. (From: [43]. © 2001 Elsevier. Reprinted with permission.)

It is interesting to compare the structure and morphology of electrodeposited  $\text{TiO}_2$  films with the sol-gel material. The observation of much larger crystallites of  $\text{TiO}_2$  film (in the range from 100 to 400 nm), electrodeposited from an aqueous mixed solution of  $\text{TiOSO}_4$ ,  $\text{H}_2\text{O}_2$ , and  $\text{HNO}_3$ , at  $-1.1\text{V}$  potential onto ITO, and subsequently annealed at  $400^\circ\text{C}$  in air for 1 hour, was reported in [40]. Large crystallites in electrodeposited  $\text{TiO}_2$  films have resulted in more pronounced XRD peaks, as compared to those of sol-gel  $\text{TiO}_2$  films having a grain size of tens of nanometers.

Electrodeposition is widely used for the fabrication of thin films of II-VI semiconductor materials. XRD data of CdTe [41] and SnSe [42] films shows a polycrystalline structure for both types of films with large grain size in the submicron range. A distinctive orthorhombic structure was observed for SnSe, while CdTe films had a (111) cubic structure. The structural improvement of CdTe films was observed after annealing at  $350^\circ\text{C}$  to  $400^\circ\text{C}$ . InSb films with a thickness up to  $1\ \mu\text{m}$  were electrodeposited onto Cu and Si substrates from an aqueous solution of  $\text{InCl}_3$ , citric acid, and sodium citrate [43]. XRD patterns of the films show a well-defined zinc blend crystallographic structure. It was also found that the structure of InSb films deposited on crystalline Si was much better than those deposited onto amorphous Cu substrates. The most exciting result recently reported was the formation of InAs and InSb thin films, as well as InAs/InSb superlattices by electrodeposition [44]. Figure 3.14 shows an XRD pattern of the InAs/InSb 41 period superlattice.

The central peak at  $2\theta = 27.869^\circ$ , and two satellites at  $26.913^\circ$  and  $28.779^\circ$ , separated from the central peak by  $-0.956^\circ$  and  $+0.910^\circ$ , respectively, correspond to a superlattice with the period of 5.5 nm. Such III-V semiconductor superlattices with the period of a few nanometers and an accuracy of each layer in the order of 0.1 nm can be really comparable (especially considering the cost) with similar superlattices produced by MBE.

A regular two-dimensional pattern of Ni nuclei was obtained by electrodeposition on an Au (111) surface (see Figure 3.15) [45]. The electrodeposition was carried out from a 5-mM solution of Ni(II) in the ionic electrolyte  $\text{AlCl}_3\text{-[BMIm]}^+\text{Cl}^-$  at potentiostatic control. It was assumed that deposition of Ni and other metals (e.g., Co), follows the structural features of Au (111) surface.

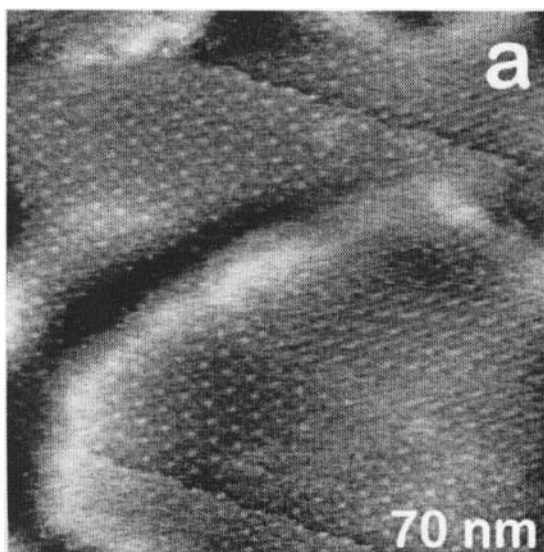
## 3.2 Elemental and Chemical Composition of Organic/Inorganic Nanostructures

### 3.2.1 Experimental Methods of Composition Study

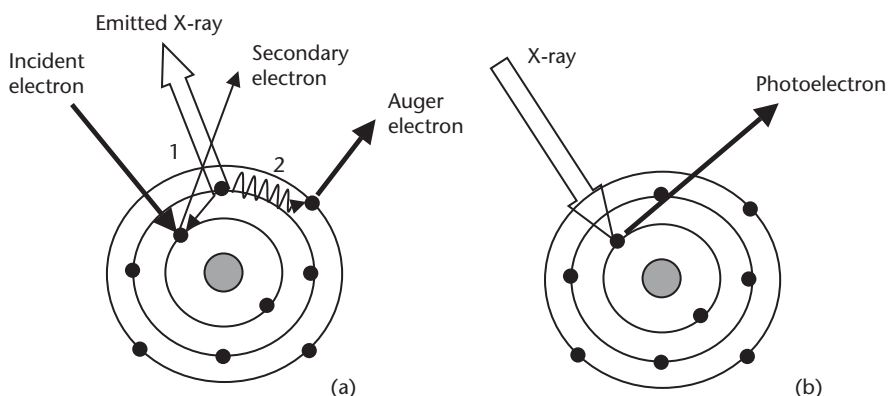
All traditional methods of elemental and chemical composition study, such as XPS, Auger spectroscopy, Raman spectroscopy, and Fourier Transformed Infrared Spectroscopy (FTIR), were adopted for nanostructural materials [11, 17, 46]. Electron spectroscopy is based upon two schemes of interaction of either high-energy electrons or X-rays with electrons on core atomic levels (see Figure 3.16).

In the first case [Figure 3.16(a)], an incident high energy electron beam may cause secondary electron emission from one of the core levels. The vacancy is immediately filled with an electron from the higher level, and results in either the emission of an electromagnetic wave in the X-ray spectral region (1), or the energy transfer to another electron and its subsequent emission (2). The second event is called the Auger process. Both processes are exploited for the elemental analysis of the material [47].

The spectrum of emitted X-rays provides a crude elemental analysis called energy dispersion X-ray (EDX) analysis. This technique goes along with standard SEM, and requires an additional X-ray detector. The accuracy of this method is not great, but it is sufficient to get a general idea of the material's elemental composition and stoichiometry. Another advantage of this technique, combined with electron



**Figure 3.15** STM image of two-dimensional nucleation of Ni electrodeposited on the surface of Au (111). (From: [44]. © 2003 Elsevier. Reprinted with permission.)



**Figure 3.16** Schemes of (a) Auger process and (b) electron photoemission.

beam scanning, is the possibility of mapping the material by plotting two-dimensional images formed by different elements. Similar information can be obtained with Auger electron spectroscopy (AES).

The method of XPS, which is based on the registration of electron spectra emitted from core atomic levels as a result of X-ray irradiation [Figure 3.16(b)], gives a more accurate information on the material's composition. The resolution of the spectra of secondary electrons emitted from the atomic levels is in the range of fractions of electron volts, which is enough to distinguish between different chemical forms of the same elements.

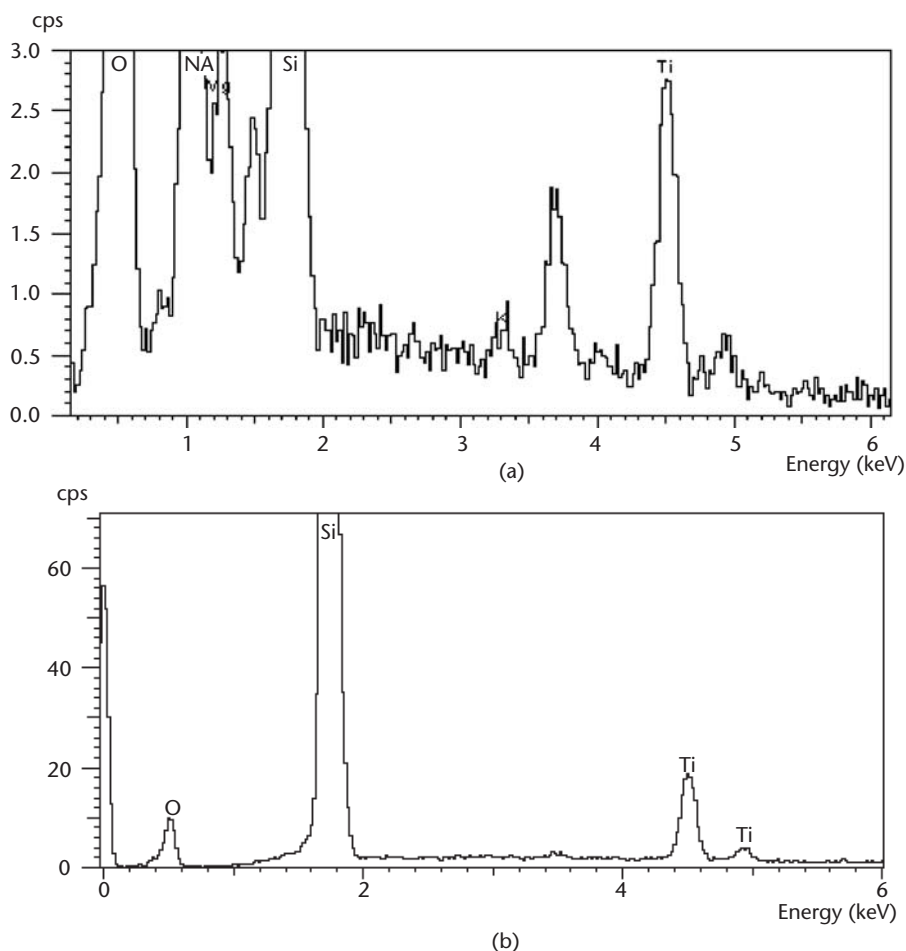
Another excellent technique for chemical analysis is infrared spectroscopy (IR), which is based upon the registration of characteristic spectra of molecular vibrations in the materials. Such spectra can be measured with either conventional IR, FTIR spectroscopy, or Raman spectroscopy. The latter is based on the registration of vibration spectra excited by a powerful laser in the visible spectral range. Raman spectral shift between the main excitation line and coupled vibration frequencies is the characteristic parameter for the recognition of molecular vibrations. An extensive database exists for vibration frequencies of different elements in different materials, which allows researchers to find chemical composition fairly easily [48].

### 3.2.2 Examples of Composition Study of Materials Prepared by Chemical Routes

Typical EDS graphs of sol-gel  $\text{TiO}_2$  films, as shown in Figure 3.17(a), demonstrate the presence of titanium and oxygen; however, it is difficult to establish the stoichiometry due to the interference of  $\text{SiO}_2$  and other oxides existing in the sol-gel film, as well as in the glass substrates [35]. Glass is a complex compound, containing a number of different elements (Si, Na, K, Mg, and Ca), as can be judged from EDS data.  $\text{TiO}_2$  films deposited by sputtering on silicon wafers yield much more defined spectra [see Figure 3.17(b)], practically without impurities, other than from silicon coming from the substrate.

XPS confirmed the formation of the PbS phase in thin films of lead phthalocyanine (PbPc) after exposure to  $\text{H}_2\text{S}$  gas [49]. The XPS peaks of both Pb-4f and S-2p in Figure 3.18(a) show a complex chemical composition of the material.

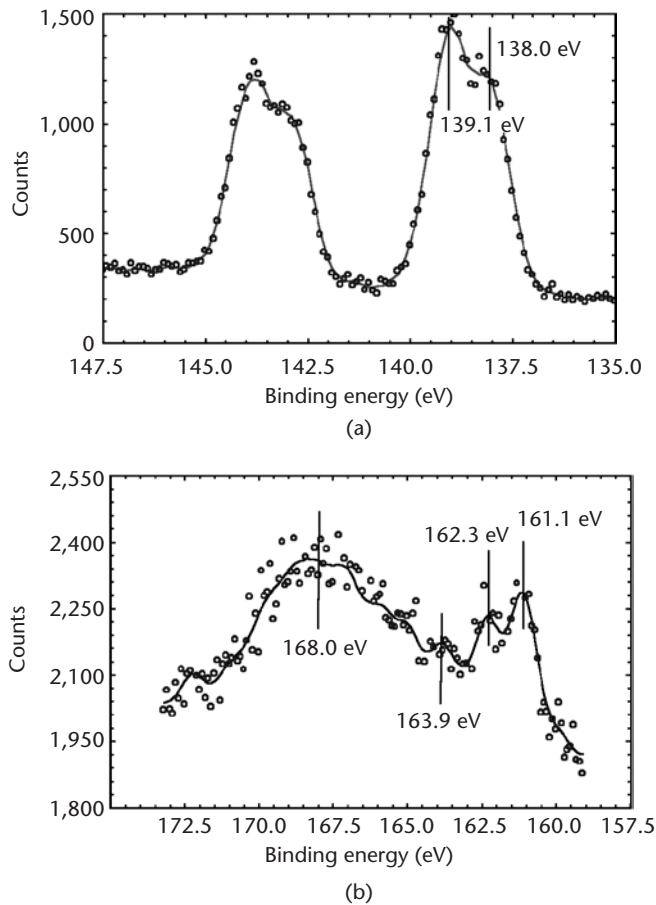




**Figure 3.17** ESD element analysis of  $\text{TiO}_2$  films produced (a) by sol-gel deposition on glass substrate, and (b) by sputtering on Si substrate. (From: [34]. © 2003 Elsevier. Reprinted with permission.)

The position of Pb-4f peak at 138.0 eV is very close to 137.8 eV, corresponding to the PbS phase [50], while the peak at 139.1 eV corresponds, most likely, to Pb in organic ligands [e.g., Pc moiety (139 eV)] [50]. The S-2p band in Figure 3.18(b) consists of several peaks of 168.0, 163.9, and 161.1 eV, due to the contribution of several phases:  $\text{SO}_2$  (168 eV), atomic S (164 eV), and PbS (161 eV), respectively. The peak at 162.3 eV most likely corresponds to S surrounded by organic ligands (162.2 eV [50])—for example, Pc moieties, due to the presence of chemical shift for both Cd and S characteristic spectral lines (see Figure 3.18). The method of XPS has also been successfully applied to confirm the formation of the stoichiometric CdS phase in both stearic acid and calixarene LB films [50].

The Raman spectra study of PbS nanoparticles in phthalocyanine (Pc) spun films [20], shown in Figure 3.19, prove the presence of Pb-S stretches at 200 and 300  $\text{cm}^{-1}$  in the film among a large number of other vibrations from 625 to 640  $\text{cm}^{-1}$  and from 970 to 990  $\text{cm}^{-1}$  typically attributed to Pc moiety. Characteristic spectral lines of Pb-S appeared as a result of exposure of PbPc spun films to  $\text{H}_2\text{S}$  gas, while test samples of metal free phthalocyanine ( $\text{H}_2\text{Pc}$ ) spun films do not show any spectral changes in the course of  $\text{H}_2\text{S}$  treatment [see Figure 3.19(c, d)].

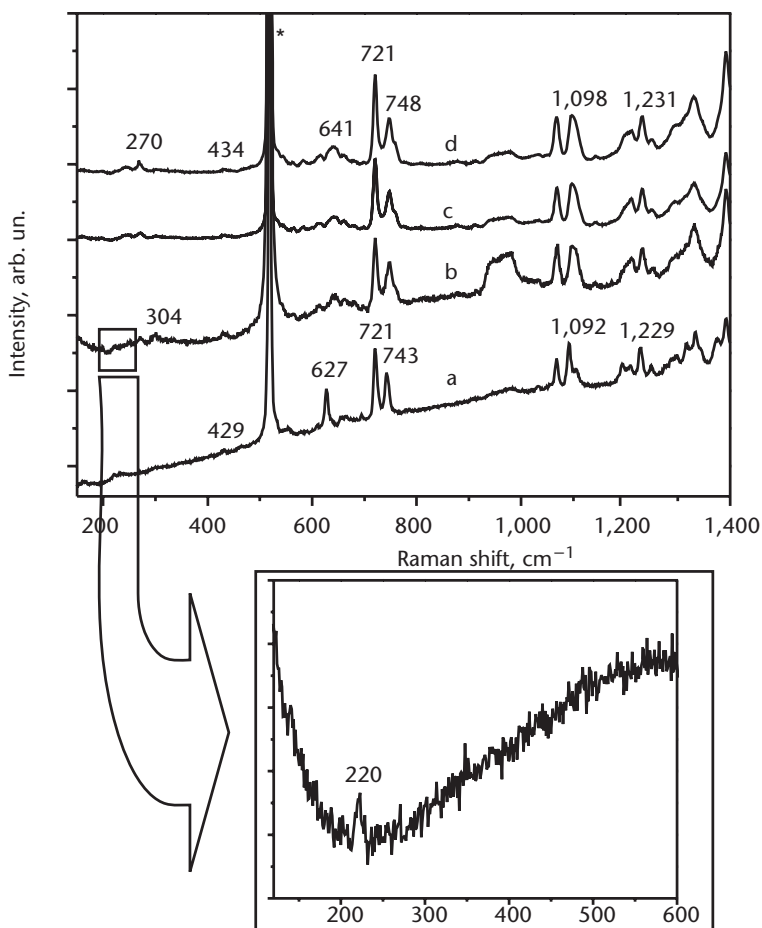


**Figure 3.18** XPS data for (a) Pb-4f<sub>5/2,7/2</sub> and (b) S-2p<sub>1/2</sub> spectral lines in PbPc/PbS-mixed spun films. (From: [48]. © 2003 IEEE. Reprinted with permission.)

### 3.2.3 Control of Impurities in Chemically Deposited Nanostructures

The problem of the registration and control of low concentrations of impurities (on the level of parts per million, or parts per billion) in organic materials is of high importance. Since organic materials have become increasingly popular in nanoelectronic device applications, their purity must be comparable to that in inorganic materials. Unfortunately, this is not always the case. Even the use of high purity grade (99.99 or  $10^{-4}$ ) chemicals during the formation of nanostructures (e.g., nanoparticles, layered structures, or thin films) does not match the grade of semiconductor materials in microelectronics, which is typically of  $10^{-6}$  and higher. That explains why materials produced by chemical routes vary in their properties so much. It recalls, to a large extent, the situation in semiconductor material technology in 1950s and 1960s, when the same types of materials produced in different laboratories showed absolutely different electrical properties. Organic materials technology is, however, progressing much faster because of great experience in materials science, advanced analytical techniques, and technologies of materials processing now available.

The importance of purity control of nanostructured materials has been recognized, and the research in this direction is constantly growing. It includes a number



**Figure 3.19** (a) Raman spectra of PbPc spun film before  $\text{H}_2\text{S}$  treatment, and (b) after  $\text{H}_2\text{S}$  treatment. (c) Spectra of metal free phthalocyanine ( $\text{H}_2\text{Pc}$ ) spun films before  $\text{H}_2\text{S}$  treatment, and (d) after  $\text{H}_2\text{S}$  treatment, shown for comparison. The inset shows the detailed Raman spectrum of PbPc film after  $\text{H}_2\text{S}$  treatment. (From: [48]. © 2003 IEEE. Reprinted with permission.)

of chemical and physical methods, such as dialysis [51], gel filtration [52], cross-flow microfiltration [53], evaporation under reduced pressure [54], ultracentrifugation [55] to reduce the presence of organic solvents, surfactants, residual monomers, and polymerization initiators. Photoluminescence measurements provide a reasonably sensitive tool (down to 0.1% in concentration) for the registration of  $\text{Ni}^{2+}$ ,  $\text{Mn}^{2+}$ , and other bivalent metal impurities in II-VI semiconductor nanoclusters [56]; or for neon, oxygen, nitrogen, and chlorine impurities trapped in sol-gel derived  $\text{MgO}:\text{Cr}$  material [57]. XPS and Auger spectroscopy provide similar sensitivity, as shown for example in [58] for Ni and Ti impurities in porous silicon.

The situation with electrically active impurities in semiconductor nanoparticles could be much more drastic, taking into account a limited number of atoms in the semiconductor clusters. Nanometer-sized clusters typically contain from  $10^3$  to  $10^4$  atoms (molecules) of the main material. The presence of just one atom of donor or acceptor impurity in the cluster, which is equivalent to a range from  $10^{19}$  to  $10^{20} \text{ cm}^{-3}$  of a bulk impurity concentration, will make the material heavily doped, and thus highly conductive, almost metallic. However, such impurity concentration is beyond



the resolution limit of Auger and X-photoelectron spectroscopy, and of optical (luminescence) methods [46, 47]. An obvious conclusion is to deploy electrical methods for impurity control in nanostructured materials, particularly in nanoparticles. Electrical methods may also be useful in monitoring the density of surface states, which play a significant role in the electrical properties of semiconductor nanoparticles.

## References

- [1] Roberts, G. G., et al., *Proceedings of the INFOS (Insulating Films on Semiconductors 83) Conference*, J. Verwey, (ed.), North Holland: Amsterdam, 1983, p. 141.
- [2] Roberts, G. G., "An Applied Science Perspective of Langmuir-Blodgett Films," *Adv. Phys.*, Vol. 34, No. 4, 1985, pp. 475–512.
- [3] Ross, J., and G. G. Roberts, *Proceedings of 2nd International Meeting on Chemical Sensors*, Bordeaux, France, 1986, p. 704.
- [4] Lvov, Y. M., and L. A. Feigin, "Langmuir Films—Preparation, Structure, Some Applications," *Kristallografiya*, Vol. 32, No. 3, 1987, pp. 800–815.
- [5] Lvov, Y. M., et al., "Small-Angle X-Ray-Analysis of Alternate-Layer Langmuir-Blodgett Films," *Phil. Mag. Lett.*, Vol. 59, No. 6, 1989, pp. 317–323.
- [6] Roberts, G. G., "Potential Application of Langmuir-Blodgett Films," in *Langmuir-Blodgett Films*, G. G. Roberts, (ed.), New York: Plenum Press, 1990.
- [7] Petty, M. C., "Characterization and Properties of Langmuir-Blodgett Films," in *Langmuir-Blodgett Films*, G. G. Roberts, (ed.), New York: Plenum Press, 1990, pp. 133–221.
- [8] Ulman, A., *An Introduction to Ultrathin Organic Films: From Langmuir-Blodgett to Self-Assembly*, Boston, MA: Academic Press, 1991.
- [9] Wegner, G., "Control of Molecular and Supramolecular Architecture of Polymers, Polymer Systems, and Nanocomposites," *Molecular Crystals and Liquid Crystals Science and Technology Section A-Molecular Crystals and Liquid Crystals*, Vol. 234, 1993, pp. 283–316.
- [10] Yarwood, J., "Fourier Transform Infrared Reflection Spectroscopy for Surface Analysis," *Analyt. Proc.*, Vol. 30, 1993, pp. 13–18.
- [11] Tredgold, R. H., *Order in Thin Organic Films*, Cambridge, England: Cambridge University Press, 1994.
- [12] Lvov, Y. M., M. R. Byre and D. Bloor, "Assembly of Multilayer Ordered Films by Alternating Adsorption of Oppositely Charged Macromolecules," *Crystall. Reports*, Vol. 39, No. 4, 1994, pp. 696–716.
- [13] Petty, M. C., M. R. Bryce, and D. Bloor, (eds.), *An Introduction to Molecular Electronics*, New York: Oxford University Press, 1995.
- [14] Ulman, A., (ed.), *Characterization of Organic Thin Films*, Boston, MA: Butterworth-Heinemann, 1995.
- [15] Tsukruk, V. V., "Assembly of Supramolecular Polymers in Ultrathin Films," *Progr. Polym. Sci.*, Vol. 22, No. 2, 1997, pp. 247–311.
- [16] Bliznyuk, V. N., A. Campbell, and V. V. Tsukruk, "Organized Multilayer Films of Charged Organic Latexes," in *Organic Thin Films: Structure and Applications*, C. W. Frank, (ed.), ACS Symposium Series 695, New York Oxford University Press, 1998, pp. 220–232.
- [17] Bonnell, D. A., *Scanning Probe Microscopy and Spectroscopy: Theory, Techniques, and Applications*, New York: Wiley-VCH, 2001.
- [18] DeStefanis, A., and A. A. G. Tomlinson, *Scanning Probe Microscopies: From Surface Structure to Nanoscale Engineering*, Enfield, NH: Trans Tech. Publications, 2001.
- [19] Gabriel, B. L., *SEM: A User's Manual for Materials Science*, Metals Park, OH: American Society for Metals, 1985.

- [20] Keyse, R. J., et al., "Introduction to Scanning Transmission Electron Microscopy," in *Microscopy Handbook*, Vol. 39, Oxford, England: BIOS Scientific Publishers, 1998.
- [21] Greffet, J.-J., and R. Carminati, "Image Formation in Near-Field Optics," *Progr. Surf. Sci.*, Vol. 56, No. 3, 1997, pp. 133–237.
- [22] Kitaigorodskii, A. L., *Organic Chemical Crystallography*, New York: Consultants Bureau, 1961.
- [23] Nabok, A. V., et al., "Size-Quantization in Extremely Small CdS Clusters Formed in Calixarene LB Films," *Thin Solid Films*, Vol. 327–329, 1998, pp. 510–514.
- [24] Lvov, Y., "Electrostatic Layer-by-Layer Assembly of Proteins and Polyions," in *Protein Architecture, Interfacing Molecular Assemblies, and Immobilization Biotechnology*, Y. Lvov and H. Mohwald, (eds.), New York: Basel/Marcel Dekker, 2000, pp. 125–167.
- [25] Nabok, A. V., et al., "Optical Study on II-VI Semiconductor Nanoparticles in Langmuir-Blodgett Films," *IEEE Trans. on Nanotechnology*, Vol. 2, No. 1, 2003, pp. 44–49.
- [26] Rama Krishna, M. V., and R. A. Freisner, "Quantum Confinement Effects in Semiconductor Clusters," *J. Chem. Phys.*, Vol. 95, No. 11, 1991, pp. 8309–8322.
- [27] Nabok, A. V., et al., "Formation of CdS Nanoclusters Within LB Films of Calixarene Derivatives and Study of Their Size-Quantization," *Mater. Sci. Eng. C*, Vol. 8–9, 1999, pp. 171–177.
- [28] Nabok, A. V., A. K. Ray, and A. K. Hassan, "Electron Beam Stimulated Formation of CdS Nanoparticles Within Calixarene Langmuir-Blodgett Films," *J. Appl. Phys.*, Vol. 88, No. 3, 2000, pp. 1333–1338.
- [29] Jiang, P., et al., "The Combining Analysis of Height and Phase Images in Tapping-Mode Atomic Force Microscopy: A New Route for the Characterization of Thiol-Coated Gold Nanoparticle Film on Solid Substrate," *Appl. Surf. Sci.*, Vol. 191, No. 1–4, 2002, pp. 240–246.
- [30] Bao, C., et al., "Preparation of Au Nanoparticles in the Presence of Low Generational Poly(amidoamine) Dendrimer with Surface Hydroxyl Groups," *Mater. Chem. & Phys.*, Vol. 81, No. 1, 2003, pp. 160–165.
- [31] Oku, T., and K. Higara, "Atomic Structures and Stability of Hexagonal BN, Diamond and Au Multiply-Twinned Nanoparticles with Five-Fold Symmetry," *Diamond and Related Materials*, Vol. 10, No. 3–7, 2000, pp. 1398–1403.
- [32] Bhattacharjee, B., et al., "Synthesis and Optical Characterization of Sol-Gel Derived Zinc Sulphide Nanoparticles Confined in Amorphous Silica Thin Films," *Mater. Chem. & Phys.*, Vol. 78, No. 2, 2002, pp. 372–379.
- [33] Flores-Acosta, M., et al., "Excitonic Absorption of Spherical PbS Nanoparticles in Zeolite A," *Solid State Commun.*, Vol. 128, No. 11, 2003, pp. 407–411.
- [34] Hassan, A. K., et al., "Structural and Electrical Studies on Sol-Gel Derived Spun TiO<sub>2</sub> Thin Films," *J. Phys. D: Appl. Phys.*, Vol. 36, No. 9, 2003, pp. 1120–1125.
- [35] Beghi, M., et al., "Structural Investigation of the Silica Titania Gel Glass-Transition," *J. Non-Cryst. Solids*, Vol. 145, No. 1–3, 1992, pp. 175–179.
- [36] Lin, Y. M., M. S. Dresselhaus, and J. Y. Ying, "Fabrication, Structure, and Transport Properties of Nanowires," *Adv. Chem. Eng.*, Vol. 27, 2001, pp. 167–203.
- [37] Persson, P., et al., "Quantum-Chemical Studies of Metal Oxides for Photoelectrochemical Applications," *Adv. Quant. Chem.*, Vol. 41, 2002, pp. 203–263.
- [38] Karuppachamy, S., et al., "Red Hybrid Organic Light-Emitting Device Fabricated with Molecularly Doped Polyimide Thin Film Containing Hole-Transporting Nanoparticles," *Solid-State Electron.*, Vol. 48, No. 5, 2004, pp. 633–640.
- [39] Karuppachamy, S., et al., "Cathodic Electrodeposition of Oxide Semiconductor Thin Films and Their Application to Dye-Sensitized Solar Cells," *Solid State Ionics*, Vol. 151, No. 1–4, 2002, pp. 19–27.
- [40] Soliman, M., et al., "Preparation and Characterization of Thin Films of Electrodeposited CdTe Semiconductors," *Renew. Energy*, Vol. 23, No. 3–4, 2001, pp. 471–481.

- [41] Zainal, Z., et al., "Electrodeposition of Tin Selenide Thin Film Semiconductor: Effect of the Electrolytes Concentration on the Film Properties," *Solar Energy Mater. & Solar Cells*, Vol. 79, No. 2, 2003, pp. 125–132.
- [42] Fulop, T., et al., "Electrodeposition of Polycrystalline InSb from Aqueous Electrolytes," *Thin Sol. Films*, Vol. 449, No. 1–2, 2003, pp. 1–5.
- [43] Wade, T. L., et al., "Electrochemical Formation of a III–V Compound Semiconductor Superlattice: InAs/InSb," *J. Electroanal. Chem.*, Vol. 500, No. 1–2, 2001, pp. 322–332.
- [44] Frailand, W., et al., "Nanoscale Electrodeposition of Metals and Semiconductors from Ionic Liquids," *Electrochem. Acta*, Vol. 48, No. 20–22, 2003, pp. 3053–3061.
- [45] Zecchina, A., et al., "Surface Structures of Oxides and Halides and Their Relationships to Catalytic Properties," *Adv. Catalysis*, Vol. 46, 2001, pp. 265–397.
- [46] Brundle, C. R., and A. D. Baker, (eds.), *Electron Spectroscopy: Theory, Techniques, and Applications*, New York: Academic Press, Vol. 1, 1977, Vol. 2, 1978.
- [47] *Vibrational Spectra and Structure: A Series of Advances*, Vol. 18, Applications of FT-IR Spectroscopy, New York: Elsevier, 1990.
- [48] Nabok, A. V., et al., "Nanocomposite Spun Films Based Upon Lead Phthalocyanine," *Proceedings of 3rd IEEE Conference on Nanotechnology*, 2003, Vol. 1–2, 2003, pp. 749–752.
- [49] Wagner, C. D., et al., "NIST X-Ray Photoelectron Spectroscopy Database," *NIST Standard Reference Database*, 20, Version 3, 4, 2003, <http://srdata.nis.gov/xps/>.
- [50] Nabok, A. V., et al., "Cadmium Sulphide Nanoparticles in Langmuir-Blodgett Films of Calixarene," *Langmuir*, Vol. 13, No. 12, 1997, pp. 3198–3201.
- [51] Rolland, A., "Clinical Pharmacokinetics of Doxorubicin in Hepatoma Patients After a Single Intravenous Injection of Free or Nanoparticle-Bound Anthracycline," *Int. J. Pharm.* Vol. 54, No. 2, 1989, pp. 113–121.
- [52] Beck, P., D. Scherer, and J. Kreuter, "Separation of Drug-Loaded Nanoparticles from Free Drug by Gel-Filtration," *J. Microencapsulation*, Vol. 7, No. 4, 1990, pp. 491–496.
- [53] Limayem, I., C. Charcosset, and H. Fessi, "Purification of Nanoparticle Suspensions by a Concentration/Diafiltration Process," *Separation and Purification Technology*, Vol. 38, No. 1, 2004, pp. 1–9.
- [54] Al Khouri-Fallouh, N., et al., "Development of a New Process for the Manufacture of Polyisobutylcyanoacrylate Nanocapsules," *Int. J. Pharm.*, Vol. 28, No. 2–3, 1986, pp. 125–132.
- [55] Krause, H. J., A. Schwarz, and P. Rohdewald, "Interfacial Polymerization, a Useful Method for the Preparation of Polymethylcyanoacrylate Nanoparticles," *Drug Dev. Ind. Pharm.*, Vol. 12, No. 4, 1986, pp. 527–552.
- [56] Yang, P., et al., "Luminescence Characteristics of ZnS Nanoparticles Co-Doped with Ni<sup>2+</sup> and Mn<sup>2+</sup>," *Opt. Mater.*, Vol. 24, No. 3, 2003, pp. 497–502.
- [57] Maghrabi, M., F. Thorne, and P. D. Townsend, "Influence of Trapped Impurities on Luminescence from MgO:Cr," *Nuclear Instruments and Methods in Physics Research, B*, Vol. 191, 2002, pp. 181–185.
- [58] Vdovenkova, T., V. Strikha, and A. Tsyganova, "Silicon Nanoparticles Characterization by Auger Electron Spectroscopy," *Surf. Sci.*, Vol. 454–456, 2000, pp. 952–956.

# Optical Properties of Organic/Inorganic Nanostructures

Optical properties of materials are very sensitive to the transition from three-dimensional (3D) bulk materials to low-dimensional systems. These low-dimensional systems include: two-dimensional (2D) surfaces, slabs and platelets; single-dimensional (1D) wires and chains; and zero-dimensional (0D) nanoparticles and nanoclusters, which are very often referred to as quantum dots. Strictly speaking, it is better to call them quasi- or pseudo- 2D, 1D, or 0D systems, since they have all three physical dimensions, although some of the dimensions are small and comparable with the wavelength of electrons, so that the electrons experience quantum confinement. Thus, the exact definition of low-dimensional systems lies in the reduction of one, two, or all three dimensions down to that quantization limit.

Physical properties of such low-dimensional systems differ from those in respective bulk materials due to the quantum confinement of electrons, and thus to the quantization of their energy. Historically, quantum effects in low-dimensional systems have been first found through the study of their optical properties, particularly, optical adsorption and luminescence spectra. In this chapter, the theoretical aspects of size quantization and its effect on optical properties will be outlined.

## 4.1 Optical Constants of Organic/Inorganic Nanostructures

### 4.1.1 Method of Ellipsometry

Optical adsorption and luminescence spectroscopy are traditional methods of material study, well described in both theoretical and experimental aspects. At the same time, methods of ellipsometry and SPR are not straightforward, either in experimental realization or in data analysis, and therefore require more detailed explanation.

Ellipsometry is an optical method based upon the registration of changes in the polarization of light after its reflection from the investigated sample. The state of polarization of the reflected electromagnetic wave can be described in terms of a ratio of complex Fresnel reflection coefficients for *s*- and *p*-components of polarized light [1]:

$$\rho = \frac{r_p}{r_s} = \tan(\Psi) \exp(i\Delta) \quad (4.1)$$

where indices  $s$  and  $p$  denote the direction perpendicular and parallel to the plane of incidence, respectively (see Figure 4.1).

Ellipsometric angles  $\Psi$  and  $\Delta$  were introduced in (4.1) as a ratio of Fresnel amplitudes of  $s$ - and  $p$ -components of polarized light and the difference in their phases ( $\delta_s$  and  $\delta_p$ ), respectively [1]:

$$\tan\Psi = \frac{|r_p|}{|r_s|}, \Delta = \delta_p - \delta_s \quad (4.2)$$

In the simple case of light reflection/refraction on the interface between two media (e.g., air and the reflective substrate), with respective refractive indices  $N_0$  and  $N_1$ , the Fresnel reflection and refraction coefficients can be written as:

$$r_p = \frac{N_1 \cos \theta_0 - N_0 \cos \theta_1}{N_1 \cos \theta_0 + N_0 \cos \theta_1}, \quad r_s = \frac{N_0 \cos \theta_0 - N_1 \cos \theta_1}{N_0 \cos \theta_0 + N_1 \cos \theta_1} \quad (4.3)$$

$$t_p = \frac{2N_0 \cos \theta_0}{N_1 \cos \theta_0 + N_0 \cos \theta_1}, \quad t_s = \frac{2N_0 \cos \theta_0}{N_0 \cos \theta_0 + N_1 \cos \theta_1} \quad (4.4)$$

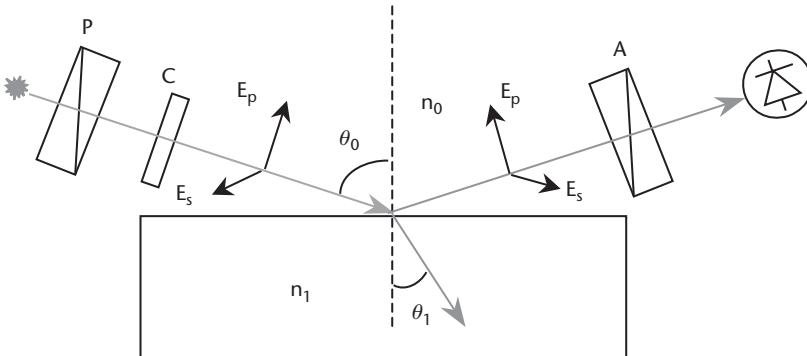
Generally, refractive indices are complex parameters  $N = n - jk$ , so Fresnel coefficients are. Substituting for  $r_s$  and  $r_p$  in (4.2) their values from (4.3), and making use of Snell's law  $N_0 \sin \theta_0 = N_1 \sin \theta_1$ , one can obtain a solution for  $N_1$  [1]:

$$N_1 = N_0 \tan \theta_0 \left[ 1 - \frac{4\rho}{(1+\rho^2)^2} \sin^2 \theta_0 \right]^{\frac{1}{2}} \quad (4.5)$$

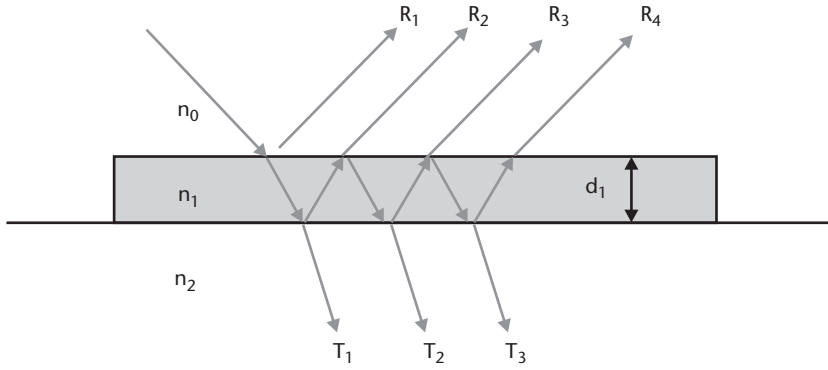
In the case of a three-layer system, consisting of a substrate (2), a film (1) on top, and an ambient (0), the solution is more complicated because of a multiple light reflection, as shown in Figure 4.2.

The total reflectance can be calculated as:

$$R = r_{01} + t_{01}t_{10}r_{12}e^{-i2\beta} + t_{01}t_{10}r_{10}r_{12}^2e^{-i4\beta} + t_{01}t_{10}r_{10}^2r_{12}^3e^{-i6\beta} + \dots \quad (4.6)$$



**Figure 4.1** The concept of ellipsometry and the scheme of PCSA null-ellipsometer: P—polarizer, C—compensator, S—sample, and A—analyzer.



**Figure 4.2** Multiple reflection from the system thin film/substrate.

Here  $r_{01}$ ,  $r_{12}$ ,  $t_{01}$ , and  $t_{10}$ , are Fresnel reflection and transmission coefficients at the 0/1(1/0) and 1/2 interfaces, respectively, and  $\beta$  is the phase thickness of the film.

$$\beta = 2\pi \left( \frac{d_1}{\lambda} \right) N_1 \cos \theta_1 = 2\pi \left( \frac{d_1}{\lambda} \right) (N_1^2 - N_0^2 \sin^2 \theta_0)^{\frac{1}{2}} \quad (4.7)$$

The summation of (4.6) for the  $p$ - and  $s$ -reflection components separately yields:

$$R_p = \frac{r_{01p} + r_{12p} e^{-i2\beta}}{1 + r_{01p} r_{12p} e^{-i2\beta}} \quad \text{and} \quad R_s = \frac{r_{01s} + r_{12s} e^{-i2\beta}}{1 + r_{01s} r_{12s} e^{-i2\beta}} \quad (4.8)$$

Now the main ellipsometric equation depends on a number of parameters of the system through Fresnel formula:

$$\tan \Psi e^{i\Delta} = \rho(N_0, N_1, N_2, d_1, \theta_0, \lambda) \quad (4.9)$$

There are two ways of solving (4.9) and (4.5). First, values of  $\Psi$  and  $\Delta$  can be found from known parameters  $N_0$ ,  $N_1$ ,  $N_2$ ,  $d_1$ ,  $\theta_0$ ,  $\lambda$  and by solving analytically respective Fresnel equations. This relatively easy task is frequently called *forward ellipsometric problem*. Second, the parameters of the reflective system, for example the refractive index ( $N_1$ ) and thickness ( $d_1$ ) of the film, can be obtained from the experimental values of  $\Psi_{exp}$  and  $\Delta_{exp}$ , a typical practical task frequently called *reverse ellipsometric problem*. The latter problem cannot be solved analytically, but only numerically, using least square techniques, which includes solving a forward problem [(4.9) or (4.5)] many times, and finding theoretical values of  $\Psi_{the}$  and  $\Delta_{the}$ , and subsequent minimization of the error function, for example:

$$E = \sqrt{(\Psi_{exp} - \Psi_{the})^2 + (\Delta_{exp} - \Delta_{the})^2} \quad (4.10)$$

The set of parameters ( $N_1$  and  $d_1$ ) corresponding to  $\Psi_{exp}$  and  $\Delta_{exp}$  at the minimum of  $E$  gives the solution of the reverse ellipsometric problem. A number of approaches based on different representations of error functions, as well as algorithms of their minimization, have been developed [2–5]. However, the main

question, whether the obtained solution is true and unique, always remains. It is a difficult problem, the discussion of which is perhaps beyond the scope of this book. The choice of the initial set of parameters for calculations is of great importance. It is always helpful to know roughly (or to make an intelligent guess) the values of parameters you want to obtain. To make sure that the obtained solution is unique, it is worth repeating calculations several times, starting from different sets of parameters. Success in ellipsometry fitting has always required a great deal of experience.

There are a large number of ellipsometry instruments starting from a simple fixed angle, single wavelength null-ellipsometer, and finishing with modern variable angle, spectroscopic instruments operating on the rotating analyzer principle, such as the M2000, made by J.A. Woollam Co., Inc.

A basic PCSA manual-operating null-ellipsometer, such as the LEF-3M (made in the Ukraine), is schematically shown in Figure 4.1. In the above scheme, the light beam from a HeNe laser ( $\lambda = 632.8$  nm) follows this path: first it goes through the polarizer (P); then it goes through the compensator (C), which is a  $\lambda/4$  plate, rotating the phase of polarization by  $90^\circ$ ; then it reflects from the investigated sample (S); and after passing the analyzer (A), the light beam targets a photodetector. The compensator is usually fixed at either  $+\pi/4$  or  $-\pi/4$  positions. The linear polarization of light reflected from the sample can be achieved by rotating the polarizer, so that the outgoing light intensity can be minimized (i.e., set almost to null) by rotating the analyzer. In fact, the minimum of light intensity can be obtained at four different sets of positions of P and A (four zones) for  $C = \pm\pi/4$ . Since the A, C, and P elements are not ideal, their readings must be averaged over four zones, in order to obtain correct values of  $\Psi$  and  $\Delta$ . Very often, two sets of readings of  $P_{1,2}$  and  $A_{1,2}$  (in two zones) at a fixed position of C (either  $+\pi/4$  or  $-\pi/4$ ) are sufficient. In this case, the values of  $\Psi$  and  $\Delta$  can be obtained as:

$$\Psi = \frac{A_1 + (\pi - A_2)}{2}, \quad \Delta = P_2 - P_1 \quad (4.11)$$

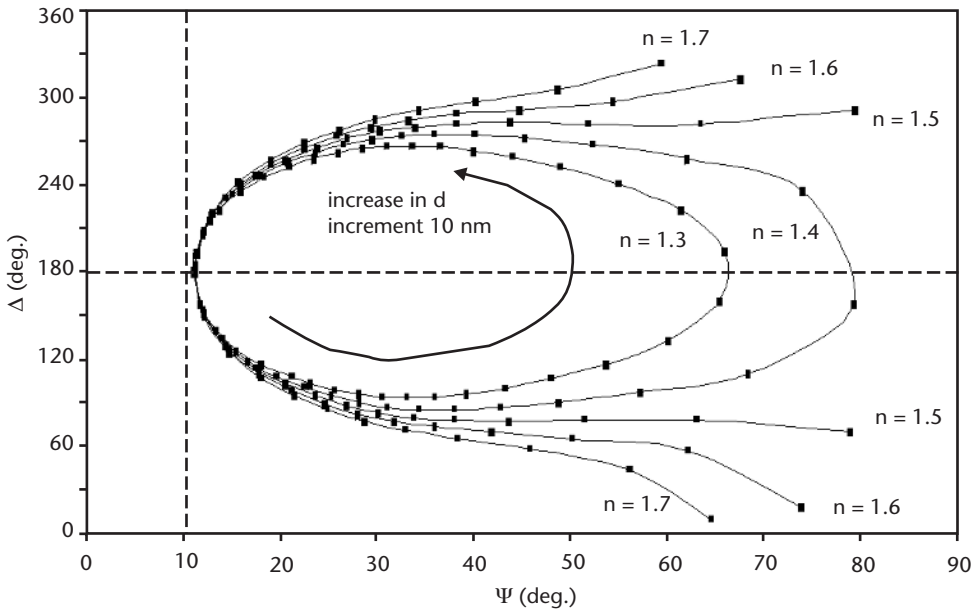
The accuracy of null-ellipsometry is usually fairly high, depending on the quality of the elements (polarizers, compensator, angle measurement units, and photodetector) used. Typical drawbacks are manual (i.e., slow) registration, difficulties in the automation, and the performance of spectral measurements.

A set of cyclic  $\Psi, \Delta(n, d)$  diagrams, as shown in Figure 4.3, is an example of a typical solution of the ellipsometric problem for an insulating (transparent) film on silicon substrate, with the following characteristics:  $n_2 = 3.867, k_2 = 0.02$  in air ( $n_0 = 1$ ) at a fixed wavelength ( $\lambda = 632.8$  nm), and the angle of incidence equal to  $70^\circ$ . Values of  $\Psi$  and  $\Delta$  lie in the range from  $0^\circ$  to  $90^\circ$ , and  $0^\circ$  to  $360^\circ$ , respectively. Every curve corresponds to a different refractive index ( $n_1$ ) of the film, while the distance along the curve (starting from the cross-point at  $\Delta = 180^\circ$ ) yields the thickness ( $d_1$ ).

It should be noted that the film thickness  $d_1$  can be found within a period of  $D_0$ , which depends on the parameters  $N_1, N_0, \lambda$ , and  $\theta_0$ , so that a total thickness  $d_1^*$  is:

$$d_1^* = d_1 + mD_0, \quad m = 0, 1, 2, \dots \quad D_0 = \frac{\lambda}{2} (N_1^2 - N_0^2 \sin^2 \theta_0)^{-\frac{1}{2}} \quad (4.12)$$





**Figure 4.3**  $\Psi, \Delta (n, d)$  diagram for insulating (transparent) film on silicon substrate.

It is assumed that media 1 and 2 are both transparent, so that  $N_1$  and  $N_2$  are real numbers. The above formula demonstrates that preliminary knowledge of the film thickness is very important.

The resolution of  $n$  and  $d$  is rather poor near the cross-point at  $\Delta = 180^\circ$ , where all curves come together (see Figure 4.3). This makes null-ellipsometry unsuitable for simultaneous evaluation of  $n$  and  $d$  for the films thinner than 10 nm. A knowledge (or intelligent guess) of one of the parameters (either  $n$  or  $d$ ) helps to overcoming the difficulty. An alternative solution is to perform measurements in two media having different refractive indices, for example, air ( $n_0 = 1$ ) and water ( $n_0 = 1.33$ ), and presenting the results in  $\Delta_1, \Delta_2$  coordinates, which gives much better resolution for the film thickness and refractive index [6].

The spectroscopic ellipsometer exploits the principle of the rotating analyzer, and typically consists of a light source, which may cover a wide spectral range (UV, visible, and IR); polarizer; rotating analyzer; and a sensitive photodetector (CCD or photoelectron multiplier). The absence of the chromatic element retarder (or compensator) makes the above scheme very suitable for spectral measurements. Spectroscopic ellipsometry has practically no restrictions on the measured film thickness; however, the sensitivity of the measurements is poor at  $\Delta$  near  $0^\circ$  and  $180^\circ$ . The signal-to-noise ratio can be significantly improved by performing a number of revolutions of the analyzer, with subsequent averaging of the  $\Psi, \Delta (\lambda)$  spectra. The spectroscopic ellipsometry method is very powerful, and allows the investigation of very complex structures, including multilayered reflective systems, composite and anisotropic materials of different nature, and rough surfaces causing light scattering and depolarization. Modern fitting software for spectroscopic ellipsometry, such as the WVASE32 supplied by J. A. Woollam Co., Inc. [7], includes a vast library of optical constants for different materials (i.e., insulators, semiconductors, and metals), as well as a number of approaches and algorithms for



data fitting of the complex systems mentioned above. However, the fitting remains a challenge, which requires a great deal of effort and experience, to find physically adequate models and to obtain mathematically unique solutions.

#### 4.1.2 Method of SPR

The SPR method is somewhat similar to ellipsometry, since it is based on the same Fresnel equations, and it has the same goal of the evaluation of parameters of thin films. The idea of SPR lies in the registration of the coupling of the incident electromagnetic wave into the surface plasmons (i.e., vibrations of free electrons in thin metal films near the metal-dielectric interface). This can be easily achieved in the Kretschmann configuration [8], as shown in the inset of Figure 4.4.

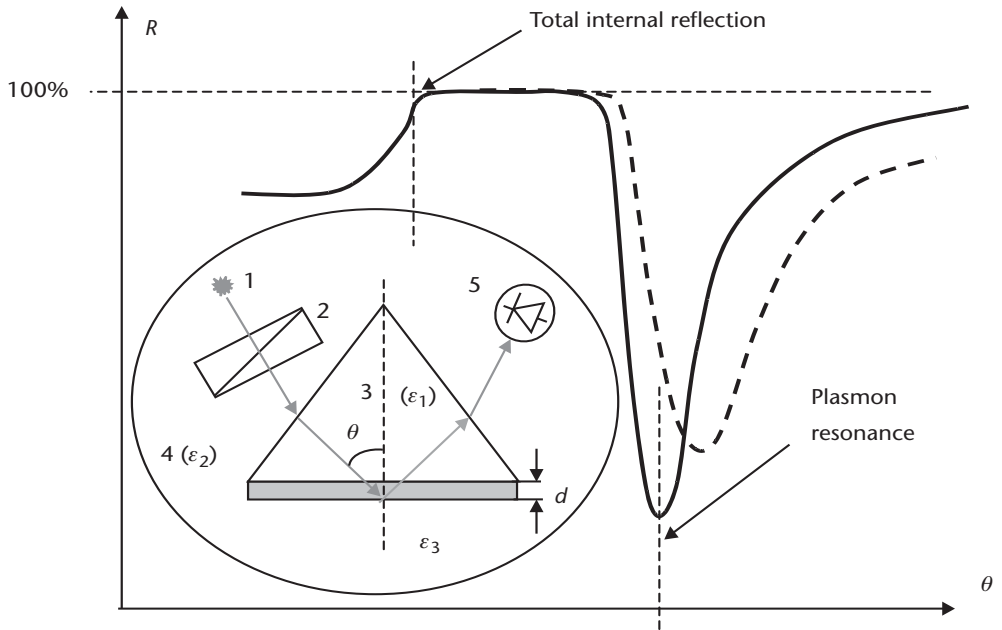
A *p*-polarized light beam (usually from a low-power HeNe laser) hits the prism, which has its bottom surface coated with a thin film (in the range from 40 to 50 nm) of highly conductive metal (e.g., gold, silver, or copper). Alternatively, the metal film can be deposited onto a glass slide, which is then brought into optical contact with the prism via the index matching fluid. If the internal incidence angle is larger than the angle of total internal reflection, then the beam reflects from the bottom of the prism, and the reflected light intensity registered with photodetector reaches its maximum. However, if the *k*-vector (or frequency) of the evanescent field penetrated into the metal film matches the frequency of plasmon oscillations, the energy will be transferred to plasmons, and the reflected light intensity will be reduced. Such conditions are often referred to as surface plasmon resonance (SPR). SPR can be registered by measuring the intensity of reflected light during the scanning of the beam over the range of angles of incidence, and thus changing the *x*-component (in the plane of the sample) of *k*-vector. A typical SPR curve, shown schematically in Figure 4.4, clearly demonstrates the resonance minimum, as well as the point of total internal reflection.

The shape of SPR curve (i.e., position, minimal reflectance, and half-width of SPR peak), depends upon the optical characteristics of the metal film (i.e., thickness, refractive index, and extinction coefficient). These parameters can be obtained by fitting the SPR curve to Fresnel's theory, using one of the least-square minimization techniques. Since the evanescent wave can penetrate through the thin metal film, the presence of the coating on top of the metal film will cause further changes (i.e., shift and broadening) in the SPR curve, as shown in Figure 4.4. The optical parameters of the coating can therefore be obtained by fitting.

The theory of SPR has been well described in a number of publications, particularly [9–15]. The reflection coefficient for a *p*-polarized light beam in the glass prism/metal film/ambient (air) three-layer system (see the inset in Figure 4.4), having respective dielectric permittivities  $\varepsilon_1$ ,  $\varepsilon_2$ , and  $\varepsilon_3$  ( $\varepsilon_1, \varepsilon_3$  are both real numbers, while  $\varepsilon_2 = \varepsilon_{r,2} + i\varepsilon_{i,2}$  is a complex number), can be described with the well-known Fresnel formula [13]:

$$r_{123} = r_{12} \frac{b_{23} + a_{23} [\operatorname{Re}(r_{12}) - i\operatorname{Im}(r_{12})] e^{2idk_x2}}{b_{23} + a_{23} [\operatorname{Re}(r_{12}) + i\operatorname{Im}(r_{12})] e^{2idk_x2}} \quad (4.13)$$

where  $r_{ij} = a_{ij}/b_{ij} = \operatorname{Re}(r_{ij}) + i\operatorname{Im}(r_{ij})$  is the reflection coefficient at the interface between layers *i* and *j*.  $k_x$  is the *x*-component (in the plane of the film) of the *k*-vector of the light incident at an angle  $\theta$ :



**Figure 4.4** Angular dependence of the reflection, often referred to as the SPR curve. Inset shows the Kretschmann geometry of SPR measurements, comprising the light source (1), polarizer (2), glass prism (3), thin metal film (4), and photodetector (5).

$$k_x = k_0 \epsilon_1^{1/2} \sin \theta = \frac{2\pi}{\pi} n_1 \sin \theta \quad (4.14)$$

The function  $R(k_x) = |r_{123}|^2$  experiences a minimum when  $b_{23} = 0$ . The surface plasmon resonance is, therefore, observed at

$$k_x^0 = k_0 \left( \frac{\epsilon_1 \epsilon_3}{\epsilon_1 - \epsilon_3} \right)^{1/2} \quad (4.15)$$

Both the reflectivity spectrum  $R(k_x)$  and its angular dependence  $R(\theta)$  can be relatively easily calculated from the parameters of the reflective system using Fresnel's formulas. The reverse problem of finding optical parameters of metal film from experimentally measured SPR curves has no analytical solution. It can be solved only numerically by fitting the experimental SPR curve to the Fresnel theory using the least square technique.

Using some approximations, however, the analytical relations between the optical parameters of metal film ( $\epsilon_2 = \epsilon_{2r} + i\epsilon_{2i}$  and  $d_2$ ) and the parameters of the SPR curve, which include the position of the resonance ( $k_{\min}$ ), minimal reflectivity ( $R_{\min}$ ) and a half-width ( $\Delta k$ ), can be established in the following form:

$$\epsilon_{2r} = \frac{\epsilon_3 k_{\min}^2}{k_{\min}^2 - \epsilon_3 k_0^2}, \epsilon_{2i} = \frac{\Delta k}{4A} (1 \pm \sqrt{R_{\min}}) \quad (4.16)$$

$$d_2 = \frac{1}{\phi} \ln \left[ \frac{\Delta k}{4B} (1 \pm \sqrt{R_{\min}}) \right] \quad (4.17)$$

It is clear from (4.16) and (4.17) that the position of SPR minimum depends entirely on the real part of the dielectric constant ( $\epsilon_{2r}$ ), while both  $R_{\min}$  and  $\Delta k$  depend on a linear combination of the imaginary part of the dielectric constant ( $\epsilon_{2i}$ ) and the film thickness ( $d$ ). The above approach has been used by Kretschmann [8] in the 1970s, when calculating facilities were limited, to evaluate parameters of metal films. The SPR data fitting now can be done fairly easily with modern PCs and fitting software.

A four-layer system, consisting of the prism ( $\epsilon_1$ ), the metal film ( $\epsilon_2, d_2$ ), the coating ( $\epsilon_3, d_3$ ), and the ambient ( $\epsilon_4$ ), is very important for a number of practical applications. This situation is more complex as compared to a three-layer system, especially considering that  $\epsilon_3$  could be a complex value. The reflection coefficient for such a system can be written as [16]:

$$r_{1234} = r_{12} \frac{Z_{1234}}{D_{1234}}, \quad (4.18)$$

where

$$D_{1234} = \left( \frac{k_{4z}}{\epsilon_4} + \frac{k_{2z}}{\epsilon_2} \right) - i \tan(k_{3z} d_3) \left( \frac{k_{4z} k_{2z}}{k_{3z}} \frac{\epsilon_3}{\epsilon_2 \epsilon_4} + \frac{k_{3z}}{\epsilon_2} \right) + r_{12} \exp(2ik_{2z} d_2) \left[ \left( \frac{k_{2z}}{\epsilon_2} - \frac{k_{4z}}{\epsilon_4} \right) - i \tan(k_{3z} d_3) \left( \frac{k_{4z} k_{2z}}{k_{3z}} \frac{\epsilon_3}{\epsilon_2 \epsilon_4} - \frac{k_{3z}}{\epsilon_2} \right) \right] \quad (4.19)$$

and  $k_{iz} = (\epsilon_i k_0^2 - k_x^2)^{1/2}$ .

The expression for  $Z_{1234}$  is similar to (4.19), but with  $r_{12}^{-1}$  instead of  $r_{12}$ .

Similar to the three-layer system, the spectrum or angular dependence of the reflectance  $R = |r_{1234}|^2$  has a minimum at certain values of  $\theta_0$  or  $\lambda_0$ . Optical parameters of the coating (e.g.,  $\epsilon_3 = \epsilon_{r3} - i\epsilon_{i3}$  or  $N_3 = n_3 - ik_3$  and  $d_3$ ) can be obtained by fitting  $R(\theta)$  or  $R(\lambda)$  SPR curves to the Fresnel formulas, assuming that the parameters for the metal film  $\epsilon_2 = \epsilon_{r2} - i\epsilon_{i2}$  and  $d_2$  were obtained earlier by fitting the SPR curve for a three layer system.

However, simple analytical relations between  $\epsilon_3 = \epsilon_{r3} - i\epsilon_{i3}$ ,  $d_3$ , and the experimental SPR curves, such as the shift between the SPR curves minima  $\Delta\theta = \theta - \theta_0$ , measured on the samples with the coating (medium 3) on the metal film (medium 2), and without it, and for the half-width of the SPR curve  $\theta_{1/2}$  measured in the four-layer system, were obtained in [10, 15]:

$$\Delta\theta = \theta - \theta_0 = \frac{2\pi}{\lambda} \frac{S_2}{n_1 \cos \theta_0} d_3 \left[ \epsilon_{r3} \left( 1 + \frac{\epsilon_{r2}}{\epsilon_{r3}^2} \right) - \epsilon_{r2} - 1 \right] \quad (4.20)$$

$$\theta_{1/2} = \frac{2\pi}{\lambda} \frac{S_2}{n_1 \cos \theta_0} d_3 \epsilon_{i3} \left( 1 - \frac{\epsilon_{r2}}{|\epsilon_3|^2} \right) \quad (4.21)$$

The scaling factor  $S_2$  in the above equations depends on the imaginary part of the dielectric permittivity of the metal film ( $\epsilon_{i2}$ ):

$$S_2 = \left( \frac{1}{-\varepsilon_{i2}} \right)^{1/2} \left( \frac{\varepsilon_{i2}}{\varepsilon_{i2} + 1} \right) \frac{1}{1 - \varepsilon_{i2}} \quad (4.22)$$

As one can see, the SPR shift  $\Delta\theta$ , caused by the presence of the transparent ( $\varepsilon_{i3} = 0$ ) film on top of the metal, depends on the linear combination of  $\varepsilon_{r3}$  and  $d_3$ , so that the simultaneous evaluation of the thickness and refractive index  $n_3 = \sqrt{\varepsilon_{r3}}$  is impossible. In the case of light-absorbing materials, where the imaginary part of the dielectric constant is nonzero, the above problem can be resolved, because of the broadening of the SPR curves.

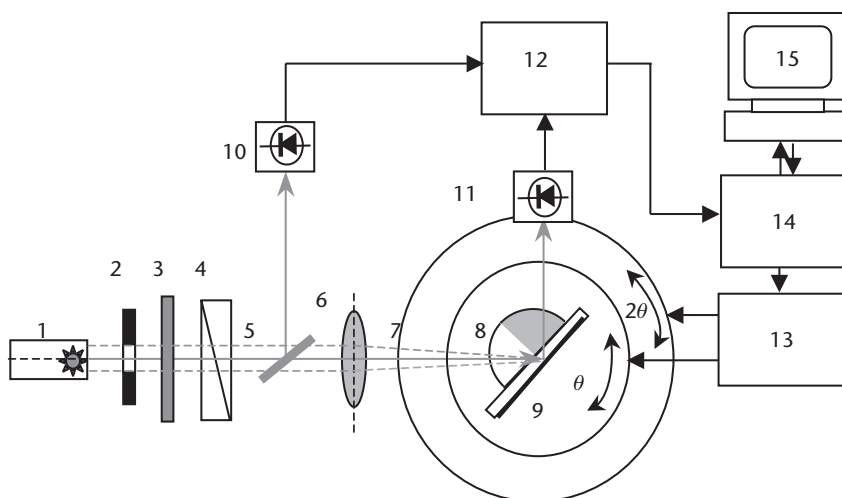
Similar to ellipsometry, the analysis and fitting of SPR data requires some experience in choosing initial parameters, limiting the range or even fixing some parameters during fitting. It is always useful to know roughly the values of thickness, refractive index, and extinction coefficient for the system studied. Two methods of ellipsometry and SPR can complement each other. For instance, both  $n$  and  $d$  values of relatively thick films (from 20 to 100 nm) can be found simultaneously with ellipsometry [see the  $\Psi, \Delta (n, d)$  diagram in Figure 4.3]. Then the obtained value for  $n$  can be used in SPR fitting as a first-guess parameter, or can be even fixed.

The SPR method has found numerous applications as a film characterization technique capable of measuring  $n$  and  $k$  with an accuracy ranging from  $10^{-4}$  to  $10^{-5}$ , and the thickness with an accuracy of  $10^{-2}$  nm. The range of measured film thicknesses, which depends on a number of parameters and can be found from (4.20) and (4.21), stretches from 20 to 50 nm, so that SPR is more suitable for characterization of thin films. Because of a high sensitivity towards  $n$ ,  $k$ , and  $d$ , as well as convenient geometry of measurements, which does not involve light propagation through the ambient, SPR has become very popular in chemical and biosensing applications. This is, however, a subject of Chapter 7.

There are several practical realizations of SPR methods, which can be split into two principally different groups, namely, spectral SPR and angular SPR. The latter approach is simpler. That is why it was adopted in a number of commercial SPR instruments, such as Biocore. A typical example of such an SPR setup is shown in Figure 4.5 [15].

The light beam from the HeNe laser (1) goes through the aperture (2), is modulated with the mechanical chopper (3), and becomes  $p$ -polarized after passing the polarizer (4). Part of the beam, reflected from the beam splitter (5) and captured with the photodetector (10), serves as a reference signal channel. Another part of the beam is focused with the lens (6) on the semicylindrical prism (8), with the gold-coated glass slide (9) attached to the back via index matching fluid. The prism is maintained on the  $\theta$ - $2\theta$  rotating stage (7). The reflected light is collected with the photodetector (11), and forms the main signal channel. The signals of the main and reference channels are fed into the lock-in amplifier (12), which is interfaced to the PC (15) via the control unit (14). The dedicated software also controls the stepper motor (13), which turns the  $\theta$ - $2\theta$  stage. The angular dependence of the reflected light intensity  $R(\theta)$  is therefore recorded with the PC.

There exist many other modifications of angular SPR techniques having different principles of light coupling, using, for example, a grating instead of a prism [17], and different methods of the registration of  $R(\theta)$  dependence. For example, the use of a fan-beam allows the registration of the  $R(\theta)$  curve instantly with the photodiode



**Figure 4.5** Experimental setup for Kretschmann-type angular SPR measurements with a semicylindrical prism fixed on the  $\theta$ - $2\theta$  rotating stage.

array [18]. The spectroscopic principle of SPR registration was adopted by several companies in their miniaturized integrated-optics SPR unit [19].

An interesting combination of SPR and ellipsometry called plasmon enhanced ellipsometry was recently reported in [20, 21]. In this method, the spectra of ellipsometric parameters  $\Psi$  and  $\Delta$  were recorded after reflection of the beam from the prism coated with thin gold film. The  $\Psi(\lambda)$  spectrum, related to the amplitude of the  $p$ -polarised component, naturally resembles the SPR curve with the characteristic dip in reflection. At the same time, the registration of the  $\Delta(\lambda)$  spectrum, representing a phase shift between  $p$ - and  $s$ - components, proved to be much more sensitive to the variations of the optical parameters of thin films in comparison with conventional SPR.

### 4.1.3 Optical Constants of Thin Organic Films

Ellipsometry and SPR have become routine methods for the characterization of thin film, particularly of thin organic films. This subject is described in a number of publications and reviews [22–24]. This chapter, however, presents some typical results and general observations of the optical properties of thin organic films.

The film periodicity in the direction perpendicular to the surface, a distinguished feature of Langmuir-Blodgett and polyelectrolyte self-assembled films, simplifies the process of simultaneous evaluation of the film thickness and refractive index. In the case of LB films of classical amphiphilic compounds, such as fatty acids, the task is even simpler, since the monolayer thickness of these compounds is known, and can be used as a first-guess value, or even as a fixed parameter.

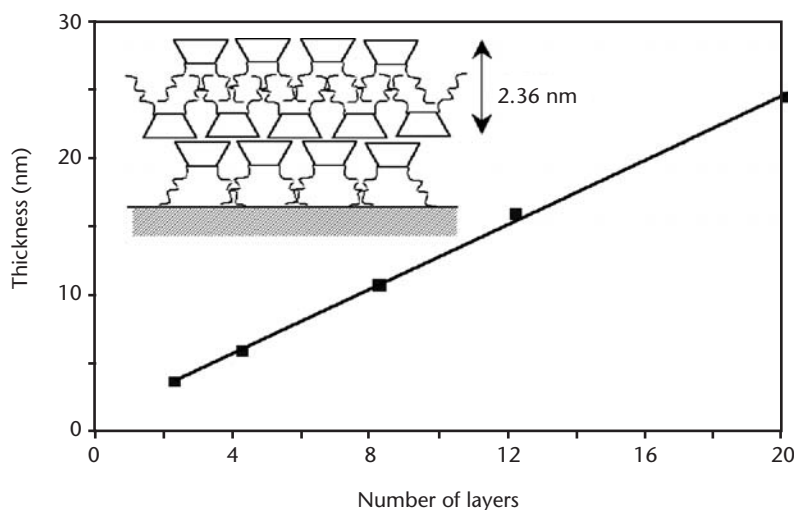
LB films of cyanoacrylic acid were studied ellipsometrically [25], and the obtained thickness of the LB bilayer, the main structure unit for Y-type LB films, corresponds well to the double length of cyanoacrylic acid (3.2 nm). The refractive index is, however, constant throughout the film, except for the first few layers close to the silicon substrate, which have slightly larger values of  $n$ . The latter can be explained by the polarization of cyanoacrylic acid molecules near the interface with silicon [25]. Such behavior is very typical for LB films deposited on silicon.

A very similar situation was observed for LB films of amphiphilic calix[4]resorcinarene derivatives: a linear dependence of the film thickness on the number of layers (see Figure 4.6), with the refractive index in the first few layers slightly larger than the value of 1.46 in the film bulk [26]. The thickness of 2.36 nm per LB bilayer, found from the slope in Figure 4.6, corresponds well to the estimated bilayer thickness of C[4]RA molecules having four substituting alkyl chains  $C_7H_{15}$  [26]. The schematic model of the C[4]RA bilayer, shown as the inset in Figure 4.6, implies both the tilt and interdigitation of alkyl chains.

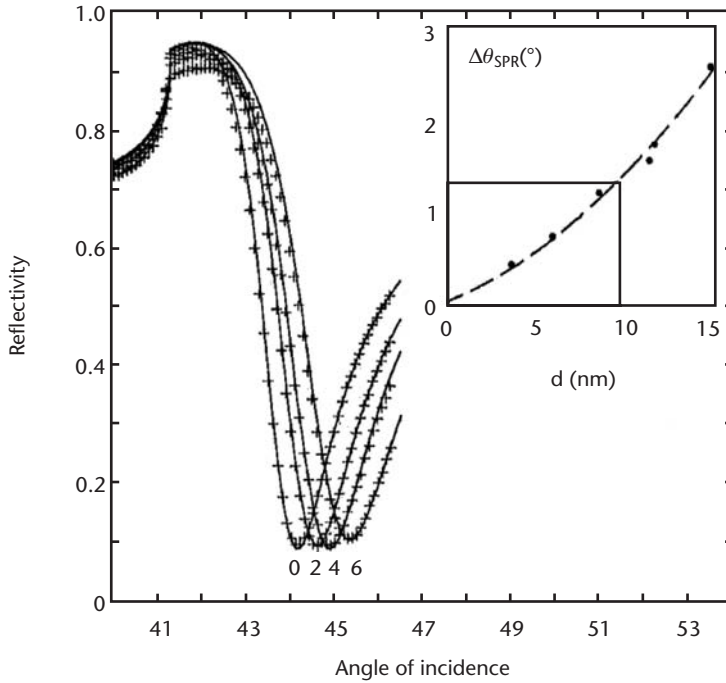
These results were later proved with independent SPR measurements [27, 28]. Figure 4.7 demonstrates a set of SPR curves shifted towards larger angles of incidence as the number of layers increased. The value of the C[4]RA monolayer thickness of 1.17 nm is found from these measurements, which is in excellent agreement with the previous ellipsometry results [26], as well as with the results of XRD [29]. It has become obvious that both LB and spun films of amphiphilic calixarene derivatives are not well ordered (perhaps spun films are less ordered than LB films), but they have the same structure unit of bowl-to-bowl oriented C[4]RA molecules with interdigitated alkyl chains. This allows us to assume the same value of refractive index for both spun and LB films, and therefore allows us to calculate the thickness of spun films [28].

Both methods of ellipsometry and SPR were deployed to study the optical parameters of electrostatically self-assembled films of PAH/PSS (see the chemical definitions in Chapter 2), and the results are shown in Figures 4.8 and 4.9, respectively.

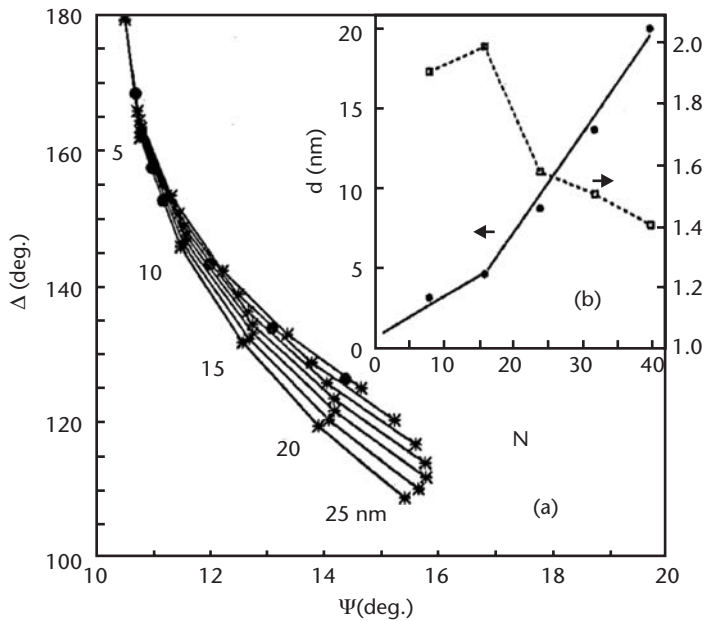
A nonlinear increase of the film thickness with an increase in the number of deposited layers was observed with both ellipsometry and SPR methods. The first few layers of PAH/PSS are thinner than subsequent layers, which is most likely due to a noncomplete surface coverage during deposition of the first few layers [30]. The refractive index of the first few PAH/PSS layers was found to be higher than that in the film bulk. The latter effect is much more pronounced than it is in LB films,



**Figure 4.6** The dependence of the thickness on the number of layers of LB film of amphiphilic  $C_7H_{15}$ -calix[4]resorcinarenes (results of the ellipsometry study). The inset schematically shows the film structure.

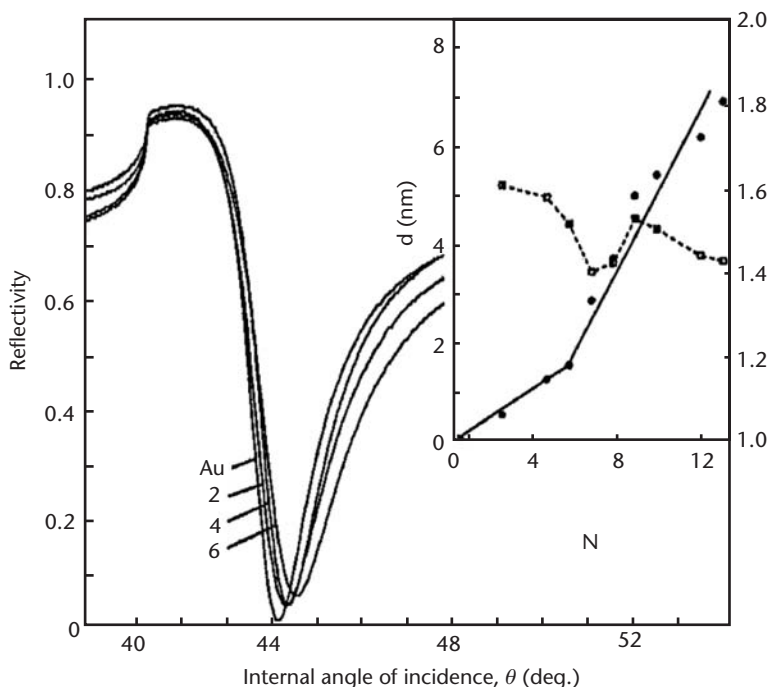


**Figure 4.7** The set of SPR curves obtained for bare gold and C[4]RA LB layers deposited on top. The number of layers is shown near the corresponding curve. The inset shows the relation between the SPR shift and film thickness. (From: [28]. © 1999 Elsevier. Reprinted with permission.)



**Figure 4.8** A set of  $\Psi, \Delta (n, d)$  diagrams calculated for a thin transparent film on silicon substrate ( $n = 3.867, k = 0, \lambda = 633 \text{ nm}$ , and  $\theta = 70^\circ$ ). The value  $n$  of the film increases from 1.4 to 2, in steps of 0.1; equidistant lines of film thickness are indicated on the graph. Experimental points for PAH/PSS film, having 8, 16, 24, 32, and 40 layers, are shown as black dots. The inset shows the dependencies of  $n$  and  $d$  on the number of layers of PAH/PSS film. (From: [30]. © 1999 Elsevier. Reprinted with permission.)



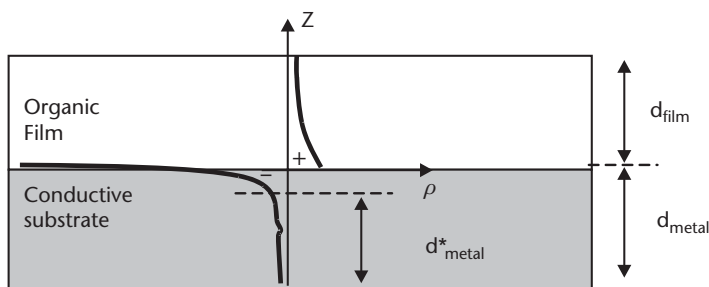


**Figure 4.9** A set of SPR curves for bare gold, and for 2, 4, and 6 PAH/PSS layers deposited on top. The inset shows the dependencies of  $n$  and  $d$  on the number of layers of PAH/PSS film. (From: [30]. © 1999 Elsevier. Reprinted with permission.)

indicating higher polarization of the substrate caused by Coulomb interaction with polyelectrolyte layers, as compared to much weaker Van der Waals interaction with LB layers. Similar results were obtained using spectroscopic ellipsometry [31].

Increasing in the refractive index of organic films near the interface with the conductive substrate (silicon in ellipsometry, and gold in SPR) seems to be a common feature of all organic thin films studied. The only reasonable explanation of the observed behavior lies in the increase of the electron density, and thus the polarization of the organic layers near the interface. Such polarization of organic films should be accompanied by the polarization of the surface of the substrate, which is particularly important in SPR experiments with thin metal films, as shown schematically in Figure 4.10. The effect of polarization of the metal film in SPR experiments was indeed observed regularly, but often treated as an artefact. The presence of organic film coating causes an increase in the refractive index and a decrease in the thickness of gold film, up to 5% from their values obtained prior to organic film deposition. Of course, the thickness of gold film is not changing physically. The thickness values, obtained by SPR fitting, are parameters of the model, which reflect the number of electrons involved in the plasmon oscillations. The electrons on the upper surface of gold film, belonging to a double layer on the organic film/gold interface, may not take part in plasmon oscillations. As a result, the effective thickness of gold film ( $d^*_{\text{metal}}$ ) in SPR experiments decreases, as illustrated in Figure 4.10. Obviously, this effect must be stronger in the case of electrostatically-bound PAH/PSS films, as compared to the less polar Van der Waals binding between metal and LB films. It becomes even stronger for highly polarizable gold colloid particles, deposited on evaporated gold film, which will be discussed later in the chapter.

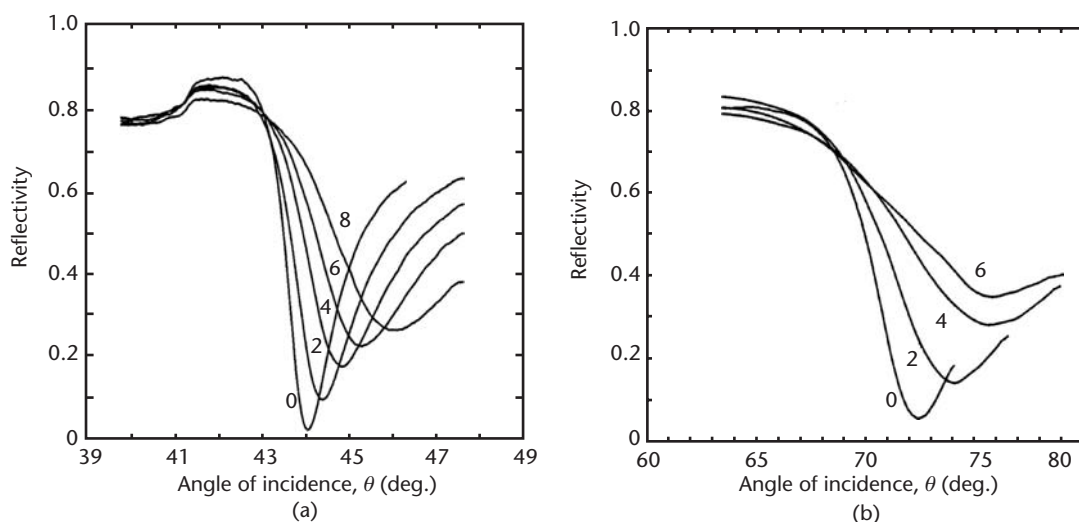




**Figure 4.10** A scheme of electron polarization on the organic film/metal film interface.

So far, we have discussed the experimental evaluation of optical characteristics on nonabsorbing organic films. The effect of the imaginary part of the refractive index ( $N = n - ik$ ), called the extinction coefficient, on the optical properties can be investigated on thin films of amphiphilic phthalocyanine derivatives. Phthalocyanines, an excellent example of light absorbing materials, having a very high absorption coefficient of about  $10^6 \text{ m}^{-1}$ , were studied extensively (see, for example, [32]), and found to have some good applications in optical devices. Phthalocyanine LB films were studied with SPR [15, 33], and typical results for this type of material are shown in Figure 4.11(a).

In addition to the shift with the increase of the number of LB layers, SPR curves experience broadening and dumping of the resonance. As mentioned in Section 4.1.2, the presence of the imaginary part of film dielectric constant (or refractive index) allows us to resolve the problem, and simultaneously to obtain the values of  $n$  and  $d$ . However, the presence of the third parameter  $k$  requires additional experimental data, in order to find a mathematically unique solution for  $d$ ,  $n$ , and  $k$ . This can be accomplished by different means. For example, the value of  $k$  can be obtained from the independent UV-vis absorption spectra measurements [e.g., from the value



**Figure 4.11** SPR curves of YbPc<sub>2</sub> LB films deposited on gold-coated glass slides, and measured in (a) air and (b) water. The number of LB layers is shown near the respective curves, with "0" denoting the non-coated samples. (From: [33]. © 1999 Taylor and Francis, Inc. Reprinted with permission.)

of absorbance ( $Abs$ ) measured at a certain wavelength ( $\lambda$ ), assuming the film thickness is known:

$$k = \frac{2303 \cdot Abs \cdot d}{4\pi \cdot \lambda} \quad (4.23)$$

and used as a first-guess parameter for SPR fitting. If the thickness is not known, then the calculation of  $k$  using (4.23) and SPR fitting for  $n$  and  $d$  can be performed in several iterations.

SPR measurements in two media having different refractive indices, for example air and water, offer an alternative simple solution of the above problem. Using a simplified version of (4.20) for the SPR shift  $\Delta\theta_{a,w}$  in both air ( $a$ ) and water ( $w$ ) ambiences:

$$\Delta\theta_{a,w} = \frac{2\pi}{\lambda n_p \cos \theta_{a,w}} \frac{(|\varepsilon_m| \varepsilon_{a,w})^{3/2}}{(|\varepsilon_m| - \varepsilon_{a,w})^2} \frac{d}{\varepsilon} (\varepsilon - \varepsilon_{a,w}) \quad (4.24)$$

where  $n_p$  is the refractive index of the prism. A simple relation for the real part of the film dielectric constant can be found [34]:

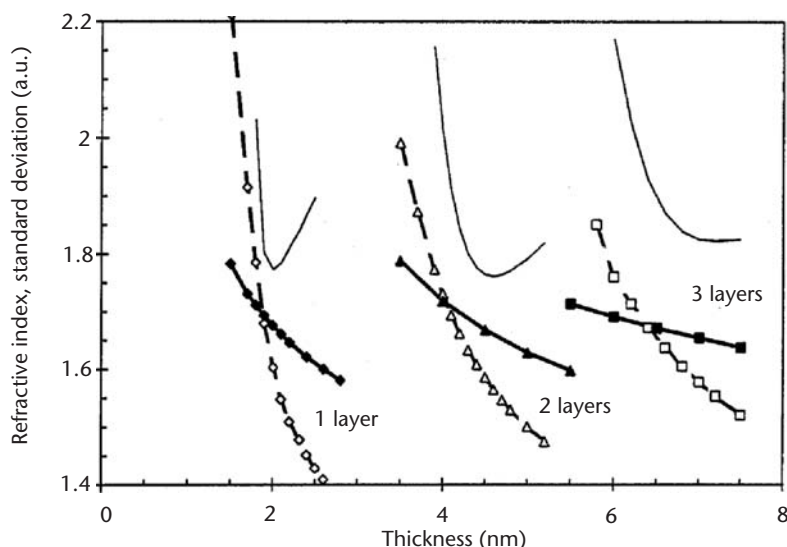
$$\varepsilon = \frac{\varepsilon_w^{5/2} \Delta\theta_a \cos \theta_a (\varepsilon_m - \varepsilon_a) - \varepsilon_a^{5/2} \Delta\theta_w \cos \theta_w (\varepsilon_m - \varepsilon_w)}{\varepsilon_w^{3/2} \Delta\theta_a \cos \theta_a (\varepsilon_m - \varepsilon_a) - \varepsilon_a^{3/2} \Delta\theta_w \cos \theta_w (\varepsilon_m - \varepsilon_w)} \quad (4.25)$$

In addition to the SPR measurements in air [see Figure 4.11(a)], another set of SPR curves were obtained by using water as the environment [see Figure 4.11(b)]. In both cases, SPR measurements were performed in the cell. Instead of solving (4.25), a simple graphical method of finding  $n$  and  $d$  was exploited. The SPR fitting was performed for the data obtained in both air and water. The values of  $n$  were obtained by SPR fitting for both media at different fixed values of  $d$ , and the dependencies of  $n(d)$  obtained were plotted in Figure 4.11. A true set of parameters  $n$  and  $d$  can be found from the intercept of the two  $n(d)$  graphs. This procedure was repeated for LB films of ytterbium bis-phthalocyanine ( $\text{YbPc}_2$ ) having different numbers of layers (1, 2, and 3) (see Figure 4.12) [33], and the obtained parameters are given in Table 4.1.

The obtained parameters are quite reasonable. The value of  $n = 1.70 \pm 0.02$  is typical for phthalocyanines; the thickness of the monolayer for this Z-type LB film is close to the diameter of  $\text{YbPc}$  molecule, which means that the  $\text{YbPc}_2$  molecules are staying vertically on the edge with respect to the surface; and the value of  $k = 0.66$  is

**Table 4.1** Optical Parameters of  $\text{YbPc}_2$  LB Films Obtained from SPR Measurements in Two Media: Air and Water

Number of LB Layers	$d$ (nm)	$n$ (at 633 nm)	$k$ (at 633 nm)
1	1.9	1.70	0.65
2	4.1	1.72	0.69
3	6.4	1.67	0.64
Average	$2.03 \pm 0.08$ per layer	$1.70 \pm 0.02$	$0.66 \pm 0.02$



**Figure 4.12** Graphical method of the calculation of  $n$  and  $k$  from the results of SPR data fitting in two media. (From: [33]. © 1999 Taylor and Francis, Inc. Reprinted with permission.)

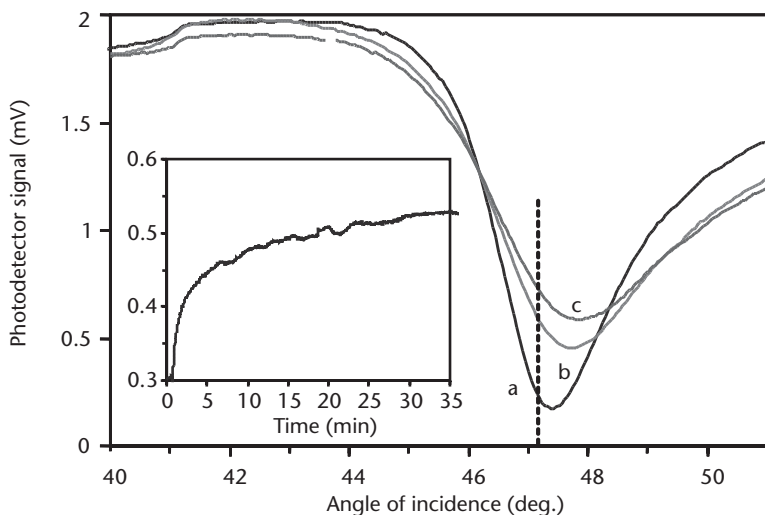
very close to that of 0.63 (at 633 nm), obtained from UV-vis absorption spectral measurements.

#### 4.1.4 Optical Parameters of Organic Films Containing Nanoparticles

The formation of II-VI semiconductor nanoparticles within LB films of respective bivalent metal salts of amphiphilic compounds, described in detail in Chapter 2, was studied with both ellipsometry and SPR. An increase in both the LB film thickness and refractive index after exposure to  $\text{H}_2\text{S}$  gas was registered first with ellipsometry [35]. It was found that the thickness of calix[8]arene LB films rises up to 1.86 nm per layer, from its initial value of 1.77 nm per layer after exposure to  $\text{H}_2\text{S}$ . The refractive index was also found to increase from 1.46 to 1.50, which was a good indication of the inclusion of the CdS phase having a larger refractive index than that of the organic film matrix.

Later, this phenomenon was studied in more detail using SPR [36]. Figure 4.13 shows the transformation of SPR curves of LB films of CdS in the course of exposure to  $\text{H}_2\text{S}$  gas, which was performed in the gas cell sealed to the sample. The results display both the shift and broadening of SPR curves, due to the formation of light-absorbing CdS clusters. In situ kinetic measurements of the reflected light intensity were performed at a fixed angle of incidence of  $47^\circ$ , chosen on the left-hand side of the SPR dip, near the minimum, to ensure a large linear range of measurements. The inset in Figure 4.13 shows the kinetics of the formation of CdS clusters, which is a reasonably fast process, reaching near-saturation in 30 to 40 minutes.

The SPR method alone does not allow the simultaneous evaluation of the thickness ( $d$ ), refractive index ( $n$ ), and extinction coefficient ( $k$ ) of LB films. The problem was solved by undertaking independent measurements of UV-vis absorption and ellipsometry in conjunction with the SPR studies [36]. The following routine was applied for data analysis: (1) values of the extinction coefficient at 633 nm were estimated from UV-vis absorption spectra measurements; (2) values of  $k$  were then used



**Figure 4.13** SPR monitoring of the formation of CdS nanoparticles within LB films of CdS. A sequence of SPR curves measured (a) initially, and in the course of exposure to H<sub>2</sub>S gas (b) after 18 minutes, and (c) after 36 minutes. The inset shows SPR kinetics at a fixed angle of incidence  $\theta^* = 47^\circ$  during exposure to H<sub>2</sub>S gas. (From: [36]. © 2003 IEEE. Reprinted with permission.)

as fixed parameters for fitting ellipsometry data, obtained for relatively thick films ranging from 10 to 40 layers; and (3) values of  $n$ , obtained from ellipsometry, were used as fixed parameters for the SPR curve fitting. The results of these calculations were presented in Table 4.2, and show the increase in all three parameters  $d$ ,  $n$ , and  $k$  of LB films after exposure to H<sub>2</sub>S gas.

The increase in LB thickness may be attributed to film swelling, caused by the formation of CdS nanoparticles within the film. Increases in both  $k$  and  $n$  are also indicative of the formation of a light-absorbing material having a refractive index higher than that of the film matrix. The effective value of refractive index,  $n^*$ , for LB film containing CdS nanoparticles can be estimated using linear superposition of values of  $n_1$  and  $n_2$  for the film matrix and CdS inclusion, respectively [36]:

$$n^* = n_1(1 - v_2) + n_2 v_2 \quad (4.26)$$

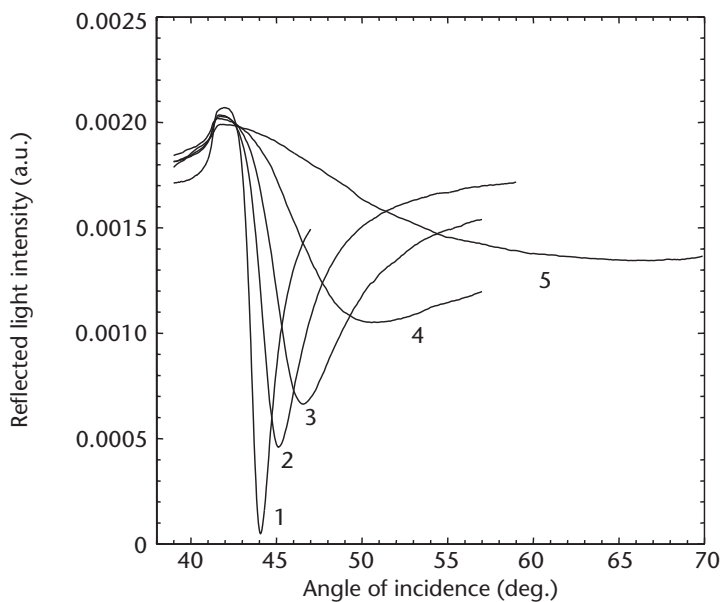
where  $v_2$  is the volume fraction of CdS in the films. A value of  $n^* = 1.71$  was found, taking  $n_2 = 2.3$  for the bulk CdS, and estimating  $v_2 = 0.2$ . The latter comes from the ratio of the concentration of Cd atoms in cadmium stearate LB films of  $10^{27} \text{ m}^{-3}$  to the concentration of atoms in the “zinc blend” cubic crystal of CdS of  $5 \times 10^{27} \text{ m}^{-3}$ . Similar calculations for calixarene (CA) LB films, having a concentration of Cd atoms of  $8 \times 10^{26} \text{ m}^{-3}$ , yield a value of  $n^* = 1.61$ . The estimated values of  $n^*$  are in

**Table 4.2** Optical Parameters of LB Films Obtained from the Absorbance, Ellipsometry, and SPR Measurements

Compound	Absorbance $k$ (at 633 nm)	Ellipsometry $N$	SPR		
			$d$ (nm/layer)	$k$	$d$ (nm/layer)
SA initial	0.0045	$1.563 \pm 0.019$	$2.42 \pm 0.090$	$0.0299 \pm 0.0060$	$2.54 \pm 0.034$
SA after H <sub>2</sub> S	0.0358	$1.616 \pm 0.026$	$2.54 \pm 0.092$	$0.0768 \pm 0.0183$	$2.56 \pm 0.045$
CA initial	0.0223	$1.514 \pm 0.008$	$1.37 \pm 0.007$	$0.0186 \pm 0.0055$	$1.33 \pm 0.058$
CA after H <sub>2</sub> S	0.0268	$1.535 \pm 0.006$	$1.39 \pm 0.005$	$0.0325 \pm 0.0066$	$1.42 \pm 0.056$

reasonable agreement, but slightly higher than the experimental values shown in Table 4.2. The effective medium approximation is anticipated to provide improved agreement between the measured and predicted values. The discrepancy also can be explained in terms of the deviation both of the refractive index, and of the concentration of Cd atoms in CdS nanoclusters from respective values for bulk CdS.

It is interesting to observe changes in SPR during the transition from pseudo-2D structures, such as thin metal film, to metal nanoclusters of pseudo-0D dimension. As found from the spectroscopic ellipsometry study in [37], the optical parameters of thin films made of nanoparticles of different metals (Cu, Co, Mo, Ta, Ni, Fe, Cr, Al, Sn, Pt, and Au) are different from those of respective bulk materials. SPR measurements were performed on thin (45-nm) gold film evaporated onto a glass slide (a classic object for SPR study), and thin films of gold colloid deposited on top by the LS method (see Chapter 2). The results, presented in Figure 4.14, show the deviation from the narrow SPR minimum for evaporated gold film (curve 1) to the much broader SPR curves of samples with deposited gold colloid (curves 2–5) [38]. Increasing the number of colloid LS layers causes further shift and substantial broadening of SPR curves. The parameters of both the evaporated gold substrate and colloid gold films obtained by fitting of SPR data are given in Table 4.3.



**Figure 4.14** SPR curves of bare gold evaporated onto a glass slide (1) and LS film of gold colloid deposited on top: (2) 1 layer, (3) 2 layers, (4) 5 layers, and (5) 10 layers.

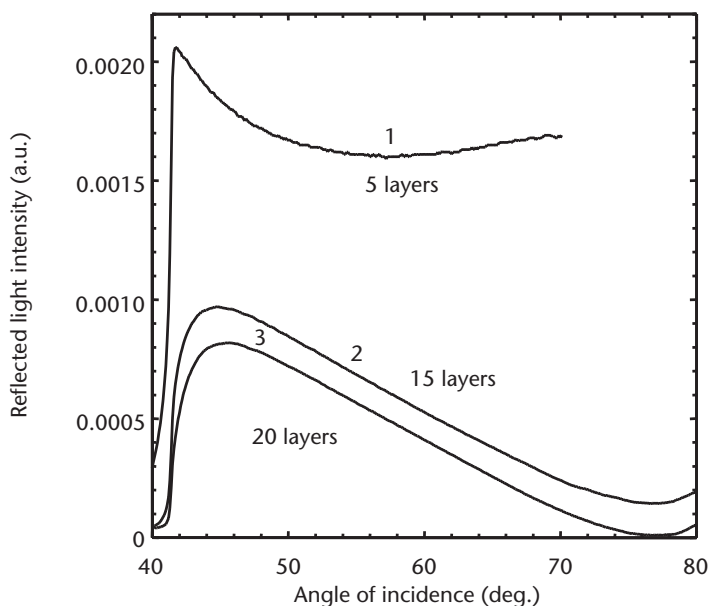
**Table 4.3** The Optical Parameters of Au Colloid LS Films Obtained from SPR

Evaporated Au Film			Colloid Au Film				Fitting Error, $E$
$N$	$K$	$d$ (nm)	Number of Layers	$n$	$k$	$d$ (nm)	
0.184	3.319	44.73	0				$5.06 \cdot 10^1$
0.190	3.326	44.68	1	0.690	2.187	9.66	$1.02 \cdot 10^1$
0.306	3.439	42.97	2	0.549	1.528	12.19	$1.83 \cdot 10^1$
0.621	3.993	30.70	5	0.564	1.357	24.39	$7.68 \cdot 10^2$

The decrease in both the refractive index and adsorption coefficient for gold colloid films is observed, while  $n$  and  $k$  values for evaporated gold substrate increases. The thickness of gold colloid films increases with the number of deposited LS layers (with a mean thickness per layer of  $7.2 \pm 1.9$  nm), which is close to what was expected for 5-nm colloid particles. The thickness of evaporated Au substrates decreases with the increase in the number of LS colloid layers deposited. Attempts to fix the optical parameters of gold substrate did not give good fitting results. The observed behavior might be caused by the redistribution of the electron density between the evaporated gold film and the colloid one. As was discussed in the previous paragraph, the increase in the refractive index in both gold substrate and colloid gold coating is believed to be caused by the polarization of both components near the interface. The number of free electrons taking part in the plasmon oscillations is therefore substantially reduced, thus reducing the effective thickness of the gold substrate.

The results in Figure 4.15 of SPR measurements on gold colloid LS films, deposited straight onto the glass slides, show a very large shift and broadening of SPR curves. The results are very similar to those obtained in [39], and present a noticeable blue shift of the absorption spectra of Au-colloid films with respect to the spectrum of bulk material. Angular positions of SPR minima, transformed into respective wavelength and energy values using (4.14), are summarized in Table 4.4.

The data shows much larger values of resonance energy for gold colloid films with respect to evaporated gold film, which is a clear indication of size quantization. The phenomenon of size quantization is the subject of following paragraphs; however, without going into details, the size of Au clusters can be roughly estimated from the values of the energy shift ( $\Delta E$ ) using a following formula:



**Figure 4.15** SPR curves of LS film of gold colloid deposited on glass slide: (1) 5 layers, (2) 15 layers, and (3) 20 layers.

**Table 4.4** SPR Resonance Energy Evaluation for Gold Colloid

Material	$\theta_{\text{SPR}}$ (degrees)	$\lambda_{\text{SPR}}$ (nm)	$E_{\text{SPR}}$ (eV)	$\Delta E$ (eV)	$a$ (nm)
Evaporated Au	44.07	600.7	2.07		
Ccolloid Au, 5 layers	57.4	495.9	2.50	0.43	2.8
Colloid Au, 15 layers	76.8	429.2	2.89	0.82	2.1
Colloid Au, 20 layers	77.1	428.6	2.90	0.83	2.1

$$a = \frac{\hbar\pi}{m\sqrt{2\Delta E}} \quad (4.27)$$

The values obtained, given in Table 4.4, are one-half the real size (5 nm) of the Au clusters used, which means that not all electrons in the gold colloid particles contribute to plasmon oscillations, and the effective particle size decreases.

## 4.2 The Effect of Quantum Confinement on Optical Properties of Low-Dimensional Systems

As was mentioned in the beginning of Chapter 4, the phenomenon of quantum confinement (i.e., size quantization) can be observed in low-dimensional systems, where the motion of electrons or other particles (i.e., holes or excitons), is restricted, at least in one dimension, by the potential energy profile. In terms of energy or wave-vector space, these particles are confined in a potential well. The energy spectra and waveforms of confined particles differ dramatically from those of free particles. The confined particles are not free anymore, since they are allowed to have only certain energies and waveforms. The energy spectra and waveforms of nanostructured materials depend on the type of restrictions in one, two, or all three dimensions in 2D, 1D, or 0D systems, respectively, as well as on the characteristic sizes of the nanostructures. These quantum phenomena become noticeable when the size of the energy well is comparable with the respective particle wavelength.

### 4.2.1 Electron in a Quantum Box

The simplest example of quantum confinement is an electron enclosed in a one-dimensional quantum box, having size  $a$  and infinitely high walls, as shown in Figure 4.16. In order to find the energy spectrum and waveforms of the confined electron, the Schrödinger equation has to be solved (see [40]):

$$\frac{d^2\Psi}{dx^2} + \frac{2mE}{\hbar^2}\Psi = V, \quad V = \begin{cases} 0, & 0 < x < a \\ \infty, & x \leq 0, x \geq a \end{cases} \quad (4.28)$$

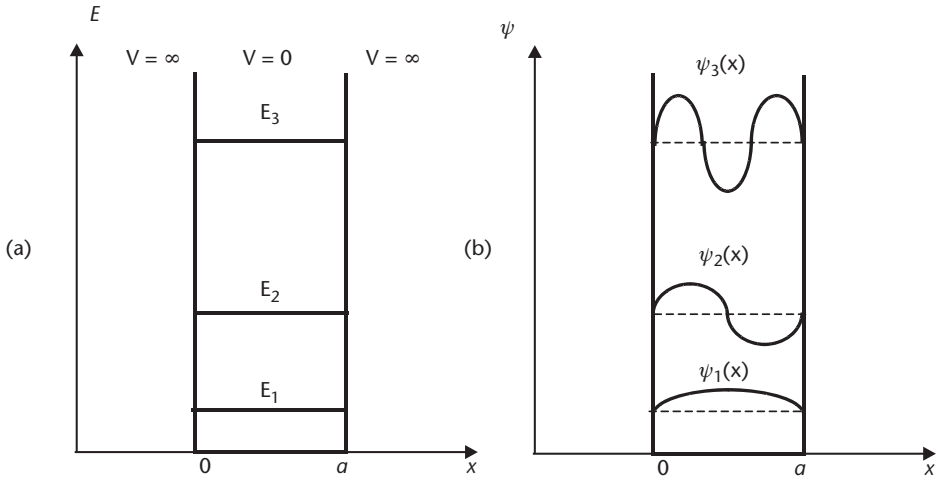
For this second-order linear differential equation, the solution can be found in the form:

$$\Psi(x) = Ae^{ikx} + Be^{-ikx} \quad (4.29)$$

At a boundary condition of  $\Psi = 0$  at  $x = 0$ , which gives  $B = -A$ , one can obtain

$$\Psi = A[e^{ikx} - e^{-ikx}] = 2iA \sin kx \quad (4.30)$$





**Figure 4.16** Electron in a quantum box: (a) the energy spectrum, and (b) wavefunctions.

Substituting (4.30) for  $\Psi$  in the Schrödinger equation, the expression for electron energy can be obtained:

$$E = \frac{\hbar^2 k^2}{2m} \quad (4.31)$$

The second boundary condition  $\Psi = 0$  at  $x = a$  sets a restriction on the values of  $k$  vector:

$$\Psi(a) = 2iA \sin ka = 0, \quad \text{so that} \quad ka = n\pi, \quad n = 1, 2, 3, \dots \quad (4.32)$$

It is obvious now that the  $k$ -vector, and thus the electron wavelength and energy, can only have certain values (e.g., quantized):

$$E_n = \frac{\hbar^2 k_n^2}{2m} = \frac{\hbar^2 \pi^2}{2ma^2} n, \quad n = 1, 2, 3, \dots \quad (4.33)$$

This formula means that the energy of size quantization should be added to the initial energy of free electron  $E = E_0 + E_n$  forming an energy ladder in the quantum box (see Figure 4.16). The effect of quantum confinement becomes noticeable when the quantum box is in the range of a few nanometers. As an example, a 1% energy increase above the ground energy level  $E_0 = 1\text{eV}$  can be found in the quantum box with the size  $a = 6\text{ nm}$ .

The quantization condition for the wavelength  $a = (\lambda/2)n$  leads to a very simple mechanical analogy, which allows us to visualize the phenomenon of size quantization. As shown in Figure 4.16, the quantum box must contain the integer number (1, 2, 3, ...) of halfwaves, a condition similar to the mechanical standing waves of a string fixed at both ends. The corresponding wavefunction is given:

$$\Psi_n(x) = 2iA \sin\left(\frac{\pi x n}{a}\right) = i\left(\frac{2}{a}\right)^{\frac{1}{2}} \sin\left(\frac{\pi x n}{a}\right) \quad (4.34)$$

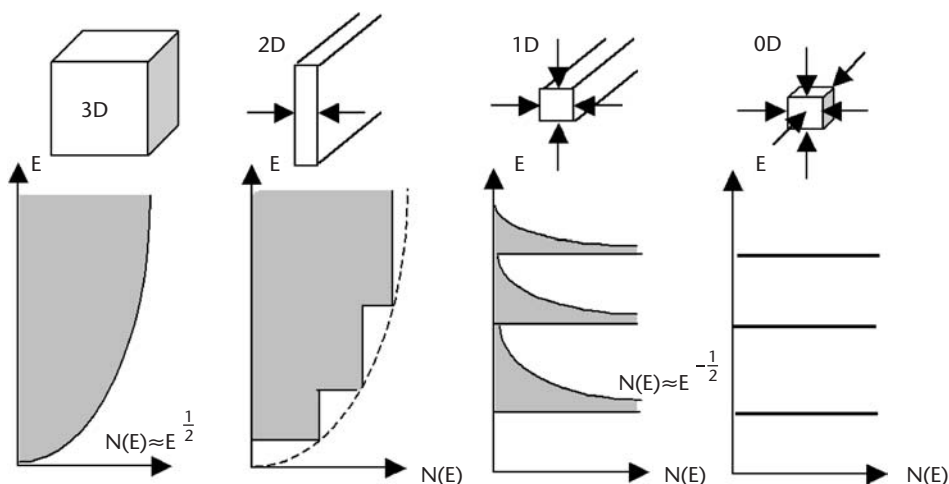
The coefficient  $A = \left(\frac{1}{2a}\right)^{\frac{1}{2}}$  can be found by the normalization of the wavefunction over the quantum box  $\int_0^a |\Psi_n(x)|^2 dx = 1$ .

The above simple problem can be useful for understanding the phenomenon of size quantization and some simple simulations, similar to that done earlier for gold colloid films.

#### 4.2.2 Quantum Confinement and the Main Optical Properties of Low-Dimensional Semiconductor Structures

The theory of quantum confinement has been particularly well developed in semiconductors. This is quite understandable, because quantum confinement historically was found first in semiconductor materials. In 1981, Ekimov and Onuschenko [41] reported on a blue shift of optical absorption spectra of halcogenide glass containing nanocrystallites of CuCl, and in 1982, the effect was explained theoretically by Efros and Efros [42]. The novelty in this is arguable, since in ancient and medieval times, artists knew that the color of mineral paints could be altered by fine milling of minerals, although they did not know about quantum mechanics. Later, halcogenide glass containing different semiconductor nanoclusters, such as sulphides, selenides, or tellurides of bivalent metals (e.g., Cd, Pb, Zn, or Cu), has become a classical object for the study of quantum phenomena [43]. The first observation of size quantization in CdS nanoparticles in LB films was reported in 1988 [44], and repeated by many other scientists for different organic and inorganic nanocomposite materials. The theory of size quantization in semiconductor nanocrystals was further developed in a number of publications [42, 43], and summarized in excellent review papers by Yoffe [45–47].

The classification of different types of low dimensional systems was given in [47], and presented in Figure 4.17, with the respective changes in the density of states in semiconductors.



**Figure 4.17** Classification of low dimensional systems, and the transformation of the density of states. (From: [47]. © 2002 Taylor and Francis, Inc. Reprinted with permission.)

The  $N(E)$  function transforms from the standard  $N(E) \sim E^{1/2}$  for three-dimensional bulk semiconductor materials, first to the staircase dependence framed into the  $E^{1/2}$  function for two-dimensional systems (e.g., thin films, slabs, and platelets), then to the series of  $E^{1/2}$  nearly-separated subbands for one-dimensional nanowires, and, finally, to the discrete energy spectrum for zero-dimensional nanoparticles.

Before going into a detailed discussion of quantum confinement, we have to remember that in II-VI and III-V semiconductors, having a direct bandgap structure, electrons and holes can be coupled together by Coulomb interaction to form excitons. Such quasi-particles, which are often called Wannier-Mott excitons or large radius excitons, can be described by the following energy dispersion in a simple hydrogen-like model for bulk semiconductors, having parabolic ( $E \sim k^2$ ) Brillouin zones, centered at  $k = 0$ , and separated by the gap  $E_g$ :

$$E = E_g - \frac{E_b}{n^2} \quad (4.35)$$

Here  $n = 1, 2, 3$ , is the exciton quantum number, and  $E_b$  is the exciton binding energy

$$E_b = \frac{\mu e^4}{2\varepsilon^2 \hbar^2} = \frac{\hbar^2}{2\mu a_B^2} \quad (4.36)$$

in which  $\varepsilon$  is the semiconductor dielectric constant,  $\mu$  is the reduced exciton mass  $\left(\frac{1}{\mu} = \frac{1}{m_e} + \frac{1}{m_b}\right)$ , and  $a_B$  is the exciton Bohr radius  $\left(a_B = \frac{\hbar^2 \varepsilon^2}{\mu e^2}\right)$ .

Usually, Wannier-Mott excitons have a large radius of a few nanometers, and low binding energy in the range from  $10^{-3}$  to  $10^{-4}$  eV, so that they exist only at low temperatures.

The importance of excitons for quantum confinement in semiconductor materials lies in the fact that the confinement conditions vary, depending on the relation between the size of the quantum well and the exciton radius. In the case of zero-dimensional semiconductor objects, such as nanoclusters, three situations should be considered [47].

First, *weak confinement*, when  $a \gg a_B$ . In such conditions, the exciton is quantized as a whole, and the energy of the main absorption band is approximately equal to:

$$E = E_g - E_b + \Delta E = E_g - E_b + \frac{\hbar^2 \pi^2}{2Ma^2} n^2 \quad (4.37)$$

where  $M = m_e + m_b$  is the exciton mass.

This approach was implemented by Efros and Efros [42] as an explanation of the experimental spectra of  $\text{CuCl}_2$  nanoclusters formed in the silica glass [41], where the first electron transition corresponding to the main adsorption band edge was presented in a form of:

$$\hbar\omega_{01} = E_g - E_b + \frac{0.67\hbar^2\pi^2}{2Ma^2} \quad (4.38)$$

The coefficient 0.67 appeared in (4.38) from the nonsymmetrical size distribution of nanoclusters in halcogenide glass, derived by Lifshitz and Slesov [48].

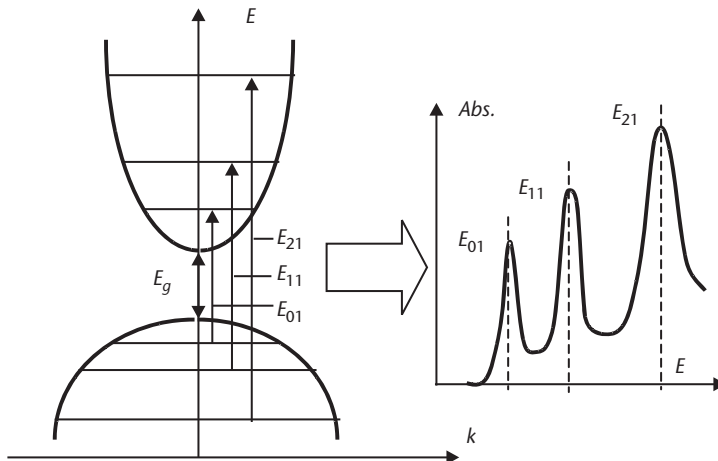
Second, *strong confinement*, when  $a \ll a_b$ . In this case, exciton does not exist, and both the electron and hole are quantized separately, forming a ladder of energy levels in conduction and valence bands, respectively. The exciton binding energy ( $E_b$ ) can be therefore neglected in the energy dispersion [42]:

$$E = \frac{\hbar^2 J_{l,n}^2}{2m_e a^2} + \frac{\hbar^2 J_{l,n}^2}{2m_h a^2} = E_g + \frac{\hbar^2 J_{l,n}^2}{2\mu a^2} \quad (4.39)$$

where  $J_{l,n}$  is the  $n$ th root of the spherical Bessels function of  $l$ th order ( $J_{0,1} = \pi = 3.14$ ,  $J_{1,1} = 4.49$ ,  $J_{2,1} = 5.76$ , ...). In other words,  $n = 1, 2, 3, \dots$  and  $l = 0, 1, 2, \dots$  are somehow similar to the principle and orbital quantum numbers, respectively. The absorption spectra therefore consist of several bands, corresponding to electron transitions between levels of size quantization for electrons in conduction band and holes in the valence band, with the selection rules of  $\Delta n, \Delta l = 0$  [35], as shown in Figure 4.18.

Third, *an intermediate confinement*, when  $a$  and  $a_b$  are comparable. This is the most difficult situation. However, it can be simplified in many practical situations, since holes are usually much heavier than electrons, so that  $a \gg a_e$  but  $a \ll a_b$ , where  $a_e$  and  $a_b$  are formally introduced as Bohr radii for electron and holes, respectively, as has been done for excitons in (4.36). In this case, only electrons are quantized in the conduction band, but the Coulomb interaction between electron and holes must be taken into account in the energy calculation:

$$E = E_g - E_b + \frac{\hbar^2 J_{l,n}^2}{2m_e a^2} \quad (4.40)$$



**Figure 4.18** Formation of the energy spectrum in the semiconductor quantum dots much smaller than Bohr radius.

The absorption spectra in this case will be formed by electron transition from the exciton level near the valence band to the levels of size quantization in the conduction band.

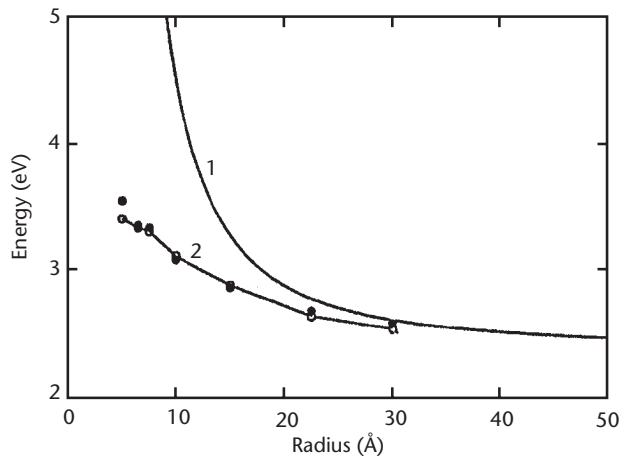
The effect of the polarization of the matrix, where II-VI particles were incorporated, was taken into account by Brus [49], by introducing a Coulomb interaction term, so that the absorption band edge is equal:

$$E = E_g + \frac{\hbar^2 \pi^2}{2\mu a^2} - \frac{1.8e^2}{\epsilon a} \quad (4.41)$$

The Coulomb term varying as  $1/a$  is a more important than the size quantization ( $1/a^2$ ) term for large crystallites, while for the small crystallites, the situation is the opposite. The nonparabolic shape of  $E(k)$  dispersion, the finite height of potential walls, and the effect of the different shape of quantum dots also have been accounted for [47]; however, they are rather minor as compared to the kinetic energy quantization and Coulomb terms in (4.41).

All the above terms have been calculated using an effective mass approximation. Direct calculations of the energy spectra of nanoclusters of different semiconductor materials, including II-V, III-V, and Si, were performed numerically using a pseudo-potential method [50, 51]. The results of the calculations were found to be closer to the experiment than to the effective mass approximation approach (4.41), as was illustrated by the dependencies of the absorption edge energy on the crystallite radius in Figure 4.19.

One of the most important practical applications of nanostructured semiconductor materials is the luminescence having the following features (as compared to the luminescence from respective bulk materials) [45, 46]: (1) blue spectral shift due to the size quantization; (2) larger oscillator strength, and thus larger intensity and more narrow luminescent spectral lines; (3) large and size-dependent Stokes spectral shift; and (4) nonlinear effects at a large intensity of excitation.



**Figure 4.19** The dependence of the energy of size quantization on the size of nanoclusters. Experimental points from zinc blende CdS: (1) calculations by Brus (4.41) [49]; and (2) calculations by the pseudopotential method. (From: [50]. © 1991 American Institute of Physics. Reprinted with permission.)

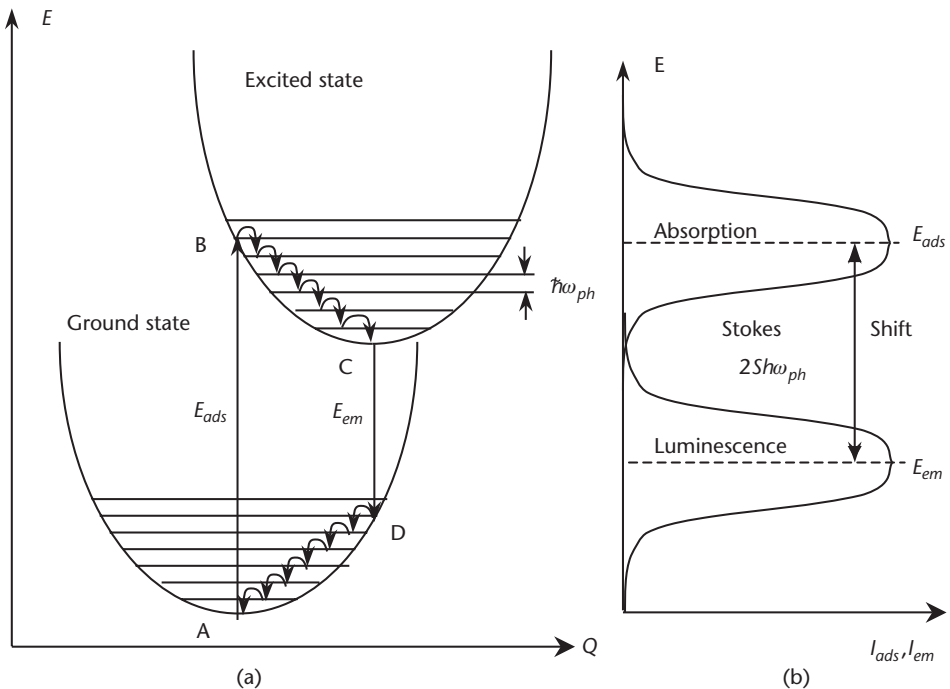
The blue spectral shift of the main adsorption and luminescence spectral lines has been already discussed in detail. The oscillator strength of excitons can be described by the following formula [47]:

$$f = \frac{2m_e^*}{\hbar^2} \Delta E |M|^2 |U_0|^2 \quad (4.42)$$

where  $\Delta E$  and  $M$  are the transition energy and dipole moment, respectively, and  $U_0$  is the factor representing the overlapping the densities of electrons and holes. In the case of weak confinement, when  $a \gg a_B$ ,  $U_0$  is independent of the cluster size. Under conditions of strong confinement ( $a < a_B$ ),  $U_0$  increases with the decrease in the cluster size as  $(a_B/a)^3$ , and thus the oscillator strength. This means that the intensity of luminescence must be much higher in small semiconductor clusters than in respective bulk materials.

The scheme of luminescence in configuration coordinates  $E(Q)$ , as shown in Figure 4.20, explains the main feature of luminescence—the red shift of the luminescent spectral line with respect to the absorption band, often referred to as the Stokes shift.

According to the Frank-Condon principle, the excitation occurs as a vertical transfer of the electron from A to B, followed by the adjustment of nuclei positions and the formation of the excited state. The time of the electron transition ( $10^{-13}$  seconds) is much smaller than the time of photoluminescence ( $10^{-8}$  seconds), so that the electron can relax to the excitation state minimum (point C) by generating a number of phonons. The vertical transition of the electron from C to D, and the



**Figure 4.20** (a) The scheme of photoluminescence electron transition in configuration coordinates, and (b) the corresponding spectra of absorption and luminescence.

subsequent light emission (luminescence) occur, followed by the relaxation to the ground state minimum (point D). The resultant energy of the emitted light is, therefore, smaller than the initial excitation energy, and the energy difference defines the Stokes shift [46]:

$$\hbar\omega_{ads} - \hbar\omega_{em} = 2S\hbar\omega_{ph} \quad (4.43)$$

The coupling constant  $S$  is a mean number of phonons generated during the electron relaxation.

The value of Stokes shift is proportional to  $(a_B/a)^3$ , and thus increases sharply with the decrease in the size of semiconductor clusters. The electron transitions in luminescence are strongly effected by a multiple degeneration of both conduction and valence bands, due to the presence of light and heavy holes, as well as by the spin orbital interaction. The selection rules for the total angular momentum projection  $F = M + s_z$  are  $F = \pm 1$ . However, in the nonspherical Q-dots, such as prolates and platellets, having noncompensated dipole moments in the  $z$ -direction, the “forbidden” transitions with  $F = \pm 2$  may become possible. This gives rise to narrow emission lines that are much more red shifted, referred to as “dark excitons” [52].

Nonlinear effects in luminescence are related to the two-photon process of the formation of biexcitons under high intensity of excitation. Biexcitons are formed as a result of the attraction of two Wannier-Mott excitons, and have a double exciton mass  $2M$ . They experimentally appeared in luminescence as a spectral line with the emission energy of [46]:

$$\hbar\omega = E_2 - E_1 = E_1 - \delta E_2 - \frac{\hbar^2 k^2}{4M} \quad (4.44)$$

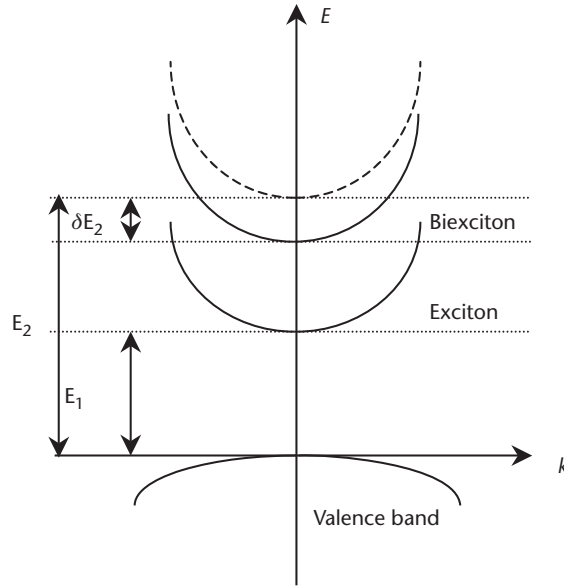
where  $E_1$  and  $E_2$  are energies of ground states of the exciton and biexciton, respectively, and  $\delta E_2 = 2E_1 - E_2$  is a binding energy of the biexciton. The scheme of the biexciton formation is shown in Figure 4.21. In effect, the formation of biexcitons is the two-phonon process appeared at the excitation energy of  $E_1 - \delta E_2/2$  [53]. With the intensity of the excitation increased, high-order multiphoton processes, such as inelastic collisions of biexcitons, may appear, and give a new sharp luminescence line at  $\hbar\omega = 2E_2 - 3E_1 = E_1 - \delta 2E_2$ .

Third harmonic generation is another typical characteristic observed in semiconductor Q-dots at a large level of illumination. The polarization of the medium ( $P$ ) induced by the external electric field ( $E$ ) can be written as:

$$P = \varepsilon_0 (\chi^{(1)} E + \chi^{(2)} E^2 + \chi^{(3)} E^3 + \dots), \quad (4.45)$$

where  $\chi^{(1)}$ ,  $\chi^{(2)}$ , and  $\chi^{(3)}$  are dielectric susceptibilities, of the first, second, and third orders, respectively. Normally,  $\chi^{(1)} \gg \chi^{(2)} \gg \chi^{(3)}$ , and the susceptibilities of higher order are not considered at all. Linear susceptibility is related to the relative dielectric permittivity ( $\varepsilon$ ) and refractive index ( $n$ ) as  $\varepsilon = n^2 = 1 + \chi^{(1)}$ , and thus is responsible for all linear phenomena in electrostatics and optics, while  $\chi^{(2)}$  and  $\chi^{(3)}$  have become noticeable at large intensities of electric field and some other special conditions. When dealing with an electromagnetic field  $E = E_0 \cos(\omega t)$ , the presence





**Figure 4.21** The scheme of the formation of biexciton.

of  $\chi^{(2)}$  and  $\chi^{(3)}$  leads to the generation of the second ( $2\omega$ ) and third ( $3\omega$ ) harmonics, respectively. The second harmonic appeared only in noncentrosymmetric structures, while the third harmonic is common for all types of materials, and particularly for nanostructures [47].

The third harmonic generation affects both the refractive index and absorption coefficient of the materials [47]:

$$n = n_0 + n_2 I \quad \text{and} \quad \alpha = \alpha_0 + \alpha_2 I \quad (4.46)$$

where  $n_2 = \frac{16\pi^2 \text{Re} \chi^{(3)}}{cn_0^2}$ ,  $\alpha_2 = \frac{16\pi^2 \text{Im} \chi^{(3)}}{cn_0^2}$ , and  $I$  is the light intensity.

The increase in the absorption coefficient causes the bleaching of the material at large intensities of laser illumination at resonance conditions, when the combined energy ( $3\hbar\omega$ ) of three photons ( $\hbar\omega$ ,  $\hbar\omega$ ,  $\hbar\omega$ ) matches one of the absorption bands in the material [54]. This phenomenon becomes quite substantial in low dimensional systems, such as 4-nm CdS Q-dots dispersed in the polymer Naflon, where the decrease in the absorbance of approximately 0.1 was observed during 40 to 500 ns of the laser illumination at 450 nm [54].

## 4.3 Optical Spectra Semiconductor Nanoparticles in Organic Films

### 4.3.1 Semiconductor Nanoparticles in LB and Spun Films

As described in Chapter 2, II-VI semiconductor nanoparticles can be formed within LB or spun films of bivalent metal salts of amphiphilic molecules in the course of the reaction with  $\text{H}_2\text{S}$  or  $\text{H}_2\text{Se}$  gas. The formation of nanoparticles was confirmed by different methods, including TEM, AFM, XPS, ellipsometry, and SPR. However, the

first experimental evidence of the formation of II-VI nanoparticles has been found using UV-vis absorption spectroscopy. These measurements in LB films of cadmium arachidate, which were initially transparent, showed the absorption band after exposure to  $\text{H}_2\text{S}$  gas [44], which was an indication of the formation of CdS nanoparticles in the film. The adsorption band appeared to be shifted towards shorter wavelength in comparison with the adsorption band of bulk CdS. A simple calculation, using (4.37) for exciton quantum confinement, allowed the estimating of particles ranging in size from 3 to 5 nm, depending on the conditions of growth. Such experiments with metal sulphide nanoparticles in LB films were repeated in many other research groups [35, 36, 55–63], using different amphiphilic compounds and different metal salts.

Typical results of this work can be illustrated by UV-vis absorption spectra (see Figure 4.22) of cadmium stearate LB films measured before and after exposure to  $\text{H}_2\text{S}$  gas.

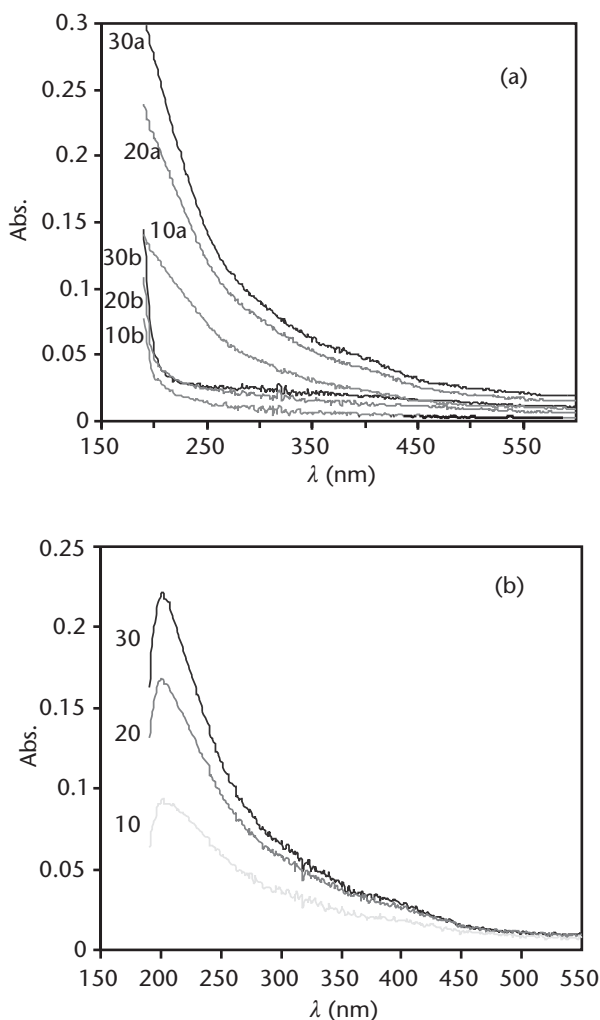
The application of (4.39) to the spectral data analysis yields the size of CdS nanoclusters from 2 to 3 nm, depending on the technological conditions (i.e., the concentration of  $\text{CdCl}_2$  and the pH of the subphase) [58]. It is important to mention that the absorption intensity is proportional to the number of deposited LB layers, which is a clear indication that the formation of CdS nanoparticles occurs in every LB bilayer, as shown in Figure 2.27. Since the AFM study in [36] revealed the platelet shape of CdS clusters in stearic acid LB films (see Figure 3.6), with the planar dimensions of 20 to 30 nm, the use of (4.39) for strong confinement in spherical II-VI semiconductor nanoparticles [42] has to be justified. In fact, the quantization should be treated separately in ( $x$ ,  $y$ ) and  $z$  directions in CdS platelets, and this results in the following expression for the energy:

$$\Delta E = \frac{\hbar^2 \pi^2}{2\mu(L_{x,y})^2} + \frac{\hbar^2 \pi^2}{2\mu(L_z)^2} \quad (4.47)$$

where  $L_{x,y}$  and  $L_z$  are the dimensions of the CdS cluster in lateral and normal directions, respectively. Because of the approximately one order of magnitude difference between the  $L_{x,y}$  of 20 to 30 nm and the  $L_z$  of 3 nm, a contribution of the first term to the quantization energy in (4.46) is negligibly small in comparison with the second term. One can conclude that the size quantization in  $z$ -direction is predominant in the above CdS platelets.

Much more interesting results were observed in the case of using amphiphilic calix[4]arene and calix[8]arene carboxylic acid molecules for the LB film deposition, and the subsequent formation of CdS nanoclusters after exposure to  $\text{H}_2\text{S}$  gas [35, 36, 59]. First, the registration of spectral changes is much more difficult, since calixarene molecules have strong absorption in the UV spectral range. Quartz slides that are transparent for UV light have to be used as substrates for deposition of calixarene LB films. Absorption spectra measured before and after exposure to  $\text{H}_2\text{S}$  gas look approximately the same, as shown in Figure 4.23(a), and the changes can be seen only after subtraction of the spectra.

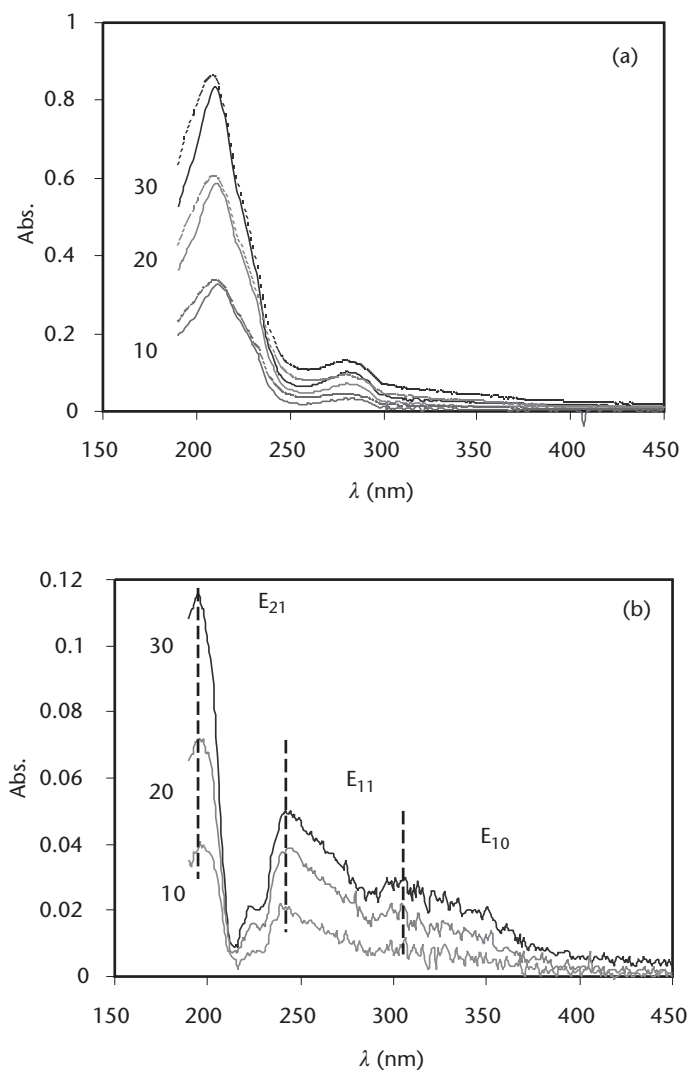
The resulting spectra of CdS nanoparticles in the calixarene film matrix, as shown in Figure 4.23(b), appears to be much more blue shifted, as compared to CdS/stearic acid films, which obviously indicates the smaller particle size. This



**Figure 4.22** (a) Absorption spectra of Cd stearate LB films measured before (curves with index "b") and after (curves with index "a") exposure to  $\text{H}_2\text{S}$  gas. The number of LB layers is shown near the respective curves. (b) Subtracted spectra corresponding to CdS phase.

proves the main idea of using cavitated compounds in order to reduce the two-dimensional diffusion of CdS molecules within LB bilayers, and to form smaller particles, presumably captured inside calixarene cavities. This process is discussed in Chapter 2, and is illustrated in Figure 2.27. A strong evidence of the model of CdS particles captured within calixarene cavities is given by X-ray diffraction measurements, which show no significant changes in the calixarene film structure after the formation of CdS within [36]. The presence of calixarene cavities is found to be a crucial factor for the formation of small CdS clusters. An attempt to form CdS clusters in the LB films of the compound chemically identical to calixarenes, but not-cyclic (e.g., formaldehyde/2,6-dihydroxy-benzoic acid copolymer), ended with much larger CdS clusters, almost identical to those formed in stearic acid [62].

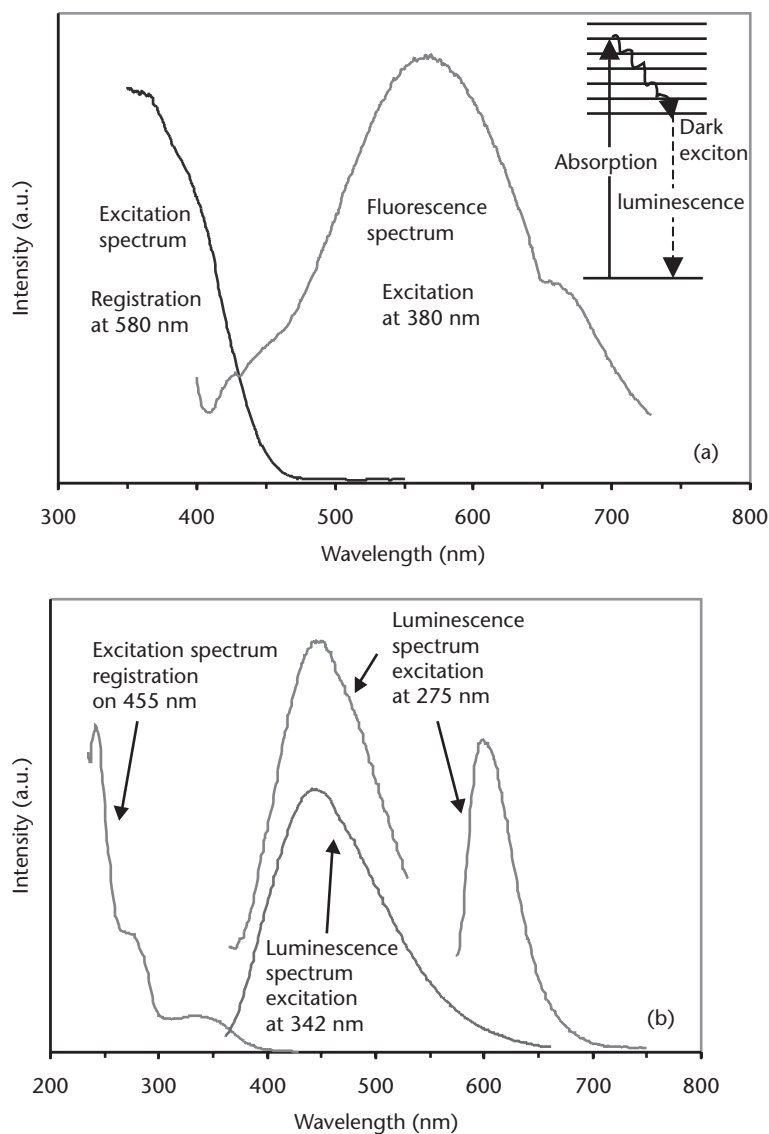
Moreover, three well-resolved spectral bands are observed in the spectra in Figure 4.23(b), which leads to an obvious suggestion that they represent the first three electron transitions ( $E_{01}$ ,  $E_{11}$ , and  $E_{21}$ ) between levels of size quantization (see



**Figure 4.23** (a) Absorption spectra of LB films of  $C_5H_{11}$ -calix[8]arene Cd salt: initial spectra of freshly-made films (solid lines), and spectra after exposure to  $H_2S$  gas (dotted lines). The number of LB layers is shown near the respective curves. (b) The subtracted spectra, corresponding to CdS phase.

Figure 4.18). Calculations of the CdS clusters size using (4.39) for all three absorption peaks yield the values of  $1.43 \pm 0.28$  nm and  $1.47 \pm 0.28$  nm for calix[4]arene and calix[8]arene films, respectively [36]. It is interesting that the difference in size of CdS clusters in calix[4]arene and calix[8]arene films is not as large as expected, considering the difference in cavity sizes of the two molecules. A possible explanation lies in the more complex, distorted conformation of quite flexible calix[8]arene rings effectively having a much smaller cavity [64].

Photoluminescence measurements were undertaken to gather conclusive information regarding the formation of CdS particles. Photoluminescence excitation (PLE) spectra of CdS nanoparticles in stearic acid LB films, as shown in Figure 4.24, closely resemble their respective absorption spectra (see Figure 4.22), as well as the spectral data reported earlier [35, 36, 59]. Stearic acid LB films have the first



**Figure 4.24** Luminescence spectra of CdS in LB films of (a) stearic acid, and (b) calix[8]arene molecules. (From: [36]. © 2003 IEEE. Reprinted with permission.)

absorption peak at 390 nm, as shown in Figure 4.24(a), while two absorption peaks occur at 280 and 340 nm for calix[8]arene LB films, as shown in Figure 4.24(b).

PL spectra of stearic acid LB films exhibit broad emission bands at approximately 570 nm, as shown in Figure 4.24(a), sandwiched between two smaller bands at 430 and 660 nm appearing as shoulders; while calixarene LB films show two luminescent peaks at 455 and 610 nm, as shown in Figure 4.24(b). Values of the emission energy, together with corresponding absorption energies, are summarized in the Table 4.5. It should be noted from Figure 4.24 that only one luminescent band appeared at 2.18 eV when the excitation at 3.63 eV was used, while a higher energy excitation at 4.51 eV yielded both luminescent bands.

The observed shift of the luminescence bands with respect to the corresponding absorption bands is large. Most likely, only the first luminescence band at 2.88 eV,

**Table 4.5** Characteristic Energies for the Luminescence of CdS Nanoparticles in LB Films

<i>Material</i>	<i>Absorption Energy (eV)</i>	<i>Emission Energy (eV)</i>	<i>Stokes Shift (eV)</i>
Stearic acid	3.10	2.88	0.22
		2.18	
		1.88	
Calix[8]arene	3.63 (first peak)	2.82	0.81
		2.03	

with the Stokes shift of 0.22 eV, represents the real resonance luminescence from the excited levels of CdS. The other two bands may be associated with impurities. Similarly, in calixarene LB films, the first band at 2.82 eV, with the energy shift of 0.81 eV, is probably due to resonance, while the second band at 2.03 eV is most likely due to the energy transfer to the impurity level.

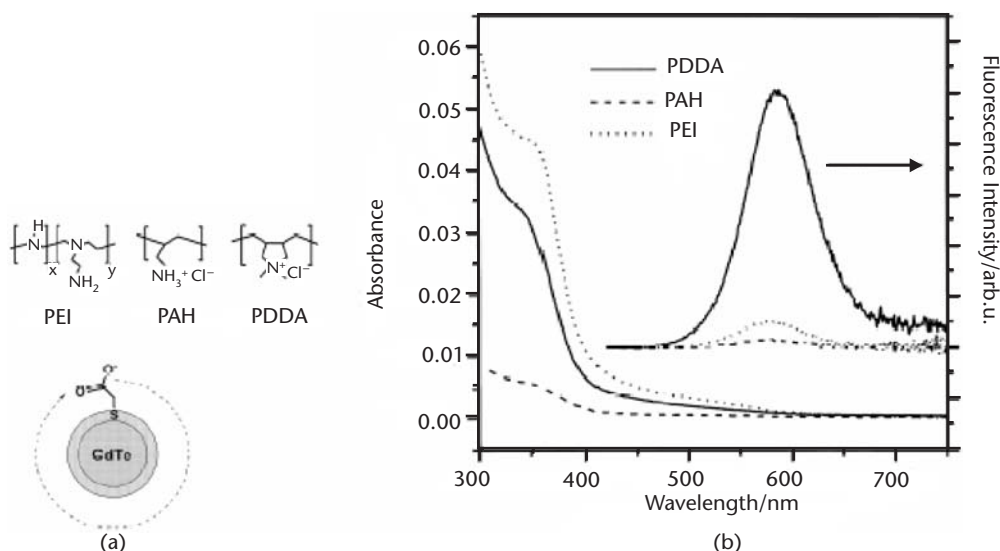
Values of the Stokes shift are found to be 0.22 and 0.81 eV for CdS nanoparticles in stearic acid and calixarene LB films, respectively. This very large Stokes shift of the luminescence of CdS nanoparticles is one of the most surprising results obtained. Typical values of the resonance Stokes shift are approximately 10 meV [46]. The formation of “dark excitons” was recently reported [46, 52], and the process is shown in the inset of Figure 4.24(a). These electron transitions that have an angular momentum projection of  $F = \pm 2$ , which are usually forbidden, can occur under special conditions, such as when II-VI semiconductor particles of prolate shape have noncompensated ( $\text{Cd}^+ - \text{S}^-$ ) dipole moments on their surface. The formation of “dark excitons” leads to a larger Stokes shift of approximately 100 meV [46, 52]. The large Stokes shift observed in the present study can be explained by assuming a platelet shape of CdS nanoparticles in LB films. The energy shift for CdS clusters in calixarene LB films is larger than that in stearic acid LB films. This difference may be explained by the fact that the effect of surface dipole moments is more pronounced in smaller CdS clusters in calixarene LB films than those embedded in stearic acid films.

The formation of semiconductor nanoparticles in LB films is one of the easiest methods, which allows the formation of various nanostructures, including unique nanoclusters consisting of several atoms, for the fundamental study of optical and electrical properties.

### 4.3.2 Semiconductor Nanoparticles in Electrostatically Self-Assembled Films

The method of electrostatic self-assembly is very promising for the formation of composite organic/inorganic nanostructures, such as superlattices formed by the alternation of layers of inorganic (e.g., metal or semiconductor) nanoparticles with layers of polycations. This technique was developed within the last decade by a number of research groups. The list of publications on this topic is given in Chapter 2.

Composite polyelectrolyte/ semiconductor nanoparticles films found some very promising applications in optoelectronics, particularly as tuneable photoluminescent and electroluminescent devices [65–70]. In these publications, different colloid particles, such as CdS, CdSe, CdTe, and CdTe/CdS core-shell particles, were deposited by the alternation with different polycations, such as poly(ethyleneimine) (PEI), poly(allylamine hydrochloride) (PAH), and poly(diallyl-dimethylammonium chloride) (PDDA), as shown in Figure 4.25.



**Figure 4.25** (a) Chemical structures of CdTe/CdS nanoparticles and polycations used, and (b) absorption/luminescence spectra of CdTe/CdS nanoparticles alternated with different polycations. (From: [67]. © 1999 Elsevier. Reprinted with permission.)

The intensity and spectra of photoluminescence of such composite films depends on three factors: (1) the particle's composition, (2) the particle's size, and (3) the interaction between colloid particles and polyelectrolytes. For example, CdTe/CdS core/shell nanoparticles, as shown in the inset of Figure 4.25, alternated with different polycations PEI, PAH and PDDA, yield different intensities of luminescence, as shown in Figure 4.25 [67]. Obviously, the luminescence is much stronger in PDDA film as compared with both PEI and PAH matrices. The presence of amine groups, known as effective fluorescent quenchers, in PEI and PAH inhibits the luminescence dramatically [67]. The pH of the solution, from which colloid particles were deposited, has a dramatic effect on the luminescence intensity because of different surface charge density. An increase in pH from 6 to 10 causes a drop in the luminescence intensity of almost 10 times [67]. A pH of 6 seems to be optimal, because a further decrease in the pH leads to poor electrostatic binding. These results show the importance of the choice of colloid particles/polyelectrolyte pairs on the luminescence efficiency.

The industrial application of II-VI semiconductor/polyelectrolyte composite films as light emitting devices is based on the effect of electroluminescence. For this purpose, films were deposited on ITO-coated glass slides, and the top metal electrode was formed by evaporation of gold. The electroluminescence can be excited in these structures by applying a voltage between the bottom and top electrodes. Physical mechanisms of photo luminescence and electroluminescence are similar regarding the light emission; however, materials must have reasonably high conductivity to provide charge carrier supply to nanoparticles. Composite polyelectrolyte/II-VI semiconductor nanoparticles have relatively high conductivity, because the thickness of polycation layers ranging in size from 0.5 to 1 nm is much smaller than the characteristic tunneling distance. Polyelectrolyte monolayers do not provide complete coverage, which leaves a number of defects and possible routes for current percolation.



Since the wavelength of the emitted light depends on both the material and the size of the nanoparticles, it is possible to vary the spectral range of light emitters. Luminescent devices of all colors for organic color displays, as well as white light emitters, are produced with this technique [65–70]. The position of the luminescence peak depends on the size of CdTe colloid particles obtained by refluxing the initial colloid solution of CdTe [70]. Extraction of colloid particles at different stages of refluxing results in different particle sizes. The smaller CdTe clusters give luminescence peaks at shorter wavelengths. The combination of all types of CdTe nanoparticles in the same film allows the coverage of nearly the entire visible spectral range of luminescence, so that such devices can be used as white light LEDs.

Because of the high efficiency of luminescence, and its wide and variable spectral range, low cost organic/inorganic LEDs are considered to be a very competitive alternative to existing solid-state devices.

## References

- [1] Asam, R. M. A., and N. M. Bashara, *Ellipsometry and Polarized Light*, 2nd ed., Amsterdam, the Netherlands: North Holland Press, 1977, 1987.
- [2] Tompkins, H. G., and W. A. McGahan, *Spectroscopic Ellipsometry and Reflectometry*, New York: John Wiley & Sons, 1999.
- [3] Aspens, D. E., “The Accurate Determination of Optical Properties by Ellipsometry” in *Handbook of Optical Constants of Solids I*, E. D. Palik, (ed.), San Diego, CA: Academic Press, 1985, pp. 89–112.
- [4] Woollam, J. A., “Variable Angle Ellipsometry,” in *Wiley Encyclopedia of Electrical and Electronic Engineering*, J. G. Webster, (ed.), New York: John Wiley & Sons, 2000, pp. 109–117.
- [5] Jellison, Jr., G. E., “Spectroscopic Ellipsometry Data Analysis: Measured Versus Calculated Quantities,” *Thin Solid Films*, Vol. 313–314, 1998, pp. 193–197.
- [6] Malmsten, M., “Ellipsometry Studies of Protein Layers Adsorbed at Hydrophobic Surfaces,” *J. Colloid and Interface Sci.*, Vol. 166, No. 2, 1994, pp. 333–342.
- [7] “Guide to Using WVASE32 Software for Spectroscopic Ellipsometry Data Acquisition and Analysis,” J. A. Woollam Co., Inc., <http://www.jawoollam.com>.
- [8] Kretschmann, E., *Z. Phys.* Vol. 241, 1971, p. 313.
- [9] Pockrand, I., “Surface Plasma Oscillations at Silver Surfaces with Thin Transparent and Absorbing Coatings,” *Surf. Sci.*, Vol. 72, No. 3, 1978, pp. 577–578.
- [10] Pockrand, I., et al., “Optical Properties of Organic Dye Monolayers by Surface Plasmon Spectroscopy,” *J. Chem. Phys.*, Vol. 69, No. 9, 1978, pp. 4001–4011.
- [11] Swalen, J. D., “Optical Wave Spectroscopy of Molecules at Surfaces,” *J. Phys. Chem*, Vol. 83, No. 11, 1979, pp. 1438–1445.
- [12] Chen, W. P., and J. M. Chen, “Use of Surface Plasma-Waves for Determination of the Thickness and Optical-Constants of Thin Metallic-Films,” *J. Opt. Soc. Am.*, Vol. 71, No. 2, 1981, pp. 189–191.
- [13] De Bruijn, H. E., R. P. H. Kooyman, and J. Greve, “Determination of Dielectric Permittivity and Thickness of a Metal Layer from a Surface-Plasmon Resonance Experiment,” *Appl. Optics*, Vol. 29, No. 13, 1990, pp. 1974–1978.
- [14] Yang, F., J. R. Samblers, and G. W. Bradberry, “Determination of the Optical-Constants and Thickness of a Highly Absorbing Film Using the Attenuated Total Reflection Technique,” *J. Modern Optics*, Vol. 38, No. 8, 1991, pp. 1441–1450.

- [15] Ray, A. K., et al., "Surface Plasmon Resonance Studies on Langmuir-Blodgett Films of Novel Octa-Substituted Metal-Free Phthalocyanine Molecules," *Phil. Mag. B*, Vol. 76, No. 6, 1997, pp. 961–971.
- [16] Vukusic, P. S., J. R. Sambles, and J. D. Write, "Surface-Plasmon Resonance Characterization of Spin-Deposited Phthalocyanine Films," *J. Mater. Chem.*, Vol. 2, No. 10, 1992, pp. 1105–1106.
- [17] Brecht, A., and G. Gauglitz, "Optimized Layer Systems for Immunosensors Based on the RIFS Transducer," *Fresenius J. Analyt. Chem.*, Vol. 349, No. 5, 1994, pp. 360–366.
- [18] Chechik, V., and C. J. M. Stirling, "Reactivity in Self-Assembled Monolayers: Effect of the Distance from the Reaction Center to the Monolayer-Solution Interface," *Langmuir*, Vol. 14, No. 1, 1998, pp. 99–105.
- [19] Slavik, R., et al., "Novel Spectral Fiber Optic Sensor Based on Surface Plasmon Resonance," *Sensors & Actuators B-Chemical*, Vol. 74, No. 1, 2001, pp. 106–111.
- [20] Westphal, P., and A. Bornmann, "Biomolecular Detection by Surface Plasmon Enhanced Ellipsometry," *Sensors and Actuators B: Chemical*, Vol. 84, No. 2–3, 2002, pp. 278–282.
- [21] Ramsdale, C. M., and N. C. Greenham, "The Optical Constants of Emitter and Electrode Materials in Polymer Light-Emitting Diodes," *J. Phys. D-Appl. Phys.*, Vol. 36, No. 4, 2003, pp. L29–L34.
- [22] Bohn, P. W., and D. J. Walls, "Challenges in the Structural Characterization of Thin Organic Films," *Mikrochimica Acta*, Vol. 1, No. 1–2, 1991, pp. 3–35.
- [23] Arwin, H., "Ellipsometry on Thin Organic Layers of Biological Interest: Characterization and Applications," *Thin Solid Films*, Vol. 377–378, 2000, pp. 48–56.
- [24] Brockman, J. M., B. P. Nelson, and R. M. Corn, "Surface Plasmon Resonance Imaging Measurements of Ultrathin Organic Films," *Ann. Re. Phys. Chem.*, Vol. 51, 2000, pp. 41–63.
- [25] Gavriluk, I. V., et al., "Langmuir-Blodgett Films Based on Cyanoacrylic Acid as Insulating Layers on Semiconductors," *Poverkhnost. Fizika. Khimiya. Mekhanika*, No. 11, 1991, pp. 93–100 (in Russian).
- [26] Nabok, A. V., et al., "Complexing Properties of Calix[4]resorcinolarene LB Films," *Thin Solid Films*, Vol. 259, No. 2, 1995, pp. 244–247.
- [27] Nabok, A. V., et al., "Study of Adsorption of Some Organic Molecules in Calix[4]resorcinolarene LB Films by Surface Plasmon Resonance," *Sensors & Actuators B*, Vol. 45, No. 2, 1997, pp. 115–121.
- [28] Hassan, A. K., et al., "Thin Films of Calix-4-Resorcinarene Deposited by Spin Coating and Langmuir-Blodgett Techniques: Determination of Film Parameters by Surface Plasmon Resonance," *Mater. Sci. Eng C*, Vol. 8–9, 1999, pp. 251–255.
- [29] Davis, F., and C. J. M. Stirling, "Spontaneous Multilayering of Calix-4-Resorcinarenes," *J. Am. Chem. Soc.*, Vol. 117, No. 41, 1995, pp. 10385–10386.
- [30] Nabok, A. V., A. K. Hassan, and A. K. Ray, "Optical and Electrical Characterisation of Polyelectrolyte Self-Assembled Thin Films," *Mater. Sci. Eng. C*, Vol. 8–9, 1999, pp. 505–508.
- [31] Schwartz, S., et al., "Polyelectrolyte Adsorption onto Planar Surfaces: A Study by Streaming Potential and Ellipsometry Measurements," *Colloids & Surfaces A*, Vol. 159, No. 2–3, 1999, pp. 491–501.
- [32] Simon, J., and J. J. Andre, *Molecular Semiconductors*, Berlin, Germany: Springer-Verlag, 1985.
- [33] Ray, A. K., et al., "Optical Studies on Composite Langmuir-Blodgett Films Containing Ytterbium Bis-Phthalocyanines," *Phil. Mag.*, Vol. 79, No. 7, 1999, pp. 1005–1019.
- [34] Hassan, A. K., et al., "Surface Plasmon Resonance Studies on Spin Coated Films of Azobenzene-Substituted Calix-4-Resorcinarene Molecules," *IEE Proc. Sci. Measur. Technol.*, Vol. 147, No. 3, 2000, pp. 137–140.

- [35] Nabok, A. V., et al., "Size-Quantization in Extremely Small CdS Clusters Formed in Calixarene Langmuir-Blodgett Films," *Thin Solid Films*, Vol. 327–329, 1998, pp. 510–514.
- [36] Nabok, A. V., et al., "II-VI Semiconductor Nanoparticles Formed by Langmuir-Blodgett Film Technique: Optical Study," *IEEE Trans. on Nanotechnology*, Vol. 2, No. 1, 2003, pp. 44–49.
- [37] Urban, F. K., et al., "Optical Properties of Nanophase Films Measured by Variable-Angle Spectroscopic Ellipsometry," *Thin Solid Films*, Vol. 408, 2002, pp. 211–217.
- [38] Nabok, A. V., S. Yvonn, and T. Richardson, "Optical Study of Langmuir-Schaeffer Films of Gold Colloid Nanoparticles," *ECOF-2004 Book of Abstracts, IX European Conference on Organised Films*, Valladolid, Spain, July 22–25, 2004, p. 154.
- [39] Brown, K. R., et al., "Hydroxylamine Seeding of Colloidal Au Nanoparticles. 3. Controlled Formation of Conductive Au Films," *Chem. Mater.*, Vol. 12, No. 2, 2000, pp. 314–323.
- [40] Kasap, S. O., *Principles of Electrical Engineering Materials and Devices*, New York: McGraw-Hill, 1997, p. 175.
- [41] Ekimov, A. I., and A. A. Onuschenko, "Quantum Size Effect in Three-Dimensional Microscopic Semiconductor Crystals," *JETP Lett.*, Vol. 34, No. 6, 1981, pp. 345–349.
- [42] Efros, A. L., and A. L. Efros, "Interband Absorption of Light in a Semiconductor Sphere," *Soviet Phys. Semicond.*, Vol. 16, No. 1982, pp. 772–775.
- [43] Ekimov, A. I., A. L. Efros, and A. A. Onuschenko, "Quantum Size Effect in Semiconductor Microcrystals," *Solid State Commun.*, Vol. 56, No. 11, 1985, pp. 921–924.
- [44] Smotkin, E. S., et al., "Size Quantization Effects in Cadmium-Sulfide Layers Formed by a Langmuir-Blodgett Technique," *Chem. Phys. Lett.*, Vol. 152, No. 2–3, 1988, pp. 265–268.
- [45] Yoffe, A. D., "Low-Dimensional Systems—Quantum-Size Effects and Electronic-Properties of Semiconductor Microcrystallites (Zero-Dimensional Systems) and Some Quasi-Two-Dimensional Systems," *Adv. in Phys.*, Vol. 42, No. 2, 1993, pp. 173–266.
- [46] Yoffe, A. D., "Semiconductor Quantum Dots and Related Systems: Electronic, Optical, Luminescence, and Related Properties of Low Dimensional Systems," *Adv. in Phys.*, Vol. 50, No. 1, 2001, pp. 1–208.
- [47] Yoffe, A. D., "Low Dimensional Systems: Quantum Size Effects and Electronic Properties of Semiconductor Microcrystallites (Zero-Dimensional Systems) and Some Quasi-Two-Dimensional Systems," *Adv. in Phys.*, Vol. 51, No. 2, 2002, pp. 799–890.
- [48] Lifshitz, I. M., and V. V. Slesov, *Soviet Phys. JETP*, Vol. 35, 1958, p. 331.
- [49] Brus, L. E., "Zero-Dimensional 'Excitons' in Semiconductor Clusters," *IEEE J. Quant. Electron.*, Vol. QE-22, No. 9, 1986, p. 1909.
- [50] Rama Krishna, M. V., and R. A. Freisner, "Quantum Confinement Effects in Semiconductor Clusters," *J. Chem. Phys.*, Vol. 95, No. 11, 1991, pp. 8309–8322.
- [51] Tomasulo, A., and M. V. Rama Krishna, "Quantum Confinement Effects in Semiconductor Clusters II," *J. Chem. Phys.*, Vol. 105, No. 12, 1996, pp. 3612–3626.
- [52] Nirmal, M., et al., "Observation of the Dark Exciton in CdSe Quantum Dots," *Phys. Rev. Lett.*, Vol. 75, No. 20, 1995, pp. 3728–3731.
- [53] Ueta, M., et al., "Excitonic Processes in Solids," *Springer Series in Solid State Sciences*, Vol. 60, 1986.
- [54] Wang, Y., "Local Field-Effect in Small Semiconductor Clusters and Particles," *J. Phys. Chem.*, Vol. 95, No. 3, 1991, pp. 1119–1124.
- [55] Zylberajch, G., A. Raudel-Teixier, and A. Barraut, "2D Monomolecular Inorganic Semiconductors, Inserted in a Langmuir-Blodgett Matrix," *Synth. Metals*, Vol. 27, No. 3–4, 1988, pp. 609–614.
- [56] Chen, H., et al., "X-Ray Photoelectron Spectroscopy Study of the Synthesis of Copper Sulphide in Langmuir-Blodgett Films," *Thin Solid Films*, Vol. 178, No. 1–2, 1989, pp. 535–540.

- [57] Weller, H., et al., "Photochemistry of Semiconductor Colloids. 14. Photochemistry of Colloidal Semiconductors—Onset of Light-Absorption as a Function of Size of Extremely Small Cds Particles," *Chem. Phys. Lett.*, Vol. 124, No. 6, 1986, pp. 557–560.
- [58] Facci, P., et al., "Formation of Ultrathin Semiconductor Films by CdS Nanostructure Aggregation," *J. Phys. Chem.*, Vol. 98, No. 50, 1994, pp. 13323–13327.
- [59] Nabok, A. V., et al., "Cadmium Sulphide Nanoparticles in Langmuir-Blodgett Films of Calixarene," *Langmuir*, Vol. 13, No. 12, 1997, pp. 3198–3201.
- [60] Wang, L. J., et al., "A Study on Inorganic Nanoparticles Amphiphilic Oligomer in Nano-Ordered Multilayer," *Mol. Cryst. & Liq. Cryst. Sci. & Technol., Section A*, Vol. 294, 1997, pp. 473–478.
- [61] Erokhin, V., et al., "Fatty Acid-Based Monoelectron Device," *Biosensors & Bioelectronics*, Vol. 12, No. 7, 1997, pp. 601–606.
- [62] Nabok, A. V., et al., "Formation of CdS Nanoclusters Within LB Films of Calixarene Derivatives and Study of Their Size-Quantization," *Mater. Sci. Eng. C*, Vol. 8–9, 1999, pp. 171–177.
- [63] Nabok, A. V., et al., "Evolution of CdS Nanoparticles Within Two-Dimensional Langmuir-Blodgett Layers," *J. Phys. D-Appl. Phys.*, Vol. 35, No. 13, 2002, pp. 1512–1515.
- [64] Gutsche, C. D., *Calixarenes*, Cambridge, England: Royal Society of Chemistry, 1989.
- [65] Gao, M., B. Richter, and S. Kirstein, "White-Light Electroluminescence from a Self-Assembled Q-CdSe/PPV Multilayer Structure," *Adv. Mater.*, Vol. 9, No. 10, 1997, pp. 802–805.
- [66] Gao, M., et al., "Strongly Photoluminescent CdTe Nanocrystals by Proper Surface Modification," *J. Phys. Chem. B*, Vol. 102, No. 43, 1998, pp. 8360–8363.
- [67] Lesser, C., M. Gao, and S. Kirstein, "Highly Luminescent Thin Films from Alternating Deposition of CdTe Nanoparticles and Polycations," *Mater. Sci. & Eng. C*, Vol. 8–9, 1999, pp. 159–162.
- [68] Gao, M., et al., "Electroluminescence Studies on Self-Assembled Films of PPV and CdSe Nanoparticles," *J. Phys. Chem. B*, Vol. 102, No. 21, 1998, pp. 4096–4103.
- [69] Gao, M., et al., "Innovative Light Emitting Materials," P. Vincenzini, and G. C. Righini, (eds.), *Advances in Sci. and Technol.*, Vol. 27, 1999, pp. 347–358.
- [70] Gao, M., et al., "Electroluminescence of Different Colors from Polycation/CdTe Nanocrystal Self-Assembled Films," *J. Appl. Phys.*, Vol. 87, No. 5, 2000, pp. 2297–2302.

# Electron Transport in Organic/Inorganic Nanostructures

## 5.1 Conductivity of Thin Films

The electrical conductivity of thin films made of either organic or inorganic materials was a subject of extensive study for decades, and the knowledge was summarized in a number of review papers and books [1–25]. The key points of both theoretical and experimental aspects of electrical conductivity of thin films are reviewed here, with the focus on quantum phenomena in conductivity, such as electron tunneling and single-electron processes, having great potential in the development of nano-electronic devices.

### 5.1.1 Definitions and Experimental Methods

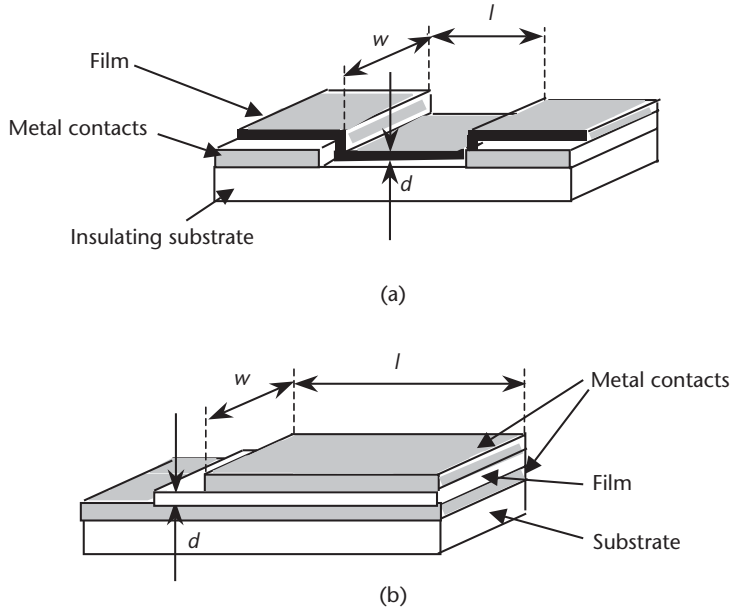
Electrical conductivity of thin films can be studied (both theoretically and experimentally) in two possible configurations: (1) conductivity in the film plane (i.e., lateral or planar conductivity), and (2) conductivity in the direction perpendicular to the film surface (i.e., normal conductivity). Experimentally, these two types of conductivity can be tested in the planar and sandwich structures, respectively, as shown in Figure 5.1.

In both cases, the conductivity can be defined as:

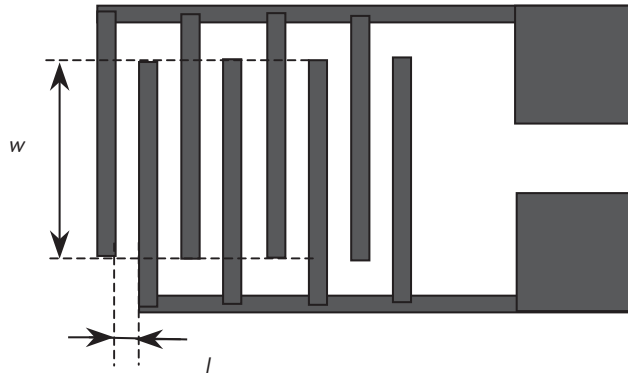
$$\sigma = \frac{I}{V} \frac{l}{A} \quad (5.1)$$

where  $V$  is the voltage applied between two electrodes, separated by the distance  $l$ , which drives the current  $I$  through the cross-section  $A$ . The units for conductivity are [ $\Omega^{-1}\text{m}^{-1}$ ] or [ $\text{Sm}^{-1}$ ]. In the planar structures,  $L$  is the minimal distance between the electrodes, and  $A = d \times w$  is a product of a film thickness  $d$  and the electrode width  $w$ ; while in sandwich structures,  $l = d$ , and  $A$  is the area of overlapping of bottom and top electrodes (see Figure 5.1). Usually, in planar structures,  $L$  is much larger and  $A$  is much smaller than the respective values in sandwich structures. These yield a much smaller measured current in planar structures, and a much larger electric field in sandwich structures. Very often, in order to increase the current, planar interdigitated electrodes can be used, as shown in Figure 5.2.

In this case, the conductivity is given:



**Figure 5.1** The structure's conductivity measurements of thin films: (a) planar structure, and (b) sandwich structure.



**Figure 5.2** Interdigitated electrodes for planar conductivity measurements.

$$\sigma = \frac{I}{V} \frac{l}{(N-1)wd} \quad (5.2)$$

where  $N$  is the number of fringes,  $l$  is the separation between fringes, and  $w$  is the overlapping of fringes. Such interdigitated electrodes can be produced by photolithography; the structures with the separation  $l$  of several tens of microns are commercially available (see, for example, [26]). With typical parameters of interdigitated electrodes available in our laboratory,  $l = 60 \mu\text{m}$ ,  $w = 3.5 \text{ mm}$ ,  $N = 16$ , and the film thickness  $d = 100 \text{ nm}$ , the minimal values of conductivity in the range from  $10^{-9}$  to  $10^{-10} \text{ (S}^{-1}\text{m}^{-1}\text{)}$  can be measured using standard electrometric equipment. Measurements of less conductive materials may suffer from the surface leakage current caused mostly by moisture in the atmosphere. Performing measurements in a vacuum or in the atmosphere of inert gases (e.g., He, Ar, or  $\text{N}_2$ ) may reduce the limit of measurable conductivity by two orders of magnitude.

Further improvement of sensitivity can be achieved by reducing the gap between planar electrodes. The structures with submicron gaps can be made either with electron-beam or SPM lithography. In the latter case, the gap can be “scratched” in the thin film of soft metal (e.g., Au, Al, or Cu) with a sharp STM or AFM tip [27, 28].

Technically, the planar conductivity of thin films (particularly, inorganic films) is very conveniently measured with the four-point probe method, as shown in Figure 5.3.

The small current between the end electrodes (1 and 4) is driven by a current source, while the voltage drop is recorded between the middle electrodes (2 and 3). This allows the elimination of the parasitic resistance of contacts. The parameter of sheet resistance ( $r_s$ ) can be obtained from these measurements, assuming that the film thickness is much smaller than its lateral dimensions [29]:

$$r_s = \frac{V}{I} g \quad (5.3)$$

where  $g$  is the geometrical factor. If the distance between the electrodes(s) is much smaller than lateral dimensions of the sample (e.g., the wafer diameter ( $\phi$ )), then  $g = \pi/\ln 2 = 4.54$ . The dependence  $g(\phi/s)$  is given in [29]. The value of  $r_s$  is measured in the unusual units of  $[\Omega/\square]$  (ohm per square), and the units may be  $\text{mm}^2$ ,  $\text{cm}^2$ ,  $\text{m}^2$ , or squares of any other dimensions. The resistivity ( $\rho$ ) and conductivity ( $\sigma$ ) of thin film can therefore be calculated as:

$$\rho = \frac{1}{\sigma} = r_s d \quad (5.4)$$

The use of sandwich structures is much more suitable than that of planar structures for the measurements of poor conducting materials. Simple comparison of the geometrical factors  $\frac{l}{A} = 10^{-2} \text{ m}^{-1}$  in (5.1) and  $\frac{l}{(N-1)dw} = 10^4 \text{ m}^{-1}$  in (5.2), calculated using the film thickness of 100 nm, the sandwich electrodes area  $A = 10 \text{ mm}^2$ , and the above dimensions for interdigitated electrodes, shows an obvious advantage of sandwich structures. However, measurements of the conductivity of

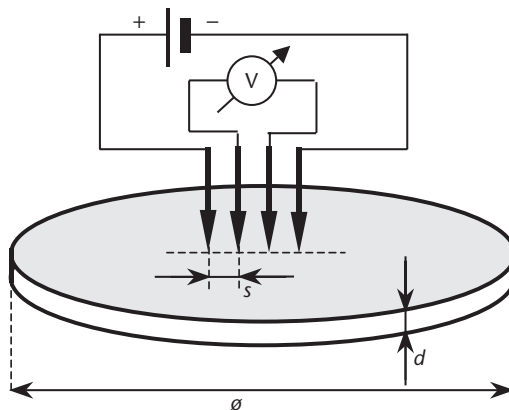


Figure 5.3 The scheme of four-point measurements.



thin films (particularly, organic thin films) in sandwich structures face a typical problem of short circuiting. There are several reasons to have short circuits in sandwich structures: (1) intrinsic (original) defects in thin films, such as pinholes in LB films, or cracks in sol-gel and electrodeposited films; (2) defects caused by the deposition of metal electrodes, such as “burning” of organic films during thermal evaporation; and (3) mechanical or chemical damage of the film, caused either by metal spring contacts to the top electrode, or by the dissolving of organic film during the application of silver-paste contacts, respectively. The latter factors can be easily eliminated by using spatially separated contacts pads on the bottom and top electrodes (see Figure 5.1). The remaining two factors lead to the formation of metal filaments across the film, which cause short circuiting.

The presence of filaments can be reduced substantially by a “gentle” evaporation of metals. First, metals with low melting points are preferable from this point of view. Obviously, gold, with a melting point of 1,064°C, is much more damaging for organic films than is aluminium (660°C) and indium (156°C). Yet, the evaporation must be carried out at a slow rate with intermediate stops to cool down the sample [30, 31]. Cooling down the substrate during metal evaporation, which can be achieved with a sample holder connected to the liquid nitrogen trap or with a Peltier cooler within a vacuum chamber, is another solution to the problem [32]. From the point of view of thermal damage, the “cold method” of sputtering of metals is perhaps better than thermal evaporation; however, metal particles still have kinetic energy high enough to damage thin organic films. The metal particles may also carry an electrical charge, and become more penetrative in the sputtering plasma.

The effect of intrinsic film defects can be reduced by maintaining high standards of deposition technology. This requires the use of clean rooms, the use of purified and filtered chemicals for film deposition, and the optimization of technological processes of film deposition and postdeposition treatments (annealing). In the case of LB films, the choice of amphiphilic molecules is of crucial importance. Rigid LB films of fatty acid molecules, usually containing a large number of pinholes and having a low melting point (80°C to 120°C), are very difficult objects for electrical testing. Polymer films, not having pinholes, and having higher melting points, are much more suitable for this purpose.

The existing metal filaments in sandwich structures can be removed by applying a large bias voltage exceeding the breakdown limit. Large electric current passing through metal filaments causes their overheating, and subsequent oxidation or evaporation. The series of consecutive high voltage sweeps gradually increases the breakdown voltage, as a result of “burning out” metal filaments. This approach was used in many experiments in thin organic films, including the classical work of Mann and Kunn on electron tunneling through the Langmuir monolayers of fatty acids [30–33].

A radical solution to the problem of short circuiting in sandwich structures is the use of either electrolyte or liquid metal top contacts. The electrolyte contact was widely used for studying inorganic semiconductors [34, 35]. This method was applied for the electrical characterization of organic thin films [36–40]. However, the range of applied voltages is limited because of the electrochemical reactions. In the case of thin films, we cannot exclude the penetration of the electrolyte through the film defects, thus causing short circuiting.

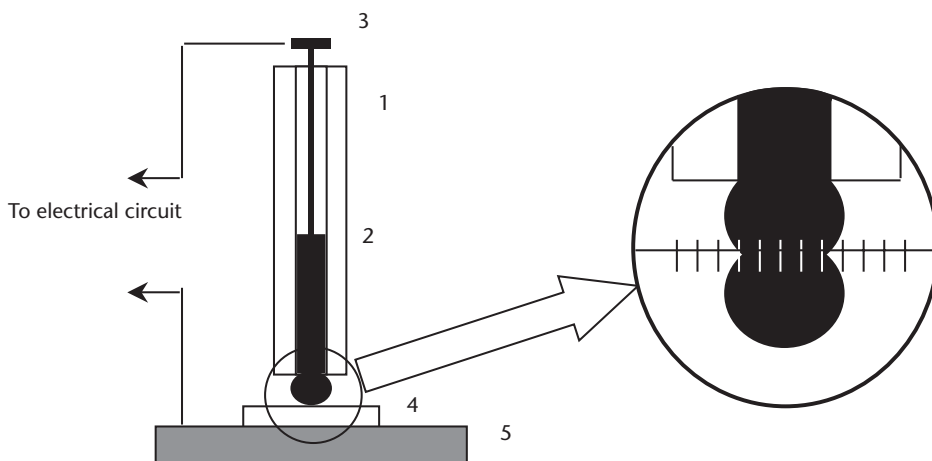
Top electrodes made of liquid metals, such as mercury or In/Ga eutectic, are much more promising. Actually, the mercury probe technique was widely adopted in microelectronics for testing deposited layers on satellite silicon wafers during the development of ICs [41]. The use of mercury electrodes for studying the electron tunneling through alkanethiols monolayers was recently reported [42–44].

A typical construction of a mercury probe [45], shown in Figure 5.4, comprises (1) a capillary tube filled with (2) mercury and (3) a metal plunge serving as an electrical contact to the mercury. The position of the probe is adjustable, and it could be brought into contact with (4) the sample fixed on (5) a metal plate. A microscope was placed horizontally, in order to observe the contact line between a mercury drop and the sample.

The inset in Figure 5.4 shows a view of the contact between a mercury drop and its mirror reflection from the sample surface. The area of the mercury electrode can thus be calculated by measuring the diameter of the contact.

The main advantage of the mercury probe is the fact that it is a nondestructive technique, and it can be used instead of the evaporation of metal contacts. This is true for a majority of inorganic materials, but is not always the case for organic films. Previous attempts to use the mercury probe for LB and spun organic films were not successful, due to a very poor adhesion in these layers. Both LB and spun films can be fatally damaged by the contact with mercury, which has a very high surface tension of 485 mN/m at room temperature. The mercury drop has become covered with a monolayer of amphiphilic material, leaving a hole in the film underneath. In contrast, polymer films, and particularly electrostatically self-assembled polyelectrolyte films, have much stronger adhesion, both to the substrate and between polyelectrolyte layers, due to electrostatic interaction; at the same time, polymer films provide the thickness precision comparable to LB films [46, 47]. These films cannot be damaged by the contact with mercury. Our experiments show no visual changes on the polymer film surface after applying the mercury probe [45, 48].

A relative disadvantage of a mercury probe is its restricted temperature range for conductivity measurements. The range between mercury's melting point of 38°C and its boiling point of 356°C is not that small. However, heating the mercury is a very



**Figure 5.4** Schematic diagram of the mercury probe: (1) capillary tube with (2) mercury, (3) metal plunge, (4) sample, and (5) metal plate. The inset shows a microscopic view of the contact.

hazardous procedure, which releases toxic mercury vapors, so it is advisable to do the temperature range measurements in the vacuum chamber. Additionally, the upper temperature is limited by the characteristic phase transitions in organic thin films.

### 5.1.2 Conductivity of Nanocrystalline Materials

As discussed in previous chapters, the majority of materials prepared by chemical routes are polycrystalline. The size of crystallites, which may vary in a wide range from tens of micrometers down to nanometers, is of a crucial importance for materials' conductivity. Even highly conductive materials (in monocrystalline form) suffer from some serious restrictions of conductivity, due to the effect of boundaries between crystallites. These restrictions are not that critical for polycrystalline metals because of their large concentrations of electrons, but they are particularly important for semiconductors. A large concentration of surface states, caused by lattice mismatching on the intercrystallite boundaries, results in the formation of potential barriers between crystallites, as shown in Figure 5.5.

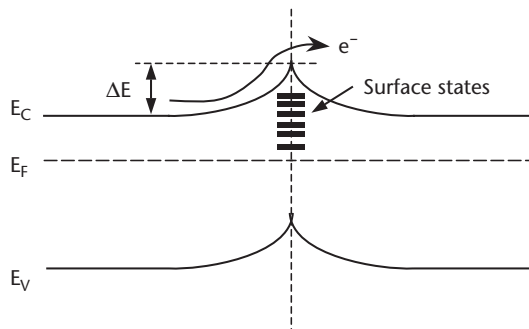
Electrons in a conduction band require extra energy to overcome the intercrystalline barrier. This results in the reduction in conductivity, due to the additional activation energy ( $\Delta E$ ) in the formula for conductivity:

$$\sigma = \sigma_0 \exp\left(-\frac{E_g + \Delta E}{2kT}\right) \quad (5.5)$$

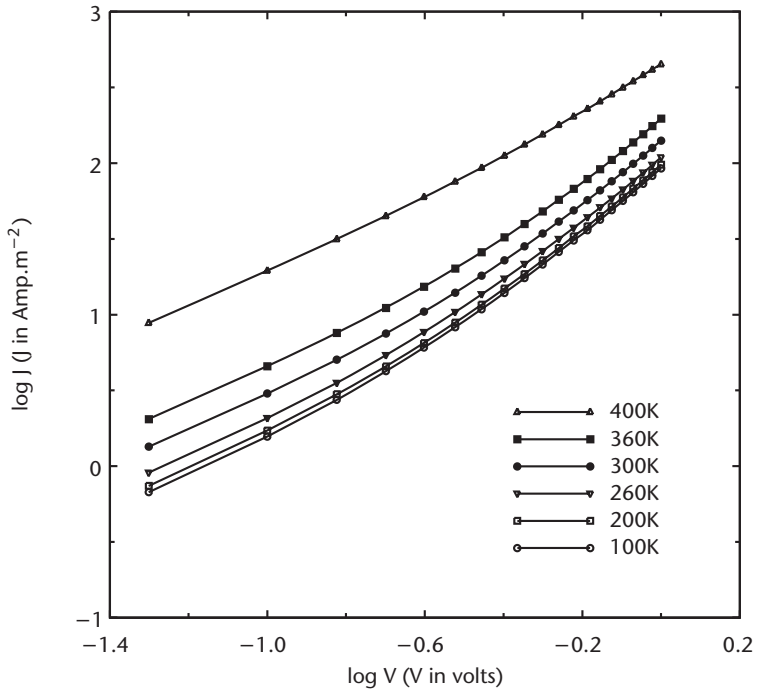
The value of this additional activation energy reflects the mechanism of electrons (holes) scattering, which may include thermally activated hopping, electric field-assisted processes such as the Pool-Frenkel mechanism, and tunneling [49]. Very often, these mechanisms coexist, so that the activation energy of conductivity for the same material may differ, depending on the electric field, the temperature, or the doping impurity concentration.

A classical, well-studied object, illustrating the effect of grain boundaries on conductivity, is sol-gel  $\text{TiO}_2$  films [50–52]. Typical features of conductivity of nanocrystalline  $\text{TiO}_2$  films processed by sol-gel/spin coating route [53] are shown in Figures 5.6 and 5.7.

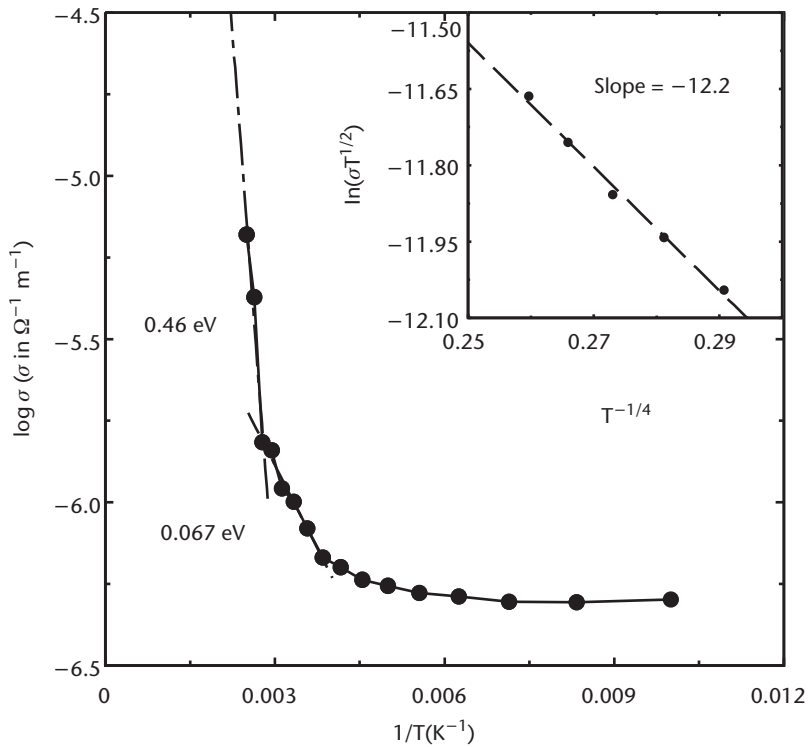
The I-V characteristics of ITO/ $\text{TiO}_2$ /Al sandwich structures measured in the temperature range from 100K to 400K, and presented in a double-logarithmic scale in Figure 5.6, exhibit changes in the conductivity mechanism. It transforms



**Figure 5.5** The formation of the potential barriers on intercrystallite boundaries.



**Figure 5.6** The  $\log(J)$ - $\log(V)$  dependencies for the ITO/TiO<sub>2</sub>/Al structure measured at different temperatures in the range from 100K to 400K. (From: [53]. © 2003 Institute of Physics. Reprinted with permission.)



**Figure 5.7** The  $\log(\sigma)$ - $1/T$  dependence for the Ohmic region. The inset shows part of the dependence plotted in  $\ln(\sigma T^{1/2})$  -  $T^{-1/4}$ . (From: [53]. © 2003 Institute of Physics. Reprinted with permission.)

from Ohmic behavior at low voltages to the space-charge limited (SCL) mechanism ( $J \approx V^m$ ), with  $m$  varying from 1.6 to 2.16 at higher voltages. Arrhenius graphs of  $\log \sigma(1/T)$ , as shown in Figure 5.7 for both ohmic and SCL regions, show the increase in the activation energy at high temperatures. Gradual increase in conductivity at  $T < 220\text{K}$  is generally associated with the variable-range hopping (VRH) conduction mechanism, described by the relation [49]:

$$\sigma = \sigma_0 \exp \left[ - \left( \frac{T_0}{T} \right)^{1/4} \right] \quad (5.6)$$

where  $\sigma_0$  is a pre-exponential factor, and  $T_0$  is a characteristic temperature coefficient, both depending on the density of the localized states at Fermi level  $N(E_F)$ :

$$\sigma_0 = \frac{3e^2 \nu}{(8\pi k)^{1/2}} \left( \frac{N(E_F)}{\alpha k T} \right)^{1/2} \quad \text{and} \quad T_0 = \frac{18\alpha^3}{k N(E_F)} \quad (5.7)$$

Here  $\nu$  is the phonon frequency at Debye temperature, and  $\alpha$  is the inverse decay length of the wave function of localized states near Fermi level. The inset in Figure 5.7 shows a linear dependence of  $\log(\sigma T^{1/2})$  on  $T^{-1/4}$  at the temperatures below 220K. This observation is consistent with (5.6), and it proves that the variable range hopping mechanism is prevalent at low temperatures.

Activation energies of 0.067 eV and 0.46 eV at high temperatures ( $T > 220\text{K}$ ) are believed to be the ionization energies of shallow and deep donor levels below the conduction band, respectively. Similar values of activated energies are reported in [54] for pressed pellets of anatase  $\text{TiO}_2$  annealed in hydrogen at  $400^\circ\text{C}$ , and they were associated with oxygen vacancies.

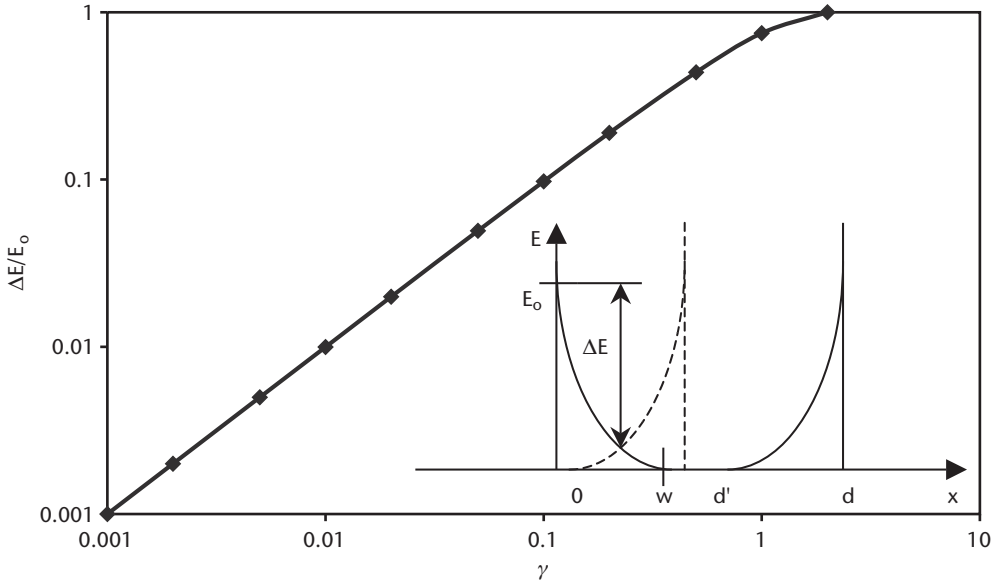
At applied voltages higher than 1.8V, when the SCL conductivity takes place, two values of activation energies 0.047 eV and 0.3 eV are obtained for the high temperature range.

The explanation of the formation of shallow traps in the  $\text{TiO}_2$  material lies in its nanocrystalline nature. The large density of surface states located on the grain boundaries in  $\text{TiO}_2$  material causes the formation of potential barriers, as shown in the inset of Figure 5.8. If the grain size ( $d$ ) is larger than a double depletion width ( $2w$ ), then the barrier height preserves its initial value of  $E_0$ . However, if the grain size is smaller than  $2w$ , the potential barriers overlap, and the resulted barrier reduces down to  $\Delta E$ , as shown in the inset of Figure 5.8.

In the case of a further reduction in  $d$ , the potential barriers may appear as small fluctuations of the conduction (valence) band edge, and may vanish completely when  $d \ll 2w$ . These energy fluctuations can be calculated as:

$$\Delta E = E_0 \left( \gamma - \frac{\gamma^2}{4} \right), \quad \text{where} \quad \gamma = \frac{d}{w} \quad (5.8)$$

The results of this simulation are shown in Figure 5.8. Assuming an initial barrier height value  $E_0 = 0.5$  eV and a donor impurity concentration in  $\text{TiO}_2$  films  $N_D = 10^{24} \text{m}^{-3}$  [55], the depletion width can be estimated as:



**Figure 5.8** Dependence of the relative barrier height on the grain size in polycrystalline materials. The inset illustrates the process of barrier reduction.

$$w = L_D \sqrt{2\beta E_0}, \text{ where } L_D = \sqrt{\frac{\epsilon_s \epsilon_0}{\beta e N_D}} \text{ is the Debye length, and } \beta = \frac{e}{kT}.$$

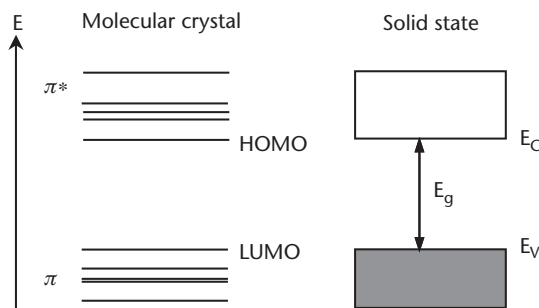
The above calculations yield  $L_D \approx 8$  nm and  $w = 50$  nm. Applying the results of this simulation (see Figure 5.8), one can conclude that for the grain size of 5 nm, the barrier height will be reduced to 0.05 eV, which is very close to the experimentally observed values of 0.047 eV for the activation energy.

### 5.1.3 Organic Semiconductors

Organic semiconductors can be defined as molecular crystals consisting of molecules with a well-developed  $\pi$ -electron system. Typical materials belonging to this class are aromatic hydrocarbons (e.g., naphthalene, anthracene, tetracene, and pentacene), porphyrines, phthalocyanines, and many others. Overlapping of  $\pi$ -electrons of neighboring molecules is not strong enough, so that the electron energy spectrum of the material is similar to the spectra of individual molecules, and therefore does not form bands. Strictly speaking, band theory is not applicable for molecular crystals, so that standard terms in solid-state physics, such as conduction band, valence band, and bandgap, must be used very carefully for the interpretation of electrical properties of organic materials. For example, the valence and conduction bands contain a certain number of electron levels, corresponding to the bonding ( $\pi$ ) and antibonding ( $\pi^*$ ) orbitals in molecular crystals, respectively; and the gap between HOMO and LUMO levels can be treated as the bandgap (see Figure 5.9).

However, the activation energy ( $\Delta E$ ) obtained from the experimental temperature dependence of molecular crystals conductivity is different from the above energy gap:

$$\sigma = \sigma_0 \exp\left(-\frac{\Delta E}{2kT}\right), \quad \Delta E = E_g + \Delta W \quad (5.9)$$



**Figure 5.9** Analogy in energy diagrams of molecular crystals and inorganic solid-state semiconductors.

The energy consists of  $E_g$ , the energy of the excitation of electron/hole pairs, and  $\Delta W$ , which is the extra energy required for the delocalization of carriers. Electron/hole pairs in molecular crystals are still bound to their native molecules, or, in other words, localized. The physics of electron localization lies in the difference between the characteristic vibration relaxation times for molecules ( $10^{-13}$  seconds) and for electrons ( $10^{-15}$  seconds), so that molecules in the lattice are frozen during movement of the electrons, thus providing electrostatic attraction. Such localization can be overcome, if it is supplied with the extra energy from phonons (e.g., vibrations of crystalline lattice). In contrast to solid-state inorganic semiconductors, which have a mobility in organic crystals with a relatively weak temperature dependence, electrons (holes) have a mobility that depends on temperature exponentially [56]:

$$\mu = \mu_0 \exp\left(-\frac{\Delta W}{2kT}\right) \quad (5.10)$$

Combining (5.10) with the conventional formula for electrons (holes) concentration  $n(p) = N_{C(V)} \exp\left(-\frac{E_g}{2kT}\right)$ , one can obtain (5.9).

Although the conductivity is described by equations similar to those in solid-state semiconductors, the use of band theory for organic semiconductors is limited by the localization of carriers. It can be understood from the Heisenberg principle of uncertainty in quantum mechanics,  $\Delta E\tau \geq \hbar$ , where  $\Delta E$  is some characteristic energy in band theory, for example a bandgap, and  $\tau$  is the electron relaxation time (or the mean time between collisions of electrons with lattice ions). Using a definition of electron mobility,  $\mu = \frac{e\tau}{m_e}$ , one can obtain the criterion for the band theory applicability:

$$\mu \geq \frac{e\hbar}{m_e \Delta E} \quad (5.11)$$

For example, by taking  $\Delta E \approx 1$  eV and the mass of a free electron, (5.11) transforms to a simple numerical criterion, concluding that, if the electron mobility is smaller than  $10^{-4}$  ( $\text{m}^2\text{V}^{-1}\text{s}^{-1}$ ), then the band theory is not applicable for this material. In other words, if a free path length of electrons in the material is smaller than the crystallographic lattice period, such electrons are localized.



So far, we discussed pure organic semiconductors; however, the presence of impurities or intrinsic defects has a crucial impact on the conductivity of these materials. For example, electronegative gases, such as O<sub>2</sub>, O<sub>3</sub>, NO<sub>x</sub>, or SO<sub>2</sub>, act as acceptor impurities, while electropositive gases, such as NH<sub>3</sub>, or CO, act as donor impurities in molecular crystals of phthalocyanines and porphyrines. That explains why organic semiconductors have much higher conductivity values in atmospheric conditions than in a vacuum [56].

A classic example of organic semiconductors is metal phthalocyanine (MePc) crystals. The chemical structure of an MePc molecule is shown in Figure 2.21. It is a very common material, having a high order of chemical purity and a relatively high melting point of approximately 400°C. These compounds can be easily modified chemically by attaching some functional groups (*R*). For example, the substitution of hydrocarbons makes these molecules soluble in organic solvents and thus suitable for LB deposition or spin coating, while the addition of ionic groups, such as SO<sub>3</sub><sup>-</sup>Na<sup>+</sup>, makes them water-soluble and suitable for electrostatic self-assembly. MePc molecules form a crystallographic lattice, in which the main structure unit is a stack of MePc molecules. Crystals of nonmodified MePc were extensively studied in the 1970s and 1980s [56]. Later in the 1990s, the interest shifted towards thin films of MePc prepared by LB deposition [57, 58] or spin coating [59, 60]. Because of their semiconducting properties, in addition to a very strong optical adsorption in the visible range, thin films of MePc have found applications in photovoltaic devices, solar cells, active optical information storage medium, lasers, optical filters, and many others devices [56, 61, 62]. Conductivity of MePc thin films was studied extensively by many research groups [63–70]. It was found that conductivity of MePc films is affected by the presence of electroactive gases, which made MePc films very attractive for gas-sensing applications. At normal atmospheric conditions, MePc films show *p*-type conductivity in the range of 10<sup>-6</sup> (Sm<sup>-1</sup>), due to the presence of acceptor impurity of oxygen. The mobility of MePc films is usually very low and varied in a wide range of 10<sup>-3</sup> ÷ 10<sup>-8</sup> (m<sup>2</sup>V<sup>-1</sup>s<sup>-1</sup>), depending on the type of metal and crystallographic structure. As mentioned previously, the use of band-theory terminology is not appropriate for phthalocyanine films. The temperature dependence of conductivity for CuPc films yields an activation energy value of 0.81 eV [56]. In a vacuum, the MePc conductivity drops down on two to three orders of magnitudes, and the temperature dependence gives a higher activation energy of 1.07 eV, most likely associated with intrinsic defects of the MePc films [56]. On the other hand, in the presence of NO<sub>x</sub> gas (a mixture of nitrogen oxides NO<sub>2</sub> and NO), the conductivity of MePc increases, because the activation energy associated with the NO<sub>x</sub> acceptor impurity is smaller (0.63 eV) [68–70]. The effect of exposure to NO<sub>x</sub> gas is not permanent, and the film conductivity recovers after continuous flushing with fresh air. Heating the sample up to 150°C to 180°C stimulates NO<sub>2</sub> desorption, and makes the recovery time much shorter [69, 70]. Even larger effects on conductivity is produced by exposure to ozone, which gives a shallower acceptor level in the bandgap of MePc materials [71]. These features of MePc films make them very attractive for gas-sensing applications [61, 62, 68–70].

Comprehensive analysis of electrical properties of all types of molecular materials is beyond the scope of this book. I can only mention two other large classes of organic materials—charge transfer complexes and conducting polymers.

Charge transfer complexes are two-component organic materials having donor and acceptor molecules in the same lattice. A typical example is a complex TTF-TCNQ (tetra-thiofulvalen-tetra-cyano-chinodimethane). The TTF donor and TCNQ acceptor molecules arranged in a regular pattern (e.g., crystallographic lattice) form a conduction and valence band, respectively [56]. The conductivity of such materials is normally high (in the range of  $1 \div 100 \text{ (Sm}^{-1}\text{)}$ ), and depends on the crystallography of the material and content of the impurities.

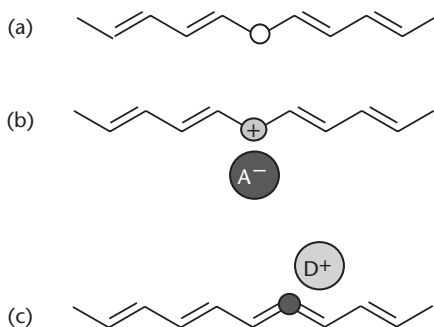
Conducting polymers are another type of organic material of extreme importance, because of their numerous applications in microelectronics and opto electronics, described in [72–75]. In contrast to the previous two types of materials, polymers have a high mobility of charge carriers, because of a huge system of delocalized electrons stretched over the whole polymer chain. Theoretically, in the simplest case of an infinite ( $C_nH_{n+1}$ ,  $n \rightarrow \infty$ ) chain having equal length of C-C bonds, there is no energy gap between HOMO and LUMO levels, so that the metallic conductivity is observed. However, in real polymers, the length of C=C and C-C bonds are different, leading to the formation of the bandgap, which may reach several electron volts. Doping polymers with donor (or acceptor) impurities leads to the formation of electrically charged defects in the system of alternated single ( $\sigma$ ) and double ( $\pi$ ) bonds, which can propagate along the polymer chain. Such defects, called solitons, act as charge carriers in polymers (see Figure 5.10).

In fact, soliton is a much more complex formation than a simple misplacement of a double bond, and it involves mechanical distortion ranging from 10 to 15 repeating units of the polymer chain. Solitons, being a singular wave in a medium with nonlinear dispersion, can propagate along the polymer chain practically without dissipation, giving rise to high drift mobility [76]. Impurity atoms play yet another important role in the conductivity of polymers, providing interconnection between individual polymer chains.

## 5.2 Electron Tunneling

### 5.2.1 The Concept and Main Features of Electron Tunneling

Tunneling is a purely quantum phenomenon of the penetration of a quantum particle (e.g., an electron) through a barrier, with the width comparable to the electron



**Figure 5.10** The formation of (a) neutral, (b) negatively charged, and (c) positively charged solitons in polyenes.

wavelength. This effect can be understood as a concept of quantum dualism, in which a quantum object combines the properties of both a particle and a wave at the same time. The exact formulation of electron tunneling can be achieved by solving a Schrödinger equation similar to (4.28) for an electron in a quantum box, changing the potential barriers to a finite height (see Figure 5.11).

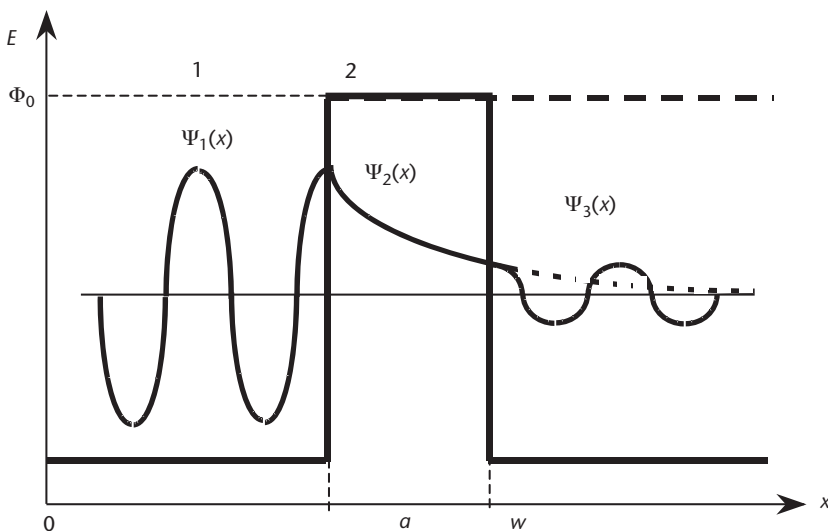
The solution gives two types of wavefunctions, as described in any quantum mechanics textbook; see, for example, [77]:

1. Periodic function  $\Psi_1(x) = A_1 e^{ikx} + B_1 e^{-ikx}$  within a quantum box  $0 < x < a$ .
2. Exponentially decaying function  $\Psi_2(x) = A_2 e^{\alpha x} + B_2 e^{-\alpha x}$  inside the barriers on both sides  $x > a$  and  $x < 0$ .

If the width of a potential barrier ( $w$ ) is comparable with the electron wavelength, then the electron wavefunction outside the barrier ( $\Psi_3(x) = A_3 e^{ikx} + B_3 e^{-ikx}$ ) is a periodical function very similar to  $\Psi_1(x)$ , but with reduced amplitudes ( $A_3 < A_1$  and  $B_3 < B_1$ ). The probability of finding the electron outside the barrier, which is equal to  $|\Psi_3|^2$ , is, therefore, nonzero. This phenomenon is called tunneling, because electrons do not jump over the barrier, but penetrate right through it.

Tunneling can be understood in terms of a simple mechanical analogy of a string stretched over three poles. If the middle pole is solid, representing an infinitely high and wide potential barrier, then the vibration of a string in one section will not be transferred to another section. If the middle pole is flexible, which is an analogy of the potential barrier with finite height and width, then the vibrations of the string will be transferred from one section to another.

The probability that the electron tunnels through the barrier, which is known as the transmission coefficient ( $D$ ), can be calculated as [77]:



**Figure 5.11** Electron wavefunctions in the quantum box with potential barriers of finite height ( $\Phi_0$ ) and width ( $w$ ), demonstrating the effect of tunneling.

$$D = \frac{|\Psi_3|^2}{|\Psi_1|^2} = D_0 \exp(-2\alpha w) \quad (5.12)$$

where  $\alpha = \frac{\sqrt{2m(\Phi_0 - E)}}{\hbar}$  is the tunneling coefficient,  $m$  is electron mass, and  $(\Phi_0 - E)$  is a potential barrier height. The value of  $\alpha$  approximately equals  $10^{-10}$  ( $\text{m}^{-1}$ ), so that the exponentially decaying tunneling current becomes negligible at the barrier width of more than 3 to 5 nm.

In the general case of tunneling through the barrier of indefinite form ( $V(x)$ ), the transition coefficient is given [78]:

$$D = D_0 \exp\left\{-\frac{1}{\hbar} \int_0^w [2m[\Phi(x) - E]^{1/2} dx]\right\} \quad (5.13)$$

The main feature of electron tunneling is the fact that electron transfers occur without consuming energy (e.g., on the same energy level). Therefore, electron tunneling current does not depend on temperature.

### 5.2.2 Electron Transfer Through Thin Organic Films

The phenomenon of tunneling was known for a long time. The theoretical possibility of tunneling was described in 1927 by F. Hund [79]. Experimentally, tunneling appeared in the spontaneous emission of  $\alpha$ -particles from atoms (e.g.,  $\alpha$ -radioactivity), and was later explained theoretically by Gamov, Guney, and Gordon [80]. The electron tunneling in semiconductors (e.g., tunneling diode effect), was first reported by Esaki in 1958 [81]. However, the main characteristic of the electron tunneling which is the exponential decay with the increase in the barrier thickness, was not proven experimentally until 1970. Mann and Kuhn proved this characteristic in their classical experimental study of tunneling current through LB monolayers of fatty acids having different chain lengths, and, therefore, thickness [30]. It was a unique achievement, from the technical point of view, to overcome the problem of short circuiting in sandwich structures with LB monolayer spacers with thickness in the range from 1.5 to 3 nm. First, those measurements were undertaken in the sandwich structures with two aluminum electrodes, which are prone to oxidation at normal atmospheric conditions. In effect, the presence of alumina makes the barrier thicker, and introduces intermediate surface states on the  $\text{Al}_2\text{O}_3/\text{Al}$  interface, which may assist tunneling [30, 31]. Second, the filaments formed during the thermal evaporation of the aluminum top electrodes [see Figure 5.4(b)], were removed by consecutive sweeps of the large dc bias [30–32, 82]. These two factors make such measurements very doubtful, and many experimental attempts to repeat this result failed. Perhaps LB monolayers are not the best objects for these kinds of measurements because of typical pinhole defects. Polymer films, particularly, electrostatically self-assembled polyelectrolytes [45, 48], or closely packed chemically self-assembled monolayers [83–85].

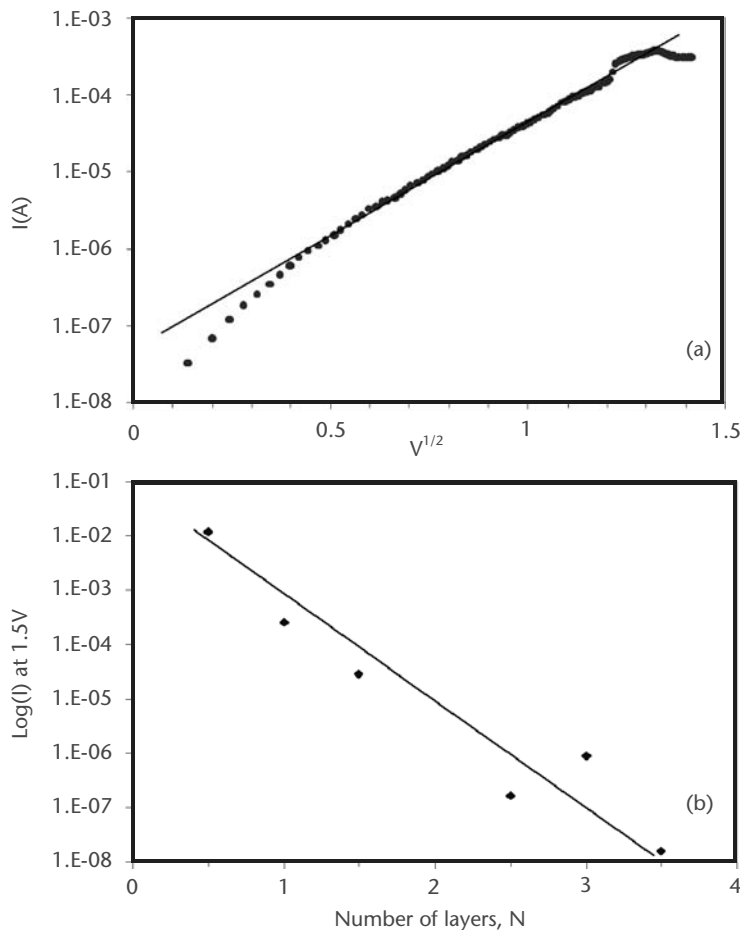
The results presented below were obtained by dc measurements on the samples of multilayered polyelectrolyte films deposited onto silicon substrates by consecutive deposition of layers of poly(allylamine) hydrochloride (PAH) and

poly(sterylsulfonate) sodium salt (PSS) [48]. The  $(\text{PAH/PSS})_N$  films having an even ( $N = 1, 2, 3, 4, 5$ ) and odd ( $N = \frac{1}{2}, 1\frac{1}{2}, 2\frac{1}{2}, 3\frac{1}{2}, 4\frac{1}{2}$ ) number of layers were produced. In order to avoid the influence of the field effect in Si substrate on electrical measurements [45], silicon wafers were heavily doped with boron.

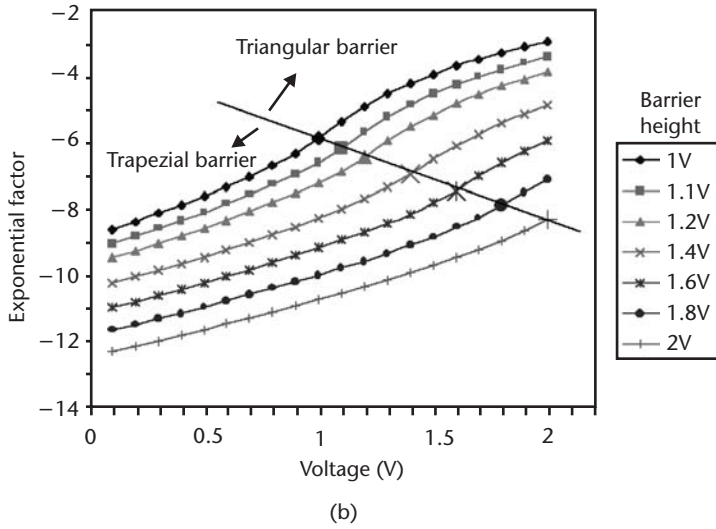
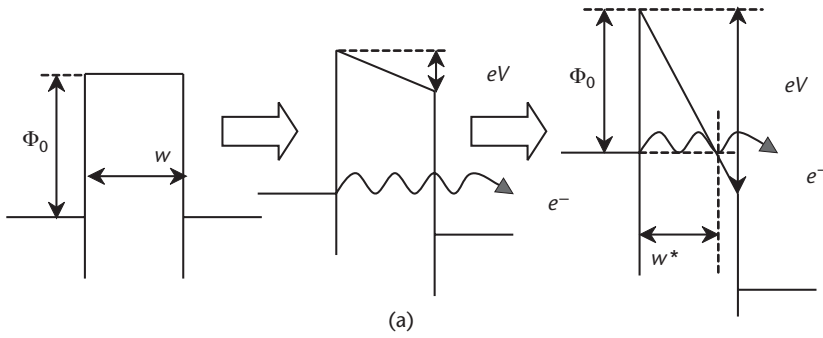
The film thickness of  $1.36 \pm 0.1$  nm per PAH/PSS layer, evenly divided between PAH and PSS sublayers, was found from ellipsometry measurements. A typical I-V characteristic of such structures looks like a straight line if plotted in the coordinates  $\log(I)$  versus  $V^{1/2}$ , as shown in Figure 5.12(a). An exponential decay of the tunneling current, measured at 1.5V dc bias, with the increase in the number of layers, is shown in Figure 5.12(b).

The following model was deployed for the interpretation of these experimental results. The initial rectangular tunneling barrier with the height  $\Phi_0$  and thickness  $W$  transforms to a trapezoidal barrier when dc bias (eV) is applied, as shown in Figure 5.13(a).

The integration of a general expression for the transparency of the tunneling barrier (5.13) yields a formula for the trapezoidal barrier:



**Figure 5.12** (a)  $\log I(V^{1/2})$  plot for one layer of PAH/PSS. (b) The dependence of the logarithm of tunneling current through  $p^+\text{Si}/(\text{PAH/PSS})_N/\text{Hg}$  structures at 1.5V on the number of layers. (From: [48]. © 2004 IEE. Reprinted with permission.)



**Figure 5.13** (a) The model of electron tunneling, from left to right: the initial rectangular barrier, the trapezoidal barrier at moderate dc bias, and the triangular barrier at large dc bias. (b) Simulated dependence of the tunneling exponential factor on bias voltage. (From: [48]. © 2004 IEE. Reprinted with permission.)

$$D = D_0 \exp \left\{ - \frac{4w\sqrt{2m}}{3\hbar} \left[ \frac{\Phi_0^{3/2} - (\Phi_0 - eV)^{3/2}}{eV} \right] \right\} \quad (5.14)$$

When a large external bias ( $eV > \Phi_0$ ) is applied, the barrier becomes triangular, with the reduced thickness of  $w^* = w \frac{\Phi_0}{eV}$ , as shown in Figure 5.13(a), and (5.14) transforms to:

$$D = D_0 \exp \left[ - \frac{4w^*\sqrt{2m}}{3\hbar} \frac{\Phi_0^{3/2}}{eV} \right] \quad (5.15)$$

The simulation of the I-V characteristics of the trapezoidal and triangular barriers have been performed using (5.14) and (5.15), and the results are presented in Figure 5.13. The linear dependence of the exponential factor on voltage transforms to the  $V^{1/2}$  dependence at large bias, due to the transformation of the barrier from

trapezoidal to triangular. The above simulation is in good qualitative agreement with the experimental data in Figure 5.12. In particular, a linear dependence of  $\log(I)$  versus  $V^{1/2}$  in Figure 5.12(b) corresponds well to (5.14), and shows that the barrier is triangular at the bias voltage applied.

The graph in Figure 5.12(b) represents an exponential law for the tunneling current  $I \approx \exp(-\alpha w)$  through the barrier having the thickness  $w = Nw_0$ , where  $w_0$  is the thickness of one PAH/PSS layer. From the slope of the graph  $\log(I)$  versus  $N$  in Figure 5.12(b), a tunneling coefficient  $\alpha = 3.3 \times 10^{-9} \text{ m}^{-1}$  was calculated, using a value of  $w_0 = 1.36 \text{ nm}$  obtained previously by ellipsometry.

Assuming that the barrier becomes triangular at a large bias, the barrier height can now be obtained from the following expression for the tunneling coefficient:

$$\alpha = \frac{4\sqrt{m} \Phi_0^{3/2}}{3\hbar \text{ eV}} \quad (5.16)$$

The calculation at  $V = 1.5 \text{ V}$  and  $m = m_p^* = 0.38 m_0$  yields  $\Phi_0 = 1.1 \text{ eV}$ . Since the tunneling of holes is actually taking place in the  $p^+ \text{ Si/PAH/PSS film/Hg}$  contact, the effective mass of holes in silicon was used in the above calculation.

The use of a nondestructive technique of mercury probe confirmed the exponential dependence of the tunneling current on the barrier width, which is the fundamental characteristic of electron tunneling.

### 5.2.3 Electron Tunneling Through Multilayered LB Films

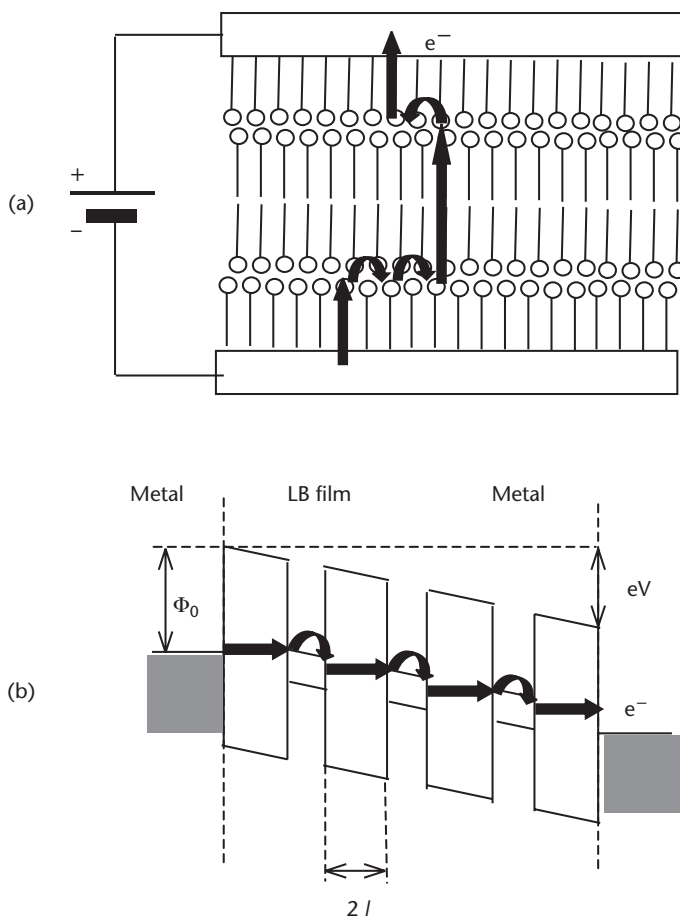
The electron transfer in multilayered LB films in the normal direction is always of great interest, and a number of publications are dedicated to this subject [86–88]. The main experimental features, such as the poor temperature dependence of dc conductivity and its independence on the number of LB layers [89, 90], are explained theoretically by Sugi [91]. The proposed model of the conductivity across Y-type LB film combines the electron tunneling through the potential barrier (formed by hydrocarbon chains), which is equal to a double chain-length ( $2l$ ), and thermally assisted hopping within planes (formed by polar head groups), as illustrated in Figure 5.14.

The current is therefore described as [91]:

$$I = I_0 (2al)^{\frac{3}{2}} \exp \left[ - (2al) - \left( \frac{4\alpha}{\pi N_t l k T} \right)^{\frac{1}{2}} \right] \quad (5.17)$$

In this formula,  $\alpha = \frac{\sqrt{(2m\Phi_0)}}{\hbar}$ ,  $m$  is the electron mass, and  $\Phi_0$  is the height of a rectangular potential barrier. The first exponential term describes tunneling through the barrier, while the second term describes Mott's electron variable-range hopping [49] between localized states, with the concentration of  $N_t \approx 10^{19} \text{ m}^{-2} \text{ eV}^{-1}$ . The effect of applied voltage can be seen, using the effective barrier height in (5.17)  $(\Phi_0^*)^{1/2} = \frac{\Phi_0^{3/2} - (\Phi_0 - eV)^{3/2}}{eV}$  for the tunneling through the series of trapezoidal barriers, as shown in Figure 5.14. There is no number of



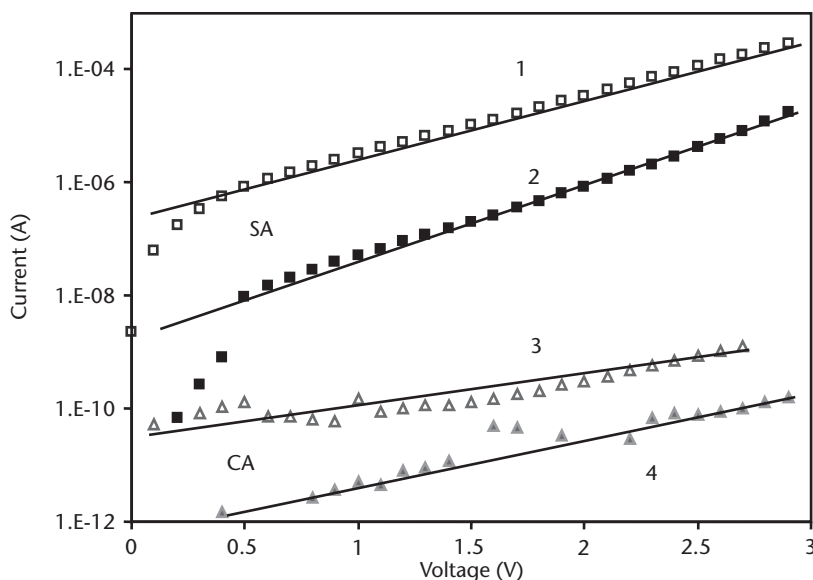


**Figure 5.14** Illustration of Sugi's model of electron transfer through LB film: (a) the scheme of electron transitions, and (b) the energy band diagram. (From: [92]. © 2002 Elsevier. Reprinted with permission.)

layers included in (5.17), so the current is invariant of the film thickness. The temperature dependence  $\ln\left(\frac{I_0}{I}\right) \sim T^{-1/2}$  is hidden in the second exponential term.

The Sugi model was recently applied for the interpretation of the conductivity of LB films containing CdS nanoparticles [92]. The technology of the formation of CdS nanoparticles in LB films of fatty acids and calixarenes is described in Chapter 2; the structure and optical properties of such composite films are discussed in Chapters 3 and 4, respectively. The presence of semiconducting CdS nanoparticles in the insulating LB films must affect the film conductivity; the increase in conductivity is naturally expected. However, the opposite happened. Figure 5.15 shows a decrease in dc for both stearic acid (SA) and calix[8]arene (CA) LB films after exposure to H<sub>2</sub>S gas, and the subsequent formation of CdS nanoparticles.

These electric measurements are carried out at room temperature in sandwich structures (Al/LB film/Al), with separated contact pads. Both types of LB films demonstrate an exponential rise of current with an increase in applied voltage, which is typical for electron tunneling through multilayered LB films [91]. Exposure of the LB films to H<sub>2</sub>S gas decreases the current readings by about two orders of



**Figure 5.15** The dc I-V characteristics of sandwich structures containing LB films of SA (1,2) and CA (3,4) before (1,3) and after (2,4)  $H_2S$  treatment. (From: [92]. © 2002 Elsevier. Reprinted with permission.)

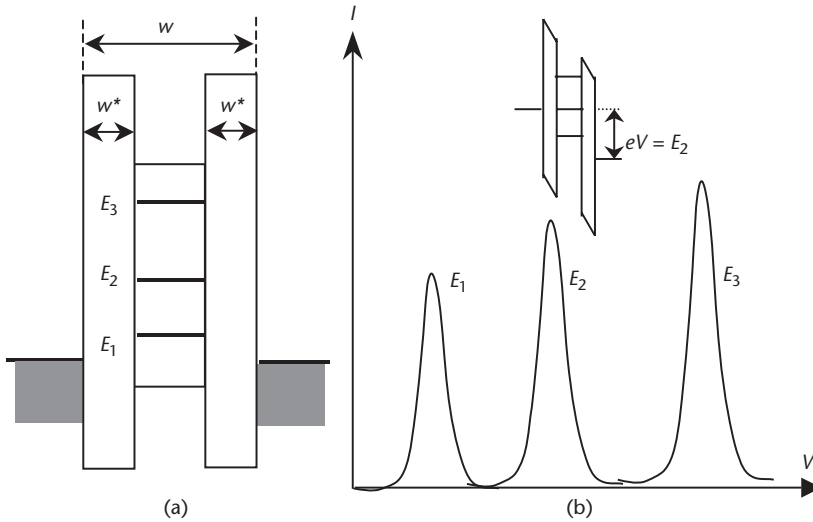
magnitude, for both SA and CA LB films. The only explanation of such behavior lies in the reduction of the layer-by-layer film order, due to the formation of CdS nanoparticles in the film. Therefore, the effect of larger CdS nanoparticles in the SA films on their conductivity is much more pronounced, as compared to the effect of smaller CdS particles in CA films. The layer-by-layer order plays a significant role in the electron transfer through LB films. A remarkable fact confirming this point is that the conductivity in much less ordered CA LB films is nearly four orders of magnitude smaller than that in well-ordered SA LB films.

All of the facts mentioned above, in addition to the very poor temperature dependence of current (i.e., a small increase by a factor of two to three within the temperature range from 270K to 370K), fit well into Sugi's model of conductivity through LB films.

#### 5.2.4 Resonance Tunneling

The phenomenon of resonance tunneling is a combination of two effects: (1) tunneling between the electron states having the same energy, and (2) size quantization of electrons in a quantum box. Consider the electron transfer through the structure consisting of a conducting (or semiconducting) quantum dot separated from two metal electrodes by thin insulating barriers. Figure 5.15 illustrates the schematic energy diagrams of this structure.

The total separation ( $w$ ) between metal electrodes is large enough to reduce the probability of direct tunneling to zero, as shown in Figure 5.16(a). However, if the Fermi level ( $E_f$ ) in the source contact matches one of the energy levels ( $E_i$ ) in the quantum dot, the tunneling will take place through a much thinner barrier  $w^*$ , via this intermediate level  $E_i$ , with the efficiency close to unity. Such resonance conditions can be achieved by the application of external dc bias, as shown in Figure 5.16(b).



**Figure 5.16** (a) Band diagram of the resonance tunneling barrier, and (b) I-V characteristic of this junction, with each peak corresponding to energy matching conditions  $eV = E_i$ ,  $i = 1, 2, 3$ .

The resulting I-V characteristics in Figure 5.16 show peaks, corresponding to the energy levels  $E_1$ ,  $E_2$ ,  $E_3$ , and so on.

Assuming the following thickness for the tunneling system ( $w^* = 2$  nm and  $w = 6$  nm) and a value of  $\alpha = 1$  nm<sup>-1</sup>, one can estimate the tunneling transparency coefficients  $D$  and  $D^*$  for energy mismatching and resonance conditions, respectively:

$$D/D_0 = \exp(-2\alpha w) = \exp(-2 \times 1 \times 6) \approx 6.14 \cdot 10^{-6}$$

$$D^*/D_0 = 2 \exp(-2\alpha w^*) = 2 \exp(-2 \times 1 \times 2) \approx 3.66 \cdot 10^{-2}$$

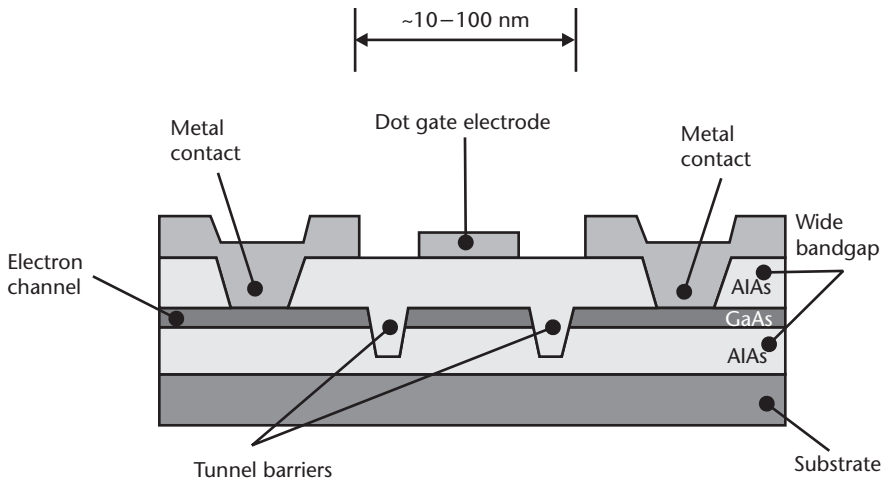
Obviously,  $D^* \gg D$ , so the system of barriers becomes conductive at resonance conditions.

The effect of resonance tunneling was discovered in 1977 by Mimura [93], and the exploration of this idea was continued in different solid-state systems [94–99]. Increased interest in resonance tunneling in the last 10 to 15 years is caused by its application in RTD, which are considered to be one of the main directions in nanoelectronics. Practical realization of RTDs has become possible because of the development of MBE. Classical RTD, based on GaAs/Al<sub>x</sub>Ga<sub>1-x</sub>As layer structures produced by MBE, is shown in Figure 5.17 [99].

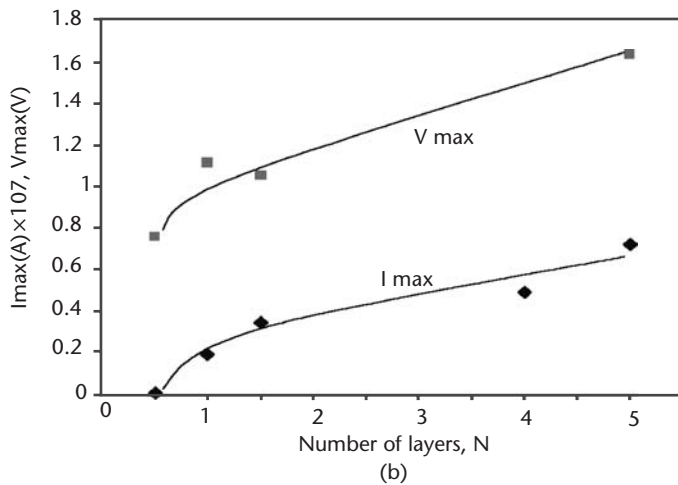
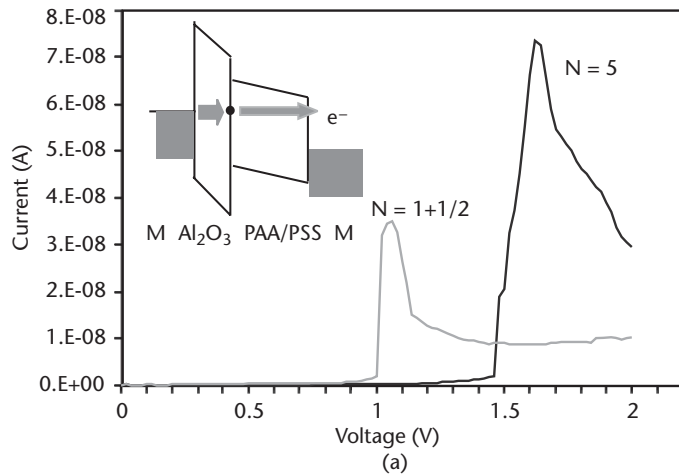
Further development of RTDs is expected in other nanostructures, of both inorganic and organic nature [100, 101]. Recent developments in organic film technology demonstrated its potential in the cost-effective fabrication of RTDs [102–104].

An example of resonance tunneling behavior is a simple structure of PAH/PSS electrostatically self-assembled film deposited on an Al-coated glass slide using a mercury probe as a top metal contact [48], as described in Section 4.2.2.

As shown in Figure 5.18(a), the peaks of current are believed to be caused by resonance tunneling via the surface electron states on the interface between PAH/PSS film and native aluminium oxide. The shift of the peak position to larger voltages with the increase in the number of layers deposited (i.e., the film thickness) supports this suggestion, as shown in Figure 5.18(b).



**Figure 5.17** Design of GaAs/AlGaAs RTD. (From: [99]. © 1996 MITRE Corporation. Reprinted with permission.)



**Figure 5.18** (a) I-V characteristics of Al/Al<sub>2</sub>O<sub>3</sub>/(PAH/PSS)<sub>N</sub> film/Hg. The number of layers (N) is shown near its respective curve. The inset shows a scheme of the resonance electron tunneling in the system. (b) The dependencies of the position of the peak and the maximum current value on the number of layers. (From: [48]. © 2004 IEE. Reprinted with permission.)

### 5.2.5 Inelastic Tunneling and Inelastic Tunneling Spectroscopy

When energy levels in the source are higher than in the drain during electron tunneling through the barrier, there is another possibility for the electron transfer, as shown in Figure 5.19. The excess of energy can be released by an exciting phonon, and if the energy of the phonon fits exactly into mismatching gap, the electron will go through. To fulfill such an inelastic tunneling process, a third body is required, which could be surface states, impurities, adsorbed molecules, or intermediate layers integrated in the barrier.

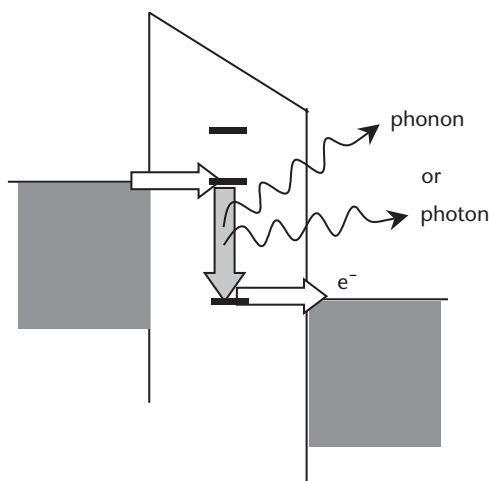
This type of tunneling has been experimentally found in the structures semiconductor (or metal)/ oxide/ metal [105–108]. The electron energy can be partially consumed to excite the vibrations (phonons) of the impurity molecules on the metal/oxide interfaces. The vibrational spectra of impurities can therefore be registered by scanning over the range of applied voltages, and measuring the current through the junction. This constitutes the idea of inelastic tunneling spectroscopy [109–111], which yields spectra similar to those obtained by IR or Raman spectroscopy. This method has been exploited for years for studying impurities on the surfaces of metals and semiconductors [112, 113].

With the invention of tunneling scanning microscopy, this method has attracted more attention because of the possibility of measuring vibrational spectra of individual molecules captured between the STM tip and conducting substrate [114–116].

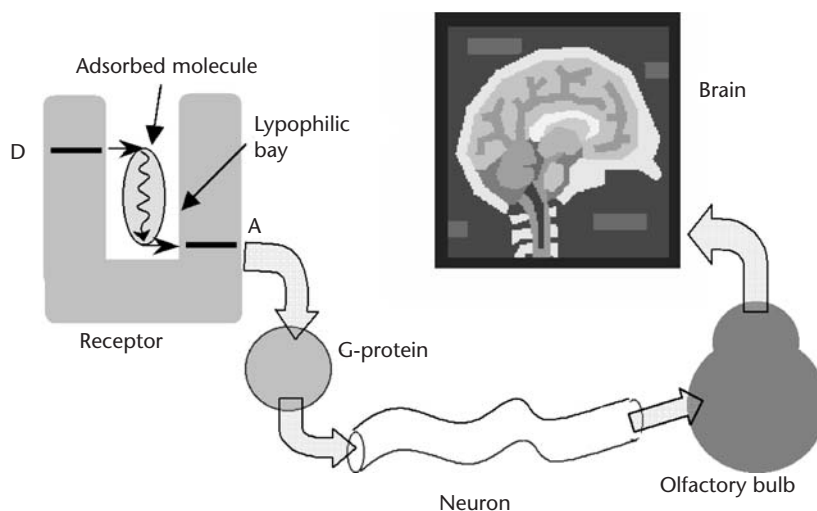
The mechanism of inelastic tunneling was considered for the explanation of conductivity features in different types of nanostructures [117–120].

Turin [121, 122] recently suggested an interesting idea that the phenomenon of inelastic tunneling might be responsible for the function of smell recognition in the human olfactory system. According to this theory of the primary act of smell recognition, the donor and acceptor levels on either side of the hydrophilic bay of smell receptors are separated by an energy gap, as shown in Figure 5.20.

If this energy matches one of the vibration energies of adsorbed molecules, the electron goes through, and triggers the following chain of events—a release of G-protein, the generation of electric pulses in the neuron, and the transfer of



**Figure 5.19** The scheme of inelastic electron tunneling, which involves the excitation of phonons (or photons).



**Figure 5.20** The mechanism of odor recognition in the human olfactory system.

electrical signals to the olfactory bulb and to the brain. The human olfactory system contains a large number of such receptors, which are separated into 20 to 30 groups (channels), each having a different energy gap between donor and acceptor levels. This covers a wide spectral range of vibrations, from 500 to 2,500  $\text{cm}^{-1}$ . The signals from these channels go to the powerful neuron computer (i.e., the human brain), which performs the final stage of signal processing and eventually smell recognition.

Another possibility of the electron energy relaxation during tunneling lies in the emission of photons. The effect of light emission stimulated by electron tunneling between the STM tip and the conducting surface via intermediate centers, such as impurity atoms and adsorbed molecules, is reported in a number of publications [123–128]. Such an effect is very promising for the future development of novel nano-optoelectronic devices.

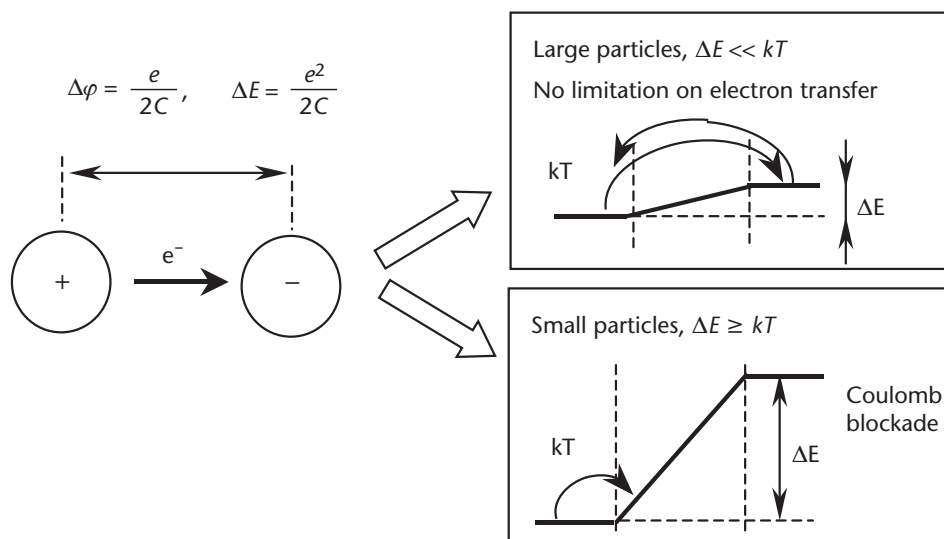
## 5.3 Single Electron Phenomena

### 5.3.1 Coulomb Blockade and Staircase I-V Characteristics

Electron transfer between nanodimensional objects is very different from the electron transfer between objects of a larger scale. Some kind of quantization in the electron transfer is observed in such structures, which opens up an absolutely new area of nanoelectronic devices operating with few electrons, often referred to as single-electron devices. As usual, a very simple physical idea provides a foundation for a whole range of single-electron phenomena.

Let us consider two particles made of a conducting material (e.g., metal or semiconductor), separated by a distance of a few nanometers, which is small enough to provide direct electron tunneling.

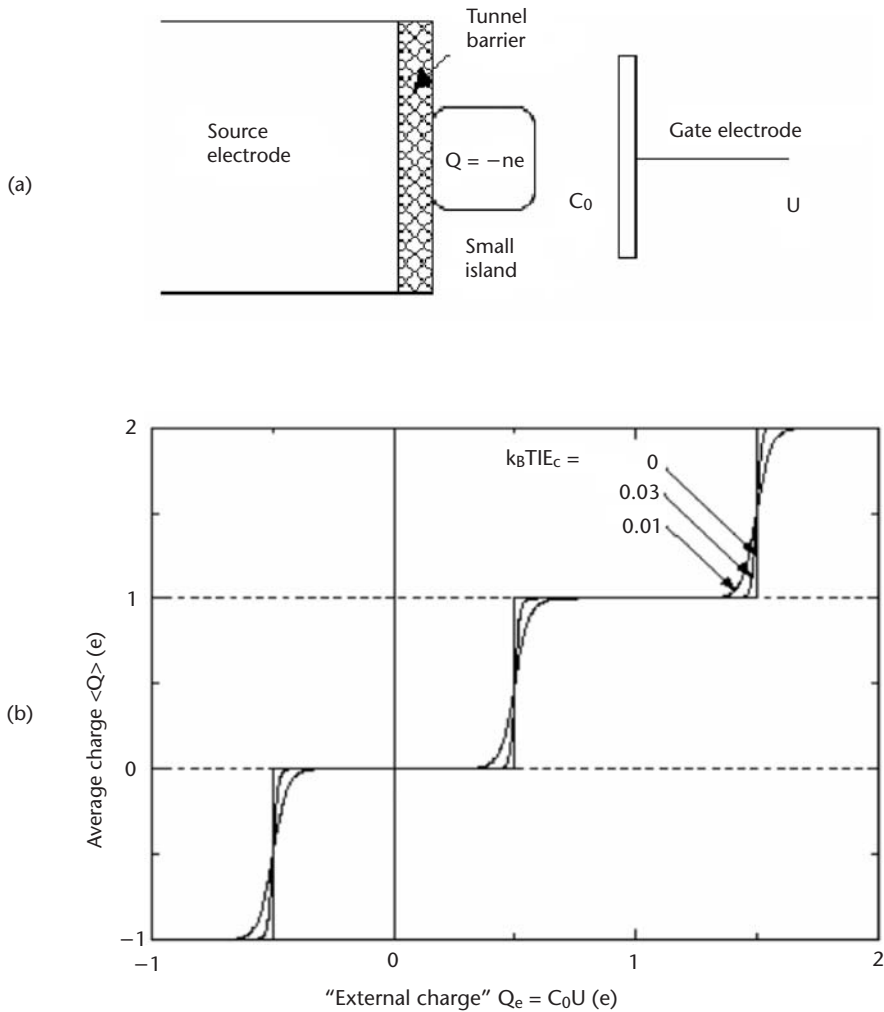
As shown in Figure 5.21, an accidental transfer of an electron from one particle to another will make them electrically charged, and will create a potential difference of  $\frac{e}{2C}$ , where  $C = \epsilon r$  is the capacitance of a spherical particle having radius  $r$  and



**Figure 5.21** Illustration of the effect of Coulomb blockade.

dielectric permittivity  $\epsilon$ . In terms of energy, a potential barrier of  $\Delta E = \frac{e^2}{2C}$  is created between the particles. For large particles (in this case, even submicron particles are considered to be large),  $\Delta E \ll kT$  even at very low temperatures, so that other electrons ignore that barrier, and can move from one particle to another, forward and back, without any hesitation. However, for small particles (tens of nanometers and smaller), this may not be the case, because the energy barrier may become comparable to, or even larger than, thermal energy ( $\Delta E \geq kT$ ). In this case, the transition of one electron creates a barrier that prevents further electron transfer between particles. This effect, called the Coulomb blockade, though quite obvious and known theoretically [129], was first observed experimentally by Likharev in 1986 [130]. In this work, the experiments were carried out in a very laborious way, by contacting 40 to 50 nm indium particles adsorbed on the oxidized metal surface with a probe, and demonstrated the effect of Coulomb blockade at 4.2K. This result was later confirmed independently by Grabert and Devoret on similar-sized metal islands formed with e-beam lithography [131], as well as by many other scientists from different groups [132–138]. However, for much smaller particles in the range from 3 to 5 nm, the Coulomb blockade was observed at room temperature [139–143].

In fact, in these publications, the Coulomb blockade effect was registered via I-V characteristics measurements, which show a staircase-like behavior typical for single-electron processes. Let us discuss this phenomenon in detail. In the structure shown in Figure 5.22(a), the nanoparticle (i.e., nanoisland) is sandwiched between two electrodes. The bottom electrode is separated from the particle by a thin barrier transparent for electron tunneling (an aluminum plate coated with a native oxide at atmospheric conditions could be an ideal surface for such experiments), while a probe electrode lies above the particle at a much larger distance. In such a structure, the tunneling of one electron from the source to the nanoisland creates a potential difference of  $e/2C$ . Further electron transfer is blocked until the external bias exceeds the value of  $e/2C$ , allowing the tunneling of a second electron.



**Figure 5.22** (a) The structure for I-V measurements, and (b) the staircase I-V characteristic demonstrating the effect of Coulomb blockade. (From: [144]. © 1999 IEEE. Reprinted with permission.)

The process of a charge transfer in the above system can be described with Gibbs free energy [144]:

$$W = \frac{Q^2}{2C} + \frac{C_0}{C}QU + \text{const} = \frac{(ne - Q_e)^2}{2C} + \text{const} \quad (5.18)$$

Here,  $Q = -ne$  is the discrete electric charge of the nanoisland, caused by the tunneling of a small number ( $n$ ) of electrons from the source;  $Q_e = C_0U$  is the external charge, which depends on the dc voltage ( $U$ ), applied to the gate electrode;  $C_0$  is the capacitance between the nanoisland and the gate electrode; and  $C$  is the total capacitance, including  $C_0$ . Taking into consideration the fact that tunneling occurs without changes in  $W$  (i.e.,  $dW/dt = 0$ ), the dependence of the electric charge ( $Q$ ) of the nanoisland on the external electric charge ( $Q_e$ ) has an obvious staircase behavior, with a single voltage step of  $\Delta U = e/C_0$ , corresponding to the transfer of a single

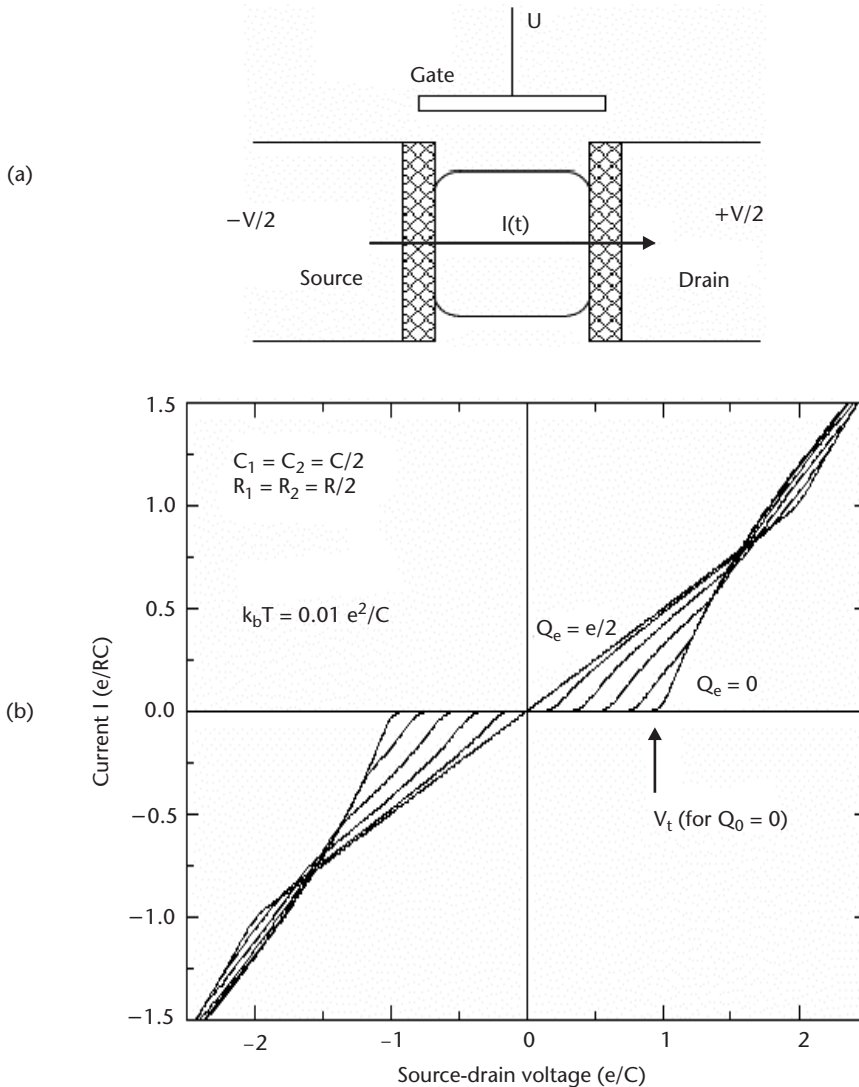


electron ( $\Delta Q = e$ ) to the island. This dependence is shown in Figure 5.22(b). At 0K, the steps would have an ideal rectangular shape, and the temperature increase would result in the smearing of the steps.

### 5.3.2 Single-Electron Devices and Their Practical Realization

The great potential of the single-electron phenomena in the application of nanoelectron devices was realized very soon after its discovery. The single-electron transistor (SET) was proposed independently by Likharev [145] and Devoret [146], and a large number of other single-electron devices evolved from it [147–154].

A three-port device is shown in Figure 5.23(a) [144]. The nanoisland is separated by tunnel junctions from the source and drain contacts. The gate contact, although separated by a larger distance from the nanoisland to prevent direct tunneling, can affect the island electrostatically.



**Figure 5.23** Single-electron transistor: (a) the structure and (b) the source-drain I-V curves for several values of the the gate voltage  $Q_e$ . (From: [144]. © 1999 IEEE. Reprinted with permission.)

The expression for the Gibbs free energy can now be written as [144]:

$$W = \frac{(ne - Q_e)^2}{2C} - \frac{eV(n_1 C_2 + n_2 C_1)}{C} + \text{const} \quad (5.19)$$

where  $n_1$  and  $n_2$  are the number of electrons passed through the barriers 1 and 2, respectively, so that the number of electrons on the island  $n = n_1 - n_2$ ; total capacitance  $C = C_0 + C_1 + C_2$ , equal to the sum of the capacitances of the gate, source, and drain;  $V$  is a source-drain voltage; and  $U$  is a gate voltage ( $Q_e = C_0 U$ ). Typical source-drain I-V characteristics are shown in Figure 5.23(b). When no gate voltage applied (i.e.,  $Q_e = 0$ ), there is no current through the transistor at low source-drain voltages ( $V$ ) because of Coulomb blockade. When the voltage reaches the threshold of  $V = e/C$ , the Coulomb blockade is overcome, and the current rises, following a nearly ohmic dependence. By applying the gate voltage ( $U = C_0 Q_e$ ), it is possible to charge the island discretely, and, therefore, remove the conditions of Coulomb blockade, and make the transistor conductive, even at small  $V$ . In fact, the I-V curve can oscillate with a period of  $\Delta U = e/C_0$  in the course of sweeping the gate voltage, as shown in Figure 5.23(b).

An SET is the simplest, most basic device, which launched a series of different single-electron devices and logic gates [144–148, 155, 156].

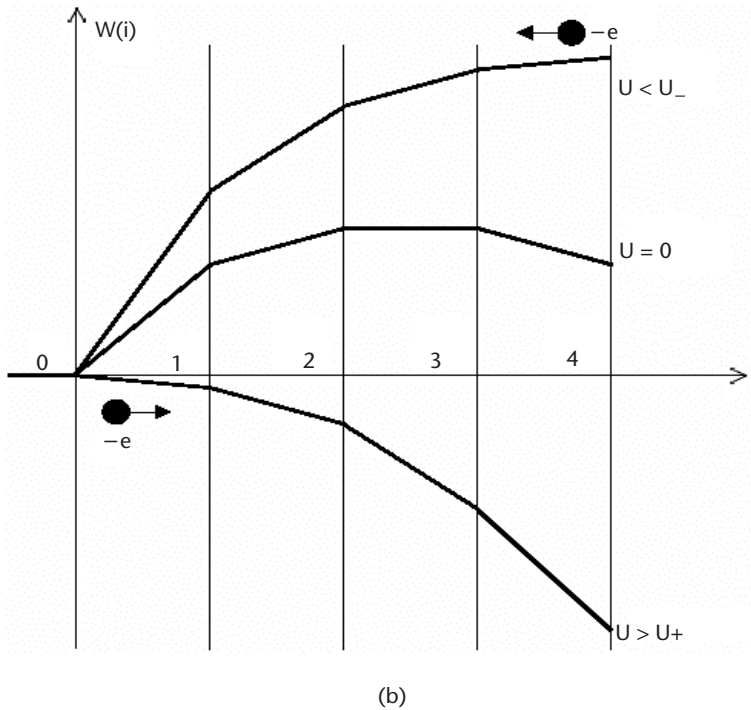
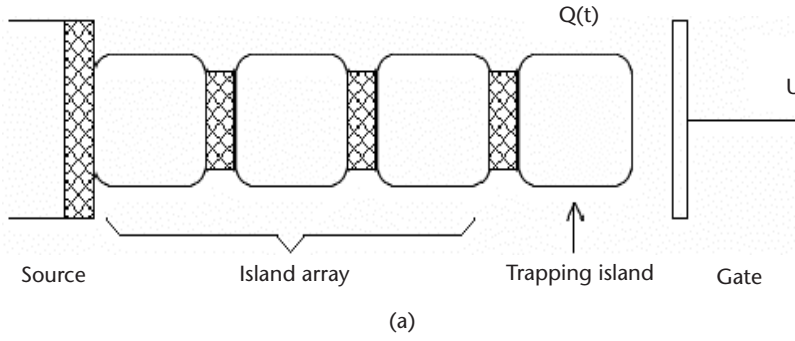
The chain of nanoislands, as shown in Figure 5.24(a), can operate as a memory [144]. The energy of the nanoislands reaches the maximum somewhere in the middle of the chain, as shown in Figure 5.24(b). By applying a certain voltage to the gate, a single electron can go through the chain of islands, and be finally trapped in the last one.

This is equivalent to “writing in” the memory devices. It can be released (i.e., the memory can be erased) by applying gate voltages of opposite polarity. Other memory devices, such as turnstile and pump, based upon the same operational principle, can be built on the nanoisland arrays [144, 157–159].

An SED can be produced by different means of nanotechnology. One of the first SETs, operating at 100K, was commercially produced by the evaporation of aluminum from two angles through the suspended mask [160]. SIMOX technology combined with electron beam lithography [161–164] seems to be the most promising technology for commercial SET fabrication. An interesting example of SET, produced by standard Si planar technology without deploying any of nanolithography facilities, is given in [165, 166]. A silicon island, formed by the conventional UV lithography on SOI substrate on the cross point of  $\text{SiO}_2/\text{Si}_3\text{N}_4$  layers, has dimensions approximately equal to 100 nm, and thus shows staircase I-V characteristics at 21K.

STM nanolithography is another excellent technique to form nanojunctions. Figure 5.25(a) shows the SET-produced 3-nm-thick Ti film by its local anodic oxidation under STM tip [167].

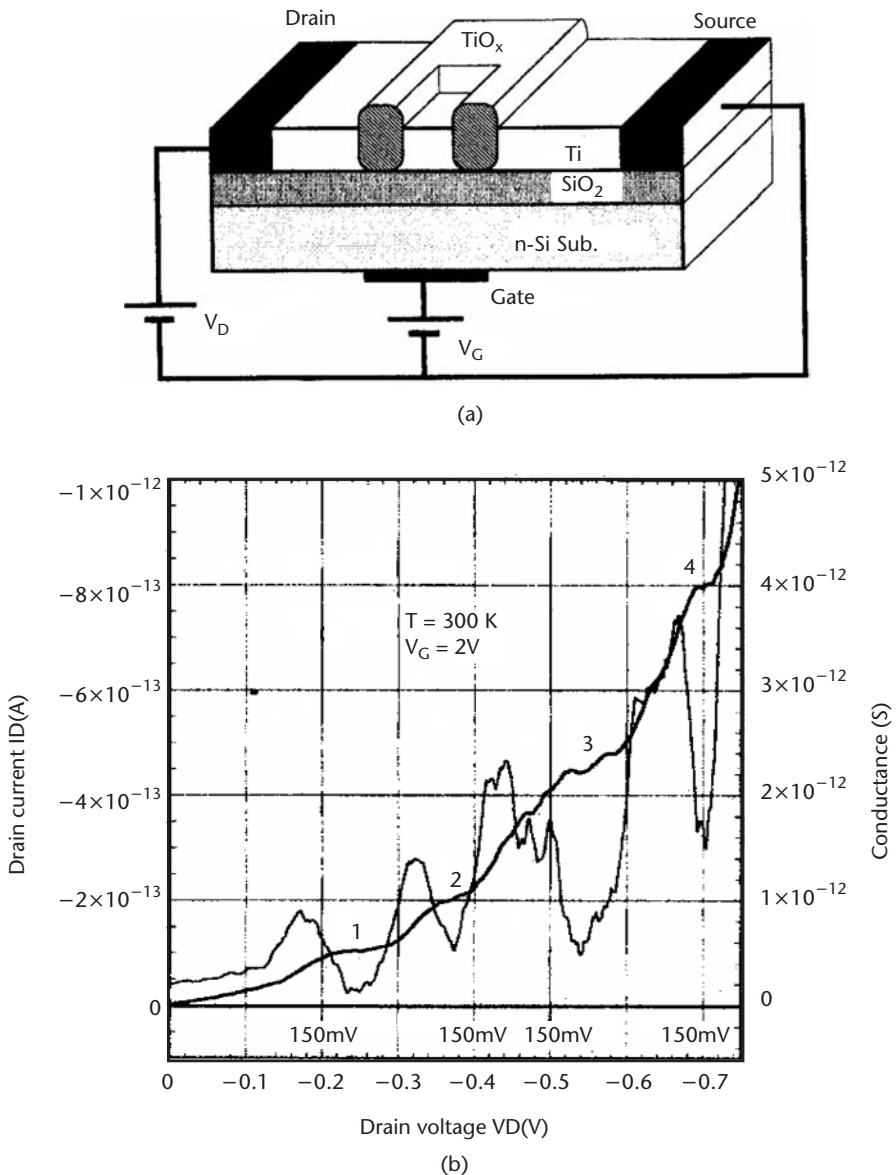
Because of the extremely small size (3 to 4 nm) of Ti islands, a well-pronounced staircase I-V characteristic was observed at room temperature, as shown in Figure 5.25(b). An even better step-resolution ( $\Delta U = e/C_0 \approx 1\text{V}$ ) was reported to be achieved on the Nb/NbO<sub>3</sub> SETs, produced by anodic oxidation, using an STM probe [168].



**Figure 5.24** Single-electron trap: (a) schematics, and (b) the electrostatic energy of an extra electron as a function of its position for three values of the gate voltage. (From: [144]. © 1999 IEEE. Reprinted with permission.)

### 5.3.3 Single-Electron Phenomena in Organic Films Containing Nanoparticles

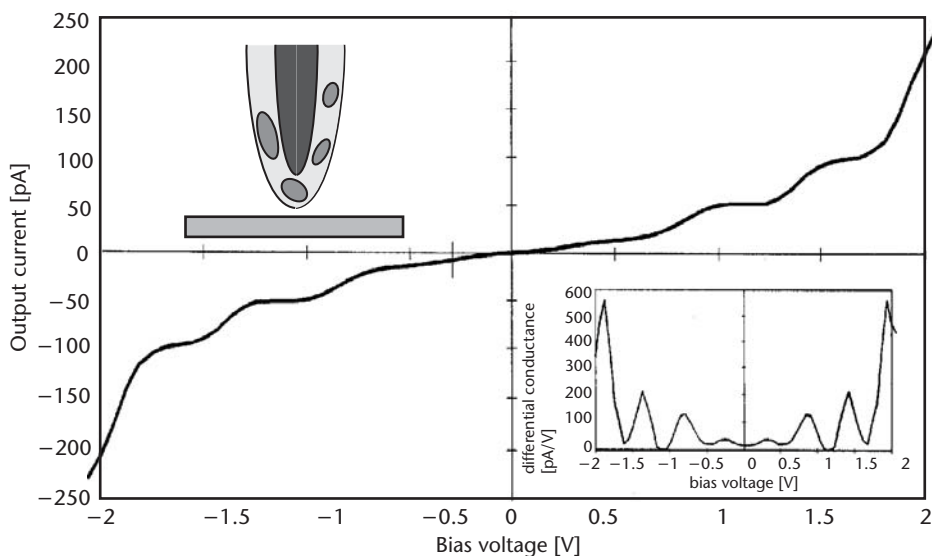
How do the organic film technology and chemical routes of the formation of nanostructures contribute to the hot subject of single-electron devices? The use of colloid nanoparticles for the realization of SED is quite obvious. In many respects, it is much easier to use well-defined colloid nanoparticles (made of either metals or semiconductors), instead of nanoislands (formed using sophisticated and expensive nanolithography). The SED can be produced by introducing nanoparticles into the preformed gap between two metal electrodes. First, the gap is larger (in the range from 10 to 20 nm), and can be produced by simpler means (e.g., e-beam, or STM-scratching lithography). Second, random deposition of 2- to 3-nm nanoparticles within a much larger gap gives a reasonably good probability of obtaining



**Figure 5.25** SET formed by STM lithography: (a) the structure and (b) the source-drain IV characteristics measured at room temperature. (From: [167]. © 1999 Taylor & Francis, Inc. Reprinted with permission.)

functioning devices. The use of self-assembly will allow the more precise deposition of nanoparticles in the gap.

The first observation of Coulomb blockade at room temperature was achieved by Erokhin, with STM current measurements in a fatty acid LB bilayer containing CdS nanoparticles [139–141]. The technology of the formation of such films is described in Chapter 2. The presence of CdS particles approximately 3 nm in size allows the registration of staircase I-V characteristics at room temperature, as shown in Figure 5.26. The difficulties with the thermal drift during STM spectroscopic measurements are overcome by depositing LB films onto the STM tip, as shown by the inset in Figure 5.26.



**Figure 5.26** The staircase I-V characteristic, measured between the STM tip coated with LB film containing CdS nanoparticles (shown as the inset on the left), and the conducting plate. The inset on the right shows the first derivative of the current. (From: [140]. © 1996 National Academy of Sciences. Reprinted with permission.)

The colloid nanoparticle approach in SET was successfully implemented by other research groups, using noble metal nanoclusters or semiconductor nanoparticles [169–172]. The use of extremely small (in the range from 1.2 to 1.4 nm) CdS clusters formed within calixarene LB films, as described in previous chapters, is a very promising direction for the fabrication of SET, having the step-resolution ranging from 1V to 2V, and operating at room temperatures (or even higher).

## References

- [1] Simon, J., and J. J. Andre, *Molecular Semiconductors*, Berlin, Germany: Springer-Verlag, 1985.
- [2] Pauwels, H., “Alternative Thin Film Solar Cells,” *Directorate-General Information Market and Innovation*, 1982.
- [3] Brundle, C. R., C. A. Evans, and S. Wilson, (eds.), *Encyclopedia of Materials Characterization: Surfaces, Interfaces, Thin Films*, Boston, MA: Butterworth-Heinemann, 1992.
- [4] Tong, H. -M., and L. T. Nguyen, (eds.), *New Characterization Techniques for Thin Polymer Films*, New York: John Wiley & Sons, 1990.
- [5] Hass, G., and M. H. Francombe, (eds.), *Physics of Thin Films: Advances in Research and Development*, Vol. 10, New York: Academic Press, 1978.
- [6] Nebel, C. E., and J. Ristain, (eds.), *Thin-Film Diamond: Semiconductors and Semimetals*, Vol. 76, Amsterdam, the Netherlands: Elsevier, 2003.
- [7] Elshabini-Riad, A. A. R., and F. D. Barlow, *Thin Film Technology Handbook*, New York: McGraw-Hill, 1997.
- [8] Sberveglieri, G., “Classical and Novel Techniques for the Preparation of SnO<sub>2</sub> Thin-Film Gas Sensors,” *Sensors & Actuators B-Chemical*, Vol. 6, No. 1–3, 1992, pp. 239–247.
- [9] Granqvist, C. G., “Transparent Conductive Electrodes for Electrochromic Devices—A Review,” *Appl. Phys. A-Mater. Sci. Process.*, Vol. 57, No. 1, 1993, pp. 19–24.

- [10] Masse, G., L. Yarzhou, and K. Djessas, "Preparation and Study of  $\text{CuXY}_2$  (X=Ga, In Y=Se, Te) Thin-Films for Solar-Cell Applications," *J. Phys. III*, Vol. 3, No. 1, pp. 2087–2099.
- [11] Maiti, S., "Recent Trends in Conducting Polymers—Problems and Promises," *Indian J. Chem. Sect A-Inorg. Phys. Theor. Anal. Chem.*, Vol. 33, No. 6, 1994, pp. 524–539.
- [12] Venkatachalam, S., and V. N. Krishnamurthy, "Polymeric Phthalocyanines and Other Electrically Conducting Polymers for Electronic and Photonic Applications—A Review," *Indian J. Chem. Sect A-Inorg. Phys. Theor. Anal. Chem.*, Vol. 33, No. 6, 1994, pp. 506–523.
- [13] Zhou, R., et al., "Phthalocyanines as Sensitive Materials for Chemical Sensors," *Appl. Organomet. Chem.*, Vol. 10, No. 8, 1996, pp. 557–577.
- [14] Mirmira, S. R., and L. S. Fletcher, "Review of the Thermal Conductivity of Thin Films," *J. Thermophys. Heat Transf.*, Vol. 12, No. 2, 1998, pp. 121–131.
- [15] Meyer, W. H., "Polymer Electrolytes for Lithium-Ion Batteries," *Adv. Mater.*, Vol. 10, No. 6, p. 439.
- [16] Drennan, J., "The Influence of Interface Structures on the Conducting Properties of Zirconia ( $\text{ZrO}_2$ )-Based Solid Electrolytes," *J. Mater. Synth. Process*, Vol. 6, No. 3, 1998, pp. 181–189.
- [17] Faria, R. M., and O. N. Oliveira, "Exploiting the Electrical Properties of Thin Films of Semiconducting Polymers," *Braz. J. Phys.*, Vol. 29, No. 2, 1999, pp. 360–370.
- [18] Park, S. H., and D. C. Lee, "A Study of the Electrical Stability Characteristics of a PVDF Organic Thin Film Fabricated by Using the Thermal Vapor Deposition Method," *J. Korean Phys. Soc.*, Vol. 35, No. 5, 1999, pp. 431–437.
- [19] Schoonman, J., "Nanostructured Materials in Solid State Ionics," *Solid State Ion.*, Vol. 135, No. 1–4, 2000, pp. 5–19.
- [20] Lue, J. T., "A Review of Characterization and Physical Property Studies of Metallic Nanoparticles," *J. Phys. Chem. Solids*, Vol. 62, No. 9–10, 2001, pp. 1599–1612.
- [21] Jiang, Z., et al., "The Structure and Gas-Sensing Property of the Coordination Compounds of Phthalocyanine," *Chin. J. Struct. Chem.*, Vol. 20, No. 5, 2001, pp. 331–338.
- [22] Van de Krol, R., and H. L. Tuller, "Electroceramics—The Role of Interfaces," *Solid State Ion.*, Vol. 150, No. 1–2, 2002, pp. 167–179.
- [23] Schoonman, J., "Nanoionics," *Solid State Ion.*, Vol. 157, No. 1–4, 2003, pp. 319–326.
- [24] Cameron, D. C., "Optical and Electronic Properties of Carbon Nitride," *Surf. Coat. Technol.*, Vol. 169, 2003, pp. 245–250.
- [25] Rumyantseva, M. N., et al., "Dopants in Nanocrystalline Tin Dioxide," *Russ. Chem. Bull.*, Vol. 52, No. 6, 2003, pp. 1217–1238.
- [26] Interdigitated Microsensor Electrodes, (ABTECH) Advanced Biosensor Technology, Richmond, VA, <http://www.abtechsci.com>.
- [27] Vanhaesendonck, C., et al., "Nanolithographic Patterning of Metal-Films with a Scanning Tunneling Microscope," *Phys. Scr.*, Vol. 55, 1994, pp. 86–89.
- [28] Li, W., M. J. Stirniman, and S. J. Sibener, "Ti Electron-Stimulated Oxidation of ni(111) at Low-Temperature," *Surf. Sci.*, Vol. 329, No. 1–2, 1995, pp. L593–L598.
- [29] Sze, S. M., *Physics of Semiconductor Devices*, New York: John Wiley & Sons, 1981.
- [30] Mann, B., and H. Kuhn, "Tunneling Through Fatty Acid Salt Monolayers," *J. Appl. Phys.*, Vol. 42, No. 11, 1971, pp. 4398–4405.
- [31] Coast, R., et al., "A Vibrational Spectroscopic Comparison of Vinyltriethoxysilane and Vinylphosphonic Acid Adsorbed on Oxidized Aluminum," *J. Adhes. Sci. Technol.*, Vol. 10, No 2, 1996, pp. 101–121.
- [32] Fischer, C. M., et al., "Organic Quantum-Wells—Molecular Rectification and Single-Electron Tunneling," *Europhysics Letters*, Vol. 28, No. 5, 1994, p. 375.
- [33] Kubota, T., W. J. Lee, and M. Iwamoto, "Inelastic Electron Tunneling Spectroscopy in Single Monolayers and Hetero-Structured Films by Using a Polyimide Barrier," *Mol. Cryst. Liq. Cryst. Sci. Technol. Sect. A-Mol. Cryst. Liq. Cryst.*, Vol. 267, 1995, pp. 223–228.



- [34] Nabok, A. V., et al., "Profile of Trapped Charge in Silicon-Nitride Films in MNOS Structures," *Physica Status Solidi A*, Vol. 82, No. 1, 1984, pp. 221–227.
- [35] Shirshov, Y. M., and A. V. Nabok, "Determination of the Profile of the Electric Charge Captured into Silicon Nitride," *Zhurnal Tekhnicheskoi Fiziki*, Vol. 53, No. 9, 1983, pp. 1830–1833 (in Russian).
- [36] Hong, H. G., W. Park, and E. Yu, "Electrochemical Evaluation of Electron Tunneling Constant in Self-Assembled Monolayer of Omega-Mercaptoalkylhydroquinone on Gold," *Bull. Korean Chem. Soc.*, Vol. 21, No. 1, 2000, pp. 23–25.
- [37] Sek, S., and R. Bilewicz, "Kinetics of Long-Range Electron Transfer Through Alkanethiolate Monolayers Containing Amide Bonds," *J. Electroanal. Chem.*, Vol. 509, No. 1, 2001, pp. 11–18.
- [38] Yamamoto, H., and D. H. Waldeck, "Effect of Tilt-Angle on Electron Tunneling Through Organic Monolayer Films," *J. Phys. Chem. B*, Vol. 106, No. 30, 2002, pp. 7469–7473.
- [39] Shao, H. B., et al., "Study of the Tunneling Mechanism for Long Range Electron Transfer in Azobenzene Self-Assembled Monolayers," *Acta Phys.-Chim. Sin.* Vol. 14, No. 9, 1998, pp. 772–777.
- [40] Gu, Y., and D. H. Waldeck, "Electron Tunneling at the Semiconductor-Insulator-Electrolyte Interface. Photocurrent Studies of the n-InP-Alkanethiol-Ferrocyanide System," *J. Phys. Chem. B*, Vol. 102, No. 45, 1998, pp. 9015–9028.
- [41] Lederman, A., "Vacuum Operated Mercury Probe for cv Plotting and Profiling," *Solid State Technol.*, Vol. 24, No. 8, 1981, pp. 123–126.
- [42] Slowinski, K., H. K. Y. Fong, and M. Majda, "Mercury-Mercury Tunneling Junctions. 1. Electron Tunneling Across Symmetric and Asymmetric Alkanethiolate Bilayers," *J. Am. Chem. Soc.*, Vol. 121, No. 31, 1999, pp. 7257–7261.
- [43] Slowinski, K., and M. Majda, "Mercury-Mercury Tunneling Junctions—Part II. Structure and Stability of Symmetric Alkanethiolate Bilayers and Their Effect on the Rate of Electron Tunneling," *J. Electroanal. Chem.*, Vol. 491, No. 1–2, 2000, pp. 139–147.
- [44] York, R. L., P. T. Nguyen, and K. Slowinski, "Long-Range Electron Transfer Through Monolayers and Bilayers of Alkanethiols in Electrochemically Controlled Hg-Hhg Tunneling Junctions," *J. Am. Chem. Soc.*, Vol. 125, No. 19, 2003, pp. 5948–5953.
- [45] Nabok, A. V., et al., "Electrical Study of Polyelectrolyte Self-Assembled Films Using Mercury Probe," *Material Science and Engineering C*, Vol. 22, No. 2, 2002, pp. 387–391.
- [46] Lvov, Y. M., G. Decher, and H. Möhwald, "Assembly, Structural Characterization, and Thermal-Behavior of Layer-by-Layer Deposited Ultrathin Films of Poly(vinyl sulfate) and Poly(allylamine)," *Langmuir*, Vol. 9, No. 2, 1993, pp. 481–486.
- [47] Lvov, Y. M., and G. Decher, "Assembly of Multilayer Ordered Films by Alternating Adsorption of Oppositely Charged Macromolecules," *Kristallografiya*, Vol. 39, No. 4, 1994, pp. 696–716.
- [48] Nabok, A. V., et al., "The Study of Electron Tunneling Through Thin Polymer Films Using Mercury Probe Technique," *IEE Proceedings, Circuits, Devices, and Systems*, Vol. 151, No. 5, 2004, pp. 461–465.
- [49] Mott, N. F., and E. A. Davis, *Electronic Processes in Non-Crystalline Materials*, 2nd ed., Oxford, England: Clarendon Press, 1979.
- [50] Diebold, U., "The Surface Science of Titanium Dioxide," *Surf. Sci. Reports*, Vol. 8, No. 5–8, 2003, pp. 53–229.
- [51] Falaras, P., "Synergetic Effect of Carboxylic Acid Functional Groups and Fractal Surface Characteristics for Efficient Dye Sensitization of Titanium Oxide," *Solar Energy Materials and Solar Cells*, Vol. 53, No. 1–2, 1998, pp. 163–175.
- [52] Paily, R., et al., "Pulsed Laser Deposition of TiO<sub>2</sub> for MOS Gate Dielectric," *Applied Surface Science*, Vol. 187, No. 3–4, 2002, pp. 297–304.
- [53] Hassan, A. K., et al., "Structural and Electrical Studies on Sol-Gel Derived Spun TiO<sub>2</sub> Thin Films," *J. Phys. D: Appl. Phys.*, Vol. 36, No. 9, 2003, pp. 1120–1125.

- [54] Reddy, K. M., S. V. Manorama, and A. R. Reddy, "Bandgap Studies on Anatase Titanium Dioxide Nanoparticles," *Mater. Chem. & Phys.*, Vol. 78, No. 1, 2002, pp. 239–245.
- [55] Tracey, S. M., A. K. Ray, and T. S. Shishiyanu, "Device Characteristics of CuPc/TiO<sub>2</sub> Heterojunctions," *IEE Proc.-Circuits, Devices and Systems*, Vol. 145, No. 5, 1998, pp. 383–387.
- [56] Simon, J., and J. J. Andre, *Molecular Semiconductors: Photoelectrical Properties and Solar Cells*, Berlin, Germany: Springer-Verlag, 1985.
- [57] Palacin, S., "Phthalocyanines in Langmuir and Langmuir-Blodgett Films: from Molecular Design to Supramolecular Architecture," *Adv. Colloid & Interface Sci.*, Vol. 87, No. 2–3, 2000, pp. 165–181.
- [58] Lee, S., K. Fukuda, and J. Anzai, "Langmuir-Blodgett Films Composed of Hydrophilic and Hydrophobic Moiety Substituted Phthalocyanines," *Mater. Sci. & Eng. C-Biomimetic Materials Sensors And Systems*, Vol. 6, No. 1, 1998, pp. 41–45.
- [59] Critchely, S. M., and M. R. Willis, "Deposition of Thin Phthalocyanine Films By Spin-Coating," *Intern. J. Electron.*, Vol. 76, No. 5, 1994, pp. 809–814.
- [60] Cook, M. J., "Thin Film Formulations of Substituted Phthalocyanines," *J. Mater. Chem.*, Vol. 6, No. 5, 1996, pp. 677–689.
- [61] Koide, N., "Synthesis and Functional-Properties of Liquid-Crystalline Polymers," *J. Synth. Organic Chem. Japan*, Vol. 49, No. 5, 1991, pp. 497–505.
- [62] Wring, S. A., and J. P. Hart, "Chemically Modified, Carbon-Based Electrodes and Their Application as Electrochemical Sensors for the Analysis of Biologically Important Compounds—A Review," *Analyst*, Vol. 117, No. 8, 1992, pp. 1215–1229.
- [63] Saleh, A. M., A. K. Hassan, and R. D. Gould, "DC Conduction Processes and Electrical Parameters of the Organic Semiconducting Zinc Phthalocyanine, ZnPc, Thin Films," *J. Phys. Chem. Solids*, Vol. 64, No. 8, 2003, pp. 1297–1303.
- [64] Ray, A. K., S. M. Tracey, and A. K. Hassan, "Conduction in Partially Monoclinic Films of Lead Phthalocyanine," *IEE Proc.-Sci., Meas. & Technol.*, Vol. 146, No. 4, 1999, pp. 205–209.
- [65] Ray, A. K., et al., "Photoconduction in Langmuir-Blodgett Films of Octa-Substituted Metal-Free Phthalocyanine Molecules," *IEE Proc.-Circuits, Devices & Systems*, Vol. 146, No. 1, 1999, pp. 44–48.
- [66] Hassan, A. K., R. D. Gould, and A. K. Ray, "Van Der Pauw Resistivity Measurements on Thermally Evaporated Copper Phthalocyanine Thin Films," *Physica Status Solidi A*, Vol. 158, No. 2, 1996, pp. K23–K25.
- [67] Saleh, A. M., R. D. Gould, and A. K. Hassan, "Dependence of AC Electrical Parameters on Frequency and Temperature in Zinc Phthalocyanine Thin-Films," *Physica Status Solidi A*, Vol. 139, No. 2, 1993, pp. 379–389.
- [68] Kazantseva, Z. I., et al., "Conductivity of the Tetra-Substituted Vanadyl and Copper Phthalocyanine Langmuir-Blodgett Films," *Poverkhnost. Physika. Khimiya. Mekhanika*, No. 8, 1991, pp. 87–93 (in Russian).
- [69] Kazantseva, Z. I., et al., "Copper Phthalocyanine Langmuir-Blodgett Films as a Sensitivity Unit for Nitrogen Oxides Sensor," *Poverkhnost. Physika. Khimiya. Mekhanika*, No. 1, 1994, pp. 65–70 (in Russian).
- [70] Nabok, A. V., et al., "Nitrogen-Oxide Gas Sensor Based on Tetra-Tertbutyl Copper Phthalocyanine Langmuir-Blodgett Films," *International Journal of Electronics*, Vol. 78, No. 1, 1995, pp. 129–133.
- [71] Van Faassen, E., and H. Kerp, "Explanation of the Low Oxygen Sensitivity of Thin Film Phthalocyanine Gas Sensors," *Sensors & Actuators B-Chemical*, Vol. 88, No. 3, 2003, pp. 329–333.
- [72] Ueda, K., M. Iwamatsu, and T. Sugimoto, "Synthesis of Tetrathiafulvalene Derivatives Synthesized with Aim at the Creation of New Organic Functionality Materials," *J. Synth. Org. Chem. Japan*, Vol. 56, No. 9, 1998, pp. 755–763.



- [73] Berzina, T. S., S. A. Shikin, and V. I. Troitsky, "The Influence of Structure Change on Electrical Properties of Conducting LB Films Produced from Hexadecyl-TCNQ and Heptadecyldimethyl-TTF Mixture," *Makromolekulare Chemie-Macromolecular Symposia*, Vol. 46, 1991, pp. 223–227.
- [74] Saxena, V., and B. D. Malhotra, "Prospects of Conducting Polymers in Molecular Electronics," *Current Appl. Phys.*, Vol. 3, No. 2–3, 2003, pp. 293–305.
- [75] Bradley, D. D. C., "Conjugated Polymer Electroluminescence," *Synthetic Metals*, Vol. 54, No. 1–3, 1993, pp. 401–415.
- [76] Bakhshi, A. K., "Electrically Conducting Polymers—From Fundamental to Applied Research," *Bull. Mater. Sci.*, Vol. 18, No. 5, 1995, pp. 469–495.
- [77] Kasap, S. O., *Electrical Engineering Materials and Devices*, New York: McGraw-Hill, 1997.
- [78] Yavorskiy, B. M., and A. A. Detlaf, *Reference Book in Physics*, Moscow, Russia: Nauka, 1979, p. 733.
- [79] Eric Weisstein's World of Physics, <http://scienceworld.wolfram.com/physics/TunnelingEffect.html>.
- [80] Gamow, G., "On Quantum Theory of Atomic Nuclei," *Z. Phys.*, Vol. 51, 1928, p. 204.
- [81] Esaki, L., "New Phenomenon in Narrow Germanium p-n Junctions," *Phys. Rev.*, Vol. 109, 1958, pp. 603–604.
- [82] Yang, D. H., et al., "Separation of Pinhole and Tunneling Electron Transfer Processes at Self-Assembled Polymeric Monolayers on Gold Electrodes," *J. Electroanal. Chem.*, Vol. 470, No. 2, 1999, pp. 114–119.
- [83] Hong, H. G., W. Park, and E. Yu, "Electrochemical Evaluation of Electron Tunneling Constant in Self-Assembled Monolayer of Omega-Mercaptoalkylhydroquinone on Gold," *Bull. Korean Chem. Soc.*, Vol. 21, No. 1, 2000, pp. 23–25.
- [84] Sek, S., and R. Bilewicz, "Kinetics of Long-Range Electron Transfer Through Alkanethiolate Monolayers Containing Amide Bonds," *J. Electroanal. Chem.*, Vol. 509, No. 1, 2001, pp. 11–18.
- [85] Yamamoto, H., and D. H. Waldeck, "Effect of Tilt-Angle on Electron Tunneling Through Organic Monolayer Films," *J. Phys. Chem. B*, Vol. 106, No. 30, 2002, pp. 7469–7473.
- [86] Faria, R. M., and O. N. Oliveira, "Exploiting the Electrical Properties of Thin Films of Semiconducting Polymers," *Braz. J. Phys.*, Vol. 29, No. 2, 1999, pp. 360–370.
- [87] Izumi, M., et al., "Recent Progress in Metallic Langmuir-Blodgett Films Based on TTF Derivatives," *Thin Solid Films*, Vol. 329, 1998, pp. 14–18.
- [88] Richard, J., P. Delhaes, and M. Vandevyver, "Electronic and Spectroscopic Properties of Conducting Langmuir-Blodgett-Films Based on Semi-Amphiphilic TCNQ Salts—A Comprehensive Comparison with Bulk Crystalline Molecular Conductors—A Review," *New J. Chem.*, Vol. 15, No. 2–3, 1991, pp. 137–148.
- [89] Sugi, M., and S. Iizima, "Single Layer Conductance of Cadmium Behenate in the Langmuir Multilayer Assembly System," *Appl. Phys. Lett.*, Vol. 34, No. 4, 1979, pp. 290–292.
- [90] Gavriluk, I. V., et al., "Langmuir-Blodgett Films Based on Cyanoacrylic Acid as Insulating Layers on Semiconductors," *Poverkhnost. Fizika. Khimiya. Mekhanika*, No. 11, 1991, pp. 93–100 (in Russian).
- [91] Sugi, M., "Langmuir-Blodgett Films—A Course Towards Molecular Electronics: A Review," *J. Mol. Electron.*, Vol. 1, No. 1, 1985, pp. 3–17.
- [92] Nabok, A. V., et al., "Electrical Characterization of LB Films Containing CdS Nanoparticles," *Mater. Sci. & Eng. C*, Vol. 22, No. 2, 2002, pp. 355–358.
- [93] Mimura, T., et al., "A New Field-Effect Transistor with Selectively Doped GaAs/n-AlxGa1-x As Heterojunctions," *Jpn. J. Appl. Phys.*, Vol. 19, No. 5, 1980, pp. L225–L227.
- [94] Capasso, F., and R. A. Kiehl, "Resonant Tunneling Transistor with Quantum Well Base and High-Energy Injection: A New Negative Differential Resistance Device," *J. Appl. Phys.*, Vol. 58, No. 3, 1985, pp. 1366–1368.

- [95] Seabaugh, A. C., J. H. Luscombe, and J. N. Randal, "Quantum Functional Devices: Present Status and Future Prospects," *Future Electron Devices (FED) Journal*, Vol. 3, Suppl. 1, 1993, pp. 9–20.
- [96] Frensley, W. R., "Gallium Arsenide Transistors," *Scientific American*, February 1987, pp. 80–87.
- [97] Wang, C. T., (ed.), *Introduction to Semiconductor Technology: GaAs and Related Compounds*, New York: John Wiley & Sons, 1990.
- [98] Mikkelsen, C. H., et al., "Coupled-Quantum-Well Field-Effect Resonant-Tunneling Transistor for Multivalued Logic Memory Applications," *IEEE Trans. Electr. Dev.*, Vol. 41, No. 2, 1994, pp. 132–137.
- [99] Montemerlo, M. S., et al., *Technologies and Designs for Electronic Nanocomputers*, McLean, VA: MITRE Corporation, 1996.
- [100] Zakhariev, B. N., and V. M. Chabanov, "Spectroscopy, Potential Barriers, and Resonances: New Progress in Quantum Design," *Phys. Part. Nuclei*, Vol. 33, No. 2, 2002, pp. 175–195.
- [101] Glattli, D. C., "Coulomb-Blockade and Off-Resonance Tunneling in Small Electronic Systems," *Physica B*, Vol. 189, No. 1–4, 1993, pp. 88–98.
- [102] York, R. L., and K. Slowinski, "Tunneling Conductivity of One- and Two-Component Alkanethiol Bilayers in Hg-Hg Junctions," *J. Electroanal. Chem.*, Vol. 550, 2003, pp. 327–336.
- [103] Fan, F. R. F., et al., "Charge Transport Through Self-Assembled Monolayers of Compounds of Interest in Molecular Electronics," *J. Am. Chem. Soc.*, Vol. 124, No. 19, 2002, pp. 5550–5560.
- [104] Lee, H. S., S. Iyengar, and I. H. Musselman, "Bias-Dependent STM Image Contrast Study of Phenyloctadecyl Ethers Physisorbed onto Highly Oriented Pyrolytic Graphite," *Langmuir*, Vol. 14, No. 26, 1998, pp. 7475–7483.
- [105] Lye, W. K., et al., "Quantitative Inelastic Tunneling Spectroscopy in the Silicon Metal-Oxide-Semiconductor System," *Appl. Phys. Lett.*, Vol. 71, No. 17, 1997, pp. 2523–2525.
- [106] Braginskii, L. S., and E. M. Baskin, "Inelastic Resonant Tunneling," *Phys. Solid State*, Vol. 40, No. 6, 1998, pp. 1051–1055.
- [107] Okur, S., and J. F. Zasadzinski, "Modification of Al-Oxide Tunnel Barriers with Organic Self-Assembled Monolayers," *J. Appl. Phys.*, Vol. 85, No. 10, 1999, pp. 7256–7262.
- [108] Jimenez-Molinos, F., et al., "Physical Model for Trap-Assisted Inelastic Tunneling in Metal-Oxide-Semiconductor Structures," *J. Appl. Phys.*, Vol. 90, No. 7, 2001, pp. 3396–3404.
- [109] Alonzo, A. C., D. A. Collins, and T. C. McGill, "Tunneling Spectroscopy of Resonant Interband Tunneling Structures," *Solid State Commun.*, Vol. 101, No. 8, pp. 607–610.
- [110] Stipe, B. C., M. A. Rezaei, and W. Ho, "Single-Molecule Vibrational Spectroscopy and Microscopy," *Science*, Vol. 280, No. 5370, 1998, pp. 1732–1735.
- [111] Stokbro, K., et al., "First-Principles Theory of Inelastic Currents in a Scanning Tunneling Microscope," *Phys. Rev. B*, Vol. 58, No. 12, 1998, pp. 8038–8041.
- [112] Mii, T., S. Tikhodeev, and H. Ueba, "Theory of Vibrational Tunneling Spectroscopy of Adsorbates on Metal Surfaces," *Surf. Sci.*, Vol. 502, 2002, pp. 26–33.
- [113] Persson, B. N. J., and H. Ueba, "Theory of Inelastic Tunneling Induced Motion of Adsorbates on Metal Surfaces," Vol. 502, 2002, pp. 18–25.
- [114] Lorente, N., and M. Persson, "Theory of Single Molecule Vibrational Spectroscopy and Microscopy," *Phys. Rev. Lett.*, Vol. 85, No. 14, 2000, pp. 2997–3000.
- [115] Sainoo, Y., et al., "Inelastic Tunneling Spectroscopy Using Scanning Tunneling Microscopy on Trans-2-butene Molecule: Spectroscopy and Mapping of Vibrational Feature," *J. Chem. Phys.*, Vol. 120, No. 16, 2004, pp. 7249–7251.
- [116] Komeda, T., et al., "Local Chemical Reaction of Benzene on Cu(110) via STM-Induced Excitation," *J. Chem. Phys.*, Vol. 120, No. 11, 2004, pp. 5347–5352.

- [117] Ness, H., and A. J. Fisher, "Coherent Electron Injection and Transport in Molecular Wires: Inelastic Tunneling and Electron-Phonon Interactions," *Chem. Phys.* Vol. 281, No. 2–3, 2002, pp. 279–292.
- [118] Haule, K., and J. Bonca, "Inelastic Tunneling Through Mesoscopic Structures," *Phys. Rev. B*, Vol. 59, No. 20, 1999, pp. 13087–13093.
- [119] Zimmerman, D. T., M. B. Weimer, and G. Agnolet, "An Adjustable Oxide-Free Tunnel Junction for Vibrational Spectroscopy of Molecules," *Appl. Phys. Lett.*, Vol. 75, No. 16, 1999, pp. 2500–2502.
- [120] Litvin, L. V., et al., "Coulomb Blockade Under Conditions of Inelastic Tunneling," *JETP Lett.*, Vol. 72, No. 5, 2000, pp. 264–268.
- [121] Turin, L., "A Spectroscopic Mechanism for Primary Olfactory Reception," *Chemical Senses*, Vol. 21, 1996, p. 773.
- [122] Turin, L., "A Method for the Calculation of Odor Character from Molecular Structure," *J. Theor. Biol.*, Vol. 216, No. 3, 2002, pp. 367–385.
- [123] Berndt, R., "Photon-Emission Induced by the Scanning Tunneling Microscope," *Scanning Microsc.*, Vol. 9, No. 3, 1995, pp. 687–693.
- [124] Pierce, D. T., et al., "Polarized Light Emission from the Metal-Metal STM Junction," *Appl. Phys. A-Mater. Sci. Process*, Vol. 66, 1998, pp. S403–S406.
- [125] Kagami, S., H. Minoda, and N. Yamamoto, "STM Light Emission from Si(111)root 3 x root 3-Ag Surface," *Surf. Sci.*, Vol. 493, No. 1–3, 2001, pp. 78–83.
- [126] Zou, Z. Q., et al., "STM-Induced Photon Emission Spectra from the Cu(100) Surface," *Surf. Sci.*, Vol. 512, No. 3, 2002, pp. L373–L378.
- [127] Dong, Z. C., et al., "Light Emission from Porphyrin Molecules Induced by a Scanning Tunneling Microscope," *Jpn. J. Appl. Phys. Part 1—Regul. Pap. Short Notes Rev. Pap.*, Vol. 41, No. 7B, 2002, pp. 4898–4902.
- [128] Deng, W., et al., "STM-Induced Photon Emission from Self-Assembled Porphyrin Molecules on a Cu(100) Surface," *J. Chem. Phys.*, Vol. 117, No. 10, 2002, pp. 4995–5000.
- [129] Kulik, I. O., and R. I. Shekhter, "Kinetic Phenomena and Charge Discreteness Effects in Granular Media," *Sov. Phys.-JETP*, Vol. 41, 1975, pp. 308–316.
- [130] Averin, D. V., and K. K. Likharev, "Coulomb Blockade of Single-Electron Tunneling, and Coherent Oscillations in Small Tunnel-Junctions," *J. Low Temp. Phys.*, Vol. 62, No. 3–4, 1986, pp. 345–373.
- [131] Lafarge, P., et al., "Direct Observation of Macroscopic Charge Quantization," *Zeitschrift Fur Physik B-Condensed Matter*, Vol. 85, No. 3, 1991, pp. 327–332.
- [132] Delsing, P., et al., "Observation of Single-Electron-Tunneling Oscillations," *Phys. Rev. B*, Vol. 42, No. 12, 1990, pp. 7439–7449.
- [133] Korotkov, A. N., D. V. Averin, and K. K. Likharev, "Single-Electron Charging of the Quantum-Wells and Dots," *Physica B*, Vol. 165, Part 2, 1990, pp. 927–928.
- [134] Kuzmin, L. S., et al., "Single-Electron Charging Effects in One-Dimensional Arrays of Ultrasmall Tunnel-Junctions," *Phys. Rev. Lett.*, Vol. 62, No. 21, 1989, pp. 2539–2542.
- [135] Kuzmin, L. S., and K. K. Likharev, "Observation of the Correlated Discrete Single-Electron Tunneling," *Jap. J. Appl. Phys., Part 1—Regular Papers, Short Notes & Review Papers*, Vol. 26, Part 2, Suppl. 26-3, 1987, pp. 1387–1388.
- [136] Kuzmin, L. S., and K. K. Likharev, "Direct Experimental-Observation of Discrete Correlated Single-Electron Tunneling," *JETP Lett.*, Vol. 45, No. 8, 1987, pp. 495–497.
- [137] Grabert, H., and M. Devoret, *Single Charge Tunneling*, New York: Plenum, 1992.
- [138] Devoret, M. H., D. Esteve, and C. Urbina, "Single-Electron Transfer in Metallic Nanostructures," *Nature*, Vol. 360, No. 6404, 1992, pp. 547–553.
- [139] Facci, P., et al., "Room-Temperature Single-Electron Junction," *Proc. NAS USA*, Vol. 93, No. 20, 1996, pp. 10556–10559.
- [140] Facci, P., et al., "Room-Temperature Single-Electron Junction," *Proc. National Academy Sciences of USA*, Vol. 93, No. 20, 1996, pp. 10556–10559.

- [141] Erokhin, V., et al., “Fatty Acid-Based Monolectron Device,” *Biosensors & Bioelectronics*, Vol. 12, No. 7, 1997, pp. 601–606.
- [142] Erokhin, V., et al., “Semiconductor Nanoparticles for Quantum Devices,” *Nanotechnology*, Vol. 9, No. 3, 1998, pp. 158–161.
- [143] Zhuang, L., L. J. Guo, and S. Y. Chou, “Silicon Single-Electron Quantum-Dot Transistor Switch Operating at Room Temperature,” *Appl. Phys. Lett.*, Vol. 72, No. 10, 1998, pp. 1205–1207.
- [144] Likharev, K. K., “Single-Electron Devices and Their Applications,” *Proc. IEEE*, Vol. 7, No. 4, 1999, pp. 606–632.
- [145] Likharev, K. K., “Single-Electron Transistors—Electrostatic Analogs of the dc Squids,” *IEEE Trans. on Magnetics*, Vol. 23, No. 2, 1987, pp. 1142–1145.
- [146] Devoret, M., and C. Glattli, “Single-Electron Transistors,” *Physics World*, Vol. 11, No. 9, 1998, pp. 29–33.
- [147] Chen, R. H., A. N. Korotkov, and K. K. Likharev, “Single-Electron Transistor Logic,” *Appl. Phys. Lett.*, Vol. 68, No. 14, 1996, pp. 1954–1956.
- [148] Ahmed, H., and K. Nakazato, “Single-Electron Devices,” *Microelectron. Eng.*, Vol. 32, No. 1–4, 1996, pp. 297–315.
- [149] Pothier, H., et al., “Single Electron Pump Fabricated with Ultrasmall Normal Tunnel Junctions,” *Physica B*, Vol. 169, No. 1–4, 1991, pp. 573–574.
- [150] Cleland, A. N., et al., “Very Low-Noise Photodetector Based on the Single Electron Transistor,” *Appl. Phys. Lett.*, Vol. 61, No. 23, 1992, pp. 2820–2822.
- [151] Turel, O., and K. Likharev, “CrossNets: Possible Neuromorphic Networks Based on Nanoscale Components,” *Inter. J. Circuit Theory & Appl.*, Vol. 31, No. 1, 2003, pp. 37–53.
- [152] Korotkov, A. N., R. H. Chen, and K. K. Likharev, “Possible Performance of Capacitively Coupled Single-Electron Transistors in Digital Circuits,” *J. Appl. Phys.*, Vol. 78, No. 4, 1995, pp. 2520–2530.
- [153] Dresselhaus, P. D., et al., “Single-Electron Tunneling in Single Junctions and Multijunction Systems,” *Physica B*, Vol. 194, Part 1, 1994, pp. 1335–1336.
- [154] Devoret, M. H., and R. J. Shoelkopf, “Amplifying Quantum Signals with the Single-Electron Transistor,” *Nature*, Vol. 406, 2000, pp. 1039–1046.
- [155] Mizuta, H., et al., “Nanoscale Coulomb Blockade Memory and Logic Devices,” *Nanotechnology*, Vol. 12, No. 2, 2001, pp. 155–159.
- [156] Fujiwara A., et al., “Double-Island Single-Electron Devices—A Useful Unit Device for Single-Electron Logic LSIs,” *IEEE Trans. Electr. Dev.*, Vol. 46, No. 5, 1999, pp. 954–959.
- [157] Nishiguchi, K., et al., “Multilevel Memory Using Single-Electron Turnstile,” *Electron. Lett.*, Vol. 40, No. 4, 2004, pp. 229–230.
- [158] Fujiwara, A., et al., “Current Quantization Due to Single-Electron Transfer in Si-Wire Charge-Coupled Devices,” *Appl. Phys. Lett.*, Vol. 84, No. 8, 2004, pp. 1323–1325.
- [159] Yano, K., et al., “Single-Electron Memory for Giga-to-Tera Bit Storage,” *Proc. IEEE*, Vol. 87, No. 4, 1999, pp. 633–651.
- [160] Nakamura, Y., C. D. Chen, and J. S. Tsai, “100-K Operation of Al-Based Single-Electron Transistors,” *Jap. J. Appl. Phys. Part 2-Letters*, Vol. 35, No. 11A, 1996, pp. L1465–L1467.
- [161] Nagase, M., et al., “Single-Electron Devices Formed by Thermal Oxidation,” *J. Electroanal. Chem.*, Vol. 559, 2003, pp. 19–23.
- [162] Takahashi, Y., et al., “Development of Silicon Single-Electron Devices,” *Physica E-Low-Dimensional Systems & Nanostructures*, Vol. 19, No. 1–2, 2003, pp. 95–101.
- [163] Takahashi, Y., et al., “Silicon Single-Electron Devices,” *J. Phys.-Condens. Matt.*, Vol. 14, No. 39, 2002, pp. R995–R1033.
- [164] Tilke, A., et al., “Silicon-Based Nanoelectronics and Nanoelectromechanics,” *Superlattices & Microstructures*, Vol. 27, No. 5–6, 2000, pp. 597–601.

- [165] Ishikuro, H., and T. Hiramoto, "Fabrication of Nano-Scale Point Contact Metal-Oxide-Semiconductor Field-Effect-Transistors Using Micrometer-Scale Design Rule," *Jap. J. Appl. Phys. Part 1*, Vol. 38, No. 1B, 1999, pp. 396–398.
- [166] Mizuta, H., et al., "Single-Electron Charging Phenomena in Nano/Polycrystalline Silicon Point Contact Transistors," *Polycrystalline Semiconductors, VII Proceedings, Solid State Phenomena*, Vol. 93, 2003, pp. 419–428.
- [167] Matsumoto, K., "Room Temperature Operated Single Electron Transistor Made by a Scanning Tunneling Microscopy/Atomic Force Microscopy Nano-Oxidation Process," *Intern. J. Electron.*, Vol. 86, No. 5, 1999, pp. 641–662.
- [168] Shirakashi, J., et al., "Single-Electron Charging Effects in Nb/Nb Oxide-Based Single-Electron Transistors at Room Temperature," *Appl. Phys. Lett.*, Vol. 72, No. 15, 1998, pp. 1893–1895.
- [169] Gasparian, V., and U. Simon, "Potential Distribution in a Finite 1-D Array of Arbitrary Mesoscopic Tunnel Junctions," *Physica B-Cond. Matter*, Vol. 240, No. 4, 1997, pp. 289–297.
- [170] Junno, T., et al., "Single-Electron Devices Via Controlled Assembly of Designed Nanoparticles," *Microel. Eng.*, Vol. 47, No. 1–4, 1999, pp. 179–183.
- [171] Shih, S. M., et al., "Two-Dimensional Arrays of Self-Assembled Gold and Sulfur-Containing Fullerene Nanoparticles," *Langmuir*, Vol. 18, No. 8, 2002, pp. 3332–3335.
- [172] Berven, C. A., et al., "Nanoparticle Based Boolean Logic," *Physica E-Low-Dimens. Syst. & Nanostruct.*, Vol. 19, No. 1–2, 2003, pp. 246–250.

# Applications of Organic/Inorganic Nanostructures in Microelectronics and Optoelectronics

## 6.1 Organic Films in Conventional Microelectronics

### 6.1.1 Organic Films as Insulating and Passivating Layers

Organic films and polymers have well-established applications in microelectronics as photoresists and passivating materials for final encapsulation of electron devices and microchips. The use of organic films as insulators in active devices, such as gate insulators in MOSFETs, was rather limited in the past, because organic materials could not compete with inorganic insulators, such as  $\text{SiO}_2$  and  $\text{Si}_3\text{N}_4$ .

Since the 1980s, organic films were always considered as possible alternatives for inorganic insulators in the course of scaling down the electron devices, following Moore's law [1]. However, the quality of organic films was not good enough. For example, LB films, despite being precise in thickness down to nanometer levels, have poor mechanical and thermal stability, as well as a large number of defects, such as pinholes, and thus have poor electrical insulating properties [2, 3]. In the last decade, as a result of great progress in organic films technologies (such as polymer film deposition and self-assembly), organic gate insulators have become a reality [4]. Gate insulators in MOSFET and CMOSFET are required to have high dielectric permittivity, which can be achieved by using composite polymer materials doped with some other organic molecules or inorganic inclusions, such as nanoparticles [5]. Another application, which requires high dielectric constant materials, includes capacitors fabricated with the metal organic chemical vapor deposition (MOCVD) technique. Some polymer/ceramic composites are able to increase the capacitance density up to  $50 \text{ nF/cm}^2$  [6].

At the same time, passivating materials must have low dielectric permittivity in order to reduce parasitic capacitances, and thus increase operating frequency [5]. Some polymer materials having low dielectric permittivity are very suitable for this purpose [7–15]. Composite and porous polymer materials offer another possibility of the fabrication of passivating layers with low dielectric permittivity [16–19]. Porous polymer structures can be formed, for example, by foaming aromatic/aliphatic polyesters under illumination and then curing at  $280^\circ\text{C}$  [20].

Dielectric properties of thin organic films, including the effect of traps and surface states on the insulator/semiconductor interface, are well studied [21]. In contrast to the  $\text{SiO}_2/\text{Si}$  system that always has a positive surface charge, which can be



reduced or overturned by the ion implantation of boron, organic (polymer) insulators may have either a negative or a positive charge, depending on the types of materials used and their chemical treatment [22]. The electric transport in metal/insulator/metal (MIM) sandwich structures with thin self-assembled organic films were studied thoroughly, using a mercury probe as one of the metal electrodes [23–26] with a view towards the application in novel nanoelectronic devices. Tunneling properties of MIM structures, particularly the tunneling decay constant, were evaluated from these measurements.

Some of polymer insulating films, prepared by the alternate deposition of polypyrrole (PPY) and polythiophene acetic acid (PTAA), demonstrate anisotropy of electrical properties, with the semiconducting behavior in the lateral direction and the metallic conductivity in the normal direction [27, 28]. Such anisotropy of conductivity is a very interesting phenomenon that may lead to the development of new nanoelectronic devices.

The advances of electrostatically self-assembled films used as passivating layers for GaAs, which does not have a native oxide, are demonstrated in [29]. The conductivity of polymers can be increased by the introduction of doping impurities. Some dopands can be initiated photochemically [30], which gives a possibility of patterning the polymer layers by the formation of conducting channels.

### 6.1.2 Active Organic/Inorganic Devices


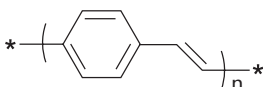
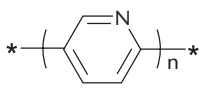
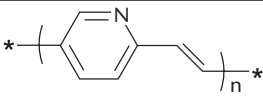
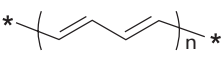
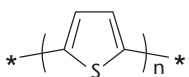
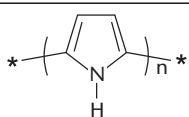
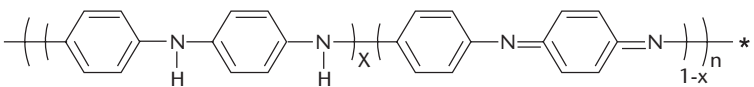
Organic materials, and, particularly, polymers, can be used for the fabrication of active electron devices (e.g., diodes, transistors, or switches) [31–36]. The foundation of this direction in microelectronics was laid in the 1990s, and it is closely related to the development of conjugated polymers [37–39]. Chemical structures of typical conjugated polymers, which are quoted throughout this chapter, are shown in Table 6.1.

Polymers in their basic (unsubstituted) forms, as shown in Table 6.1, are insoluble. To make them soluble in organic solvents, and thus suitable for film deposition (e.g., by spin-coating), different substituting side groups are introduced. The electrical conductivity feature of these polymers is due to the formation of a delocalized (or conjugated)  $\pi$ -electron system, and the conductivity can be increased by doping with either donor (e.g., Na, K, Li, or Ca) or acceptor (e.g.,  $I_2$ , Cl,  $PF_6$ ,  $BF_6$ , or  $AsF_6$ ) impurities. The conducting properties of these polymers can vary from insulating (with typical conductance of  $10^{-8}$  S/m), to semiconducting ( $10^{-3}$  S/m), and to metallic ( $10^2$  S/cm), depending on the substituting groups and doping.

More recent works report on the formation of organic heterojunction diodes by depositing LB multilayers of a polyaniline/stearic acid 1:1 mixture onto films of poly(3-methylthiophene) electro-polymerized onto gold electrodes [40]. The above diodes demonstrate a high rectification factor. Low cost field-effect transistors can be formed from poly(3-octylthiophene), poly(3-dodecylthiophene), Arylamino-poly(phenylene-vinylene), poly(2-methoxy, 5 ethyl (2' hexyloxy) paraphenylenevinylene), and pentacene from a soluble precursor, and with silicon dioxide or poly(4-vinylphenol) as a gate insulator [41].

Polymer junction field-effect transistors (JFET) can be fabricated using poly(3,4-ethylene-dioxythiophene)/poly(styrene sulfonate) (PEDT/PSS) as the channel, and poly(2,5-hexyloxy p-phenylene cyanovinylene) (CNPPV) as the gate

**Table 6.1** Chemical Structures of Typical Conjugated Polymers

	Poly(para-phenylene)
	Poly(para-phenylene vinylene)
	Poly(para-pyridine)
	Poly(para-phenylene vinylene)
	Trans-polyacetylene
	Polythiophene
	Polypyrrol
	Polyaniline: leucoemeraldine ( $x = 1$ ); emeraldine ( $x = 0.5$ ); pernigraniline ( $x = 0$ )

layer [42]. The advantages of these devices lie in their mechanical flexibility, light weight, and low cost. They show a current of  $13.8 \mu\text{A}$  at zero gate voltage, and a pinch-off at 1V, which are parameters very similar to conventional JFET devices.

An interesting example of molecular memory devices is shown in [43]. The phase transitions in ultrathin polyelectrolyte multilayers of poly(allylamine hydrochloride)/poly(styrenesulfonic acid) (PAH/PSS) are observed in response to changes in the pH of the environment. These films exhibit a history-dependent swelling behavior and molecular conformational memory. Well-studied traditional organic materials, such as phthalocyanines, can be also used in organic field-effect transistors (OFET) [44].

The use of polymer transistors as light emitting devices was recently reported. Semiconducting conjugated polymer poly(3-hexylthiophene) (P3HT) was used as the hole-transport layer for a polymer LED in [45], while poly[9,9-di(ethylhexyl)fluorene] was used as interdigitated source/drain electrodes on the Si/SiO<sub>2</sub> substrate in [46]. The original rubbing technique of molecular alignment of poly(3-alkylthiophene) was proposed in [47] for the fabrication of field-effect transistor (FET) devices, which results in anisotropy of conductivity ranging from 5 to 20 for the current in parallel and orthogonal directions, with respect to the friction



direction. The combination of polymer materials with traditional inorganic materials is very common in polymer microelectronics. Conjugated polymer thin film transistors are fabricated using silicon dioxide ( $\text{SiO}_2$ ) and polyimide films as a dual layer gate dielectric on a plastic substrate [48]. The dual layer gate dielectric shows good insulating properties and a flat band voltage of 0.5V. Direct assembly of molecules on silicon surfaces was used in [49] for the fabrication of hybrid organic-semiconductor transistors. Aryl diazonium salts were used to assemble covalently on a hydride-passivated, oxide-free n-type Si(111) surface. The monolayer modifies the electrical properties of the interface, and exhibits nonlinear current-voltage characteristics.

The charge transfer and capturing processes on the organic/inorganic and organic/organic interfaces were studied recently in [50, 51], with a view to applications in hybrid organic/inorganic electron devices. With the same purpose, the exciton processes in organic/inorganic structures were studied in [52].

An all-polymer transistor was demonstrated in [53]. All components were produced by the low-cost method of jet printing. In this type of transistor, having a channel length of  $5\ \mu\text{m}$ , the high electron mobility  $0.002\ \text{m}^2\text{V}^{-1}\text{s}^{-1}$ , and the on-off current switching ratio of 10 were achieved. Recent advances in polymer microelectronic devices were demonstrated in [54], which reports on the fabrication of a digital circuit containing 171 transistors that are able to convert a parallel word of four bits into a serial bit sequence. The polymer poly(3,3"-dihexyl-2,2':5',2"-terthiophene) (PDHTT) was used as a semiconducting material.

The advanced technology of molecular beam epitaxy was considered for the fabrication of hybrid organic/inorganic photonic and electronic devices [55]. The organic molecular beam deposition technology allows the reproducible growth of complex layer sequences, with a defined thickness of various organic semiconductors in combination with dielectric films, and with conducting layers of metals and indium tin oxide (ITO). For example, organic/inorganic heterostructure diodes based on thin crystalline films of 3,4,9,10-perylenetetracarboxylic dianhydride (PTCDA) on III-V semiconductors were produced. Such devices were operated in the gigahertz frequency range.

Scaling down the size of electron devices requires advance methods of patterning. In addition to the well-established electron beam lithography, the electron holography method has been proposed recently as a high resolution imaging technique for the fabrication of organic electron devices [56]. Another possibility is to use AFM lithography for patterning of polymer layers [57, 58].

## 6.2 Organic/Inorganic Optoelectronic Devices

Optoelectronics is the area in which organic films and organic-inorganic nanostructures have found their main applications in the last decade. These achievements are reviewed in [59–63]. Organic-inorganic composites represent a very interesting class of materials with great potential in optoelectronics applications. The unique features of these materials related to the phase interpenetration can be used in electronic and optoelectronic devices, as well as for bioencapsulation, chromatographic separation, catalysis, and nanolithography [59]. For instance, LEDs produced by

chemical routes demonstrate longer lifetime, lower power consumption, higher brightness, and better spectral purity, as compared to solid-state LEDs [60]. In recent years, significant progress has been achieved in the synthesis of various types of polymer-nanocomposites, and in understanding their optical and electrical properties. As a result, organic nanocomposite devices, such as light emitting diodes, photovoltaic devices, and solar cells, have been developed using methods of thin organic films, such as chemical and electrostatic self-assembly, contact printing, and spin coating [63]. As compared to solid-state devices, the main advantage of the optoelectronic devices prepared by chemical routes is their cost effectiveness. Moreover, novel composite materials based upon conductive polymers, such as poly(aniline), substituted poly(paraphenylenevinyls), or poly(thiophenes), when mixed with semiconducting nanoparticles, such as CdS, CdSe, CuS, or ZnS, show new properties of materials; such properties include interpenetrating networks, p-n nanojunctions, or “fractal” p-n interfaces [63], which are not achievable by traditional microelectronics technologies. The main applications of organic nanostructures in optoelectronics are outlined below.

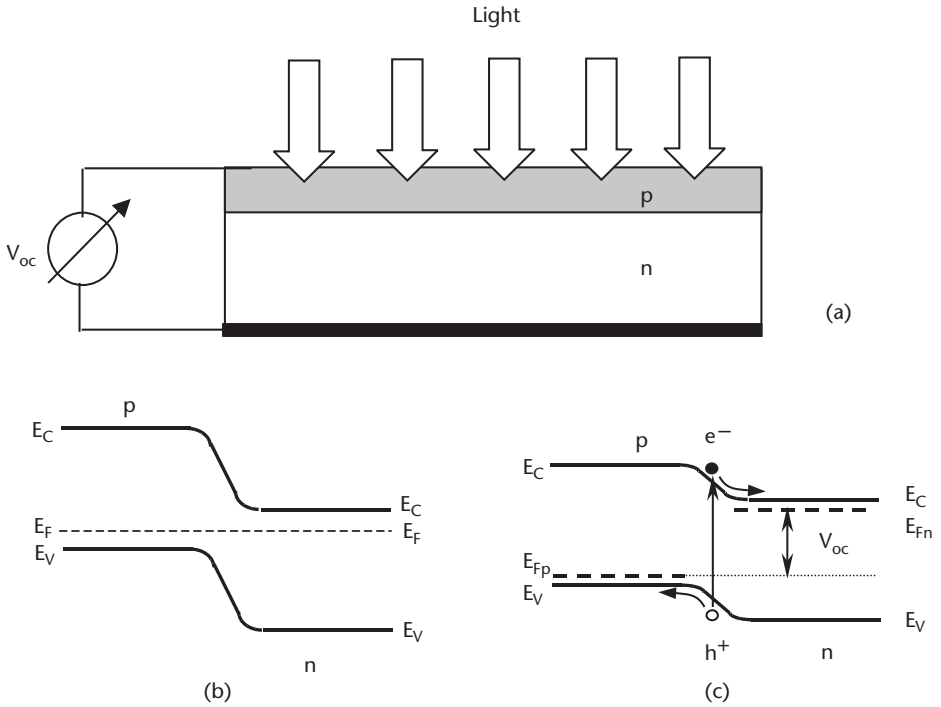
### 6.2.1 Nanostructured Photovoltaic Devices and Solar Cells

Photovoltaic devices and solar cells are examples of a traditional application area, where organic and inorganic materials work together and complement each other in the same device. Typically, the solar cell is a shallow p-n junction that separates the hole-electron pairs generated by light, and thus creates the voltage on the electrodes (see Figure 6.1).

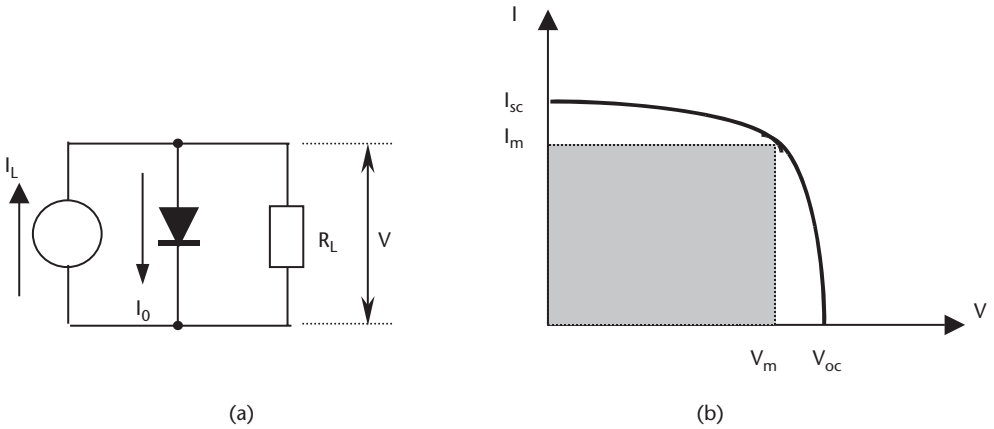
The majority of commercial solar cells are made of silicon [64]. The technology of silicon solar cells has reached a state of perfection, resulting in a high efficiency of solar energy conversion (up to 28%) [65]. This is close to the theoretical limit of silicon solar cells. At the same time, solar cells made of other semiconductor materials, such as II-VI and III-V (e.g., cascaded heterojunctions), are able to achieve much higher efficiency, up to 70% [65]. Another important factor in solar cell development is the cost. Monocrystalline silicon devices are expensive though effective. A search for alternative materials (e.g., other semiconductors, organic materials, polymers, or composite heterostructures) for photovoltaic devices and solar cells is constantly being pursued. For example, less expensive polycrystalline silicon devices are not as effective as the monocrystalline devices, but this lower efficiency does not prevent their applications in a number of areas where the maximal efficiency is not essential.

The efficiency of solar cells can be derived from the equivalent circuit and current-voltage characteristic of the p-n junction [65]. The equivalent circuit, shown in Figure 6.2(a), contains the current source ( $I_{sc}$ ) due to the generation of electron-hole pairs, the p-n junction, and the load resistor ( $R_L$ ).

By varying the value of  $R_L$  from 0 to  $\infty$ , one can plot the load characteristic, as shown in Figure 6.2(b).  $R_L = 0$  represents the case of the short circuit condition, with the short circuit current equal to the current source  $I = I_{sc}$ , but  $V = 0$ . Another extreme at  $R = \infty$  gives open circuit conditions, with  $I = 0$  and  $V = V_{oc}$ . The optimal value of  $R_L$  allows the extraction of the maximum power from the solar cell,  $P_m = I_m V_m$ , which is shown as a dark rectangular area in Figure 6.2(b). Using the Schottky formula for the current-voltage characteristic of a p-n junction,



**Figure 6.1** (a) Schematic diagram of the p-n junction solar cell. Energy band diagrams of a p-n junction (b) in the darkness, and (c) under illumination.



**Figure 6.2** (a) Equivalent circuit of the p-n junction under illumination, and (b) the load characteristic of the p-n junction solar cell.

$$I = I_0 [\exp(eV/kT) - 1] \tag{6.1}$$

where  $I_0$  is the reverse saturated current, one can now obtain the open circuit voltage and the output power

$$V_{oc} \approx \frac{kT}{e} \ln\left(\frac{I}{I_0}\right) \tag{6.2}$$

$$P = IV = I_0 V [\exp(eV/kT) - 1] - IV \quad (6.3)$$

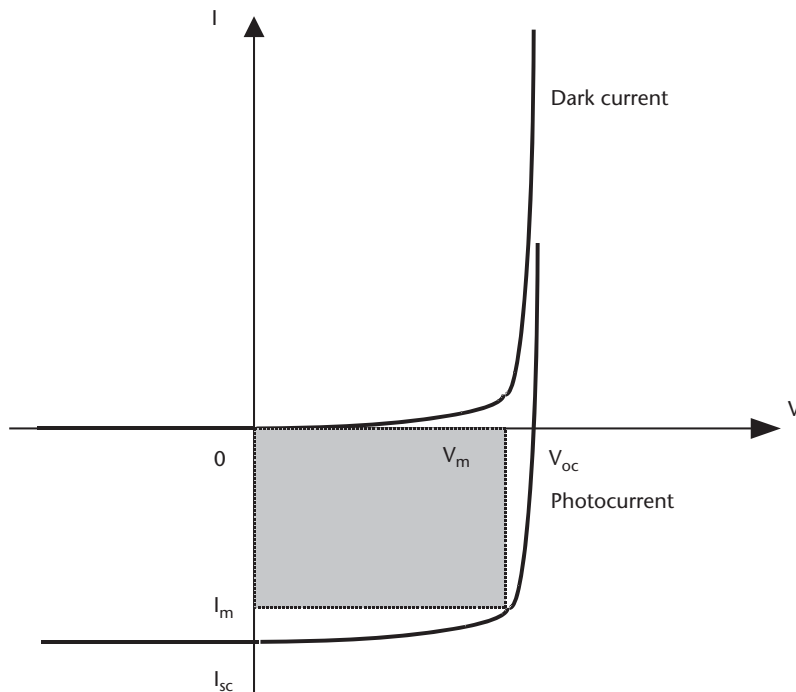
The maximal power can be found from the condition of  $dP/dV = 0$ :

$$P_m = I_m V_m \approx I \left[ V_{oc} - \frac{kT}{e} \left( \ln \left( 1 + \frac{eV_m}{kT} \right) - 1 \right) \right] = \frac{I}{e} E_m \quad (6.4)$$

where  $E_m$  is the maximal energy extracted from the solar cell. The efficiency of a solar cell ( $\eta$ ) can therefore be defined as:  $\eta = \frac{E_m}{E_{light}}$ , where  $E_{light}$  is the energy of light incident of the solar cell.

One purely methodological problem of solar cell measurements has to be addressed at this stage. Although the Schottky formula for the current-voltage characteristic of p-n junctions is used in the above derivation, it does not mean that solar cells have to be studied by measuring their I-V characteristics. In a majority of publications, the measurements of I-V curves in the darkness and under illumination are used to evaluate the maximum power, as shown in Figure 6.3.

The critical points,  $I_{sc}$  and  $V_{oc}$ , are the same as on the load characteristic [see Figure 6.2(b)]. However, the I-V dependence in the fourth quarter might vary because of different physical conditions, such as the position of quasi-Fermi levels, the recharge of the traps or surface states, or the injection of carriers from contacts. In some situations, both methods of I-V and load characteristics can give the same results, but this is not always the case for heterostructures, multilayered structures,



**Figure 6.3** I-V characteristics of p-n junctions in the darkness and under illumination, and the evaluation of the maximal power.

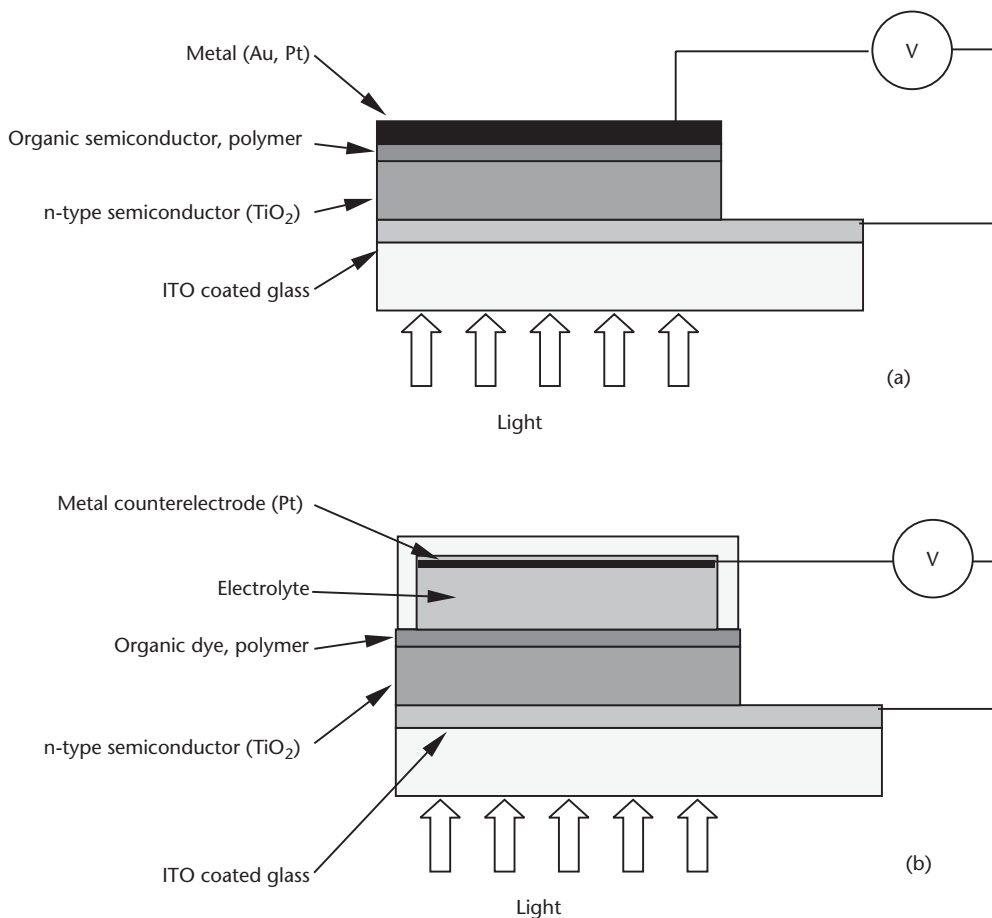
and organic materials. The recommendation is to use the more universal load characteristic method with a high resistance input voltmeter and a variable load resistor, as shown in Figure 6.2. We are not supposed to apply a voltage to a solar cell, but to extract it.

The efficiency can be calculated numerically or graphically for p-n junctions made from certain semiconducting materials, by using the solar spectrum and the dependence of  $E_m$  on the bandgap of semiconductors,  $E_m(E)$  [65]. The calculation yields the maximum possible value of 31% for the p-n homojunction made from the material with  $E_g = 1.35$  eV, which is close to GaAs. In fact, all semiconductor materials having  $E_g$  in the range of  $1.1 \div 1.5$  eV give the same efficiency of approximately 30%. Therefore, the efficiency of modern silicon solar cells, which range from 25% to 28%, is very close to the theoretical limit. It is interesting that the cascaded p-n junctions with different  $E_g$  or heterojunctions can give much high efficiency up to 72% [65]. This fact stimulates the research in the solar cells based on new semiconductor materials and their combinations in cascades and heterostructures.

During the last 30 years, all possible combinations of materials in p-n junctions and metal-semiconductor Schottky contacts were tested as photodetectors and solar cells. The most suitable combinations for solar cells applications can be separated into two classes. First, there are either purely solid-state devices, built on either single type semiconductor materials, similar to that shown in Figure 6.1(a), or heterojunctions consisting of two or more different semiconductor materials, including organic semiconductors or conducting polymers. Second, there are devices based on dye-sensitized semiconductor electrodes with an electrolyte contact, often referred to as Graetzel's cells [66]. The homojunction devices are mostly based on silicon, including polycrystalline and hydrogenated amorphous silicon. These devices are described in [67], and are not considered here. Both designs (solid-state devices and electrolyte contact devices) are shown in Figure 6.4.

The common characteristic of both designs is the transparent substrate (glass or polymer), with the conductive ITO coating. The n-type semiconducting layer must be transparent in the visible range. One of the best materials of this kind is  $\text{TiO}_2$ , which can be produced by different experimental techniques, including chemical routes of sol-gel [68, 69] or electrodeposition [70].

Since  $\text{TiO}_2$  does not absorb light in the visible range, a layer of light-absorbing organic material (i.e., a sensitizing layer) must be deposited on top. This can be a thin film of organic semiconductors, such as phthalocyanines [68, 71] that have a very strong adsorption coefficient (in the range from  $10^4$  to  $10^5$   $\text{cm}^{-1}$ ) in the visible spectral range, and, at the same time, have a p-type conductivity, which helps to separate the electron-hole pairs generated by light. Many other organic materials are used as light-absorbing and hole-conducting media [72], including porphyrines [73] or cyanine and merocyanine dyes [74]. Conjugated polymers are another excellent choice of light-absorbing and conducting materials for solid-state solar cells [75–79]. Conjugated polymers can be used in photovoltaic devices in many different ways: as light-harvesting materials, and a hole conducting material [75–84]; as n-type materials for charge separation [79, 85]; and as materials for both top and bottom contacts [86]. A combination of the above has resulted in the fabrication of fully plastic photovoltaic devices and solar cells [85]. Great progress in organic solar cells has been recently achieved using fullerene C60 as a light-harvesting material [87–90].



**Figure 6.4** (a) Solid-state photovoltaic cell, and (b) electrolyte photovoltaic cell.

Fullerene/conjugated polymer bulk heterojunctions, formed by two interpenetrating donor-acceptor networks, improves the efficiency of solar cells, and shows the way for commercial development of fully plastic photovoltaic devices. The same concept of interpenetrating networks is exploited in the case of carbon nanotubes/polymer composite materials having twice the quantum efficiency compared to standard ITO-based devices [91].

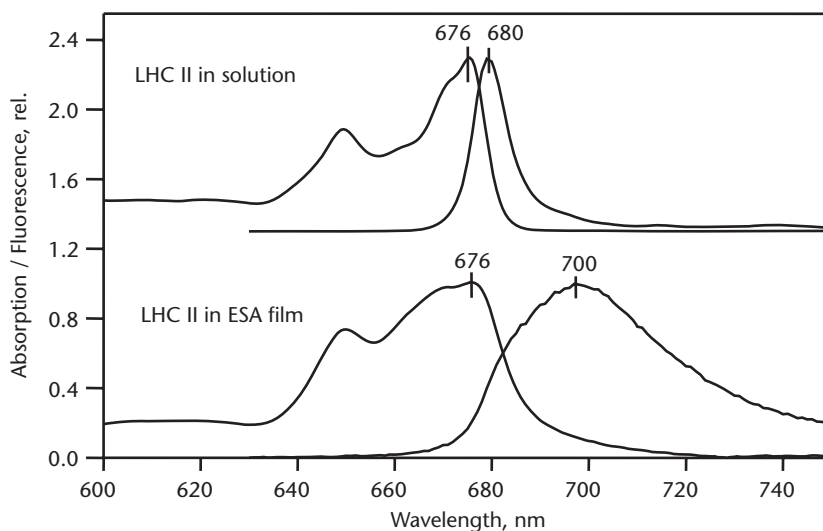
The main criterion for selecting the light-harvesting layer is a high quantum yield and the best possible coverage of the visible spectral range. Ruthenium complexes are very good candidates for this role [92–95]. Sometimes combinations of two or more different dyes are used in order to cover the entire solar spectrum [96–98].

It is difficult to imagine a light-harvesting complex more efficient than chlorophyll, which is why solar cells, sensitized with either chlorophyll derivatives or natural light-harvesting complexes containing chlorophyll, is a very promising direction in solar cell development [99–101]. An attempt to deposit a light-harvesting complex (LHC-II) extracted from leaves onto solid substrates, using the electrostatic self-assembly technique, has been done in [102]. The absorption spectra of

LHC-II/PAH ESA films demonstrate two characteristic adsorption bands, one in a range from 435 to 470 nm, and another at 680 nm, with a linear dependence of the absorbance on the number of LHC-II/PAH layers deposited. The films retained their optical activity. Their luminescence spectra, as shown in Figure 6.5, are similar to that of LHC-II in solution, but slightly broadened, perhaps due to the aggregation of LHC-II complexes in the solid phase. A larger Stokes shift of the LHC-II luminescence, observed in ESA films, can be attributed to the strong Coulomb interaction between LCH-II and polycation layers.

Ideally, the light-harvesting organic layer must have a p-type conductivity, and form a heterojunction with an n-type titania layer, in order to separate electron-hole pairs generated by light. Alternatively, charge separation can be achieved by bringing dye molecules into direct contact with the electrolyte containing ion redox-couples. As a result of the photoelectrochemical reaction between the dye and the electrolyte, electrons drain into  $\text{TiO}_2$ , and positive ions in the electrolyte drift and discharge on the metal counterelectrode (usually made of chemically inert Pt). For this type of device, the area of the dye/semiconductor interaction must be as large as possible, which can be achieved by using porous  $\text{TiO}_2$  layers [103–105]. Such nanoporous semiconductor layers can be formed by depositing and sintering titania nanoparticles [106]. Other semiconductor layers of metal nanoparticles can improve the efficiency of solar cells because of their sensitizing properties [107–110]. Other semiconductors, such as metal oxide [111–114] and II-V [115–118] semiconductor materials, can be used as photocathodes.

The role of the electrolyte is very important for the performance of Graetzel's solar cells. A typical drawback of electrolytic solar cells is the limitation on the ion drift through the electrolyte, with the immediate effect on the efficiency at a high level of irradiation. In order to improve the performance, some additives that increase the ion conductivity of the electrolytes must be used. From the engineering point of view, liquid contact is not preferred, due to the extra effort of sealing the device, the high probability of the electrolyte leaking out or drying, and the



**Figure 6.5** Fluorescence (excitation and emission spectra) of LHC-II in (top) solution, and (bottom) ESA film.



temperature limitations. The use of highly conductive solid electrolytes might be an excellent engineering solution for solar cells [119–122].

However, fully solid-state solar cell devices are preferable for industry. The heterojunctions based on II-VI [123–130] and III-V materials [131–134], produced by the chemical techniques of either electrodeposition or sol-gel [135], can offer a cost-effective alternative to silicon solar cells. Such heterostructures have the potential for further development, with the goal of achieving the theoretically predicted light conversion efficiency of approximately 70%. Some other cost-effective techniques, such as screen-printing [136] or layer-by-layer electrostatic self-assembly [137], can be successfully exploited for solar cell fabrication.

The characteristics of solar cells and their performance, including light conversion efficiency and long term stability, are studied extensively in [138–145], and the conclusions can be summarized as follows. Silicon-based solar cells are still the most popular and commercially viable, but they have almost reached the theoretical maximum of the efficiency. Electrolyte-based solar cells are very inexpensive, but the efficiency of the best devices is typically in the range from 7% to 10%. However, they are not stable, and their characteristics tend to degrade during exploitation. Other typical faults include drying out or leaking out of the electrolyte, and the resultant environmental problems. Very often, their efficiency under full sun illumination can drop dramatically due to the limitation of ion supply. The dry solar cells based on solid electrolytes have a lower efficiency, approximately 8% in the best designs, but have more potential for long-term stability and exploitation. Purely solid-state semiconductor solar cells, with their efficiency reaching 18%, constitute a very promising direction in solar cells research and development, because of their potentially very high efficiency (approximately 70%) and stability. There are some concerns, however, regarding the cost, mechanical flexibility, and environmental effects of toxic halcogenide components. The use of conductive polymer or polymer/inorganic composites in solar cells constitutes a very promising direction, especially considering the unique mechanical properties of these materials.

### 6.2.2 Light-Emitting Devices

Light-emitting devices (LEDs) are one the main applications of materials processed by chemical routes, which include purely organic materials, nanostructured inorganic materials, and their composites. The discovery of conducting polymers [146–148], which was awarded the Nobel Prize in Chemistry in 2000, has resulted in a great development of polymer-based devices, such as diodes, transistors, light-emitting devices, and photovoltaic devices. Similar to sensors, a huge variety of organic materials (as compared to the rather limited selection of inorganic semiconductors) can offer greater electronic and optical properties [149]. This results in the commercial production of organic LEDs which have high efficiency and brightness, cover the entire visible spectral range, and offer unique mechanical properties (e.g., flexibility and light weight). Finally, they are substantially less expensive than solid-state LEDs.

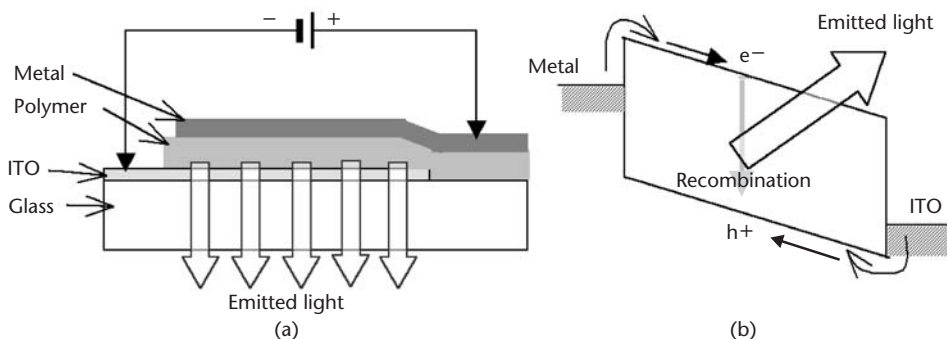
The physics background of light-emitting devices is the effect of electroluminescence discussed in Chapter 4. LEDs prepared by chemical routes can be separated into two classes: (1) LEDs based on semiconducting polymers, and (2) LEDs based on nanostructured inorganic materials, mostly colloid semiconductor nanoparticles.

The operational principles of polymer LEDs were developed in 1990s (see [150–169]), and they are described briefly next. Polymer LEDs are typically deposited on the transparent insulating substrates with transparent conductive coating, for example, ITO coated glass. Sometimes, instead of ITO, transparent conductive polymers can be used. The polymer layer (or layers) can be deposited by spin coating, and metal electrodes are evaporated on top. The structure of a polymer-based LED is shown in Figure 6.6, along with the respective band diagrams.

The injection of carriers from the metal contact is accompanied by the direct recombination of the carriers in the polymer bulk. Polymer LEDs can operate as monopolar or bipolar devices, depending on the concentration of electrons and holes, and their mobility. In bipolar devices, the injection and conductivity of both types of carriers (electrons and holes) takes place [157]. The scheme in Figure 6.6 is very simple. In reality, it is much more complex, and comprises several polymer layers serving as blocking layers for holes or electrons, thus providing monopolar operation conditions [158]. The efficiency of polymer LEDs is not high. The theoretical analysis shows that the luminescence yield in polymer LEDs cannot be more than one-fourth of the photoluminescence, due to spin statistic; however, a much smaller luminescent yield, approximately 5% or less, is observed experimentally [157]. The efficiency of LEDs can be substantially improved by using metals with a low work function (e.g., Ca instead of Al [158]).

A large number of different conjugated polymer materials were exploited for the development of LEDs. They include poly(vinylene) [150], poly(phenylene ethynylene) [170], PPV [171], oxadiazole [172], thienylene-phenylene copolymers [173], and many others. Polymer-based LEDs cover the entire visible spectral range, particularly, the blue region [174–180]. The combination of different types of conjugated polymers in the same device allows the fabrication of white LEDs, due to overlapping of their emission spectra [181]. Recent reports discuss the formation of novel polyfluorene based LEDs, having high power efficiency and bright emission in the blue spectral region [178–180, 182–187]. A slightly different approach in LED fabrication is proposed in [188], using solid electrolytes and polyelectrolytes. LEDs based on silicon alternated copolymers are proposed in [189].

Following the trend of scaling down microelectronic and opto electronic devices, the arrays of submicron-size LEDs have been fabricated [190]. The shape of microLEDs arrays is a subject of an investigation with the aim of further improvement of LED efficiency [191–193].



**Figure 6.6** (a) Schematic diagram of a polymer LED, and (b) its energy band diagram.

An alternative approach in LED development is based on the use of inorganic semiconductor nanoparticles. The principles of electroluminescence in semiconductor nanostructures is described in Chapters 4 and 5. The efficiency of the luminescence of inorganic materials is generally higher than that of organic ones. The principles of LEDs based on nanostructured inorganic semiconductor materials is described in [194, 195]. The control of the spectral position of the emission band can be achieved by varying the size of nanocrystallites or nanoparticles [196–210].

Traditionally, nanoparticles made of II-VI and III-V semiconductors, having direct band recombination, constitute the majority of LEDs [197–201]. The interesting observation of anti-Stokes photoluminescence (i.e., photon energy upconversion) from size-quantized CdSe and InP nanocrystalline colloids is reported in [200]. The explanation of anti-Stokes photoluminescence involves surface states.

Some other methods of processing of nanostructured materials, such as sol-gel [202], laser ablation [203], and sono-chemistry [204], can be exploited for the formation of light-emitting nanostructured materials. In the latter method, a combination of the standard colloid chemistry approach with ultrasonic treatment has resulted in the nanoparticles of well-controlled size and low dispersion in size, which is very important for the production of electron devices, particularly LEDs. As described in Chapters 2 and 4, the method of electrostatic self-assembly can be very useful for the deposition of thin films containing semiconductor nanoparticles, used in the formation of LEDs covering the whole visible spectral, as well as white light emitters [205–210].

Other semiconductor materials can be used in LEDs, including silicon, which is a nondirect gap material that shows no luminescence in the bulk form. However, nanostructured silicon, which derives from porous silicon, shows reasonable amounts of luminescence in the visible range [211, 212].

The combination of conducting polymers with inorganic semiconductor nanoparticles is another very promising direction in the development of optoelectronic devices, particularly LEDs [60, 118, 208, 213–215].

Conjugated conducting (semiconducting) polymers can be nanostructured, using either electrophoresis [216] or the reverse micelle method [217]. This gives an additional means to control the luminescence spectral bands of polymers, by varying the size of clusters. Another original method of the formation of nanosized polymers is the use of dendrimers [218]. Fullerene molecules C<sub>60</sub>, which can be regarded as oligomers, can also be exploited in optoelectronic devices [87–90, 219].

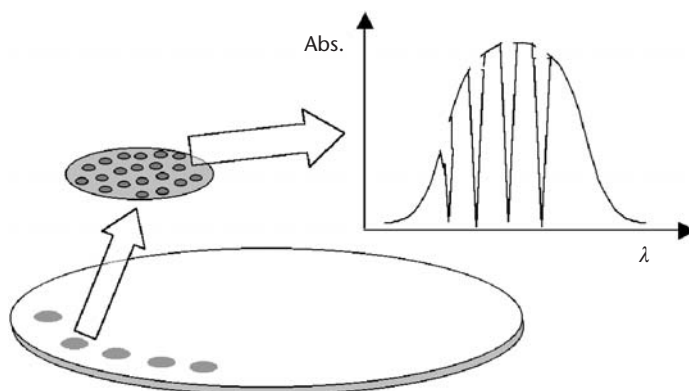
### 6.2.3 Optical Memory Devices

The idea of optical memory devices was suggested in the 1980s during the first wave of interest in molecular electronics. Theoretical aspects of optical molecular memory were well understood by that time. The phenomena of photochromism and electrochromism (the basis of modern optical memory devices) were known, and organic molecules having the necessary properties were synthesized and studied [220]. What was missing were reliable nanotechnologies and analytical tools for the commercial development and fabrication of optical memory devices. It took from 10 to 15 years until optical memory devices started to appear on the market. A number of optical memory devices ready for commercial development were reported in the 1990s [221–227].

Several physical phenomena are exploited in optical memory devices. The list includes photochromism, electrochromism, thermochromism, and magnetochromism. These phenomena are based on spectral changes of the material caused by photo excitation, applied voltage, changes in the temperature, and magnetic field, respectively. The criteria for their commercial application in optical memory devices are the stability of optical spectral changes, their spatial resolution, and reversibility (i.e, the ability to erase or rewrite the information). For example, reversible color changes (between yellow and blue) in thin films of charge transfer (CT) complexes of tetrakis[3,5-bis(trifluoromethyl)phenyl]borate are reported in [221]. The photochromic effect in polymer-TCNQ charge transfer complexes at 830-nm illumination is reported in [225]. The electrochromic effect (i.e., a reversible switch from green to red, in response to the application of an external bias of +1.2V and -1.5V, respectively), was observed in polymer films of poly(1-vinyl-2-pyrrolidinone-co-N,N'-methylenbisacrylamide (PVPD) containing organic electrochromics *p*-diacetylbenzene (*p*-DAB), dimethyl- or diethyl terephthalate [222].

In addition to the spin coating and casting deposition techniques typical for polymer materials, the sol-gel technology was suggested for the fabrication of optical storage media [226]. Hybrid organic-inorganic materials (i.e., ceramics modified with organic materials) are produced by this technique, and show both photochromic and thermochromic behavior. Thermo-optic switching behavior is also observed in 4',7-dihydroxyflavylium medium, which may lead to the development of write-read-erase molecular memory devices [228]. Another promising direction of optical memory is the use of liquid crystals with the photo-induced chiral transformations of chromophores [229, 230].

Other mechanisms of optical memory involve the magneto-optic effect, spectral hole burning (SHB) [223, 224], and nonlinear optics (e.g., two-photon absorption) [227, 231]. The effect of SHB is observed in polymers with imbedded organic dyes, rare Earth elements, or inorganic II-VI and III-V semiconductors [232–235]. Normally, the absorption spectra of such materials are inhomogeneously broadened due to the aggregation of chromophores. The illumination of the SHB material with a high intensity laser beam, having the spectral band much narrower than that of the broad spectral line of chromophore aggregates, causes a large number of HOMO-LUMO electron transitions, and thus an exhaustion of HOMO levels. A



**Figure 6.7** The scheme of the spectral hole burning (SHB) optical memory.

narrow gap (hole) in the absorption spectra appears after the laser illumination. Using tunable powerful lasers, it is possible to “burn” a number of “spectral holes” in the absorption spectral band, as shown in Figure 6.7.

The spectral position of the “hole” gives an additional parameter to the spatially resolved pixels, and allows a huge increase in the memory capacity, by a factor ranging from  $10^3$  to  $10^9$  times, depending on a number of spectral holes burned in one pixel [232, 236]. The generation of phonons, however, acts in the opposite direction of “healing” the spectral holes, and thus causes the spontaneous erasing of the information. That is why the operating temperature of SHB memory devices is limited to 77K (the temperature of liquid nitrogen). Recent progress in optical storage materials made possible the operation of SHB optical memory at room temperature [237, 238].

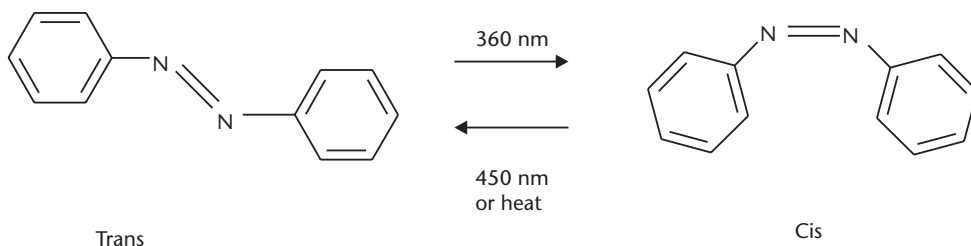
Another obvious method of increasing the density of stored information is to use smaller memory dots (pixels), preferably in submicron, or even nanometer, range. Near-field scanning optical microscopy (NFSOM) seems to be an ideal technical tool to achieve this [239, 240]. The cis-trans transition in azobenzene dyes, as shown in Figure 6.8, accompanied by the characteristic spectral changes in azobenzene dye molecules [241], is exploited for optical switching [240].

The use of NFSOM for writing in self-assembled films of azobenzene derivatives is demonstrated in [240, 242–244]. The electromagnetic field, amplified hundreds of times under the nanotip, becomes sufficient to cause cis-trans transitions in an azobenzene film in a local nanometer-size area under the tip. The required image can be formed by scanning the tip over the film. Another nanoscopic technique of surface potential (scanning Kelvin probe) is used in the above works to visualize the effect of writing [243].

In the last decade, conducting polymers have become the main building blocks of optical memory devices [245–250]. A natural way of increasing the memory capacity is the decrease in the size of elementary pixels by using nanoparticles. Recent reports discuss the development of optical memory devices based on films containing semiconductor nanoparticles [251–253] and polymer/nanoparticles composites [254–257].

### 6.3 Quantum Nanoelectronic Devices

Principles of quantum electron devices are described in Chapter 5. Two types of quantum electronics devices, RTDs and SETs, are discussed in detail, and several examples of RTDs and SETs produced by chemical methods are given.



**Figure 6.8** Trans-cis transition in the azobenzene dye.

Nanostructured materials produced by chemical methods can be successfully used for the fabrication of RTDs and SETs. As mentioned in Chapter 5, SETs can be simply formed by placing metal or semiconductor colloid nanoparticles in the gap of planar tunneling junctions, formed by nanolithography [258, 259]. Organic analogs of RTDs can be created in conducting polymer superlattices [260–263]. This section, however, is mostly focused on quantum dot devices.

### 6.3.1 Quantum Computing

The idea of quantum computing using the array of quantum dots was developed theoretically during last three decades [264–269]. Let us consider a two-dimensional matrix of cells having several logic states (0 and 1 in the simplest case), where each cell can interact with the closest neighboring cells. The mathematical meaning of the interaction between cells lies in the ability of a cell to change its logic state depending on the logic states of its neighbors. Such systems, called cellular automata, were a popular subject of computer modeling. A good example of such a system is the computer game “Life” [270], which operates in a two-dimensional matrix of square cells. The color of each cell depends on the colors of the eight neighboring cells, following some simple rules. For example, in the simplest case of binary (black and white) “Life,” the cell is black (logic “1,” or live cell), if it has more than one black neighbor. The cell dies (becomes white, or logic “0”) from overpopulation, when four or more neighbors are black. Exactly three black neighbors give birth to a new black cell. The matrix can be triggered by the initial generation of a number of black cells. The color (logic state) of the cells updates in regular time intervals following the PC clock. Such simple rules produce fascinating results. The matrix becomes alive, with some patterns moving about, changing shape, growing and shrinking, or appearing and disappearing. Some patterns show unstable behavior and disappear (die) soon after the generation; some patterns are stable in either the stationary, pulsating, or moving forms, and can live eternally. Even this simplest version of “Life” is fascinating to watch, but the multicolor version of “Life,” in which new rules can be designed and applied, is really something special. It is not just a game; it is a future of computing with some very interesting mathematics behind it. Without going deeply into cellular automata mathematics, it can be said that, depending on the relations between neighboring cells, the matrix can perform some mathematical operations (e.g., integration or Fourier decomposition). In some cases, the patterns generated by the matrix show fractal behavior, with the reproduction of the same shapes scaled up or down.

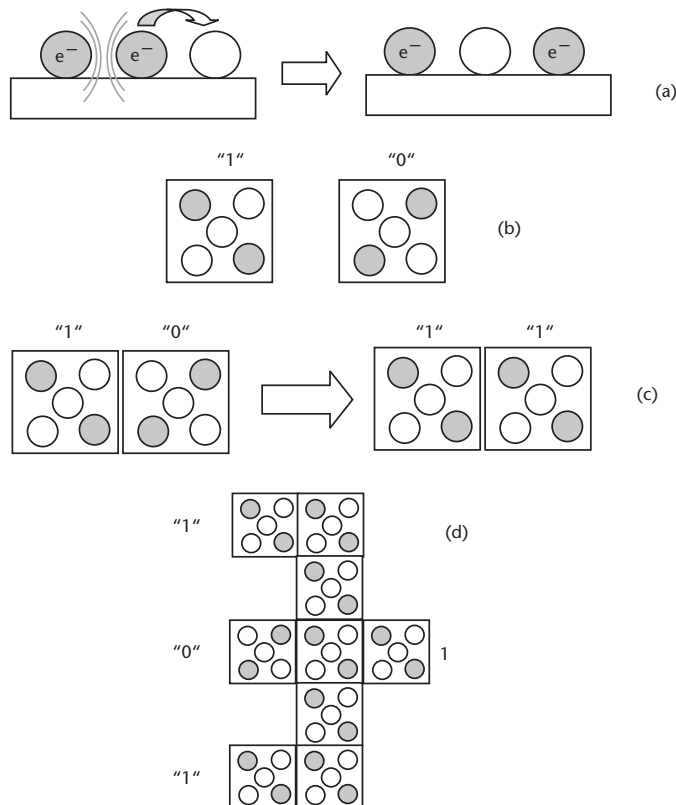
In order to transfer the principles of cellular automation from the software level to the real quantum computing systems, two steps must be taken: first, arrange the quantum dots (i.e., nanoparticles, or nanoislands) into regular two-dimensional arrays; and, second, establish connections between the QDs by means of some physical interaction (e.g., optical, magnetic, or electrical). Then, the matrix of QDs has to be connected to input and output devices. From this point of view, fractal properties of the matrix can be a great help in transferring the signal pattern from the nanometer scale QDs to the micrometer scale of input and output devices. Cellular automata may help to resolve the biggest problem of future super-computers, which will have elementary devices in the nanometer scale, and will require a physical connection (i.e., addressing) to each cell.



Cellular automata, based on the principles of parallel computing, have another great advantage of high reliability. In contrast to conventional computers, which are based on binary logic gates and are thus very sensitive to the failure of a small number of logic cells, cellular automata can operate even when a large number (up to 20%) of cells are faulty [270].

A simple example of arrays of QDs interacting electrostatically is described in [220]. In the array of nanoparticles, which are firmly paced on the substrate and separated by small gaps comparable with the electron tunneling distance ranging from 2 to 3 nm, the electron charge can propagate along the chain following the relay mechanism, as shown in Figure 6.9(a). The driving force of such electron transfer is the electrostatic interaction between two negatively charged neighboring particles. As a result of this electrostatic repulsion, the electron will be transferred to the next particle.

However, the electron relay transfer in such a simple chain of nanoparticles is not reliable. Much better stability can be achieved using a cell containing five particles, as shown in Figure 6.9(b). This cell has two stable configurations, which can be treated as logical states “0” and “1.” As shown in Figure 6.9(c), the situation of two neighboring cells, having different configurations “1” and “0” (or “0” and “1”), is not energetically favorable (and thus not stable), and should be transformed to more energetically favorable (stable) situations of “1” and “1” (or “0” and “0”).



**Figure 6.9** (a) Electrostatic interaction in the linear array of quantum dots, (b) two stable logical states in five-dot cell, (c) switching process in the five-dot cell, and (d) majority gate made of five-dot cells. (From: [220]. © 1996 MITRE Corporation. Reprinted with permission.)



Therefore, the information can be transported along the row of five-dot cells. A number of logic gates can be created using these five-dot cells [220]. A simple example of the majority gate is shown in Figure 6.9(d). Such logic gates may constitute the basis of large scale computing systems.

The scheme shown above is still binary and suitable to sequential computing, but it does not require the wiring of every logical cell. More sophisticated systems of quantum dots that have anisotropic interaction between cells can work as cellular automata and perform parallel computing. Several physical principles of the operation of QD arrays were suggested recently, which includes resonance tunneling devices [271], single electron tunneling transistors [272], superconducting Josephson junctions [273], and dipole-dipole coupling [274]. A very promising idea of spintronic devices, based upon quantum dots with the electron spin as a logic state and spin-spin interaction between the QD, was developed in [275–280].

The progressive ideas of parallel quantum computing and cellular automation are adopted in silicon nanoelectronics, and are considered to be a possible road map for future nanoelectronic computers [281, 282]. It is interesting to note that the physical limitations of complementary metal-oxide-semiconductor (CMOS) devices are admitted in [282], and some other devices, such as single-electron transistors, were suggested for future applications, as well as for wireless architecture of quantum computing.

### 6.3.2 Practical Realization of Arrays of Quantum Dots

Chemical methods for the fabrication of nanostructures have found their application niche in a strong competition with traditional physical methods in solid-state microelectronics [283, 284]. In many respects, it is much easier to form regular arrays of nanoparticles on solid-state surfaces by using the principles of self-assembly, rather than by using very the expensive techniques of MBE or nanolithography. MBE is not suitable for this task, and does not provide the required level of regularity of QDs. Electron beam lithography may not give the required nanometer resolution for nanoislands. STM manipulation seems to be ideal for the formation of QDs in the required shape and arrangement [285, 286], but it is too slow to be considered as a practical technological tool in nanoelectronics. This section presents examples of different chemical approaches to the formation of regular arrays of quantum dots and attempts at their experimental realization.

The formation of regular arrays was attempted several times using gold colloid nanoparticles, which are a classical object in the field. The formation of chains of Au-55(PPh<sub>3</sub>)(12)Cl-6 clusters between tungsten tips on an SiO<sub>2</sub> surface is reported in [287, 288]. Measurements of I-V characteristics in these nanowires show the effect of Coulomb blockade at room temperature. The method of encapsulation of QDs in nanometer-thick silica shells is exploited in [289]. The obtained core-shell nanoparticles were deposited on solid surfaces to form two-dimensional and three-dimensional arrays of a macroscopic size with uniform particle spacing. A new approach to the ordering of gold colloid particles on the interface between water and dichloromethane is proposed in [280]. The water phase, which contains amphiphilic molecules of per-6-deoxy-6-thio- $\alpha$ -cyclodextrin (1) or poly(vinylpyrrolidone) (2), is covered by a thin film of [Au-55(PPh<sub>3</sub>)(12)Cl-6] in dichloromethane. The

interaction of the molecular cluster with the thiol groups forms clusters that are perfectly ordered in the hexagonal or cubic lattices. This is proven experimentally using TEM in [290]. The spontaneous formation of nanoparticle arrays on the air-water interface is reported in [291], where circular domains of nanoparticles are formed at low concentrations of nanoparticles on the water surface, while at high concentrations, the stripes appeared.

Electrical properties of one-dimensional arrays of gold clusters are studied in [292], and single electron transport features are confirmed in such systems.

The formation of superlattices that consist of layers of various quantum dots and their electrical properties are reviewed in [293]. Regular arrays of gold nanoparticles are formed on the surface of  $\text{SiO}_2$  via alkylthiols [294]. In this work, 3.7-nm gold nanoparticles, which are self-assembled on the surface of  $\text{SiO}_2$  between two metal electrodes of the tunneling junction, exhibit a nonlinear Coulomb charging behavior.

The substrate plays a significant role in the formation of regular arrays of nanoparticles. The modification of (100) and (111) surfaces of silicon and germanium with diacetylenes is considered a promising method for the formation of ordered nanostructures on top [295]. Theoretical analysis shows that attachments of diacetylenes on  $\text{Si}(100)\text{-}2\times 1$ ,  $\text{Ge}(100)\text{-}2\times 1$ , and  $\text{Si}(111)\text{-}7\times 7$  surfaces could produce monolayers of reactive cumulenic and/or enynic surface species capable of binding metal nanoparticles. The use of regular structures of adsorbed biopolymers for the arrangement of gold nanoparticles is demonstrated in [296].

Gold clusters encapsulated in the carboxylic anhydride shell can be successfully immobilized on amine-functionalized silica substrates, providing an ordered, two-dimensional arrangement in the gold cluster monolayers [297]. More advanced patterning of gold colloid arrays can be achieved with the AFM nanooxidation technique [298]. The surface of silicon was selectively oxidized, first by using a scanning AFM tip. Then, gold nanoparticles were self-assembled only on the oxidized patches via monolayers of amino-terminated molecules.

Gold nanoparticles are not unique in their ability to self-assemble. Regular arrays of nanoparticles of other materials (e.g., metals, semiconductors, or polymers) also can be formed by self-assembly [299–301]. The same strategy of the formation of regular assemblies can be applied to nanowires, nanotubes, and polynucleotides, as building blocks of nanoelectronic devices [302].

Nanowires and nanotubes have become the most popular objects in nanoelectronic research, because of their obvious applications in nanoelectronic and optoelectronic devices and sensors [303]. The most common approach in the formation of quantum wires is the use of porous materials (e.g., porous silicon, or silica) as templates. Fabrication of nanomaterials using porous alumina templates is described in [304–306].

A very interesting method of the synthesis of silver nanowires inside calix[4]hydroquinone nanotubes is described in [307]. The inner surface of calix[4]hydroquinone nanotubes contains hydrogen bonds, which can be used for the electrochemical synthesis of silver nanoparticles inside. Carbon nanotubes have become the most popular object of this kind due to their unique properties (e.g., exceptional mechanical strength, and high conductivity), and a wide range of possible applications in nanoelectronic devices and sensors [91, 308–318].

Another extremely promising direction of nanoelectronics is the formation hybrid nanobiological devices combining inorganic nanostructures (e.g., nanoparticles, nanowires, or nanotubes), with biological objects (e.g., proteins, or cells) [319, 320]. However, these exciting topics are beyond the scope of this book.

## References

- [1] Moore, G., "Progress in Digital Integral Electronics," *International Electron Device Meeting (IEDM), Tech. Digest*, 1975, pp. 11–13.
- [2] Petty, M. C., M. R. Bryce, and D. Bloor, (eds.), *An Introduction to Molecular Electronics*, London, England: Edward Arnold, 1995.
- [3] Petty, M. C., *Langmuir-Blodgett Films: An Introduction*, Cambridge, England: Cambridge University Press, 1996.
- [4] Hedrick, J. L., "From Spin-On to Self-Assembly: Current and Future Opportunities for Polymer Science in Advanced Microelectronics," *Abstr. Pap. Am. Chem. Soc.*, Vol. 225, No. 2, 2003.
- [5] Opila, R. L., and J. Eng, "Thin Films and Interfaces in Microelectronics: Composition and Chemistry as Function of Depth," *Prog. Surf. Sci.*, Vol. 69, No. 4–6, 2002, pp. 125–163.
- [6] Misman, O., et al., "PWB Compatible High Value Integral Capacitors by MOCVD," *J. Mater. Sci.-Mater. Electron.*, Vol. 11, No. 9, 2000, pp. 657–660.
- [7] Maier, G., "Low Dielectric Constant Polymers for Microelectronics," *Prog. Polym. Sci.*, Vol. 26, No. 1, 2001, pp. 3–65.
- [8] Chung, D. D. L., "Polymer-Matrix Composites for Microelectronics," *Polym. Polym. Compos.*, Vol. 8, No. 4, 2000, pp. 219–229.
- [9] Silvis, H. C., et al., "Design of Nanoporous Polyarylene Polymers for Use as Low-k Dielectrics in Microelectronic Devices," *Acs Symposium Series*, Vol. 874, 2004, pp. 187–198.
- [10] Bai, Y. Q., et al., "Photosensitive Polynorbornene Based Dielectric. I. Structure-Property Relationships," *J. Appl. Polym. Sci.*, Vol. 19, No. 5, 2004, pp. 3023–3030.
- [11] Hu, W., et al., "Synthesis of Fluorine-Containing Poly (aryl ether) with Low Dielectric Constant," *Chem. J. Chin. Univ.-Chin.*, Vol. 24, No. 1, 2003, pp. 184–185.
- [12] Chiniwalla, P., et al., "Multilayer Planarization of Polymer Dielectrics," *IEEE Trans. Adv. Packag.*, Vol. 24, No. 1, 2001, pp. 41–53.
- [13] Yamada, Y., "Siloxane Modified Polyimides for Microelectronics Coating Applications," *High Perform. Polym.*, Vol. 10, No. 1, 1998, pp. 69–80.
- [14] Buckley, L. J., and A. W. Snow, "Physical Properties and Microelectronic Applications of Low Permittivity Fluoromethylene Cyanate Ester Resins," *Vac. Sci. Technol.*, Vol. 15, No. 2, 1997, pp. 259–266.
- [15] Spassova, E., et al., "Low-Permittivity Evaporated Polymer-Polyimide," *Vacuum*, Vol. 47, No. 11, 1996, pp. 1345–1346.
- [16] Larlus, O., et al., "Silicalite-1/Polymer Films with Low-k Dielectric Constants," *Appl. Surf. Sci.*, Vol. 226, No. 1–3, 2004, pp. 155–160.
- [17] Boey, F. Y. C., A. I. Y. Tok, and W. J. Clegg, "Porous Reaction-Sintered AlN Tapes for High-Performance Microelectronics Application," *J. Mater. Res.*, Vol. 17, No. 2, 2002, pp. 306–314.
- [18] Xu, Y., et al., "Synthesis and Characterization of Porous Polymeric Low Dielectric Constant Films," *J. Electron. Mater.*, Vol. 30, No. 4, 2001, pp. 309–313.
- [19] Xu, Y. H., et al., "Dielectric Property and Microstructure of a Porous Polymer Material with Ultralow Dielectric Constant," *Appl. Phys. Lett.*, Vol. 75, No. 6, 1999, pp. 853–855.
- [20] Shi, F. F., L. A. Schneggenburger, and J. Economy, "New Photoimageable Dielectric Insulating Copolyester Thin Films: Synthesis and Characterization," *J. Appl. Polym. Sci.*, Vol. 63, No. 9, 1997, pp. 1199–1211.

- [21] Koehler, M., and I. Biaggio, "Influence of Diffusion, Trapping, and State Filling on Charge Injection and Transport in Organic Insulators," *Phys. Rev. B*, Vol. 68, No. 7, 2003, Art. No. 075205.
- [22] Kazantseva, Z. I., et al., "Physical Properties of Dielectric Langmuir-Blodgett Films on Silicon," *Ukrainskii Fizicheskii Zhurnal*, Vol. 34, No. 9, 1989, pp. 1398–1404 (in Russian).
- [23] Chabinyk, M. L., et al., "Molecular Electronics with a Metal-Insulator-Metal Junction Based on Self-Assembled Monolayers," *ACS Symposium Series*, Vol. 844, 2003, pp. 16–35.
- [24] Holmlin, R. E., et al., "Electron Transport Through Thin Organic Films in Metal-Insulator-Metal Junctions Based on Self-Assembled Monolayers," *J. Am. Chem. Soc.*, Vol. 124, No. 29, 2002, pp. 8762–8762.
- [25] Nabok, A. V., et al., "Electrical Study of Polyelectrolyte Self-Assembled Films Using Mercury Probe," *Material Science and Engineering C*, Vol. 22, 2002, pp. 387–391.
- [26] Nabok, A. V., et al., "The Study of Electron Tunneling Through Thin Polymer Films Using Mercury Probe Technique," *IEE Proceedings, Circuits, Devices, and Systems*, Vol. 151, No. 5, 2004, pp. 461–465.
- [27] De Oliveira, H. P., and C. P. De Melo, "Temperature and Frequency Dependence of the Electrical Properties of Thin Organic Films," *Mol. Cryst. Liquid Cryst.*, Vol. 374, 2002, pp. 527–536.
- [28] De Oliveira, H. P., F. L. Dos Santos, and C. P. De Melo, "Low Temperature Behavior of the Resistivity of Thin Organic Films," Vol. 121, No. 1–3, *Synth. Met.*, 2001, pp. 1429–1430.
- [29] Asai, K., et al., "An Application of Electrolytic Deposition for the Electronic Passivation of GaAs-Surfaces Through the Formation of Thin Organic Films," *Surf. Sci.*, Vol. 306, No. 1–2, 1994, pp. 37–41.
- [30] Sentein, C., et al., "Influence of Stereoregularity on the Photoinitiated Electrical Conductivity of Poly(3-alkylthiophenes)," *Synth. Met.*, Vol. 83, No. 1, 1996, pp. 27–37.
- [31] Punkka, E., and M. F. Rubner, "Molecular Heterostructure Devices Composed of Langmuir-Blodgett-Films of Conducting Polymers," *J. Electron. Mater.*, Vol. 21, No. 11, 1992, pp. 1057–1063.
- [32] Bohler, A., et al., "Organic Heterostructures for Electronic and Photonic Devices," *Physica E*, Vol. 2, No. 1–4, 1998, pp. 562–572.
- [33] Sentein, C., et al., "Molecular Rectification in Oriented Polymers," *J. Chim. Phys.-Chim. Biol*, Vol. 95, No. 6, 1998, pp. 1331–1334.
- [34] Parthasarathy, G., et al., "A Metal-Free Cathode for Organic Semiconductor Devices," *Appl. Phys. Lett.*, Vol. 72, No. 17, 1998, pp. 2138–2140.
- [35] Sentein, C., et al., "Study of Orientation Induced Molecular Rectification in Polymer Films," *Opt. Mater.*, Vol. 9, No. 1–4, 1998, pp. 316–322.
- [36] Rogers, J. A., Z. N. Bao, and V. R. Raju, "Nonphotolithographic Fabrication of Organic Transistors with Micron Feature Sizes," *Appl. Phys. Lett.*, Vol. 72, No. 21, 1998, pp. 2716–2718.
- [37] Yu, G., and A. J. Heeger, "High Efficiency Photonic Devices Made with Semiconducting Polymers," *Synth. Met.*, Vol. 85, No. 1–3, 1997, pp. 1183–1186.
- [38] Friend, R. H., "Semiconductor Device Physics with Conjugated Polymers," *Phys. Scr.*, Vol. T66, 1996, pp. 9–15.
- [39] Yu, G., "High Performance Photonic Devices Made with Semiconducting Polymers," *Synth. Met.*, Vol. 80, No. 2, 1996, pp. 143–150.
- [40] Riul, A., C. A. Mills, and D. M. Taylor, "The Electrical Characteristics of a Heterojunction Diode Formed from an Aniline Oligomer LB-Deposited onto Poly(3-methylthiophene)," *J. Mater. Chem.*, Vol. 10, No. 1, 2000, pp. 91–97.
- [41] Scheinert, S., and G. Paasch, "Fabrication and Analysis of Polymer Field-Effect Transistors," *Phys. Status Solidi A-Appl. Res.*, Vol. 201, No. 6, 2004, pp. 1263–1301.
- [42] Cui, T. H., Y. X. Liu, and K. Varshneyan, "Fabrication and Characterization of Polymeric p-Channel Junction FETs," *IEEE Trans. Electron Devices*, Vol. 51, No. 3, 2004, pp. 389–393.

- [43] Hiller, J., and M. F. Rubner, "Reversible Molecular Memory and pH-Switchable Swelling Transitions in Polyelectrolyte Multilayers," *Macromolecules*, Vol. 36, No. 11, 2003, pp. 4078–4083.
- [44] Ben Chaabane, R., et al., "Study of Organic Thin Film Transistors Based on Nickel Phthalocyanine: Effect of Annealing," *Thin Solid Films*, Vol. 427, No. 1–2, 2003, pp. 371–376.
- [45] Li, Z. L., et al., "Patterning-Free Integration of Polymer Light-Emitting Diode and Polymer Transistor," *Appl. Phys. Lett.*, Vol. 84, No. 18, 2004, pp. 3558–3560.
- [46] Ahles, M., et al., "Light Emission from a Polymer Transistor," *Appl. Phys. Lett.*, Vol. 84, No. 3, 2004, pp. 428–430.
- [47] Nagamatsu, S., et al., "Effects of Molecular Alignment on Carrier Transport in Organic Transistors," *Synth. Met.*, Vol. 137, No. 1–3, 2003, pp. 923–924.
- [48] Park, S. K., et al., "Electrical and Mechanical Properties of Low Temperature Evaporated Silicon Dioxide/Polyimide Dual-Layer Insulator for Plastic-Based Polymer Transistor," *Thin Solid Films*, Vol. 429, No. 1–2, 2003, pp. 231–237.
- [49] Wang, W., et al., "Electrical Characterization of Metal-Molecule-Silicon Junctions," *Ann. NY Acad. Sci.*, Vol. 1006, 2003, pp. 36–47.
- [50] Veenstra, S. C., and H. T. Jonkman, "Energy-Level Alignment at Metal-Organic and Organic-Organic Interfaces," *J. Polym. Sci. Pt. B-Polym. Phys.*, Vol. 41, No. 21, 2003, pp. 2549–2560.
- [51] Yan, L., and Y. L. Gao, "Interfaces in Organic Semiconductor Devices," *Thin Solid Films*, Vol. 417, No. 1–2, 2002, pp. 101–106.
- [52] Ichikawa, M., et al., "Exciton Dynamics in Organic Semiconductor Devices: Investigation of Exciton-Charge Carrier Interactions as Revealed by Photoluminescence Responses," *Jpn. J. Appl. Phys. Part 2—Lett.*, Vol. 40, No. 10A, 2001, pp. L1068–L1070.
- [53] Sirringhaus, H., et al., "High-Resolution Inkjet Printing of All-Polymer Transistor Circuits," *Science*, Vol. 290, No. 5499, 2000, pp. 2123–2126.
- [54] Krumm, J., et al., "A Polymer Transistor Circuit Using PDHTT," *IEEE Electron Device Lett.*, Vol. 25, No. 6, 2004, pp. 399–401.
- [55] Kowalsky, W., et al., "Organic Molecular Beam Deposition: Technology and Applications in Electronics and Photonics," *PCCP Phys. Chem. Chem. Phys.*, Vol. 1, No. 8, 1999, pp. 1719–1725.
- [56] Simon, P., et al., "Electron Holography of Organic and Biological Materials," *Adv. Mater.*, Vol. 15, No. 17, 2003, pp. 1475–1481.
- [57] Jahromi, S., et al., "In situ Polymerisation of Pyrrole in Nanochannels Produced by Means of AFM Lithography," *ChemPhysChem*, Vol. 3, No. 8, 2002.
- [58] Hagedorn, M. S., et al., "Silicon Metal-Oxide-Semiconductor Field-Effect Transistor with Gate Structures Defined by Scanned Probe Lithography," *J. Vac. Sci. & Technol. B*, Vol. 14, No. 6, 1996, pp. 4153–4156.
- [59] Castelvetro, V., and C. De Vita, "Nanostructured Hybrid Materials from Aqueous Polymer Dispersions," *Adv. Colloid Interface Sci.*, Vol. 108–09, 2004, pp. 167–185.
- [60] Kovac, J., L. Peternai, and O. Lengyel, "Advanced Light Emitting Diodes Structures for Optoelectronic Applications," *Thin Solid Films*, Vol. 433, No. 1–2, 2003, pp. 22–26.
- [61] Forrest, S. R., "Active Optoelectronics Using Thin-Film Organic Semiconductors," *IEEE J. Sel. Top. Quantum Electron.*, Vol. 6, No. 6, 2000, pp. 1072–1083.
- [62] Caciali, F., "Organic Semiconductors for the New Millennium," *Philos. Trans. R. Soc. Lond. Ser. A-Math. Phys. Eng. Sci.*, Vol. 358, No. 1765, 2000, pp. 173–192.
- [63] Godovsky, D. Y., "Device Applications of Polymer-Nanocomposites," *Adv. Polymer Sci.*, Vol. 53, 2000, pp. 163–205.
- [64] Donati, S., *Photodetectors: Devices, Circuits, and Applications*, Upper Saddle River, NJ: Prentice-Hall, 2000.
- [65] Sze, S. M., *Physics of Semiconductor Devices*, 2nd ed., New York: John Wiley & Sons, 1981.



- [66] Redmond, G., D. Fitzmaurice, and M. Graetzel, "Visible-Light Sensitization by Cis-bis(thiocyanato)bis(2,2'-bipyridyl-4,4'-dicarboxylato)ruthenium(II) of a Transparent Nanocrystalline ZnO Film Prepared by Sol-Gel Techniques," *Chem. Mater.*, Vol. 6, No. 5, 1994, pp. 686–691.
- [67] Rath, J. K., "Low Temperature Polycrystalline Silicon: A Review on Deposition, Physical Properties and Solar Cell Applications Solar Energy," *Materials and Solar Cells*, Vol. 76, No. 4, 2003, pp. 431–487.
- [68] Ray A. K., S. M. Tracey, and S. N. B. Hodgson, "Photoelectric Measurements on Chloroaluminium Phthalocyanine/Titanium Oxide Heterojunctions," *J. Sol-Gel Sci. Technol.*, Vol. 22, No. 1–2, 2001, pp. 15–22.
- [69] Ray, A. K., et al., "Optical Studies on Sol-Gel Derived Titanium Dioxide Films," *IEE Proc.-Sci. Meas. Technol.*, Vol. 147, No. 6, 2000, pp. 301–305.
- [70] Kavan, L., et al., "Preparation of TiO<sub>2</sub> (Anatase) Films on Electrodes by Anodic Oxidative Hydrolysis of TiCl<sub>3</sub>," *J. Electroanal. Chem.*, Vol. 346, No. 1–2, 1993, pp. 291–307.
- [71] Lehn, J. M., and C. W. Rees, (eds.), *Molecular Semiconductors: Photoelectric Properties and Solar Cells*, Berlin, Germany: Springer-Verlag, 1985.
- [72] Pfeiffer, M., et al., "Controlled p-Doping of Pigment Layers by Cosublimation: Basic Mechanisms and Implications for Their Use in Organic Photovoltaic Cells," *Solar Energy Materials and Solar Cells*, Vol. 63, No. 1, 2000, pp. 83–99.
- [73] Campbell, W. M., et al., "Porphyrins as Light Harvesters in the Dye-Sensitized TiO<sub>2</sub> Solar Cell," *Coordination Chemistry Reviews*, Vol. 248, No. 9–10, 2004, pp. 817–833.
- [74] Sayama, K., et al., "Efficient Sensitization of Nanocrystalline TiO<sub>2</sub> Films with Cyanine and Merocyanine Organic Dyes," *Solar Energy Materials and Solar Cells*, Vol. 80, No. 1, 2003, pp. 47–71.
- [75] Braun, D., "Semiconducting Polymer LEDs," *Materials Today*, Vol. 5, No. 6, 2002, pp. 32–39.
- [76] Kumara, G. R. R. A., et al., "Dye-Sensitized Solar Cell with the Hole Collector p-CuSCN Deposited from a Solution in n-propyl sulphide," *Solar Energy Materials and Solar Cells*, Vol. 69, No. 2, 2001, pp. 195–199.
- [77] Murakoshi, K., et al., "Fabrication of Solid-State Dye-Sensitized TiO<sub>2</sub> Solar Cells Combined with Polypyrrole," *Solar Energy Materials and Solar Cells*, Vol. 55, No. 1–2, 1998, pp. 113–125.
- [78] Arango, A. C., et al., "Efficient Titanium Oxide/Conjugated Polymer Photovoltaics for Solar Energy Conversion," *Adv. Mater.*, Vol. 12, No. 22, 2000.
- [79] Breeze, A. J., et al., "Improving Power Efficiencies in Polymer-Polymer Blend Photovoltaics," *Solar Energy Mater. & Solar Cells*, Vol. 83, No. 2–3, 2004, pp. 263–271.
- [80] Arango, A. C., P. J. Brock, and S. A. Carter, "Photovoltage in Conjugated Polymer Photovoltaics with a Titanium Dioxide Anode," *Organic Nonlinear Optical Materials and Devices. Symposium Materials Research Society*, Warrendale, PA, 1999, pp. 149–153.
- [81] Gamboa, S. A., et al., "Photovoltaic Structures Based on Polymer/Semiconductor Junctions," *Solar Energy Mater. & Solar Cells*, Vol. 55, No. 1–2, 1998, pp. 95–104.
- [82] Salafsky, J. S., W. H. Lubberhuizen, and R. E. I. Schropp, "Photoinduced Charge Separation and Recombination in a Conjugated Polymer-Semiconductor Nanocrystal Composite," *Chem. Phys. Lett.*, Vol. 290, No. 4–6, 1998, pp. 297–303.
- [83] Yongxiang, L., J. Hagen, and D. Haarer, "Novel Photoelectrochromic Cells Containing a Polyaniline Layer and a Dye-Sensitized Nanocrystalline TiO<sub>2</sub> Photovoltaic Cell," *Synth. Metals*, Vol. 94, No. 3, 1998, pp. 273–277.
- [84] Sicot, L., et al., "Dye Sensitized Polythiophene Solar Cells," *Synth. Metals*, Vol. 102, No. 1–3, 1999, pp. 991–992.
- [85] Onoda, M., K. Tada, and K. Yoshino, "Photoinduced Charge Transfer of Conducting Polymer Composites," *IEICE Trans. Electron.*, Vol. E81-C, No. 7, 1998, pp. 1051–1056.
- [86] Arias, A. C., et al., "Doped Conducting-Polymer-Semiconducting-Polymer Interfaces: Their Use in Organic Photovoltaic Devices," *Phys. Rev. B-Condensed-Matter*, Vol. 60, No. 3, 1999, pp. 1854–1860.

- [87] Knol, J., and J. C. Hummelen, "Fullerene Derivatives as Components for Plastic Photovoltaic Cells," *Proceedings of the Symposium on Recent Advances in the Chemistry and Physics of Fullerenes and Related Materials*, Vol. 6, Electrochem. Soc., Pennington, NJ, 1998, pp. 1123–1127.
- [88] Brabec, C. J., et al., "Realization of Large Area Flexible Fullerene-Conjugated Polymer Photocells: A Route to Plastic Solar Cells," *Synth. Metals*, Vol. 102, No. 1–3, 1999, pp. 861–865.
- [89] Wang, G., et al., "Enhanced Photovoltaic Response of PVK/C<sub>60</sub> Composite Films," *Physica B*, Vol. 279, No. 1–3, 2000, pp. 116–119.
- [90] Matoussi, H., et al., "Photovoltaic Heterostructure Devices Made of Sequentially Adsorbed Poly(phenylene vinylene) and Functionalized C<sub>60</sub>," *Appl. Phys. Lett.*, Vol. 77, No. 10, 2000, pp. 1540–1542.
- [91] Ago, H., et al., "Composites of Carbon Nanotubes and Conjugated Polymers for Photovoltaic Devices," *Adv. Mater.*, Vol. 11, No. 15, 1999, pp. 1281–1285.
- [92] Saito, Y., et al., "Photo-Sensitizing Ruthenium Complexes for Solid State Dye Solar Cells in Combination with Conducting Polymers as Hole Conductors," *Coordination Chemistry Reviews*, Vol. 248, No. 13–14, 2004, pp. 1469–1478.
- [93] Nazeeruddin, M. K., et al., "Stepwise Assembly of Amphiphilic Ruthenium Sensitizers and Their Applications in Dye-Sensitized Solar Cell," *Coordination Chemistry Reviews*, Vol. 248, No. 13–14, 2004, pp. 1317–1328.
- [94] Islam, A., H. Sugihara, and H. Arakawa, "Molecular Design of Ruthenium(II) Polypyridyl Photosensitizers for Efficient Nanocrystalline TiO<sub>2</sub> Solar Cells," *J. Photochemistry and Photobiology A: Chemistry*, Vol. 158, No. 2–3, 2003, pp. 131–138.
- [95] Tai, W.-P., K. Inoue, and J.-H. Oh, "Ruthenium Dye-Sensitized SnO<sub>2</sub>/TiO<sub>2</sub> Coupled Solar Cells," *Solar Energy Materials and Solar Cells*, Vol. 71, No. 4, 2002, pp. 553–557.
- [96] Kubo, W., et al., "Dye-Sensitized Solar Cells: Improvement of Spectral Response by Tandem Structure," *J. Photochemistry and Photobiology A: Chemistry*, Vol. 164, No. 1–3, 2004, pp. 33–39.
- [97] Perera, V. P. S., et al., "A Solar Cell Sensitized with Three Different Dyes," *Solar Energy Materials and Solar Cells*, Vol. 85, No. 1, 2004, pp. 91–98.
- [98] Otaka, H., et al., "Multicolored Dye-Sensitized Solar Cells," *J. Photochemistry and Photobiology A: Chemistry*, Vol. 164, No. 1–3, 2004, pp. 67–73.
- [99] Amao, Y., Y. Yamada, and K. Aoki, "Preparation and Properties of Dye-Sensitized Solar Cell Using Chlorophyll Derivative Immobilized TiO<sub>2</sub> Film Electrode," *J. Photochemistry and Photobiology A: Chemistry*, Vol. 164, No. 1–3, 2004, pp. 47–51.
- [100] Amao, Y., and T. Komori, "Bio-Photovoltaic Conversion Device Using Chlorine-e6 Derived from Chlorophyll from Spirulina Adsorbed on a Nanocrystalline TiO<sub>2</sub> Film Electrode," *Biosensors and Bioelectronics*, Vol. 19, No. 8, 2004, pp. 843–847.
- [101] Nsengiyumva, S., et al., "Capacitance Measurements of Photovoltaic Cells Based on Mixed Monolayers of Chlorophyll A and Sulfoquinovosyldiacylglycerol," *Sol. Energy Mater. Sol. Cells*, Vol. 45, No. 3, 1997, pp. 211–225.
- [102] Nabok, A. V., et al., "II-VI Semiconductor Nanoparticles Formed by Langmuir-Blodgett Film Technique. Optical Study," *Proceedings of 2002 2nd IEEE Conference on Nanotechnology, (IEEE-NANO 2002)*, Washington, D.C., August 26–28, 2002, pp. 261–264.
- [103] Karapire, C., C. Zafer, and S. Ili, "Studies on Photophysical and Electrochemical Properties of Synthesized Hydroxy Peryleneimides in Nanostructured Titania Thin Films," *Synthetic Metals*, Vol. 145, No. 1, 2004, pp. 51–60.
- [104] Saito, Y., et al., "Morphology Control of Mesoporous TiO<sub>2</sub> Nanocrystalline Films for Performance of Dye-Sensitized Solar Cells," *Solar Energy Materials and Solar Cells*, Vol. 83, No. 1, 2004, pp. 1–13.
- [105] Koelsch, M., et al., "Electrochemical Comparative Study of Titania (Anatase, Brookite, and Rutile) Nanoparticles Synthesized in Aqueous Medium," *Thin Solid Films*, Vol. 451–452, 2004, pp. 86–92.



- [106] Shen, Y.-C., et al., "Co-Sensitization of Microporous TiO<sub>2</sub> Electrodes with Dye Molecules and Quantum-Sized Semiconductor Particles," *Colloids and Surfaces A: Physicochemical and Engineering Aspects*, Vol. 175, No. 1–2, 2000, pp. 135–140.
- [107] Westphalen, U., et al., "Metal Cluster Enhanced Organic Solar Cells," *Solar Energy Materials and Solar Cells*, Vol. 61, No. 1, 2000, pp. 97–105.
- [108] Wen, C., et al., "Effects of Silver Particles on the Photovoltaic Properties of Dye-Sensitized TiO<sub>2</sub> Thin Films," *Solar Energy Materials and Solar Cells*, Vol. 61, No. 4, 2000, pp. 339–351.
- [109] Diamant, Y., et al., "Core-Shell Nanoporous Electrode for Dye Sensitized Solar Cells: The Effect of Shell Characteristics on the Electronic Properties of the Electrode," *Coordination Chemistry Reviews*, Vol. 248, No. 1–3, 2004, pp. 1271–1276.
- [110] Shen, Q., D. Arae, and T. Toyoda, "Photosensitization of Nanostructured TiO<sub>2</sub> with CdSe Quantum Dots: Effects of Microstructure and Electron Transport in TiO<sub>2</sub> Substrates," *J. Photochemistry and Photobiology A: Chemistry*, Vol. 164, No. 1–3, 2004, pp. 75–80.
- [111] Bandaranayake, M. P., et al., "Dye-Sensitized Solar Cells Made from Nanocrystalline TiO<sub>2</sub> Films Coated with Outer Layers of Different Oxide Materials," *Coordination Chemistry Reviews*, Vol. 248, No. 1–3, 2004, pp. 1271–1281.
- [112] Zhang, X.-T., et al., "Al<sub>2</sub>O<sub>3</sub>-Coated Nanoporous TiO<sub>2</sub> Electrode for Solid-State Dye-Sensitized Solar Cell," *Solar Energy Materials and Solar Cells*, Vol. 80, No. 3, 2003, pp. 315–326.
- [113] Keis, K., et al., "Nanostructured ZnO Electrodes for Dye-Sensitized Solar Cell Applications," *J. Photochemistry and Photobiology A: Chemistry*, Vol. 148, No. 1–3, 2002, pp. 57–64.
- [114] Tennakone, K., et al., "Dye-Sensitized Composite Semiconductor Nanostructures," *Physica E: Low-Dimensional Systems and Nanostructures*, Vol. 14, No. 1–2, 2002, pp. 190–196.
- [115] Kumar, S. K., et al., "CdTe Photovaltic Sintered Films," *J. Phys. & Chem. of Solids*, Vol. 61, No. 11, 2000, pp. 1809–1813.
- [116] Sirohi, S., and T. P. Sharma, "Bandgaps of Cadmium Telluride Sintered Film," *Optical Materials*, Vol. 13, No. 2, 1999, pp. 267–269.
- [117] Kumar, V., et al., "Structural and Optical Properties of Sintered Cd<sub>1-x</sub>Zn<sub>x</sub>S Films," *Optical Materials*, Vol. 11, No. 1, 1998, pp. 29–34.
- [118] Mattoussi, H., et al., "Electroluminescence from Heterostructures of Poly(phenylene vinylene) and Inorganic CdSe Nanocrystals," *J. Appl. Phys.*, Vol. 83, No. 12, 1998, pp. 7965–7974.
- [119] Ueki, S. H., et al., "Quasi-Solid Dye Sensitized Solar Cells Solidified with Chemically Cross-Linked Gelators: Control of TiO<sub>2</sub>/Gel Electrolytes and Counter Pt/Gel Electrolytes Interfaces," *J. Photochemistry and Photobiology A: Chemistry*, Vol. 164, No. 1–3, 2004, pp. 117–122.
- [120] Komiya, R., et al., "Highly Efficient Quasi-Solid State Dye-Sensitized Solar Cell with Ion Conducting Polymer Electrolyte," *J. Photochemistry and Photobiology A: Chemistry*, Vol. 164, No. 1–3, 2004, pp. 123–127.
- [121] Katsaros, G., et al., "A Solvent-Free Composite Polymer/Inorganic Oxide Electrolyte for High Efficiency Solid-State Dye-Sensitized Solar Cells," *J. Photochemistry and Photobiology A: Chemistry*, Vol. 149, No. 1–3, 2002, pp. 191–198.
- [122] Nogueira, A. F., and M. M.-A. De-Paoli, "A Dye Sensitized TiO<sub>2</sub> Photovoltaic Cell Constructed with an Elastomeric Electrolyte," *Solar Energy Mater & Solar Cells*, Vol. 61, No. 2, 2000, pp. 135–141.
- [123] Schulmeyer, T., et al., "Influence of Cu(In,Ga)Se<sub>2</sub> Bandgap on the Valence Band Offset with CdS," *Thin Solid Films*, Vol. 451–452, 2004, pp. 420–423.
- [124] Santana-Aranda, M. A., and M. Meléndez-Lira, "Screen Printed Cd<sub>Sx</sub>Te<sub>1-x</sub> Films, Structural and Optical Characterization," *Applied Surface Science*, Vol. 175–176, 2001, pp. 538–542.

- [125] Romeo, N., et al., "Growth of Polycrystalline CdS and CdTe Thin Layers for High Efficiency Thin Film Solar Cells," *Materials Chemistry and Physics*, Vol. 66, No. 2–3, 2000, pp. 201–206.
- [126] Boyle, D. S., et al., "Novel Approach to the Chemical Bath Deposition of Chalcogenide Semiconductors," *Thin Solid Films*, Vol. 361–362, 2000, pp. 150–154.
- [127] Benamar, E., et al., "Electrodeposited Cadmium Selenide Films for Solar Cells," *Annales de Chimie Science des Matériaux*, Vol. 23, No. 1–2, 1998, pp. 369–372.
- [128] Winz, K., et al., "Novel Light-Trapping Schemes Involving Planar Junctions and Diffuse Rear Reflectors for Thin-Film Silicon-Based Solar Cells," *Solar Energy Materials and Solar Cells*, Vol. 49, No. 1–4, 1997, pp. 195–203.
- [129] Nenmark, G. F., "Defects in Wide Band Gap II-VI Crystals," *Materials Science and Engineering: R: Reports*, Vol. 21, No. 1, 1997, pp. 1–46.
- [130] Sebastian, P. J., "The Transport and Optical Properties of CdSe-CdTe Pseudobinary Thin Films," *Thin Solid Films*, Vol. 245, No. 1–2, 1994, pp. 132–140.
- [131] Mauk, M. G., J. R. Balliet, and B. W. Feyock, "Large-Grain (1-mm), Recrystallized Germanium Films on Alumina, Fused Silica, Oxide-Coated Silicon Substrates for III-V Solar Cell Applications," *J. Crystal Growth*, Vol. 250, No. 1–2, 2003, pp. 50–56.
- [132] Ringel, S. A., "Hydrogen-Extended Defect Interactions in Heteroepitaxial InP Materials and Devices," *Solid-State Electronics*, Vol. 41, No. 3, 1997, pp. 359–380.
- [133] Andreev, V. M., and V. D. Rumyantsev, "A3B5 Based Solar Cells and Concentrating Optical Elements for Space PV Modules," *Solar Energy Materials and Solar Cells*, Vol. 44, No. 4, 1996, pp. 319–332.
- [134] Hardtdegen, H., and P. Giannoules, "An Outstanding Innovation in LP-MOVPE: Use of Nitrogen as the Carrier Gas," *III-Vs Review*, Vol. 8, No. 3, 1995, pp. 34–39.
- [135] Mane, R. S., and C. D. Lokhande, "Chemical Deposition Method for Metal Chalcogenide Thin Films," *Materials Chemistry and Physics*, Vol. 65, No. 1, 2000, pp. 1–31.
- [136] Ma, T., et al., "Preparation and Properties of Nanostructured TiO<sub>2</sub> Electrode by a Polymer Organic-Medium Screen-Printing Technique," *Electrochemistry Communications*, Vol. 5, No. 4, 2003, pp. 369–372.
- [137] Takenaka, S., et al., "Layer-by-Layer Self-Assembly Replication Technique: Application to Photoelectrode of Dye-Sensitized Solar Cell," *Thin Solid Films*, Vol. 438–439, 2003, pp. 346–335.
- [138] Ferber, J., R. Stangl, and J. Luther, "An Electrical Model of the Dye-Sensitized Solar Cell," *Solar Energy Materials and Solar Cells*, Vol. 53, No. 1–2, 1998, pp. 29–54.
- [139] Kron, G., et al., "Electrical Characterisation of Dye Sensitised Nanocrystalline TiO<sub>2</sub> Solar Cells with Liquid Electrolyte and Solid-State Organic Hole Conductor," *Thin Solid Films*, Vol. 403–404, 2002, pp. 242–246.
- [140] Frank, A. J., N. Kopidakis, and J. Van de Lagemaat, "Electrons in Nanostructured TiO<sub>2</sub> Solar Cells: Transport, Recombination and Photovoltaic Properties," *Coordination Chemistry Reviews*, Vol. 248, No. 1–3, 2004, pp. 1165–1179.
- [141] Durrant, J. R., S. A. Haque, and E. Palomares, "Towards Optimization of Electron Transfer Processes in Dye Sensitised Solar Cells," *Coordination Chemistry Reviews*, Vol. 248, No. 1–3, 2004, pp. 1247–1257.
- [142] Murakoshi, K., et al., "Importance of Binding States Between Photosensitizing Molecules and the TiO<sub>2</sub> Surface for Efficiency in a Dye-Sensitized Solar Cell," *J. Electroanalytical Chemistry*, Vol. 396, No. 1–2, 1995, pp. 27–34.
- [143] Ferber, J., and J. Luther, "Computer Simulations of Light Scattering and Absorption in Dye-Sensitized Solar Cells," *Solar Energy Materials and Solar Cells*, Vol. 54, No. 1–4, 1998, pp. 265–275.
- [144] Peter, L. M., and K. G. U. Wijayantha, "Intensity Dependence of the Electron Diffusion Length in Dye-Sensitised Nanocrystalline TiO<sub>2</sub> Photovoltaic Cells," *Electrochemistry Communications*, Vol. 1, No. 12, 1999, pp. 576–580.

- [145] Sommeling, P. M., et al., "Long-Term Stability Testing of Dye-Sensitized Solar Cells," *J. Photochemistry and Photobiology A: Chemistry*, Vol. 164, No. 1–3, 2004, pp. 137–144.
- [146] Shirakawa, H., "The Discovery of Polyacetylene Film: The Dawning of an Era of Conducting Polymers," *Synth. Met.* Vol. 125, No. 1, 2002, pp. 3–10.
- [147] McDiarmid, A. G., "Synthetic Metals: A Novel Role for Organic Polymers," *Synth. Met.*, Vol. 125, 2002, pp. 11–22.
- [148] Heeger, A. J., "Semiconducting and Metallic Polymers: The Fourth Generation of Polymeric Materials," *Synth. Met.*, Vol. 125, 2002, pp. 23–42.
- [149] Guillon, D., et al., "Organic Materials with Optical Properties," *Analysis*, Vol. 28, No. 2, 2000, pp. 99–102.
- [150] Onoda, M., et al., "Organic Electroluminescence Devices Using Poly(arylene vinylene) Conducting Polymers," *Jpn. J. Appl. Phys. Part 1—Regul. Pap. Short Notes Rev. Pap.*, Vol. 32, No. 9A, 1993, pp. 3895–3899.
- [151] Panero, S., S. Passerini, and B. Scrosati, "Conducting Polymers—New Electrochromic Materials for Advanced Optical Devices," *Molecular Crystals and Liquid Crystal*, Vol. 230, 1993, pp. 337–349.
- [152] Scrosati, B., "Conducting Polymers—New Frontiers and Prospectives," *Mater. Sci. Eng. B-Solid State Mater. Adv. Technol.*, Vol. 12, No. 4, 1992, pp. 369–373.
- [153] Ioannidis, A., et al., "Current-Voltage Characteristic of Organic Light Emitting Diodes," *Appl. Phys. Lett.*, Vol. 72, No. 23, 1998, pp. 3038–3040.
- [154] Bidan, G., et al., "Conducting Polymers as a Link Between Biomolecules and Microelectronics," *Synth. Met.*, Vol. 102, No. 1–3, 1999, pp. 1363–1365.
- [155] Braun, D., "Semiconducting Polymer LEDs," *Materials Today*, Vol. 5, No. 6, 2002, pp. 32–39.
- [156] Heeger, A. J., "Light Emission from Semiconducting Polymers: Light-Emitting Diodes, Light-Emitting Electrochemical Cells, Lasers and White Light for the Future," *Sol. State Comm.*, Vol. 107, No. 11, 1998, pp. 673–679.
- [157] Blom, P. W. M., and M. J. M. De Jong, "Device Operation of Polymer Light-Emitting Diodes," *Philips J. of Research*, Vol. 51, No. 4, 1998, pp. 479–494.
- [158] Braun, D., "Electronic Injection and Conduction Processes for Polymer Devices," *J. Polymer Sci., B-Polymer Physics*, Vol. 41, No. 21, 2003, pp. 2622–2629.
- [159] Burroughes, J. H., et al., "Light-Emitting Diodes Based on Conjugated Polymers," *Nature*, Vol. 347, No. 6293, 1990, pp. 539–541.
- [160] Braun, D., and A. J. Heeger, "Visible-Light Emission from Semiconducting Polymer Diodes," *Appl. Phys. Lett.*, Vol. 58, No. 18, 1991, pp. 1982–1984.
- [161] Gustafsson, G., et al., "Flexible Light-Emitting Diodes Made from Soluble Conducting Polymers," *Nature*, Vol. 357, No. 6378, 1992, pp. 477–479.
- [162] Pei, Q., et al., "Polymer Light-Emitting Electrochemical Cells," *Science*, Vol. 269, No. 5227, 1995, pp. 1086–1088.
- [163] Skotheim, T. A., (ed.), *Handbook of Conducting Polymers*, New York: Marcel Dekker, 1986.
- [164] Yu, G., C. Zhang, and A. J. Heeger, "Dual-Function Semiconducting Polymer Devices—Light-Emitting and Photodetecting Diodes," *Appl. Phys. Lett.*, Vol. 64, No. 12, 1994, pp. 1540–1542.
- [165] Parker, I. D., "Carrier Tunneling and Device Characteristics in Polymer Light-Emitting Diodes," *J. Appl. Phys.*, Vol. 75, No. 3, 1994, pp. 1656–1666.
- [166] Yang, Y., and A. J. Heeger, "Polyaniline as a Transparent Electrode for Polymer Light-Emitting-Diodes—Lower Operating Voltage and Higher Efficiency," *Appl. Phys. Lett.*, Vol. 64, No. 10, 1994, pp. 1245–1247.
- [167] Hide, F., et al., "Laser Emission from Solutions and Films Containing Semiconducting Polymer and Titanium Dioxide Nanocrystals," *Chem. Phys. Lett.*, Vol. 256, No. 4–5, 1996, pp. 424–430.

- [168] Arango, A. C., S. A. Carter, and P. J. Brock, "Charge Transfer in Photovoltaics Consisting of Interpenetrating Networks of Conjugated Polymer and TiO<sub>2</sub> Nanoparticles," *Appl. Phys. Lett.*, Vol. 74, No. 12, 1999, pp. 1698–1700.
- [169] Carter, S. A., J. C. Scott, and P. J. Brock, "Enhanced Luminance in Polymer Composite Light Emitting Devices," *Appl. Phys. Lett.*, Vol. 71, No. 9, 1997, pp. 1145–1147.
- [170] Hirohata, M., et al., "Electroluminescence in Conducting Polymers Based on Poly(phenylene ethynylene), *Synth. Met.*, Vol. 85, No. 1–3, 1997, pp. 1273–1274.
- [171] Brouwer, H. J., et al., "LEDs Based on Conjugated PPV Block Copolymers," *Synth. Met.*, Vol. 84, No. 1–3, 1997, pp. 881–882.
- [172] Peng, Z. H., and J. H. Zhang, "New Oxadiazole-Containing Conjugated Polymer for Single-Layer Light-Emitting Diodes," *Chem. Mat.*, Vol. 11, No. 4, 1999, pp. 1138–1143.
- [173] Bouachrine, M., et al., "A Thienylene-Phenylene Copolymer with Di(ethylene oxide) Side Chains and Its Use in Light Emitting Diodes," *Synth. Met.*, Vol. 126, No. 2–3, 2002, pp. 241–244.
- [174] Sun, Y. M., "Synthesis and Optical Properties of Novel Blue Light-Emitting Polymers with Electron Affinitive Oxadiazole," *Polymer*, Vol. 42, No. 23, 2001, pp. 9495–9504.
- [175] Baek, N. S., et al., "Exploratory Synthesis and Luminescence Study of the First pi-Conjugated Tin-Based Alternating Copolymers for Blue Light-Emitting Diodes at the Very Low Operating Voltage," *Macromolecules*, Vol. 35, No. 25, 2002, pp. 9282–9288.
- [176] Fujii, A., T. Sonoda, and K. Yoshino, "Preparation, Optical Properties and Yellow Electroluminescence of Water-Soluble Poly(p-phenylene vinylene)," *Jpn. J. Appl. Phys. Part 2—Lett.*, Vol. 39, No. 3AB, 2000, pp. L249–L252.
- [177] Tada, K., et al., "Blue-Green Electroluminescence in Copolymer Based on Poly(1,4-phenylene ethynylene)," *Jpn. J. Appl. Phys. Part 2—Lett.*, Vol. 35, No. 2B, 1996, pp. L251–L253.
- [178] Liu, B., et al., "Blue-Light-Emitting Fluorene-Based Polymers with Tunable Electronic Properties," *Chem. Mater.*, Vol. 13, No. 6, 2001, pp. 1984–1991.
- [179] Wohlgenannt, A., and Z. V. Vardeny, "Photophysics Properties of Blue-Emitting Polymers," *Synth. Metals*, Vol. 125, No. 1, 2001, pp. 55–63.
- [180] Wu, F. I., et al., "Novel Oxadiazole-Containing Polyfluorene with Efficient Blue Electroluminescence," *Chem. Mater.*, Vol. 15, No. 1, 2003, pp. 269–274.
- [181] Paik, K. L., et al., "White Light-Emitting Diodes from Novel Silicon-Based Copolymers Containing Both Electron-Transport Oxadiazole and Hole-Transport Carbazole Moieties in the Main Chain," *Macromolecules*, Vol. 35, No. 18, 2002, pp. 6782–6791.
- [182] Bliznyuk, V. N., et al., "Electrical and Photoinduced Degradation of Polyfluorene Based Films and Light-Emitting Devices," *Macromolecules*, Vol. 32, No. 2, 1999, pp. 361–369.
- [183] Bernius, M., et al., "Fluorene-Based Polymers—Preparation and Applications," *J. Mater. Sci.-Mater. Electron.*, Vol. 11, No. 2, 2000, pp. 111–116.
- [184] Tessler, N., et al., "Properties of Light Emitting Organic Materials Within the Context of Future Electrically Pumped Lasers," *Synth. Metals*, Vol. 115, No. 1–3, 2000, pp. 57–62.
- [185] Setayesh, S., et al., "Polyfluorenes with Polyphenylene Dendron Side Chains: Toward Non-Aggregating, Light-Emitting Polymers," *J. Am. Chem. Soc.*, Vol. 123, No. 5, 2001, pp. 946–953.
- [186] Wilkinson, C. I., et al., "Enhanced Performance of Pulse Driven Small Area Polyfluorene Light Emitting Diodes," *Appl. Phys. Lett.*, Vol. 79, No. 2, 2001, pp. 171–173.
- [187] Peng, Q., et al., "New Series of Highly Phenyl-Substituted Polyfluorene Derivatives for Polymer Light-Emitting Diodes," *J. Polymer Sci. A-Polymer Chemistr.*, Vol. 42, No. 12, 2004, pp. 2985–2993.
- [188] Neher, D., et al., "Light-Emitting Devices Based on Solid Electrolytes and Polyelectrolytes," *Polym. Adv. Technol.*, Vol. 9, No. 7, 1998, pp. 461–475.
- [189] Kim, H. K., et al., "Novel Silicon-Based Alternating Copolymers: Synthesis, Photophysical Properties, and Tunable EL Colors," *Macromol. Symp.*, Vol. 192, 2003, pp. 135–149.

- [190] Granstrom, M., and O. Inganäs, "Flexible Arrays of Submicrometer-Sized Polymeric Light Emitting Diodes," *Adv. Mater.*, Vol. 7, No. 12, 1995, pp. 1012–1017.
- [191] Fujii, A., et al., "Optical Properties of Self-Assembled Thin Film of Poly(p-phenylenevinylene)s and Its Application to Light-Emitting Devices with Microdisk Geometry," *Jpn. J. Appl. Phys. Part 2—Lett.*, Vol. 42, No. 6B, 2003, pp. L693–L696.
- [192] Fujii, A., et al., "Polymer Electroluminescent Diodes with Microcylindrical Geometry," *Synth. Met.*, Vol. 102, No. 1–3, 1999, pp. 1010–1011.
- [193] Fujii, A., et al., "Polymer Electroluminescent Diodes with Ring Microcavity Structure," *Jpn. J. Appl. Phys. Part 2—Lett.*, Vol. 37, No. 6B, 1998, pp. L740–L742.
- [194] Trindade, T., P. O'Brien, and N. L. Pickett, "Nanocrystalline Semiconductors: Synthesis, Properties, and Perspectives," *Chem. Mat.*, Vol. 13, No. 11, 2000, pp. 3843–3858.
- [195] Shipway, A. N., E. Katz, and I. Willner, "Nanoparticle Arrays on Surfaces for Electronic, Optical, and Sensor Applications," *Chem. Phys. Chem.*, Vol. 1, No. 1, 2000, pp. 18–52.
- [196] Hryciw, A., et al., "Effects of Particle Size and Excitation Spectrum on the Photoluminescence of Silicon Nanocrystals Formed by Ion Implantation," *Nuclear Instrum. & Methods in Phys. Research-B: Beam Interactions with Materials and Atoms*, Vol. 222, No. 3–4, 2004, pp. 469–476.
- [197] Rogach, A. L., "Nanocrystalline CdTe and CdTe(S) Particles: Wet Chemical Preparation, Size-Dependent Optical Properties and Perspectives of Optoelectronic Applications," *Mater. Sci. & Eng. B*, Vol. 69–70, 2000, pp. 435–440.
- [198] Li, X., et al., "Light-Emitting Boron Nitride Nanoparticles Encapsulated in Zeolite ZSM-5," *Microporous and Mesoporous Materials*, Vol. 40, No. 1–3, 2000, pp. 263–269.
- [199] Bagaev, E. A., et al., "Photoluminescence from Cadmium Sulfide Nanoclusters Formed in the Matrix of a Langmuir-Blodgett Film," *Semiconductors*, Vol. 37, No. 11, 2003, pp. 1321–1325.
- [200] Poles, E., et al., "Anti-Stokes Photoluminescence in Colloidal Semiconductor Quantum Dots," *Appl. Phys. Lett.*, Vol. 75, No. 7, 1999, pp. 971–973.
- [201] Kershaw, S. V., et al., "Development of IR-Emitting Colloidal II-VI Quantum-Dot Materials," *IEEE J. Sel. Top. Quantum Electron.*, Vol. 6, No. 3, 2000, pp. 534–543.
- [202] Copeland, T. S., et al., "Synthesis and Luminescent Properties of Mn<sup>2+</sup>-Doped Zinc Silicate Phosphors by Sol-Gel Methods," *J. Luminescence*, Vol. 97, No. 3–4, 2002, pp. 168–173.
- [203] Huisken, F., et al., "Laser Production and Deposition of Light-Emitting Silicon Nanoparticles," *Appl. Surf. Sci.*, Vol. 154–155, 2000, pp. 305–313.
- [204] Gedanken, A., "Using Sonochemistry for the Fabrication of Nanomaterials," *Ultrason. Sonochem.*, Vol. 11, No. 2, 2004, pp. 47–55.
- [205] Gao, M., B. Richter, and S. Kirstein, "White-Light Electroluminescence from a Self-Assembled Q-CdSe/PPV Multilayer Structures," *Adv. Mater.*, Vol. 9, No. 10, 1997, pp. 802–805.
- [206] Gao, M., et al., "Strongly Photoluminescent CdTe Nanocrystals by Proper Surface Modification," *J. Phys. Chem. B*, Vol. 102, No. 43, 1998, pp. 8360–8363.
- [207] Lesser, C., M. Gao, and S. Kirstein, "Highly Luminescent Thin Films from Alternating Deposition of CdTe Nanoparticles and Polycations," *Mater. Sci. & Eng. C*, Vol. 8–9, 1999, pp. 159–162.
- [208] Gao, M., et al., "Electroluminescence Studies on Self-Assembled Films of PPV and CdSe Nanoparticles," *J. Phys. Chem. B*, Vol. 102, No. 21, 1998, pp. 4096–4103.
- [209] Gao, M., et al., "Innovative Light Emitting Materials," *Advances in Sci. and Technol.*, Vol. 27, 1999, pp. 347–358.
- [210] Gao, M., et al., "Electroluminescence of Different Colors from Polycation/CdTe Nanocrystal Self-Assembled Films," *J. Appl. Phys.*, Vol. 87, No. 5, 2000, pp. 2297–2302.
- [211] Kocka, J., I. Pelant, and A. Fejfar, "Light Emitting Silicon, Recent Progress," *J. Non-Cryst. Sol.*, Vol. 198–200, Part 2, 1996, pp. 857–862.
- [212] Lie, L. H., et al., "Preparation and Characterisation of Luminescent Alkylated-Silicon Quantum Dots," *J. Electroanal. Chem.*, Vol. 538, 2002, pp. 183–190.



- [213] Kim, Y., H. Lim, and C-S. Ha, "Red Hybrid Organic Light-Emitting Device Fabricated with Molecularly Doped Polyimide Thin Film Containing Hole-Transporting Nanoparticles," *Sol.-State Electron.*, Vol. 48, No. 5, 2004, pp. 633–640.
- [214] Mattoussi, H., et al., "Electroluminescence from Heterostructures of Poly(phenylene vinylene) and Inorganic CdSe Nanocrystals," *J. Appl. Phys.* Vol. 83, No. 12, 1998, pp. 7965–7974.
- [215] Bliznyuk, V., et al., "Self-Assembled Nanocomposite Polymer Light-Emitting Diodes with Improved Efficiency and Luminance," *Adv. Mater.*, Vol. 11, No. 15, 1999, p. 1257.
- [216] Tada, K., and M. Onoda, "Preparation and Application of Nanostructured Conjugated Polymer Film by Electrophoretic Deposition," *Thin Solid Films*, Vol. 438–439, 2003, pp. 365–368.
- [217] Liggins, R. T., and H. M. Burt, "Polyether-Polyester Diblock Copolymers for the Preparation of Paclitaxel Loaded Polymeric Micelle Formulations," *Adv. Drug Deliv. Rev.*, Vol. 54, No. 2, 2002, pp. 191–202.
- [218] Priel, S., et al., "Scaling Properties in the Molecular Structure of Three-Dimensional, Nano-sized Phenylene-Based Dendrimers as Studied by Atomistic Molecular Dynamics Simulations," *Carbon*, Vol. 41, No. 12, 2003, pp. 2269–2283.
- [219] Zhu, D., et al., "Design, Synthesis and Properties of Functional Materials Based on Fullerene," *Synth. Met.*, Vol. 133–134, 2003, pp. 679–683.
- [220] Montemerlo, M. S., et al., "Technologies and Designs for Electronic Nanocomputers," MITRE Corp., McLean, VA, 1996.
- [221] Nagamura, T., "Optical Memory By Novel Photoinduced Electrochromism," *Mol. Cryst. Liq. Cryst.*, Vol. 224, 1993, pp. 75–83.
- [222] Tsutsumi, H., et al., "Polymer Gel Films with Simple Organic Electrochromics for Single-Film Electrochromic Devices," *J. Polymer Sci. Part A-Polymer Chem.*, Vol. 30, No. 8, 1992, pp. 1725–1729.
- [223] Pope, M., "Prospects for Electronic Processes in Organic Materials," *Mol. Cryst. Liq. Cryst.*, Vol. 230, 1993, pp. 1–22.
- [224] Cik, G., and M. Bardosova, "Reversible Optical Memory," *Chemicke Listy*, Vol. 87, No. 10, 1993, pp. 690–696.
- [225] Kim, J., et al., "Optical Memory Media Via Polymer-TCNQ Charge-Transfer Complex," *Synth. Metals*, Vol. 71, No. 1–3, 1995, pp. 2215–2216.
- [226] Levy, D., "Recent Applications of Photochromic Sol-Gel Materials," *Mol. Cryst. Liq. Cryst. Sci. Technol. Sect. A-Mol. Cryst. Liq. Cryst.*, Vol. 297, 1997, pp. 31–41.
- [227] Dvornikov, A. S., and P. M. Rentzepis, "Novel Organic ROM Materials for Optical 3D Memory Devices," *Opt. Commun.*, Vol. 136, No. 1–2, 1997, pp. 1–6.
- [228] Pina, F., et al., "Thermal and Photochemical Properties of 4',7-dihydroxyflavylium in Water-Ionic Liquid Biphasic Systems: A Write-Read-Erase Molecular Switch," *Angew. Chem.-Int. Edit.*, Vol. 43, No. 12, 2004, pp. 1525–1527.
- [229] Shibaev, V., A. Bobrovsky, and N. Boiko, "Photoactive Liquid Crystalline Polymer Systems with Light-Controllable Structure and Optical Properties," *Progress in Polymer Science*, Vol. 28, No. 5, 2003, pp. 729–836.
- [230] Shibaev, V., A. Bobrovsky, and N. Boiko, "Light-Responsive Chiral Photochromic Liquid Crystalline Polymer Systems," *J. Photochem. & Photobiol. A: Chemistry*, Vol. 155, No. 1–3, 2003, pp. 3–19.
- [231] Polyzos, I., et al., "Two-Photon Absorption Properties of Novel Organic Materials for Three-Dimensional Optical Memories," *Chem. Phys. Lett.*, Vol. 369, No. 3–4, 2003, pp. 264–268.
- [232] Hirao, K., "Photonics Glass for PHB Holographic Memory," *J. Non-Cryst. Solids*, Vol. 196, 1996, pp. 16–25.
- [233] Renge, I., "Symmetry and Hole-Burning Properties of Porphyrins," *J. Luminescence*, Vol. 98, No. 1–4, pp. 213–220.

- [234] Qiu, J., et al., "Valence Manipulation by Lasers of Samarium Ion in Micrometer-Scale Dimensions Inside Transparent Glass," *Solid State Commun.*, Vol. 113, No. 6, 1999, pp. 341–344.
- [235] Sugiyama, Y., et al., "Hole Burning Spectroscopy of InAs Self-Assembled Quantum Dots for Memory Application," *Physica E: Low-Dimensional Systems and Nanostructures*, Vol. 7, No. 3–4, 2000, pp. 503–507.
- [236] Neifeld, M. A., and L. Zhang, "Limits on the Bitwise Information Density of Spectral Storage," *Optics Commun.*, Vol. 177, No. 1–6, 2000, pp. 171–179.
- [237] Ham, B. S., P. R. Hemmer, and M. S. Shariar, "Observation of Laser-Jitter-Enhanced Hyperfine Spectroscopy and Two-Photon Spectral Hole-Burning," *Optics Commun.*, Vol. 164, No. 1–3, 1999, pp. 129–136.
- [238] Kravets, V. G., "Multilevel High-Capacity Optical Memory," *J. Opt. Technol.*, Vol. 67, No. 12, 2000, pp. 1054–1058.
- [239] Shen, Y., et al., "Hybrid Near-Field Optical Memory and Photofabrication in Dye-Doped Polymer Film," *Optics Comm.*, Vol. 200, No. 1–6, 2001, pp. 9–13.
- [240] Karageorgiev, P., et al., "Modification of the Surface Potential of Azobenzene-Containing Langmuir-Blodgett Films in the Near Field of a Scanning Kelvin Microscope Tip by Irradiation," *Langmuir*, Vol. 16, No. 13, 2000, pp. 5515–5518.
- [241] Maack, J., et al., "Molecular Cis-Trans Switching in Amphiphilic Monolayers Containing Azobenzene Moieties," *Thin Solid Films*, Vol. 242, No. 1–2, 1994, pp. 122–126.
- [242] Stiller, B., et al., "Optically Induced Switching of Azobenzene Containing Self-Assembling Monolayers Investigated by Kelvin Probe and Scanning Force Microscopy," *Mol. Cryst. Liquid Cryst.*, Vol. 355, 2001, pp. 401–413.
- [243] Stiller, B., et al., "Scanning Kelvin Microscopy as a Tool for Visualization of Optically Induced Molecular Switching in Azobenzene Self-Assembling Films," *Surface & Interface Analysis*, Vol. 30, No. 1, 2000, pp. 549–551.
- [244] Stiller, B., et al., "Self-Assembled Monolayers of Novel Azobenzenes for Optically Induced Switching," *Mater. Sci. Eng. C-Biomimetic Supramol. Syst.*, Vol. 8–9, 1999, pp. 385–389.
- [245] Liang, Y., A. S. Dvornikov, and P. M. Rentzepis, "A Novel Non-Destructible Readout Molecular Memory," *Optics Communications*, Vol. 223, No. 1–3, 2003, pp. 61–66.
- [246] Somani, P. R., and S. Radhakrishnan, "Electrochromic Materials and Devices: Present and Future," *Mater. Chem. & Phys.*, Vol. 77, No. 1, 2003, pp. 117–133.
- [247] Wolak, M. A., et al., "Optical Properties of Photochromic Fluorinated Indolylfulgides," *J. Photochem. & Photobiol. A: Chemistry*, Vol. 144, No. 2–3, 2001, pp. 83–91.
- [248] Barachevsky, V. A., "Applied Aspects of Organic Photochemistry," *High Energy Chem.*, Vol. 37, No. 1, 2003, pp. 6–16.
- [249] Wu, C. C., C. W. Chen, and T. Y. Cho, "Three-Color Reconfigurable Organic Light-Emitting Devices," *Appl. Phys. Lett.*, Vol. 83, No. 4, July 28, 2003, pp. 611–613.
- [250] Wolak, M. A., et al., "Optical and Thermal Properties of Photochromic Fluorinated Adamantylidene Indolylfulgides," *J. Photochem. Photobiol. A-Chem.*, Vol. 147, No. 1, 2002, pp. 39–44.
- [251] Maenosono, S., et al., "Optical Memory Media Based on Excitation-Time Dependent Luminescence from a Thin Film of Semiconductor Nanocrystals," *Jpn. J. Appl. Phys. Part 1—Regul. Pap. Short Notes Rev. Pap.*, Vol. 39, No. 7A, 2000, pp. 4006–4012.
- [252] Zeng, H., et al., "Irradiation Assisted Fabrication of Gold Nanoparticles-Doped Glasses," *J. Cryst. Growth*, Vol. 267, No. 1–2, 2004, pp. 156–160.
- [253] Dardona, S., et al., "Holeburning in Rare Earth Doped Nanoparticles of MgS," *J. of Luminesc.*, Vol. 107, No. 1–4, 2004, pp. 182–186.
- [254] Yang, H., et al., "Preparation and Optical Constants of the Nano-Crystal and Polymer Composite  $\text{Bi}_4\text{Ti}_3\text{O}_{12}$ /PMMA Thin Films," *Optics & Laser Technology*, Vol. 37, No. 4, 2005, pp. 259–264.



- [255] Yang, H., et al., "Preparation and Transmission Loss of the Nano-Crystal and Polymer Composite Film BTO/PMMA," *Optics & Laser Technology*, Vol. 35, No. 4, 2003, pp. 291–294.
- [256] Tsutsumi, H., Y. Nakagawa, and K. Tamura, "Single-Film Electrochromic Devices with Polymer Gel Films Containing Aromatic Electrochromics," *Solar Energy Mater. & Solar Cells*, Vol. 39, No. 2–4, 1995, pp. 341–348.
- [257] Tyson, D. S., C. A. Bignozzi, and F. N. Castellano, "Metal-Organic Approach to Binary Optical Memory," *J. Am. Chem. Soc.*, Vol. 124, No. 17, pp. 4562–4563.
- [258] Persson, S. H. M., et al., "A Self-Assembled Single-Electron Tunneling Device," *Molecular Electronics: Sci. & Technol. Annals, N.Y. Acad. Sci.*, Vol. 852, 1998, pp. 188–196.
- [259] Persson, S. H. M., L. Olofsson, and L. Gunnarsson, "A Self-Assembled Single-Electron Tunneling Transistor," *Appl. Phys. Lett.*, Vol. 74, No. 17, 1999, pp. 2546–2548.
- [260] Shimidzu, T., "Approaches to Ultimate Functional Polymers: Quantum Functional and Molecular Engineering Materials," *Macromol. Symp.*, Vol. 175, 2001, pp. 177–184.
- [261] Shimidzu, T., "Approaches to Polymer Superlattice and Molecular Device," *Macromol. Symp.*, Vol. 104, 1996, pp. 127–135.
- [262] Shimidzu, T., "Functionalized Conjugating Polymers: From Molecule and Ions Transporting Membranes to Advanced Electronic and Photonic Materials," *Pure Appl. Chem.*, Vol. 67, No. 12, 1995, pp. 2039–2046.
- [263] Shimidzu, T., T. Iyoda, and H. Segawa, "Advanced Materials by Functionalization of Conjugated Polymers," *Macromol. Symp.*, Vol. 101, 1996, pp. 207–218.
- [264] Feynman, R. P., "Simulating Physics with Computers," *Int. J. Theor. Phys.*, Vol. 21, No. 6–7, 1982, pp. 467–488.
- [265] Preskill, J., "Battling Decoherence: The Fault-Tolerant Quantum Computer," *Physics Today*, Vol. 52, No. 6, 1999, pp. 24–30.
- [266] Cory, D. G., et al., "Experimental Quantum Error Correction," *Phys. Rev. Lett.*, Vol. 81, No. 10, 1998, pp. 2152–2155.
- [267] Preskill, J., "Quantum Computing: Pro and Con," *Proc. R. Soc. London Ser. A-Math. Phys. Eng. Sci.*, Vol. 454, No. 1969, pp. 469–486.
- [268] Steane, A., "Quantum Computing," *Rep. Prog. Phys.*, Vol. 61, No. 2, 1998, pp. 117–173.
- [269] Deutsch, D., and A. Ekert, "Quantum Computation," *Physics World*, Vol. 11, No. 3, 1998, pp. 47–52.
- [270] Gardner, M., "Mathematical Games. The Fantastic Combinations of John Conway's New Solitaire Game 'Life,'" *Scientific American*, Vol. 223, 1970, pp. 120–123.
- [271] Roychowdhury, V. P., D. B. Janes, and S. Bandyopadhyay, "Nanoelectronic Architecture for Boolean Logic," *Proc. IEEE*, Vol. 85, No. 4, 1997, pp. 574–588.
- [272] Goodnick, S. M., and J. Bird, "Quantum-Effect and Single-Electron Devices," *IEEE Trans. on Nanotechnology*, Vol. 2, No. 4, 2003, pp. 368–385.
- [273] Wendin, G., "Scalable Solid-State Qubits: Challenging Decoherence and Read-Out," *Philos. Trans. R. Soc. Lond. Ser. A-Math. Phys. Eng. Sci.*, Vol. 361, No. 1808, 2003, pp. 1323–1338.
- [274] Milburn, G. J., "Quantum Computing Using a Neutral Atom Optical Lattice: An Appraisal," *Fortschritte Phys.-Prog. Phys.*, Vol. 48, No. 9–11, 2001, pp. 957–964.
- [275] Golovach, V. N., and D. Loss, "Electron Spins in Artificial Atoms and Molecules for Quantum Computing," *Semicond. Sci. Technol.*, Vol. 17, No. 4, 2002, pp. 355–366.
- [276] Burkard, G., and D. Loss, "Quantum Information Processing Using Electron Spins in Quantum Dots," *Acta Phys. Pol. A*, Vol. 100, No. 2, 2001, pp. 109–127.
- [277] Leuenberger, M. N., and D. Loss, "Spintronics and Quantum Computing: Switching Mechanisms for Qubits," *Physica E*, Vol. 10, No. 1–3, 2001, pp. 452–457.
- [278] Sukhorukov, E. V., and D. Loss, "Spintronics and Spin-Based Qubits in Quantum Dots," *Phys. Status Solidi B-Basic Res.*, Vol. 224, No. 3, 2001, pp. 855–862.

- [279] Calarco, T., et al., "Quantum Computing with Trapped Particles in Microscopic Potentials," *Fortschritte Phys.-Prog. Phys.*, Vol. 48, No. 9–11, 2000, pp. 945–955.
- [280] Burkard, G., H. A. Engel, and D. Loss, "Spintronics and Quantum Dots for Quantum Computing and Quantum Communication," *Fortschritte Phys.-Prog. Phys.*, Vol. 48, No. 9–11, 2000, pp. 965–986.
- [281] Clark, R. G., et al., "Progress in Silicon-Based Quantum Computing," *Philos. Trans. R. Soc. Lond. Ser. A-Math. Phys. Eng. Sci.*, Vol. 361, No. 1808, 2003, pp. 1451–1471.
- [282] Wang, K. L., "Issues of Nanoelectronics: A Possible Roadmap," *J. Nanosci. Nanotechnol.*, Vol. 2, No. 3–4, 2002, pp. 235–266.
- [283] Fischer, C. M., M. Burghard, and S. Roth, "Microelectronic and Nanoelectronic Aspects in Conjugated Systems," in "New Materials: Conjugated Double Bond Systems," *Mater. Sci. Forum*, Vol. 191, 1995, pp. 149–157.
- [284] Rosei, F., "Nanostructured Surfaces: Challenges and Frontiers in Nanotechnology," *J. Phys.-Condes. Matter.*, Vol. 16, No. 17, 2004, pp. S1373–S1436.
- [285] Eigler, D. M., C. P. Lutz, and W. E. Rudge, "An Atomic Switch Realisation with Tunneling Microscope," *Nature*, Vol. 352, 1991, pp. 600–603.
- [286] Saenz, J. J., and N. Garcia, "Quantum Atom Switch: Tunneling of Xe Atoms," *Phys. Rev. B, Cond. Matt.*, Vol. 47, 1993, pp. 7537–7541.
- [287] Schmid, G., and Y. P. Liu, "Quasi One-Dimensional Arrangements of Au-55(PPh<sub>3</sub>)(12)Cl-6 Clusters and Their Electrical Properties at Room Temperature," *Nano Lett.*, Vol. 1, No. 8, 2001, pp. 405–407.
- [288] Vidoni, O., et al., "Quasi One-Dimensional Gold Cluster Arrangements," *J. Mater. Chem.*, Vol. 11, No. 12, 2001, pp. 3188–3190.
- [289] Mulvaney, P., et al., "Silica Encapsulation of Quantum Dots and Metal Clusters," *J. Mater. Chem.*, Vol. 10, No. 6, 2000, pp. 1259–1270.
- [290] Schmid, G., and N. Beyer, "A New Approach to Well-Ordered Quantum Dots," *Eur. J. Inorg. Chem.*, No. 5, 2000, pp. 835–837.
- [291] Sear, R. P., et al., "Spontaneous Patterning of Quantum Dots at the Air-Water Interface," *Phys. Rev. E*, Vol. 59, No. 6, 1999, pp. R6255–R6258.
- [292] Brousseau, L. C., et al., "Electronic Properties of Single Au Nanocrystals and Synthesis of 1-Dimensional Nanocrystal Arrays," *Mater. Res. Bull.*, August 1998, pp. 129–137.
- [293] Collier, C. P., T. Vossmeier, and J. R. Heath, "Nanocrystal Superlattices," *Annu. Rev. Phys. Chem.*, Vol. 49, 1998, pp. 371–404.
- [294] Andres, R. P., et al., "Self-Assembly of a Two-Dimensional Superlattice of Molecularly Linked Metal Clusters," *Science*, Vol. 273, No. 5282, 1996, pp. 1690–1693.
- [295] Lu, X., et al., "Producing Reactive Species on Si(100), Ge(100), and Si(111) Surfaces by Attachments of Diacetylenes," *J. Phys. Chem. B*, Vol. 108, No. 14, 2004, pp. 4478–4484.
- [296] Warner, M. G., and J. E. Hutchison, "Arrangement of Functionalized Gold Nanoparticles Using Biopolymer Scaffolds: Progress Toward the Development of New Building Blocks for Nanoelectronic Devices," *Abstr. Pap. Am. Chem. Soc.*, Vol. 225, 2003, p. 257.
- [297] Akamatsu, K., et al., "Highly Reactive Intermediate-Functionalized Gold Clusters: Synthesis and Immobilization on Silica Supports Through Amide-Forming Coupling," *J. Mater. Chem.*, Vol. 12, No. 10, 2002, pp. 2862–2865.
- [298] Li, Q. G., J. W. Zheng, and Z. F. Liu, "Site-Selective Assembly of Gold Nanoparticles on Silicon Using AFM Nano-Oxidation Technique," *Chem. J. Chin. Univ.-Chin.*, Vol. 22, No. 7B, 2001, pp. 1216–1218.
- [299] Lin, Y., et al., "Photonic Pseudo-Gap-Based Modification of Photoluminescence from CdS Nanocrystal Satellites Around Polymer Microspheres in a Photonic Crystal," *Appl. Phys. Lett.*, Vol. 81, No. 17, 2002, pp. 3134–3136.
- [300] Shim, M., and P. Guyot-Sionnest, "N-Type Colloidal Semiconductor Nanocrystals," *Nature*, Vol. 407, No. 6807, 2000, pp. 981–983.

- [301] Somasundaran, P., "Simple Colloids in Simple Environments Explored in the Past, Complex Nanoids in Dynamic Systems to be Conquered Next: Some Enigmas, Challenges, and Strategies," *J. Colloid Interface Sci.*, Vol. 256, No. 1, pp. 3–15.
- [302] Khomutov, G. B., et al., "Interfacial Nanofabrication Strategies in Development of New Functional Nanomaterials and Planar Supramolecular Nanostructures for Nanoelectronics and Nanotechnology," *Microelectron. Eng.*, Vol. 69, No. 2–4, 2003, pp. 373–383.
- [303] Lee, C., et al., "Molecular Wires and Gold Nanoparticles as Molewares for the Molecular Scale Electronics," *Curr. Appl. Phys.*, Vol. 2, No. 1, 2002, pp. 39–45.
- [304] Davydov, D. N., et al., "Field Emitters Based on Porous Aluminum Oxide Templates," *J. Appl. Phys.*, Vol. 86, No. 7, 1999, pp. 3983–3987.
- [305] Shingubara, S., "Fabrication of Nanomaterials Using Porous Alumina Templates," *J. Nanopart. Res.*, Vol. 5, No. 1–2, 2003, pp. 17–30.
- [306] Keating, C. D., and M. J. Natan, "Striped Metal Nanowires as Building Blocks and Optical Tags," *Adv. Mater.*, Vol. 15, No. 5, 2003, pp. 451–454.
- [307] Kim, K. S., "Self-Assembled Organic Nanotubes and Self-Synthesized Silver Subnanowire Arrays in an Ambient Solution Phase," *Curr. Appl. Phys.*, Vol. 2, No. 1, 2002, pp. 65–69.
- [308] Ahmad, S., "Carbon Nanostructures Fullerenes and Carbon Nanotubes," *IETE Tech. Rev.*, Vol. 16, No. 3–4, 1999, pp. 297–310.
- [309] Yu, M. F., "Fundamental Mechanical Properties of Carbon Nanotubes: Current Understanding and the Related Experimental Studies," *J. Eng. Mater. Technol.-Trans. ASME*, Vol. 126, No. 3, 2004, pp. 271–278.
- [310] Harris, P. J. F., "Carbon Nanotube Composites," *Int. Mater. Rev.*, Vol. 49, No. 1, 2004, pp. 31–43.
- [311] Ando, T., "Carbon Nanotubes and Exotic Transport Properties," *Physica E*, Vol. 22, No. 1–3, 2004, pp. 656–661.
- [312] Dresselhaus, M. S., and H. Dai, "Carbon Nanotubes: Continued Innovations and Challenges," *MRS Bull.*, Vol. 29, No. 4, 2004, pp. 237–239.
- [313] McEuen, P. L., and J. Y. Park, "Electron Transport in Single-Walled Carbon Nanotubes," *MRS Bull.*, Vol. 29, No. 4, 2004, pp. 272–275.
- [314] Jayaraman, K., et al., "Recent Advances in Polymer Nanofibers," *J. Nanosci. Nanotechnol.*, Vol. 4, No. 1–2, 2004, pp. 52–65.
- [315] Lin, Y., et al., "Advances Toward Bioapplications of Carbon Nanotubes," *J. Mater. Chem.*, Vol. 14, No. 4, 2004, pp. 527–541.
- [316] Milne, W. I., et al., "Carbon Nanotubes as Field Emission Sources," *J. Mater. Chem.*, Vol. 14, No. 6, 2004, pp. 933–943.
- [317] Xu, J., "Nanotube Electronics: Non-CMOS Routes," *Proc. IEEE*, Vol. 91, No. 11, 2003, pp. 1819–1829.
- [318] Baxendale, M., "The Physics and Applications of Carbon Nanotubes," *J. Mater. Sci.-Mater. Electron.*, Vol. 14, No. 10–12, 2003, pp. 657–659.
- [319] Huang, X. Y., and M. Zheng, "Programmable Assembling Metallic Nanoparticles with Biological Molecules for Nanoelectronic Devices and Sensors," *Abstr. Pap. Am. Chem. Soc.*, Vol. 225, 2003, pp. 243243.
- [320] Prokop, A., "Bioartificial Organs in the Twenty-First Century—Nanobiological Devices," *Ann. NY Acad. Sci.*, Vol. 944, 2001, pp. 472–490.

# Chemical and Biosensors

## 7.1 Classification and Main Parameters of Chemical and Biosensors

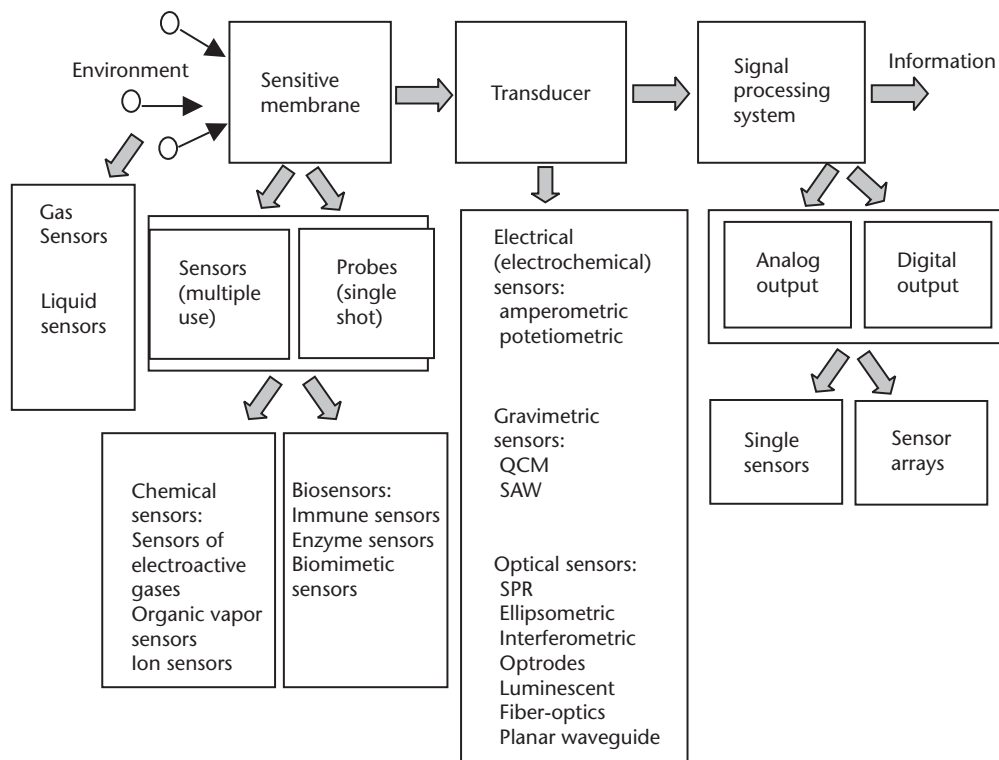
While the implementation of organic films and chemical nanotechnologies microelectronics and optoelectronics is the subject of ongoing discussions and competitions with solid-state technologies, their major role in the development of chemical and biosensors cannot be argued at all. The enormous variety of organic and bioorganic compounds, and the practically unlimited possibilities of their further chemical synthesis, cannot be compared with the rather limited choices of inorganic materials used in chemical and biosensors.

The role of chemical and biosensors has become extremely important in modern computer-controlled systems, used in such areas as biomedical instrumentation, environmental control systems, and expert systems for food industry and agriculture, where sensors provide an interface between the environment and the computer-controlled systems. The number of publications on chemical and biosensors for the last two decades reaches 10,000, which includes many excellent reviews and monographs [1–23]. This area, however, is still evolving, and this chapter gives a short review of recent developments in sensors, as well as the summary of existing knowledge.

### 7.1.1 Main Definitions and Classification of Sensors

Chemical and biosensors can be defined as devices that transform different chemical or biochemical reactions (including adsorption of molecules) into some measurable physical parameters. A simple scheme of chemical and biosensors comes from the above definition. As shown in Figure 7.1, a typical chemical or biosensor consists of three main parts: (1) a sensitive membrane, where the molecular recognition or chemical reactions occur; (2) a transducer, which serves as an interface between the sensor and environment, and transforms the molecular adsorption and/or chemical reactions into some physical parameters; and (3) a signal processing system to quantify this physical parameter, and to deliver information in a suitable form to the external receiver.

The above scheme is very general and allows various deviations and transformations. In many cases, the sensitive membrane may combine both functions of molecular recognition and transducing. The signal processing system largely depends on the type of information required, and it can vary from a simple visualization, to sophisticated dataforms for further computer analysis.



**Figure 7.1** Classification of chemical and biosensors.

The scheme in Figure 7.1 leads to more detailed systematic of sensors. In other words, sensors can be systematized by the type of chemical reaction registered, or by the type of transducer, or by the approach in signal processing and information representation.

Starting with the analyzed environment, sensors can be formally divided into two categories: gas sensors, and sensors working in a liquid environment. Moving to the sensitive membrane, two types of sensors can be defined, depending on the nature of chemical processes taking place in the membrane: sensors of multiple use, and single shot (or disposable) sensors. Furthermore, sensors of both inorganic and organic molecules having relatively small molecular weight are called chemical sensors, while sensors of much larger biological molecules are called biosensors. The common characteristic for all sensitive membranes is that they must provide a function of molecular recognition; in other words, a selective adsorption of (or reaction with) molecules from the environment. The type of chemical processes in the membrane triggers three classifications: electro-active gas sensors, organic vapor sensors, and ion sensors.

According to this principle, biosensors can be also divided into two large classes: (1) sensors based upon highly specific binding of biomolecules, such as reactions between antibodies and antigens in immune sensors, and (2) catalytic sensors, which, in addition to specific binding of analyte molecules from the environment,

decompose them into smaller products. A typical example of the latter biosensor is an enzyme sensor, which contains enzyme molecules in the membrane that act as catalysts to decompose small molecules of substratum from the environment. Typically, the membranes of biosensors contain natural bioactive molecules, such as antibodies or enzymes, which might be very expensive. At the same time, there exists the less expensive option of biomimetic sensors having artificial synthetic receptors, which can mimic the main natural biofunctions. However, both the sensitivity and selectivity of biomimetic sensors are not as good as in the natural biosensors.

Sensors can be classified by the transducing principle. The main types of transducers, as shown in Figure 7.1, include:

1. *Electrical (or electrochemical) transducers*, which transform chemical reactions into electrical signals—either electric current (amperometric sensors), or voltage (potentiometric);
2. *Gravimetric sensors*, which register changes in the mass due to molecular adsorption, and consist of two subclasses—quartz crystal microbalance (QCM), and surface acoustic wave (SAW) devices;
3. *Optical sensors*, which are a large group of devices based on different principles. Surface plasmon resonance (SPR), ellipsometry, and interferometry measure changes in the refractive index and thickness of membranes caused by different chemical and biochemical reactions. Optrodes register attenuation of the light intensity, while luminescent sensors measure the intensity of luminescence (fluorescence). The principle of optrodes or interferometry can be implemented using fiber optic sensors and planar waveguides.

More detailed descriptions and comparisons of different transducing principles will be given in Section 7.2.

Sensors also can be grouped according to the signal processing routine used. Depending on the final signal form, sensors can be divided into digital and analog devices. Although the digital form of the output signals is the most common because of compatibility with computing systems, analog forms of output signals are still preferable for a simple visualization of sensor response.

The most common form of sensor device is a single sensor, which ideally responds to a particular type of analyte molecule. In real sensor devices, selectivity and sensitivity must be as high as possible, as will be discussed below. However, there exists an alternative approach of using several sensors simultaneously (i.e., a sensor array). In this case, each sensor device may not be necessarily very sensitive and selective, but the possibility of molecular recognition appears when these sensors work together. If the sensitivity of these devices towards different analyte molecules differ in several times, it might be sufficient to recognize molecules by the analysis of the images in the  $n$ -dimensional space that are formed by responses of  $n$ -sensor devices. This can be understood in a simple example of a sensor array consisting of two devices (S1 and S2) that have slightly different sensitivities to two different analytes (A1 and A2); for example, S1 is more sensitive to A1, and S2 is more sensitive to A2, respectively. The two-dimensional graph of sensor responses (R1

and R2), shown in Figure 7.2, gives two different areas for two analytes (A1 and A2), which allows us to distinguish easily between A1 and A2, and then to quantify them.

This approach can be easily extended to the n-dimensional space using dedicated software. Artificial neural network (ANN) systems software can be effectively deployed for such data analysis. Without going into details of the very complex subject of ANN expert systems, it can be stated that ANN can be realized using standard computing facilities (PCs), and widely available software, such as MatLab. The recognition process consists first in “training” the ANN software by feeding data into a PC. Such data includes the responses of different sensors (R1, R2, ..., Rn) to different analytes (A1, A2, ..., An) of different concentrations (C1, C2, ..., Cn). During this process, the weight coefficients of the links between neurones are tuned. On the second stage of the analysis, the response to unknown mixtures of analytes can be compared to the existing database, and the ANN system calculates the composition of the mixture, as well as the concentration of individual analytes. Such sensor arrays combined with ANN systems have become very popular in chemical and biosensing, and have found numerous applications in various systems in food industry, agriculture, pharmacy, health care, and environmental control.

### 7.1.2 Parameters of Sensors

One of the most important parameters of chemical and biosensors is their sensitivity. The exact definition of sensitivity is the changes of some measurable values ( $I$ ), caused by changes in the concentration ( $C$ ) of registered analyte molecules [19]:

$$S = \frac{dI}{dC} \quad (7.1)$$

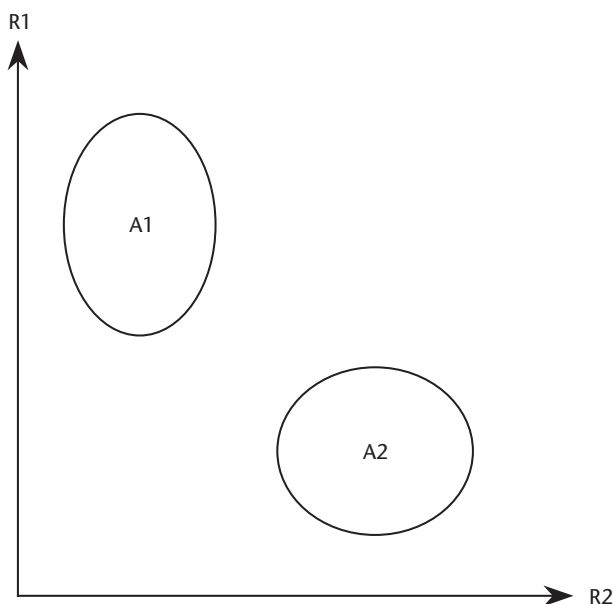


Figure 7.2 Illustration of the recognition of two analytes (A1 and A2) with a two-sensor array.



This definition is not very convenient for the comparison of different physical parameters. It is better to operate with relative changes in the signal  $i = \frac{I}{I_0}$ , where  $I_0$  is the maximum possible signal corresponding to the situation in which all adsorption sites are occupied with analyte molecules. In this sense, the sensitivity is directly related to the isotherm of adsorption, which is defined as the dependence of the number of occupied adsorption sites on the concentration of adsorbing molecules in the environment. In a simple case of the reversible adsorption of molecules on the surface containing a certain fixed number of adsorption sites, the isotherm of adsorption can be represented by the Langmuir adsorption isotherm [24]:

$$\theta = \frac{K_a C}{1 + K_a C} \quad (7.2)$$

where  $\theta$  is the surface coverage,  $C$  is the concentration of molecules in the environment, and  $K_a$  is the equilibrium coefficient.  $K_a$  depends on the temperature and the activation energies of adsorption and desorption:

$$K_a = \frac{[S - M]}{[S][M]} = \frac{\theta}{(1 - \theta)C} = \exp\left(\frac{E_{des} - E_{ads}}{RT}\right) \quad (7.3)$$

In (7.3),  $[S - M] \sim \theta$ ,  $[S] \sim 1 - \theta$ , and  $[M] \sim C$  denote, respectively, the sites occupied by analyte molecules, empty sites, and free molecules in the environment.

In the case of adsorption in the bulk of a thin film (i.e., a sensitive membrane), when the diffusion of analyte molecules into the film is fast, and thus can be neglected, the adsorption isotherm is described by Brunauer-Emmett-Teller (BET) equation [24]:

$$\theta = \frac{\theta_{\max} K_b C}{(C_{\max} - C)[(1 + (K_b - 1)C/C_{\max})]} \quad (7.4)$$

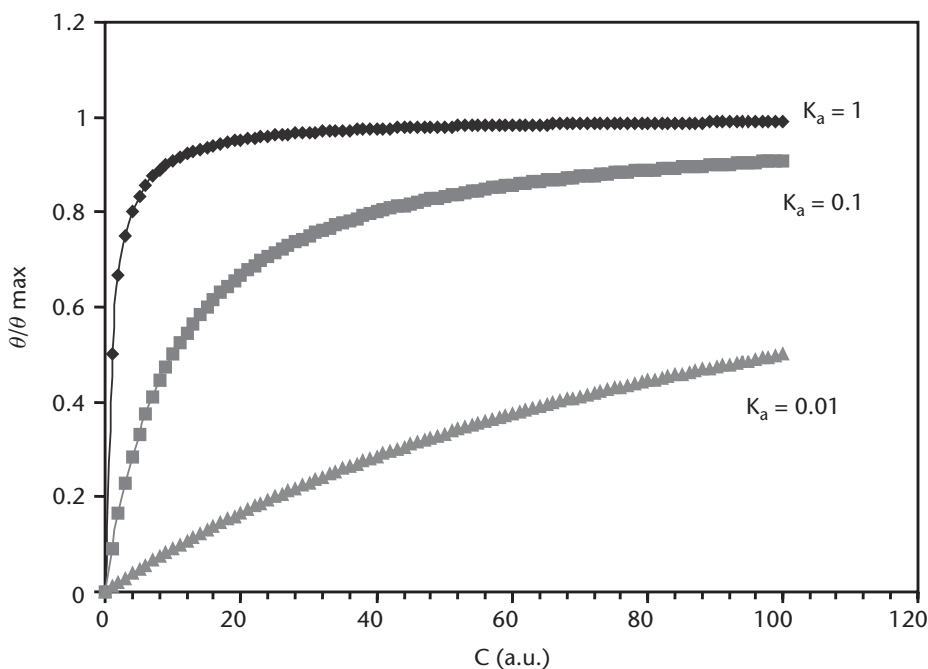
where  $\theta_{\max}$  is the maximal coverage that can be achieved at a certain concentration of analyte molecules  $C_{\max}$ , and  $K_b$  is the coefficient similar to  $K_a$  in (7.2) and (7.3).

The dependence (7.3) is not linear, as shown in Figure 7.3, with the occupation of adsorption sites reaching its maximum.

Therefore, the sensitivity defined in (7.1) is not constant, but varies on different stages of adsorption. For example, from (7.3) for the Langmuir adsorption, assuming that the signal  $I$  is proportional to the surface coverage  $\theta$ , the sensitivity  $S$  can be found as:

$$S = \frac{dI}{dC} = \frac{1}{(1 + K_a C)^2} \quad (7.5)$$

However, in practical terms of sensor devices, we often substitute the term of sensitivity with the range of measurable concentrations of analyte molecules, or even with the minimal possible registered concentration, which can be distinguished from the noise level. The concentration of analyte molecules can be measured in



**Figure 7.3** Langmuir adsorption isotherm at different values of  $K_a$ .

absolute units of weight (e.g., g/L, mg/mL, or ng/mL); in molar concentration (M/L); or in relative units such as parts per million (ppm), which represents the number of analyte molecules per million of the main molecules in the environment.

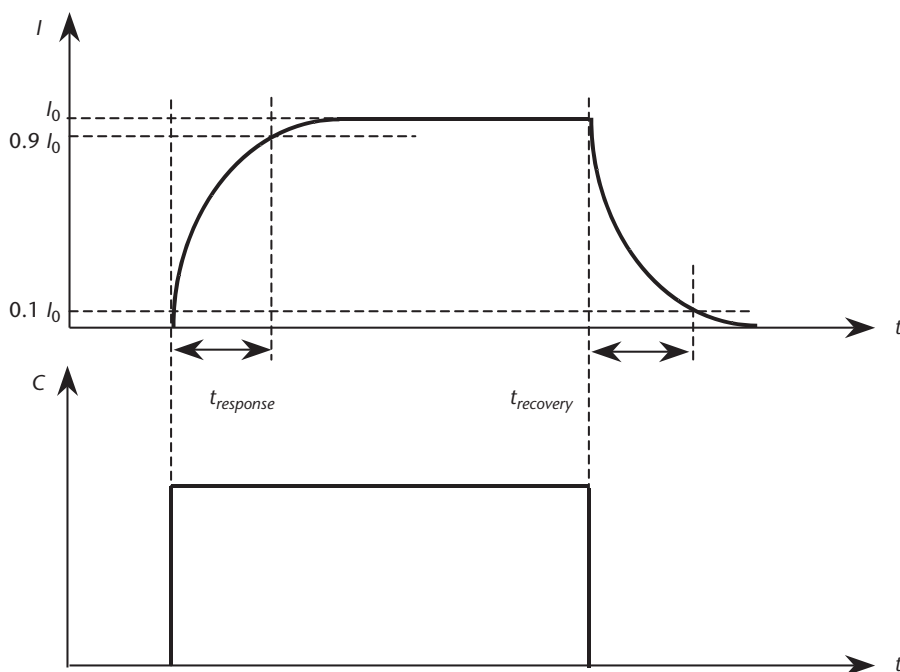
Another very important parameter of chemical and biosensors is the selectivity. In the case of a sensor responding to  $n$  different analytes with respective sensitivities  $S_i = \frac{dl_i}{dC_i}$  ( $i = 1, 2, \dots, n$ ), they can be compared by their ratio  $\Lambda_{ij} = \frac{S_i}{S_j}$ , which is called the selectivity. At the initial stage of adsorption, when the output signal of the sensor is proportional to the analyte concentration ( $I \sim C$ ), the selectivity is simply equal to the ratio of the respective equilibrium constants [19]:

$$\Lambda_{ij} = \frac{K_a^i}{K_a^j} \quad (7.6)$$

Adsorption kinetics, or time dependence in the case of either Langmuir or BET adsorption, can be described by a simple exponential dependence [24]:

$$N = N_0 \left[ 1 - \exp\left(-\frac{t}{\tau_a}\right) \right] \quad (7.7)$$

where  $N$  is the number of occupied binding sites,  $N_0$  is the total number of binding sites, and  $\tau_a$  is the characteristic time of adsorption. This dependence is shown in Figure 7.4 as a response to a rectangular pulse of concentration of analyte molecules. The response time, defined as the time when the signal reaches 90% of its maximum, is  $t_{\text{response}} = 2.3\tau_a$ .



**Figure 7.4** The response of a sensor to a pulse of concentration of analyte.

A very important feature of chemical and biosensors is their ability to recover the main state of the sensitive membrane, and thus the initial value of a physical measurable parameter, after removing the source of analyte molecules from the environment. The sensor recovery depends on the desorption rate of analyte molecules. Typically, the exponential decay in the occupation of adsorption sites depends on a characteristic time of desorption ( $\tau_d$ ) [24]:

$$N = N_0 \exp\left(-\frac{t}{\tau_d}\right) \quad (7.8)$$

Typically, the recovery time, defined as the time when the signal returns to the level of 10% higher than the initial value,  $t_{\text{recovery}} = 2.3\tau_d$ .

In the case of simple adsorption of analyte molecules on binding sites, the characteristic times of adsorption and desorption are the same ( $\tau_a = \tau_d$ ). If, however, some chemical reactions take place during adsorption, so that the postadsorption state of the analyte molecules is different, the characteristic times,  $\tau_a$  and  $\tau_d$ , may become completely different.

Diffusion of the analyte molecules has a great impact on the sensor kinetics of the response, causing a delay in the response and the deviation from simple exponential behavior [18, 19].

The recovery (response) time is in a reciprocal relation with the binding constant (or selectivity); that is, the higher the selectivity of adsorption (which presumes stronger binding of the analyte molecules), the longer the desorption (recovery) time required. From the point of view of sensor development, both extreme situations, when either a full recovery or complete nonrecovery takes place, are acceptable. In

the first case, the device behaves like an ideal sensor of a multiple use. In the second case, we have a single shot sensor (or probe), which can be disposable (or, at least, a sensitive membrane is disposable, and can be easily replaced for little extra cost). An intermediate situation of noncomplete recovery of the sensor is not favorable. If this situation occurs, an automatic adjustment of the initial level is required, which can be done fairly easily with modern electronics.

## 7.2 Physical Transducing Principles for Sensors

### 7.2.1 Gravimetric Sensors

The use of gravimetric sensors is one of the simplest and most established transducing techniques. It is based upon the interaction of the acoustic waves with the material, and the transformation of either added mass or changes in the acoustic wave velocity due to molecular adsorption or chemical or biosensor reactions on the surface. Two well-known types of gravimetric sensors are bulk acoustic wave (BAW) devices, also known as quartz crystal microbalance (QCM), and surface acoustic wave (SAW) devices.

QCM transducers are usually made of AT-cut quartz crystals with gold electrodes evaporated on both sides and connected to wires with the clumps, as shown in Figure 7.5.

The operational principle of QCM lies in the registration of a resonance frequency of quartz crystal, which is affected by the added mass of adsorbed molecules. The relation between the added mass ( $\Delta m$ ) and changes in resonance frequency ( $\Delta f$ ) is governed by Saurbrey equation [25]:

$$\Delta f = -\frac{2f_0^2}{A(\rho_q \mu_q)^{1/2}} \Delta m \quad (7.9)$$

where  $f_0$  is the initial resonance frequency of quartz crystal,  $\rho = 2.648 \text{ (g} \cdot \text{cm}^{-3}\text{)}$  and  $\mu_q = 2.947 \cdot 10^{11} \text{ (g} \cdot \text{cm}^{-1} \cdot \text{s}^{-2}\text{)}$  are the density and shear modulus of quartz, respectively, and  $A$  is the area of overlapping of gold electrodes (see Figure 7.5). The surface of QCM can be coated with a film (membrane) that is sensitive to some

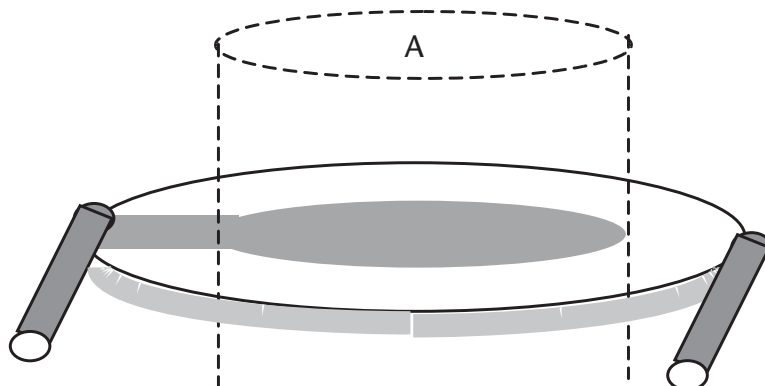


Figure 7.5 Quartz crystals with evaporated gold electrodes and clump contacts.

particular analyte molecules. The requirements for the coating are as follows: (1) it must be rigid and homogeneous, in order not to damp the oscillations; and (2) the frequency shift should not exceed 1% from the main resonance frequency, in order to fulfill the linearity of (7.9).

If the latter criterion is obeyed for the absorption of analyte molecules, and the frequency remains within the linear range of (7.9), then a linear relation between the frequency changes ( $\Delta f$  [Hz]) of AT-cut quartz crystal and the added mass ( $\Delta m$  [g]) is given by the following empirical equation [18]:

$$\Delta f = -2.3 \cdot 10^{-6} f_0^2 \frac{\Delta m}{A} \quad (7.10)$$

Typical commercial AT-cut quartz crystals having  $f_0 = 10$  MHz and  $A = 1$  cm<sup>2</sup> give the sensitivity of 0.3 Hz/ng. Considering the noise level of quartz oscillators of approximately 10 Hz, the minimal registered mass is approximately 30 ng, which is sufficient for the registration of large molecules. That is why QCM sensors found their application in biosensing, particularly immune-sensing.

For decades, the method of QCM was regarded as a “dry” method, to be used in a gaseous medium or vacuum. This fact limited the application of QCM devices. Contact between quartz crystals and viscous liquid media leads to the damping of the oscillations, and therefore makes it difficult to deploy QCM for in situ monitoring of bioreactions. However, recent progress in using thickness shire mode (TSM) resonators in liquid media has overcome the above difficulties, and widely exploit QCM in biosensing [26–32]. The main idea is to measure the whole impedance spectra of a TSM resonator, and then to fit the experimental data to the Butterworth-Van-Dyke (BVD) equivalent circuit model [33], as shown in Figure 7.6. Each element in this model represents a physical property of the crystal. In Figure 7.6,  $R$  represents the energy loss mostly arising from viscous effects;  $L$  represents the initial mass/motional inertia of the system;  $C$  is related to the mechanical elasticity of the quartz; and  $C_p$  determines the admittance away from resonance, and

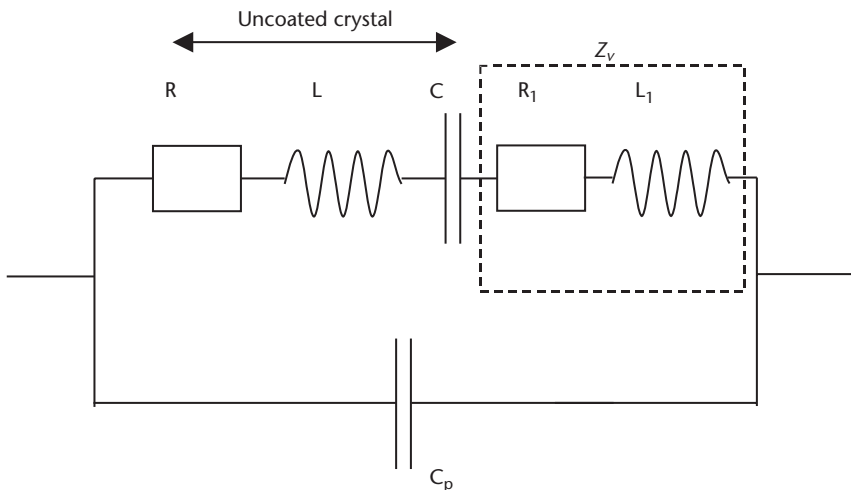


Figure 7.6 BVD equivalent circuit for QCM impedance measurements.

consists of the capacitance of the quartz between the electrodes and the parasitic capacitance of the crystal fixture.

The deposition of a viscoelastic film onto the crystal surface can be described by the additional elements  $R_1$  and  $L_1$ , representing a measure of energy dissipation in the film, and mass loading, respectively [33]. Changes in these two parameters caused by adsorption of analyte guest molecules can be obtained by fitting experimental impedance spectra to the equivalent circuit [33], and can provide additional information for the analysis of sensor response.

The following equation is used for fitting of the measured admittance spectra to the BVD model [33]:

$$Y(\omega) = G + jB = \frac{1}{Z_m + Z_v} + j\omega C_p \quad (7.11)$$

where  $Z_m(\omega) = R + j\omega L + \frac{1}{j\omega C}$ ,  $Z_v = R_1 + j\omega L_1$  and  $\omega = 2\pi f$ .

The admittance spectra is observed by two singularities called parallel and series resonance, with respective resonance frequencies  $f_s$  and  $f_p$ , related to BVD model parameters by:

$$f_s = \frac{1}{2\pi\sqrt{(L + L_1)C}} \quad \text{and} \quad f_p = \frac{1}{2\pi} \sqrt{\left[ \frac{1}{(L + L_1)} \left( \frac{1}{C} + \frac{1}{C_p} \right) \right]} \quad (7.12)$$

Using this approach, the effect of the viscous liquid medium due to parameters  $R$  and  $L$  can be separated from the effect introduced by the membrane ( $R_1$ ,  $L_1$ ). Changes in the parameters  $R_1$  and  $L_1$  caused by adsorption of analyte guest molecules can be obtained from the fitting, and can provide additional information for the analysis of sensor response.

The SAW method is based upon the registration of changes in the velocity of surface acoustic waves due to molecular adsorption. Typical SAW devices consist of two pairs of interdigitated electrodes deposited on the surface of a piezoelectric material, such as quartz, ZnO, LiNo, or AlN, as shown in Figure 7.7. One pair of interdigitated electrodes is connected to the generator, and acts as a transmitter to

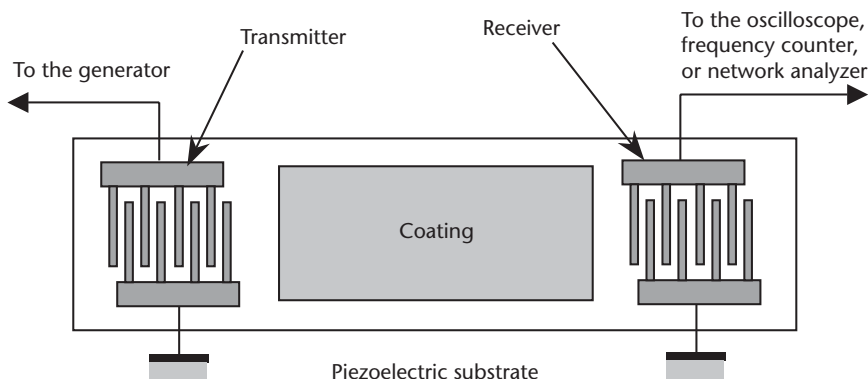


Figure 7.7 The scheme of a SAW device.

excite surface acoustic waves in the material; the other pair receives the signal propagated along the surface of the substrate.

There are several possibilities of performing SAW sensing measurements. The simplest method is to register the time delay of the signal between the transmitter and the receiver, using an oscilloscope, and then to evaluate the acoustic wave velocity. Another possibility is to measure the resonance frequency ( $f_0$ ), which is related to the parameters of the equivalent circuit, such as parallel transducer resistance ( $R_p$ ) [18]:

$$R_p = (8k^2 f_0 C_s N^2)^{-1} \quad (7.13)$$

where  $N$  is the number of pair of fringes in the interdigitated electrodes, and  $C_s$  is the capacitance per electrode. Modern network analyzers are capable of recording the whole spectra of the amplitude and phase of the transmitted signal, and performing in situ fitting to the equivalent circuit.

Similar to QCM, changes in the resonance frequency of SAW can be associated with added mass of adsorbed molecules:

$$\Delta f = (k_1 + k_2) f_0^2 \frac{\Delta m}{A} \quad (7.14)$$

where  $k_1$  and  $k_2$  are the parameters of the piezoelectric substrates.

Since the resonance frequency of SAW devices range typically in the hundreds of megahertz, their sensitivity towards the molecular adsorption is up to two orders of magnitude higher than that for QCM (BAW) devices. SAW transducers have become very attractive for sensing applications [34–36], despite their high cost compared to QCM. Similar to QCM, SAW devices operate in a gaseous medium [37, 38]. However, the use of sheer mode oscillation allows the use of SAW devices in liquids, which is more suitable for in situ biochemical sensing [39, 40].

## 7.2.2 Electrical and Electrochemical Sensors

Electrical, including electrochemical, transducers are the most common commercial sensor devices, mostly due to their low cost, but also due to the simplicity of construction and reliability of the performance. Two large classes of the electrical transducers can be defined as amperometric and potentiometric.

Amperometric sensors measure changes in the current of either chemiresistors or electrochemical electrodes, while potentiometric sensors are based on the effect of adsorbed molecules on the surface potential of materials.

The simplest amperometric sensor is a chemiresistor, having the value of resistance dependent on the molecular adsorption or on chemical reactions [18]. Different materials can be used for chemiresistors fabrication: compressed powder pellets [41], metal oxide semiconductors [42], conducting polymers [43–47], or organic semiconductors [48–52]. The various materials have different mechanisms of conductivity and relations to the environment.

Some electrically active analyte molecules may act as impurities, which have a significant impact on the conductivity of these materials. For example, oxidizing (or electronegative) gases, such as NO, NO<sub>2</sub>, SO<sub>2</sub>, O<sub>2</sub>, O<sub>3</sub>, Cl<sub>2</sub>, or HCl, act as acceptor

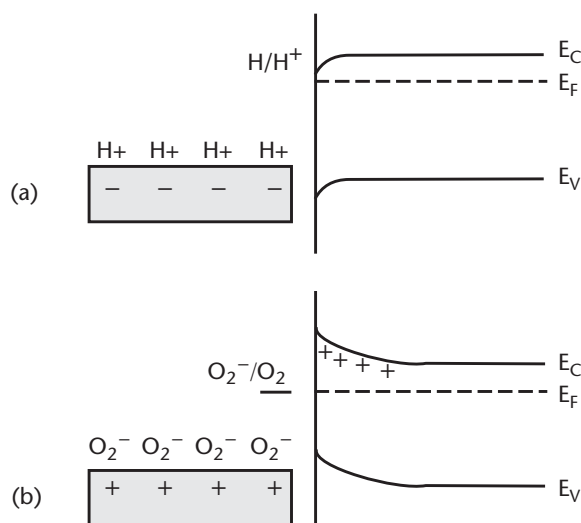


impurities for the crystalline metal phthalocyanine thin films [48, 51]. The effect of these impurities depends on their activation energy for conductivity. Some rare earth bis-phthalocyanines, such as YbPc2 or LtPc2 which have three electron states (i.e., oxidized, neutral, and reduced), show the effect of their conductivity in the presence of both oxidizing and reducing gases, such as CO, NH<sub>3</sub>, or hydrocarbons [52]. Conductivity of some polymers may depend on electroactive impurities in a similar way. However, some other mechanisms, such as the protonation/deprotonation of the polymers, or some chemical reactions with analyte molecules, may have an impact on their conductivity. All mechanisms mentioned above affect the bulk conductivity of materials.

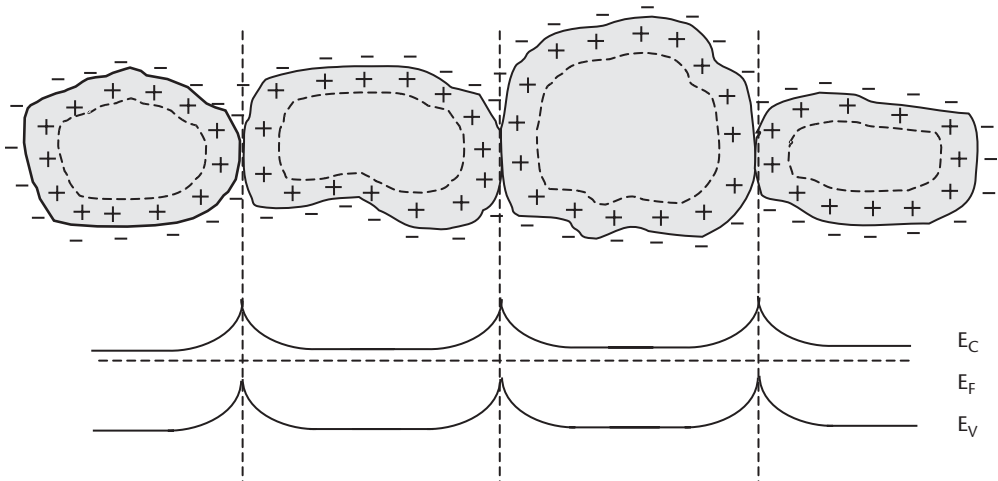
The surface effects may also significantly contribute to the conductivity of materials. For example, the adsorption of positive or negative ions on the surface of thin films of oxide semiconductors may affect the space charge layer on the semiconductor surface, and thus the film conductivity. This effect can be understood from the band diagram shown in Figure 7.8.

Adsorption of different ions on the semiconductor surface forms the mirror image charge on the semiconductor surface. Adsorption of H<sup>+</sup> ions forms the accumulation layer on the surface of an n-type semiconductor, and thus increases the conductivity, while adsorption of O<sub>2</sub><sup>-</sup> ions forms the depletion layer, and thus decreases the conductivity. Some other redox pairs, such as F/F<sup>-</sup>, may even cause the inversion of the surface conductivity. The situation can be more complicated if surface states are considered.

The surface effects in conductivity are more pronounced in porous polycrystalline materials prepared by chemical routes, such as sol-gel and electrodeposition. Similar to compressed powder materials, the lattice mismatching on the grain boundaries of micro- (nano) crystallites leads to the formation of potential barriers on the boundaries between crystallites (see Figure 7.9). Adsorption of different molecules on the grain boundaries affects the barrier height and the space-charge width, and thus the conductivity through polycrystalline materials.



**Figure 7.8** Energy band diagrams of n-type semiconductors with adsorbed of (a) H<sup>+</sup> and (b) O<sub>2</sub><sup>-</sup> ions on the surface.



**Figure 7.9** The formation of the potential barriers on the intercrystallite boundaries.

Another type of amperometric transducer is based on the direct measurements of current during electrochemical reactions [53, 54]. These measurements are usually performed in the three-electrode electrochemical cell. In such systems, the ionic current flows between the working electrode, which is coated with a sensitive layer (membrane), and the Pt counterelectrode, while all potentials are measured against the reference electrode (e.g., the AgCl/Cl electrode). The electrolyte must contain a redox pair, which provides a constant supply of ions to the system. The value of the current depends on the ion concentration.

This method is very convenient for the registration of enzyme reactions. Starting from the model reaction of glucose decomposition catalyzed by the enzyme Glucose oxidase, the electrochemical amperometric principle has become extremely popular in biosensors. The main attraction of this approach is low cost, which is why 90% of present-day commercial biosensors are amperometric.

The formation of a double layer on the surface of materials, mentioned above, constitutes the principle of potentiometric sensor devices. The dependence of the surface potential  $\varphi$  on the concentrations of molecules involved in the electrochemical reaction  $A + B = C + D$  taking place on the surface is given by Nernst equation [55]:

$$\varphi = \varphi_0 - \frac{RT}{nF} \ln \left( \frac{[C][D]}{[A][B]} \right) \quad (7.15)$$

in which  $\varphi_0$  is the initial surface potential,  $R$  and  $F$  are gas and Faraday constants, respectively, and  $n$  is the number of electrical charges involved in the electrochemical reaction. In the case of simple adsorption of, for example, hydrogen ions, the change in the surface potential is equal to:

$$\Delta\varphi = \frac{RT}{F} \ln \left( \frac{[H^+]}{H} \right) = 59(mV) \times \log \left( \frac{[H^+]}{H} \right) \quad (7.16)$$

The Nernst equation, therefore, sets the theoretical upper limit on the sensitivity of potentiometric devices, which is 59 mV per decade of concentration.

Different experimental techniques can be used for the measurements of surface potential. The Kelvin probe method [56] gives direct information on the surface potential. This method, as shown in Figure 7.10, is based upon the registration of the displacement current between the investigated sample and the vibrating electrode, which can be written as:

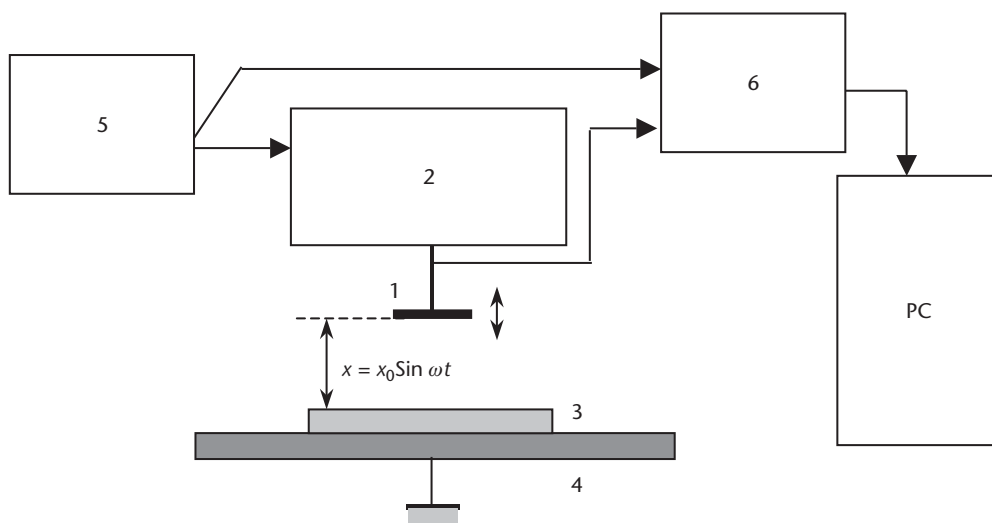
$$I = \frac{dQ}{dt} = \varphi \frac{dC}{dt} \quad (7.17)$$

If the separation between the electrode and the substrate oscillates at a frequency  $\omega$ , with  $x = x_0 \exp(-i\omega t)$ , then the current is equal to:

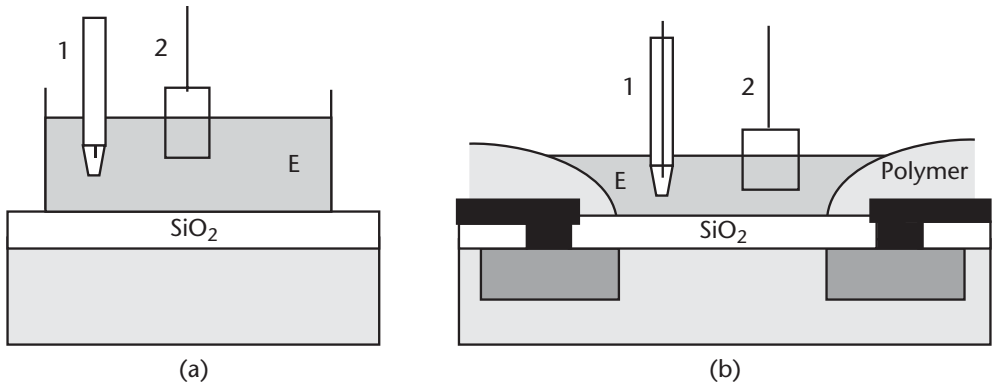
$$I = -i\varphi\omega \frac{\varepsilon\varepsilon_0 A}{x_0} \exp(-i\omega t) = -i\varphi\omega C_0 \exp(-i\omega t) \quad (7.18)$$

where  $C_0 = \frac{ee_0 A}{x_0}$ . The amplitude of the first harmonic of the oscillations is proportional to the surface potential. The method is very simple and reliable; however, it has not found a wide application in chemical sensing.

The most successful experimental realization of the potentiometric principle lies in the use of MIS structures and MOSFETs [57–59]. Strictly speaking, there must be electrolyte-oxide-semiconductors (EOS) in the above structures, since the electrolyte is used instead of a metal electrode. In the construction shown in Figure 7.11 [60, 61], source and drain electrodes are insulated from the electrolyte by the polymer coating.



**Figure 7.10** Experimental setup for Kelvin probe measurements comprising: gold plated electrode (1) fixed on the vibrator (2); investigated sample (3) fixed on the metal plate (4); generator (5); and lock-in amplifier (6) interfaced to PC.



**Figure 7.11** (a) EOS and (b) EOSFET as potentiometric transducers: (E) electrolyte, (1) reference electrode, and (2) Pt electrode.

The measurements are performed in the cell attached to the EOS structure, or EOSFET. A dc voltage is applied between the substrate and platinum electrode, and all voltages are measured against the reference electrode (Ag/AgCl). The characteristic parameters of the above devices, such as the flat-band voltage of MIS structures and the threshold voltage of MOSFETs, depend on the adsorbed ion concentration in the solution according to (7.16). MOSFETs are particularly popular sensing devices because they are fabricated with standard microelectronic technology. However, the sensitivity of these devices is limited to 59 mV per decade of concentration.

MOSFET transistors can be used as gas sensors, if the analyte gas molecules react with metal film and change the surface potential. An example of this type of device is a hydrogen sensor on palladium (Pd) gate ChemFET [18, 62, 63]. Pd film acts as a catalyst for molecular hydrogen, and triggers a following chain of events: (1)  $H_2$  transforms in its atomic form (H); (2) hydrogen atoms diffuse through the Pd film, and form a dipole layer on the Pd/SiO<sub>2</sub> interface; and (3) causes changes in the work function of Pd ( $\Phi_{Pd}$ ), which affects the threshold voltage of ChemFET. The change in the threshold voltage ( $\Delta V_T$ ) is therefore proportional to the concentration of hydrogen in the environment:

$$\Delta V_T = \Delta \Phi_{Pd} = -\Delta p N_H \epsilon_0 \quad (7.19)$$

where  $\Delta p$  is the change in the dipole moment caused by atomic hydrogen of concentration  $N_H$  ( $N_{H_2}$ ), which depends on the concentration of molecular hydrogen.

Such devices can operate at room temperature; however, their sensitivity and, particularly, recovery are much better at temperatures of approximately 150°C. Such ChemFET can be also used for detection of other gases, such as  $H_2S$  or  $NH_3$ , which can dissociate on the surface of the Pd-gate and release atomic hydrogen [18].

The adsorption FET (ADFET), which is a depletion mode ChemFET having a porous metal gate (or no gate at all) and a very thin oxide layer, can be directly used for the detection of polar molecules, such as  $NH_3$ , HCl, CO, NO, or  $NO_2$  [18]. The electric charge of the adsorbed molecules,  $eN_{ads}$ , produces an additional electric field (voltage),  $\Delta V = \frac{eN_{ads}A}{\epsilon_0 \epsilon_{ox} d_{ox}}$ , which controls the current through the channel. In order

to have a maximum effect of the adsorbed molecules, the oxide layer must be as thin as possible, without being too susceptible to electrical breakdown.

Another very promising gas sensing device, proposed in [64, 65], is based on MOSFETs with an incomplete gate electrode that does not cover the whole channel length (see Figure 7.12).

The adsorbed molecules of some gases or vapors dissociate in the electric field near the gate edge, and then diffuse along the surface. As a result of the surface charging, the MOSFET, which was initially off, eventually turns on with some delay. The delay time ( $t_d$ ) depends on the diffusion coefficient ( $D$ ) of analyte molecules,  $t_d = \Delta L^2/D$ , which allows the recognition of analyte molecules by their diffusion time.

### 7.2.3 Optical Sensors

The area of optical sensors is the largest, and is, perhaps, the most promising direction in chemical and biosensing, because of the high sensitivity of some optical methods (e.g., interferometry), as compared to gravimetric and electrical sensors. Optical transducers are based on the interaction of light with the sensitive membrane, and they respond to changes in the optical properties of the material caused by chemical or biochemical reactions. Two main groups of optical transducers can be defined: (1) passive optical devices, which register changes in the thickness ( $d$ ) and the refractive index ( $n$ ) of the membrane; and (2) active optical devices, which register either changes in the imaginary part of the refractive index, or the extinction coefficient ( $k$ ), which related is to light losses or light emitting (i.e., fluorescence or luminescence). The first group includes ellipsometry, SPR, interferometry, and fiber optics; the second group includes absorption and luminescent spectroscopy.

The principles of SPR are discussed in Chapter 4. The SPR method found its main application in chemical and biosensing, because of its relatively easy and inexpensive experimental realization. There are several commercial SPR instruments, such as BIAcore [66], SPR-4 and SPR-5 [67], FT-SPR from GWC Technologies, Inc.

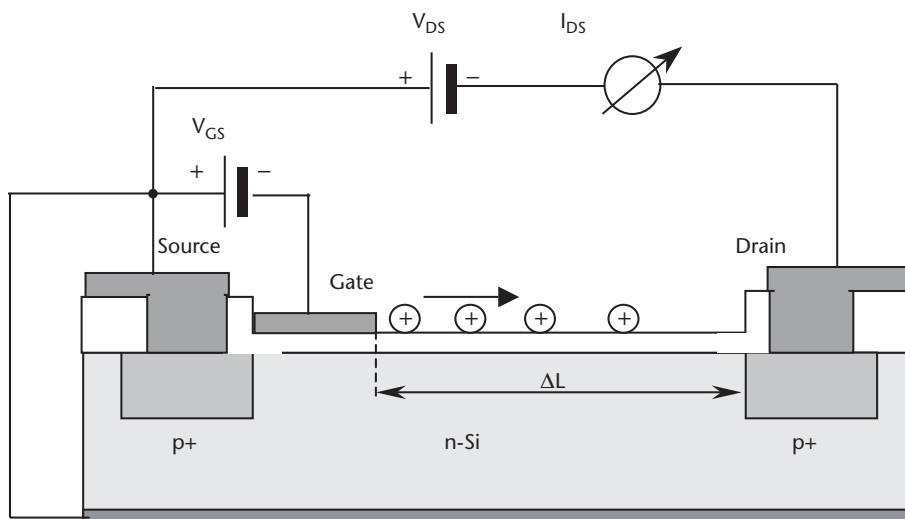


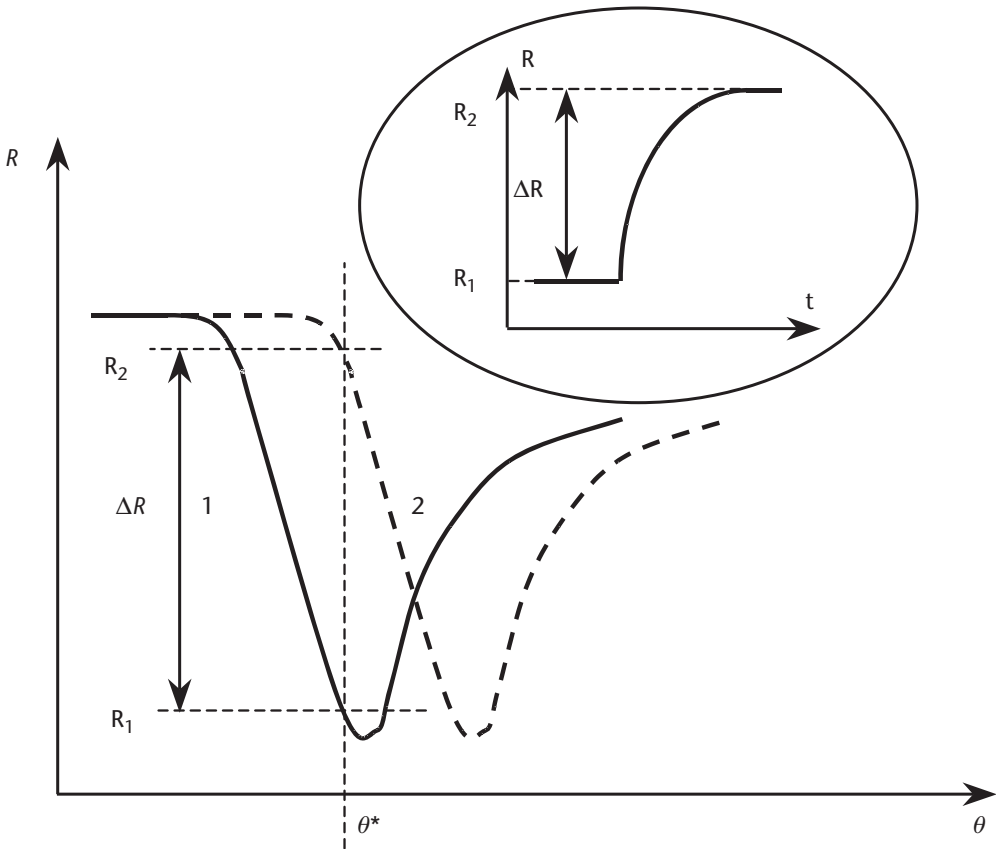
Figure 7.12 Incomplete gate MOSFETs as a gas sensor.

[68], and SPEETA from Texas Instrument [69], all of which are widely used for different sensing applications, particularly immune sensing. Parameters of the sensing membrane deposited on the surface of the prism, which include the thickness ( $d$ ), the refractive index ( $n$ ) and the extinction coefficient ( $k$ ), can be evaluated from SPR fitting. The accuracy of these parameters reaches 0.1 nm,  $10^{-5}$ , and  $10^{-4}$ , respectively. As shown in Chapter 4, the simultaneous evaluation of  $d$  and  $n$  from the SPR measurements is impossible. Very often, we have to make an assumption on the values of either  $d$  or  $n$ . In the case of the registration of rather large biomolecules, it is more appropriate to set the value of the refractive index to 1.4, which is a typical value for proteins, and only consider changes in the thickness. In the case of the adsorption of small molecules in the bulk of the sensitive membrane, the thickness can be considered to be constant; thus, the shift of the SPR curve is associated with changes in the refractive index. The broadening and dumping of the SPR minimum can be interpreted as an increase in the  $k$ -value. The interpretation of changes in SPR curves depends largely on the preliminary knowledge of the system and requires a great deal of experience.

For many practical applications, however, SPR fitting is not required. The response of the SPR transducer to chemical reactions, biochemical reactions, or molecular adsorption can be monitored as the time dependence of the reflected light intensity at a fixed angle of incidence. The choice of the angle of incidence is important for maintaining the linearity and wide dynamic range of the response. To fulfill these criteria, the angle of incidence is usually chosen on the left side of the SPR, on its linear part, and as close as possible to the SPR minimum, as shown in Figure 7.13. The linear dynamic range  $\Delta R$  can be defined as a vertical projection of a left linear part of the SPR curve. The typical SPR kinetics is shown as the inset in Figure 7.13.

More sensitive technique of ellipsometry is not as popular as SRP in sensing application. The main disadvantage of the ellipsometry method, apart from the need for more expensive equipment, is that the laser beam goes through the investigated medium, and therefore makes in situ measurements very difficult. Changes in the refractive index of the medium, caused by the injection of different solutions (e.g., gases) into the cell, interfere with changes in the film optical parameters. This problem can be overcome by using a combination of SPR and ellipsometry, called internal ellipsometry [70–73]. In this method, which has been mentioned briefly in Chapter 4, the light propagation geometry is similar to SPR. As shown in Figure 7.14, the polarized light enters the prism at normal incidence, and reflects from the bottom of the prism, which is in optical contact with a glass slide that has a thin gold film in the range from 30 to 50 nm deposited on top.

Under conditions of total internal reflection, SPR may occur, when the  $k_x$  component of the incident wave vector matches the  $k$ -vector of surface plasmons in the gold film. The choice of the prism is therefore very important. When a standard BK7 glass prism ( $n = 1.515$ ) is used, the angles of total internal reflection are  $41.3^\circ$  and  $61.4^\circ$  for air and ambient water, respectively. Therefore, the prism must have an angle larger than the total internal reflection. For example, a  $45^\circ$  prism is suitable for measurements in the air, and  $65^\circ$  to  $70^\circ$  prisms work perfectly in an aqueous medium. Using a spectroscopic ellipsometric instrument with the above prism/gold film attachment, the spectra of two ellipsometric parameters  $\Psi$  and  $\Delta$  can be recorded. Parameter  $\Psi$  represents the amplitude ratio of  $p$ - and  $s$ -components of



**Figure 7.13** The illustration of the choice of the angle of incidence ( $\theta^*$ ) for SPR kinetic measurements: (1) initial SPR curve, and (2) SPR curve shifted due to a chemical reaction in the membrane. The inset shows the SPR kinetics.

polarized light ( $tn\Psi = A_p/A_s$ ), and therefore the spectra  $\Psi(\lambda)$  closely resembles the SPR curve  $R(\theta)$ , measured in the Kretschmann-type SPR instruments (see Figure 7.15).

The relation between the two dependencies,  $R(\theta)$  and  $\Psi(\lambda)$ , can be established by the following relation, assuming that  $A_s$  is constant over the measurable spectral range:

$$k_x = \frac{2\pi}{\lambda} n_1 \sin \theta \tag{7.20}$$

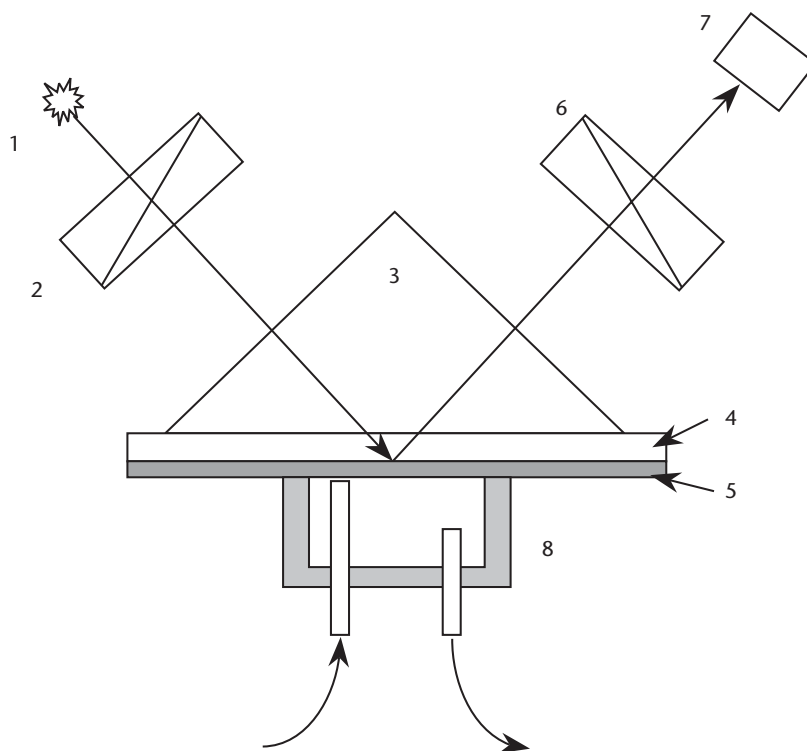
where  $n_1$  is the refractive index of the prism.

At the same time, the spectra of another ellipsometric parameter  $\Delta$ , which is a phase shift between  $p$ - and  $s$ -components of polarized light ( $\Delta = \varphi_p - \varphi_s$ ), exhibit a sharp, almost vertical drop from  $270^\circ$  to  $90^\circ$  at the wavelength close to the surface plasmon resonance, as shown in Figure 7.15.

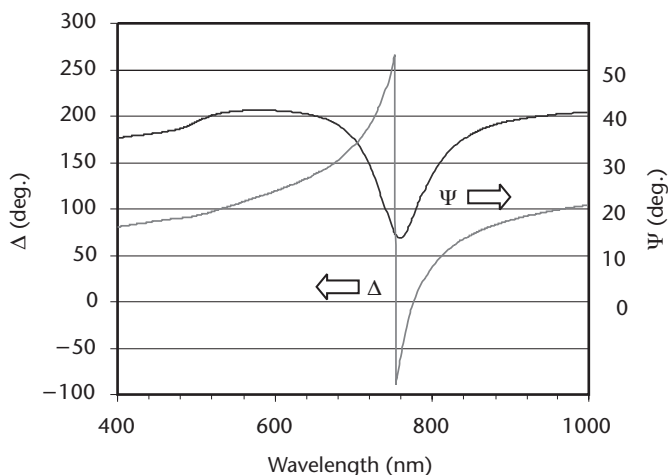
A thin film (or adsorbed layer) presented on the gold surface causes the shift of both  $\Psi(\lambda)$  and  $\Delta(\lambda)$ , as shown in Figure 7.16.

It seems that the  $\Delta(\lambda)$  spectrum is more sensitive than  $\Psi(\lambda)$  to the small changes in the optical parameters of gold film and coating. The internal ellipsometry method



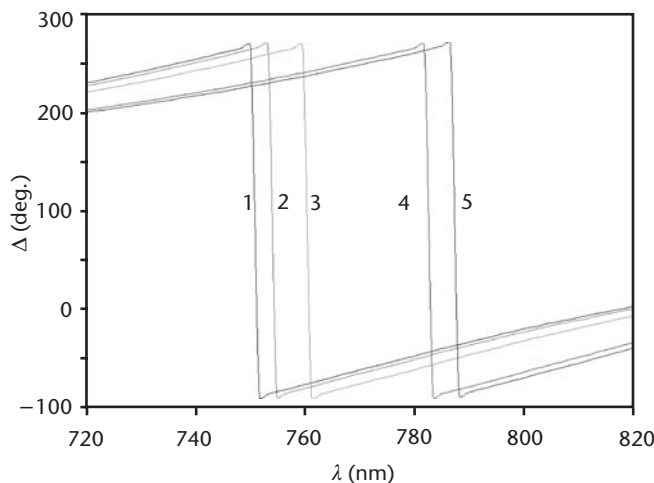


**Figure 7.14** Schematic experimental setup for internal ellipsometry, comprising of a white light source (1); polarizer (2); prism (3); glass slide (4) with evaporated thin gold film (5), brought into optical contact with the prism via index matching fluid; rotating analyzer (6); photodetector (7), consisting of fiber optics, diffraction grating, and photodiode array; and the reaction cell (8) with inlet and outlet tubes.



**Figure 7.15** Typical spectra  $\Psi(\lambda)$  and  $\Delta(\lambda)$  for gold-coated glass slide.

is very suitable for the detection of molecular adsorption, and chemical and biological reactions, when the reaction cell is attached to the gold film, as shown in Figure 7.14. Figure 7.16 shows a typical set of  $\Delta(\lambda)$  spectra corresponding to consecutive adsorption steps: bare gold, PAH layer, protein A, atrazine antiserum, and



**Figure 7.16**  $\Delta(\lambda)$  spectra measured in the Tris/HCl buffer solution after consecutive adsorption steps: (1) bare gold, (2) PAH, (3) Protein A (*Staphylococcus Aureus*), (4) atrazine antiserum, and (5) atrazine.

atrazine. The remarkable fact is that the adsorption of relatively small molecules of herbicide atrazine ( $M \sim 200$ ) produces a noticeable spectral shift, while conventional SPR measurements do not show it. Another obvious advantage of the internal ellipsometry sensing technique is that the beam does not pass through the investigated medium.

Two practical recommendations for the above method are mentioned. First, the use of a chromium sublayer improves the adhesion of gold to the glass slide, which makes the gold coating more robust and reusable in sensing experiments. Second, the use of a semicylindrical prism allows the measurements at different angles of incidence without changing the prism. However, in this case, the beam diameter must be very small, ranging from 50 to 100  $\mu\text{m}$ , as compared to the prism curvature.

The fitting of the experimental spectra to the Fresnel theory can be accomplished with commercial software, such as WVASE32, from J. A. Woollam Co., Inc. This software contains a vast library of the optical constants of materials, and various models and algorithms for data analysis.

The example of the models obtained by fitting for bare gold film and coating on top is shown in Table 7.1.

The model in Table 7.1. is reversed, as compared to conventional ellipsometry fitting models, so that the prism is taken as an ambient, the studied medium is considered as the substrate, and the adsorbed layer appears between the substrate (medium) and gold film. All adsorbed films were treated in the same way by applying a Cauchy model  $\left( n(\lambda) = A + \frac{B}{\lambda^2} + \frac{C}{\lambda^4} \right)$ . The parameters of the Cauchy model, as

**Table 7.1** The Model for Fitting of the Internal Ellipsometry Results

Medium	Thickness (nm)	Refractive Index $N(\lambda) = n - ik$
Ambient (glass prism BK7)	>10	From the WVASE32 library
Gold film	36.8	From the WVASE32 library
PAH film	1.3	Cauchy model from the VASE32 library: $A = 1.415, B = 0.01, C = 0$
Substrate (aqueous buffer solution)	>10	From the WVASE32 library

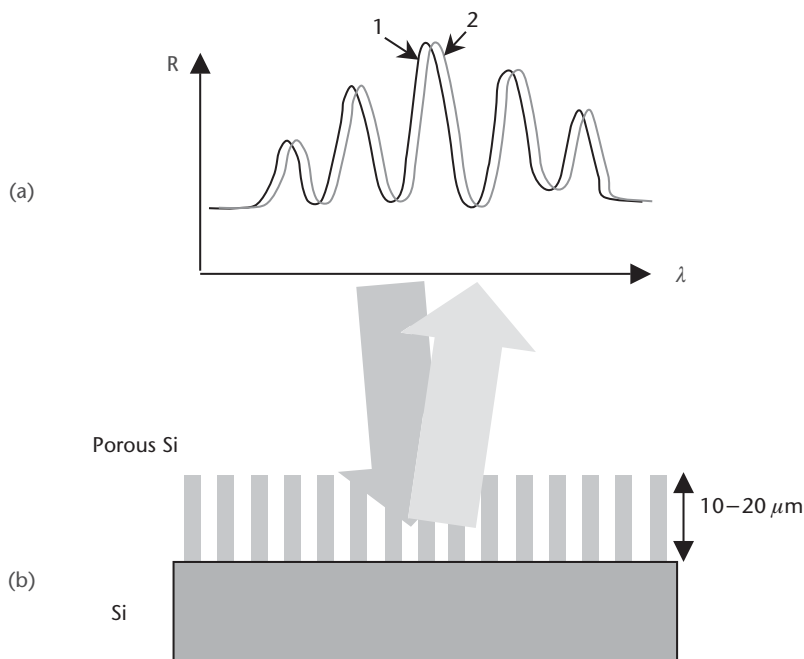
shown in Table 7.1, are kept constant in further calculations. The values of the film thickness for consecutive steps of adsorption of PAH, Protein A, antiserum (AS) atrazine, and atrazine, obtained by fitting the data as shown in Figure 7.16, are summarized in Table 7.2.

Interferometry, being the most sensitive optical technique, has found a number of applications in chemical and biosensing. One of the simplest techniques is the Fabry-Perot interferometry on porous silicon [74]. This sensor combines a high sensitivity of interferometry and a high surface area (i.e., adsorption area) of porous silicon (PS). The interferometry fringes are observed on the spectra of the light reflected from the PS sample due to the interference of two beams reflected from the top surface of porous silicon and the Si/PS interface, as shown in Figure 7.17.

The condition for the observation of maxima of reflected light intensity is  $m\lambda = 2nd$ , where  $n$  and  $d$  are the refractive index and the thickness of the PS layer, respectively, and  $m = 1, 2, 3, \dots$ . The number and position of interference fringes depend on the refractive index ( $n$ ) of PS layer. Adsorption of a large concentration of analyte molecules in PS, which is from  $10^2$  to  $10^3$  times larger than that on the flat surface, leads to the substantial changes in refractive index, and thus to the shift of the interference pattern. The spectral changes due to the adsorption of protein in PS are shown in Figure 7.17.

**Table 7.2** Values of the Film Thickness on Different Steps of Adsorption Obtained by Fitting of the Results of Internal Ellipsometry (Cauchy Model with the Fixed Parameters  $A = 1.415$ ,  $B = 0.01$ , and  $C = 0$ )

Film Thickness (nm)	PAH	Protein A	AS Atrazine	Atrazine
	1.3	3.7	6.2	10.9



**Figure 7.17** The Fabry-Perot interferometry technique of porous silicon, and the interference spectral fringes measured: (a) initial spectrum, and (b) the spectrum after protein adsorption.

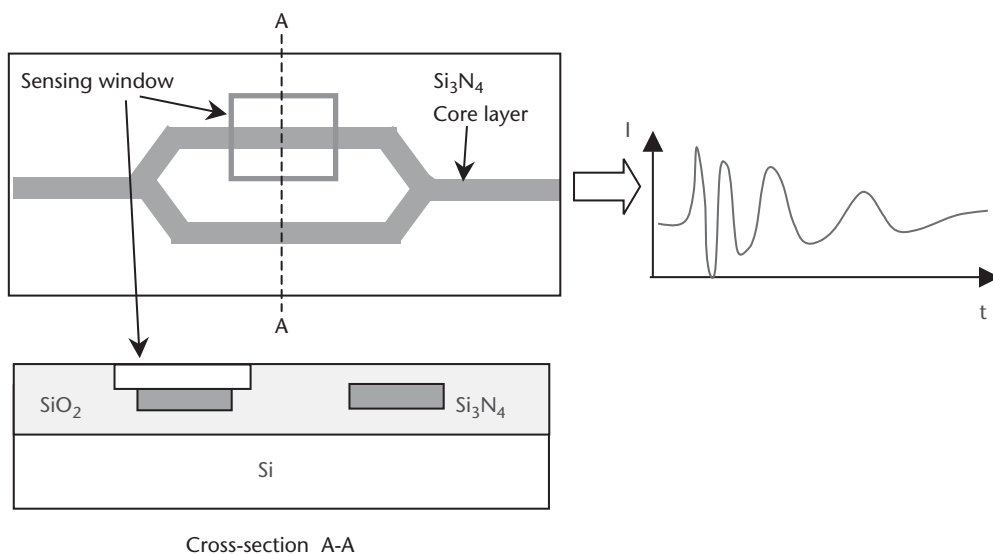
Another popular interferential transducer is Mach-Zhender (MZ) interferometer [75–79]. This device consists of a planar waveguide, having a core layer with a slightly larger refractive index than that of the cladding. The waveguide splits into two branches, as shown in Figure 7.18, with one of the branches having a sensing window etched in the top cladding layer, which exposes the core to the environment. This branch, with the window coated with a chemically sensitive layer (membrane), forms a sensing channel, while the other branch serves as a reference.

The output signal of MZ inteferometer forms by the interference of two waves from two branches at the point in which they meet, and thus depends on the phase difference between the main and reference channels. In the course of adsorption of molecules, or some chemical or biochemical reactions in the sensitive membrane, accompanied by changes in the refractive index, the phase shift between two branches will develop, and result in periodic changes in the output signal, as shown in Figure 7.18.

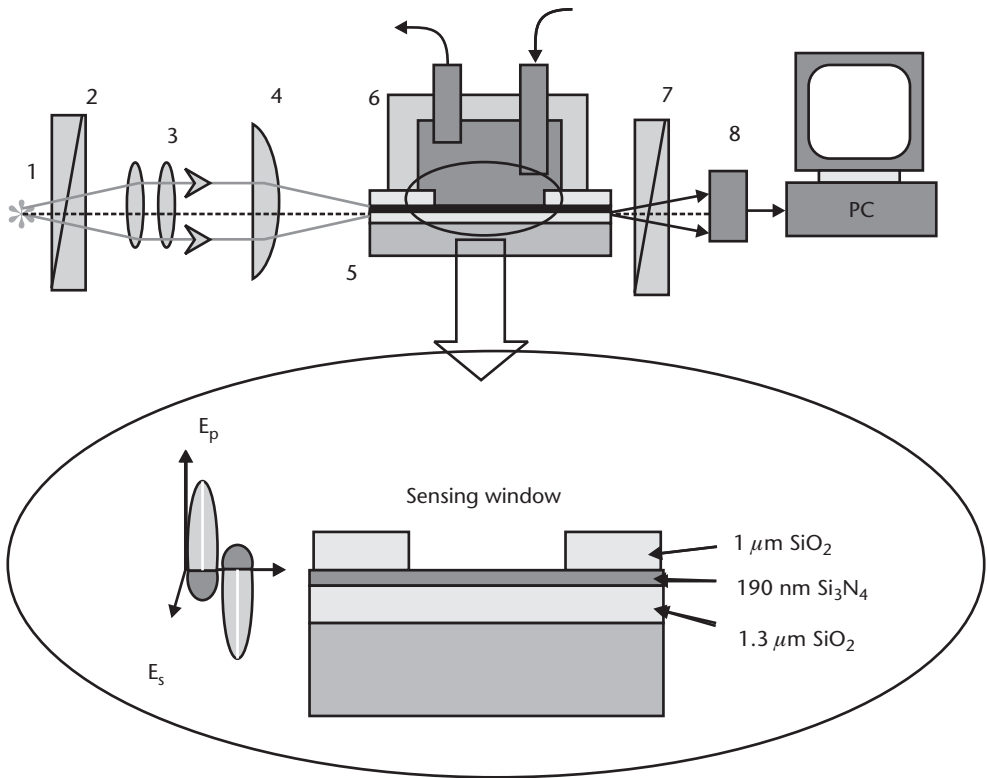
$$I = \sin(\varphi_1 - \varphi_2) \quad (7.21)$$

In the last decade, MZ interferometers produced from different materials (e.g., glass or silicon wafers) and different technologies have become very common in chemical and biosensing [76, 80, 81].

The same idea of an interferential transducer can be realized in a simple planar waveguiding structure, with no grooving and splitting of the core [82, 83]. The experimental setup for such measurements is shown in Figure 7.19. The waveguide can be fabricated with standard silicon planar technology by thermal oxidation of an Si wafer, followed by CVD deposition of silicon nitride, and then by a silicon oxide layer. The waveguiding structure  $\text{SiO}_2/\text{Si}_3\text{N}_4/\text{SiO}_2$  with thicknesses of  $1.5 \mu\text{m}$ ,  $0.2 \mu\text{m}$ , and  $1.5 \mu\text{m}$ , respectively, as shown in the inset of Figure 7.19, accommodates a single mode of HeNe laser (or semiconductor laser-diode) beam ( $\lambda = 633$



**Figure 7.18** Mach-Zhender interferometer: the top view and cross-section along the A-A line. The inset shows periodic changes in the output signal.



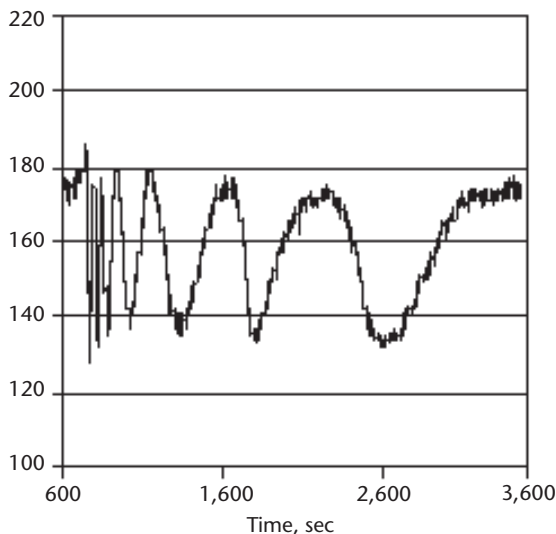
**Figure 7.19** The experimental setup for planar polarization interferometry comprising of a diode-laser (1); polarizer (2); beam collimator (3); semicylindrical lens (4); planar waveguide (5) with the cell (6) attached; analyzer (7); and optical power meter (8) interfaced to PC. The inset shows an enlarged cross-section of the planar waveguide.

nm). A sensing window is etched in the top  $\text{SiO}_2$  layer. When a polarized laser beam propagates through such a waveguide, the  $p$ -component of electromagnetic wave can be affected by molecular adsorption or chemical and biochemical reactions, while the  $s$ -component is almost intact, and serves as a reference. The phase difference between  $p$ - and  $s$ -components, developed in the course of reaction, causes the rotation of the polarization, which can be registered by placing the analyzer in the output. The resultant periodic changes in the output light intensity is very similar to that in the MZ interferometer:

$$I = \sin(\varphi_p - \varphi_s) \quad (7.22)$$

The planar polarization interferometer (PPI) described above was used for the registration of adsorption of proteins [83] and immune reactions [84, 85]. A typical response of a PPI device on adsorption of proteins (e.g., fibrinogen) is shown in Figure 7.20.

The period of the output signal changes (i.e., increases) in the course of adsorption because the adsorption rate is going down. The number of fringes on the time dependence of the output signal is related to the amount of adsorbed analyte. The peculiarity of using both MZ and PPI devices lies in a very slow rate of adsorption. Rapid injection of the investigated solution into the cell may cause a high frequency



**Figure 7.20** Typical response of PPI to adsorption of fibrinogen.

fast response, which is difficult to register without missing several initial interference fringes.

It is worth mentioning one more very interesting and promising transducing technique—long period fiber grating (LPG) [86–88], which is also based upon the registration of changes in the refractive index. The main element of such a transducer is the core of the fiber optics with the dots of slightly larger refractive index written along the core with a certain period (i.e., grating). In contrast to Bragg fiber gratings, which have a short period comparable with the wavelength of light propagating through it (thus experiencing reflection at a certain wavelength, matching Bragg diffraction conditions), LPGs have a period in the millimeter range [86–88]. In the section of the fiber containing LPG, the light propagating through the fiber is leaked to the cladding, and recoupled to the core, which can interact with the environment. The fiber is coated with a sensitive layer (membrane), so that the changes in the refractive index of the membrane due to the chemical reactions affect the output light intensity. Such transducers caused the great interest of many research groups, due to the possibility of remote sensing. However, the drawback of this method is its very narrow range of matching the values of the refractive indices of cladding and sensitive membrane [89]. If this condition is not fulfilled, the sensitivity of LPG drops dramatically.

Very often chemical or biochemical reactions in the sensitive membrane may cause some optical activity, such as light absorption or emission (e.g., luminescence or fluorescence).

In this case, spectroscopic methods can be deployed for transducing action. For example, conventional UV-visible spectroscopy can be used for the registration of changes in optical absorption of chromophore molecules embedded into the membranes caused by changes in the pH value [90, 91]. However, the minimum value of absorbance of approximately  $10^{-3}$  in the majority of commercial UV-visible spectrophotometers sets a limit to the sensitivity of such sensor devices. The light absorption can register at a much lower level using powerful monochromatic light sources

(e.g., lasers and LEDs), and sensitive photodetectors (e.g., photomultipliers and CCDs). Such sensor devices, based upon the registration of the intensity of monochromatic light, are called optrodes. These devices can be realized using fiber optics with the tip coated with sensitive membrane.

The sensitivity of optrodes can be improved dramatically by using the attenuated total reflection (ATR) of light in planar waveguides [92–94]. If a monochromatic light beam is coupled into the planar waveguide, the light propagates at a steep angle, close to the critical angle  $\theta_c = \sin^{-1}\left(\frac{n_1}{n_2}\right) = 46.8^\circ$ , due to a large difference in refractive indices of the  $\text{Si}_3\text{N}_4$  core ( $n_2 = 2.0$ ) and the  $\text{SiO}_2$  cladding ( $n_1 = 1.46$ ), as shown in Figure 7.21.

The number of reflections ( $N$ ), which the light beam experiences within the sensing window, can be calculated as:

$$N = \frac{L}{d_2} \cot \theta_c \quad (7.23)$$

For this structure, the ratio of the window length to the core layer thickness,  $L/d_2 = 2 \cdot 10^4$ , yields approximately  $10^4$ .

If the membrane deposited on top of the sensing window is transparent, then nothing happens, and the light propagates through the waveguide practically without dissipation. However, if the membrane contains chromophore molecules, which absorb light at the wavelength used, the light losses will occur at every reflection, due to the evanescent field penetrating into the membrane. The resultant light intensity coming from the waveguide is governed by Beer's law:

$$I = I_0 \exp(-\alpha_3 d_3 N) \quad (7.24)$$

where  $\alpha_3$  and  $d_3$  are the absorption coefficient and the thickness of the membrane, respectively. Here,  $d_3$  is assumed to be much smaller than the penetration depth of

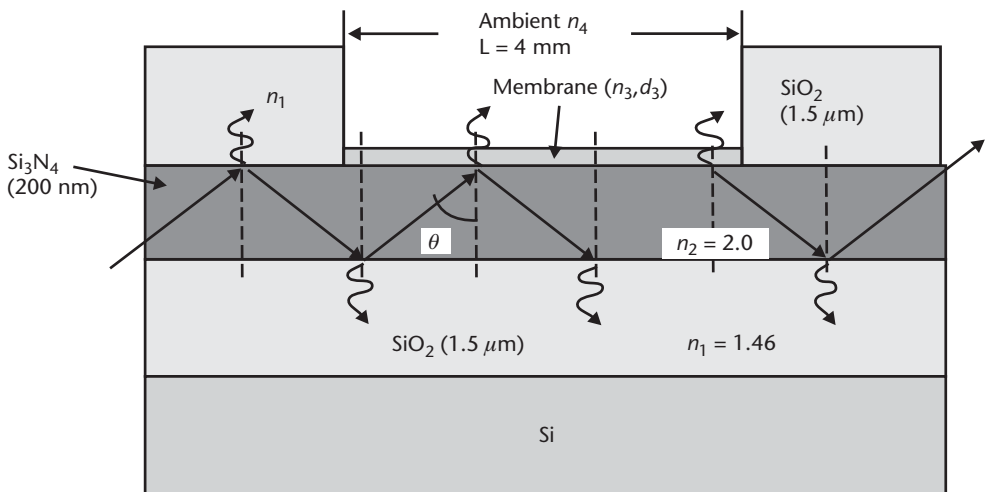


Figure 7.21 Silicon-based planar waveguide as ATR transducer.



the evanescent field. Therefore, the sensitivity of planar waveguide ATR transducer is expected to be 10,000 higher than that of the conventional absorption spectroscopy.

The experimental setup for planar waveguide ATR measurements is similar to that described in Figure 7.19, but without polarizing elements. As an example, a monolayer of copper phthalocyanine (CuPc) molecules ( $d_3 = 1.5$  nm, and  $\alpha_3 \approx 10^7$  m<sup>-1</sup>) exhibits a large attenuation of  $\frac{I}{I_0} = \exp(-300)$ . Experiments have shown that two monolayers of CuPc molecules, deposited on top of the sensing window of the planar waveguide, reduce the output light intensity down to a noise level. The experimental value of the gain in sensitivity is slightly smaller, and is reported to range from 800 to 1,000 [93].

An effective value of complex refractive index  $N^* = n^* - ik^*$  should be considered for relatively thick membrane coatings. Taking into account an exponential decay of the evanescent field,  $E(x) = E_0 \exp(-\Gamma x)$ , the real and imaginary parts of the refractive index can be calculated as:

$$n^* = n_3 + (n_4 - n_3) \exp(-\Gamma d_3) \quad (7.25)$$

$$k^* = k_3 [1 - \exp(-\Gamma d_3)] \quad (7.26)$$

where  $k_3 = \frac{\alpha_3 \lambda}{4\pi}$ , and  $n_4$  is the ambient refractive index.

The ATR planar waveguide optrode described above is an extremely sensitive tool for the registration of small changes in optical absorption in the membrane caused by different chemical and biochemical reactions.

Measurements of the luminescence or fluorescence spectra (or, simply, total luminescence intensity over the whole spectral range) is a very promising transducing principle, which has found many applications in chemical and biosensors [95–97]. The membrane containing active luminophore molecules can be deposited, for example, on the tips of the fiber optics. An experimental problem of the separation of the incident light from powerful excitation light sources and low intensity of luminescence can be a difficult technical task. It can be resolved in planar waveguide devices, which are described in two applications, PPI and ATR. The same planar waveguide transducer can be used for the registration of luminescence, if the sensitive membrane contains luminophore molecules, as shown in Figure 7.22.

In the above transducer, the light emission occurs as a result of the excitation of luminophore molecules by the evanescent field during multiple reflection in the planar waveguide. This method is used in several sensing applications [95–97], including the registration of immune reactions between luminophore labeled antibodies in the membrane and respective antigens in the ambient [97].

The electroluminescence method works as a combination of electrical and optical transducing techniques. For example, electroluminescence from porous silicon is found to be sensitive to adsorption of some proteins [98, 99]. Unfortunately, the electroluminescence mechanism in porous silicon is still not yet fully understood, and the luminescence is not stable. However, recent progress in the stabilization of electroluminescence using a polyelectrolyte coating improves the situation [100]. Therefore, the advantage of PS sensors in a huge adsorption area can be exploited in full capacity.

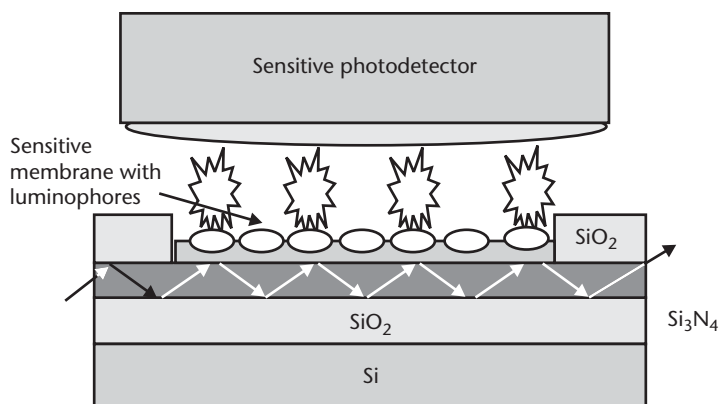


Figure 7.22 Planar waveguide as a luminescent biosensor.

## 7.3 Nanostructured Materials for Sensing

In this section, several examples of sensors based upon nanostructured materials of either organic or inorganic origin are introduced.

### 7.3.1 Sensors Based on Inorganic Materials

One of the main directions in sensor development is based on metal oxide chemiresistors. The operational principle of this type of sensor is explained earlier in this chapter. Sensors based on thin films of metal oxides (e.g., SnO<sub>2</sub>, ZnO, TiO<sub>2</sub>, WO<sub>3</sub>, and In<sub>2</sub>O<sub>3</sub>) have been used for decades for the sensing of various gases, including oxidizing gases (e.g., NO<sub>x</sub>, SO<sub>2</sub>, HCl, Cl<sub>2</sub>, and O<sub>3</sub>), reduction gases (e.g., CO, NH<sub>3</sub>, and short hydrocarbons) [101–104], organic vapors (e.g., alcohols, ketons, aromatic compounds, and hydrocarbons) [105, 106], and many other gases. The sensors' affinity largely depends on the structure of the metal oxides, their impurities, and the temperature. The properties of metal oxides are known to be very technology-dependent, with the consequences of poor reproducibility [18, 19]. From the point of view of the classical gas sensing approach towards the development of highly sensitive and selective sensor devices, metal oxides are not impressive, because of their rather poor selectivity and reproducibility. However, metal oxide chemiresistors are ideal for the development of sensor arrays. The focus of publications has largely shifted towards multisensors in the last 10 years [107–116]. Electron-nose devices based upon metal oxides have become widespread and commercially available. For example, the Alpha M.O.S. Fox 3000 is used for the analysis of various substances (e.g., olive oil, vines, coffee beans, meat, perfumes, and solvents) of commercial interest to the food, agriculture, pharmacy, and chemical industries. It has been recently reported on the application of metal oxide for the analysis of liquid substances with a view toward applications in biosensing [117].

Solid electrolytes are other very promising materials for chemical sensing. These composite materials, such as zirconia [118], lithium lanthanum titanate [119], and lanthanum molybdenum oxides [120], are ionic conductors, so that they are ideally suitable for the registration of different electrochemical reactions. The range of application of solid electrolytes is very wide, ranging from electroactive gases and

vapors [121–123] to hydrocarbons [124]. Solid electrolytes can be used for chemical analysis in liquid media, and particularly for biosensing applications [125, 126].

The conductivity of thin films prepared from metal nanoparticles has been found to be sensitive to adsorption of electroactive gases and organic vapors [127–132]. Since colloid metal nanoparticles are usually coated with some organic layer (shell) to stabilize their growth, it is expected that such nanostructured films do not show metallic conductivity. The conductivity somewhat resembles semiconducting behavior with some characteristic activation energy, which is most likely related to the electron-hopping between metal nanoparticles. The reduction in the conductivity of nanoparticle films in the presence of organic vapors, which act as solvents for the organic shell, can be explained by the penetration of solvent molecules between particles, thus increasing the distance between particles, or the hopping length [127]. Adsorption of electroactive molecules on the nanoparticles' surface may cause the redistribution of the electron density in metal clusters, which changes the film conductivity [127, 128]. In the case of films made of semiconductor nanoparticles, electroactive gases may act as an acceptor or donor impurities, which affects the film conductivity [127–129]. Because of well-defined electrochemical behavior, nanoparticles have found applications in enzyme and biosensors [130–132]. Sensors based on nanoparticles have a promising future, especially in nanosensors using modern nanoprobe techniques.

The SPR optical method can be deployed as a transducing technique for nanoparticle sensors. The film of Au-CdS nanoparticles displays the SPR response to the reaction of acetylcholine decomposition catalyzed by the enzyme AcetylcholineEsterase [133]. This work also studies the inhibition of the enzyme with environmental pollutants.

### 7.3.2 Sensors Based on Organic Materials

As mentioned earlier, organic materials can offer many more opportunities for sensing applications than can inorganic materials, simply because of the much larger variety of organic compounds. During the last two decades, the subject of molecular electronics was split in several directions, and the direction of chemical and biosensors was the most successful among them. Organic sensing materials can be separated in two large classes: first, polymer materials, particularly conducting polymers; and second, organic films, consisting of monomer molecules.

The conducting polymer approach in sensing is rapidly increasing. Large numbers of sensing devices have been recently proposed, and some of them have been implemented into commercial products. Chemiresistors made of conducting polymers [134–136] seem to be the most advanced sensing devices capable of the registration of gases, vapors, and electrochemical reactions in liquid phase. This approach, similar to metal oxide sensors, is successfully implemented in commercially available sensor arrays [137–139].

Apart from amperometric polymer transducers, other electrical potentiometric transducers based upon conducting polymers have been reported [140]. Other transducing techniques, such as SPR, are used in conjunction with polypyrrole coating [141]. In the past decade, conducting polymers that are able to detect electrochemical reactions in contact with a liquid phase have found wide applications as biosensors (e.g., enzyme sensors) and biosensor arrays [142–152].

As briefly mentioned in this chapter, organic semiconductors are ideally suitable materials for sensors, both electrical and optical. Phthalocyanines (Pc), as one of the most explored organic semiconductors, are widely used as gas sensors [153–156]. Both electric conductivity and optical properties (i.e., absorption spectra) depend very much on the chemical structure of Pc molecules: the type of central metal (or other) atom; the type of substituting groups, and their position and number; and the molecular arrangement (i.e., packing) of Pc molecules in molecular crystals [48].

The effect of electronegative gases on the conductivity of Pc films is well-studied, and is widely exploited in gas sensing [48, 51, 153]. Electronegative gases attract electrons from the central part of metal phthalocyanine molecules, with an effect on optical absorption spectra. This effect constitutes the basis of optical Pc gas sensors, which use UV-visible spectroscopy, SPR, and interferometry as transducing techniques [154, 156].

Rare earth Bis-phthalocyanine molecules are more interesting for gas sensing applications, because of three states of Pc moiety: oxidized, neutral, and reduced, each with its characteristic absorption spectra signature. The presence of electronegative and electropositive gases may cause switching between these states, which can be registered with optical techniques, such as SPR [157–161]. An even more pronounced redox behavior is observed in the absorption spectra of LB films of amphiphilic porphyrins. All three spectral bands are clearly resolved, and the switch between those three states can be done by exposure to the electroactive gases [162–166]. The observed optical switching behavior can be measured with a UV-visible spectrophotometer; or by the measurement of the light intensity at a fixed wavelength of a laser diode. The recovery time can be substantially reduced at elevated temperatures, which can be produced by an embedded heating element. Portable NO<sub>x</sub> sensors have been designed on this principle [163].

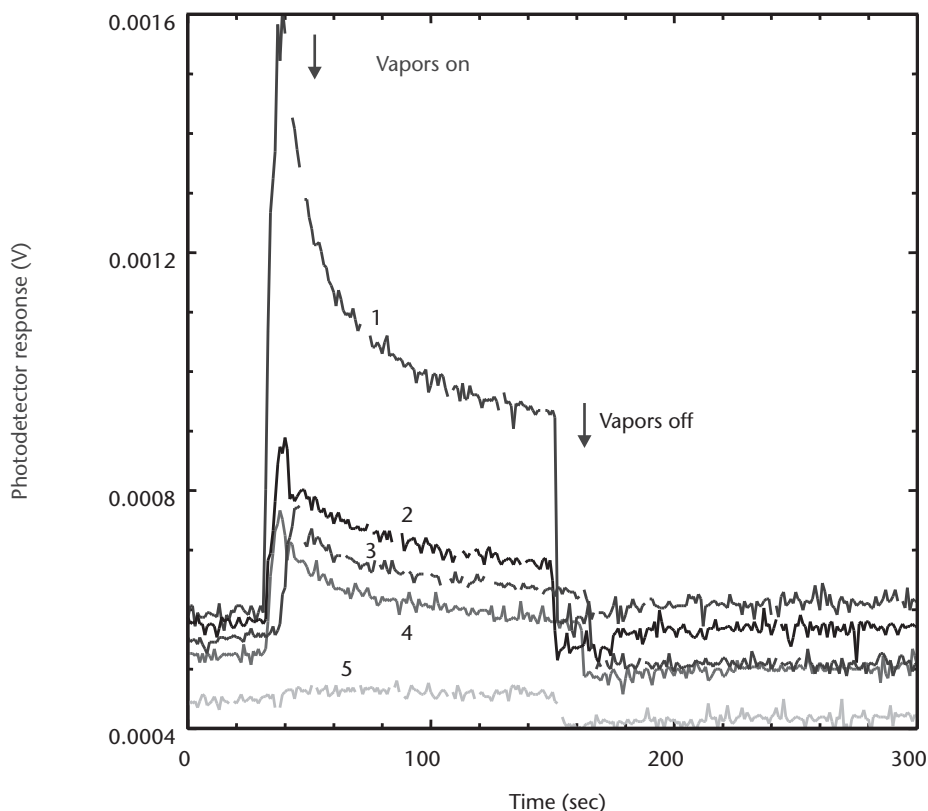
### 7.3.3 Organic Vapor Sensors Based on Calixarenes

Calixarenes, as well as other cavitand molecules, are widely used in chemical and biosensors. These molecules are considered as binding sites of high specificity, and affinity-mimicking natural bioreceptors. The tunable specificity can be achieved by using different functional groups in calixarene molecules. Unmodified calix[n]arenes and calix[4]resorcinarenes, whose chemical structures are shown in Figures 2.22 and 2.23, are known as ion selective compounds [167], with their binding constants showing good correlation between the size of the cavity and ion radius. Amphiphilic calixarenes are lipophilic, and soluble in the majority of organic solvents, and they can be deposited onto solid substrates using LB and spin coating methods, as discussed in Chapter 2. Such thin films of calixarene derivatives contain bowl-to-bowl dimers as the main structure unit, and are therefore extremely hydrophobic [168]. Films made of amphiphilic calixarene derivatives are nanoporous, and, in addition to internal cavities of calixarene molecules, contains pores, which are formed between calixarene molecules, and between interdigitated hydrocarbon chains, as shown in Figure 2.24.

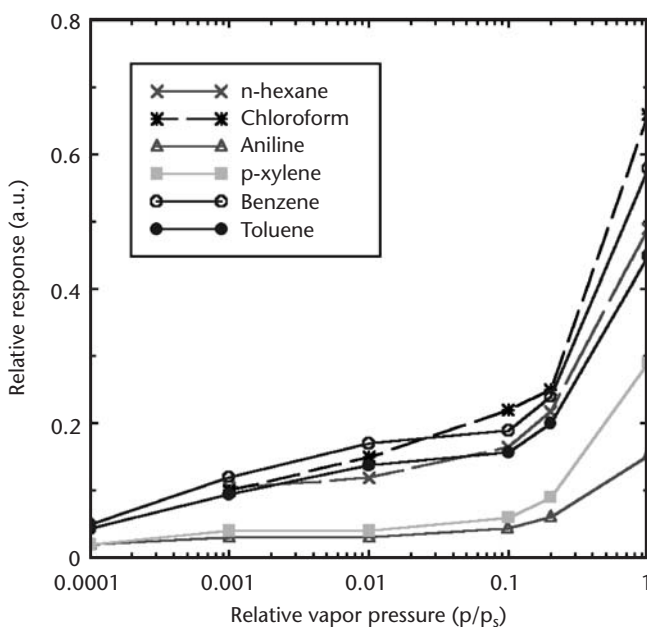
Quite naturally, such nanoporous lipophilic films may work perfectly as sensitive membranes for organic vapors. The first experiments with LB films of amphiphilic calix[4]resorcinarenes [169] were successful, showing that the films swell

after exposure to some organic vapors, such as hexane and benzene. Further study of the adsorption of organic molecules in calixarene films using methods of SPR, ellipsometry, and QCM [170–172], shows the following features:

1. Adsorption of organic vapors, such as hexane, benzene, toluene, and *n*-xylene, in their high concentration, comparable to the saturated vapor pressure ( $p_s$ ), causes an increase in the mass, thickness, and refractive index of calixarene thin films.
2. The adsorption is fast, and full recovery can be achieved after flushing the samples with fresh air, as can be seen from the SPR kinetics diagrams in Figure 7.23.
3. Isotherms of adsorption obtained from QCM measurements show practically no selectivity, as can be judged from Figure 7.24. At low concentrations of adsorbates, presented in relative vapor pressure units ( $p/p_s$ ), all curves line up, which indicates a common physicochemical mechanism of adsorption. However, when the vapor pressure reaches the level of 10% ÷ 20% from  $p_s$ , the amount (mass) of adsorbed molecules increases.



**Figure 7.23** The kinetics of the SPR response of Azo-C[4]RA LB films (4 layers) to benzene vapor of different concentrations: (1)  $p_s$ , (2)  $p_s/10$ , (3)  $p_s/100$ , (4)  $p_s/1,000$ , and (5)  $p_s/10,000$ , where  $p_s$  is the saturated vapor pressure. (From: [171]. © 2000 Royal Society of Chemistry. Reprinted with permission.)



**Figure 7.24** Isotherms of adsorption of different organic vapors in Azo-C[4]RA LB films obtained with SPR. (From: [171]. © 2000 Royal Society of Chemistry. Reprinted with permission.)

This situation resembles the phenomenon of capillary condensation of water vapors in microporous materials [24]. According to the Kelvin formula:

$$p_s = p_{so} \exp\left(-\frac{2V\gamma}{rRT} \cos \theta\right) \quad (7.27)$$

the saturated vapor pressure ( $p_s$ ) inside the cylindrical pores of the radius  $r$  can be substantially smaller than that in normal atmospheric conditions ( $p_{so}$ ). The exponential factor in (7.27) contains the molar volume ( $V$ ) and surface tension ( $\gamma$ ) of the adsorbate and the wetting angle ( $\theta$ ) in the capillary (in the case of full wetting,  $\theta = 0$  and  $\cos \theta = 1$ ). In the microporous media, which have a pore size in the micrometer range, the deviation from the BET absorption isotherm started to appear at pressures very close to  $p_{so}$ .

The concept of capillary condensation can be formally expanded towards nanoporous lipophilic calixarene films [171]. Applying (7.27) to the adsorption of organic vapors in calixarene films with the mean pore radius of 1 nm, one can estimate the value of  $p_s = 0.2p_{so}$  [171]. The obtained value corresponds perfectly well to that observed in Figure 7.24, which shows a threshold of  $0.2p_{so}$  for the absorption increase.

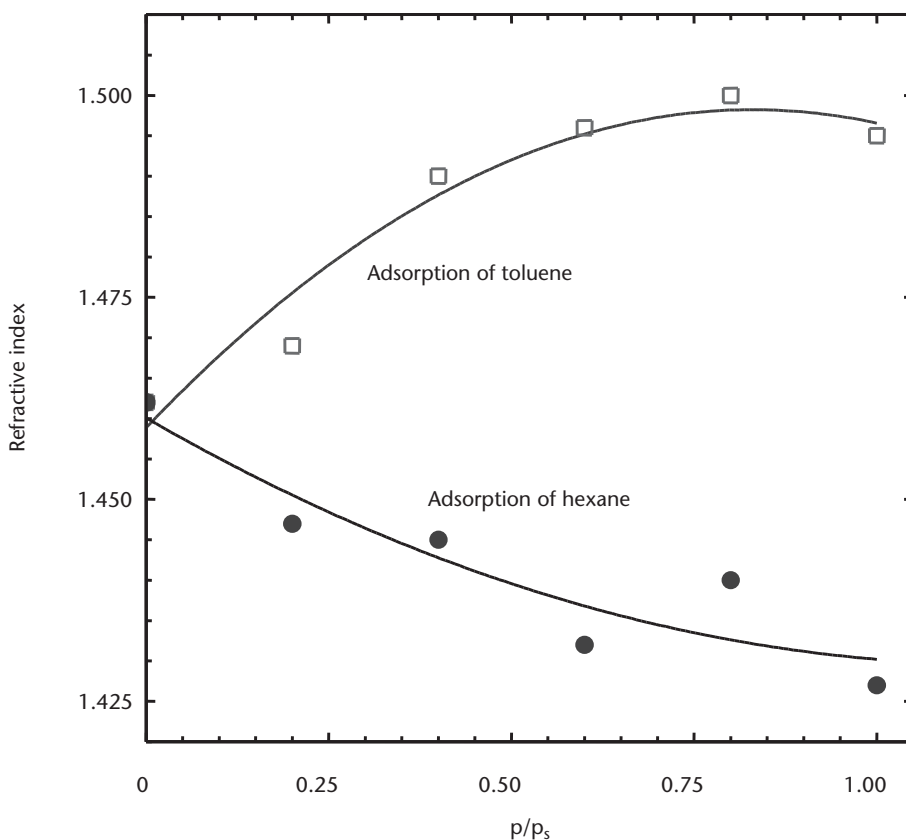
The model of the adsorption of organic vapors in calixarene films now becomes clear. At low concentrations of organic vapors, the conventional BET theory can be applied for their adsorption in relatively thick calixarene films. The Langmuir theory is more suitable for monolayers. When the vapor pressure exceeds the threshold of  $0.1p_s \div 0.2p_s$ , vapor condensation (i.e., the formation of a liquid phase) occurs within nanopores in the film bulk, and results in a sharp increase in the amount (mass) of adsorbed molecules, accompanied by changes in optical parameters of calixarene films.

Detailed ellipsometric study of adsorption of hexane and benzene shows an increase in the film thickness for all organic vapors studied, which corresponds to the concept of swelling of calixarene films. The film refractive index, however, behaves differently, depending on the type of adsorbed molecules. For example, as shown in Figure 7.25, the refractive index increases in the course of adsorption of toluene, and decreases when hexane is absorbed.

The above behavior can be understood using capillary condensation theory. Since the refractive index of liquid hexane  $n_{\text{hexane}} = 1.37$  is less than  $n = 1.46$  for calixarene film, the condensation of hexane will cause the reduction in the film refractive index. It is opposite for the condensation of toluene having  $n_{\text{toluene}} = 1.49$ , and therefore causes an increase in the film refractive index.

A sharp increase in the signal on SPR kinetics curves most likely corresponds to the formation of the liquid phase on the film surface, followed by its diffusion in the film bulk.

Another interesting fact, which falls into the concept of capillary condensation, is that the exposure of calixarene films in the atmosphere of short hydrocarbons, such as propane and butane, does not cause any substantial changes to either the optical properties of calixarene films or their mass. The only explanation is that both propane and butane do not condense at room temperature (i.e., their boiling point is



**Figure 7.25** The dependencies of the refractive index of P-C[4]RA LB films (20 layers) on the concentration of toluene and hexane vapors. (From: [171]. © 2000 Royal Society of Chemistry. Reprinted with permission.)

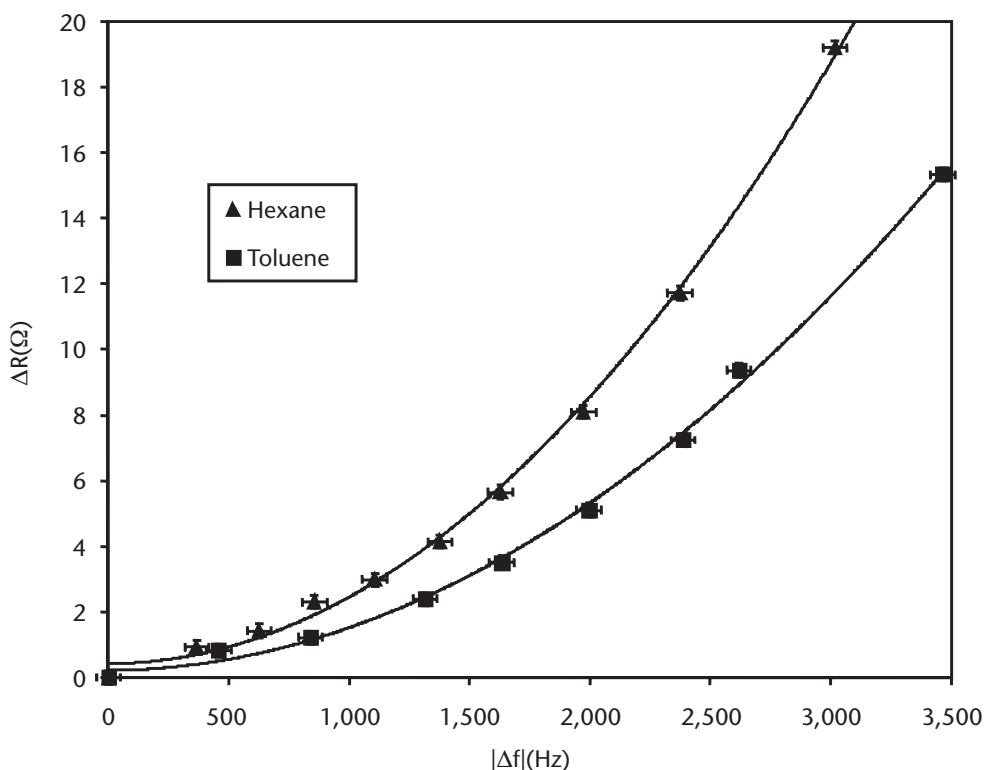


below 0°C). Gaseous propane and butane, however, cause practically no change in either the mass or the refractive index of calixarene films.

The effect of capillary condensation of organic vapors in the LB or spun films of amphiphilic calixarenes has been used for the development of QCM sensor alarm devices, which are used to detect high, pre-explosive vapor concentrations of a wide class of organic solvents [173]. The list includes benzene, toluene, ethylbenzene, and xylene (BTEX) vapors, which belong to the aromatic family, which also includes hydrocarbons, chloro-hydrocarbons, alcohols, and ketons. The response is fast, and the devices are fully recoverable. The registered concentration ranges from 0.1 LEL to HEL, where LEL and HEL represent low and high explosion limits. No selectivity is observed, which is not absolutely required for alarm sensors. The device should give an early warning when the 0.1 LEL level of any type of explosive organic vapors is exceeded.

The task of vapor recognition can be resolved, however, using QCM impedance spectra measurements, as described in Section 7.2.1 [174, 175]. Two parameters obtained from the impedance data analysis,  $L(\Delta f)$  and  $R$ , correspond to the mass load and viscosity of calixarene films, respectively, and give additional information for vapor recognition. As shown in Figure 7.26, the vapors can be identified by their unique ratio of  $\Delta f/R$ .

Further expansion of this research towards the impedance spectra analysis of QCM sensor array may lead to the development of expert systems for the analysis of complex mixtures of organic vapors of relatively high concentrations.



**Figure 7.26** The dependence of  $\Delta R$  against  $\Delta f$  for hexane and toluene vapors. (From: [175]. © 2004 Elsevier. Reprinted with permission.)

## 7.4 Biosensors

### 7.4.1 Composite Membranes for Biosensing

The key element of biosensors is a sensitive membrane, which contains bioactive molecules and provides selective binding of analyte molecules and their reactions. The immobilization of active biomolecules in the membrane is, therefore, the most important aspect of the formation of sensitive membranes. It is very important to provide the reliable integration and preservation of a native structure of biological material. It is also important to achieve the situation in which recognizing elements are presented in their maximum density on the transducer surface, and their active centers are exposed to a solution for the interaction with analytes. These are the main conditions for providing maximum sensitivity of bioanalysis.

The following conditions have to be fulfilled in order to design the correct combination of biological molecules with the transducer surface.

1. *Maximum preservation of the activity of immobilized biomolecules.* The immobilized biomolecules must keep their structure and functions as long as possible in both working and storage conditions. The lifetime of bio-membranes of several months is considered to be very good.
2. *High density of immobilized molecules on the transducer surface.* This results in the high sensitivity of biosensors. From this point of view, relatively thick, multilayered membranes have an advantage over monolayers. On the other hand, the permeability of the membrane for the analyte molecules becomes an important consideration when thick membranes are used. There must be an optimal choice of the film thickness for particular membranes and analyte molecules to provide maximum sensitivity. An alternative approach is to use highly porous materials, such as porous silicon, for adsorption. It seems that a combination of highly porous substrates with a highly accessible monolayer sensitive coating offers the highest sensitivity.
3. *Exposition of the majority of active sites to the solution.* This is another important problem of immobilization. If biomolecules are randomly oriented in the membrane, some of their active sites are not available for the interaction (i.e., binding) with the analyte molecules. Ordered molecular structures with the uniform orientation of the host biomolecules are favorable.
4. *Good adhesion of biomolecules to the transducer surface.* This is an important factor improving the stability of biosensors.
5. *Simplicity and low cost of the formation of sensitive membranes.* This is particularly important for single-shot sensors having disposable, reusable, and easily replaceable sensitive membranes on the transducer surface.

It is difficult to fulfill all these conditions in one sensor, but a reasonable compromise is necessary.

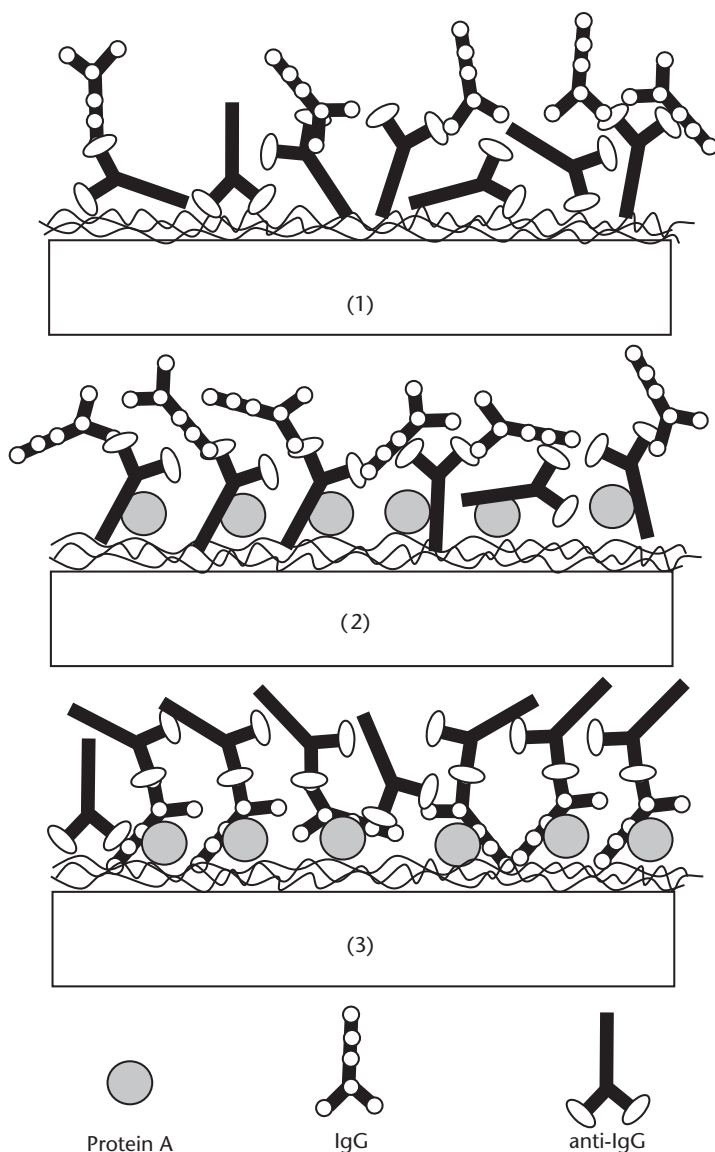
There are three approaches for the immobilization of biomolecules listed here.

1. *Physical adsorption of biomolecules, including adsorption in porous materials.* It may work for some proteins [176]. However, in the majority of

- cases, protein molecules are not stable on the solid surfaces, and are prone to change their structure (i.e., decompose or untangle) and to lose functions.
2. *Covalent binding of biomolecules to the transducer surface.* This is performed via some intermediate compounds, including bifunctional agents, such as glutaraldehyde (GA) [98, 177, 178]. Some of the intermediate agents, such as 3-amino-propyltriethoxysilane or amino-thiols, may form covalent bonds with the silicon and gold substrates, respectively, but have weaker interaction with proteins via amine groups.
  3. *Entrapment of biomolecules into gels.* Examples include alginate gels [176, 179, 180], using different methods of ion-, photo-, electro- and electron-beam polymerization, along with other substances. Bioactive molecules can be adsorbed into commercially available membranes made of cellulose or Biodine C (B) [176]. Proteins can be deposited by the LB method [181] and become enclosed between polar groups of amphiphilic compounds, such as phospholipids. A relatively new method of polyelectrolyte (or electrostatic) self-assembly [182] allows the immobilization of electrically charged proteins between layers of polyions having an opposite electric charge [183].

The latter group of methods provide natural conditions, primarily the required local pH, for biomolecules, and allow preserving their activity for a long time. The LB film and electrostatic self-assembly methods constitute a powerful tool in molecular engineering, due to their the ability to produce layer-by-layer deposition of different molecules, such as proteins, enzymes, immune components, organic chromophore, and luminophore molecules, and due to their ability to produce composite and multifunctional membranes for biosensing. For a number of reasons, polyelectrolyte self-assembly is more suitable for biomembranes. Polyelectrolyte films are hydrophilic, in contrast to hydrophobic LB films, and provide excellent permeability for some low molecular weight products. Another advantage lies in the good adhesion of polyelectrolytes due to a strong Coulomb interaction, as compared to the weak Van der Waals binding in LB films. Thermal stability of polyelectrolytes are much better than that in LB films having a low melting point. The experimental realization of electrostatic deposition, as discussed in Chapter 2, is very simple, as compared to the LB method, and does not require special equipment. In most cases, the deposition can be done manually in a beaker, or even in situ by consecutive injections of required solutions into the reaction cell [184].

Some adsorbed biomolecules, such as immunoglobulines (IgG), antibodies (AB), or antigens (AG), require a certain orientation on the solid surface in order to have their binding sites directed to the solution, allowing these biomolecules to bind their counterparts (AG or AB, respectively). This can be achieved by the introduction of intermediate layers of either lectins or protein A from *Staphylococcus Aureus* [176, 185]. The technique of electrostatic self-assembly is the most suitable for this task, since the layers of protein A and IgG can be deposited consecutively on top of the PAH layer [176, 185]. Immune components having binding sites to protein A at the second constant domain [186] become oriented towards the solution, as shown in Figure 7.27.



**Figure 7.27** Schematic model of the immune reaction: (1) binding of IgG on anti-IgG, immobilized on top of the PAA layer; (2) binding of IgG on anti-IgG, deposited on top of protein A; and (3) binding of anti-IgG on IgG, deposited on top of protein A.

### 7.4.2 Immune Sensors

As mentioned earlier, specific binding of antibodies with native antigens is usually accompanied by a substantial increase in the mass and thickness of the sensitive membranes. Therefore, gravimetric methods of QCM and SAW, and optical methods of SPR, ellipsometry, or interferometry are the obvious choice for the registration of immune reactions. The following examples of the registration of AB/AG binding reactions demonstrate the advantages of the optical methods.

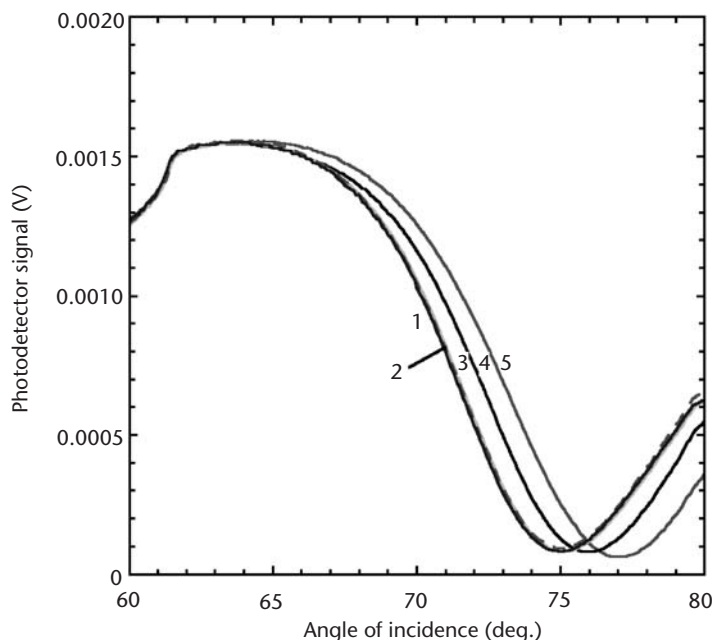
The pair of human IgG and polyclonal goat on human IgG antibodies (anti-IgG) was chosen as a model object for monitoring immune reactions. The method of

electrostatic self-assembly (ESA) was used as the immobilization technique. Other chemicals used were Bovin Serum Albumin (BSA) and Protein A from *Staphylococcus aureus*, and (poly)allylamine hydrochloride (PAH) as polycation. The initial 1 mg/mL solutions of the above biocompounds were prepared in a Trizma/HCl buffer, having a slightly alkaline pH in the range from 7.5 to 8.2. In such conditions, the above proteins and IgG molecules were negatively charged, and suitable for the electrostatic deposition on top of the PAH layer. The series of SPR measurements were performed using the setup shown in Figure 4.5. All adsorption steps were performed in the reaction cell attached to the SPR instrument by the injection of the required solutions.

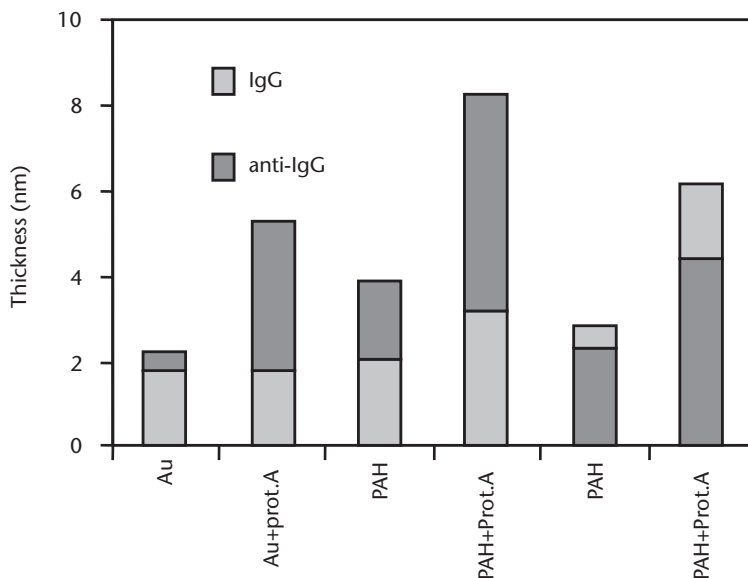
The set of SPR curves in Figure 7.28 shows a typical adsorption sequence.

The adsorption of BSA was carried out as a control experiment, in order to fill the binding sites which remained after the adsorption of the protein A. Since the shift of the curve (3) is very small with respect to the curve (2), it can be assumed that all sites on the surface of the PAH layer were already filled with the protein A. In order to provide the registration of the specific interaction only, further experiments were carried out, using both immune components mixed with BSA. The shifts of curve (4) with respect to (3), and of curve (5) with respect to (4), are similar, which indicates similar effective thicknesses of the IgG and anti-IgG layers.

Such measurements were carried out using different sequences of adsorption, and the results of SPR fitting are summarized in the bar-chart diagram in Figure 7.29. The value of  $n = 1.42$ , which is typical for proteins, is used as a fixed parameter for all bio-organic layers during SPR fitting, so that the shift of SPR curves corresponds to changes in film thickness. The analysis of this data, as shown in Figure 7.29, shows that:



**Figure 7.28** The set of SPR curves measures in buffer solution the sequence: (1) initial curve on the PAH/(PSS/PAH)<sub>3</sub> layer, (2) after adsorption of protein A, (3) after adsorption of BSA, (4) after adsorption of IgG, and (5) after binding of anti-IgG.

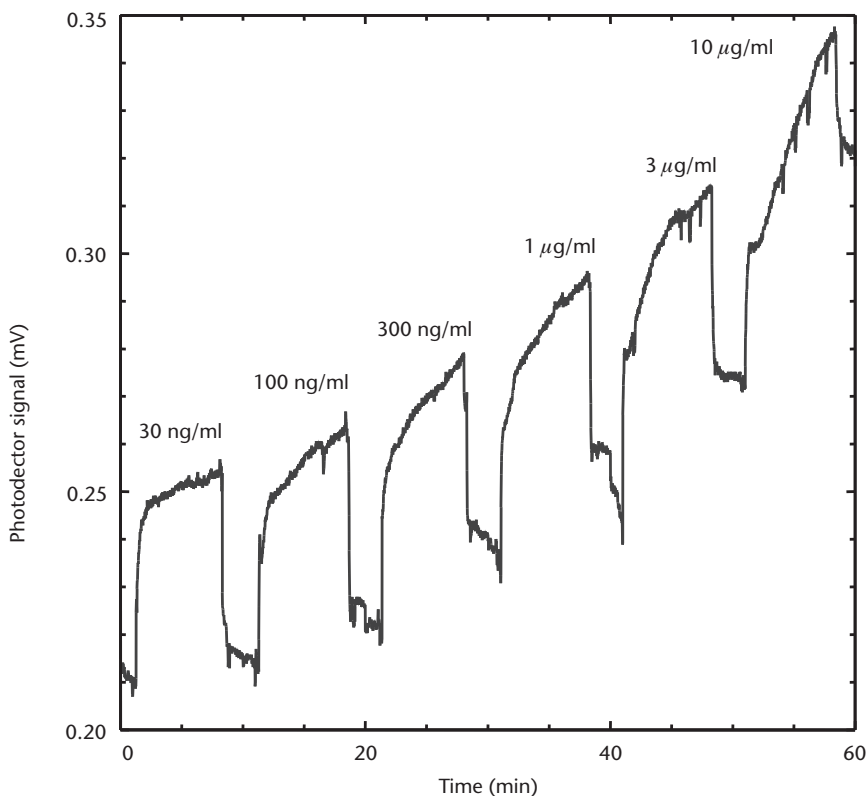


**Figure 7.29** Results of SPR fitting show the changes of the film thickness caused by adsorption of one of the immune components (IgG or anti-IgG) and binding its counterpart (anti-IgG or IgG, respectively).

1. The adsorption of the immune component (anti-IgG) is more effective on the PAH layer than on bare gold.
2. The presence of the protein A increases the efficiency of the immune reaction, which is in agreement with the model of orientation of immunoglobulins in Figure 7.25.
3. The adsorption of anti-IgG on the top of IgG is more efficient than it would be in the reverse order, possibly because of the difference in the number of binding sites available. Anti-IgG molecules have only two binding sites to IgG, while IgG molecules contain several antigenic determinants to bind anti-IgG. Therefore, the amount of the specifically bound IgG on the top of anti-IgG should be less than in the previous case of the IgG/anti-IgG complex formation.

Figure 7.30 demonstrates typical kinetics of the immune reaction, which is the binding of anti-IgG molecules with previously immobilized IgG. The reaction was performed with anti-IgG concentrations in the range from 10 to 30 ng/mL.

Each injection of anti-IgG causes an increase in the response, followed by its decrease after flushing with buffer. The true effect of the binding anti-IgG molecules can be evaluated by the comparison of the baselines before and after each cycle of adsorption and washing. The observed rise of the baseline can be attributed to the specific binding of anti-IgG molecules. The relative response as a function of the anti-IgG concentration is shown in Figure 7.31. At concentrations higher than 3 g/mL, a sharp increase in the response is observed. It is probably caused by nonspecific binding of anti-IgG. Additional washing of the sample with Twin-20 buffer shows a complete recovery of the response, as shown in curve 1 of Figure 7.31, due to the washing out of nonspecifically bound anti-IgG molecules.



**Figure 7.30** Kinetics of the adsorption of various concentration of anti-IgG on top of immobilized IgG.

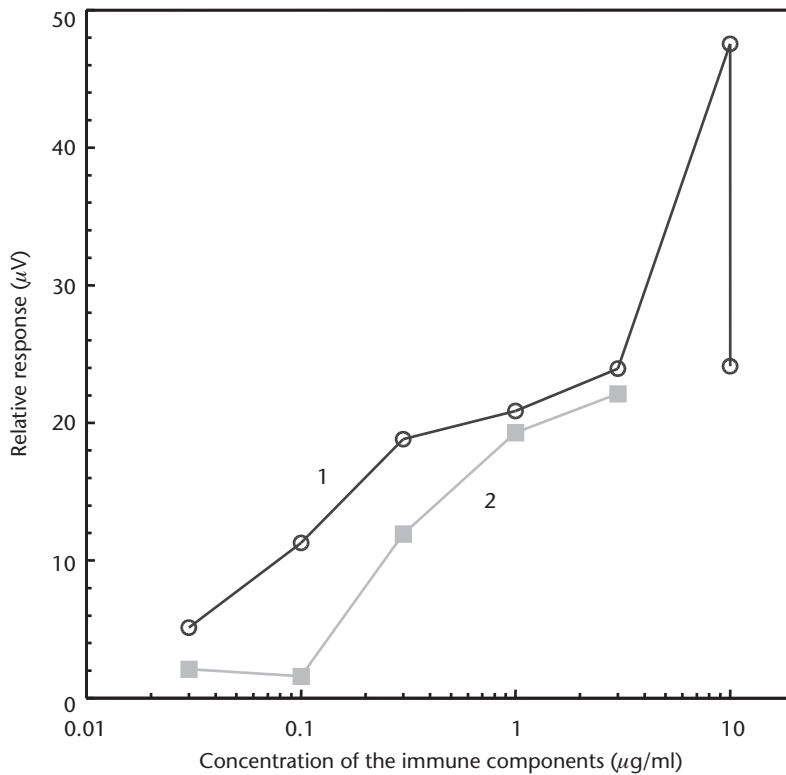
Similar kinetics are obtained in the case of the immune reaction in reverse order—binding IgG from solutions of various concentrations with the previously immobilized anti-IgG. Concentration as a function of the relative response is shown in Figure 7.31. Both dependencies in Figure 7.31 are very similar, which confirms full reversibility of the immune reaction. A slightly lower response in the case of binding IgG with anti-IgG is believed to be caused by a fewer number of reactive sites on the immobilized anti-IgG layer, as is shown by the SPR fitting results in Figure 7.29.

As shown in Figure 7.31, the lowest concentration of IgG registered with SPR is 30 ng/mL, which is close to the limit for the SPR method. Further increases in sensitivity can be achieved by using interferometric techniques, such as PPI. The operation principle of this device is discussed earlier in this chapter. Typical results obtained with PPI are shown in Figure 7.32 [187, 188].

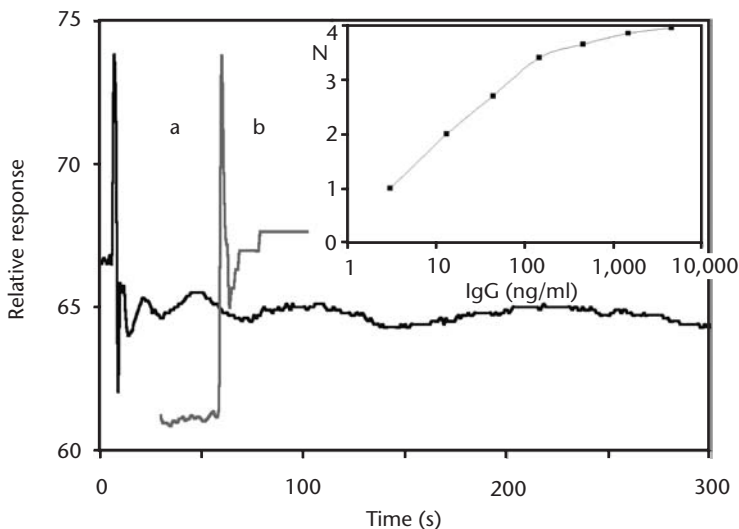
A multiperiodic response reflects the changes in the phase shift between *p*- and *s*-components of the polarized light propagating through the waveguide, due to IgG/anti-IgG specific binding. Adsorption of anti-IgG molecules from its 100 mM/mL solution onto the PAH layer results in more than six periods of phase change, while binding of 1 ng/mL of IgG on top of anti-IgG produces much smaller changes.

The concentration dependence of the response of PPI, as shown in the inset in Figure 7.32, resembles the Langmuir adsorption isotherm, which is expected for





**Figure 7.31** Concentration dependence of the SPR response for: (1) binding of anti-IgG on top of IgG, and (2) binding of IgG on top of anti-IgG.



**Figure 7.32** Typical responses of PPI on: (a) the immobilization of anti-IgG from its 100 g/mL solution, and (b) the binding of IgG from its 1 ng/mL solution. The inset shows the dependence of the number of interference fringes on the concentration of IgG.

IgG binding on the surface containing anti-IgG binding sites. This method seems to be very sensitive and promising for biosensing, since nearly an entire period of signal changes is observed in response to the binding of 1 ng/mL of IgG, as shown in

Figure 7.32. The response of the PPI sensor is a number of periods of phase changes, which is not easy to register. This is, perhaps, one of the main disadvantages of PPI sensors.

The immune assay approach is widely used for the registration of nonbiological compounds, including environmental toxins such as pesticides and herbicides [189]. However, this is not easy for the QCM, SAW, and SPR methods, since the analytes have relatively low molecular weight. As shown earlier in the chapter, the internal ellipsometry method is much more promising for this purpose. The same applies to PPI sensors, which have a great potential in the registration of low molecular weight analytes.

### 7.4.3 Enzyme Sensors

As discussed earlier in this chapter, the registration of enzyme reactions is a routine task for electrical and electrochemical methods. The majority of enzyme sensors on the market are electrochemical. The main advantages of electrochemical methods are simplicity and low cost. The sensitivity of electrochemical methods is not great, but it is sufficient for the majority of biomedical applications. However, there is another aspect of the use of enzyme reactions to monitor environmental pollutants, such as heavy metal ions, pesticides, and herbicides, which act as inhibitors of enzyme activity. This is a universal approach to the monitoring of the pollutants, which have different chemical natures. Instead of developing a number of sensors specific to every pollutant, a better solution can be achieved with an enzyme sensor array, in which each enzyme is inhibited differently by different toxins. Such enzyme sensor arrays have been developed, using the potentiometric principle of registration. A six-channel array of Si/SiO<sub>2</sub> capacitors with different enzymes deposited on top (GlucoseOxidase, Ethyryl- and Butyryl-CholineEsterase, and Urease) was capable of the recognition and evaluation of heavy metal ions and phosphor-organic pesticides [190, 191]. The sensitivity of such sensor arrays is in the parts-per-million range, which is at the limit of electrochemical sensors, but not high enough for environmental control tasks. Further increases in the sensitivity can be achieved with optical methods.

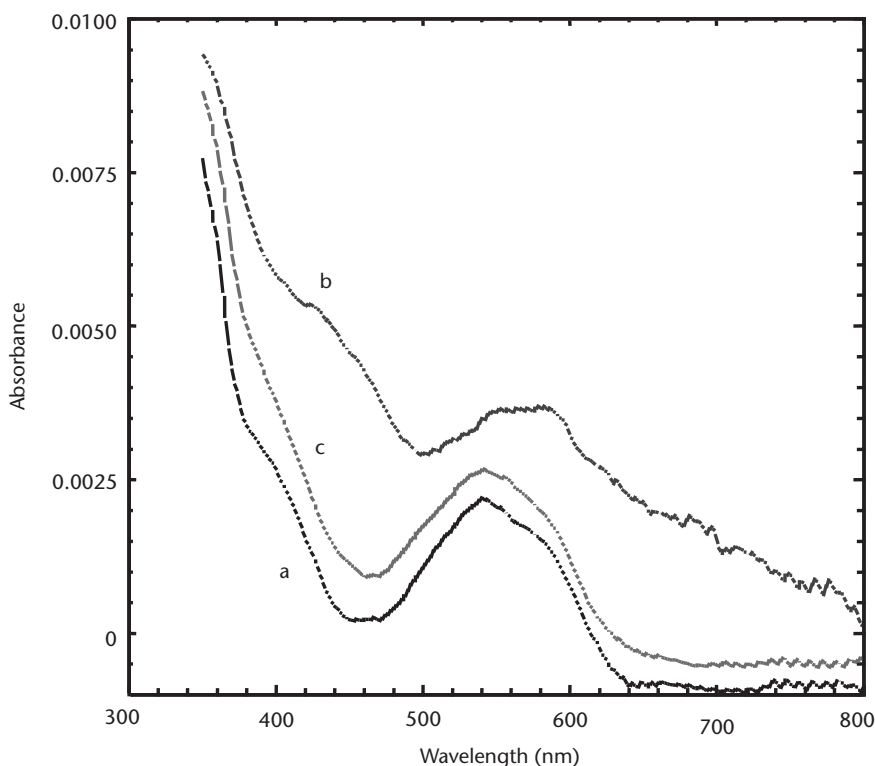
Traditional optical biosensing methods based on the registration of refractive index (e.g., SPR, ellipsometry, and interferometry) do not seem to be sensitive enough for the registration of the low molecular weight products of enzyme reactions. The only method of optical registration of enzyme reactions is to use the optrode principle described earlier in this chapter. The sensitive membranes of optrode sensors contain chromophore molecules, which respond to changes in the local pH caused by products of enzyme reactions [192]. The idea of pH sensitive optrode was successfully realized in [193] using a (poly)pyrrole membrane with embedded Prussian blue chromophore and enzyme immobilized on top. The electrostatic self-assembly method offers a better option of building composite sensitive membranes by the consecutive deposition of layers of chromophore molecules containing anionic groups, with layers of polycations, and then layers of negatively charged enzymes alternated with polycations, as described in Chapter 2.

Composite films consisting of cyclo-tetra-chromotropyrene (CTCT) tetrasulfonic salt chromophores and (poly)allylamine hydrochloride (PAH) have been produced and tested for their response to ammonia [194]. The UV-visible absorption

spectra of such films shows the effect of exposure to ammonia in both vapor and liquid forms, as shown in Figure 7.33.

The reduction in the intensity of the 440-nm band, and the appearance of a band at 560 nm, results from a multiple deprotonation of CTCT chromophore [195] in alkaline pH caused by the presence of ammonia. This fact is interesting in itself, since it shows the way of the registration of ammonia. This work evolves further [196] by depositing, in alternation with PAH, a few layers of the enzyme Urease on top of the CTCT/PAH film. The changes in the UV-visible absorption spectra of this film after soaking in the urea (i.e., substratum) solution are very similar to the previous situation of CTCT/PAH reaction with ammonia (see Figure 7.33), which implies similar chemical processes in the above films. Indeed, one of the products of the urea decomposition is ammonia, which can diffuse in the film bulk, causing the deprotonation of CTCT molecules, and resulting in the characteristic changes in the UV-visible spectra.

Furthermore, the soaking of CTCT/PAH/Urease composite films in a  $\text{CdCl}_2$  solution has resulted in the reduction of the absorbance at 440 nm, as a result of the inhibition of the enzyme Urease. These results demonstrate the method of registration of enzyme reactions and their inhibitions with the optrode transducers. This idea has been explored further, using composite films with other enzyme/chromophore pairs. For example, the Thymol blue/CTCT/Acetyl CholineEsterase films show some characteristic changes after soaking in the acetylcholine solution, as well as showing the effect of the inhibition of Acetyl CholineEsterase by PVDP pesticide [197].

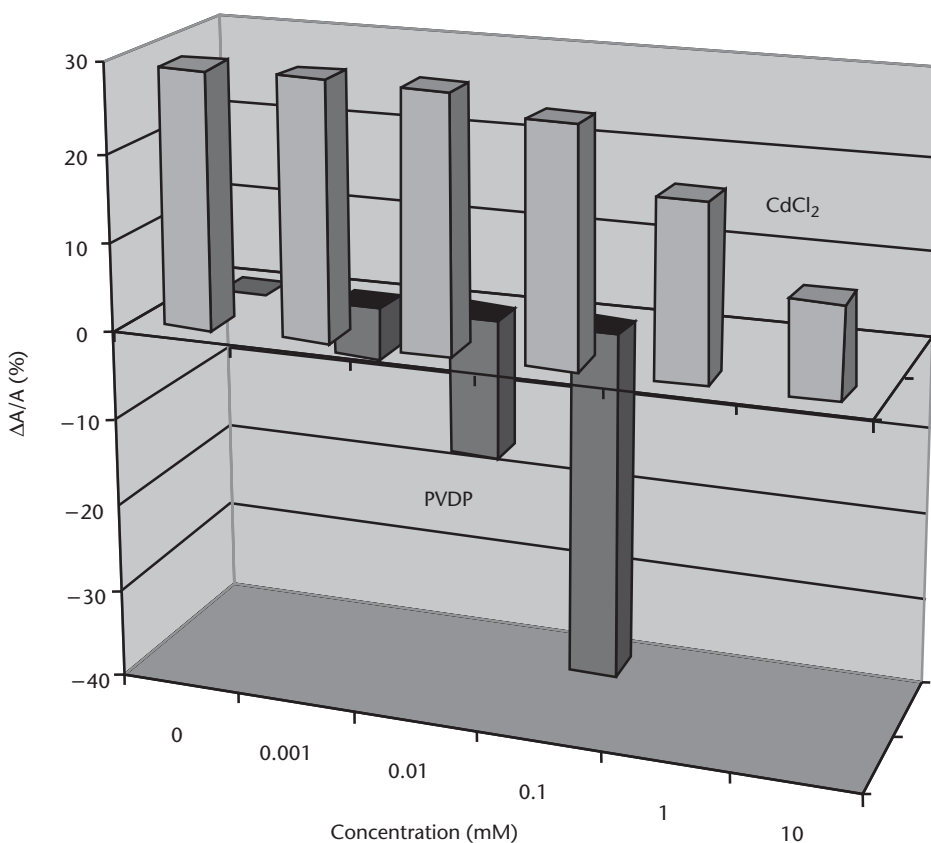


**Figure 7.33** The effect of ammonia vapors on UV-visible spectra of CTCT/PAH film: (a) initial spectrum; (b) after 5-minute exposure to ammonia; and (c) after flushing with air.

The diagram in Figure 7.34 shows the dependencies of the relative changes in the absorbance at 440 nm of the two enzyme/chromophore composites on the concentrations of  $\text{Cd}^{2+}$  ions and DVDP, respectively. Negative values of  $\Delta A/A$  for Thymol Blue/Acetyl CholineEsterase films indicate the increase in absorbance during the course of enzyme reaction to acetylcholine decomposition, as well as the decrease in pH value.

As shown in Figure 7.34, the minimum registered concentrations of  $\text{Cd}^{2+}$  and DVDP are approximately  $10^{-5} \div 10^{-6}$  M, which is similar to what has been demonstrated in [190, 191] for the same enzymes and inhibitors, but with the potentiometric method.

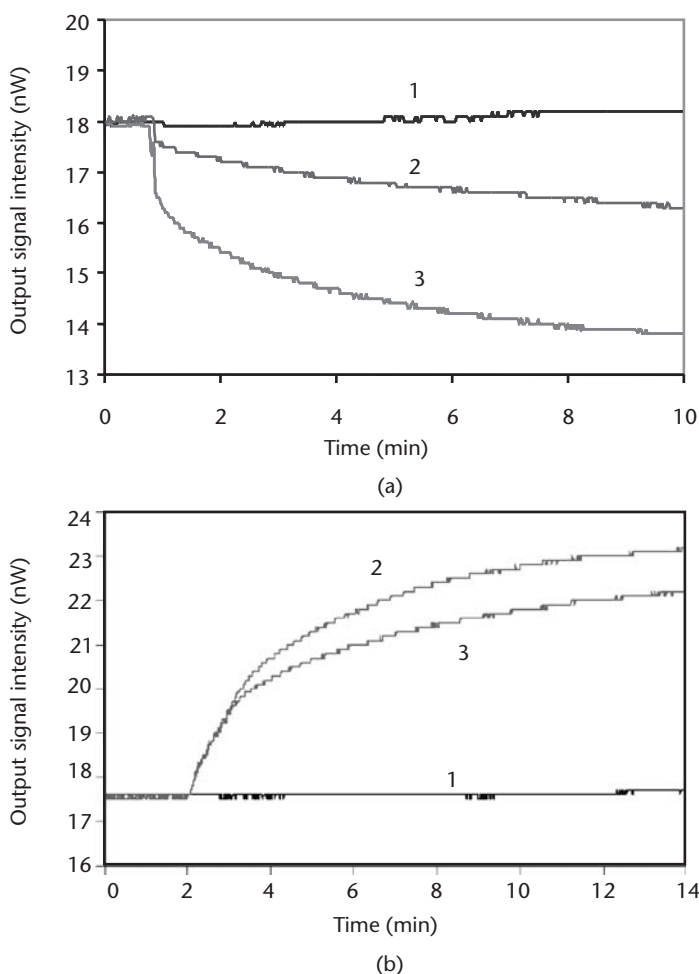
Remarkable progress in the direction of optical enzyme sensors has been achieved by deploying the ATR method in the planar  $\text{Si}_3\text{N}_4$  waveguides [184, 198, 199]. As discussed earlier in this chapter, this method showed a sensitivity of nearly three orders of magnitude higher than the UV-visible spectroscopy method. Planar waveguides were initially coated with three to four layers of CTCT/PAH, placed on the stage of the experimental setup (see Figure 7.19), and attached to the reaction cell. The deposition of enzymes, such as Urease, Acetyl- and Butiryl



**Figure 7.34** Bar-chart diagram of the effect of  $\text{Cd}^{2+}$  ions and DVDP pesticide on the relative changes of absorbance of two composite membranes containing pairs of CTCT/Urease and Thymol Blue/Acetyl CholineEsterase, respectively.

CholineEsterase, onto of the CTCT/PAH film was carried out in the cell, as were the reactions of decomposition of substrata and inhibition of enzymes.

Typical responses of planar waveguides coated with composite CTCT/Urease films are shown in Figure 7.35(a). The intensity of the outcoming light is decreasing during the course of the reaction of urea decomposition catalyzed by the enzyme Urease, as shown in Figure 7.35(b). The observed attenuation of the light intensity is a consequence of the increased adsorption coefficient at 630 nm, due to the deprotonation of CTCT chromophore at high (i.e., alkaline) pH [195]. In the test experiment, the CTCT/PAH membrane without Urease shows no response to the injection of urea solution [Figure 7.35(a), curve 1]. Injection of buffer solution containing 10 parts per billion of Imidacloprid also resulted in a decrease in the signal [Figure 7.35(a), curve 3], although smaller when compared to the untreated



**Figure 7.35** Typical responses of the planar waveguide enzyme sensors to the injection of the respective substratum solutions into the cell. (a) The reaction with 100-mM urea solution: curve 1—CTCT membrane without enzyme Urease; curve 2—CTCT/Urease membrane; and curve 3—CTCT/Urease membrane after exposure to a 10 parts per billion solution of Imidacloprid. (b) The reaction with 100-mM Acetylcholine solution: curve 1—CTCT membrane without enzyme AChE; curve 2—CTCT/AChE membrane; and curve 3—CTCT/AChE membrane after exposure to a 1 part-per-billion solution of DVDP.

membrane [Figure 7.35(a), curve 2]. The observed behavior can be understood in terms of the inhibition of the activity of the Urease enzyme by Imidacloprid pesticide.

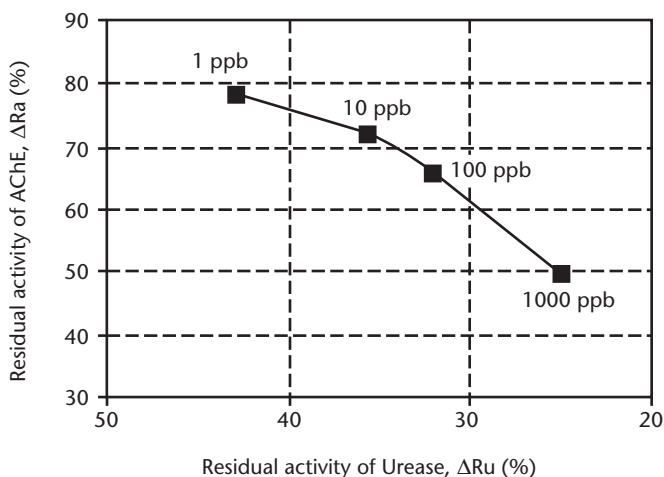
Similar experiments are undertaken on waveguides coated with CTCT/AChE membranes, and the typical responses are shown in Figure 7.35(b). In contrast to CTCT/Urease membranes, the injection of the substratum Acetylcholine causes an increase in the outgoing light intensity [Figure 7.35(b), curve 2]. Such behavior reflects the increased optical absorption in the membrane at 630 nm, due to the protonation of CTCT chromophore at low (i.e., acidic) pH as a result of the enzyme reaction [195]. The presence of a 1 part per billion (DVDP) pesticide inhibits the activity of AChE, and therefore reduces the sensor response [Figure 7.35(b), curve 3]. The test experiment on the membrane without enzyme AChE shows no response [Figure 7.35(b), curve 1].

The concentration dependence of the sensor response in Figure 7.36 shows that Urease is strongly inhibited by DVDP. However, the concentration dependence is not well pronounced, while Imidacloprid is a weaker inhibitor, but the concentration dependence is much stronger.

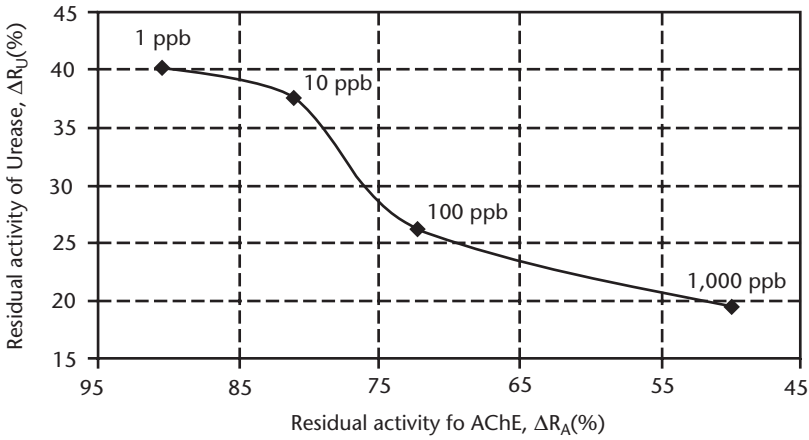
The comparison of the two sensors having CTCT/Urease and CTCT/AChE membranes, presented in Figure 7.36, shows that AChE is much less affected by DVDP than is Urease. The results obtained contradict previous observations of the inhibition of AChE by phosphororganic pesticides [190, 191]. However, the concentrations of inhibitors studied in those works are three orders of magnitude higher than in our case.

A series of experiments on the inhibition effect of  $\text{Cd}^{2+}$  and  $\text{Pb}^{2+}$  ions have been carried out on planar waveguides coated with both CTCT/Urease and CTCT/AChE membranes. The dependence of the residual activity of enzyme Urease on different concentrations of  $\text{Cd}^{2+}$  and  $\text{Pb}^{2+}$  ions is shown in Figure 7.37.

As shown in Figure 7.37, lead is a stronger inhibitor for the enzyme Urease than is cadmium. The comparison of responses of CTCT/Urease and CTCT/AChE membranes, given in Figure 7.37, shows that  $\text{Pb}^{2+}$  ions have much less effect on AChE activity than that on Urease. The effect of heavy metal ions on the activity of



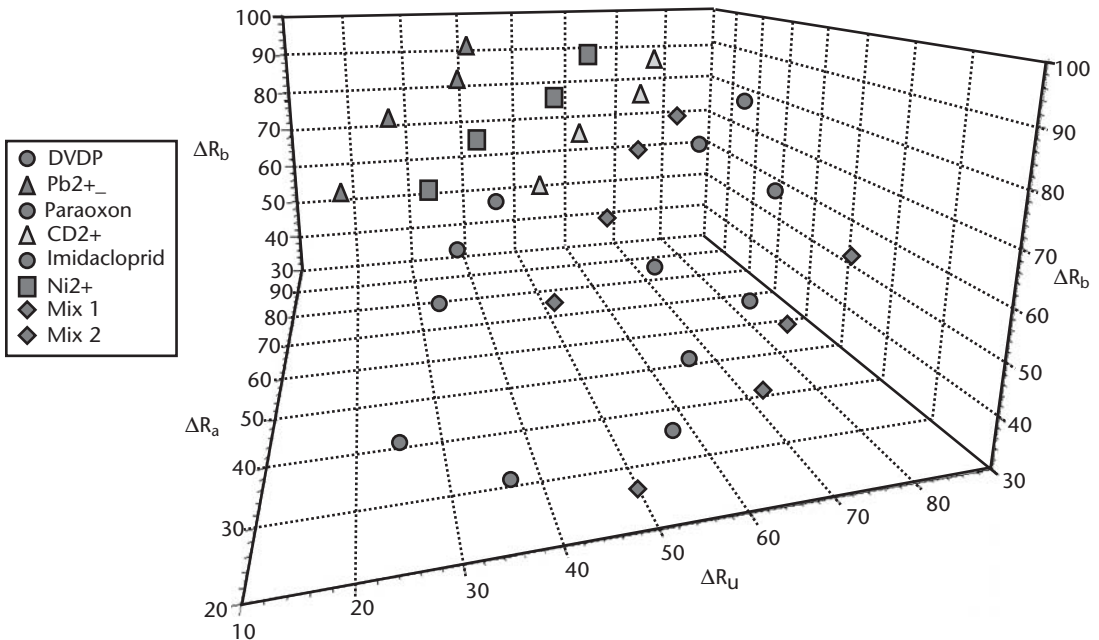
**Figure 7.36** Comparison of the residual activities of enzymes Urease and AChE after their inhibition by DVDP.



**Figure 7.37** Comparison of the residual activities of enzymes Urease and AChE after their inhibition by Pb<sup>2+</sup> ions.

both Urease and AChE is permanent, since there is no recovery of the initial sensor response after a thorough flushing of the system with water and a pure buffer solution.

The results are truly remarkable, since traces of heavy metal ions and pesticides in very small concentrations in the parts per billion range were registered. The results show an obvious possibility of pattern recognition of heavy metal ions (Cd<sup>2+</sup> and Pb<sup>2+</sup>) and of pesticides (Imidacloprid and DVDP), by using two planar waveguides coated with Urease or Acetylcholin Esterase, which have different responses to different pollutants.



**Figure 7.38** Pseudo-3D diagram of the residual enzyme activities of three channels of the planar waveguides, coated with Urease, and Acetyl- and Butyryl-CholineEsterase, to different heavy metal ions and pesticides.



Further research in this direction has been carried out using a sensor array experimental setup with four-channel waveguides. Each channel is coated with a different enzymes: Urease; Acetyl- and Butyryl-CholineEsterase; and with the fourth channel left uncoated to serve as a reference. The experiments were performed by injecting different substrata solutions into respective channels, and recording simultaneously the light intensity coming through each channel. The results are summarized in Figure 7.38, as a pseudo-3D graph of the responses of all three channels on different inhibitors.

Each inhibitor produces a line of experimental points corresponding to different concentrations. All of these lines corresponding to heavy metals ions ( $\text{Cd}^{2+}$ ,  $\text{Pb}^{2+}$ , and  $\text{Ni}^{2+}$ ) and pesticides (Imidacloprid, DVDP, and Paraxon) are clearly separated, and thus provide a pattern for the recognition of pollutants. The responses to the mixtures of pollutants, as shown in Figure 7.38, allow an identification as follows. Mix 1 consists of  $\text{Cd}^{2+}$  and Imidacloprid in approximately equal proportions, and Mix 2 contains mostly Paraxon. Further work using ANN software for pattern recognition is currently underway.

## References

- [1] Blum, L. J., *Bio- and Chemi-Luminescent Sensors*, London, England: World Scientific, 1997.
- [2] Edmonds, T. E., (ed.), *Chemical Sensors*, London, England: Blackie, 1987.
- [3] Seiyama, T., et al., (eds.), "Chemical Sensors," *Proceedings of the International Meeting on Chemical Sensors*, Fukuoka, Japan, September 19–22, 1983.
- [4] Jones, B. E., (ed.), *Current Advances in Sensors*, Bristol, England: Adam Hilger, 1987.
- [5] Kirianaki, N. V., et al., *Data Acquisition and Signal Processing for Smart Sensors*, New York: John Wiley & Sons, 2002.
- [6] Carstens, J. R., *Electrical Sensors and Transducers*, Upper Saddle River, NJ: Prentice-Hall, 1993.
- [7] Krohn, D. A., *Fiber Optic Sensors: Fundamentals and Applications*, 2nd ed., Research Triangle Park, NC: Instrument Society of America, 1992.
- [8] Wolfbeis, O. S., (ed.), *Fiber Optic Chemical Sensors and Biosensors*, Vol. 1, Boca Raton, FL: CRC Press, 1991.
- [9] Udd, E., (ed.), *Fiber Optic Sensors: An Introduction for Engineers and Scientists*, New York: John Wiley & Sons, 1991.
- [10] Sberveglieri, G., (ed.), *Gas Sensors: Principles, Operation, and Developments*, Boston, MA: Kluwer Academic, 1992.
- [11] Wild, P., *Industrial Sensors and Applications for Condition Monitoring*, London, England: Mechanical Engineering Publications, 1994.
- [12] Van der Horn, G., and J. L. Huijsing, *Integrated Smart Sensors: Design and Calibration*, Boston, MA: Kluwer Academic, 1998.
- [13] Webster, J. G., (ed.), *The Measurement, Instrumentation and Sensors Handbook*, Boca Raton, FL: CRC Press, 1999.
- [14] Sellergren B., (ed.), *Molecularly Imprinted Polymers: Man-Made Mimics of Antibodies and Their Applications in Analytical Chemistry*, Oxford, England: Elsevier, 2001.
- [15] Dakin, J., and B. Culshaw, *Optical Fiber Sensors: Principles and Components*, Norwood, MA: Artech House, 1988.
- [16] Janata, J., *Principles of Chemical Sensors*, New York: Plenum, 1989.

- [17] Diamond, D., (ed.), *Principles of Chemical and Biological Sensors*, New York: John Wiley & Sons, 1998.
- [18] Sze, S. M., (ed.), *Semiconductor Sensors*, New York: John Wiley & Sons, 1994.
- [19] Göpel, W., J. Hesse, and J. N. Zemel, (eds.), *Sensors: A Comprehensive Survey, Vol. 1, Fundamentals and General Aspects*, New York: VCH, 1989.
- [20] Göpel, W., J. Hesse, and J. N. Zemel, (eds.), *Sensors: A Comprehensive Survey, Vol. 2, Chemical and Biochemical Sensors*, New York: VCH, 1991.
- [21] Göpel, W., J. Hesse, and J. N. Zemel, (eds.), *Sensors: A Comprehensive Survey, Vol. 3, Chemical and Biochemical Sensors, Part II*, New York: VCH, 1992.
- [22] Göpel, W., J. Hesse, and J. N. Zemel, (eds.), *Sensors: A Comprehensive Survey, Vol. 8, Micro and Nano Sensor Technology Trends in Sensor Markets*, New York: VCH, 1995.
- [23] Moseley, P. T., and B. T. Tofield, (eds.), *Solid State Gas Sensors*, Bristol, England: Adam Hilger, 1987.
- [24] Gregg, S. J., and K. S. W. Sing, *Adsorption, Surface Area and Porosity*, New York: Academic Press, 1967.
- [25] Sauerbrey, G., "Verwendung von Schwingquarzen zur Wägung dünner Schichten und zur Mikrowägung," *Zeitschrift für Physik*, Vol. 155, 1959, pp. 206–213.
- [26] Lucklum, R., and P. Hauptmann, "The *f*-R QCM Technique: An Approach to an Advanced Sensor Signal Interpretation," *Electrochimica Acta*, Vol. 45, 2000, pp. 3907–3916.
- [27] Lucklum, R., and P. Hauptmann, "The Quartz Crystal Microbalance: Mass Sensitivity, Viscoelasticity and Acoustic Amplification," *Sensors and Actuators B: Chemical*, Vol. 70, 2000, pp. 30–36.
- [28] Hauptmann, P., et al., "Using the Quartz Microbalance Principle for Sensing Mass Changes and Damping Properties," *Sensors and Actuators A: Physical*, Vol. 37–38, 1993, pp. 309–316.
- [29] Behling, C., R. Lucklum, and P. Hauptmann, P., "Response of Quartz-Crystal Resonators to Gas and Liquid Analyte Exposure," *Sensors and Actuators A: Physical*, Vol. 68, 1998, pp. 388–398.
- [30] Zimmerman, B., et al., "Electrical Characterisation of High-Frequency Thickness-Shear-Mode Resonators by Impedance Analysis," *Sensors and Actuators B: Chemical*, Vol. 76, 2001, pp. 47–57.
- [31] Behling, C., R. Lucklum, and P. Hauptmann, "Possibilities and Limitations in Quantitative Determination of Polymer Shear Parameters by TSM Resonators," *Sensors and Actuators A: Physical*, Vol. 61, 1997, pp. 260–266.
- [32] Sakti, S. P., et al., "Disposable TSM-Biosensor Based on Viscosity Changes of the Contacting Medium," *Biosensors and Bioelectronics*, Vol. 16, 2001, pp. 1101–1108.
- [33] Ballatine, D. S., et al., *Acoustic Wave Sensors Theory, Design and Physico Chemical Applications*, New York: Academic Press, 1997.
- [34] Benes, E., et al., "Sensors Based on Piezoelectric Resonators," *Sensors and Actuators A: Physical*, Vol. 48, No. 1, 1995, pp. 1–21.
- [35] Nieuwenhuizen, M. S., and J. L. N. Hartevelde, "An Automated SAW Gas Sensor Testing System," *Sensors and Actuators A: Physical*, Vol. 44, No. 3, 1994, pp. 219–229.
- [36] Déjous, C., et al., "A Surface Acoustic Wave Gas Sensor: Detection of Organophosphorus Compounds," *Sensors and Actuators B: Chemical*, Vol. 24, No. 1–3, 1995, pp. 58–61.
- [37] Reibel, J., et al., "Gas Analysis with SAW Sensor Systems," *Sensors and Actuators B: Chemical*, Vol. 65, No. 1–3, 2000, pp. 173–175.
- [38] Rebière, D., et al., "Surface Acoustic Wave Detection of Organophosphorus Compounds with Fluoropolyol Coatings," *Sensors and Actuators B: Chemical*, Vol. 43, No. 1–3, 1997, pp. 34–39.
- [39] Luppá, P. B., L. J. Sokoll, and D. W. Chan, "Immunosensors—Principles and Applications to Clinical Chemistry," *Clinica Chimica Acta*, Vol. 314, No. 1–2, 2001, pp. 1–26.

- [40] Barié, N., and M. Rapp, "Covalent Bound Sensing Layers on Surface Acoustic Wave (SAW) Biosensors," *Biosensors and Bioelectronics*, Vol. 16, No. 9–12, 2001, pp. 979–987.
- [41] Madou, M. J., and S. R. Morrison, *Chemical Sensing with Solid State Devices*, New York: Academic Press, 1989.
- [42] Weimar, U., and W. Gopel, "Chemical Imaging: II. Trends in Practical Multiparameter Sensor Systems," *Sensors and Actuators, B: Chemical*, Vol. 52, No. 1–2, 1998, pp. 143–161.
- [43] Jain, S., et al., "Humidity Sensing with Weak Acid-Doped Polyaniline and Its Composites," *Sensors and Actuators B: Chemical*, Vol. 96, No. 1–2, 2003, pp. 124–129.
- [44] Fang, Q., et al., "Micro-Gas-Sensor with Conducting Polymers," *Sensors and Actuators B: Chemical*, Vol. 84, No. 1, 2002, pp. 66–71.
- [45] Sakurai, Y., et al., "Novel Array-Type Gas Sensors Using Conducting Polymers, and Their Performance for Gas Identification," *Sensors and Actuators B: Chemical*, Vol. 83, No. 1–3, 2002, pp. 270–275.
- [46] Potje-Kamloth, K., "Chemical Gas Sensors Based on Organic Semiconductor Polypyrrole," *Critical Reviews in Analytical Chemistry*, Vol. 32, No. 2, 2002, pp. 121–140.
- [47] Gangopadhyay, R., and D. Amitabha, "Conducting Polymer Composites: Novel Materials for Gas Sensing," *Sensors and Actuators B: Chemical*, Vol. 77, No. 1–2, 2001, pp. 326–329.
- [48] Simon, J., and J. J. Andre, *Molecular Semiconductors, Photoelectrical Properties and Solar Cells*, J. M. Lehn, and Ch. W. Rees, (eds.), Berlin, Germany: Springer-Verlag, 1985.
- [49] Potje-Kamloth, K., "Chemical Gas Sensors Based on Organic Semiconductor Polypyrrole," *Critical Reviews in Analytical Chemistry*, Vol. 32, No. 2, 2002, pp. 121–140.
- [50] Adhikari, B., and S. Majumdar, "Polymers in Sensor Applications," *Progress in Polymer Science*, Vol. 29, No. 7, 2004, pp. 699–766.
- [51] Nabok, A. V., et al., "Nitrogen-Oxide Gas Sensor Based on Tetra-tertbutyl Copper Phthalocyanine Langmuir-Blodgett Films," *International Journal of Electronics*, Vol. 78, No. 1, 1995, pp. 129–133.
- [52] Rodríguez-Méndez, M. L., et al., "Langmuir-Blodgett Films of Lanthanide Diphthalocyanines as Environmental Tobacco Smoke Sensors," *Sensors and Actuators B: Chemical*, Vol. 18, No. 1–3, 1994, pp. 89–92.
- [53] Estela, J. M., and V. Cerd, "Application of Flowing-Stream Techniques to Water Analysis: Part II. General Quality Parameters and Anionic Compounds: Halogenated, Sulphur and Metalloid Species," *Talanta*, Vol. 62, No. 1, 2004, pp. 1–15.
- [54] Reymond, F., et al., "Electrochemistry at Liquid/Liquid Interfaces: Methodology and Potential Applications," *Electrochimica Acta*, Vol. 45, No. 15–16, 2000, pp. 2647–2662.
- [55] Hill, J. W., and D. K. Kolb, *Chemistry for Changing Times*, 9th ed., Upper Saddle River, NJ: Prentice Hall, 2001.
- [56] Baikie, I. D., et al., "Automatic Kelvin Probe Compatible with Ultrahigh Vacuum," *Rec. Sci. Instrum.*, Vol. 60, 1989, p. 930.
- [57] Ru-Qin, Yu., Z. Zong-Rang, and S. Guo-Li, "Potentiometric Sensors: Aspects of the Recent Development," *Sensors and Actuators B: Chemical*, Vol. 65, No. 1–3, 2000, pp. 150–153.
- [58] Holzinger, M., J. Maier, and W. Sitte, "Potentiometric Detection of Complex Gases: Application to CO<sub>2</sub>," *Solid State Ionics*, Vol. 94, No. 1–4, 1997, pp. 217–225.
- [59] Di Benedetto, L. T., et al., "Field-Portable Flow-Injection Analysers for Monitoring of Air and Water Pollution," *Talanta*, Vol. 43, No. 6, 1996, pp. 915–925.
- [60] Alexander, P. W., and P. Bergveld, "Development of an Ion-Sensitive Solid State Device for Neuro-Physiological Measurements," *IEEE Trans. Biomed. Eng.*, Vol. BME-17, 1990, p. 70.
- [61] Alegret, S., et al., "Flow-Through pH ISFET + Reference-ISE as Integrated Detector in Automated FIA Determination," *Sensors & Actuators*, Vol. B7, 1992, p. 555.
- [62] Lundstrom, I., M. S. Shivaraman, and C. M. Svensson, "A Hydrogen Sensitive Pd-Gate MOS transistor," *J. Appl. Phys.*, Vol. 46, 1975, p. 3876.

- [63] Lundstrom, I., and D. Sodeberg, "Hydrogen Sensitive MOS Structures, Part 2: Characterisation," *Sensors & Actuators*, Vol. 2, 181/1982, p. 105.
- [64] Shirshov, Y. M., V. V. Omelchuk, and A. I. Shkreby, "Ion Diffusion in Films Condensed on the Surface of the Si-SiO<sub>2</sub> System Dielectric," *Ukr. Fiz. Zhurnal*, Vol. 26, No. 6, 1981, pp. 967-972.
- [65] Wilkop, T., et al., "The Detection of Organic Contaminations in Water with Calixarene Coated Electrodes," in *Novel Methods to Study Interfacial Layer*, D. Mobius, and R. Miller, (eds.), Amsterdam, the Netherlands: Elsevier, 2001, pp. 427-438.
- [66] Fivash, M., E. M. Towler, and R. J. Fisher, "BIAcore for Macromolecular Interaction," *Current Opinion in Biotechnology*, Vol. 9, No. 1, 1998, pp. 97-101.
- [67] Beketov, G. V., et al., "Surface Plasmon Resonance Spectroscopy: Prospects of Superstrate Refractive Index Variation for Separate Extraction of Molecular Layer Parameters," *Sensors and Actuators B: Chemical*, Vol. 48, No.1-3, 1998, pp. 432-438.
- [68] Frutos, A. G., S. C. Weibel, and R. M. Corn, "Rear-Infrared Surface Plasmon Resonance Measurements of Ultrathin Films. 2. Fourier Transform SPR Spectroscopy," *Anal. Chem.*, Vol. 71, No. 18, 1999, pp. 3935-3940.
- [69] Chinowsky, T. M., et al., "Performance of the SPREETA 2000 Integrated Surface Plasmon Resonance Affinity Sensor," *Sensors and Actuators B*, Vol. 6954, 2003, pp. 1-9.
- [70] Westphal, P., and A. Bornmann, "Biomolecular Detection by Surface Plasmon Enhanced Ellipsometry," *Sensors and Actuators B*, Vol. 84, 2002, pp. 278-282.
- [71] Poksinski, M., and H. Arwin, "In Situ Monitoring of Metal Surfaces Exposed to Milk Using Total Internal Reflection Ellipsometry," *Sensors and Actuators B*, Vol. 94, 2003, pp. 247-252.
- [72] Poksinski, M., and H. Arwin, "Protein Monolayers Monitored by Internal Reflection Ellipsometry," *Thin Solid Films*, Vol. 455-456, 2004, pp. 716-721.
- [73] Bortchagovsky, E. G., et al., "Fullerene Embedded Langmuir-Blodgett Films Probed by Spectroscopic Ellipsometry," *SPIE*, Vol. 3359, 1998, pp. 38-44.
- [74] Min, H.-K., H.-S. Yang, and S. M. Cho, "Extremely Sensitive Optical Sensing of Ethanol Using Porous Silicon," *Sensors and Actuators B: Chemical*, Vol. 67, No. 1-2, 2000, pp. 199-202.
- [75] Gauglitz, G., and J. Ingenhoff, "Influence of Thin Superstrate Films on Evanescent Waves in Surface Waveguides," *Ber. Bunsen. Phys. Chem.*, Vol. 95, 1991, pp. 1558-1563.
- [76] Schmitt, H. M., et al., "An Integrated System for Optical Biomolecular Interaction Analysis," *Biosens. & Bioelectron.*, Vol. 12, No. 8, 1997, pp. 809-816.
- [77] Klotz, A., A. Brecht, and G. Gauglitz, "Channel Waveguide Mode Beat Interferometer," *Sensors & Actuators B*, Vol. 38-39, 1997, pp. 310-315.
- [78] Heideman, R. G., R. P. H. Kooyman, and J. Greeve, "Performance of a Highly Sensitive Optical Waveguide Mach-Zehnder Immunosensor," *Sensors and Actuators B*, Vol. 10, 1993, pp. 209-217.
- [79] Schubert, T., et al., "Refractive Index Measurements Using an Integrated Mach-Zehnder Interferometer," *Proc. of Euroensors X*, Leuven, Belgium, September 8-11, 1996, p. 3.
- [80] Drapp, B., et al., "Integrated Optical Mach-Zehnder Interferometers as Simazine Immuno-brobes," *Sensors & Actuators B*, Vol. 38-39, 1997, pp. 277-282.
- [81] Weisser, M., et al., "Specific Bio-Recognition Observed with an Integrated Mach-Zehnder Interferometer," *Biosensors and Bioelectronics*, Vol. 14, 1999, pp. 405-411.
- [82] Shirshov, Y. M., et al., "A Sensor Based on the Planar Polarization Interferometer," *Sensors and Actuators A*, Vol. 68, 1998, pp. 384-387.
- [83] Shirshov, Y. M., et al., "Analysis of the Response of Planar Interferometer to Molecular Layer Formation: Fibrinogen Adsorption on Silicon Nitride Surface," *Biosensors & Bioelectronics*, Vol. 16, 2001, pp. 381-390.
- [84] Nabok, A. V., "Composite Polyelectrolyte Self-Assembled Films for Chemical and Bio-Sensing," in *Novel Methods to Study Interfacial Layers*, D. Mobius, and R. Miller, (eds.), Amsterdam, the Netherlands: Elsevier, 2001, pp. 351-370.

- [85] Nabok, A. V., et al., "Registration of Immuno-Globuline AB/AG Reaction with Planar Polarization Interferometer," *Proceedings of SPIE, Biochemical and Biomolecular Sensing, Environmental and Industrial Sensing, Photonics East*, Boston, MA, November 5–8, 2000, pp. 4200–4201.
- [86] De Vries, M., et al., "Photoinduced Grating-Based Optical Fiber Sensors for Structural Analysis and Control," *Eng. Struct.*, Vol. 20, No. 3, 1998, pp. 205–210.
- [87] Allsop, T., L. Zhang, and I. Bennion, "Detection of Organic Aromatic Compounds in Paraffin by a Long-Period Fiber Grating Optical Sensor with Optimized Sensitivity," *Optics Comm.*, Vol. 191, No. 3–6, 2001, pp. 181–190.
- [88] Keith, J., S. Puckett, and G. E. Pacey, "Investigation of the Fundamental Behavior of Long-Period Grating," *Talanta*, Vol. 61, No. 4, 2003, pp. 417–421.
- [89] Hou, R., et al., "Modelling of Long-Period Fibre Grating Response to Refractive Index Higher Than That of Cladding," *Meas. Sci. & Technol.*, Vol. 12, No. 10, 2001, pp. 1709–1713.
- [90] Kawabata, Y., H. Sugamoto, and T. Imasaka, "Micro-Optrode for Urea Using an Ammonium Ion-Sensitive Membrane Covered with a Urease-Immobilized Membrane," *Analitica Chimica Acta*, Vol. 283, 1993, pp. 689–694.
- [91] Konski, R., and O. S. Wolfbeis, "Composite Films of Prussian Blue and N-Substituted Polypyrroles: Covalent Immobilisation of Enzymes and Application to Near Infrared Optical Biosensing," *Biosensors & Bioactuators*, Vol. 14, 1999, pp. 87–92.
- [92] Plowman, T. E., S. S. Saavedra, and W. M. Reichert, "Planar Integrated Optical Methods for Examining Thin Films and Their Surface Adlayers," *Biomaterials*, Vol. 19, No. 4–5, 1998, pp. 341–355.
- [93] Nabok, A. V., S. Haron, and A. K. Ray, "Silicon Planar Waveguide for Biosensing," *IEE Nano-Biotechnology*, Vol. 150, No. 1, 2003, pp. 25–29.
- [94] Haron, S., A. Nabok, and A. K. Ray, "Optical Bio-Sensing Transducer Based on Silicon Waveguide Structure Coated with Polyelectrolyte Nanolayers," *Proceedings of SPIE*, Vol. 5119, 2003, pp. 100–108.
- [95] Singer, E., et al., "Fiber Optic Sensor for Oxygen Determination in Liquids," *Sensors and Actuators A: Physical*, Vol. 42, No. 1–3, 1994, pp. 542–546.
- [96] Duveneck, G. L., et al., "Novel Bioaffinity Sensors for Trace Analysis Based on Luminescence Excitation by Planar Waveguides," *Sensors and Actuators B: Chemical*, Vol. 38, No. 1–3, 1997, pp. 88–95.
- [97] Schuderer, J., et al., "Development of a Multichannel Fluorescence Affinity Sensor System," *Anal. Chem.*, Vol. 72, No. 16, 2000, pp. 3942–3948.
- [98] Starodub, V. M., et al., "Control of Myoglobin Level in a Solution by an Immune Sensor Based on the Photoluminescence of Porous Silicon," *Sensors and Actuators B: Chemical*, Vol. 58, No. 1–3, 1999, pp. 409–414.
- [99] Starodub, V. M., L. L. Fedorenko, and N. F. Starodub, "Optical Immune Sensors for the Monitoring Protein Substances in the Air," *Sensors and Actuators B: Chemical*, Vol. 68, No. 1–3, 2000, pp. 40–47.
- [100] Tsargorodskaya, A., A. V. Nabok, and A. K. Ray, "Study of Electroluminescence in Porous Silicon for Sensing Applications," *IEE Proceedings—Circuits, Devices and Systems*, Vol. 50, No. 4, 2003, pp. 355–359.
- [101] Meixner, H., and U. Lampe, "Metal Oxide Sensors," *Sens. Actuator B-Chem.*, Vol. 33, No. 1–3, 1996, pp. 198–202.
- [102] Hockensmith, C. M., J. C. Goldsby, and T. Kacic, "Thermal Studies of New Precursors to Indium-Tin Oxides for Use as Sensor Materials in the Detection of NO<sub>x</sub>," *Thermochim. Acta.*, Vol. 341, 1999, pp. 315–322.
- [103] Sung, J. H., et al., "Sensing Characteristics of Tin Dioxide/Gold Sensor Prepared by Coprecipitation Method," *Sens. Actuator B-Chem.*, Vol. 66, No. 1–3, 2000, pp. 149–152.



- [104] Malyshev, V. V., and A. V. Pisyakov, "Dynamic Properties and Sensitivity of Semiconductor Metal-Oxide Thick-Film Sensors to Various Gases in Air Gaseous Medium," *Sens. Actuator B-Chem.*, Vol. 96, No. 1–2, 2003, pp. 413–434.
- [105] Broda, S., and W. H. Schnitzler, "Chemosensory Systems for Analysis of Volatile Aroma Compounds in Food," *Dtsch. Lebensm.-Rundsch.*, Vol. 94, No. 1, 1998, pp. 13–16.
- [106] Kohl, D., et al., "Systematic Studies on Responses of Metal-Oxide Sensor Surfaces to Straight Chain Alkanes, Alcohols, Aldehydes, Ketones, Acids and Esters Using the SOMMSA Approach," *Sens. Actuator B-Chem.*, Vol. 70, No. 1–3, 2000, pp. 43–50.
- [107] Garcia-Gonzalez, D. L., and R. Aparicio, "Classification of Different Quality Virgin Olive Oils by Metal-Oxide Sensors," *Eur. Food Res. Technol.*, Vol. 218, No. 5, 2004, pp. 484–487.
- [108] Penza, M., and G. Cassano, "Recognition of Adulteration of Italian Wines by Thin-Film Multisensor Array and Artificial Neural Networks," *Anal. Chim. Acta.*, Vol. 509, No. 2, 2004, pp. 177–196.
- [109] Pasini, P., et al., "Use of a Gas-Sensor Array for Detecting Volatile Organic Compounds (VOC) in Chemically Induced Cells," *Anal. Bioanal. Chem.*, Vol. 378, No. 1, 2004, pp. 76–83.
- [110] Cococcioni, M., B. Lazzerini, and F. Marcelloni, "An Artificial Olfactory System for Quality and Geographical Discrimination of Olive Oils," *Knowledge-Based Intelligent Information and Engineering Systems, Pt. 2, Proceedings*, Vol. 2774, 2003, pp. 647–653.
- [111] Garcia-Gonzalez, D. L., and R. Aparicio, "Virgin Olive Oil Quality Classification Combining Neural Network and MOS Sensors," *J. Agric. Food Chem.*, Vol. 51, No. 12, 2003, pp. 3515–3519.
- [112] Boothe, D. D. H., and J. W. Arnold, "Electronic Nose Analysis of Volatile Compounds from Poultry Meat Samples, Fresh and After Refrigerated Storage," *J. Sci. Food Agric.*, Vol. 82, No. 3, 2002, pp. 315–322.
- [113] Dewettinck, T., K. Van Hege, and W. Verstraete, "The Electronic Nose as a Rapid Sensor for Volatile Compounds in Treated Domestic Waste Water," *Water Res.*, Vol. 35, No. 10, 2001, pp. 2475–2483.
- [114] Capone, S., et al., "Analysis of Vapours and Foods by Means of an Electronic Nose Based on a Sol-Gel Metal Oxide Sensors Array," *J. Sens. Actuator B-Chem.*, Vol. 69, No. 3, 2000, pp. 230–235.
- [115] Hudon, G., C. Guy, and J. Hermia, "Measurement of Odor Intensity by an Electronic Nose," *J. Air Waste Manage. Assoc.*, Vol. 50, No. 10, 2000, pp. 1750–1758.
- [116] Wijesundera, C., and T. Walsh, "Evaluation of an Electronic Nose Equipped with Metal Oxide Sensors for Cheese Grading," *Aust. J. Dairy Technol.*, Vol. 53, No. 2, 1998, pp. 141–141.
- [117] Chibirova, F. K., et al., "Semiconductor Metal Oxide Sensors in Water and Water Based Biological Systems," *Sensors*, Vol. 3, No. 10, 2003, pp. 451–457.
- [118] Maskell, W. C., "Progress in the Development of Zirconia Gas Sensors," *Solid State Ion.*, Vol. 134, No. 1–2, 2000, pp. 43–50.
- [119] Stramare, S., V. Thangadurai, and W. Weppner, "Lithium Lanthanum Titanates: A Review," *Chem. Mat.*, Vol. 15, No. 21, 2003, pp. 3974–3990.
- [120] Georges, S., et al., "The LAMOX Family of Fast Oxide-Ion Conductors: Overview and Recent Results," *J. New Mat. Electrochem. Syst.*, Vol. 7, No. 1, 2004, pp. 51–57.
- [121] Mobius, H. H., "Galvanic Solid Electrolyte Cells for the Measurement of CO<sub>2</sub> Concentrations," *J. Solid State Electrochem.*, Vol. 8, No. 2, 2004, pp. 94–109.
- [122] Ramamoorthy, R., P. K. Dutta, and S. A. Akbar, "Oxygen Sensors: Materials, Methods, Designs and Applications," *J. Mater. Sci.*, Vol. 38, No. 21, 2003, pp. 4271–4282.
- [123] Menil, F., V. Coillard, and C. Lucat, "Critical Review of Nitrogen Monoxide Sensors for Exhaust Gases of Lean Burn Engines," *Sens. Actuator B-Chem.*, Vol. 67, No. 1–2, 2000, pp. 1–23.

- [124] Maskell, W. C., "Progress in the Development of Zirconia Gas Sensors," *Solid State Ion.*, Vol. 134, No. 1–2, pp. 43–50.
- [125] Jobst, G., et al., "Thin-Film Clark-Type Oxygen Sensor-Based on Novel Polymer Membrane Systems for In-Vivo and Biosensor Applications," *Biosensors & Bioelectronics*, Vol. 8, No. 3–4, 1993, pp. 123–128.
- [126] Suzuki, H., A. Sugama, and N. Kojima, "Micromachined Clark Oxygen Electrodes and Biosensors," *Fujitsu Scientific & Technical Journal*, Vol. 28, No. 3, 1992, pp. 393–401.
- [127] Shipway, A. N., E. Katz, and I. Willner, "Nanoparticle Arrays on Surfaces for Electronic, Optical, and Sensor Applications," *Chemphyschem*, Vol. 1, No. 1, 2000, pp. 18–52.
- [128] Ryabtsev, S.V., et al., "Interaction of Metal Nanoparticles with a Semiconductor in Surface-Doped Gas Sensors," *Semiconductors*, Vol. 35, No. 7, 2001, pp. 835–839.
- [129] Panchapakesan, B., et al., "Nanoparticle Engineering and Control of Tin Oxide Microstructures for Chemical Microsensor Applications," *Nanotechnology*, Vol. 12, No. 3, 2001, pp. 336–349.
- [130] Hernandez-Santos, D., M. B. Gonzalez-Garcia, and A. C. Garcia, "Metal-Nanoparticles Based Electroanalysis," *Electroanalysis*, Vol. 14, No. 18, 2002, pp. 1225–1235.
- [131] Katz, E., I. Willner, and J. Wang, "Electroanalytical and Bioelectroanalytical Systems Based on Metal and Semiconductor Nanoparticles," *Electroanalysis*, Vol. 16, No. 1–2, 2004, pp. 19–44.
- [132] Baraton, M. I., and L. Merhari, "Advances in Air Quality Monitoring Via Nanotechnology," *J. of Nanoparticle Research*, Vol. 6, No. 1, 2004, pp. 107–117.
- [133] Zayats, M., et al., "Probing Photo-Electrochemical Processes in Au-CdS Nanoparticle Arrays by Surface Plasmon Resonance: Application for the Detection of Acetylcholine Esterase Inhibitors," *J. Am. Chem. Soc.*, Vol. 125, No. 51, 2003, pp. 16006–16014.
- [134] Bidan, G., "Electroconducting Conjugated Polymers—New Sensitive Matrices to Build up Chemical or Electrochemical Sensors—A Review," *Sens. Actuator B-Chem.*, Vol. 6, No. 1–3, 1992, pp. 45–56.
- [135] Barisci, J. N., C. Conn, and G. G. Wallace, "Conducting Polymer Sensors," *Trends Polym. Sci.*, Vol. 4, No. 9, 1996, pp. 307–311.
- [136] Lavrik, N. V., et al., "Composite Olyaniline/Calixarene Langmuir-Blodgett Films for Gas Sensing," *Nanotechnology*, Vol. 7, 1996, pp. 1–5.
- [137] Privat, E., et al., "Techniques for Ethanol Removal Before Discrimination of Alcoholic Drinks Using Electronic Noses (A Review)," *Sci. Aliments*, Vol. 18, No. 5, 1998, pp. 459–470.
- [138] Leclerc, M., "Optical and Electrochemical Transducers Based on Functionalized Conjugated Polymers," *Adv. Mater.*, Vol. 11, No. 18, 1999, pp. 1491–1500.
- [139] Sarig, Y., "Potential Applications of Artificial Olfactory Sensing for Quality Evaluation of Fresh Produce," *J. Agr. Eng. Res.*, Vol. 77, No. 3, 2000, pp. 239–258.
- [140] Rover, L., G. D. Neto, and L. T. Kubota, "Potentiometric Transducers Based in Conducting Polymers: Analytical Applications," *Quim. Nova*, Vol. 20, No. 5, 1997, pp. 519–527.
- [141] Yu, J. C. C., and E. P. C. Lai, "Polypyrrole Film on Miniaturized Surface Plasmon Resonance Sensor for Ochratoxin A Detection," *Synth. Met.*, Vol. 143, No. 3, 2004, pp. 258–264.
- [142] Emr, S. A., and A. M. Yacynych, "Use of Polymer-Films in Amperometric Biosensors," *Electroanalysis*, Vol. 7, No. 10, 1995, pp. 913–923.
- [143] Trojanowicz, M., and T. K. V. Krawczyk, "Electrochemical Biosensors Based on Enzymes Immobilized in Electropolymerized Films," *Mikrochim. Acta*, Vol. 121, No. 1–4, 1995, pp. 167–181.
- [144] Schuhmann, W., "Conducting Polymer Based Amperometric Enzyme Electrodes," *Mikrochim. Acta*, Vol. 121, No. 1–4, 1995, pp. 1–29.
- [145] Adeloju, S. B., and G. G. Wallace, "Conducting Polymers and the Bioanalytical Sciences: New Tools for Biomolecular Communications—A Review," *Analyst*, Vol. 121, No. 6, 1996, pp. 699–703.



- [146] Skladal, P., and L. Macholan, "Biosensors—Present State and Future Trends," *Chem. Listy*, Vol. 91, No. 2, 1997, pp. 105–113.
- [147] Sadik, O. A., "Bioaffinity Sensors Based on Conducting Polymers: A Short Review," *Electroanalysis*, Vol. 11, No. 12, 1999, pp. 839–844.
- [148] Gerard, M., A. Chaubey, and B. D. Malhotra, "Application of Conducting Polymers to Biosensors," *Biosens. Bioelectron.*, Vol. 17, No. 5, 2002, pp. 345–359.
- [149] Pal, P. S., and P. Sarkar, "Polymers in Biosensors—A Review," *J. Indian Chem. Soc.*, Vol. 79, No. 3, 2002, pp. 211–218.
- [150] Ramanaviciene, A., and A. Ramanavicius, "Application of Polypyrrole for the Creation of Immunosensors," *Crit. Rev. Anal. Chem.*, Vol. 32, No. 3, 2002, pp. 245–252.
- [151] Shah, J., and E. Wilkins, "Electrochemical Biosensors for Detection of Biological Warfare Agents," *Electroanalysis*, Vol. 15, No. 3, 2003, pp. 157–167.
- [152] Vidal, J. C., E. Garcia-Ruiz, and J. R. Castillo, "Recent Advances in Electropolymerized Conducting Polymers in Amperometric Biosensors," *Microchim. Acta*, Vol. 143, No. 2–3, 2003, pp. 93–111.
- [153] Zhou, R., et al., "Phthalocyanines as Sensitive Materials for Chemical Sensors," *Appl. Organomet. Chem.*, Vol. 10, No. 8, 1996, pp. 557–577.
- [154] Zhu, D. B., Y. Q. Liu, and Y. Xu, "Recent Progress of Study on the Molecular Thin Films for Electronics," *Mol. Cryst. & Liq. Cryst. Sci. & Technol., Section A-Mol. Cryst. & Liq. Cryst.*, Vol. 294, 1997, pp. 1–6.
- [155] Engelkamp, H., and R. J. M. Nolte, "Molecular Materials Based on Crown Ether Functionalized Phthalocyanines," *J. Porphyrins & Phthalocyanines*, Vol. 4, No. 5, 2000, pp. 454–459.
- [156] Jiang, Z., et al., "The Structure and Gas-Sensing Property of the Coordination Compounds of Phthalocyanine," *Chinese J. Struct. Chem.*, Vol. 20, No. 5, 2001, pp. 331–338.
- [157] De Saja, R., et al., "Array of Lutetium Bisphthalocyanine Sensors for the Detection of Trimethylamine," *Mater. Sci. Eng. C-Biomimetic Supramol. Syst.*, Vol. 8–9, 1999, pp. 565–568.
- [158] Rodriguezmendez, M. L., et al., "Response Of Chemically-Modified Prpc(2), Prpc(2)(T) and Gdpc(2)(T) Langmuir-Blodgett-Films to Tobacco-Smoke," *Sens. Actuator B-Chem.*, Vol. 25, No. 1–3, 1995, pp. 643–646.
- [159] Rodriguezmendez, M. L., et al., "Langmuir-Blodgett-Films of Lanthanide Diphthalocyanines as Environmental Tobacco-Smoke Sensors," *Sens. Actuator B-Chem.*, Vol. 18, No. 1–3, 1994, pp. 89–92.
- [160] Souto, J., R. Aroca, and J. A. Desaja, "Surface-Enhanced Resonance Raman-Scattering of a NO<sub>2</sub>-Bisphthalocyanine Adduct in Langmuir-Blodgett Monolayers," Vol. 22, No. 12, 1991, pp. 787–790.
- [161] Ray, A. K., et al., "Optical Studies on Composite Langmuir-Blodgett Films Containing Ytterbium Bis-phthalocyanines," *Phil. Mag.*, Vol. 79, No. 7, 1999, pp. 1005–1019.
- [162] Brook, R. A., et al., "Mixed Monolayer LB Films of EHO and Calix[8]arene," *J. Mater. Sci. Eng. C-Biomimetic Supramol.* Vol. 22, No. 2, 2002, pp. 427–432.
- [163] Pedrosa, J. M., et al., "Influence of Molecular Organization of Asymmetrically Substituted Porphyrins on Their Response to NO<sub>2</sub> Gas," *Langmuir*, Vol. 18, No. 20, 2002, pp. 7594–7601.
- [164] Smith, V. C., et al., "Chlorine Sensing Properties of Porphyrin Thin Films," *Thin Solid Films*, Vol. 285, 1996, pp. 911–914.
- [165] Grieve, M. B., et al., "An Investigation of the Optical-Properties of Tetraphenylporphyrin Derivatives in Langmuir and Langmuir-Blodgett-Films," Vol. 243, No. 1–2, 1994, pp. 581–586.
- [166] Hudson, A. J., et al., "Characterization and Langmuir-Blodgett Deposition of Novel Porphyrin Compounds," *Mol. Cryst. Liq. Cryst. Sci. Technol. Sect. A-Mol. Cryst. Liq.*, Vol. 234, 1993, pp. 385–390.

- [167] Gutsche, C. D., *Calixarenes*, Cambridge, England: Royal Society of Chemistry, 1989.
- [168] Davis, F., et al., "Order and Structure in Langmuir-Blodgett Mono- and Multilayers of Resorcarenes," *Langmuir*, Vol. 14, No. 15, 1998, pp. 4180–4185.
- [169] Nabok, A. V., et al., "Complexing Properties of Calix[4]resorcinolarene LB Films," *Thin Solid Films*, Vol. 259, No. 2, 1995, pp. 244–247.
- [170] Nabok, A., et al., "Study of Adsorption of Some Organic Molecules in Calix[4]resorcinolarene LB Films by Surface Plasmon Resonance," *Sensors and Actuators B*, Vol. 45, No. 2, 1997, pp. 115–121.
- [171] Nabok, A. V., A. K. Hassan, and A. K. Ray, "Condensation of Organic Vapours Within Nanoporous Calixarene Thin Films," *J. Mater. Chem. (RSC)*, Vol. 10, 2000, pp. 189–194.
- [172] Hassan, A. K., et al., "Kinetic Study of BTEX Vapour Adsorption onto Surfaces of Calix-4-resorcinolarene Films," *Appl. Surf. Sci.*, Vol. 182, 2001, pp. 49–54.
- [173] Ray, A. K., et al., "Organic Vapours Sensor," U.K. Patent No. 0217125.4, July 24, 2002.
- [174] Holloway, A. F., et al., "New Method of Vapour Discrimination Using the Thickness Shear Mode (TSM) Resonator," *Sensors*, Vol. 3, 2003, pp. 170–174.
- [175] Holloway, A. F., et al., "Impedance Analysis of the Thickness Shear Mode Resonator for Organic Vapour Sensing," *Sensors and Actuators*, Vol. 99, No. 2–3, 2004, pp. 355–360.
- [176] Starodub, V. M., et al., "Approaches for Structured Immobilisation of Recognising Elements on the Transducer Surface of Biosensors," in *Nanostructured Materials and Coatings for Biomedical and Sensor Applications*, Y. G. Gogotsi, and I. V. Uvarova, (eds.), *NATO Science Series, Series II: Mathematics, Physics and Chemistry*, Vol. 102, 2003, pp. 311–325.
- [177] Koudelka, M., et al., "In-Vivo Behaviour of Hypodermically Implanted Microfabricated Glucose Sensors," *Biosensors and Bioelectronics*, Vol. 6, No. 1, 1991, pp. 31–36.
- [178] Yao, T., and K. Takashima, "Amperometric Biosensor with a Composite Membrane of Sol-Gel Derived Enzyme Film and Electrochemically Generated Poly(1,2-diamino-benzene) Film," *Biosensors & Bioelectronics*, Vol. 13, No. 1, 1998, pp. 67–73.
- [179] Khan, G. F., "Organic Charge Transfer Complex Based Printable Biosensor," *Biosensors and Bioelectronic*, Vol. 11, No. 12, 1996, pp. 1221–1227.
- [180] Schmidt, A., C. Standfuss-Gabisch, and U. Bilitewski, "Microbial Biosensor for Free Fatty Acids Using an Oxygen Electrode Based on Thick Film Technology," *Biosensors & Bioelectronics*, Vol. 11, No. 11, 1996, pp. 1139–1145.
- [181] Bersina, T. S., et al., "Langmuir-Blodgett Films Composed of Monolayers of Amphiphilic Molecules and Adsorbed Soluble Proteins," *Thin Solid Films*, Vol. 285, 1996, pp. 757–761.
- [182] Lvov, Y., G. Decher, and H. Möhwald, "Assembly, Structural Characterization, and Thermal Behavior of Layer-by-Layer Deposited Ultrathin Films of Poly(vinylsulfate) and Poly(allylamine)," *Langmuir*, Vol. 9, 1993, pp. 481–486.
- [183] Lvov, Y. M., and G. B. Sukhorukov, "Protein Architecture: Assembly of Ordered Films by Means Alternated Adsorption of Opposite Charged Macromolecules," *Biologicheskije Membrany*, Vol. 14, No. 3, 1997, pp. 229–250.
- [184] Nabok, A. V., S. Haron, and A. K. Ray, "Silicon Planar Waveguide for Biosensing," *IEE Nano-Biotechnology*, Vol. 150, No. 1, 2003, pp. 25–29.
- [185] Starodub, N. F., et al., "Immobilisation of Biocomponents for Immune Optical Sensors," *Ukrainian Bio-Chemical Journal*, Vol. 73, No. 5, 2001, pp. 55–64.
- [186] Dancil, K. P. S., D. P. Greiner, and M. J. Sailor, "A Porous Silicon Optical Biosensor: Detection of Reversible Binding of IgG to a Protein A-Modified Surface," *J. Am. Chem. Soc.*, Vol. 121, No. 34, 1999, pp. 7925–7930.
- [187] Nabok, A. V., et al., "Composite Polyelectrolyte Self-Assembled Films for Chemical and Bio-Sensing," in *Novel Methods to Study Interfacial Layers*, D. Mobius, and R. Miller, (eds.), Amsterdam: Elsevier, 2001, pp. 351–370.

- [188] Nabok, A. V., et al., "Registration of Immuno-Globuline AB/AG Reaction with Planar Polarization Interferometer," *Proceedings of SPIE, Biochemical and Biomolecular Sensing, Environmental and Industrial Sensing, Photonics East*, Boston, MA, November 5–8, 2000, pp. 4200–4201.
- [189] Zelikoff, J. T., "Immunotoxicology Across Species Lines," *Developmental & Comparative Immunology*, Vol. 21, No. 2, 1997, p. 121.
- [190] Kukla, A. L., et al., "Multienzyme Electrochemical Sensor Array for Determination of Heavy Metal Ions," *Sensors and Actuators B: Chemical*, Vol. 57, No. 1–3, 1999, pp. 213–218.
- [191] Starodub, N. F., et al., "Multi-Enzymatic Electrochemical Sensor: Field Measurements and Their Optimisation," *Analytica Chimica Acta*, Vol. 385, No. 1–3, 1999, pp. 461–466.
- [192] Kawabata, Y., H. Sugamoto, and T. Imasaka, "Micro-Optrode for Urea Using an Ammonium Ion-Sensitive Membrane Covered with a Urease-Immobilized Membrane," *Analytica Chimica Acta*, Vol. 283, No. 2, 1993, pp. 689–694.
- [193] Konski, R., and O. S. Wolfbeis, "Composite Films of Prussian Blue and N-Substituted Polypyrroles: Covalent Immobilisation of Enzymes and Application to Near Infrared Optical Biosensing," *Biosensors & Bioelectronics*, Vol. 14, No. 1, 1999, pp. 87–92.
- [194] Nabok, A. V., et al., "Polyelectrolyte Self-Assembled Thin Films Containing Cyclo-tetrachromotropyrene for Chemical and Bio-Sensing," *Mater. Sci & Eng. C*, Vol. 8–9, 1999, pp. 123–126.
- [195] Poh, B. L., and C. S. Lim, "Complexations of Amines with Water-Soluble Cyclo-tetrachromotropyrene," *Tetrahedron*, Vol. 46, No. 10, 1990, pp. 3651–3658.
- [196] Nabok, A., et al., "Composite Polyelectrolyte Self-Assembled Films for Optical Biosensors," *Proceedings of SPIE's 6th Annual Intern. Symposium on Smart Structures and Materials*, March 1–5, 1999, pp. 3673–3729.
- [197] Nabok, A. V., et al., "Enzyme/Indicator Optrodes for Detection of Heavy Metal Ions and Pesticides," *SPIE Proc., Biochemical and Biomolecular Sensing, Environmental and Industrial Sensing, Photonics East*, Boston, MA, November 5–8, 2000, pp. 4200–4207.
- [198] Haron, S., A. Nabok, and A. K. Ray, "Optical Bio-Sensing Transducer Based on Silicon Waveguide Structure Coated with Polyelectrolyte Nano Layers," *Proceedings of SPIE*, Vol. 5119, 2003, pp. 100–108.
- [199] Nabok, A. V., S. Haron, and A. K. Ray, "Optical Enzyme Sensors Based upon Silicon Planar Waveguide Coated with Composite Polyelectrolyte Film," *Appl. Surf. Sci.*, Vol. 238, No. 1–4, 2004, pp. 423–428.

# About the Author

Alexei Nabok is a senior lecturer at the Material and Engineering Research Institute at Sheffield Hallam University and a leader of the research group there. In 1968, Dr. Nabok finished his secondary education at the prestigious Ukrainian Physical-Mathematical Boarding School and entered T. G. Shevchenko Kiev State University. After graduating from the Radio-Physics Department of this university in 1973, he obtained a degree in radiophysics and electronics, equivalent to an M.Sc. His first job was in the Kiev Research Institute of Microdevices within the microelectronic firm Kristal. In 1980, Dr. Nabok joined the Institute of Semiconductor Physics of the Academy of Sciences of the Ukraine. In 1984, he obtained a degree of candidate of physical-mathematical sciences (equivalent to a Ph.D.) in physics of semiconductors and dielectrics. The topic of his dissertation was “Processes of Charge Transfer and Capture in the System Electrolyte-Silicon Nitride-Silicon Oxide-Silicon.”

After finishing his dissertation, Dr. Nabok continued working at the Institute of Semiconductor Physics as a senior research scientist. In 1985, he joined the Research Laboratory of Molecular Electronics, which at the time had just been created within the Institute, and appeared among a group of enthusiasts who developed this new area of research in the Ukraine. Dr. Nabok established himself as a leading specialist in this field in the Ukraine and soon became the head of the Laboratory of Molecular Electronics. In 1995, he was rewarded by the Ukrainian State Committee with the title of senior research scientist.

During 1995–1996, Dr. Nabok visited the United Kingdom and worked as a visiting research scientist at Sheffield University and Sheffield Hallam University. In 1997, he joined the research group of Professor A. K. Ray at the School of Engineering of Sheffield Hallam University. He became a leading specialist in the field of organic film technology, nanostructures, and sensors. Dr. Nabok is an internationally recognized scientist, an author of more than 90 publications, a regular participant of different international conferences and meetings, a referee in a number of scientific journals, a Fellow of the Institute of Nanotechnology (United Kingdom), and a holder and participant of a number of research grants from the United Kingdom and Europe.



# Index

## A

ABAB-type LB films, 38–39  
activation energy for conductivity, 142  
adsorption FET, 219  
adsorption kinetics, 210  
AFM  
    contact mode, 74, 79  
    noncontact mode, 74  
    tapping mode, 73, 79, 80  
alkoxide sol-gel route, 20, 22, 23  
alternated LB layers, 38–39  
amperometric enzyme sensors, 217  
amperometric sensors, 207, 215  
amphiphilic molecules, 33, 35–38, 42, 45, 22,  
    136, 188  
analog signal sensors, 207  
angular (Kretschmann) SPR, 103–104  
array of QDs, 186–188, 200,  
artificial neuron network (ANN), 16, 208,  
    220, 251  
atomic force microscopy (AFM), 6, 13, 15,  
    17, 22, 49, 57, 73–75, 79–81, 84,  
    85, 123, 135, 174, 189  
atrazine, 225  
attenuated total reflection (ATR), 229  
ATR sensor (transducer), 229, 230, 247  
Auger spectroscopy, 87–88, 91  
azobenzene dye, 185

## B

band theory applicability, 141, 142  
biexciton, 121–122  
biomimetic sensors, 207  
biosensors, 207, 208, 210, 211, 217, 230,  
    232, 233, 238–51  
blue spectral shift, 119, 120  
Bohr radius of exciton, , 117, 118  
Bragg diffraction, 75–76, 79, 228  
Bragg fiber grating, 228  
Brunauer-Emmett-Teller (BET) equation, 209

Butterworth-Van-Dyke (BVD) equivalent  
    circuit, 213, 214  
BVD model, 214, 214

## C

calixarene LB films, 43–45, 52, 53, 80, 123,  
    126, 127, 162  
optical parameters, 104–5  
capillary condensation, 235–37  
cascaded p-n junctions solar cell, 178  
catalytic sensors (or enzyme sensors), 206–7  
CdS nanoparticles in LB films  
    absorption spectra, 116, 122–25, 127  
    effect of the electron beam, 81  
    effect of temperature, 51–53  
    formation, 49–53, 150  
    luminescence spectra, 126  
    morphology, 79–81  
    optical parameters, 111  
    SPR study, 110–111  
CdS platelets, 123  
cellular automata, 4, 6, 186–88  
charge transfer complexes, 143, 144, 184  
ChemFET, 219  
chemical routes in nanotechnology, 10, 11,  
    58, 59, 71, 72, 138, 160, 175, 178,  
    181, 216  
chemical self-assembly, 10, 15, 16, 59, 72  
chemical sensors, 57, 206  
chemically self-assembled nanoparticles  
    (morphology and crystallography),  
    81–84  
chlorophyll, 179  
cis-trans transition, 185  
classification of sensors, 205–7  
colloid nanoparticles, 10, 13, 15, 16, 20, 48,  
    57, 71, 83, 160, 186, 188  
composite ESA films, 29–33  
composite ESA membranes for biosensing,  
    30, 245–47

- composite LB films, 43–48  
 compressed powder pellet sensors, 215  
 conducting polymers, 10, 144, 178, 181, 183, 185  
 conductive polymer sensors, 215, 232  
 conductivity measurements, 133–38  
 conductivity  
   definition, 133, 134  
   of LB films containing CdS nanoparticles, 149–51  
 conjugated polymers, 172–173, 182  
 copper phthalocyanine, 29, 230  
 Coulomb blockade, 3, 5, 10, 156, 157, 159, 161, 188  
 Coulomb interaction, 27, 107, 117–19, 180, 239  
 crystallography study (methods), 75–79  
 cyclo-tetra-chromotropyrene (CTCT), 29–31, 246–49
- D**
- dark current, 177  
 dark exciton, 121, 12  
 density of states in low dimensional systems, 116  
 digital signal sensors, 207  
 dye-sensitized layer, 178
- E**
- ECFM, 73  
 electrical sensors (transducers), 207, 215–20  
 electrochemical sensors (transducers), 207, 215–20, 245  
 electrochromism, 23, 183, 184  
 electrodeposited films (morphology and crystallography), 85–86, 136  
 electrodeposition, 16–18, 58, 72, 84, 86, 87, 178, 181, 216  
 electroluminescence, 128, 181–83, 230  
 electrolyte-oxide-semiconductor (EOS) structures, 218, 219  
 electrolytic photovoltaic cell, 178–81  
 electron beam lithography, 6, 9, 159, 174  
 electron diffraction, 49, 75–76, 81–84  
 electron in a quantum box, 114–16, 145  
 electron tunneling, 2–5, 133, 136, 137, 144–55, 187, 188  
   through ESA films, 147–149  
   field effect, 147–49  
   through LB films, 147, 149–151  
   theory, 145–46  
   through thin films, 146  
 electrostatic self-assembly (ESA), 9, 10, 23–33, 71, 72, 79, 127, 143, 175, 179–83, 239–41, 245  
 electrostatically interacted QDs, 187  
 elemental and chemical composition (methods), 87–88  
 ellipsometric equipment, 98  
 ellipsometric sensors (transducers), 207, 221  
 ellipsometry, 45, 49, 95–100, 103–5, 107, 110–12, 147, 149, 207, 220–24, 234, 240, 245  
   data fitting (Cauchy model), 225  
   equation, 95  
   theory, 95–97  
 energy dispersion X-ray analysis (EDX, ESD), 87–89  
 enzyme sensors, 206–7, 232, 245–48  
 EOSFET, 219  
 equilibrium coefficient, 209  
 ESA deposition  
   equipment, 27–28  
   of biomolecules, 29–32  
   of molecular aggregates, 29–30  
   of nanoparticles, 31–33  
 ESA films  
   layer-by-layer structure, 78  
   optical parameters, 105–7  
 evanescent field, 100, 229, 230  
 exciton, 117–19, 121, 123, 126, 174
- F**
- Fabry-Perot interferometer as a sensor, 225  
 fatty acid(s), 10, 33–41, 45, 48, 76, 104, 136, 146, 150, 161  
 fill factor, 176  
 five-dot cell, 187  
 forward ellipsometric problem, 97  
 four-point probe, 135  
 fractal behaviour of QDs, 186  
 fractal p-n junctions, 175  
 Frank-Condon principle, 120  
 Fresnel  
   coefficients, 96  
   equation, 96, 100, 102  
   formula, 97, 100  
   fullerene, 46, 178  
 Fourier transformed infrared (FTIR) spectroscopy, 87, 88



**G**

- game “life,” 186
- gas sensors, 206, 219, 220, 233
- gold colloid, 13, 15, 32, 33, 81, 83, 107, 112–14, 116, 188–89
  - film sensors, 232,
  - LB films (SPR study), 112–14
  - QDs, 188–89
- Graetzel’s solar cell, 178
- grain boundaries (effect on conductivity), 138–41
- gravimetric sensors (transducers), 207, 212–15

**H**

- heterojunction diodes, 172, 180
- hollow polyelectrolyte shells, 33–34

**I**

- II–VI semiconductor layers, 53–54
- II–VI semiconductor nanoparticles
  - in ESA films, 127
  - in LB films (technology) 48–54
- II–VI semiconductor superlattices, 53–54
  - immobilization, 30, 47, 189, 238–44
  - of biomolecules, 238
  - by covalent binding, 239
  - by entrapment, 239
  - by ESA method, 239
  - by physical adsorption, 238
- immune sensors, 206, 240–45
- impurities in nanostructured materials, 90–91, 215, 216, 231, 232
- incomplete gate MOSFET sensor, 220
- inelastic tunneling, 154–55
  - spectroscopy, 154–55
- inhibition of enzymes, 232, 246–50
- interdigitated electrodes, 22, 133–135, 214, 215
- interferometric sensors (transducers), 207, 225–28, 243
- intermediate confinement, 118
- interpenetrating networks, 175, 179
- I–V characteristic(s), 5, 6, 10, 138, 147, 148, 151, 152, 156, 157, 159, 161, 162, 177, 188

**K**

- Kelvin formula, 235
- Kelvin probe method, 73, 185, 218
- Kiessig fringes, 76, 79

- Kretschmann configuration (geometry), 100–2, 104, 222

**L**

- Langmuir adsorption, 209, 243
- Langmuir balance, 34, 36, 37
- Langmuir monolayer, 35, 36, 38
- Langmuir-Blodgett (LB) films, 5, 33–43, 45–50, 52, 53, 57, 71, 76, 77, 79–81, 83, 89, 104, 105, 107–11, 116, 123–27, 136, 137, 149–51, 161, 162, 171, 233–36, 239
- Langmuir-Shaeffer (LS) deposition (films), 47–48, 112, 113
- layer-by-layer structure, 76–79
- LB deposition conditions, 41–42
- LB films
  - of colloid nanoparticles, 47
  - layer-by-layer structure, 76–77
  - morphology, 80
  - optical parameters, 104–5
- LB trough(s), 40–41
- LFM, 73
- Lifshitz-Slesov model, 51, 118
- light-emitting devices or LED(s), 173–75, 181–83, 229
  - on conducting polymers, 181–82
  - on semiconductor nanoparticles, 182–83
- light-harvesting complex, 178–79
- load characteristic, 175–78
- localization of electrons, 142
- long period fiber grating (LPG) sensor, 228
- low-dimensional systems (optical properties), 114–22
- luminescence, 14, 92, 95, 119–21, 126–29, 180, 182, 183, 207, 228, 230
- luminescent (fluorescent) sensors (transducers), 207, 228

**M**

- Mach-Zhender (MZ) interferometer as a sensor, 184
- maximal power of solar cell, 177
- mercury probe, 137–138, 149, 152, 172
- metal oxide sensors, 215, 216, 231, 232
- metal phthalocyanines, , 143, 178, 216, 233
- metal phthalocyanine films (conductivity), 143
- MFM, 73
- molecular beam epitaxy (MBE), 1, 5, 6, 10, 13, 54, 58, 86, 152, 174, 188

molecular electronics, 1, 4, 6, 9, 34, 43, 183, 232  
Moore's law, 1  
morphology study (methods), 72–75  
multisensor (or sensor array), 207, 208, 231, 245, 251

## N

nanocrystalline materials  
  conductivity, 138–141  
nanoparticle film sensors, 232  
nanostructural (nanostructured) materials, 11, 71, 87, 90, 92, 114, 183, 231  
Nernst equation, 217, 218  
neutron diffraction, 76–77  
nonlinear optical phenomena, 119, 121–122, 144, 184, 189  
normal conductivity, 133  
null-ellipsometry, 96, 98, 99

## O

open circuit voltage, 175  
optical enzyme sensors, 245–51  
optical immune sensors, 241–45  
optical memory devices, 184–85  
optical sensors (transducers), 207, 220–31  
optrode(s), 207, 228–30, 245, 246  
  enzyme sensor, 245–47  
organic active devices, 172–74  
organic field effect transistors (OFET), 173  
organic insulating layers, 171–72  
organic light-emitting diode (LED), 173–75  
organic passivating layers, 171–72  
organic semiconductors, 142, 143, 174, 178, 215, 233  
  conductivity, 141–44  
  sensors, 215, 232  
organic vapor sensors on calixarene films, 233–37  
orientation of the immune components via protein A, 239–40  
oscillator strength, 120

## P

palladium gate ChemFET hydrogen sensor, 219  
parallel computing, 6, 187–188  
pattern recognition, 208, 250–251  
PbS, 53, 54, 84, 88–91  
photochromism (photochromic), 183, 184  
photocurrent, 177

photovoltaic devices, 16, 21, 22, 33, 57, 87, 143, 175, 178, 179, 181  
phthalocyanine LB films, 43–44, 108  
phthalocyanine sensors, 216, 233  
physical limitations of semiconductor electronics, 2, 4, 188  
planar conductivity, 133–135  
planar polarization interferometer (PPI) as a sensor, 226–28, 230, 243–45  
planar waveguide, 226–30, 248  
  ATR enzyme sensor array, 249–51  
  ATR enzyme sensor, 247–251  
  ATR sensor, 229, 230  
  luminescence (fluorescence) sensors, 230, 231  
plasmon-enhanced ellipsometry, 104  
polyanion(s), 23–25, 27, 77, 79  
polycation(s), 23–25, 27, 32, 33, 77, 79, 127, 128, 180, 241, 254  
polyelectrolyte(s), 18, 23–28, 31, 33, 34, 58, 78, 104, 107, 127, 128, 137, 146, 173, 182, 230, 239  
polymer field effect transistors (PFET), 172–73  
porous silicon (PS), 91, 183, 189, 225, 230, 238  
porous silicon (PS) sensors, 225, 230, 238  
potentiometric sensors, 217  
PPI immune sensor, 227–30, 243–45  
PS luminescent sensors, 230

## Q

QCM sensor(s), 15, 240, 245  
QCM impedance analysis, 213  
quantum computing, 6, 86  
quantum confinement, 115  
quantum dot(s) (QDs), 3, 4, 6, 10, 18, 59, 95, 118, 119, 151, 186–89  
quantum nanoelectronic devices, 4, 185–90  
quartz crystal microbalance (QCM), 28, 207, 212, 215, 234, 237, 240, 245

## R

Raman spectroscopy (spectra), 87–89, 91, 154  
recovery of the sensor, 144, 211, 212, 219, 233, 234, 242, 250  
recovery time, 211  
rectangular barrier, 148–49  
reflectance, 96, 100  
registration  
  of heavy metal ions, 246–51

- of pesticides, 246–251
  - relative changes in the signal, 209
  - resistivity, 22, 135
  - resonance tunneling, 3–5, 10, 54, 151–53, 188
    - device(s) (RTDs), 4, 5, 10, 54, 152, 153, 185, 186, 188
    - in thin films, 152–153
  - response (of a sensor), 211, 214, 221, 227, 228, 232, 234, 235, 237, 242–45, 248–50
  - response time, 211
  - reverse ellipsometric problem, 97
  - reverse micelle, 14, 183
  - ruthenium complex, 178
- S**
- sandwich structure(s), 133–36, 138, 146, 150, 151, 172
  - Saurbrey equation, 212–13
  - scanning electron microscopy (SEM), 9, 15, 17, 22, 72, 73, 80, 81, 84, 85, 87, 172
  - scanning near-field optical microscopy (SNOM), 73, 74
  - scanning nanoprobe techniques, 6, 7, 13, 73, 75, 81
  - scanning tunneling microscopy (STM), 1, 6–10, 13, 15, 18, 49, 73, 79, 81, 87, 135, 154, 159, 160
  - second harmonic generation, 121–22
  - selectivity (of sensors), 207, 208, 210, 211, 231, 234, 237
  - sensitive membrane, 205, 207, 209–212, 220, 221, 226, 228–30, 238
  - sensitivity, 208, 209
  - sensors of multiple use, 206, 212
  - sensors working in liquid environment, 206
  - sheet resistance, 135
  - short circuit, 175, 177
    - current, 175
  - signal processing system, 205
  - single electron device(s) (SED), 4, 5, 10, 53, 158–60, 186
  - single electron transistor(s) (SET), 5, 10, 158, 159, 161, 188
  - single sensor(s), 208
  - single shot sensors (or probes), 206, 212, 238
  - single-electron phenomena, 155–162
  - single-electron trap, 159–160
  - size quantization, 11, 95, 113–16, 118, 119, 123, 124, 151
    - in CdS nanoparticles, 123
  - small (low) angle X-ray diffraction (SAXD), 45, 76–78
  - solar cell(s), 16, 21, 22, 57, 87, 143, 175–81
    - efficiency, 175, 178
  - sol-gel, 19–23, 57–59, 71, 72, 84–86, 88, 89, 91, 136, 138, 178, 181–84, 216
    - deposition, 18–23
    - dip-coating, 21
    - films (morphology and crystallography), 84–85
  - spin-coating, 22
  - sol-gel TiO<sub>2</sub>
    - composition, 89
    - conductivity, 138–141
    - morphology and crystallography, 84–85
  - solid electrolyte sensors, 181, 182, 231
  - solid state photovoltaic cell, 178–81
  - soliton(s), 144
  - specific binding sensors (or immune sensors), 206
  - spectral hole burning, 184–185
  - spectroscopic ellipsometry, 98, 99, 107, 112
  - spectroscopic SPR, 104
  - spin-coating, 15, 19, 22, 27, 54–59, 84, 143, 172, 175, 182, 184, 233
  - spin-coating (theory), 54–56
  - SPM, 73, 135
  - SPR, 45, 49, 95, 100–14, 122, 206, 207, 220–22, 224, 232–36, 240–45
  - SPR
    - practical realization, 103
    - theory, 100–3
    - curve, 100–1
    - immune sensor, 241–43
    - measurements in two media, 109–10
  - sensors (transducers), 207, 220–21
  - staircase-like I-V characteristic, 5, 6, 10, 156–59, 161, 162
- STM**
- (atomic) manipulation, 8, 188
  - nanolithography, 7, 10, 159
- Stokes shift, 120, 121, 127, 180
- strong confinement, 118, 120, 123
- Sugi model, 149, 150
- surface states, 92, 138, 140, 146, 154, 171, 177, 183, 216
  - effect on conductivity, 138–141
- surface acoustic wave (SAW) devices, 206, 207, 212, 214–15, 240, 245
- surface coverage, 26, 105, 209
- surface plasmons, 100, 221
  - quantum confinement, 113–114

surface pressure, 36, 37, 40, 42, 46  
  area (P-A) diagram, 33, 36–38, 42  
surface tension, 36, 50, 137, 235

## T

thermochromism, 184  
thickness shire mode (TSM) resonators, 213  
thin-film conductivity, 133–144  
thin-film technologies (comparison), 58  
third harmonic generation, 121–22  
TiO<sub>2</sub>, 9, 15, 17, 18, 21–23, 26, 31, 33, 57,  
  84–86, 88, 89, 138–40, 178–80, 231  
total internal reflection ellipsometry (TIRE),  
  104, 221–25  
transducer, 7, 205, 206, 215, 217, 221, 226,  
  228–30, 238, 239  
transfer ratio, 38, 43  
transmission coefficient, 97, 145, 146  
transmission electron microscopy (TEM), 73  
trapezoidal barrier, 148–49  
triangular barrier, 148–49  
tuneable luminescence, 128

two-dimensional diffusion (theory), 50–51  
two-photon processes, 121, 184

## W

Wannier-Mott exciton, 117, 121  
weak confinement, 117, 120  
Wilhelmy balance, 36, 40

## X

X-type LB films, 38–39  
xerogel, , 19–21, 23  
X-ray diffraction (XRD), 22, 23, 45, 75–76,  
  79, 84, 86, 105, 124  
X-ray photoelectron spectroscopy (XPS),  
  49, 87–88, 90, 91, 122

## Y

Y-type LB films, 38–39, 104, 149

## Z

Z-type LB films, 38–39, 109

---

## Recent Titles in the Artech House Microelectromechanical Systems (MEMS) Series

*Fundamentals and Applications of Microfluidics*, Nam-Trung Nguyen  
and Steven T. Wereley

*Introduction to Microelectromechanical (MEM) Microwave Systems*,  
Héctor J. De Los Santos

*An Introduction to Microelectromechanical Systems Engineering*, Nadim Maluf  
*MEMS Mechanical Sensors*, Stephen Beeby et al.

*Organic and Inorganic Nanostructures*, Alexei Nabok

*RF MEMS Circuit Design for Wireless Communications*, Héctor J. De Los Santos

For further information on these and other Artech House titles,  
including previously considered out-of-print books now available through our  
In-Print-Forever® (IPF®) program, contact:

Artech House  
685 Canton Street  
Norwood, MA 02062  
Phone: 781-769-9750

Fax: 781-769-6334  
e-mail: [artech@artechhouse.com](mailto:artech@artechhouse.com)

Artech House  
46 Gillingham Street  
London SW1V 1AH UK  
Phone: +44 (0)20 7596-8750

Fax: +44 (0)20 7630-0166  
e-mail: [artech-uk@artechhouse.com](mailto:artech-uk@artechhouse.com)

Find us on the World Wide Web at:  
[www.artechhouse.com](http://www.artechhouse.com)

---